Development of a Locoregional Astatine-211 Radiotherapy Targeting Syndecan-1 in a Syngeneic Mouse Model of Glioblastoma

Loris Roncali

THESE DE DOCTORAT

DE
L'UNIVERSITÉ D'ANGERS
SOUS LE SCEAU DE
LA COMUE ANGERS – LE MANS

ÉCOLE DOCTORALE N° 605 - BIOLOGIE-SANTE
SPECIALITE : « NEURO-ONCOLOGIE NUCLEAIRE »

PAR
Loris Roncali

Development of a Locoregional Astatine-211 Radiotherapy Targeting Syndecan-1 in a Syngeneic Mouse Model of Glioblastoma

Thèse présentée et soutenue à Angers, le 20/11/2023

Unité de recherche : INSERM U1307 - CNRS U6075 - CRCI²NA
(Centre de Recherche en Cancérologie et Immunologie intégrée Nantes-Angers)

Équipe 2: Nuclear Oncology
Équipe 5: Design and Application of Innovative Locoregional treatments in Glioblastoma (GLIAD)

Composition du Jury :

Présidente du Jury : Hélène CASTEL	Directrice de Recherche, Université de Rouen Normandie
Rapporteurs : Anna GOLEBIEWSKA	Directrice de Recherche, Luxembourg Institute of Health
John PRIOR	Professeur des Universités - Praticien Hospitalier, Université de Lausanne
Examinatrices : Anne-Sophie SALABERT	Maître de Conférence - Patricien Hospitalier, Université de Toulouse
Hélène CASTEL	Directrice de Recherche, Université de Rouen Normandie
Directeur de thèse : Emmanuel GARCION	Directeur de Recherche, Université d'Angers
Co-directeur de thèse : Michel CHÉREL	Professeur des Universités - Praticien Hospitalier, Université de Nantes
Co-encadrant de thèse : François HINDRÉ	Maître de Conférence, Université d'Angers

Acknowledgements

First and foremost, I would like to express my deep gratitude to Dr. Emmanuel Garcion for welcoming me into the GLIAD team. I am also truly thankful to Prof. Michel Chérel and Prof. Françoise Kraeber-Bodéré for welcoming me into the Nuclear Oncology team. These past four years have been an invaluable experience.

I will first express my appreciation to the jury members for dedicating their time to assess my work. I would like to thank Prof. John Prior and Dr. Anna Golebiewska for the honor of serving as reviewers for this thesis. I extend my thanks to Dr. Hélène Castel and Dr. Anne-Sophie Salabert for agreeing to review this work as examiners.

I would like to give special thanks to Dr. Emmanuel Garcion, my thesis supervisor. Your mentorship and trust gave me confidence throughout this project, and our many conversations have been essential during my PhD journey. You provided the perfect balance between guidance and autonomy, and thus contributed to my growth as a young researcher. I'm grateful for your positivity, humor, and all our engaging chats, whether they were about science or just life.

I am also deeply grateful to Prof. Michel Chérel, my thesis co-supervisor, for his dedication to this work and for his guidance during these for years. Your communicative passion for research and our fruitful discussions on various topics, related or not to science, have helped me to gain in maturity. Thank you for your expertise, your honesty, and your trust.

I extend my sincere thanks to Dr. François Hindré, my thesis co-advisor. Your strong expertise in nuclear medicine and your constructive feedback were crucial. Your sharp analytical skills played a key role in advancing this project.

I would like to thank Dr. Céline Beauvillain and Dr. Samuel Valable for being part of my individual monitoring committee throughout this thesis. I am grateful for your advice and your kind support.

This thesis was made possible thanks to funding from LabEx IRON 2. I would lie to express my gratitude for this financial support, and especially the extension of my contract, which allowed me to continue my work and make significant advancements for my research project.

A big thank you to the GLIAD and Nuclear Oncology teams for their warm welcome. Thank you for your support and encouragement over the past four years. This thesis journey introduced me to many wonderful individuals within these teams. Many of you played an important role in this research project, for which I am deeply grateful. A special thanks to all the co-authors of my main paper, who were also deeply involved in its review.

To Dr. Séverine Marionneau-Lambot, thank you for your deep involvement in this project. Your commitment, especially during the in vivo experiments and the astate evenings, as well as monitoring the mice, was crucial for the success of this work. You are a pillar of the team, and I feel lucky to have worked with you on this project. I cannot thank you enough for all the help and support you have given me, and for your calm, kindness, and support.

To Dr. Charlotte Roy, it's been a great time working with you. I have fond memories of our times with Séverine during the experiments in Nantes and those astatine evenings. Thank you for your many tips, for your positivity, hard work, and drive for excellence which have been a source of motivation for me.

To Sebastien Gouard, thank you for your guidance and your help, especially with the Beaver and the PET/CT experiments, which was really helpful. Thank you for your hands-on approach, for your great availability and you sense of humor.

To Sylvie Avril, thank you for your help with cell culture and your consistent support throughout the project. Your availability and willingness to address my questions and concerns truly reflect your dedication and character.

I would like to extend my heartfelt thanks to the chemistry crew led by Dr. François Guérard within the Nuclear Oncology team. My special thanks go to both Dr. François Guérard and Dr. Romain Eychenne for their vast expertise in radiochemistry and for handling the radiolabeling of antibodies which were essential for this study.

To Dr. Audrey Rousseau, thank you for your great availability and for the analysis and interpretation of my histological cryosections. Your expertise as an anatomopathologist is remarkable and I am grateful to have been able to benefit from it.

To Dr. Mathilde Allard, I'm deeply grateful for your expertise and guidance, especially when it came to flow cytometry data analysis on FlowJo.

To my postdoc and doctoral colleagues from GLIAD, Dr. Rodolfo Molina-Pena, Dr. Natalia Ferreira, Dr. Amel Djoudi, Maël Bouillon, and Arianna Rinaldi: Working with each of you has been a true pleasure. Your spirit of collaboration, mutual respect and support have greatly enriched my journey. It was an honor to be a part of some of your projects. The camaraderie, encouragement, and valuable feedback we shared have been essential to get through these tough years of work.

To Laurence Sindji, Dr. Anne Clavreul, and Lisa Mellier, Thank you for your diverse technical expertise, your support, your good spirits, and your advice during these thesis years.

I am deeply thankful to the rest of the GLIAD team, Pr. Frank Boury, Dr. Florence Dumas, Dr. Claudia Monteiro-Menei, and Dr. Laetitia Bassset, for the positive interactions and discussions we had.

A heartfelt thank you to my fellow PhD students, engineers, and technicians from the Nuclear Oncology team: Nina, Charlotte, Mylène, Romain, Ludovic, Alexandre, Cassandra, Nour, Mathilde, Fred, and Romain. The team's working atmosphere largely depends on you all, with your constant good spirits, sense of solidarity, and humor. I also want to thank the rest of the Nuclear Oncology team whom I've had the pleasure to work or discuss with: Dr. Nicolas Chouin, Dr. Joëlle Gaschet, Pr. Yannick Guilloux, Dr. Jean-François Gestin, Pr. Alain Faivre-Chauvet, Dr. Latifa Rbah-Vidal, Dr. Marie-Hélene Gaugler, and Dr. Françoise Leost, as well as those I've only briefly crossed paths with. A special nod to Alexandre, Joelle, Nicolas, and Jean-François for the nice memories from our time in Cape Town during the TAT12 symposium.

I want to express my gratitude to Dr. Florence Franconi, Dr. Laurent Lemaire, and Dr. Samuel Bonnet from the PRISM platform for their availability and assistance during all the MRI sessions. A big thanks to Dr. Catherine Guillet and Jérôme Cayon from the PACEM platform for their expertise and availability. I'm also thankful to Dr. Nicolas Jouand and Cécile Daussy from the Cytocell platform for their precious help in designing my flow cytometry experiments. I thank the staff of the MicroPicell platform, especially Philippe Hulin and Magalie Feyeux, for assisting me with the brain section analysis. My acknowledgements also go to the staff from the UTE animal facility in Nantes and SCAHU in Angers. I would like to thank to the administrative staff for their efficiency and readiness, and especially Stéphanie Pinot for managing my travel arrangements to Nantes, often at the last minute.

Lastly, I want to thank my friends for their support and genuine curiosity about my work. I would like to thank my family, especially my parents and sister. The desire to make you proud while pursuing my passion has been a driving force behind this journey. I am very grateful to my parents for instilling in me a sense of curiosity and a strong work ethic, and for their unfailing support throughout my studies, especially during these last few months of writing. To my sister, thank you for always believing in me, for your emotional support, for our inside jokes and our deep conversations about everything.

Table of content

CHAPTER I - Introduction 1

I. The central nervous system 3
1. The meninges 3
2. Cell populations within the brain parenchyma 5
3. The cerebral barriers 7

II. Glioblastoma 9
1. Epidemiology 9
2. Gliomas classification 9
3. Key mutations 11
4. Molecular subtypes 12
5. The glioblastoma niches 14

III. The standard of care for glioblastoma 18
1. Diagnosis 18
2. The Stupp protocol 19
3. Surgical approaches 20
4. Chemotherapy 21
5. Radiotherapy 22
6. Mechanisms of radioresistance 30

IV. Radionuclide therapy 31
1. Particles used in radionuclide therapy 32
2. Administration route 34
3. Vectors and therapeutic targets 35

References 39

CHAPTER II - Scope and aims 55

Scope and aims 57

CHAPTER III - Current Landscape and Future Directions of Targeted-Alpha-Therapy for Glioblastoma Treatment 59

Introduction 63

I. Glioblastoma: a confined solid tumor 65
1. The blood-brain barrier (BBB) 65
2. Hypoxic niches 72
3. Glioblastoma stem-like cells (GSLCs) 74
4. Cancer-associated fibroblasts (CAFs) 75
5. The immune landscape of GB 76

II. Primary α-emitters for targeted-α-therapy of glioblastoma 79
1. Astatine-211 79
2. Actinium-225 83
3. Bismuth-213 88
4. Promising α-emitters for the treatment of GB 91

III. Preclinical challenges and prospects 92
1. *In vivo* models 92
2. Targeting innovations and emerging vectors 95
3. Therapeutic combinations 100
Conclusion 103
References 104
CHAPTER IV - Brain Intratumoral Astatine-211 Radiotherapy Targeting Syndecan-1 Cures Glioblastoma and Elicits Memory Immunity in Mice 131
Introduction 135
Results 137
1. *In vivo* GL261 tumors as a relevant model to target SDC1 in GB 137
2. The 9E7.4 mAb enables a prolonged and localized cerebral retention of ^{125}I in tumor-bearing mice 139
3. Locoregional treatment of GB with ^{211}At-9E7.4 TAT leads to improved survival and minimal toxicity 140
4. Activity-dependent radionecrosis resolves over time only in the case of a 100 kBq injection of TAT 143
5. Locoregional ^{211}At-9E7.4 TAT decreases the occurrence of secondary tumors 143
6. Locoregional ^{211}At-9E7.4 TAT elicits vascular remodeling and local inflammation after 7 days 147
7. Locoregional ^{211}At-9E7.4 TAT protects the brain from contralateral tumor injection 147
8. Locoregional ^{211}At-9E7.4 TAT elicits the activation of immune memory 149
Discussion 151
Methods 156
1. Ethical statement 156
2. Mice 156
3. Cell line 157
4. 9E7.4 mAb production 157
5. ^{125}I or ^{211}At-labeling of 9E7.4 and IgG2a, κ mAb 157
6. Orthotopic tumor grafts 158
7. MRI 159
8. Radioconjugates locoregional injection 159
9. Biodistribution 160
10. Digital autoradiography 160
11. Survival and rechallenge studies 160
12. Histopathological analysis 161
13. Immunofluorescence 161
14. PET/CT 162
15. Flow cytometry 162
16. Statistical analysis 163
References 164
Supplementary Figures 171
CHAPTER V – General discussion 187
I. Therapeutic strategy 189
1. Locoregional TAT as first-line treatment 189
2. Selecting ^{211}At for the treatment of GB 190
3. Vectorization with the 9E7.4 mAb targeting SDC1 190

4. SDC1 as a therapeutic target for GB 191
II. Evaluation of the TAT distribution *in vivo* 191
1. Cerebral distribution 191
2. Global distribution 193
III. Therapeutic efficacy of the TAT 193
1. Impact on the tumor 193
2. Effect on tumor dissemination 194
IV. Microenvironmental responses to TAT 194
1. The vascular component 194
2. The immune component 195
V. Conclusions and perspectives 196
References 199
APPENDICES 203
Appendice I - Review: Targeting Tumor Associated Macrophages to Overcome Conventional Treatment Resistance in Glioblastoma 205
Appendice II - Article: LentiRILES, a miRNA-ON Sensor System for Monitoring the Functionality of miRNA in Cancer Biology and Therapy 225
Appendice III - Article: Rapamycin-Loaded Lipid Nanocapsules Induce Selective Inhibition of the mTORC1-Signaling Pathway in Glioblastoma Cells 245
Appendice IV - Article: Implantable SDF-1α-loaded Silk Fibroin Hyaluronic Acid Aerogel Sponges as an Instructive Component of the Glioblastoma Ecosystem: Between Chemoattraction and Tumor Shaping into Resection Cavities 261

List of figures

CHAPTER I - Introduction

Fig. 1 | The four cranial meninges……..……..…….....4
Fig. 2 | Interactions between glial cell and neurons within the CNS……..……....……6
Fig. 3 | Structure of the blood-brain barrier…….……....…..……8
Fig. 4 | The 2021 WHO classification of the major diffuse gliomas in adult…….…...……10
Fig. 5 | Diversity of transcriptomic states of GB cells and compositions of subtypes of GB…...……12
Fig. 6 | Main propositions of transcriptomic classification for GB. ……...……..……13
Fig. 7 | Illustration of the glioblastoma niches. ……....……..……17
Fig. 8 | MR imaging of a patient with glioblastoma. ……...……..……18
Fig. 9 | Schedule of the Stupp protocol. ……..……..……19
Fig. 10 | Mechanism of action of temozolomide……..……22
Fig. 11 | Primary repair mechanisms for DSBs induced by ionizing radiations…….....……24
Fig. 12 | Bystander and abscopal effects triggered by tumor irradiation. ……...……..……25
Fig. 13 | FET and FDOPA as amino acid tracers for PET in GB.....……27
Fig. 14 | General mechanisms of radioresistance in GB. ……...……..……30
Fig. 15 | Characteristics of β particles, α particles and Auger electrons. ……...……..……33
Fig. 16 | PET/CT scans of an mCRPC patient treated with ^{225}Ac-PSMA-617…..…… 34
Fig. 17 | T1-weighted MRI of intratumoral CED injection of gadolinium-labeled chemotherapy…...…35
Fig. 18 | Current clinical and preclinical studies on targeted radionuclide therapy for GB…….....36
Fig. 19 | Roles of syndecans in ECM alterations during cancer development……...…...……37

CHAPTER III - Current Landscape and Future Directions of Targeted-Alpha-Therapy for Glioblastoma Treatment

Fig. 1 | Strategies to cross the BBB and BTB for systemic treatments of GB……...…….....…....68
Fig. 2 | Locoregional strategies for the treatment of GB…….....…….……72
Fig. 3 | Main characteristics of the TME to consider for the design of future TAT in GB….....77
Fig. 4 | Energy, Linear energy transfer (LET) and tissue range of β^- and α-emitters.....…80
Fig. 5 | Decay schemes and main characteristics of ^{211}At, ^{225}Ac, and ^{213}Bi…….....…81
Fig. 6 | Overview of current preclinical models and strategies for TAT in GB…….....……96

CHAPTER IV - Brain Intratumoral Astatine-211 Radiotherapy Targeting Syndecan-1 Cures Glioblastoma and Elicits Memory Immunity in Mice

Fig. 1 | *In vivo* GL261 tumors as a relevant model to target SDC1 in GB…..……...138
Fig. 2 | The 9E7.4 mAb enables a prolonged and localized cerebral retention of ^{125}I in tumor-bearing mice……..…….....……..139
Fig. 3 | Locoregional treatment of GB with ^{211}At-9E7.4 TAT leads to improved survival and minimal toxicity.....……..141
Fig. 4 | Dose-dependent radionecrosis gradually resolves over time with the most effective dose of 100 kBq…….....……144
Fig. 5 | Locoregional ^{211}At-9E7.4 TAT decreases the occurrence of secondary tumors…….....…146
Fig. 6 | Locoregional ^{211}At-9E7.4 TAT elicits vascular remodeling and local inflammation after 7 days…….....……148
Fig. 7 | Locoregional ^{211}At-9E7.4 TAT protects the brain from tumor reinjection…….....……150
Fig. 8 | Locoregional ^{211}At-9E7.4 TAT elicits the activation of immune memory…….....….152

Supplementary Fig. 1 | Biodistribution study of ^{125}I-9E7.4 and ^{125}I-IgG2a, k conjugates in GB-bearing C57BL/6JRj mice…….....…….....……...174
Supplementary Fig. 2 | Individual weight monitoring of C57BL/6JRj mice during the survival study…….....……..175
Supplementary Fig. 3 | Long-term monitoring of hematological toxicity in surviving mice….....176
Supplementary Fig. 4 | Individual monitoring of hematological toxicity in control groups of the survival study…….....…….....……..177
Supplementary Fig. 5 | Individual monitoring of hematological toxicity in sacrificed mice treated with TAT during the survival study…….....……..178
Supplementary Fig. 6 | Long-term monitoring of toxicity in surviving mice…….....……...179
Supplementary Fig. 7 | Individual monitoring of toxicity in control groups of the survival study…….....…….....……..180
Supplementary Fig. 8 | Individual monitoring of toxicity in sacrificed mice treated with TAT during the survival study…….....……181
Supplementary Fig. 9 | T1-weighted MRI images and individual tumor growth follow-up during the survival study…….....…….....…...182
Supplementary Fig. 10 | T1-weighted MRI images and individual weight follow-up during the rechallenge study…….....……183
Supplementary Fig. 11 | Investigation of naïve and CD44$^-$/CD62L$^-$ T cell phenotypes in the blood of rechallenged animals…….....185

CHAPTER V - General discussion

Fig. 1 | Intravenous versus intracranial biodistribution of radiolabeled 9E7.4…….....…….192

Fig. 2 | Hydrogel-based local drug delivery systems for post-operative radiotherapy…….....…….197

List of tables

CHAPTER III - Current Landscape and Future Directions of Targeted-Alpha-Therapy for Glioblastoma Treatment

Table 1 | Preclinical studies of targeted-a-therapy in GB *in vivo* models…….....….85

Table 2 | Completed pilot studies and clinical trials in high-grade glioma treated with TAT.....90

CHAPTER IV - Brain Intratumoral Astatine-211 Radiotherapy Targeting Syndecan-1 Cures Glioblastoma and Elicits Memory Immunity in Mice

Table 1 | Summary of the survival study…….....…….....……..142

Table 2 | Histopathological analysis of brain sections 7 days after local injection of the ^{211}At–9E7.4 TAT…….....…….....…….....……145

Supplementary Table 1 | Median fluorescence intensity ratios from Flow cytometry analysis between IgG2a, κ and mAb 9E7.4…….…….....…….....…173

Supplementary Table 2 | ^{211}At purity and radiochemical purity of the ^{211}At-9E7.4 and ^{211}At-IgG2a, κ conjugates…….…….....…….....…173

Supplementary Table 3 | Detailed statistical analysis of the survival study…….....……..……173

Supplementary Table 4 | Summary of the rechallenge study…..……...….....…184

Abbreviations

3D-CRT	three-dimensional conformal radiation therapy
5-ALA	5-aminolevulinic acid
53BP1	p53-binding protein 1
Ac	actinium
AC	astrocyte
AIC	5-amino-imidazole-4-carboxamide
ALP	alkaline phosphatase
ALT	alanine transaminase
AMT	adsorptive-mediated transcytosis
AML	acute myeloid leukemia
APC	antigen-presenting cell
ASCL1	achaete-scute family bHLH transcription factor 1
ATADA3A	ATPase family AAA domain -containing 3A
At	astatine
ATP	adenosine triphosphate
ATRX	alpha-thalassemia X-linked intellectual disability
BBB	blood-brain barrier
BBTB	blood-brain tumor barrier
BCB	blood-cerebrospinal fluid barrier
BED	biologically effective dose
BER	base excision repair
Bi	bismuth
BRCA	breast cancer susceptibility protein
BTB	blood-tumor barrier
C	carbon
CAF	cancer-associated fibroblast
CDKN2A/B	cyclin-dependent kinase inhibitor 2a/b
CED	convection-enhanced delivery
Chk1	checkpoint kinase 1
CLI	Cerenkov luminescence imaging
CNS	central nervous system
CSF	cerebrospinal fluid
CT	computed tomography
CTLA-4	cytotoxic t-lymphocyte-antigen-4
CTM	carrier-mediated transcytosis
CTV	clinical target volume
Cu	copper
CXCR4	c-x-c chemokine receptor type 4
DAMP	damage associated molecular pattern
DARPin	designed ankyrin repeat proteins
DCE-MRI	dynamic contrast-enhanced magnetic resonance imaging
DDR	DNA damage response
DOTA	1-,4-,7-,10-tetraazcy-clododecane-1,4-,7-,10-tetra acetic acid
DNA	desoxyribonucleic acid
DNA-PK	DNA-dependent protein kinase
DNMT	DNA methyltransferase
DSB	double-strand break
EANO	european association of neuro -oncology
EBRT	external beam radiation therapy
ECM	extracellular matrix
EGF	epidermal growth factor
EMT	epithelial-mesenchymal transition
EOR	extent of resection
ESTRO	european society for therapeutic radiology and oncology
F	fluorine
FAP	fibroblast activation protein
FAPi	fibroblast activation protein inhibitor
FET	[^{18}f]fluoro-ethyl-l-tyrosine
FDA	food and drug administration
FDOPA	l-3,4-dihydroxy-6-[^{18}f]fluoro-phenylalanine
FDG	fluorodeoxyglucose
FGF	fibroblast growth factor
FLAIR	fluid attenuated inversion recovery
Fr	francium
FUS	focus ultrasound
Ga	gallium
GB	glioblastoma
GEP-NET	gastroentero-pancreatic neuroendocrine tumors
GFAP	glial fibrillary acidic protein
GPCR	G protein-coupled receptor
GRPR	gastrin-releasing peptide receptors
GSLCs	glioma stem-like cells

GTV	growth tumor volume
H	hydrogen
HDAC	histone deacetylase
HGF	hepatocyte growth factor
HIF	hypoxia-inducible factor
HR	homologous recombination
HRE	hypoxia-response element
I	iodine
i.c.	intracranial
ICI	immune checkpoint inhibitors
IDH	isocitrate deshydrogenase
IL	interleukine
IL13RA2	interleukine-13 receptor subunit α2
IMRT	intensity-modulated radiation therapy
i.n.	intranasal
i.p.	intraperitoneal
i.t.	intratumoral
i.v.	intravenous
KPS	Karnofsky performance score
LAT1	L-type amino acid transporter 1
LD_{10}	lethal dose for 10% of animals
LET	linear energy transfer
Lu	lutetium
LV	left ventricle
mAb	monoclonal antibody
MC1R	melanocortin 1 receptor
mCRPC	metastatic castration-resistant prostate cancer
MET	L-[methyl-^{11}c]-methionine
MES	mesenchymal cell
MDC1	mediator of DNA damage checkpoint protein 1
MDSC	myeloid-derived suppressor cell
MGMT	O6-methylguanine-DNA methyltransferase
MHC-I	major histocompatibility complex I
MITC	5-(3-methyltriazol-1yl)imidazole -4-carboxamide
MM	multiple myeloma
MMP	matrix metalloproteinase
miRNA	microRNA
MRI	magnetic resonance imaging
MTD	maximal tolerated dose
mTOR	mammalian target of rapamycin
MVP	microvascular proliferation
N	nitrogen
Na	sodium
NADPH	nicotinamide adenine dinucleotide phosphate
NER	nucleotide excision repair
NF1	neurofibromin 1
NHEJ	non-homologous end joining
NIR	near infrared
NK	natural killer cell
NK1R	neurokinin type 1 receptor
NO	nitric oxide
NPC	neural progenitor cell
NSC	neural stem cell
NVU	neurovascular unit
O	oxygen
OPC	oligodendrocyte precursor cells
OPN	osteopontin
OS-d	overall survival from the diagnosis
OS-t	overall survival from the start of the treatment
PARP	poly(ADP-ribose) polymerase
PAMP	pathogen associated molecular pattern
Pb	lead
PBMCs	peripheral blood mononuclear cells
PD-1	programmed cell death protein 1
PDGF	platelet-derived growth factor
PD-L1	programmed death-ligand 1
PDX	patient-derived xenograft
PDOX	patient-derived orthotopic xenograft
PDT	photodynamic radiotherapy
PET	positron-emission tomography
PFS	progression-free survival
Phe	phenylalanine
PI3K	phosphoinositide 3-kinase
PKM2	M2 isoform of pyruvate kinase
Po	polonium
PRRT	peptide receptor radionuclide therapy
PSMA	prostate-specific membrane antigen
Pt	platinum
Ra	radium
Re	rhenium
RNA	ribonucleic acid
RNT	radionuclide therapy

ROS	reactive oxygen species
RTM	receptor-mediated transport
RV	right ventricle
scRNA-seq	single-cell RNA sequencing
SDC1	syndecan-1
SGZ	subgranular zone
SLYM	subarachnoid lymphatic-like membrane
SPECT	single photon emission computed tomography
SRS	stereotactic radiosurgery
SSB	single-strand break
SSTR	somatostatin receptor
SVZ	subventricular zone
TAA	tumor-associated antigen
TAM	tumor-associated macrophage
TAT	targeted-α-therapy
Tb	terbium
TCA	tricarboxylic acid
T_{CM}	central memory T cell
T_{EM}	effector memory T cell
TERT	telomerase reverse transcriptase
TGF	transforming growth factor
Th	thorium
Th1	helper T cell 1
TIL	tumor-infiltrating lymphocyte
Tl	thallium
TLR	toll-like receptor
TME	tumor microenvironment
TMZ	temozolomide
TNF	tumor necrosis factor
Treg	regulatory T cell
T_{RM}	resident memory T cell
TRT	targeted radionuclide therapy
TTFs	tumor treating fields
U	uranium
USMB	ultrasound-stimulated microbubbles
VE-cadh	vascular endothelial cadherin
VEGF	vascular endothelial growth factor
VMAT	volumetric modulated arc therapy
WHO	world health organization
Y	yttrium

Foreword

Cancer continues to be a significant hurdle in medical research, stemming from cellular imbalances that result in abnormal growth behaviors. At the cellular level, the onset of cancer can be viewed as a failure of the intrinsic mechanisms of the body. Each cell, guided by its genetic instructions, follows strict rules governing its growth, division, and function. Maintaining these rules is crucial. Yet, when genetic mutations occur, whether due to external factors like environmental toxins, radiation, and certain pathogens, or internal reasons such as genetic errors or inherited tendencies, they can create conditions conducive to cancer development.

These mutations disrupt vital cellular pathways that control growth, programmed cell death, and DNA repair. As cells bypass these checkpoints, they gather more mutations, enabling the unchecked proliferation of cancerous cells. The variety of these mutated cells within a tumor suggests that cancer is not a singular disease but a collection of related disorders, each defined by its molecular features and clinical outcomes. Recent strides in molecular oncology have revealed the complex origins of cancer. It is clear that its roots go beyond just genetic changes. Alterations in DNA methylation, irregularities in non-coding RNA sequences, and shifts in cell metabolism, along with changes in the surrounding environment of the tumor, play pivotal roles in cancer development and growth. This complex origin highlights the importance of a holistic approach to cancer research, drawing knowledge from genomics, cell biology, biochemistry, and other fields.

This thesis will focus on glioblastoma, the most aggressive tumor of the central nervous system. Its persistent resistance to conventional treatments emphasizes the pressing need for innovative therapeutic strategies. Specifically, glioblastoma exhibits a high level of radioresistance, which contributes to its inevitable recurrence. Subsequent chapters will explore the emerging field of targeted radionuclide therapy, which seeks to apply internal radiation in a targeted and tumor-specific manner, with the aim of bypassing this resistance and offering a more effective treatment.

Chapter I provides a general introduction that outlines the brain, the characteristics of glioblastoma, its therapeutic management, and the limitations of the standard of care approaches. It also offers an overview of radionuclide therapy. Chapter II sets out the general scope and objectives of this research project.

Chapter III is a comprehensive review of scientific literature on targeted radionuclide therapy, with an emphasis on the use of α radionuclides. The aim of this section is to contextualize the strategies currently under preclinical and clinical investigation, considering the unique features of glioblastoma in terms of its location, microenvironment, and resistance mechanisms to therapies. The goal is to learn from past advancements to pinpoint future challenges in this field.

Chapter IV details the design and *in vivo* application of a targeted radionuclide therapy using the radionuclide astatine-211, aiming to propose a more effective and non-harmful treatment for glioblastoma. Experimental data are presented and discussed in this section, which is currently under review for publication. Chapter V is a general discussion that juxtaposes our experimental findings with the limitations and challenges identified in the scientific literature. It offers medium and long-term prospects for this therapeutic approach.

CHAPTER I

Introduction

I. The central nervous system

1. The meninges

The central nervous system (CNS) comprises the brain and the spinal cord. It oversees the nervous system and processes data from the peripheral nervous system. Additionally, it orchestrates signals originating from the body's peripheral organs. The brain resides within the cranial cavity and is safeguarded by the skull. The spinal cord, positioned caudally relative to the brain, is located within the vertebral canal and is shielded by the vertebrae[1]. The brain is enveloped by four layers designated as “meninges”. These membranes serve a protective function for the brain, ensuring its secure positioning within the cranial vault and acting as shock absorbers. This functionality hinges on the dynamics of cerebrospinal fluid (CSF), generated by the choroid plexuses situated in the cerebral ventricles. The modulation of CSF is intricately managed by the blood-CSF interface at the choroid plexuses and the arachnoid layer[2]. The meninges modulate the homeostasis of the CNS by overseeing the blood, lymphatic, and CSF systems (Fig. 1)[3].

Recent research has unveiled the role of the meninges in the immune regulation of the CNS at the boundaries of the brain. This revelation challenges the longstanding notion of "immune privilege", which posits the brain as an entity isolated from the immune system. This historical concept stems from initial observations regarding the presence of the blood-brain barrier (BBB), which maintains a restrictive vasculature within the CNS, thereby limiting the entry of peripheral immune cells into the cerebral tissue[4]. Similarly, the observed lack of lymphatic circulation within the parenchyma has further reinforced this paradigm. The validity of this concept is increasingly debated in light of recent findings. Whether it is the observed breach of the BBB in certain brain disorders, allowing peripheral immune cells to access the cerebral tissue[5], the discovery of the glymphatic system managing the circulation of CSF[6], or the mobilization of immune cells from the bone marrow in response to cerebral tissue damage[7], the traditional understanding of brain immune regulation is being re-evaluated.

Dura mater. The dura mater is the outermost of the meninges. It is a thick, dense, and fibrous membrane anchored to the skull on one side and to the arachnoid mater on the other. This layer contains a vasculature and a lymphatic network which facilitates the exit of blood from the brain and the return of CSF to circulation[8]. It also serves as a residency for a multitude

of cells from the innate and adaptive immunity[9]. The dura mater engages with the adjacent bone marrow of the skull *via* the connection between the diploic vein and dural vessels[10].

Arachnoid mater. The arachnoid mater is an intermediate thin layer of the meninges, situated beneath the dura mater. This membrane is not vascularized and exhibits tissue extensions toward the pia mater, resembling a spiderweb-like structure. The subarachnoid space, positioned between the arachnoid mater and the pia mater, facilitates the flow of CSF. The main roles of the CSF are to protect the brain and spinal cord and to provide them with nutrients while taking away waste. Along with the CSF, the brain's main arteries are located in the subarachnoid space[3].

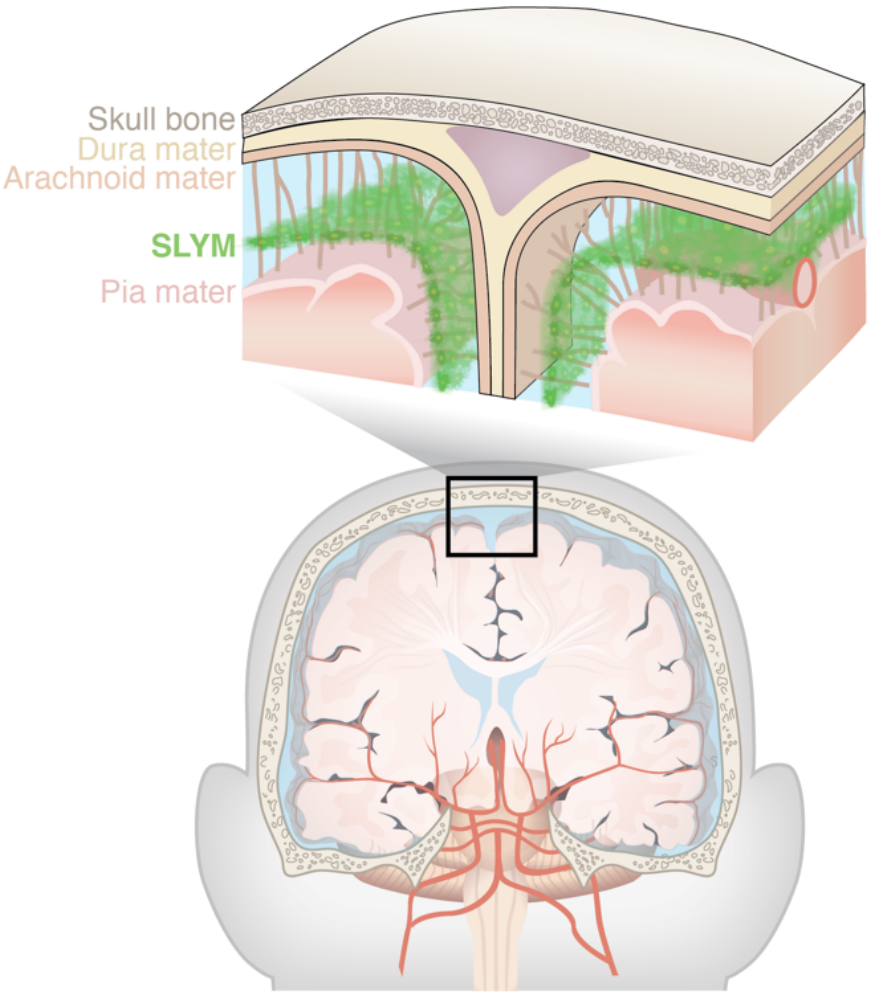

Fig. 1 | **The four cranial meninges.** A schematic representation of the four layers that constitute the meninges. Notably, the subarachnoid lymphatic-like membrane (SLYM) compartmentalizes the subarachnoid space. It contains a leukocyte population equivalent to that of the dura mater, suggesting a role in CNS immune responses. (From Møllgård *et al.* 2023)[11]

Subarachnoid lymphatic-like membrane. The subarachnoid lymphatic-like membrane (SLYM) is a recently identified meningeal layer that compartmentalizes the subarachnoid space. It facilitates direct exchanges between the CSF and venous blood. This membrane is rich in myeloid cells and could hold significant implications in response to inflammation[11].

Pia mater. The pia mater is the innermost layer of the meninges and directly adheres to the surface of the brain and the spinal cord. Along with the arachnoid mater, they are referred to as the leptomeninges. This region is highly vascularized to supply nutrients to the brain. Within the spinal cord, it contributes to maintaining its structural rigidity[12].

2. Cell populations within the brain parenchyma

The cerebral parenchyma represents the functional tissue of the brain. It encompasses neurons and glial cells, which include astrocytes, oligodendrocytes, microglia, and oligodendrocyte precursor cells (OPC; Fig. 2). During developmental stages, all these cell types derive from neural stem cells (NSCs)[13,14]. In mature organisms, two primary stem cell reservoirs can be identified within the CNS: the subventricular zone (SVZ) and the subgranular zone (SGZ) of the dentate gyrus in the hippocampus[15,16].

Neurons. Neurons are the functional units of the nervous system. They are electrically excitable cells transmitting signals throughout the body *via* both chemical and electrical mechanisms. They consist of a soma, axons, and dendrites. The axon facilitates the transmission of efferent signals, while the dendrites receive afferent signals. The axonal terminals release neurotransmitters, converting an electrical signal into a chemical one. This transmission is regulated by ion movements, primarily potassium, sodium, and chloride, through voltage-dependent ion channels[17]. The majority of neuron cell bodies are housed in the gray matter, which accounts for 10% of the cerebral parenchyma. It forms the cerebral cortex and encompasses the basal ganglia. The white matter constitutes 90% of the parenchyma and is composed of axons and dendrites that convey neural information between neurons and to peripheral organs[18,19]. The white matter also houses supportive glial cells[20].

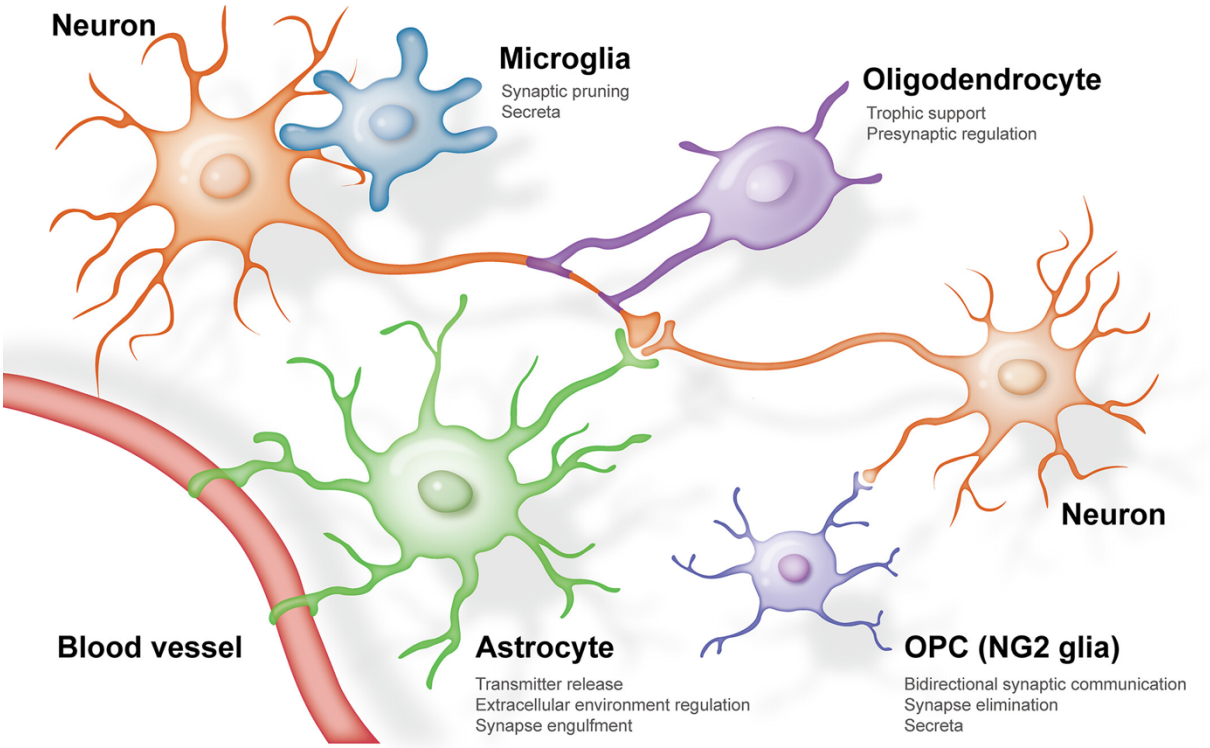

Fig. 2 | **Interactions between glial cell and neurons within the CNS.** Composition of neural cells in the mature brain. Within the mammalian CNS, glial cells are typically categorized into astrocytes, activated microglia, oligodendrocytes, and oligodendrocyte progenitor cells (often referred to as NG2 glia)**.** (From Liu *et al*., 2023)[21]

Astrocytes. Astrocytes constitute the majority of glial cells. They play a pivotal role in the homeostasis of the CNS by recycling neurotransmitters, regulating the ionic balances, modulating synaptogenesis and synaptic transmission, and maintaining the integrity of the blood-brain barrier (BBB) that separates the brain from systemic circulation[22–24]. A vast array of astrocyte subsets exists, with functions that remain largely uncharted. Recent technological advancements have enabled the identification of some of these subsets using single-cell RNA sequencing (scRNA-seq) techniques[25]. Broadly, astrocytes are modulated either by neurodevelopmental transcriptional programs or by stimuli such as neurotransmitters, cytokines, ions, and microbial metabolites[26]. For instance, a recent study highlighted the existence of a specialized subpopulation equipped with a glutamate release machinery similar to that found in synapses. These astrocytes play a role in the functioning of the cortico-hippocampal circuit[27]. Current research is particularly focused on the plasticity of these subsets and their interconvertibility.

Oligodendrocytes. Oligodendrocytes provide the myelin that surrounds the axons of neurons. Myelin is an extension of their plasma membrane that wraps around axons concentrically to ensure rapid nerve conduction. On the axon, there are domains interspersed between myelin segments, called nodes of Ranvier, which concentrate sodium and potassium channels essential for the transmission of action potentials. Axons are myelinated along almost their entire length, isolating them from the cerebral parenchyma. Thus, oligodendrocytes release extracellular vesicles from the myelin layer, facilitating the exchange of small metabolites to maintain axonal integrity[28]. They can also release cytokines to regulate immune responses. A recent study further emphasized their capacity to modulate the microglia phenotype, suggesting a role in influencing microglia's response during inflammation[29]. Oligodendrocytes originate from oligodendrocyte precursor cells (OPC), a highly proliferative cell population. These OPCs also perform various other functions, such as inducing angiogenesis, presenting antigens, and forming synapses with neurons[30–32].

Microglia. Microglia consist of the resident tissue macrophages of the CNS. They are the first cells to respond in the event of brain injury, due to their receptors for damage-associated molecular patterns (DAMPs) and pathogen-associated molecular patterns (PAMPs). They can interact with other cell types in the CNS, including neurons and oligodendrocytes. As such, they regulate a significant number of CNS functions, including synaptogenesis, adult neurogenesis, and neuroinflammation[33]. Traditionally, microglia is artificially categorized into two phenotypic classes: M1 and M2. The M1 phenotype is associated with pro-inflammatory and neurotoxic activity, while the M2 phenotype is linked to anti-inflammatory and neuroprotective functions[34]. However, single-cell technologies have revealed a significant spatial and temporal heterogeneity in microglia, which deviates considerably from this binary classification[35].

3. The cerebral barriers

The blood-CSF barrier (BCB). The BCB is an epithelio-endothelial structure located in the choroid plexus of the ventricles. This barrier is composed of a vascularized stroma enveloped by epithelial cells, with the stroma itself containing fenestrated capillaries surrounded by connective tissue and immune cells[36]. The ventricular side of this stroma is lined by cuboidal epithelial cells, to which epiplexus cells with phagocytic capabilities adhere. These cells function as scavengers within the brain's ventricular system[37]. Morphologically, the

choroid plexus varies across different ventricles, being thin in the lateral ventricle, lobulated in the fourth, and with an intermediate size in the third. Beyond its primary role in CSF production and forming the BCB, the choroid plexus could be involved in the circadian regulatory system[38]. Furthermore, the BCB has been shown to possess chemosensory receptors, potentially playing a role in monitoring and regulating brain fluid composition[39].

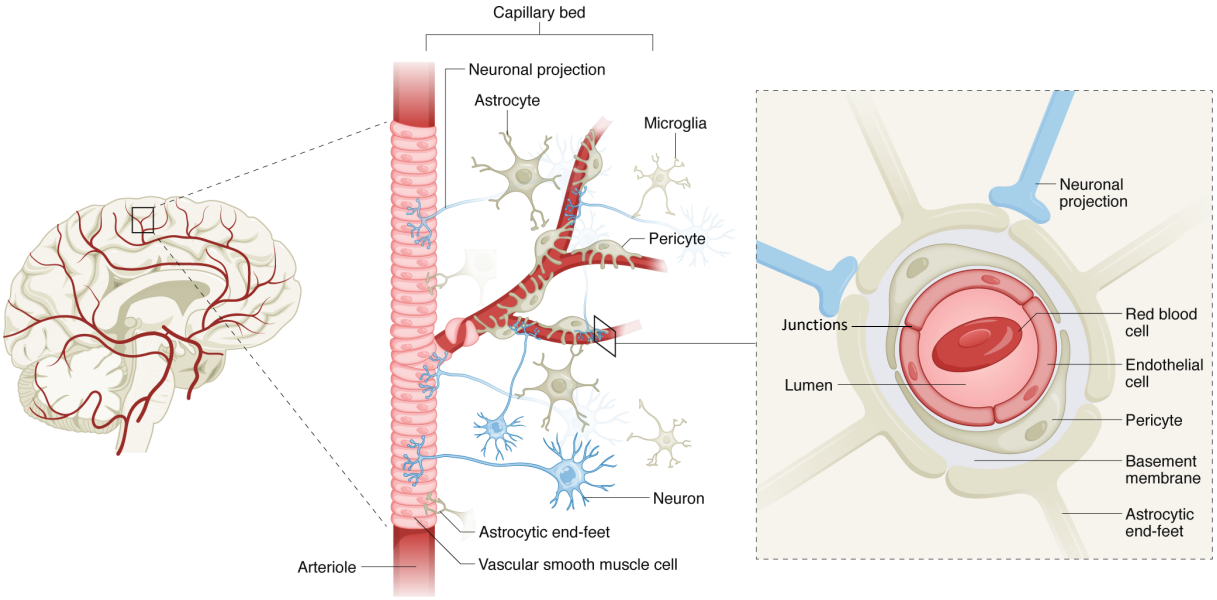

Fig. 3 | **Structure of the blood-brain barrier.** The BBB consists of epithelial cells, connected by tight junctions, which are surrounded by pericytes within the basal membrane. Astrocytic endfeet form an interface with the basal membrane. Neurons extend projections to the astrocytic endfeet. This entire structure is referred to as the neurovascular unit. (From Barisano *et al*. 2022)[40]

The blood-brain barrier (BBB). The BBB is a multifaceted structure that separates the CNS from the systemic circulation and thus ensures an optimal environment for neuronal functions. It is composed of a capillary basement membrane and three cellular components: endothelial cells, pericytes, and astrocytic end-feet (Fig. 3). The primary roles of the BBB are to maintain neural homeostasis, protect against harmful agents, facilitate communication between the CNS and peripheral systems, and supply essential nutrients to the brain. This is accomplished through several mechanisms: restricting the paracellular diffusion of hydrophilic entities, overseeing the active transport of essential nutrients, managing the efflux transport of hydrophobic molecules, and controlling the transendothelial migration of blood cells and potential pathogens[4]. In the BBB, endothelial cells exhibit unique characteristics compared to their counterparts elsewhere in the organism. They lack fenestrations, possess more robust tight junctions, and demonstrate limited pinocytic vesicular transport, ensuring a restricted

paracellular movement of hydrophilic entities[41]. Tight junctions are situated between cerebral endothelial cells and establish a selective barrier that restricts the entry of most substances from the bloodstream. Pericytes, situated within the capillary basement membrane, are essential for angiogenesis, microvessel integrity and differentiation, and the establishment of endothelial tight junctions[42]. Astrocyte end-feet, which envelop the vessel wall, are pivotal in initiating and sustaining the tight junctions and allow interactions between neurons and the vascular system[43].

II. Glioblastoma

1. Epidemiology

GB remains the most aggressive tumor of the CNS[44]. Its annual incidence ranges between 3.26 and 5.02 cases per 100,000 population[44–46]. GB constitutes 14.2% of all primary tumors of the brain and other CNS structures and accounts for 50.1% of primary malignant brain tumors. The incidence of GB exhibits a marked age-related trend. While the tumor predominantly manifests in the elderly population, its incidence is considerably rarer in the pediatric demographic, representing only 2.7% of all brain and other CNS tumors in individuals aged 0-19 years. This age-related predilection becomes even more accentuated with the highest incidence rates observed among individuals within the age range of 75 to 84 years. Furthermore, gender-based disparities in GB incidence are evident, with the male population exhibiting a 1.6-fold increased risk compared to its female counterpart. Only 6.9% of diagnosed patients can expect a survival duration beyond five years post-diagnosis[44].

2. Gliomas classification

The World Health Organization (WHO) has been classifying gliomas since 1979, initially basing their categorization on histopathological criteria. In 2007, Louis *et al.* classified GB as a grade 4 diffuse astrocytoma, the highest grade among brain tumors. This classification emphasized the predominantly astrocytic composition of GB and its aggressive nature. This aggressiveness was evident from its high mitotic activity, significant endothelial proliferation, and the presence of necrotic foci as a consequence of rapid tumor growth, leading to hypoxic niches within the tumor[47]. This classification soon revealed its shortcomings, leading to discrepancies in diagnoses and varied tumor progressions among patients. Advances in molecular biology facilitated the identification of genetic characteristics of brain tumors.

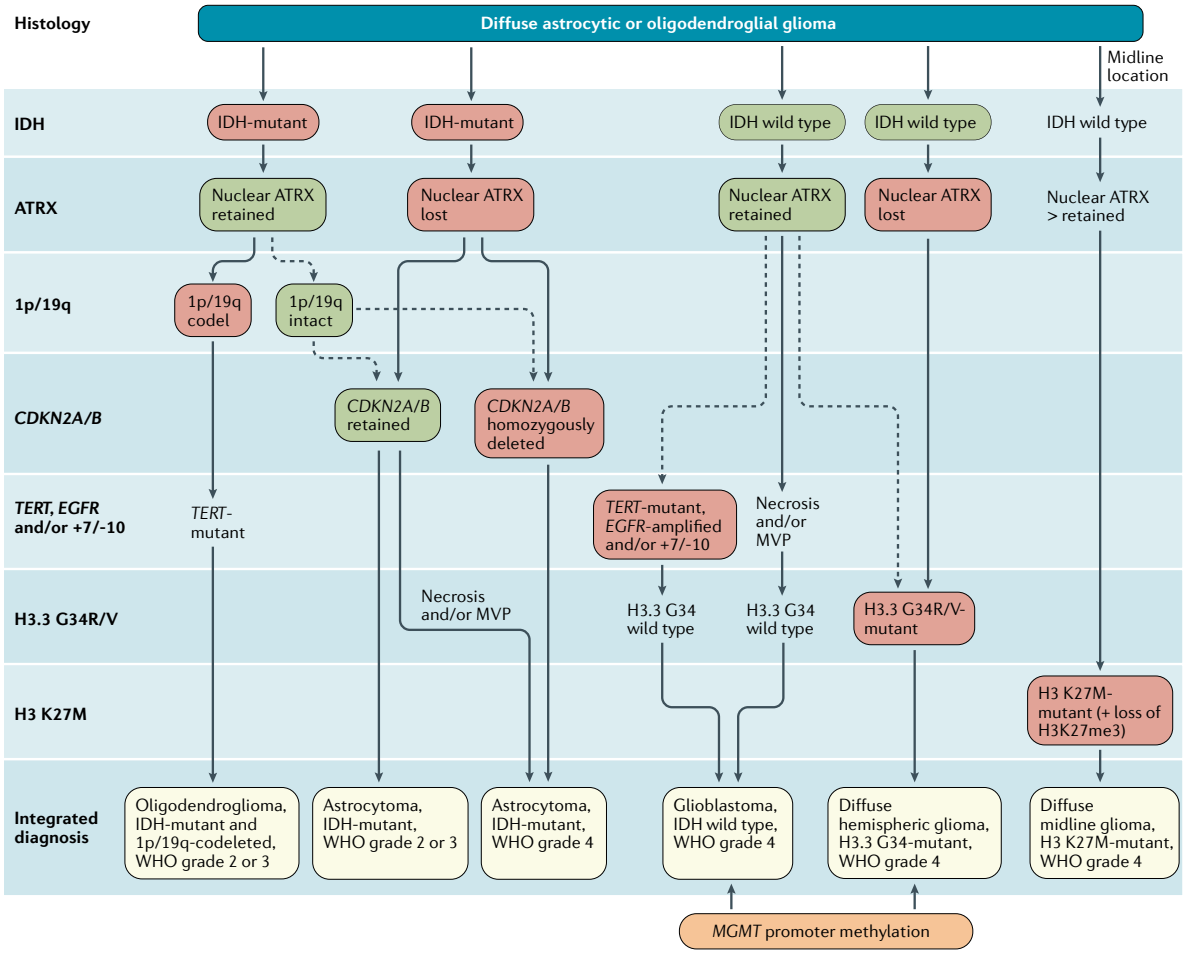

Fig. 4 | **The 2021 WHO classification of the major diffuse gliomas in adult.** GBs are classified as grade 4 IDH wild-type gliomas, exhibiting necrosis and microvascular proliferation (MVP) and/or a mutation in the TERT gene, amplification of the EGFR gene, and/or a gain of chromosome 7 and a loss of chromosome 10. They are also characterized by methylation of the MGMT gene promoter. *WHO: World Health Organization; IDH: isocitrate dehydrogenase; ATRX: alpha-thalassemia X-linked intellectual disability; CDKN2A/B: cyclin-dependent kinase inhibitor 2A/B, EGFR: epidermal growth factor receptor, TERT: telomerase reverse transcriptase, MGMT: O6-methylguanine-DNA methyltransferase.* (From Weller *et al.*, 2021)[48]

Consequently, in 2016, the updated classification of brain tumors incorporated these genetic and epigenetic criteria. The primary genetic criterion was the mutation of the gene encoding for isocitrate dehydrogenase 1 (IDH1). This mutation was found in 10% of GBs and served as a marker for poor prognosis. GBs with wild-type IDH were categorized into three morphological subtypes: giant cell, epithelioid, and gliosarcoma. The "not otherwise specified" (NOS) category encompassed GBs for which the IDH status has not been investigated[49].

The 5th edition of the CNS classification by WHO continues the integration of both molecular and histological criteria (Fig. 4). However, significant modifications are evident. GBs now only encompass IDH wild-type gliomas. Consequently, certain diffuse astrocytomas and anaplastic astrocytomas are now classified under the "glioblastoma" label. Conversely, previous IDH-mutant GB are now categorized as grade 4 astrocytomas. The molecular

signature for GB diagnosis has evolved to specifically identify the absence of IDH gene mutation, coupled with the presence of a telomerase reverse transcriptase (TERT) promoter mutation, gene amplification of epidermal growth factor receptor (EGFR), or a change in the copy number of chromosomes 7 and 10 (+7/-10)[50].

3. Key mutations

TERT promoter. Mutations in the promoter of TERT are observed in approximately 70-80% of GB[51]. TERT is the catalytic component of the telomerase enzyme, which is a specialized reverse transcriptase responsible for maintaining telomere length. Telomeres are nucleoprotein structures situated at chromosome ends, essential for maintaining chromosomal stability. With each cell division, telomeres undergo reduction in length, ultimately resulting in cellular senescence or apoptosis[52]. However, the relationship between TERT mutations and specific features of GB remains a matter of debate. Recent studies suggest that such mutations do not influence the prognosis of GB patients, nor do they affect the methylation status of the MGMT gene promoter[53].

EGFR. Genomic alterations in EGFR are among the most prevalent in GB, occurring in approximately 50% of cases[54]. EGFR, a receptor tyrosine kinase, undergoes physiological activation upon ligand binding, leading to dimerization and subsequent phosphorylation of its C-terminal tail[55]. This receptor plays pivotal roles in various physiological and pathological pathways. The EGFR variant III (EGFRvIII) stands out as the predominant EGFR mutation, found in half of the GB cases that express EGFR. This variant is notably associated with unfavorable patient outcomes and resistance to chemoradiotherapy. More specifically, EGFRvIII stimulates the phosphoinositide 3-kinase (PI3K) / Akt / mammalian target of rapamycin (mTOR) pathway and mitogen-activated protein kinases (MAPKs) signaling pathways, orchestrating the regulation of tumor growth, survival, angiogenesis, and metabolism[56–58]. EGFR impacts the tumor microenvironment (TME) by attracting immunosuppressive cells while also inhibiting T cell and natural killer cell activation. Additionally, changes in EGFR elevate the levels of immunosuppressive molecules and cytokines[59].

MGMT. The methylation of the O6-methylguanine-DNA methyltransferase (MGMT) gene promoter stands as a significant biomarker for GB and serves as a predictive factor for the

response to temozolomide (TMZ) chemotherapy. MGMT, a DNA-repair protein, is crucial in removing alkyl groups from the O6 position of guanine, a key site for DNA alkylation. Interestingly, the DNA methylation induced by TMZ specifically targets this O6 position, making it a primary contributor to its cytotoxic effect. The MGMT protein counteracts the effects of alkylating therapeutic agents by rectifying alkylated guanine residues at the DNA level. Thus, methylation of CpG islands within the MGMT promoter region suppresses its transcription, potentially serving as a predictive biomarker for resistance to TMZ[60].

4. Molecular subtypes

Genome-wide transcriptomic analyses have facilitated the classification of GB based on distinct molecular signatures. As a result, Wang *et al.* GB categorized GBs into three primary subtypes: proneural (PN), classical (CL), and mesenchymal (ME)[62,63]. It is worth noting that this classification predates the recent updates by the WHO and thus encompasses IDH-mutant gliomas. The classical subtype is characterized by amplifications or mutations in EGFR. The proneural subtype, more prevalent in younger patients, is marked by amplifications or mutations in platelet-derived growth factor receptor α (PDGFRA) and homozygous deletions in cyclin dependent kinase inhibitor 2A (CDKN2A). The mesenchymal subtype, rooted in the

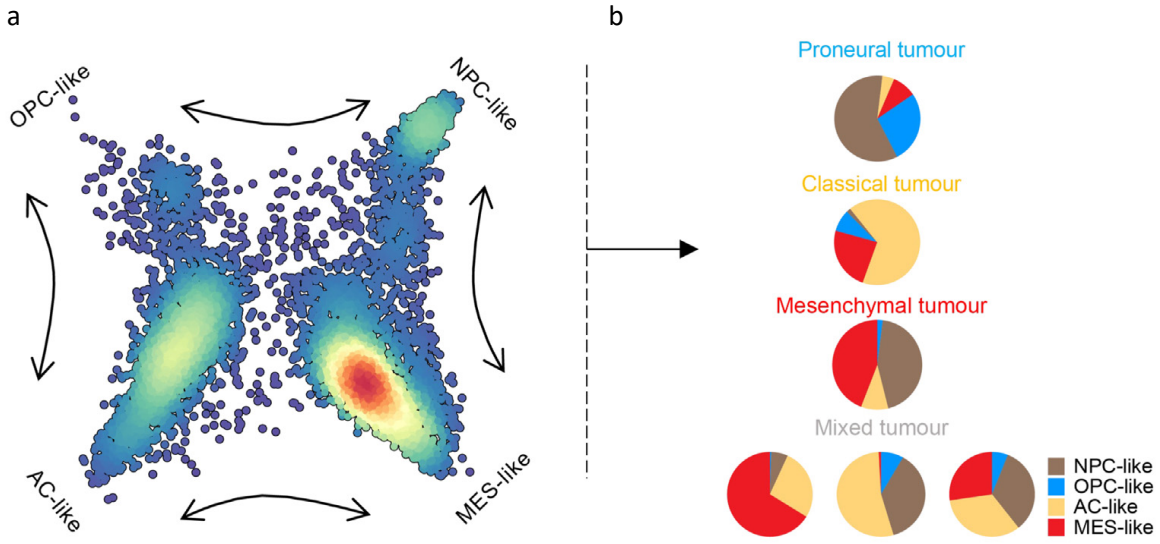

Fig. 5 | **Diversity of transcriptomic states of GB cells and compositions of GB subtypes**. **a** GB cells reflect the transcriptomic patterns of oligodendrocyte precursors (OPC-like), neural progenitors (NPC-like), astrocytes (AC-like), and mesenchymal cells (MES-like). The populations of NPC-, AC-, OPC-, and MES-like cells are in a dynamic balance, transitioning among the four transcriptomic profiles. **b** The proneural, classical, and mesenchymal tumor subtypes consist of varying proportions of NPC-, AC-, OPC-, and MES-like cells. The predominant subtype is determined by the most abundant cell population within the tumor. Tumors with a mixed profile contain roughly equal parts of two or more cell populations. (From De Silva *et al.* 2023)[61]

astroglial lineage, exhibits mutations in neurofibromin 1 (NF1) and deletions in phosphatase and tensin homolog (PTEN). It seems likely that most GB tumors exhibit features spanning multiple subtypes, underscoring the pronounced intra- and intertumoral heterogeneity, with individual cells displaying diverse gene expression patterns[64].

Therefore, GB cells exhibit transcriptomic signatures that closely resemble various cell types, including neural progenitor cells (NPCs), oligodendrocyte precursor cells (OPCs), astrocytes (ACs), and mesenchymal cells (MES). This has led to the categorization of GB into distinct subtypes such as NPC-like, OPC-like, AC-like, and MES-like. Specifically, classical GB predominantly consists of AC-like and MES-like cells. Proneural GB is primarily characterized by NPC-like and OPC-like cells. Mesenchymal GB is mainly composed of MES-like and OPC-like cells. Additionally, "mixed tumors" display equivalent proportions of two or more cellular populations[64] (Fig. 5).

Other transcriptomic approaches, including studies by Phillips *et al.* in 2006[65] and Garofano *et al.* in 2021, have suggested alternative classifications (Fig. 6). These findings underscore the inherent plasticity and heterogeneity of GB. Phillips *et al.*'s approach aligns with the already discussed classification of Wang *et al.,* discussed earlier in this section, in which the "classical" subtype corresponds to the "proliferative" subtype in Phillips's classification. Notably, Garofano *et al.* introduced a fourth subtype termed "mitochondrial" which is associated with the most favorable patient outcomes[66] (Fig. 6).

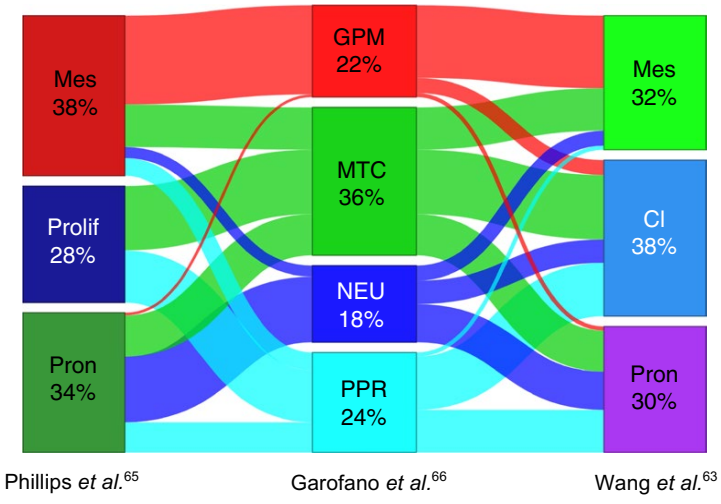

Fig. 6 | **Main propositions of transcriptomic classification for GB.** Garofano *et al*. conducted pathway-based analysis of single glioma cells and established four distinct clusters for GBs, including glycolytic/plurimetabolic (GPM), mitochondrial (MTC), neuronal (NEU) and proliferative/progenitor (PPR). *Mes: mesenchymal, Prolif: proliferative, Pron: proneural, Cl: classical.* (From Garofano *et al*., 2021)[66]

The studies underscore the profound heterogeneity and plasticity of GB cells. However, these cells progress along known neurodevelopmental differentiation pathways. Despite their ability to change lineage during development, they originate from a limited number of attractor states[67]. De Silva *et al.* underlined that halting GB dedifferentiation, which leads to the generation of GSLCs, requires terminal differentiation of the cells[61]. Thus, the induction of neurogenic differentiation has been explored and has demonstrated its potential to reduce the tumorigenicity of GSLCs by inhibiting Notch, a receptor promoting proliferation during neurogenesis, and overexpressing achaete-scute family bHLH transcription factor 1 (ASCL1), a transcription factor involved in neural differentiation[68].

5. The glioblastoma niches

The heterogeneity and plasticity observed through these transcriptomic studies contribute to the development of various tumor microenvironments (TME) depending on the GB subtype. Distinct regions of the TME display diverse morphological and metabolic traits, which influence tumor heterogeneity and its survival prospects[69]. The TME relies on the interaction of tumor cells, comprising GB stem-like cells (GSLCs), with the extracellular matrix and with a variety of non-cancerous cells. GSLCs have the ability to self-renew and differentiate into various cell types, and therefore play a significant role in tumor invasion and resistance to therapies. In GB, they reside within three main niches which directly influence distinct cellular behaviors (Fig. 7).

Perivascular niche. The perivascular niche is characterized by an expansion of microvascular structures. It serves as a maintenance site for GSLCs, which are in direct contact with the vascular epithelium. The perivascular niche is a heterogeneous construct with various types of microvessels. Four distinct patterns have been described. The "microvascular sprouting" refers to healthy capillary vessels produced by physiological angiogenesis. "Vascular clusters" are aggregates of blood vessels whose bodies are not interconnected. "Vascular garlands" describe an aberrant spiral arrangement of vessels. Lastly, "glomeruloid vascular proliferation" refers to the aggregation of multiple vessels with their bodies connected[70].

In GB, oxygen deprivation stimulates the release of pro-angiogenic factors such as vascular endothelial growth factor (VEGF), transforming growth factor β (TGF-β), FGFs,

angiopoietin-1, and EGF. These factors interact with endothelial cell receptors, leading to vessel wall dissolution and endothelial cell basement membrane degradation. Subsequent ECM remodeling by matrix metalloproteinases (MMPs) facilitates endothelial cell migration and proliferation, forming an endothelial tube-like structure. This structure is eventually stabilized by a mature vascular basement membrane and surrounding mural cells, resulting in a new vessel[71]. The swift expansion of the vasculature results in the emergence of inadequately functional vessels and a varied disruption of the BBB, leading to the infiltration of peripheral immune cells, including monocytes/macrophages, neutrophils, and myeloid-derived suppressor cells (MDSCs), which further drive tumor progression[72,73].

In addition to angiogenesis, several mechanisms of vessel formation are involved in GB[74]. Vasculogenesis refers to the formation of blood vessels from bone marrow-derived endothelial progenitor cells, predominantly observed in the late stages of GB development [75] Vascular mimicry, on the other hand, describes vessels that lack epithelial cells, with tubular walls primarily composed of extracellular matrix components[76]. Another phenomenon is GB-endothelial cell transdifferentiation, where GSLCs undergo transdifferentiation into endothelial-like cells[77]. Additionally, during vascular co-option, tumor cells navigate along the basolateral surface of existing vessels, eventually integrating these intact vessels into the tumor mass. This process predominantly occurs at the invasive front during the early oncogenic phase and operates independently of VEGF signaling[78].

The perivascular niche exhibits elevated levels of pro-inflammatory cytokines such as tumor necrosis factor α (TNF-α), interleukine 6 (IL-6), and IL-8. TNF-α plays an essential role in tumor development and angiogenesis[79]. IL-6, secreted within the GB TME by neurons, microglia, astrocytes, TAMs, and peripheral monocytes, is instrumental in promoting angiogenesis and cellular proliferation[80,81]. IL-8 stands out as a primary inducer of angiogenesis and also governs the maintenance and proliferation of GSLCs[82,83].

Hypoxic niche. The formation of inconsistent blood vessels, as previously discussed, produces collapsed vessels in some areas of the tumor and results in reduced oxygen tension within tissues. This oxygen deprivation, called hypoxia, subsequently leads to the formation of a necrotic foci surrounded by pseudopalisading cells, which is a peripherally migrating wave of cells escaping the hypoxic region[84].

Hypoxic signaling is orchestrated by hypoxia-inducible factors (HIFs). HIFs are heterodimer constituted of an α and a β subunit. HIFβ is constitutively expressed in cells while HIFα exhibits an unstable expression due to its rapid degradation in the presence of oxygen. Under hypoxic conditions, the HIFα subunit stabilizes and undergoes nuclear translocation to bind HIFβ and recognize the Hypoxia Response Element (HRE) located on the promoter regions of its target genes. This binding modulates various cellular processes, including survival, glycolysis, pH regulation, migration, and invasion[85]. It also regulates pluripotency-associated transcription factors such as Oct3/4, Nanog, and Sox2, molecules associated with epithelial-to-mesenchymal transition (EMT) like chemokine receptor 4 (CXCR4), Snail, and Twist, and angiogenic factors, notably VEGF[86]. A recent study also indicated the capacity of the hypoxic niche to attract TAMs and cytotoxic T cells through the release of the chemokine CCL8 and the cytokine IL-1β, to reprogram them towards an immunosuppressive phenotype[87].

Invasive niche. In addition to its migratory capacity to escape hypoxic regions, GB can invade healthy brain tissue but do not metastasize to peripheral organs through blood or lymphatic pathways. Infiltration is led by individual cells that have to detach from the tumor mass to engage into invasive behavior. The invasive front progresses following the pathways of anatomical structures such as those of perivascular space and white matter. They can also reach distant sites in the brain parenchyma and the leptomeningeal space[88].

Invasion is performed through a mesenchymal invasion mechanism, which relies on interactions with the ECM and progression driven by the contractility of the actin cytoskeleton[89]. Consequently, the composition of the ECM directly influences the invasive properties of GB[90]. ECM is physiologically composed of hyaluronic acid, proteoglycans, and glycoproteins to structure the extracellular space. Therefore, GB cells are able to influence the ECM composition by producing their own basement membrane components such as laminin, vitronectin, fibronectin, tenascin C, and collagen[91].

The progression operates through an attachment-detachment phenomenon. During this process, GB cells advance by contracting their cytoskeleton, establish strong adhesion to the ECM through the expression of integrins, and subsequently secrete MMPs to degrade the ECM behind them[92]. This mechanism is further modulated by communication between the tumor core and the invasive fronts[93].

Located at the border between the tumor and healthy parenchyma, the invasive niche has access to functional blood vessels and interacts with a larger number of cells from the TME. However, its progression leads to alterations in the BBB, particularly by disrupting the interactions maintained by astrocytic end-feet with the basal membrane[94]. Thus, communication with the vascular endothelial cells contribute to the self-renewal of GSLCs, as they release of Jagged 1/2, ligands for Notch receptors, and nitric oxide (NO) which activate Notch signaling[95]. Similarly, angiopoietin activates the Tie2 receptor, leading to the expression of extracellular adhesion molecules like N-cadherin and integrin β1, potentially enhancing GSLC invasion[96].

During tumor progression, invasive niches can be submerged by cellular proliferation, subsequently leading to the formation of a hypoxic niche. This hypoxic environment then prompts neovascularization, transitioning into a perivascular niche configuration. This structural evolution is both spatial and temporal, resulting in the successive development of specific TMEs[97].

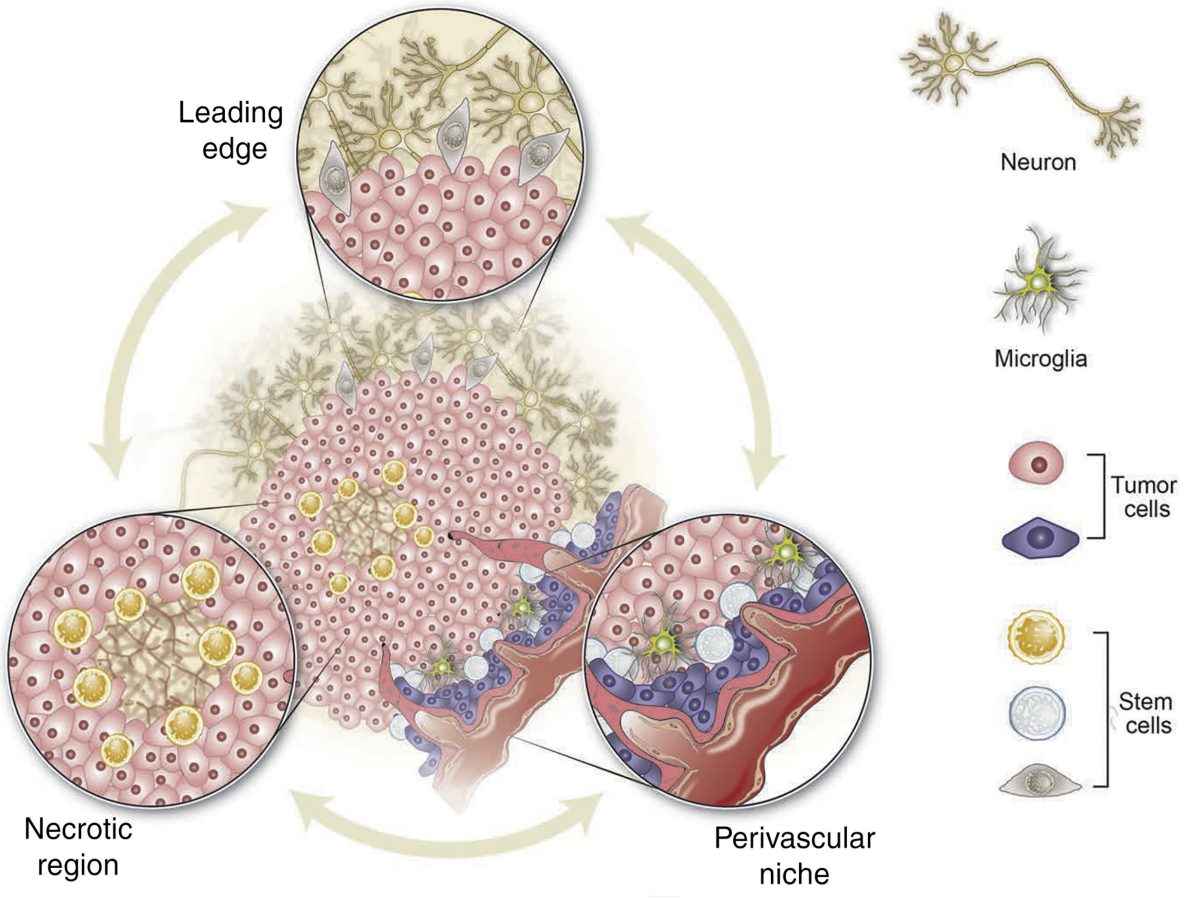

Fig. 7 | **Illustration of the glioblastoma niches.** (From Praguer *et al.*, 2020)[67]

III. The standard of care for glioblastoma

1. Diagnosis

The emergence of GB produces diverse symptoms depending on the cerebral region affected by the tumor. Thus, GB most commonly develops in the frontal lobe (40%), followed by the temporal lobe (29%), the parietal lobe (14%), and the occipital lobe (3%)[98]. It has been demonstrated that tumors affecting the temporal lobe are associated with a decreased overall survival compared to other tumors[99]. The most frequently observed symptoms are: drowsiness (87%), progressive neurological (51%) and cognitive (33%) deficits, seizures (45%), incontinence (40%), and headaches (33%). Increased intracranial pressure is the predominant cause of these symptoms and is responsible for the majority of related deaths. During monitoring, the age and neurological functions of the patient are considered. Functional impairment is assessed using the Karnofsky Performance Score (KPS). The KPS is a 11-point scale correlating to percentage ranging from 100% to 0%, where 100% indicates a patient capable of normal activity and work without the need for special care, and 0% means death[100].

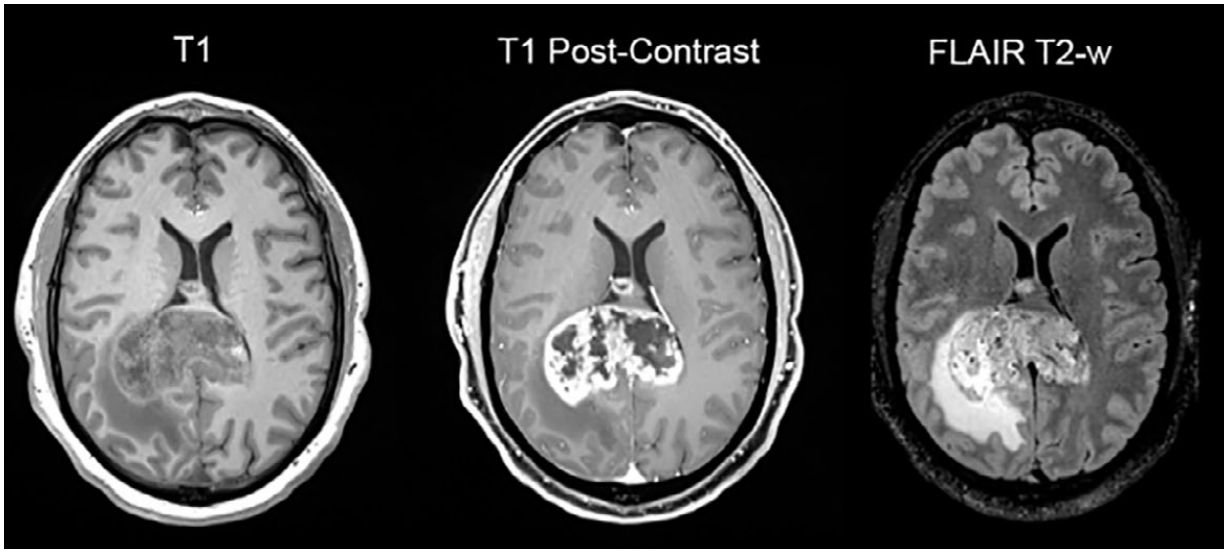

Fig. 8 | **MR imaging of a patient with glioblastoma.** From left to right: pre-contrast T1-weighted, post-contrast T1 weighted, T2-weighted FLARI images. The T1-weighted sequence typically displays soft tissues in isointensity or hypointensity and water in hypointensity. The addition of gadolinium, a contrast agent, allows to enhance the quality of the image by shortening the relaxation time of protons within tissues. The T2-weighted FLAIR sequence shows soft tissues in hyperintensity and water also in hyperintensity. In addition, it suppresses the signal from the CSF, making it useful for detecting lesions near the cerebral ventricles. (From Hirschler *et al.*, 2023)

Magnetic resonance imaging (MRI) is essential for the diagnosis of brain tumors. The European Association of Neuro-Oncology (EANO) guidelines advocate for the use of MRI sequences T1, T2, and T2-weighted fluid attenuated inversion recovery (FLAIR) both pre- and

post-administration of a gadolinium-based contrast agent (Fig. 8). Pseudoprogression, defined as the enlargement of the primary tumor or the emergence of a new lesion, must be taken into account if an anomaly is observed in the first month after a localized therapeutic intervention[48].

2. The Stupp protocol

Until the 1970s, surgical resection was the only treatment option for patients diagnosed with GB. The advent of radiotherapy in the late 1970s demonstrated enhanced treatment efficacy, and the combination of surgery and radiotherapy quickly became the standard of care[101,102]. In 2005, Stupp *et al.* incorporated chemotherapy into the standard treatment regimen using TMZ, an alkylating agent[103,104].

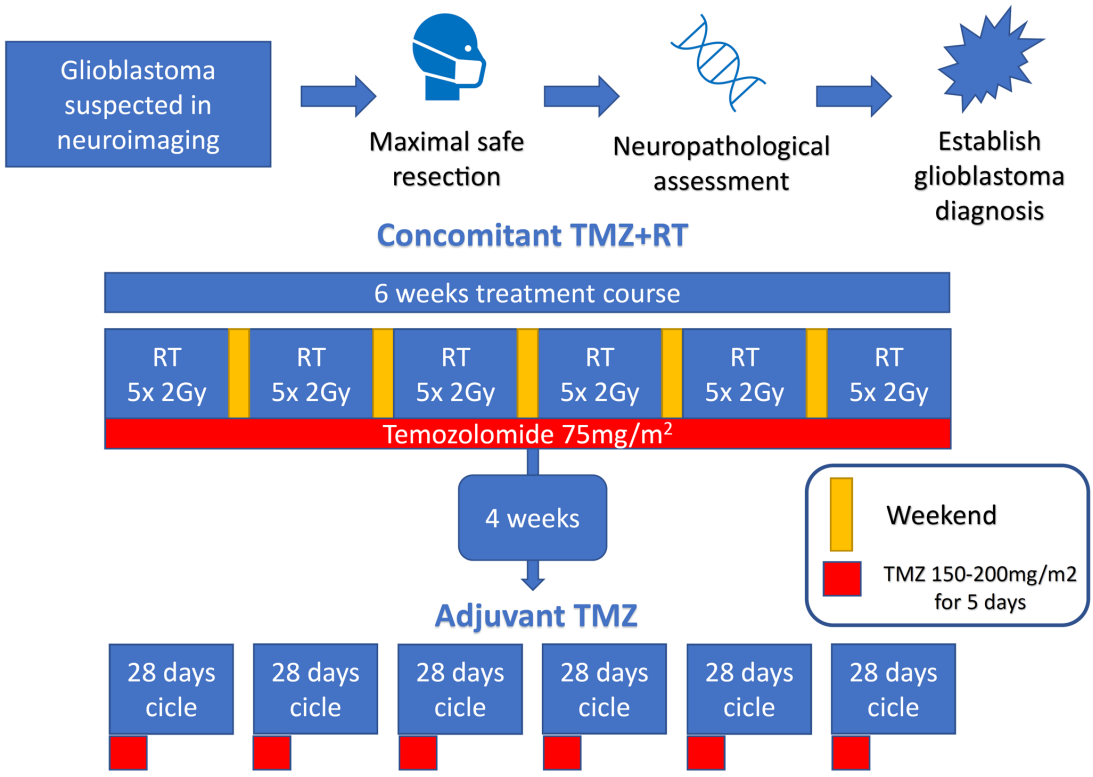

Fig. 9 | **Schedule of the Stupp protocol.** *TMZ: temozolomide, RT: radiotherapy, Gy: Gray.* (From Batistella *et al.*, 2021)[106]

Following a GB diagnosis, a combined approach of radiotherapy and chemotherapy is initiated approximately five weeks post-diagnosis. The patient undergoes focal, megavoltage X-ray radiation, receiving a dose of 2 Gy for each session. This focal irradiation, targeting only the resection bed, is distinct from whole-brain irradiation. Focal irradiation is generally

considered safer as it spares the non-tumor-affected parts of the brain from radiation exposure. The patient undergoes 30 of these sessions, administered five days per week during six weeks, resulting in a cumulative dose of 60 Gy. Concurrently, the patient is prescribed an oral dose of TMZ, at a daily dosage of 75 mg/m^2 of body surface area. After this phase, there is a four-week break where neither radiotherapy nor TMZ is administered. Subsequently, the adjuvant chemotherapy phase begins. During this phase, The dosage for each cycle ranges from 150 to 200 mg/m^2 of TMZ over a 5-day period. This is followed by a 21-day break without the drug. Depending on the tolerance of the patient, up to six of these cycles may be conducted (Fig. 9).

Despite the intensive therapeutic regimen, the median survival for patients does not exceed 15 months[103]. In 2017, Perry *et al.* conducted a randomized clinical trial with patients over the age of 65 to evaluate the added benefit of TMZ chemotherapy in conjunction with a short-course radiotherapy (40 Gy in 15 fractions). This combination resulted in an extended overall survival[105]. Consequently, this protocol has become the standard prescription for elderly patients diagnosed with GB.

3. Surgical approaches

In the case of GB, overall survival is closely linked to the extent of resection (EOR). Achieving a resection greater than 98% of the tumor mass can significantly improve the prognosis of patients[107,108]. Due to the invasive characteristics of GB and the existence of scattered tumor cells that remain undetected by MRI, the challenge of expanding the resection beyond the boundaries defined by contrast-enhanced MRI, while maintaining surgical safety, persists.

Fluorescence-guided resection. Fluorescence techniques have been used to enable a more targeted and safer tumor resection. The synthetic 5-aminolevulinic acid (5-ALA), when metabolized, produces a fluorescent metabolite, protoporphyrin IX, which accumulates in high concentrations in cancer cells[109]. Its application in glioma surgery has been shown to enhance the EOR and improve progression-free survival (PFS)[110]. The fluorescence from 5-ALA helps distinguish between the tumor core, healthy tissue, and areas of cancer infiltration, helping in more precise removal. However, not all GB uptake 5-ALA, and the intensity of fluorescence can vary based on the tumor subtype[111]. Fluorescein, a fluorescent compound, accumulate in brain regions with abnormal cellularity and vascularization due to its binding with blood

proteins and subsequent exclusion from normal tissue by the BBB. This allows for real-time imaging of tumors, particularly their margins[112]. However, some GBs maintain BBB integrity, leading to potential false negatives. Additionally, fluorescein can accumulate in non-tumor areas, especially post-surgical sites. Despite these problems, the use of fluorescein in GB microsurgical resection has been linked to increased gross total resection rates and overall survival[113]. Combination with 5-ALA is also possible to maximize EOR and thus improve the outcome of patients[114].

Neuronavigation and mapping. Neuronavigation is a standard tool applied during surgery to ensure the safety of resection. It encompasses a set of imaging techniques including intraoperative MRI, intraoperative ultrasound, confocal intraoperative microscopy, and intraoperative mass spectrometry, all of which provide real-time information during surgery[115]. Brain mapping further facilitates extended resection by pinpointing anatomical areas responsible for critical functions, such as motor and language, ensuring their preservation during the procedure. Preoperative mapping can be achieved using navigated transcranial magnetic stimulations, functional MRI, magnetoencephalography, or diffusion tensor imaging fiber tracking. Conversely, intraoperative mapping uses direct cortical or subcortical stimulations[116]. In some cases, awake surgery may be required to conduct intraoperative language mapping[117,118].

Regrettably, recurrence is inevitable, even after resection of all radiographic abnormalities detected on T1-weighted and T2-weighted FLAIR images. This perspective has led to the view of GB as a whole-brain tumor, not solely curable by surgical intervention[119.] Furthermore, a recent study has shown that surgical resection triggers the self-renewal of GSLCs through pleiotrophin, thereby contributing to tumor recurrence[120].

4. Chemotherapy

GB chemotherapy is conducted using the TMZ alkylating agent. As previously mentioned, its use has been approved by the FDA in 2005. In 2023, the FDA extended its use for newly diagnosed and refractory anaplastic astrocytomas. This molecule is inactive and stable at acidic pH. At physiological pH, the hydrolysis of TMZ results in the formation of 5-(3-methyltriazol-1-yl)imidazole-4-carboxamide (MITC). Then, MITC is hydrolyzed in 5-amino-imidazole-4-carboxamide (AIC) and methyldiazoliumn which reacts with DNA and

releases its methyl groups. Consequently, it can add methyl groups to the nitrogen (N7) and oxygen (O6) of guanine and the oxygen (O3) of adenine in the DNA molecule. N7 methyl-guanine accounts for 70% of the adducts generated by TMZ. These additions cause base mismatches as well as single and double-strand breaks in DNA. The non-repair of these breaks results in a cell cycle arrest in the G2/M phase and cell death through apoptosis.

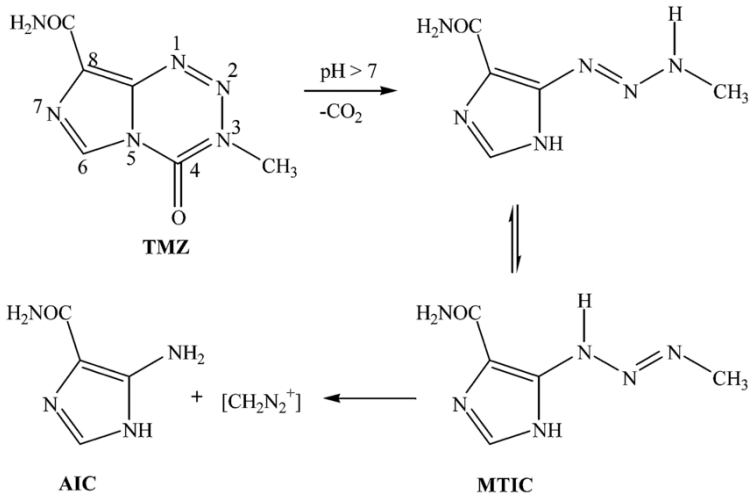

Fig. 10 | **Mechanism of action of temozolomide.** At physiological pH, the hydrolysis of TMZ results in the formation of 5-(3-methyltriazol-1-yl)imidazole-4-carboxamide (MITC). Then, MITC is hydrolyzed in 5-amino-imidazole-4-carboxamide (AIC) and methyldiazoliumn ($CH_2N_2^+$) which reacts with DNA and releases its methyl groups. (From Martinho *et al.*, 2015)[125]

Unfortunately, TMZ represents a significant factor in GB resistance. Due to the high mutational load and heterogeneity of GB, only 50% of patients respond to TMZ[121]. The only predictive marker for TMZ response to date is the MGMT promoter methylation status[122]. Furthermore, the heterogeneity of the BBB permeability limits the accumulation of TMZ within the tumor[123]. Metabolically, the acidosis generated by tumor hypoxia would prevent the proper metabolism of TMZ, thereby reducing its efficacy[124].

5. Radiotherapy

a. Biological effects

ROS production. In the extracellular environment, ionization of water molecules by radiation leads to its radiolysis and the generation of reactive oxygen species (ROS). ROS include the superoxide anion O_2^-, hydroxyl radicals OH·, and hydrogen peroxide H_2O_2. These species are toxic for tumor cells and cerebral parenchyma[126]. Ionizing radiation also amplifies the endogenous ROS levels within mitochondria[127], compromising their membrane integrity, which in turn becomes more permeable and releases an increased amount of ROS[128]. This

elevated ROS concentration disrupts the mitochondrial electron transport chain, inducing a redox imbalance[129]. Cellular antioxidant systems can counteract this oxidative stress. For instance, superoxide dismutase can convert OH· to H_2O_2, which is subsequently transformed by catalases and peroxidases into H_2O and O_2[130,131]. If oxidative stress persists, it can lead to lipid peroxidation, protein misfolding in the endoplasmic reticulum, and DNA breaks.

DNA Damage. Irradiation induces DNA damage, either directly or indirectly, manifesting as base damage, single-strand breaks (SSBs) or double-strand breaks (DSBs). Additionally, radiation can cause complex DNA damage with multiple non-DSB lesions, called clustered DNA damage. Such complex damages necessitate prolonged activation of the repair system, potentially resulting in incomplete repair and mutation induction[132]. The type of DNA damage and the repair mechanisms involved vary based on the type of particle and the energy level they emit. For instance, a recent study demonstrated that high-energy particles generate apurinic/apyrimidinic sites and thymine glycol near DSBs. This triggers the initiation of a specific repair pathway, notably involving DNA polymerase θ[133]

Upon the formation of classical DSBs, DNA damage repair sensors such as ataxia-telangiectasia mutated (ATM), ataxia-telangiectasia and Rad3-related (ATR) and DNA-dependent protein kinase (DNA-PK) are activated and recruit downstream DNA repair pathway proteins[134]. The phosphorylation of ATR, DNA-PK, and γH2AX, and the recruitment of mediator of DNA damage checkpoint protein 1 (MDC1) to DNA damage foci facilitates the assembly of DNA repair proteins, including breast cancer type 1 susceptibility protein 1 (BRCA1), BRCA2, and p53-binding protein 1 (53BP1)[135]. The phosphorylation of checkpoint kinases, Chk1 and Chk2, also contributes to this pathway. Collectively, these events stabilize and activate p53, which in turn activates p21, inducing cell cycle arrest[136]. This sets the stage for DSB repair mechanisms. The non-homologous end joining (NHEJ) pathway is initiated by the Ku70/Ku80 heterodimer, while the homologous recombination (HR) pathway is orchestrated by the MRN complex (Mre11/Rad50/Nbs1). Alternative DSB-repair pathways, such as alternative end joining (alt-EJ) and single-strand annealing (SSA), can also be initiated (Fig. 11). Depending on the nature of the lesion, repair mechanisms differ. For instance, SSBs are predominantly repaired *via* nucleotide excision repair (NER) or base excision repair (BER) pathways. The outcome of an irradiated tumor cell is contingent upon its inherent genomic instability and the status of its DNA repair machinery. In instances of incomplete DNA repair, p53 promotes apoptosis through the pro-apoptotic factors Puma, Noxa, and Bax[137].

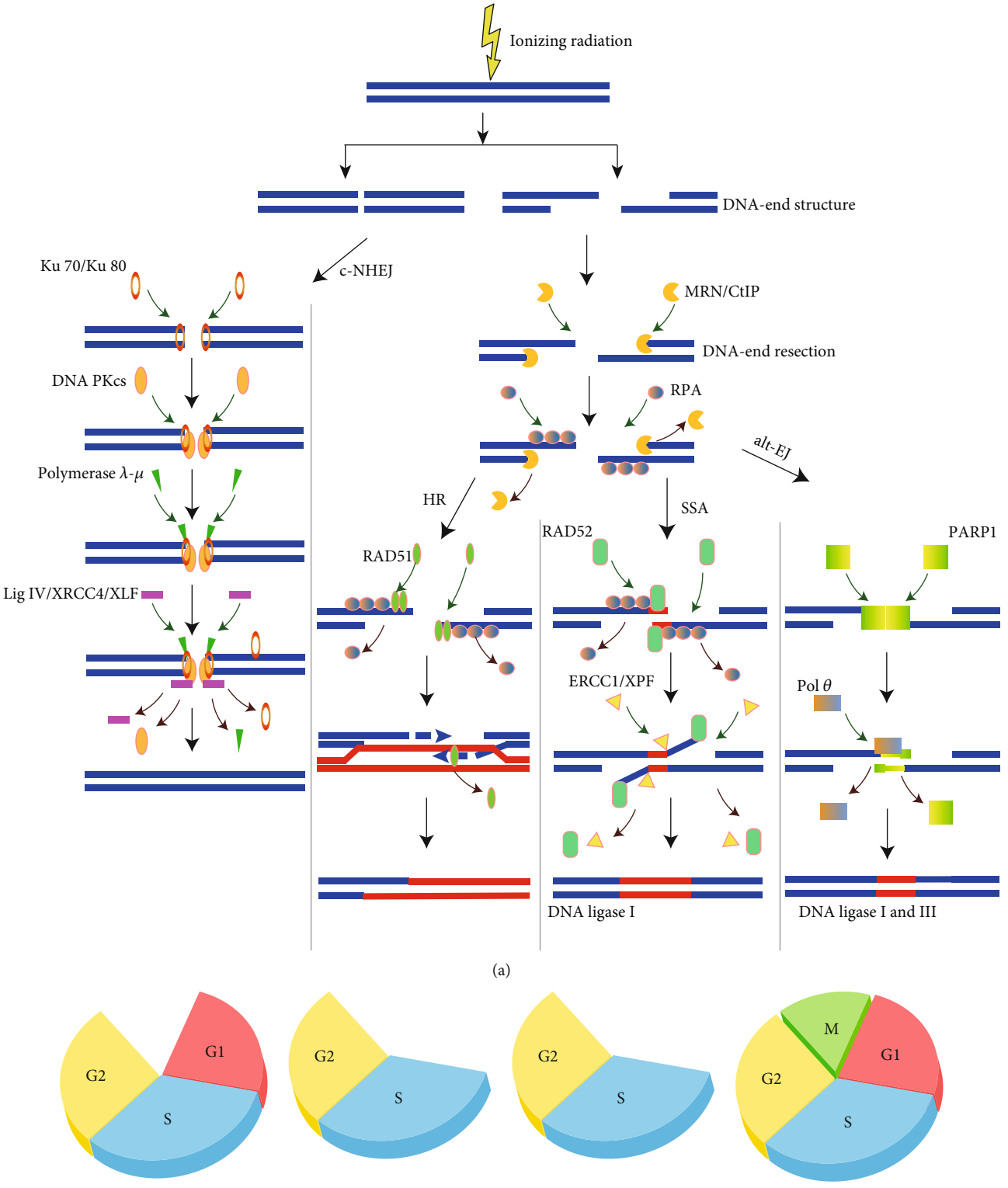

Fig. 11 | **Primary repair mechanisms for DSBs induced by ionizing radiations.** When DNA is damaged by ionizing radiation (IR), creating double-strand breaks (DSBs) with either blunt ends or short single-strand ends, the classical nonhomologous end joining (c-NHEJ) repair process begins. This is initiated by the attachment of the Ku70/80 heterodimer, followed by the involvement of DNA-PKcs and polymerase. If the DNA is resected, other repair pathways like homologous recombination (HR), alternative end joining (alt-EJ), and single-strand annealing (SSA) are activated, each requiring different proteins for the repair process. These major repair pathways for IR-induced DNA DSBs are dependent on the cell cycle stage. (From Zhao *et al.*, 2020)[138]

Bystander and abscopal effects. Beyond their direct action on irradiated cells, ionizing radiations produce distant effects impacting neighboring non-irradiated cells. The outcomes of these effects are diverse, including a reduced clonogenic survival, increase in genomic instability, a heightened frequency of sister chromatid exchange, augmented micronuclei, chromosomal aberrations, accumulation of γH2AX foci, and induction of apoptosis[139]. Bystander effects can be conveyed through direct contact with irradiated cells *via* intercellular gap junctions, transmitting Ca^{2+}, nucleotides, and peptides. Moreover, release of cytokines and chemokines, such as IL-6, IL-8, TGF-β, TNFα, NO, and ROS, contribute to a more distant communication[140]. Macrophages are involved in the bystander signaling by releasing factors like TNFα, NO, and superoxide nitrogen[139]. Furthermore, radiotherapy may promote T cell trafficking towards the tumor through local inflammation[141] Irradiated cells also communicate through the release of exosomes to propagate either cytotoxic or cytoprotective signals, depending on the context[142,143]. Lastly, bystander cells can also impact irradiated cells, particularly their response to radiation[144].

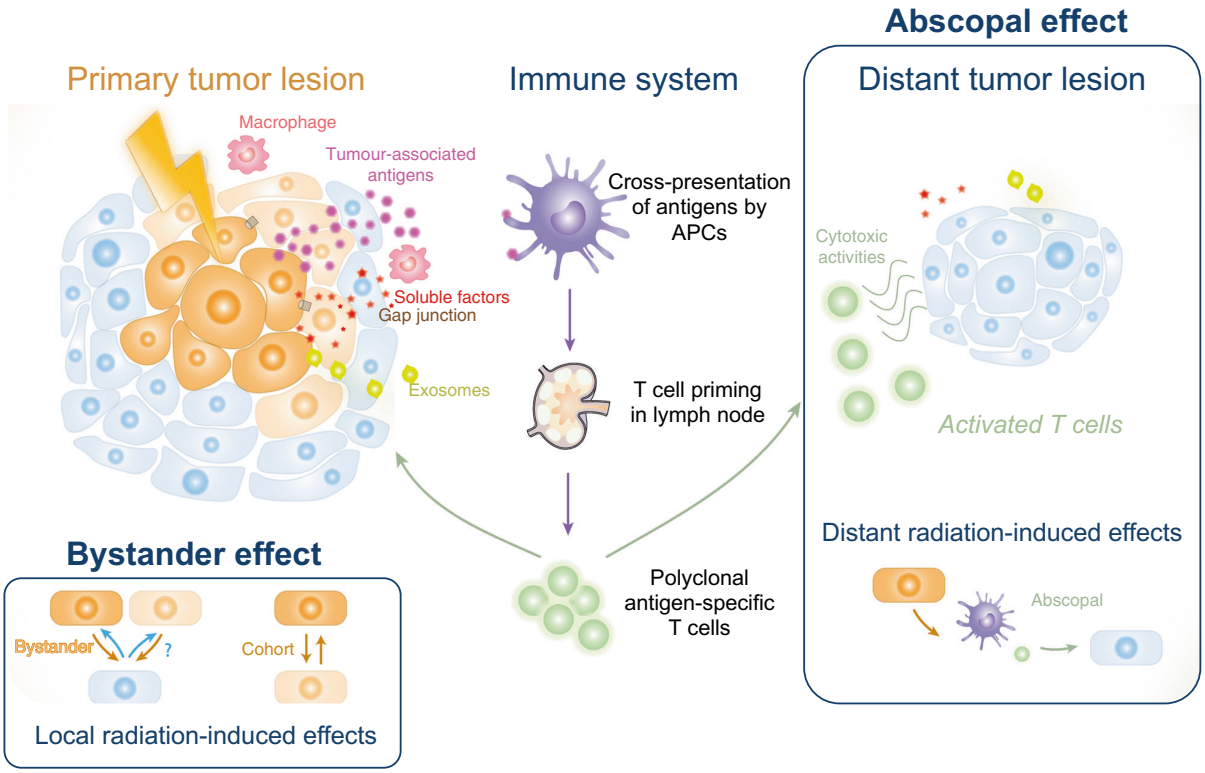

Fig. 12 | **Bystander and abscopal effects triggered by tumor irradiation.** Within the primary irradiated lesion, two local effects are observed: bystander effects between high-dose or low-dose targeted cells and non-irradiated cells, and cohort effects between high and low-dose targeted cells. Irradiation causes cancer cells to undergo immunogenic cell death, releasing tumor-associated antigens (TAAs), which activate the immune system, particularly antigen-presenting cells (APCs) and macrophages. APCs present these TAAs to T cells, leading to a systemic immune response against tumors both within and outside the irradiated area, the latter being termed the abscopal effect. Exosomes are believed to play a role in these non-targeted effects both locally and distantly. (From Daguenet *et al.*, 2020)[145]

The abscopal effect denotes the systemic response following tumor irradiation. It is based on the release of tumor-associated antigens (TAAs) and danger-associated molecular patterns (DAMPs) due to radiotherapy, which are then recognized by the immune system. Crucially, antigen-presenting cells cross-present the TAAs to T cells in lymph nodes. These T cells subsequently undergo clonal proliferation, targeting not only the primary lesion but also distant tumor sites within the body. This model is supported by evidence that radiotherapy can modulate the expression of TAAs on tumor surfaces[146], expression of adhesion molecules on epithelial cells for leukocytes recruitment, maturation of dendritic cells[147], and the behavior of cytotoxic T cells[148].

b. Clinical practice for external radiotherapy

The standard treatment for GB also relies on external beam radiation therapy (EBRT) as described in the Stupp protocol. This method involves directing X-ray beams through the skin and tissues to target and eliminate tumor cells, while trying to minimize damage to the healthy brain parenchyma.

Target delineation strategy. The primary challenge in treating GB is defining the tumoral volume to target. The volume to be treated, called the clinical target volume (CTV), is determined by MRI with a T2/FLAIR sequence. Abnormalities on T2/FLAIR suspected to be edema are not included in the CTV. Current guidelines from the European Society for Therapeutic Radiology and Oncology (ESTRO) and the EANO recommend to apply a 1.5 cm margin to the gross tumor volume (GTV) to define the CTV. This was previously recommended at 2 cm, as studies indicated that 80% of GB recurrences occurred within 2cm of the GTV. However, recent studies have reported similar outcomes with margins ranging from 0.5 to 1.5 cm[149].

Pre-treatment imaging. The primary imaging modalities applied are contrast-enhanced 3D T1-weighted and T2/FLAIR sequences. While these MRI protocols offer high-quality spatial resolution, the T2/FLAIR sequences present challenges as their signals can indicate oedema, inflammation, post-operative changes, or gliosis. Thus, they are not always specific to tumor infiltration. However, T2/FLAIR can be instrumental in identifying suspected tumor infiltration areas, especially when discerning between tumor and oedema[150,151].

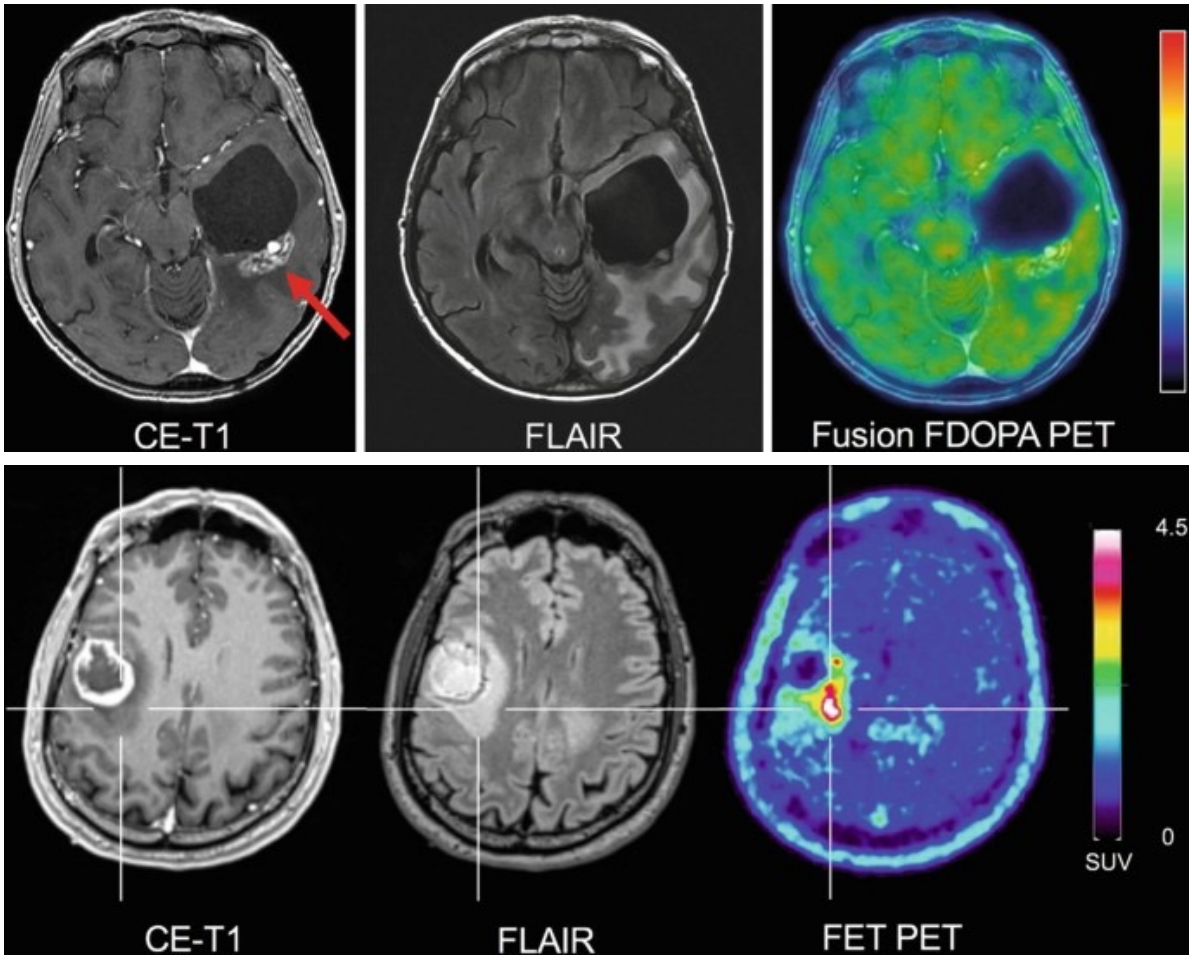

Fig. 13 | **FET and FDOPA as amino acid tracers for PET in GB.** Comparison of T1-weighted and T2-weighted MR imaging with L-3,4-dihydroxy-6-[^{18}F]fluorophenylalanine (FDOPA and [18F]fluoro-ethyl-l-tyrosine (FET) PET. Both tracer uptakes rely on L-type amino acid transporter to specifically accumulate within the tumor mass. (From Galldiks *et al.*, 2019)[156]

In addition, imaging using computed tomography (CT), positron emission tomography (PET), or PET-CT can be implemented to obtain supplementary information. CT scan employs X-rays and electronic detectors to capture multiple projections from various angles. These projections are then processed to produce detailed cross-sectional images, of the body's internal tissues and structures[152]. In a PET scan, the patient is injected with a radiopharmaceutical containing a positron-emitting radionuclide. This radionuclide distributes within tissues based on its carrier molecule and emits positrons. When a positron encounters a free electron, they annihilate, producing two photons emitted in opposite directions. External detectors capture these photons, and their origin is localized, allowing for the visualization of the distribution of the radiopharmaceutical within the body. This provides insights into physiological processes at the cellular level[153]. Regarding PET imaging, the most effective amino acid tracers for detecting metabolically active GB are suggested to be L-[methyl-^{11}C]-methionine (MET), [^{18}F]fluoro-ethyl-l-tyrosine (FET), and L-3,4-dihydroxy-6-[^{18}F]fluorophenylalanine (FDOPA). These

radiolabeled amino acids demonstrate selective uptake in brain tumors through their transport by L-type amino acid transporter 1 (LAT1), which is overexpressed in malignant tumors[154–157].

Dose fractionation. Although the Stupp protocol is based on a fractionation of a total dose of 60 Gy, other protocols have tested different dose fractionation approaches. Hyperfractionation involves a reduction of the emitted dose combined with an increase of the irradiation frequency. However, a retrospective study highlighted the absence of significant added value with a protocol of 1.8 Gy / 2x per day in 30 fractions, for a total of 54 Gy[158]. Hypofractionation has also been explored in clinical settings. The Perry protocol, as previously discussed, is now routinely adopted for elderly patients. However, the biologically effective dose (BED) for 40 Gy in 15 fractions is lower than that of 60 Gy in 30 fractions, indicating that these patients might be receiving suboptimal dosing. In fact, Perlow *et al*. recently reported a better overall survival with a hypofractionated regimen of 52.5 Gy in 15 fractions (BED equivalent to the Stupp protocol) compared to Perry's protocol[159]. Another study reported equivalent outcomes between hypofractionated radiotherapy and the classical radiotherapy protocol, but underlined a reduced lymphopenia during treatment[160].

Advancements for EBRT. Three-dimensional conformal radiation therapy (3D-CRT) is a radiotherapy technique that integrates imaging methods like CT, MRI, PET, or PET-CT to create a 3D image of the patient's tumor. This allows the delivery of a focused dose while minimizing exposure to healthy tissues. This approach has become a standard in radiotherapy treatment. Advancements in 3D-CRT have been developed to refine the precision of the irradiating beams[161].

Intensity-modulated radiation therapy (IMRT) is an advanced form of 3D-CRT that offers enhanced dose distribution to target volumes, especially for concave and irregular shapes. Unlike traditional radiotherapy, IMRT uses a multi-leaf collimator (MLC) to modulate the intensity of radiation beams by computer optimization. After the definition of the CTV and dose parameters, the movement of the MLC is computer-optimized to minimize exposure to adjacent normal tissue and organs at risk. IMRT can also simultaneously deliver specific radiation doses to different targets[162].

With volumetric modulated arc therapy (VMAT), the radiation dose is consistently administered as the gantry of the linear accelerator (LINAC) revolves around the patient, either in a single or multiple arcs. This method refines the dose distribution to the tumor by adjusting

the intensity of the radiation beam, dose rate, and the speed of rotation. VMAT reduces treatment duration and the number of monitor units used[162].

Stereotactic radiosurgery (SRS) applies several beams of high-energy X-rays, γ-rays, or protons that converge on a specific, visually-identified area. This radiation delivery is very precise. By intersecting multiple beams, the targeted area receives a high therapeutic dose, while nearby healthy brain tissue gets a minimal dose. This method can be adjusted accurately, ensuring quick energy dissipation outside the targeted area and saving healthy tissue. The sharp decrease in radiation in adjacent tissues ensures minimal side effects. Some techniques allow a submillimeter precision and the application of fractionated doses[163].

Photodynamic radiotherapy (PDT) uses photosensitive agents that preferentially accumulate in tumor tissues. These agents are activated when exposed to intense, non-thermal visible light of a particular wavelength. This activation triggers a photodynamic response driven by ROS, causing damage to macromolecules like DNA, RNA, lipids, and proteins, ultimately leading to the death of cancer cells[164]. 5-ALA presents notable benefits compared to other photosensitizers. Multiple research efforts have underscored the effectiveness of 5-ALA-driven PDT in treating GBM, showing *in vitro* cytotoxicity rates reaching up to 80% and substantial tumor tissue necrosis in rat studies[165,166].

FLASH radiotherapy (FLASH-RT) is a technique that enables the emission of an ultra-high dose electron beam, on the order of 10^6 Gy/s. This allows for irradiation over exposure times in the microsecond range[167]. A study showed that FLASH-RT fractionated regimen was able to control glioma growth in a mouse model while preserving neurocognitive functions. This benefit is partly attributed to a lower production of ROS compared to conventional radiotherapy[168].

Internal radiotherapy. Brachytherapy is a technique wherein radionuclides are internally positioned close to or within the treatment site, emitting high-energy particles. The radiation dose depends on the selected radionuclide. GammaTile® represents a novel brachytherapy approach, incorporating four cesium-131 spheres embedded within a collagen matrix. Recently endorsed by the FDA, this surgically-targeted radiation therapy is implanted immediately post-surgical resection in patients. It's a permanent, biocompatible implant operating based on the decay of cesium-131. This radionuclide undergoes electron capture, emitting characteristic low-energy X-ray photons and electrons[169].

6. Mechanisms of radioresistance

Despite the achieved advancements in external radiotherapy, GB remains significant radioresistant because of its its genomic heterogeneity and its microenvironment, involving hypoxic niches, metabolic alterations, GSLCs, microRNAs or regulations of cell cycle and DNA-damage responses (Fig. 14).

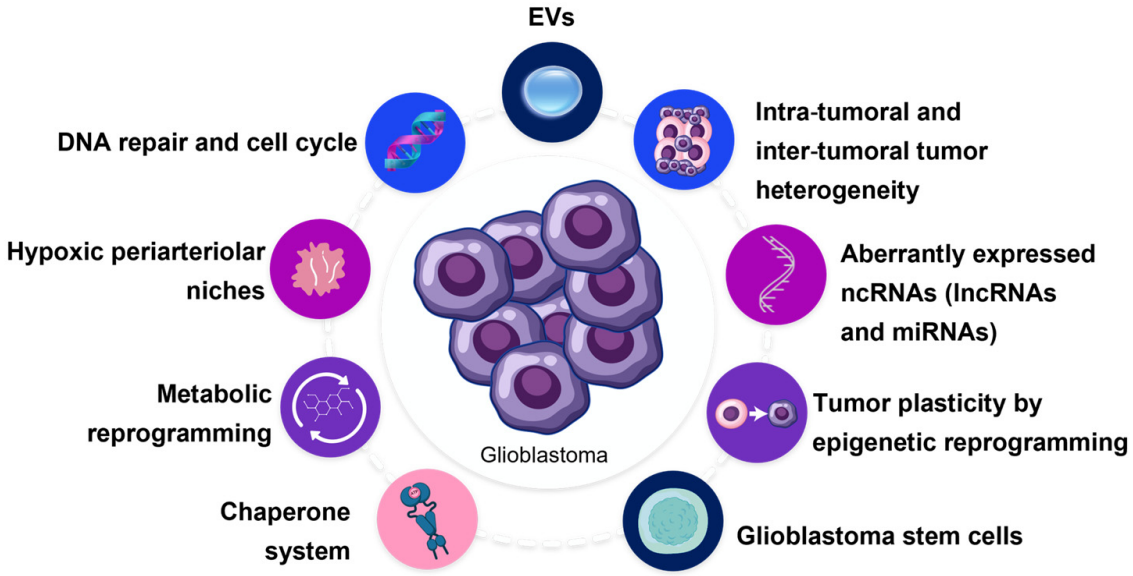

Fig. 14 | **General mechanisms of radioresistance in GB.** (From Burko *et al.*, 2023)[174]

Hypoxia. DNA damage caused by X-rays in conventional radiotherapy is largely due to the production of ROS within cells, rather than direct irradiation of the DNA molecule itself. Consequently, the efficacy of radiotherapy is significantly oxygen-dependent, and is therefore reduced in hypoxic niches where ROS cannot be generated. Furthermore, in hypoxic conditions, HIF-α is able to activate the transcription of the Oct4 gene, responsible for GSLCs self-renewal[170]. Chronic hypoxia can activate the NHEJ protein DNA-PK to efficiently repair radiation-induced DNA damage, and downregulates the HR protein Rad51, resulting in less HR pathway repair[171–173].

Metabolic alterations. GB cells exhibit elevated glycolytic activity and a dominance of the pentose phosphate pathway, which results in an excessive production of nicotinamide adenine dinucleotide phosphate (NADPH)[175]. NADPH plays a crucial role in redox homeostasis and the cellular antioxidant system, thereby shielding cells from oxidative stress. Radiation therapy increases this glucose utilization in GB cells, and the M2 isoform of pyruvate kinase (PKM2) have been shown to participate to the rewiring of glucose metabolism to enhance

antioxidant responses[176]. In response to radiation, IDH1 wild-type promotes NADPH production, contributing to radioresistance[177]. In addition, a high GB expression of ATPase family AAA domain-containing 3A (ATADA3A), a mitochondrial protein regulating communication with the endoplasmic reticulum, is associated with radioresistance of GB[178]. Radiations also upregulate autophagy which increases production of tricarboxylic acid (TCA) cycle metabolites such as citrate, succinate, fumarate, and malate, leading to an increase of adenosine triphosphate (ATP) production and high oxygen consumption rate[179].

GSLCs. GSLCs are known to enhance GBM radioresistance by amplifying the activation of DNA damage checkpoint pathways and inherently overactivating the PI3K/Akt and PTEN pathways. In particular, $CD133^+$ GSLCs, when exposed to radiation, predominantly activate DNA damage checkpoint proteins like Chk1 and Chk2. This allows them to repair radiation-induced DNA damage more efficiently than $CD133^-$ cells[180,181]. The increased production of ROS scavengers in GSLCs, *via* genes like superoxide dismutase, superoxide reductase, glutathione peroxidase, and catalase, protects them from damage caused by ROS, potentially enhancing tumor resistance to radiation[182].

IV. Radionuclide therapy

The advancement of radionuclide therapy (RNT) emerges as a promising avenue to address the inability of standard treatments, especially EBRT, to achieve complete eradication of GB. This modality capitalizes on the vectorization of high-energy particles for internalized tumor targeting and eradication. The methodology can encompass passive vectors, like nanoparticles, for localized intratumoral delivery, or active, precision-guided vectors suitable for both systemic and localized injections. In this context, we refer to it as targeted radionuclide therapy (TRT). RNT employs radionuclides characterized by their low penetration and high energy, leading to more ionizing emissions (such as β^-, α, or Auger e^- emitters) (Fig. 15). Notably, some radionuclides also emit γ or β^+ radiations, which are advantageous for the diagnostic imaging of GB. These radionuclides, due to their dual capability of both diagnosis and therapy, are termed theranostic radiopharmaceuticals. Theranostic pairs can also be established with a radiopharmaceutical dedicated to therapy and another to diagnostic, with the same vectorization strategy. This synergistic approach optimizes treatment personalization, ensuring interventions are precisely aimed at the affected cells or tissues[183]. This section briefly

introduces RNT. The design of therapeutic strategies for GB, including the choice of radionuclides, vectors and targets will be discussed in Chapter III.

1. Particles used in radionuclide therapy

The physicochemical properties of high-energy particles provide the opportunity to develop diverse strategies, considering both the emitted energy and the path taken within tissue (Fig. 15). Linear energy transfer (LET) refers to the amount of energy deposited by an ionizing particle as it travels through matter. It is expressed in keV/µm. Particles with a low LET, have a long ionization path and deposit little energy along their route. Conversely, particles with a high LET, like α particles, release much more energy but over a shorter distance. LET indicates the biological damage a radiation can cause and therefore influences the type of DNA damage it can produce[184].

β-emitters. β^- radionuclides such as iodine-131 (^{131}I), yttrium-90 (^{90}Y), and lutetium-177 (^{177}Lu) were the first ones to be clinically investigated for GB treatment[185–189]. They have shorter tissue penetration (1-10 mm) than X-rays, their emission energy is ranging between 0.1 and 2.3 MeV, and their LET is 0.2 keV/µm. Clinically, β^-emitters have been used in approved treatments for non-Hodgkin lymphoma, neuroendocrine tumors, and metastatic castration-resistant prostate cancer, with drugs like Zevalin®, Bexxar®, Lutathera®, and Pluvicto®[190–192].

α-emitters. α-emitters are characterized by a limited tissue penetration (50-100 µm), a high energy emission (2-10 MeV), and a high linear energy transfer (100 keV/µm)[193]. They also retain efficacy under hypoxic conditions[194]. In 2013, the FDA approved the use of radium-223 (^{223}Ra) dichloride (Xofigo®) for treating mCRPC[195]. In the context of GB, α-emitters are seen as optimal for addressing both primary tumors and post-surgical remnants, minimizing damage to healthy tissues. Recent clinical investigations have affirmed the safety and effectiveness of targeted-α therapies (TATs) using radionuclides like astatine-211 (^{211}At), bismuth-213 (^{213}Bi), and actinium-225 (^{225}Ac) in GB treatments[196–201].

Auger electrons (AEs). The majority of AEs exhibit extremely low energy (< 1 keV), even if some AEs exhibit high peak energies, such as 78.2 keV with a maximum range of 87 mm for platinum-195m (^{195m}Pt). This energy is released over a span of less than 500 nm in tissues, which is considerably shorter than the range of α particles[202].

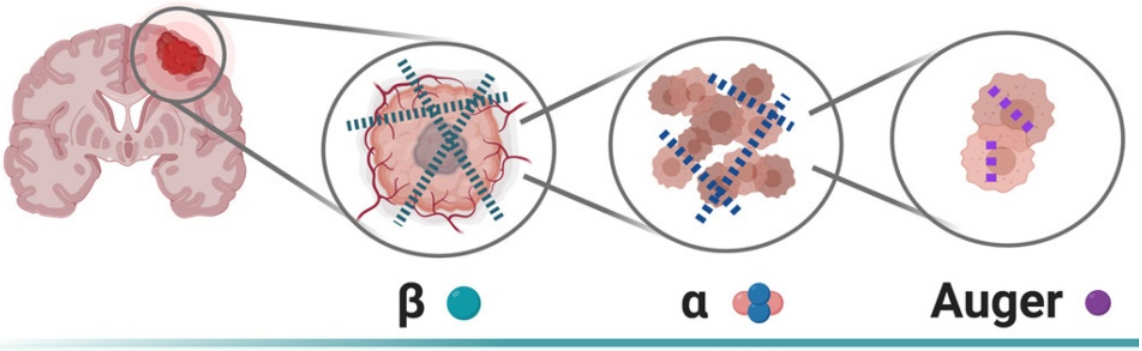

	β	α	Auger
Range	up to few mm	40-100 µm	<100 nm
Crossfire effect	+++++	+	-
Uniform radiation dose	+++++	++	-
Homogeneous antigen expression	+	++	+++++
Affinity and specificity for the target	+	+++++	+++++
LET and RBE	0.2-2 keV/µm +	50-230 keV/µm +++++	1-23 keV/µm ++++
Stability *in vivo*	++	+++++	+++++
High SA	+	+++	+++++
Dependence on hypoxia, dose rate effects or cell cycle position	+++	-	-
Daughter products with extra emissions	-	+++++ e.g. ^{211}At, ^{225}Ac, ^{223}Ra, ^{213}Bi	-

Fig. 15 | **Characteristics of β particles, α particles and Auger electrons.** *LET: Linear energy transfer, RBE: relative biological effectiveness, SA: specific activity.* (From Bolcaen *et al.*, 2021)[183]

The choice of an appropriate radionuclide for GB RNT is influenced by multiple factors. Foremost, its availability and the scale of its production are essential. Key considerations include its physicochemical characteristics, half-life, tissue range, and the potential toxicity of daughter radionuclides during decay. The vectorization approach, whether passive or active, the feasibility of radiolabeling the vector, and the vector biological half-life are crucial. The choice of the biological target is also significant regarding its expression levels in GB cells and surrounding healthy tissues. Intracellular target expression might favor a strategy based on Auger electrons, whose limited tissue range requires internalization by target cells. Additionally, the mode of administration plays a decisive role in the comprehensive selection framework.

2. Administration route

Systemic approach. Intravenous delivery of RNT is ideal when aiming to target multiple tumor sites concurrently. This approach is particularly effective for circulating tumor cells, as in leukemia or multiple myeloma, or metastases that arise from the vascular dissemination of tumor cells. For instance, Kratochwil *et al.* showcased the efficacy of the α-emitter ^{225}Ac using this method in patients with metastatic castration-resistant prostate cancer with a complete response in imaging PET/CT. This study also highlighted the superiority of the ^{225}Ac over the β$^-$-emitter ^{177}Lu, which had been previously administered to the patient (Fig. 16)[203].

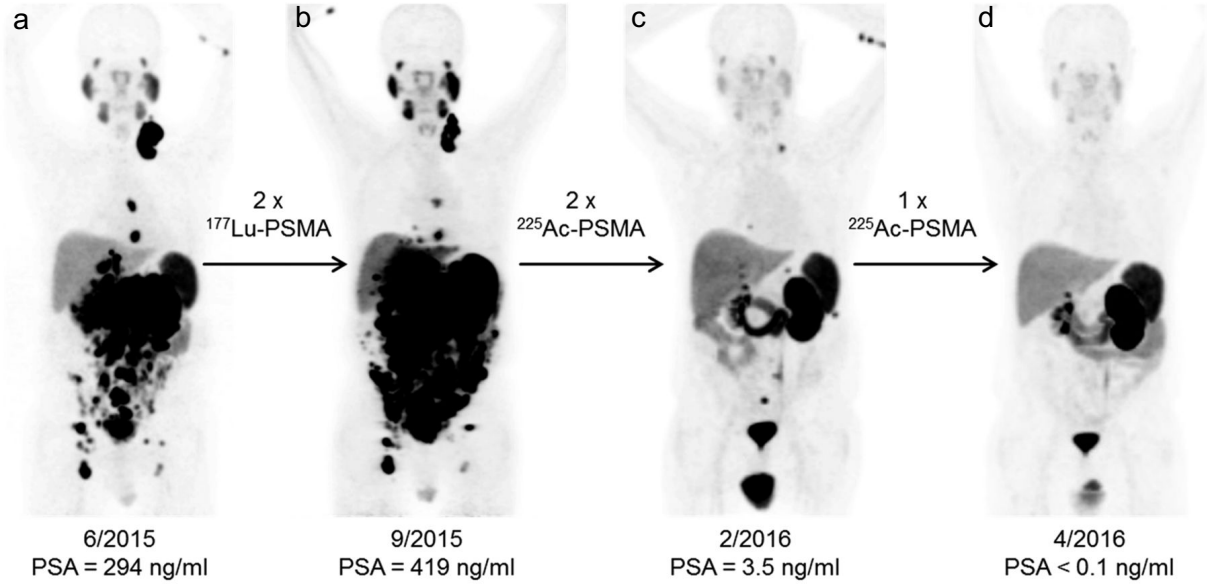

Fig. 16 | **PET/CT scans of an mCRPC patient treated with ^{225}Ac-PSMA-617.** Gallium-68-PSMA-11 PET/CT. The patient underwent two cycles of ^{177}Lu-PSMA-617 and three cycles of ^{225}Ac-PSMA-617. **a** Initial tumor spread. **b** Tumor progression after second cycle of ^{177}Lu-PSMA-617. **c,d** Complete response after 3 cycles of ^{225}Ac-PSMA-617. (From Kratochwil *et al.*, 2016)[203]

In the management of GB, RNT can be delivered intravenously. This method requires targeted vectorization, possibly using an antibody or peptide, to ensure the specific distribution of radioactivity within the tumor. While this strategy offers the advantage of minimally invasive administration, it relies on blood circulation, the vascularization of the tumor, and also the BBB, which remains intact in certain tumoral regions. This challenge can be partially mitigated by the judicious selection of the radionuclide. Optimal tissue penetration can assist in targeting distant hypoxic niches from blood vessels. However, this might also elevate the potential harm to surrounding healthy tissues.

Locoregional approach. The locoregional approach provides an alternative for GB treatment, allowing for the direct intratumoral administration of the radioconjugate of interest. To ensure homogeneous distribution, convection-enhanced delivery (CED) has proven effective. This method employs stereotactic insertion of catheters either directly into the tumor or the post-operative cavity (Fig. 17). These catheters are linked to pumps that provide a steady, positive-pressure micro-infusion of the chosen agent into the target area using bulk flow principle, typically at rates between 0.1 to 10 µl/min, as opposed to a single bolus injection[204,205]. By leveraging a pressure gradient instead of a concentration gradient, concerns regarding the molecular weight and diffusivity of the therapeutic agent are sidestepped. This ensures a homogeneous delivery of drugs in low concentrations to a designated brain area, enhancing its intratumoral volume of distribution. CED can impact areas spanning centimeters in brain tissue, while diffusion-reliant methods are limited to a millimeter scale[206].

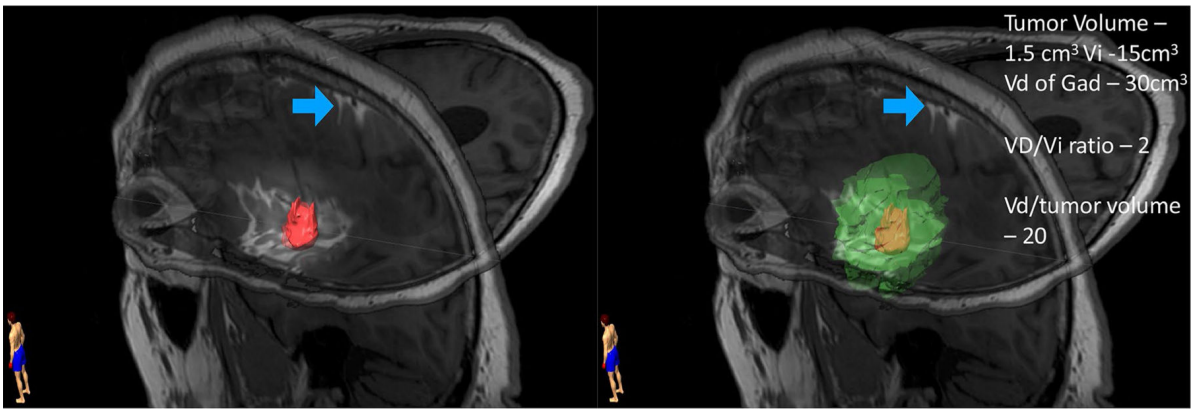

Fig. 17 | **T1-weighted MRI of intratumoral CED injection of gadolinium-labeled chemotherapy.** The injection volume is indicated in red. The distribution volume is indicated in green. Blue arrow indicates back flow in the subarachnoid space. (From D'Amico *et al.*, 2021)

3. Vectors and therapeutic targets

Passive approach. A passive vectorization strategy can be used for locoregional delivery in RNT. In this context, the vector serves to shield the radionuclide, thereby enhancing its intratumoral retention time. For instance, our research group has previously evaluated the therapeutic potential of lipid nanocapsules loaded with rhenium-188 (^{188}Re), a β^--emitter, administered *via* CED in an orthotopic rodent model of GB. This approach yielded a therapeutic efficacy of 83%. Numerous vectors are suitable for passive targeting strategies, including liposomes, micelles, magnetic nanoparticles, and gold nanoparticles. Notably, gold nanoparticles are appealing due to their ability to enhance the efficacy of radiotherapy. When

exposed to radiation, these particles can emit secondary low-energy electrons that increase the nearby delivered radiation dose, thereby amplifying the cytotoxic effect on tumor cells.

Targeted approach. Targeted radionuclide therapy for GB focuses on directing radionuclides precisely to tumor cells, minimizing impact on adjacent healthy tissues. Several vectors have been developed for this purpose. Among these, monoclonal antibodies and their derivates are designed to identify and bind to specific antigens prevalent on GB cells. Radiolabeled peptides, targeting overexpressed tumor receptors, offer another promising approach. Additionally, nanoparticles like gold or liposomes can be functionalized with ligands or antibodies to hone in on GB cells specifically. The great challenge of this approach is the relevant choice of the target, as GB exhibits a strong intratumoral heterogeneity and an evolutive TME directly influencing its expression of potential biomarkers.

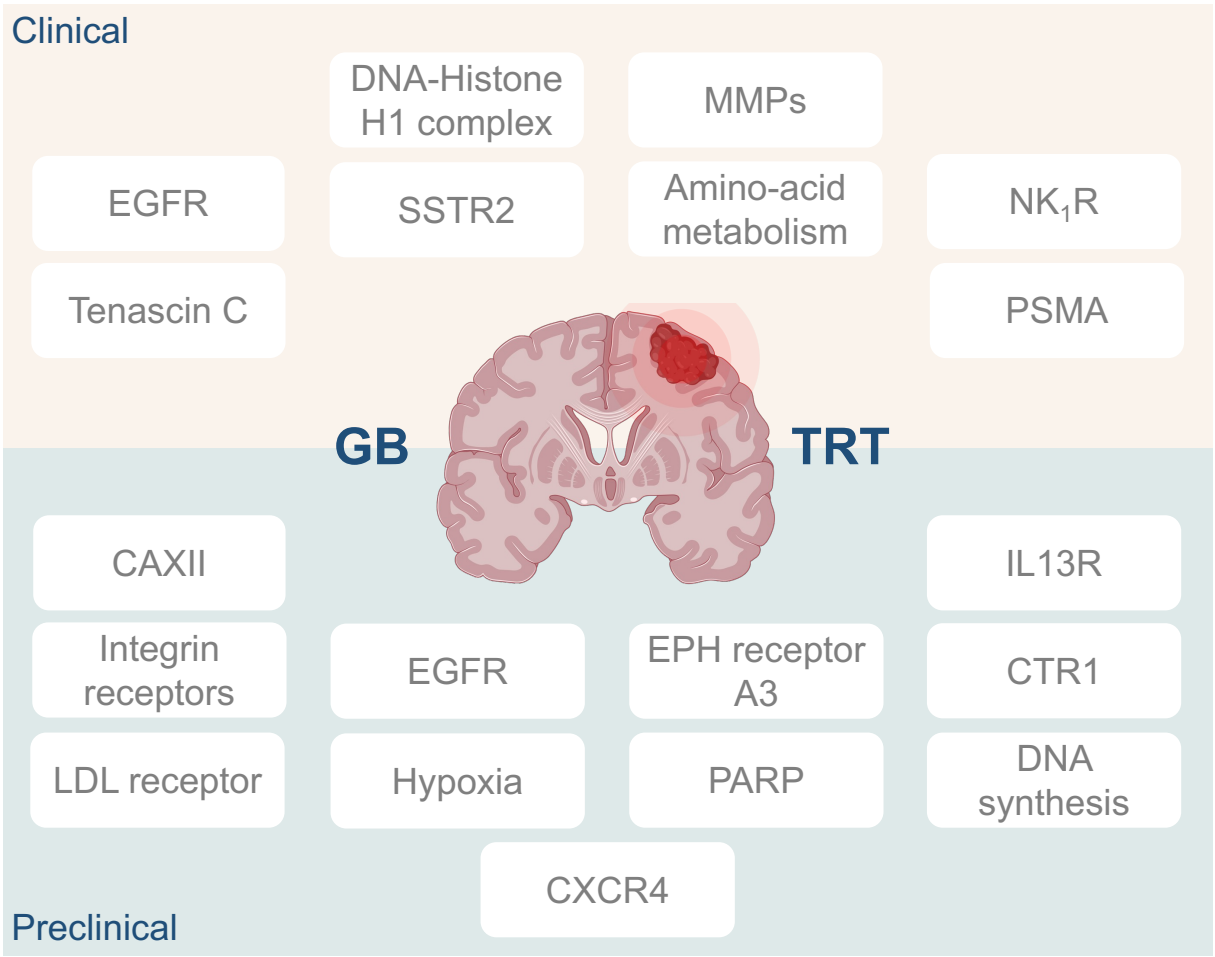

Fig. 18 | **Current clinical and preclinical studies on targeted radionuclide therapy for GB.** *GB: glioblastoma, TRT: targeted radionuclide therapy, EGFR: epidermal growth factor, SSTR2: somatostatin receptor 2, MMP: matrix metalloproteinase, NK_1R: neurokinin receptor, PSMA: prostate-specific membrane antigen, CAXII: carbonic anhydrase XII, LDL: low density liprotein, CXCR4: chemokine receptor 4, PARP: EPH: ephrin, IL13R: inerleukine-13 receptor, CTR1: copper transporter 1.* (Created with Biorender - biorender.com, adapted from Bolcaen *et al.*, 2021)[183]

New therapeutic targets. Numerous therapeutic targets have been explored both preclinically and clinically for GB therapy (Fig. 18) and some of them will be discussed in Chapter III. Various components of GB have been addressed, such as the ECM, DNA damage, or hypoxia.

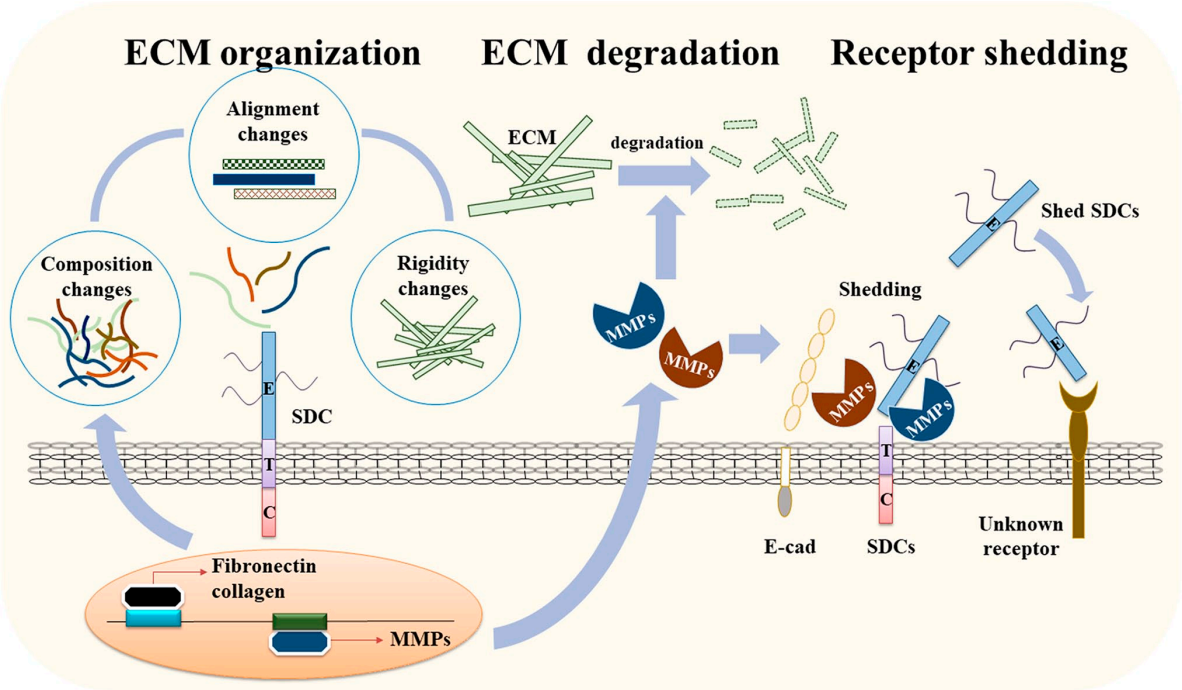

Fig. 19 | **Roles of syndecans in ECM alterations during cancer development.** Syndecan (SDC) influences the structure and properties of the extracellular matrix (ECM), including its stiffness, which is vital for cancer functions. SDC controls enzymes like matrix metalloproteinases (MMPs) that regulate the turnover of the ECM. It also attaches MMPs to the cell surface, activating them to break down the ECM and cell receptors. Additionally, released SDC affects cancer cell actions and processes like angiogenesis. (From Jang *et al*., 2020)[220]

One emerging target of particular interest within the GB landscape is the syndecan proteoglycan family, especially syndecan-1 (SDC1). SDC1 is a transmembrane heparan sulfate proteoglycan, characterized by its external domain adorned with heparan-sulfate and chondroitin-sulfate glycosaminoglycans. Serving as a co-receptor for an array of growth factors, chemokines, and cytokines, SDC1 is instrumental in modulating cellular processes like growth, proliferation, adhesion, and migration.[207]. In the brain, SDC1 is predominantly expressed in the choroid plexus and is involved adult neurogenesis by fostering the proliferation of NSCs in the SVZ[208]. Furthermore, SDC1 plays a crucial role in maintaining the integrity of the ECM. It directly orchestrates the expression and secretion of ECM components, thereby influencing its overall structure[209–211]. Specifically, SDC1 facilitates the fibronectin fibrillogenesis in ECM *via* integrin, and therefore regulates ECM fiber orientation[212] (Fig. 19).

Additionally, as a docking receptor, SDC1 has been identified in several studies to offer binding sites for MMP-2, -7, -9, and 13 on the cell surface[213]. Notably, in cancers like breast, colon, and pancreatic, SDC1 is recognized to bind MMP-7 on the cellular surface[214–216]. During the invasive progression of cancer, as MMPs degrade the ECM, they also cleave SDC1[217], which subsequently can bind to VEGFR2, promoting cellular invasion[218] (Fig. 19). Additionally, in breast cancer contexts, SDC1 plays a role in immune evasion by connecting VEGFR2 to VLA-4, thereby hindering LFA-1 mediated T cell migration[219].

In GB, elevated SDC1 expression is associated with a poor prognosis in GB[221]. SDC1 is a crucial bridge between tumor cells and their microenvironment, facilitating interactions with the ECM and a range of growth factors and cytokines. Therefore, it influences tumor proliferation[222], invasion[222,223], and angiogenesis[224]. In its shed form, SDC1 induces radioresistance of GB by promoting interactions between lysosomes and autophagosomes, thus ensuring a sustained autophagic activity in irradiated cells[225]. SDC1 may also modulate the EMT in GB, akin to its function in other malignancies, given its regulation by NF-κB[226] and its pronounced expression in the mesenchymal phenotype of GB[227]. Its translocation to the nucleus could inhibit the activation of pro-EMT genes, including NF-κB and TGF-β[228] . In addition to its multiple roles in the development of GB, its position at the interface between tumor cells and the ECM makes it an ideal target to disrupt the tumoral ecosystem of GB.

References

1. Thau, L., Reddy, V. & Singh, P. Anatomy, Central Nervous System. *BMJ* **1**, 478–478 (2022).
2. Atchley, T. J., Vukic, B., Vukic, M. & Walters, B. C. Review of Cerebrospinal Fluid Physiology and Dynamics: A Call for Medical Education Reform. *Neurosurgery* **91**, 1–7 (2022).
3. Ghannam, J. Y. & Kharazi, K. A. Al. Neuroanatomy, Cranial Meninges. *StatPearls* (2023).
4. Wu, D. *et al.* The blood–brain barrier: structure, regulation, and drug delivery. *Signal Transduction and Targeted Therapy 2023 8:1* **8**, 1–27 (2023).
5. Elwood, E., Lim, Z., Naveed, H. & Galea, I. The effect of systemic inflammation on human brain barrier function. *Brain Behav Immun* **62**, 35–40 (2017).
6. Iliff, J. J. *et al.* A paravascular pathway facilitates CSF flow through the brain parenchyma and the clearance of interstitial solutes, including amyloid β. *Sci Transl Med* **4**, (2012).
7. Mazzitelli, J. A. *et al.* Cerebrospinal fluid regulates skull bone marrow niches via direct access through dural channels. *Nature Neuroscience 2022 25:5* **25**, 555–560 (2022).
8. Louveau, A. *et al.* Structural and functional features of central nervous system lymphatic vessels. *Nature* **523**, 337–341 (2015).
9. Buckley, M. W. & McGavern, D. B. Immune dynamics in the CNS and its barriers during homeostasis and disease. *Immunol Rev* **306**, 58–75 (2022).
10. Merlini, A. *et al.* Distinct roles of the meningeal layers in CNS autoimmunity. *Nat Neurosci* **25**, 887–899 (2022).
11. Møllgård, K. *et al.* A mesothelium divides the subarachnoid space into functional compartments. *Science (1979)* **379**, 84–88 (2023).
12. Adeeb, N. *et al.* The pia mater: a comprehensive review of literature. *Childs Nerv Syst* **29**, 1803–1810 (2013).
13. Ge, W. P., Miyawaki, A., Gage, F. H., Jan, Y. N. & Jan, L. Y. Local generation of glia is a major astrocyte source in postnatal cortex. *Nature 2012 484:7394* **484**, 376–380 (2012).
14. Gage, F. H. & Temple, S. Neural Stem Cells: Generating and Regenerating the Brain. *Neuron* **80**, 588–601 (2013).
15. Doetsch, F., Caille, I., Lim, D. A., Garcia-Verdugo, J. M. & Alvarez-Buylla, A. Subventricular zone astrocytes are neural stem cells in the adult mammalian brain. *Cell* **97**, 703–716 (1999).
16. Gage, F. H. Mammalian Neural Stem Cells. *Science (1979)* **287**, 1433–1438 (2000).
17. Ludwig, P. E., Reddy, V. & Varacallo, M. Neuroanatomy, Neurons. *StatPearls* (2023).
18. Mercadante, A. A. & Tadi, P. Neuroanatomy, Gray Matter. *StatPearls* (2023).

19. Suárez-Solá, M. L. *et al.* Neurons in the white matter of the adult human neocortex. *Front Neuroanat* **3**, 682 (2009).
20. Fields, R. D. Change in the Brain's White Matter: The role of the brain's white matter in active learning and memory may be underestimated. *Science* **330**, 768 (2010).
21. Liu, Y. *et al.* Interactions of glial cells with neuronal synapses, from astrocytes to microglia and oligodendrocyte lineage cells. *Glia* **71**, 1383–1401 (2023).
22. Volterra, A. & Meldolesi, J. Astrocytes, from brain glue to communication elements: the revolution continues. *Nat Rev Neurosci* **6**, 626–640 (2005).
23. Alvarez, J. I., Katayama, T. & Prat, A. Glial influence on the blood brain barrier. *Glia* **61**, 1939–1958 (2013).
24. Abbott, N. J., Rönnbäck, L. & Hansson, E. Astrocyte-endothelial interactions at the blood-brain barrier. *Nat Rev Neurosci* **7**, 41–53 (2006).
25. Clark, I. C. *et al.* Barcoded viral tracing of single-cell interactions in central nervous system inflammation. *Science* **372**, (2021).
26. Lee, H. G., Wheeler, M. A. & Quintana, F. J. Function and therapeutic value of astrocytes in neurological diseases. *Nature Reviews Drug Discovery 2022 21:5* **21**, 339–358 (2022).
27. de Ceglia, R. *et al.* Specialized astrocytes mediate glutamatergic gliotransmission in the CNS. *Nature 2023* 1–10 (2023) doi:10.1038/s41586-023-06502-w.
28. Krämer-Albers, E. M. & Werner, H. B. Mechanisms of axonal support by oligodendrocyte-derived extracellular vesicles. *Nature Reviews Neuroscience 2023 24:8* **24**, 474–486 (2023).
29. Boccazzi, M. *et al.* The immune-inflammatory response of oligodendrocytes in a murine model of preterm white matter injury: the role of TLR3 activation. *Cell Death & Disease 2021 12:2* **12**, 1–12 (2021).
30. Yuen, T. J. *et al.* Oligodendrocyte-Encoded HIF Function Couples Postnatal Myelination and White Matter Angiogenesis. *Cell* **158**, 383–396 (2014).
31. Kirby, L. *et al.* Oligodendrocyte precursor cells present antigen and are cytotoxic targets in inflammatory demyelination. *Nature Communications 2019 10:1* **10**, 1–20 (2019).
32. Moura, D. M. S., Brennan, E. J., Brock, R. & Cocas, L. A. Neuron to Oligodendrocyte Precursor Cell Synapses: Protagonists in Oligodendrocyte Development and Myelination, and Targets for Therapeutics. *Front Neurosci* **15**, (2021).
33. Hammond, B. P., Manek, R., Kerr, B. J., Macauley, M. S. & Plemel, J. R. Regulation of microglia population dynamics throughout development, health, and disease. *Glia* **69**, 2771–2797 (2021).

34. Guo, S., Wang, H. & Yin, Y. Microglia Polarization From M1 to M2 in Neurodegenerative Diseases. *Front Aging Neurosci* **14**, 815347 (2022).
35. Healy, L. M., Zia, S. & Plemel, J. R. Towards a definition of microglia heterogeneity. *Communications Biology 2022 5:1* **5**, 1–6 (2022).
36. Wolburg, H. & Paulus, W. Choroid plexus: Biology and pathology. *Acta Neuropathol* **119**, 75–88 (2010).
37. Carpenter, S. J., McCarthy, L. E. & Borison, H. L. Electron microscopic study on the epiplexus (Kolmer) cells of the cat choroid plexus. *Zeitschrift für Zellforschung und Mikroskopische Anatomie* **110**, 471–486 (1970).
38. Quintela, T. *et al.* The choroid plexus harbors a circadian oscillator modulated by estrogens. *Chronobiol Int* **35**, 270–279 (2018).
39. Spector, R., Keep, R. F., Robert Snodgrass, S., Smith, Q. R. & Johanson, C. E. A balanced view of choroid plexus structure and function: Focus on adult humans. *Exp Neurol* **267**, 78–86 (2015).
40. Barisano, G. *et al.* Blood–brain barrier link to human cognitive impairment and Alzheimer's disease. *Nature Cardiovascular Research 2022 1:2* **1**, 108–115 (2022).
41. Betz, A. L., Firth, J. A. & Goldstein, G. W. Polarity of the blood-brain barrier: distribution of enzymes between the luminal and antiluminal membranes of brain capillary endothelial cells. *Brain Res* **192**, 17–28 (1980).
42. Sengillo, J. D. *et al.* Deficiency in mural vascular cells coincides with blood-brain barrier disruption in Alzheimer's disease. *Brain Pathol* **23**, 303–310 (2013).
43. Zhao, Z., Nelson, A. R., Betsholtz, C. & Zlokovic, B. V. Establishment and Dysfunction of the Blood-Brain Barrier. *Cell* **163**, 1064–1078 (2015).
44. Ostrom, Q. T. *et al.* CBTRUS Statistical Report: Primary Brain and Other Central Nervous System Tumors Diagnosed in the United States in 2015–2019. *Neuro Oncol* **24**, v1–v95 (2022).
45. Fabbro-Peray, P. *et al.* Association of patterns of care, prognostic factors, and use of radiotherapy–temozolomide therapy with survival in patients with newly diagnosed glioblastoma: a French national population-based study. *J Neurooncol* **142**, 91–101 (2019).
46. Davis, F. G. *et al.* Glioblastoma incidence rate trends in Canada and the United States compared with England, 1995-2015. *Neuro Oncol* **22**, 301–302 (2020).
47. Louis, D. N. *et al.* The 2007 WHO Classification of Tumours of the Central Nervous System. *Acta Neuropathol* **114**, 97 (2007).
48. Weller, M. *et al.* EANO guidelines on the diagnosis and treatment of diffuse gliomas of adulthood. *Nat Rev Clin Oncol* **18**, 170–186 (2021).

49. Louis, D. N. *et al.* The 2016 World Health Organization Classification of Tumors of the Central Nervous System: a summary. *Acta Neuropathol* **131**, 803–820 (2016).
50. Louis, D. N. *et al.* The 2021 WHO Classification of Tumors of the Central Nervous System: a summary. *Neuro Oncol* **23**, 1231–1251 (2021).
51. Olympios, N. *et al.* TERT Promoter Alterations in Glioblastoma: A Systematic Review. *Cancers (Basel)* **13**, 1–19 (2021).
52. Kim, N. W. *et al.* Specific association of human telomerase activity with immortal cells and cancer. *Science* **266**, 2011–2015 (1994).
53. Giunco, S. *et al.* Prognostic role and interaction of TERT promoter status, telomere length and MGMT promoter methylation in newly diagnosed IDH wild-type glioblastoma patients. *ESMO Open* **8**, (2023).
54. Oprita, A. *et al.* Updated Insights on EGFR Signaling Pathways in Glioma. *Int J Mol Sci* **22**, 1–21 (2021).
55. Zhang, X., Gureasko, J., Shen, K., Cole, P. A. & Kuriyan, J. An allosteric mechanism for activation of the kinase domain of epidermal growth factor receptor. *Cell* **125**, 1137–1149 (2006).
56. An, Z., Aksoy, O., Zheng, T., Fan, Q. W. & Weiss, W. A. Epidermal growth factor receptor and EGFRvIII in glioblastoma: signaling pathways and targeted therapies. *Oncogene* **37**, 1561–1575 (2018).
57. Thorpe, L. M., Yuzugullu, H. & Zhao, J. J. PI3K in cancer: divergent roles of isoforms, modes of activation and therapeutic targeting. *Nat Rev Cancer* **15**, 7–24 (2015).
58. Deschênes-Simard, X., Kottakis, F., Meloche, S. & Ferbeyre, G. ERKs in cancer: friends or foes? *Cancer Res* **74**, 412–419 (2014).
59. Li, X. P., Guo, Z. Q., Wang, B. F. & Zhao, M. EGFR alterations in glioblastoma play a role in antitumor immunity regulation. *Front Oncol* **13**, 1236246 (2023).
60. Hegi, M. E. *et al.* MGMT gene silencing and benefit from temozolomide in glioblastoma. *N Engl J Med* **352**, 997–1003 (2005).
61. De Silva, M. I., Stringer, B. W. & Bardy, C. Neuronal and tumourigenic boundaries of glioblastoma plasticity. *Trends Cancer* **9**, 223–236 (2023).
62. Verhaak, R. G. W. *et al.* Integrated Genomic Analysis Identifies Clinically Relevant Subtypes of Glioblastoma Characterized by Abnormalities in PDGFRA, IDH1, EGFR, and NF1. *Cancer Cell* **17**, 98–110 (2010).
63. Wang, Q. *et al.* Tumor Evolution of Glioma-Intrinsic Gene Expression Subtypes Associates with Immunological Changes in the Microenvironment. *Cancer Cell* **32**, 42-56.e6 (2017).

64. Neftel, C. *et al.* An Integrative Model of Cellular States, Plasticity, and Genetics for Glioblastoma. *Cell* **178**, 835-849.e21 (2019).
65. Phillips, H. S. *et al.* Molecular subclasses of high-grade glioma predict prognosis, delineate a pattern of disease progression, and resemble stages in neurogenesis. *Cancer Cell* **9**, 157–173 (2006).
66. Garofano, L. *et al.* Pathway-based classification of glioblastoma uncovers a mitochondrial subtype with therapeutic vulnerabilities. *Nat Cancer* **2**, 141–156 (2021).
67. Prager, B. C., Bhargava, S., Mahadev, V., Hubert, C. G. & Rich, J. N. Glioblastoma Stem Cells: Driving Resilience through Chaos. *Trends Cancer* **6**, 223–235 (2020).
68. Park, N. I. *et al.* ASCL1 Reorganizes Chromatin to Direct Neuronal Fate and Suppress Tumorigenicity of Glioblastoma Stem Cells. *Cell Stem Cell* **21**, 209-224.e7 (2017).
69. Perrin, S. L. *et al.* Glioblastoma heterogeneity and the tumour microenvironment: implications for preclinical research and development of new treatments. *Biochem Soc Trans* **47**, 625–638 (2019).
70. Chen, J. *et al.* The pathological structure of the perivascular niche in different microvascular patterns of glioblastoma. *PLoS One* **12**, e0182183 (2017).
71. Ahir, B. K., Engelhard, H. H. & Lakka, S. S. Tumor Development and Angiogenesis in Adult Brain Tumor: Glioblastoma. *Molecular Neurobiology 2020 57:5* **57**, 2461–2478 (2020).
72. De Bock, K., Cauwenberghs, S. & Carmeliet, P. Vessel abnormalization: another hallmark of cancer?: Molecular mechanisms and therapeutic implications. *Curr Opin Genet Dev* **21**, 73–79 (2011).
73. Azzi, S., Hebda, J. K. & Gavard, J. Vascular permeability and drug delivery in cancers. *Front Oncol* **3 AUG**, 57195 (2013).
74. Hardee, M. E. & Zagzag, D. Mechanisms of Glioma-Associated Neovascularization. *Am J Pathol* **181**, 1126–1141 (2012).
75. Folkins, C. *et al.* Glioma tumor stem-like cells promote tumor angiogenesis and vasculogenesis via vascular endothelial growth factor and stromal-derived factor 1. *Cancer Res* **69**, 7243–7251 (2009).
76. Folberg, R. & Maniotis, A. J. Vasculogenic mimicry. *APMIS* **112**, 508–525 (2004).
77. Tso, C. L. *et al.* Primary Glioblastomas Express Mesenchymal Stem-Like Properties. *Molecular Cancer Research* **4**, 607–619 (2006).
78. Baker, G. J. *et al.* Mechanisms of Glioma Formation: Iterative Perivascular Glioma Growth and Invasion Leads to Tumor Progression, VEGF-Independent Vascularization, and Resistance to Antiangiogenic Therapy. *Neoplasia* **16**, 543–561 (2014).

79. Brat, D. J., Bellail, A. C. & Van Meir, E. G. The role of interleukin-8 and its receptors in gliomagenesis and tumoral angiogenesis. *Neuro Oncol* **7**, 122–133 (2005).
80. Goswami, S., Gupta, A. & Sharma, S. K. Interleukin-6-Mediated Autocrine Growth Promotion in Human Glioblastoma Multiforme Cell Line U87MG. *J Neurochem* **71**, 1837–1845 (1998).
81. Liddelow, S. A. *et al.* Neurotoxic reactive astrocytes are induced by activated microglia. *Nature* **541**, 481–487 (2017).
82. Infanger, D. W. *et al.* Glioblastoma stem cells are regulated by interleukin-8 signaling in a tumoral perivascular niche. *Cancer Res* **73**, 7079–7089 (2013).
83. Yoshida, S. *et al.* Involvement of interleukin-8, vascular endothelial growth factor, and basic fibroblast growth factor in tumor necrosis factor alpha-dependent angiogenesis. *Mol Cell Biol* **17**, 4015–4023 (1997).
84. Rong, Y., Durden, D. L., Van Meir, E. G. & Brat, D. J. 'Pseudopalisading' necrosis in glioblastoma: a familiar morphologic feature that links vascular pathology, hypoxia, and angiogenesis. *J Neuropathol Exp Neurol* **65**, 529–539 (2006).
85. Majmundar, A. J., Wong, W. J. & Simon, M. C. Hypoxia inducible factors and the response to hypoxic stress. *Mol Cell* **40**, 294 (2010).
86. Mimeault, M. & Batra, S. K. Hypoxia-inducing factors as master regulators of stemness properties and altered metabolism of cancer- and metastasis-initiating cells. *J Cell Mol Med* **17**, 30 (2013).
87. Sattiraju, A. *et al.* Hypoxic niches attract and sequester tumor-associated macrophages and cytotoxic T cells and reprogram them for immunosuppression. *Immunity* **56**, 1825-1843.e6 (2023).
88. Farin, A. *et al.* Transplanted glioma cells migrate and proliferate on host brain vasculature: a dynamic analysis. *Glia* **53**, 799–808 (2006).
89. Byrne, K. M. *et al.* Bistability in the Rac1, PAK, and RhoA Signaling Network Drives Actin Cytoskeleton Dynamics and Cell Motility Switches. *Cell Syst* **2**, 38–48 (2016).
90. Ulrich, T. A., De Juan Pardo, E. M. & Kumar, S. The mechanical rigidity of the extracellular matrix regulates the structure, motility, and proliferation of glioma cells. *Cancer Res* **69**, 4167–4174 (2009).
91. Marino, S. *et al.* The Extracellular Matrix in Glioblastomas: A Glance at Its Structural Modifications in Shaping the Tumoral Microenvironment—A Systematic Review. *Cancers 2023, Vol. 15, Page 1879* **15**, 1879 (2023).
92. Cha, J., Kang, S. G. & Kim, P. Strategies of Mesenchymal Invasion of Patient-derived Brain Tumors: Microenvironmental Adaptation. *Sci Rep* **6**, (2016).

93. Bastola, S. *et al.* Glioma-initiating cells at tumor edge gain signals from tumor core cells to promote their malignancy. *Nat Commun* **11**, (2020).
94. Watkins, S. *et al.* Disruption of astrocyte-vascular coupling and the blood-brain barrier by invading glioma cells. *Nat Commun* **5**, (2014).
95. Charles, N. *et al.* Perivascular Nitric Oxide Activates Notch Signaling and Promotes Stem-like Character in PDGF-Induced Glioma Cells. *Cell Stem Cell* **6**, 141–152 (2010).
96. Liu, D. *et al.* Tie2/TEK Modulates the Interaction of Glioma and Brain Tumor Stem Cells with Endothelial Cells and Promotes an Invasive Phenotype. *Oncotarget* **1**, 700–709 (2010).
97. Hambardzumyan, D. & Bergers, G. Glioblastoma: Defining Tumor Niches. *Trends Cancer* **1**, 252–265 (2015).
98. Larjavaara, S. *et al.* Incidence of gliomas by anatomic location. *Neuro Oncol* **9**, 319 (2007).
99. MacKintosh, C. *et al.* Does location matter? Characterisation of the anatomic locations, molecular profiles, and clinical features of gliomas. *Neurol Neurochir Pol* **54**, 456–465 (2020).
100. Schag, C. C., Heinrich, R. L. & Ganz, P. A. Karnofsky performance status revisited: reliability, validity, and guidelines. *J Clin Oncol* **2**, 187–193 (1984).
101. Sheline, G. E. Radiation therapy of brain tumors. *Cancer* **39**, 873–881 (1977).
102. Walker, M. D., Strike, T. A. & Sheline, G. E. An analysis of dose-effect relationship in the radiotherapy of malignant gliomas. *Int J Radiat Oncol Biol Phys* **5**, 1725–1731 (1979).
103. Stupp, R. *et al.* Radiotherapy plus concomitant and adjuvant temozolomide for glioblastoma. *N Engl J Med* **352**, 987–996 (2005).
104. Stupp, R. *et al.* Effects of radiotherapy with concomitant and adjuvant temozolomide versus radiotherapy alone on survival in glioblastoma in a randomised phase III study: 5-year analysis of the EORTC-NCIC trial. *Lancet Oncol* **10**, 459–466 (2009).
105. Perry, J. R. *et al.* Short-Course Radiation plus Temozolomide in Elderly Patients with Glioblastoma. *N Engl J Med* **376**, 1027–1037 (2017).
106. Batistella, G. N. de R. *et al.* Approaching glioblastoma during COVID-19 pandemic: current recommendations and considerations in Brazil. *Arq Neuropsiquiatr* **79**, 167–172 (2021).
107. Brown, T. J. *et al.* Association of the Extent of Resection With Survival in Glioblastoma: A Systematic Review and Meta-analysis. *JAMA Oncol* **2**, 1460–1469 (2016).
108. Kotrotsou, A. *et al.* Multi-center study finds postoperative residual non-enhancing component of glioblastoma as a new determinant of patient outcome. *J Neurooncol* **139**, 125–133 (2018).
109. Hadjipanayis, C. G. & Stummer, W. 5-ALA and FDA approval for glioma surgery. *J Neurooncol* **141**, 479–486 (2019).

110. Picart, T. *et al.* Is fluorescence-guided surgery with 5-ala in eloquent areas for malignant gliomas a reasonable and useful technique? *Neurochirurgie* **63**, 189–196 (2017).
111. Sánchez-Ortega, J. F., Aguas-Valiente, J., Sota-Ochoa, P. & Calatayud-Pérez, J. Glioblastoma with primitive neuronal component: A case report and considerations of fluorescence-guided surgery. *Surg Neurol Int* **11**, (2020).
112. Smith, E. J., Gohil, K., Thompson, C. M., Naik, A. & Hassaneen, W. Fluorescein-Guided Resection of High Grade Gliomas: A Meta-Analysis. *World Neurosurg* **155**, 181-188.e7 (2021).
113. Acerbi, F. *et al.* Fluorescein-guided surgery for resection of high-grade gliomas: A multicentric prospective phase II study (FLUOGLIO). *Clinical Cancer Research* **24**, 52–61 (2018).
114. Della Puppa, A., Munari, M., Gardiman, M. P. & Volpin, F. Combined Fluorescence Using 5-Aminolevulinic Acid and Fluorescein Sodium at Glioblastoma Border: Intraoperative Findings and Histopathologic Data About 3 Newly Diagnosed Consecutive Cases. *World Neurosurg* **122**, e856–e863 (2019).
115. Sales, A. H. A. *et al.* Surgical Treatment of Glioblastoma: State-of-the-Art and Future Trends. *J Clin Med* **11**, (2022).
116. Ottenhausen, M., Krieg, S. M., Meyer, B. & Ringel, F. Functional preoperative and intraoperative mapping and monitoring: increasing safety and efficacy in glioma surgery. *Neurosurg Focus* **38**, E3 (2015).
117. Hervey-Jumper, S. L. *et al.* Awake craniotomy to maximize glioma resection: methods and technical nuances over a 27-year period. *J Neurosurg* **123**, 325–339 (2015).
118. Bajunaid, K. M. & Ajlan, A. M. Awake craniotomy. *Neurosciences Journal* **20**, 248–252 (2015).
119. Agarwal, S., Sane, R., Oberoi, R., Ohlfest, J. R. & Elmquist, W. F. Delivery of molecularly targeted therapy to malignant glioma, a disease of the whole brain. *Expert Rev Mol Med* **13**, (2011).
120. Knudsen, A. M. *et al.* Surgical resection of glioblastomas induces pleiotrophin-mediated self-renewal of glioblastoma stem cells in recurrent tumors. *Neuro Oncol* **24**, 1074–1087 (2022).
121. Arora, A. & Somasundaram, K. Glioblastoma vs temozolomide: can the red queen race be won? *Cancer Biol Ther* **20**, 1083 (2019).
122. Hegi, M. E. *et al.* MGMT Gene Silencing and Benefit from Temozolomide in Glioblastoma . *New England Journal of Medicine* **352**, 997–1003 (2005).
123. Sarkaria, J. N. *et al.* Is the blood–brain barrier really disrupted in all glioblastomas? A critical assessment of existing clinical data. *Neuro Oncol* **20**, 184 (2018).

124. Stéphanou, A. & Ballesta, A. pH as a potential therapeutic target to improve temozolomide antitumor efficacy : A mechanistic modeling study. *Pharmacol Res Perspect* **7**, (2019).
125. Martinho, O. *et al.* In vitro and in vivo studies of temozolomide loading in zeolite structures as drug delivery systems for glioblastoma. *RSC Adv* **5**, 28219–28227 (2015).
126. Zou, Z., Chang, H., Li, H. & Wang, S. Induction of reactive oxygen species: an emerging approach for cancer therapy. *Apoptosis* **22**, 1321–1335 (2017).
127. Leach, J. K., Tuyle, G. Van, Lin, P.-S., Schmidt-Ullrich, R. & Mikkelsen, R. B. Ionizing Radiation-induced, Mitochondria-dependent Generation of Reactive Oxygen/Nitrogen 1. *Cancer Res* **61**, 3894–3901 (2001).
128. Tulard, A., Hoffschir, F., De Boisferon, F. H., Luccioni, C. & Bravard, A. Persistent oxidative stress after ionizing radiation is involved in inherited radiosensitivity. *Free Radic Biol Med* **35**, 68–77 (2003).
129. Kam, W. W. Y. & Banati, R. B. Effects of ionizing radiation on mitochondria. *Free Radic Biol Med* **65**, 607–619 (2013).
130. Bhuyan, K. C. & Bhuyan, D. K. Superoxide dismutase of the eye Relative functions of superoxide dismutase and catalase in protecting the ocular lens from oxidative damage. *Biochimica et Biophysica Acta (BBA) - General Subjects* **542**, 28–38 (1978).
131. Glorieux, C. & Calderon, P. B. Catalase, a remarkable enzyme: Targeting the oldest antioxidant enzyme to find a new cancer treatment approach. *Biol Chem* **398**, 1095–1108 (2017).
132. Mavragani, I. V. *et al.* Complex DNA Damage: A Route to Radiation-Induced Genomic Instability and Carcinogenesis. *Cancers (Basel)* **9**, (2017).
133. Yi, G. *et al.* DNA polymerase θ-mediated repair of high LET radiation-induced complex DNA double-strand breaks. *Nucleic Acids Res* **51**, 2257–2269 (2023).
134. Blackford, A. N. & Jackson, S. P. ATM, ATR, and DNA-PK: The Trinity at the Heart of the DNA Damage Response. *Mol Cell* **66**, 801–817 (2017).
135. Thompson, L. H. Recognition, signaling, and repair of DNA double-strand breaks produced by ionizing radiation in mammalian cells: The molecular choreography. *Mutation Research/Reviews in Mutation Research* **751**, 158–246 (2012).
136. Weinberg, W. C. & Denning, M. F. p21WAF1 Control of Epithelial Cell Cycle and Cell Fate. *http://dx.doi.org/10.1177/154411130201300603* **13**, 453–464 (2002).
137. Kuribayashi, K., Finnberg, N., Jeffers, J. R., Zambetti, G. P. & El-Deiry, W. S. The relative contribution of pro-apoptotic p53-target genes in the triggering of apoptosis following DNA damage in vitro and in vivo. *Cell Cycle* **10**, 2380–2389 (2011).

138. Zhao, L. *et al.* The Determinant of DNA Repair Pathway Choices in Ionising Radiation-Induced DNA Double-Strand Breaks. *Biomed Res Int* **2020**, (2020).
139. Rzeszowska-Wolny, J., Przybyszewski, W. M. & Widel, M. Ionizing radiation-induced bystander effects, potential targets for modulation of radiotherapy. *Eur J Pharmacol* **625**, 156–164 (2009).
140. Prise, K. M. & O'Sullivan, J. M. Radiation-induced bystander signalling in cancer therapy. *Nat Rev Cancer* **9**, 351 (2009).
141. Herrera, F. G., Bourhis, J. & Coukos, G. Radiotherapy combination opportunities leveraging immunity for the next oncology practice. *CA Cancer J Clin* **67**, 65–85 (2017).
142. Al-Mayah, A. H. J., Irons, S. L., Pink, R. C., Carter, D. R. F. & Kadhim, M. A. Possible Role of Exosomes Containing RNA in Mediating Nontargeted Effect of Ionizing Radiation. *https://doi.org/10.1667/RR2868.1* **177**, 539–545 (2012).
143. Kumar Jella, K. *et al.* Exosomes Are Involved in Mediating Radiation Induced Bystander Signaling in Human Keratinocyte Cells. *https://doi.org/10.1667/RR13337.1* **181**, 138–145 (2014).
144. Widel, M., Przybyszewski, W. M., Cieslar-Pobuda, A., Saenko, Y. V. & Rzeszowska-Wolny, J. Bystander normal human fibroblasts reduce damage response in radiation targeted cancer cells through intercellular ROS level modulation. *Mutat Res* **731**, 117–124 (2012).
145. Daguenet, E. *et al.* Radiation-induced bystander and abscopal effects: important lessons from preclinical models. *British Journal of Cancer 2020 123:3* **123**, 339–348 (2020).
146. Lugade, A. A. *et al.* Local radiation therapy of B16 melanoma tumors increases the generation of tumor antigen-specific effector cells that traffic to the tumor. *J Immunol* **174**, 7516–7523 (2005).
147. Reits, E. A. *et al.* Radiation modulates the peptide repertoire, enhances MHC class I expression, and induces successful antitumor immunotherapy. *J Exp Med* **203**, 1259–1271 (2006).
148. Garnett, C. T. *et al.* Sublethal irradiation of human tumor cells modulates phenotype resulting in enhanced killing by cytotoxic T lymphocytes. *Cancer Res* **64**, 7985–7994 (2004).
149. Niyazi, M. *et al.* ESTRO-EANO guideline on target delineation and radiotherapy details for glioblastoma. *Radiother Oncol* **184**, (2023).
150. Wen, P. Y. *et al.* Updated response assessment criteria for high-grade gliomas: response assessment in neuro-oncology working group. *J Clin Oncol* **28**, 1963–1972 (2010).
151. Li, M. *et al.* T2/FLAIR Abnormity Could be the Sign of Glioblastoma Dissemination. *Front Neurol* **13**, 819216 (2022).
152. Goldman, L. W. Principles of CT and CT Technology. *J Nucl Med Technol* **35**, 115–128 (2007).

153. Omami, G., Tamimi, D. & Branstetter, B. F. Basic principles and applications of 18F-FDG-PET/CT in oral and maxillofacial imaging: A pictorial essay. *Imaging Sci Dent* **44**, 325 (2014).
154. Sharma, R. *et al.* A comparison study of 11C-methionine and 18F-fluorodeoxyglucose positron emission tomography-computed tomography scans in evaluation of patients with recurrent brain tumors. *Indian J Nucl Med* **31**, 93 (2016).
155. Glaudemans, A. W. J. M. *et al.* Value of 11C-methionine PET in imaging brain tumours and metastases. *Eur J Nucl Med Mol Imaging* **40**, 615–635 (2013).
156. Galldiks, N., Lohmann, P., Cicone, F. & Langen, K. J. FET and FDOPA PET Imaging in Glioma. *Glioma Imaging: Physiologic, Metabolic, and Molecular Approaches* 211–221 (2019) doi:10.1007/978-3-030-27359-0_13/COVER.
157. Roach, J. R., Plaha, P., McGowan, D. R. & Higgins, G. S. The role of [18F]fluorodopa positron emission tomography in grading of gliomas. *J Neurooncol* **160**, 577–589 (2022).
158. Lewitzki, V. *et al.* Accelerated hyperfractionated radiochemotherapy with temozolomide is equivalent to normofractionated radiochemotherapy in a retrospective analysis of patients with glioblastoma. *Radiat Oncol* **14**, (2019).
159. Perlow, H. K. *et al.* Dose-escalated accelerated hypofractionation for elderly or frail patients with a newly diagnosed glioblastoma. *J Neurooncol* **156**, 399–406 (2022).
160. Kim, N. *et al.* Clinical Outcomes of Moderately Hypofractionated Concurrent Chemoradiotherapy for Newly Diagnosed Glioblastoma. *Yonsei Med J* **64**, 94–103 (2023).
161. Koka, K., Verma, A., Dwarakanath, B. S. & Papineni, R. V. L. Technological Advancements in External Beam Radiation Therapy (EBRT): An Indispensable Tool for Cancer Treatment. *Cancer Manag Res* **14**, 1421 (2022).
162. Scaringi, C., Agolli, L. & Minniti, G. Technical Advances in Radiation Therapy for Brain Tumors. *Anticancer Res* **38**, 6041–6045 (2018).
163. Redmond, K. J. & Mehta, M. Stereotactic Radiosurgery for Glioblastoma. *Cureus* **7**, (2015).
164. Mang, T. S. Lasers and light sources for PDT: past, present and future. *Photodiagnosis Photodyn Ther* **1**, 43–48 (2004).
165. McNicholas, K., MacGregor, M. N. & Gleadle, J. M. In order for the light to shine so brightly, the darkness must be present-why do cancers fluoresce with 5-aminolaevulinic acid? *Br J Cancer* **121**, 631–639 (2019).
166. Mazurek, M., Szczepanek, D., Orzyłowska, A. & Rola, R. Analysis of Factors Affecting 5-ALA Fluorescence Intensity in Visualizing Glial Tumor Cells-Literature Review. *Int J Mol Sci* **23**, (2022).

167. Li, L., Yuan, Y. & Zuo, Y. A review of the impact of FLASH radiotherapy on the central nervous system and glioma. *Radiat Med Prot* **3**, 208–212 (2022).
168. Montay-Gruel, P. *et al.* Hypo-fractionated FLASH-RT: An effective treatment against glioblastoma that significantly reduces neurocognitive side effects in mice. *Clin Cancer Res* **27**, 775 (2021).
169. Ekhator, C. *et al.* GammaTile: Comprehensive Review of a Novel Radioactive Intraoperative Seed-Loading Device for the Treatment of Brain Tumors. *Cureus* **14**, (2022).
170. Covello, K. L. *et al.* HIF-2α regulates Oct-4: effects of hypoxia on stem cell function, embryonic development, and tumor growth. *Genes Dev* **20**, 557–570 (2006).
171. Bouquet, F. *et al.* A DNA-dependent stress response involving DNA-PK occurs in hypoxic cells and contributes to cellular adaptation to hypoxia. *J Cell Sci* **124**, 1943–1951 (2011).
172. Bindra, R. S. *et al.* Down-Regulation of Rad51 and Decreased Homologous Recombination in Hypoxic Cancer Cells. *Mol Cell Biol* **24**, 8504 (2004).
173. Marampon, F. *et al.* Hypoxia sustains glioblastoma radioresistance through ERKs/DNA-PKcs/HIF- 1α functional interplay. *Int J Oncol* **45**, 2121–2131 (2014).
174. Burko, P. *et al.* Molecular Pathways Implicated in Radioresistance of Glioblastoma Multiforme: What Is the Role of Extracellular Vesicles? *International Journal of Molecular Sciences 2023, Vol. 24, Page 4883* **24**, 4883 (2023).
175. Levine, A. J. & Puzio-Kuter, A. M. The Control of the Metabolic Switch in Cancers by Oncogenes and Tumor Suppressor Genes. *Science (1979)* **330**, 1340–1344 (2010).
176. Bailleul, J. *et al.* PKM2 rewires glucose metabolism during radiation therapy to promote an antioxidant response and glioblastoma radioresistance. *Neuro Oncol* (2023) doi:10.1093/NEUONC/NOAD103.
177. Calvert, A. E. *et al.* Cancer-Associated IDH1 Promotes Growth and Resistance to Targeted Therapies in the Absence of Mutation. *Cell Rep* **19**, 1858–1873 (2017).
178. You, W. C. *et al.* Mitochondrial protein ATPase family, AAA domain containing 3A correlates with radioresistance in glioblastoma. *Neuro Oncol* **15**, 1342–1352 (2013).
179. Kim, J. *et al.* NRBF2-mediated autophagy contributes to metabolite replenishment and radioresistance in glioblastoma. *Experimental & Molecular Medicine 2022 54:11* **54**, 1872–1885 (2022).
180. Bao, S. *et al.* Glioma stem cells promote radioresistance by preferential activation of the DNA damage response. *Nature* **444**, 756–760 (2006).

181. Castellino, R. C. & Durden, D. L. Mechanisms of disease: the PI3K-Akt-PTEN signaling node--an intercept point for the control of angiogenesis in brain tumors. *Nat Clin Pract Neurol* **3**, 682–693 (2007).

182. Chang, L. *et al.* Cancer stem cells and signaling pathways in radioresistance. *Oncotarget* **7**, 11002–11017 (2016).

183. Bolcaen, J. *et al.* A perspective on the radiopharmaceutical requirements for imaging and therapy of glioblastoma. *Issue 16 Theranostics* **11**, 7911–7947 (2021).

184. Hunter, N. & Muirhead, C. R. Review of relative biological effectiveness dependence on linear energy transfer for low-LET radiations. *Journal of Radiological Protection* **29**, 5 (2009).

185. Bigner, D. D. *et al.* Phase I studies of treatment of malignant gliomas and neoplastic meningitis with 131I-radiolabeled monoclonal antibodies anti-tenascin 81C6 and anti-chondroitin proteoglycan sulfate Me1-14 F (ab')2--a preliminary report. *J Neurooncol* **24**, 109–122 (1995).

186. Reardon, D. A. *et al.* Phase II trial of murine (131)I-labeled antitenascin monoclonal antibody 81C6 administered into surgically created resection cavities of patients with newly diagnosed malignant gliomas. *J Clin Oncol* **20**, 1389–1397 (2002).

187. Cokgor, I. *et al.* Phase I trial results of iodine-131-labeled antitenascin monoclonal antibody 81C6 treatment of patients with newly diagnosed malignant gliomas. *J Clin Oncol* **18**, 3862–3872 (2000).

188. Grana, C. *et al.* Pretargeted adjuvant radioimmunotherapy with Yttrium-90-biotin in malignant glioma patients: A pilot study. *Br J Cancer* **86**, 207 (2002).

189. Casacó Parada, A. *et al.* Phase I single-dose study of intracavitary-administered Nimotuzumab labeled with 188 Re in adult recurrent high-grade glioma. *Cancer Biol Ther* **7**, 333–339 (2008).

190. Grillo-López, A. J. Zevalin: the first radioimmunotherapy approved for the treatment of lymphoma. *Expert Rev Anticancer Ther* **2**, 485–493 (2002).

191. Friedberg, J. W. & Fisher, R. I. Iodine-131 tositumomab (Bexxar®): radioimmunoconjugate therapy for indolent and transformed B-cell non-Hodgkin's lymphoma. *Expert Rev Anticancer Ther* **4**, 18–26 (2004).

192. Strosberg, J. *et al.* Health-Related Quality of Life in Patients With Progressive Midgut Neuroendocrine Tumors Treated With 177Lu-Dotatate in the Phase III NETTER-1 Trial. *J Clin Oncol* **36**, 2578–2584 (2018).

193. Sgouros, G., Bodei, L., McDevitt, M. R. & Nedrow, J. R. Radiopharmaceutical therapy in cancer: clinical advances and challenges. *Nature Reviews Drug Discovery 2020 19:9* **19**, 589–608 (2020).

194. Wulbrand, C. *et al.* Alpha-particle emitting 213Bi-anti-EGFR immunoconjugates eradicate tumor cells independent of oxygenation. *PLoS One* **8**, (2013).

195. Parker, C. *et al.* Alpha emitter radium-223 and survival in metastatic prostate cancer. *N Engl J Med* **369**, 213–223 (2013).

196. Kneifel, S. *et al.* Local targeting of malignant gliomas by the diffusible peptidic vector 1,4,7,10-tetraazacyclododecane-1-glutaric acid-4,7,10-triacetic acid-substance p. *Clin Cancer Res* **12**, 3843–3850 (2006).

197. Cordier, D. *et al.* Targeted alpha-radionuclide therapy of functionally critically located gliomas with 213Bi-DOTA-[Thi8,Met(O2)11]-substance P: a pilot trial. *Eur J Nucl Med Mol Imaging* **37**, 1335–1344 (2010).

198. Zalutsky, M. R. *et al.* Clinical experience with alpha-particle emitting 211At: treatment of recurrent brain tumor patients with 211At-labeled chimeric antitenascin monoclonal antibody 81C6. *J Nucl Med* **49**, 30–38 (2008).

199. Krolicki, L. *et al.* Prolonged survival in secondary glioblastoma following local injection of targeted alpha therapy with 213Bi-substance P analogue. *Eur J Nucl Med Mol Imaging* **45**, 1636–1644 (2018).

200. Królicki, L. *et al.* Safety and efficacy of targeted alpha therapy with 213Bi-DOTA-substance P in recurrent glioblastoma. *Eur J Nucl Med Mol Imaging* **46**, 614–622 (2019).

201. Królicki, L. *et al.* Dose escalation study of targeted alpha therapy with [225Ac]Ac-DOTA-substance P in recurrence glioblastoma - safety and efficacy. *Eur J Nucl Med Mol Imaging* **48**, 3595–3605 (2021).

202. Bolcaen, J. *et al.* Marshalling the Potential of Auger Electron Radiopharmaceutical Therapy. *J Nucl Med* **64**, 1344–1351 (2023).

203. Kratochwil, C. *et al.* 225Ac-PSMA-617 for PSMA-Targeted α-Radiation Therapy of Metastatic Castration-Resistant Prostate Cancer. *J Nucl Med* **57**, 1941–1944 (2016).

204. Hunt Bobo, R. *et al.* Convection-enhanced delivery of macromolecules in the brain. *Proc Natl Acad Sci U S A* **91**, 2076–2080 (1994).

205. D'Amico, R. S., Aghi, M. K., Vogelbaum, M. A. & Bruce, J. N. Convection-enhanced drug delivery for glioblastoma: a review. *J Neurooncol* **151**, 415–427 (2021).

206. Lonser, R. R., Sarntinoranont, M., Morrison, P. F. & Oldfield, E. H. Convection-enhanced delivery to the central nervous system. *J Neurosurg* **122**, 697–706 (2015).

207. Bernfield, M. *et al.* Functions of cell surface heparan sulfate proteoglycans. *Annu Rev Biochem* **68**, 729–777 (1999).

208. Mouthon, M. A. *et al.* Syndecan-1 Stimulates Adult Neurogenesis in the Mouse Ventricular-Subventricular Zone after Injury. *iScience* **23**, (2020).
209. Beauvais, D. L. M. & Rapraeger, A. C. Syndecans in tumor cell adhesion and signaling. *Reproductive Biology and Endocrinology 2004 2:1* **2**, 1–12 (2004).
210. Choi, Y., Chung, H., Jung, H., Couchman, J. R. & Oh, E. S. Syndecans as cell surface receptors: Unique structure equates with functional diversity. *Matrix Biol* **30**, 93–99 (2011).
211. Shen, B., Delaney, M. K. & Du, X. Inside-out, outside-in, and inside-outside-in: G protein signaling in integrin-mediated cell adhesion, spreading, and retraction. *Curr Opin Cell Biol* **24**, 600 (2012).
212. Yang, N. & Friedl, A. Syndecan-1-Induced ECM Fiber Alignment Requires Integrin αvβ3 and Syndecan-1 Ectodomain and Heparan Sulfate Chains. *PLoS One* **11**, e0150132 (2016).
213. Yu, W. H. & Woessner, J. F. Heparan sulfate proteoglycans as extracellular docking molecules for matrilysin (matrix metalloproteinase 7). *J Biol Chem* **275**, 4183–4191 (2000).
214. Su, G., Blaine, S. A., Qiao, D. & Friedl, A. Shedding of syndecan-1 by stromal fibroblasts stimulates human breast cancer cell proliferation via FGF2 activation. *J Biol Chem* **282**, 14906–14915 (2007).
215. Wang, X. *et al.* Shed Syndecan-1 is involved in chemotherapy resistance via the EGFR pathway in colorectal cancer. *Br J Cancer* **111**, 1965 (2014).
216. Sanderson, R. D. & Yang, Y. Syndecan-1: a dynamic regulator of the myeloma microenvironment. *Clin Exp Metastasis* **25**, 149–159 (2008).
217. Endo, K. *et al.* Cleavage of syndecan-1 by membrane type matrix metalloproteinase-1 stimulates cell migration. *J Biol Chem* **278**, 40764–40770 (2003).
218. Jung, O. *et al.* Heparanase-induced shedding of syndecan-1/CD138 in myeloma and endothelial cells activates VEGFR2 and an invasive phenotype: prevention by novel synstatins. *Oncogenesis* **5**, (2016).
219. Jung, O., Beauvais, D. M., Adams, K. M. & Rapraeger, A. C. VLA-4 phosphorylation during tumor and immune cell migration relies on its coupling to VEGFR2 and CXCR4 by syndecan-1. *J Cell Sci* **132**, (2019).
220. Jang, B. *et al.* Emerging Role of Syndecans in Extracellular Matrix Remodeling in Cancer. *J Histochem Cytochem* **68**, 863–870 (2020).
221. Xu, Y., Yuan, J., Zhang, Z., Lin, L. & Xu, S. Syndecan-1 expression in human glioma is correlated with advanced tumor progression and poor prognosis. *Mol Biol Rep* **39**, 8979–8985 (2012).

222. Shi, S. *et al.* Syndecan-1 knockdown inhibits glioma cell proliferation and invasion by deregulating a c-src/FAK-associated signaling pathway. *Oncotarget* **8**, 40922–40934 (2017).
223. Chen, J. *et al.* Effects of syndecan-1 on the expression of syntenin and the migration of U251 glioma cells. *Oncol Lett* **14**, 7217 (2017).
224. Francescone, R. A. *et al.* Role of YKL-40 in the angiogenesis, radioresistance, and progression of glioblastoma. *J Biol Chem* **286**, 15332–15343 (2011).
225. Zeng, L. *et al.* SDC1-TGM2-FLOT1-BHMT complex determines radiosensitivity of glioblastoma by influencing the fusion of autophagosomes with lysosomes. *Theranostics* **13**, 3725–3743 (2023).
226. Couchman, J. R. Syndecan-1 (CD138), Carcinomas and EMT. *International Journal of Molecular Sciences 2021, Vol. 22, Page 4227* **22**, 4227 (2021).
227. Watanabe, A. *et al.* Expression of syndecans, a heparan sulfate proteoglycan, in malignant gliomas: participation of nuclear factor-kappaB in upregulation of syndecan-1 expression. *J Neurooncol* **77**, 25–32 (2006).
228. Kumar-Singh, A. *et al.* Nuclear syndecan-1 regulates epithelial-mesenchymal plasticity in tumor cells. *Biology (Basel)* **10**, (2021).

CHAPTER II

Scope and aims

Scope and aims

GB remains a major public health challenge. With no cure available and current treatments only offering limited life extension, there is a clear need to explore new therapeutic strategies. Targeted radionuclide therapy (TRT) shows potential as a method to deliver a vectorized radionuclide targeting tumor cells, aiming to destroy them. Clinical advancements in TRT with β^--emitters, such as the introduction of treatments like Zevalin® and Bexxar® for non-Hodgkin's lymphoma, and more recently, ^{177}Lu-based Lutathera® and Pluvicto® for the treatment of NET and mCRPC, highlighted the progress achieved in this field. In 2013, the first targeted-α-therapy (TAT) based on ^{223}Ra dichloride (Xofigo®) was approved by the FDA for the treatment of mCRPC. In this context, this thesis aims to develop a TAT for GB, capable to address two distinct clinical situations by eliminating: i) the tumor in patients who are inoperable surgically, ii) the residual cells that are inaccessible after resection surgery. The α-emitting radionuclide ^{211}At presents interesting prospects due to its physicochemical properties to develop a targeted therapy. SDC1, described as a poor prognosis factor in many cancers, is emerging as a key biomarker in the development of GB. Targeting SDC1 with the 9E7.4 rat mAb thus seems relevant for the delivery of TAT (^{211}At-9E7.4) *via* intracranial administration.

The objectives of this thesis are as follows:

- Evaluate the global and cerebral distribution of ^{211}At-9E7.4 TAT to determine its *in vivo* stability and estimate potential toxicity risks.
- Assess the efficacy and toxicity of TAT in an orthotopic and syngeneic mouse model.
- Determine both short and long-term effects on microenvironment at the immune level

The core of thesis is divided into the two next chapters. Chapter III provides a comprehensive review of the advancements made by TAT in treating GB. It focuses on how TAT has been employed, considering the specific characteristics of GB. The primary aim of this chapter is to identify challenges, benefits, and potential areas of improvement. Chapter IV introduces our development and application of the ^{211}At-9E7.4 TAT. This study explores the efficacy of this therapy in a syngeneic, orthotopic murine model of GB. The results we delivered could offer valuable insights into how this particular form of TAT might be used in treating GB in the future.

CHAPTER III

Current Landscape and Future Directions of Targeted-Alpha-Therapy for Glioblastoma Treatment

Loris Roncali, François Hindré, Emmanuel Garcion* & Michel Chérel*

Review

Current Landscape and Future Directions of Targeted-Alpha-Therapy for Glioblastoma Treatment

Loris Roncali[1,2], François Hindré[1,3], Emmanuel Garcion[1,4*] & Michel Chérel[2,5*]

[1] Université d'Angers, Inserm U1307, CNRS U6075, Nantes Université, CRCI[2]NA, Angers - France

[2] Nantes Université, Inserm U1307, CNRS U6075, Université d'Angers, CRCI[2]NA, Nantes - France

[3] PRIMEX (Plateforme de Radiobiologie et d'Imageries Expérimentales), SFR 4208, University of Angers, Angers - France

[4]PACEM (Plateforme d'Analyse Cellulaire et Moléculaire), SFR 4208, Université d'Angers, Angers – France

[5]ICO (Institut de Cancérologie de l'Ouest) - René Gauducheau Cancer Center, Saint-Herblain - France

[*]Corresponding authors: emmanuel.garcion@univ-angers.fr (Emmanuel Garcion), michel.cherel@univ-nantes.fr (Michel Chérel)

Abstract

Despite two decades of intensive research, conventional therapeutic protocols failed to provide a definitive solution to treat glioblastoma (GB). Therefore, it remains the most aggressive malignancy of the central nervous system, and emerging strategies have yet to produce consistent satisfactory outcomes. Because of its specific localization and intricate characteristics, GB is as a uniquely regulated solid tumor with a strong resistance to therapy. Recent advances in targeted radionuclide therapy (TRT), particularly with the introduction of α-emitting radionuclides, have unveiled potential avenues for GB management. Recent preclinical and clinical studies underscored promising advancements for targeted-α-therapy (TAT), but these therapeutic approaches exhibit a vast design heterogeneity, encompassing diverse radionuclides, vectors, target molecules, and administration modalities. This Review seeks to critically assess the therapeutic landscape of GB through the perspective of TAT. In doing so, we hope to identify existing challenges and draw insights that might pave the way towards a more effective therapeutic approach.

Key points

- Glioblastoma is a whole brain disease with distinct features when compared to other solid tumors
- Emerging targets, vectors and α radionuclides hold promise towards therapeutic success in GB
- Preclinical models should prioritize standardization through fidelity to human GB and standard-of-care protocol
- TAT is compatible with targeted therapeutic combinations

Introduction

Glioblastoma (GB) remains the most aggressive form of brain tumors. Since 2005, the therapeutic landscape has been largely shaped by the Stupp regimen, which consists, when feasible, in a surgical resection, followed by a combination of radiotherapy and temozolomide chemotherapy. However, this approach is limited by a 15-month median survival of patients[1]. Despite two decades of therapeutic exploration, advancements which mainly rely on the standard protocol and remain insufficient. During this time, bevacizumab, an anti-angiogenic monoclonal antibody approved by the Food and Drug Administration (FDA), has improved patients' quality of life but fails to prolong survival[2]. Meanwhile, Tumor Treating Fields (TTFs), using low-intensity, intermediate-frequency electric fields aimed at the tumor, have marked a noteworthy addition to GB treatment but still lack curative potential[3,4]. Lastly, the advent of immunotherapy, despite showing preclinical promise, has not produced substantial phase III clinical trial success[5,6].

The resistance of GB to treatments results from its multifaceted heterogeneity[7–9]. This diverse landscape is driven by factors such as genomic instability[10], the presence of hypoxic niches[11], and the pivotal role of glioblastoma stem-like cells (GSLCs)[12], which establish a pro-tumoral microenvironment strengthening immunosuppression[13] and tumor infiltration[14]. In addition, the blood-brain barrier (BBB) exacerbates treatment challenges, preventing nearly all small-molecule drugs from brain entry[15].

Targeted radionuclide therapy (TRT) offers potential breakthroughs. This modality, compatible with systemic and locoregional administrations, permits various vectorization methods, promoting high-energy radionuclide combinations that may annihilate tumors. This strategy is based on exposure of cells to radiation, which results in both direct and indirect cellular impacts. The direct effects arise from energy transfer, leading to phenomena such as DNA damage and cross-fire effects. On the other hand, indirect effects stem from the generation of reactive oxygen species (ROS) *via* H_2O radiolysis and radiation-induced bystander effects. These bystander effects involve signal propagation from radiated to neighboring cells, triggering apoptosis in cells not immediately exposed to ionizing radiation. This phenomenon could potentially elicit immune response, known as “abscopal effect”.

Initial investigations prioritized β^- radioisotopes, like iodine-131 (^{131}I), yttrium-90 (^{90}Y), or lutetium-177 (^{177}Lu), due to their shorter tissue penetration (1-10 mm) compared to X-rays

used in external beam radiation[16–21]. These radioisotopes exhibit an average emission energy ranging from 0.1 to 2.3 MeV and a linear energy transfer (LET, which describes the amount of energy deposited per length unit) of 0.2 keV/µm. In the early 2000s, successful clinical trials involving β^--emitters resulted in the approval and subsequent market introduction of two treatments for non-Hodgkin lymphoma based on an anti-CD20 monoclonal antibody (mAb) labeled with ^{90}Y (^{90}Y-ibritumomab tiuxetan, Zevalin®)[22], or with ^{131}I (^{131}I-tositumomab, Bexxar®)[23]. In 2018, the FDA has approved the combination of the somatostatin analog DOTATE with ^{177}Lu (^{177}Lu-DOTATATE, Lutathera®) for the treatment of neuroendocrine tumors[24]. Additionally, ^{177}Lu-labeled PSMA-617 (^{177}Lu vipivotide tetraxetan, Pluvicto®) has been greenlit in 2022 for treating adult patients with prostate-specific membrane antigen (PSMA)-positive metastatic castration-resistant prostate cancer (mCRPC)[25].

However, the tissue penetration of β^--emitters remains substantial and does not always guarantee the preservation of healthy tissue surrounding the irradiated areas[26]. The emergence of α-emitters in nuclear medicine has the potential to bring about a paradigm shift. Outclassing β^- emitters, α emitters present shorter tissue penetration (50-100 µm), higher energy emissions (2-10 MeV), higher linear energy transfer (100 keV/µm)[27], and a maintained efficacy in hypoxic conditions[28]. Significant clinical outcomes have already been demonstrated, leading to the FDA's approval in 2013 of the α radionuclide radium-223 (^{223}Ra) dichloride (Xofigo®) for the treatment of mCRPC[29], which lacked effective therapeutic options at the time. In the case of GB, α-emitters may represent ideal candidates for eliminating both the primary tumor masses and residual tumor post-surgery, while preserving healthy tissues. Recent clinical studies have validated both the safety and efficacy of targeted-α therapies (TATs) leveraging astatine-211 (^{211}At), bismuth-213 (^{213}Bi), and actinium-225 (^{225}Ac) in GB scenarios, with supportive findings regarding survival of GB rodent models.

This Review aims to trace the ascent of TAT in GB treatment. Here, we discuss previous preclinical and clinical studies involving TAT strategies to treat GB, from radioelement selection to vectorization strategies and administration considerations. Considering the distinctive characteristics of GB as a whole-brain tumor, this comprehensive assessment intends to streamline future TAT endeavors, and to unveil potential successful therapeutic combinations.

I. Glioblastoma: a confined solid tumor

GB represents a distinctive solid tumor due to its location within the brain. The brain benefits from a unique regulation with specific biological interfaces: the BBB, the blood-cerebrospinal fluid (CSF) barrier (BCB), and the meningeal barrier[30]. The BCB is located between the blood and the cerebral cisterns containing the CSF. It is formed by endothelial and epithelial cells of the choroid plexuses and subarachnoid spaces. The meningeal barrier is formed of four distinct layers called meninges which provide physical protection of the brain parenchyma as well as local immune regulation[31,32]. Both BCB and meninges are involved in the clearance of the CNS fluids. Furthermore, the brain features a specialized immune control system, with its own immune cells called microglia, and interaction with peripheral immune cells[33]. The presence of neural stem cell (NSC) niches in areas such as the subventricular zone[34] and the dentate gyrus of the hippocampus[35] contribute to further increase this complexity. These niches contribute to the intricacy of the regulatory mechanisms of the brain. In the case of GB, various niches within the tumor microenvironment (TME) play a role in regulating tumor development and providing protection against the immune system. Recent investigations have revealed that GB is synaptically incorporated into neural circuits, subsequently affecting neuronal operations and compromising cognitive functions. These perturbations reciprocally facilitate tumoral proliferation[36–38]. The interplay of all these factors collectively contributes to the inaccessibility of the tumor and its resistance to conventional therapies.

1. The blood-brain barrier (BBB)

The BBB is a highly regulated and selective interface that separates the central nervous system from the systemic circulation. This critical barrier plays a pivotal role in governing various physiological functions, such as regulation of cerebral hemodynamics, maintenance of ionic homeostasis, provision of cerebral nutrition, and control of neurotransmitter concentrations. Simultaneously, it acts as a guardian by restricting the passage of plasma-derived molecules and by shielding the brain from potential neurotoxic agents[39].

Structure and functions. The BBB primarily consists of specialized endothelial cells in cerebral blood vessels. These cells exhibit distinct properties and functions compared to their counterparts in peripheral tissues. Notable features include the presence of inter-endothelial adherens and tight junctions[40] as well as an enriched population of mitochondria[41]. Tight

junctions effectively reduce paracellular transport across the endothelium and create a clear separation between the luminal and basolateral compartments. As a result, only small molecules like oxygen (O_2), carbon dioxide (CO_2), and small lipophilic compounds, weighing less than 400 Da, can freely pass through, while others require receptor-mediated transport or endocytic mechanisms. Adherens junctions also play a crucial role in maintaining BBB integrity by regulating paracellular diffusion between endothelial cells. These molecular complexes establish intercellular adhesion by linking with the actin cytoskeleton through catenin proteins.

Pericytes are the second cellular component involved in BBB function. They envelop nearly 100% of the cerebral endothelium. Pericytes are situated along the walls of blood capillaries and are embedded in the basement membrane, allowing for close communication with endothelial cells. They control various functions, including cerebral blood flow and regulation of neuroinflammation[42]. Additionally, they have a direct influence on the regulation of tight junctions among endothelial cells[43]. Lastly, astrocytes, the most abundant glial cell population, cover the basal membrane of the BBB with their end-feet, bridging connections between neurons and the vascular system[44]. While some of their specific functions within the BBB remain the subject of debate, it is well-established that their presence is crucial for orchestrating key checkpoints in brain metabolism[45].

Collectively, this assembly is referred to as the neurovascular unit (NVU) when associated with neurons. It is worth noting that the BBB is absent in certain regions of the brain, such as the circumventricular organs and the choroid plexus. Furthermore, the protection provided to cerebral vasculature is heterogeneous, depending on the type of blood vessel and is regulated by various forms of neurovascular complexes[46].

Disruption of the BBB in GB. While it was once widely accepted that the BBB was uniformly breached in GB-bearing patients, recent clinical data have questioned this assumption[47,48]. In the context of GB, the disruption of the BBB occurs due to hypoxia-driven expression of vascular endothelial growth factor (VEGF), which leads to disorganized angiogenesis and the formation of immature and more permeable blood vessels within the tumor mass[49,50]. Clinical detection of brain tumors typically involves magnetic resonance imaging (MRI) *via* T1-weighted contrast-enhanced sequences and T2-weighted Fluid Attenuated Inversion Recovery (FLAIR) volumes[51]. T1-weighted imaging can grossly detect BBB disruption but does not provide insights into the variability of this rupture, which can differ among patients and even within the same tumor.

To address this issue, dynamic contrast-enhanced MRI (DCE-MRI) is used to quantitatively measure the transport of contrast agents across different contrast-enhancing regions. This technique employs pharmacokinetic modeling and dynamic imaging acquisition to estimate vascular permeability[52,53]. Other studies using alternative MRI techniques and positron-emission tomography (PET) have also revealed tumor regions extending beyond the contrast-enhanced areas seen in MRI scans. These findings, combined with the analysis of surgically removed tissue, support the concept of an intact BBB in these regions. Consequently, areas of BBB disruption give rise to a distinct pathology-specific interface known as the blood-tumor barrier (BTB) or blood-brain tumor barrier (BBTB). The BTB is characterized by an abnormal distribution of pericytes and a loss of connection to astrocytic end-feet and neurons, which are displaced by GB cells during tumor growth. A decrease in the expression of junctional proteins is also observed. Despite being termed "hyper-permeable", this interface remains heterogeneous and retains some characteristics of the BBB[54]. In this context, the challenge of drug administration through the bloodstream and thus the passage through both the BBB and BTB are crucial considerations for achieving uniform and effective treatment of GB with TAT.

Strategies to cross the BBB. To overcome the challenges posed by the heterogeneity of BBB and BTB disruptions in GB, various invasive and non-invasive strategies have been developed to facilitate drug delivery to the tumor site (Fig. 1). This section aims to highlight some of these approaches, while a comprehensive review has been published by Wu *et al.*[15].

Transcytosis represents an initial non-invasive approach to cross the BBB. It can occur through paracellular mechanisms, involving the modulation of tight junction protein expression to facilitate the passage of molecules between endothelial cells. For example, minoxidil sulfate is an activator of the adenosine 50-triphosphate-sensitive potassium channel (K_{ATP} channel) able to increase the BBB permeability by attenuating the tight junction proteins[55]. Alternatively, transcellular transcytosis allows for the transport of molecules through various mechanisms, including passive diffusion of small hydrophobic molecules, carrier-mediated transcytosis (CTM) for small molecules mimicking endogenous substrates, receptor-mediated transport (RTM) for macromolecules, and adsorptive-mediated transcytosis (AMT) for cationic macromolecules or mAb[56]. For example, in a recent study, Tylawsky *et al*. performed an intact-BBB crossing with a caveolin-1-mediated transcytosis of fucoidan nanoparticles targeting P-selectin. The use of this vector led to an extended survival with reduced bone and healthy tissue toxicity

in a murine medulloblastoma model[57]. In TATs designed for GB, CTM is commonly used for the delivery of radiopharmaceuticals, using peptides like substance P or phenylalanine (Phe) to facilitate BBB penetration[58,59], as well as mAb targeting tenascin[60,61].

Thus, modifying the pharmacokinetics of radiopharmaceuticals can also facilitate the transportation of drugs that are typically impermeable to the BBB. Consequently, conjugates combining drugs with carriers or ligands have been investigated. The engineering of vectors such as liposomes[62–65], lipidic nanocapsules[66–68] or polymers[69,70] has indeed demonstrated an effective penetration of the BBB. Gold nanoparticles show promising results as well to target the GB[71,72].

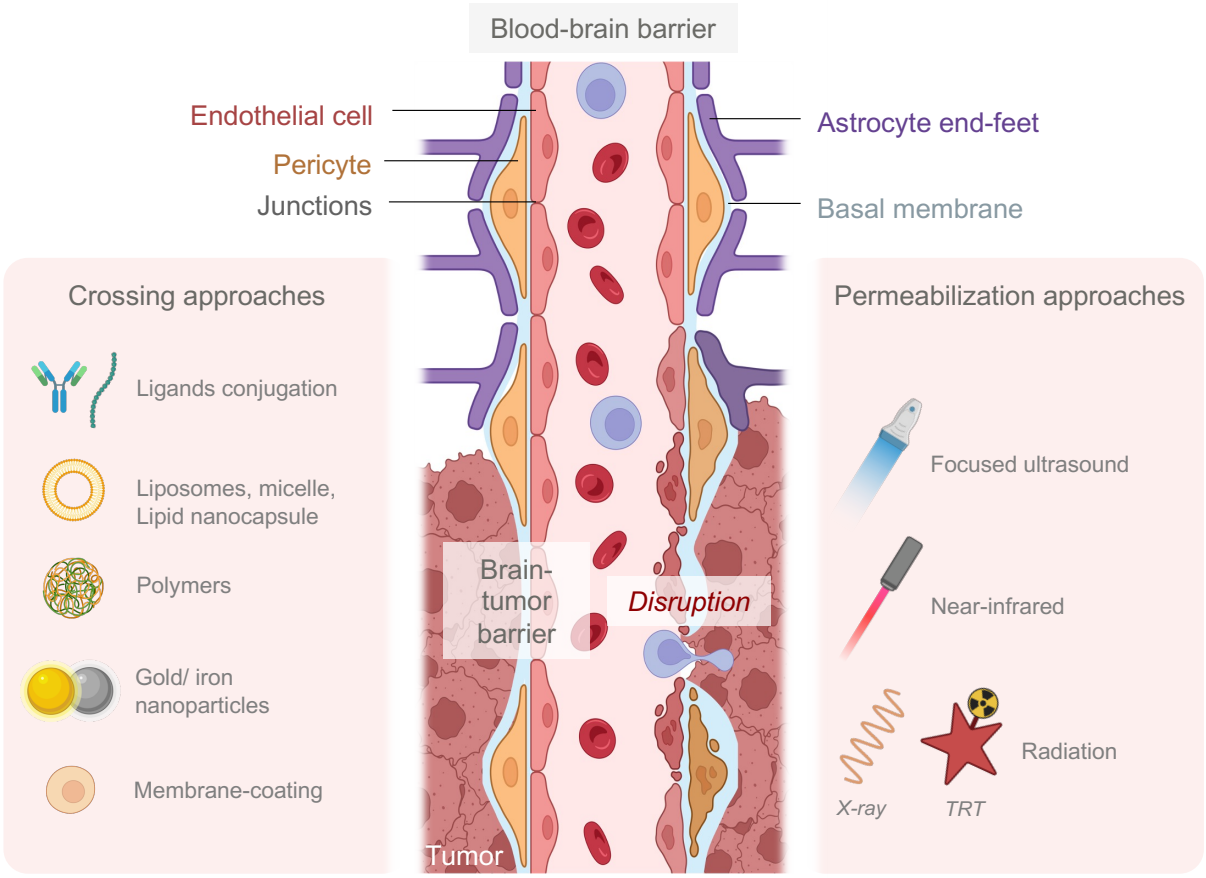

Fig. 1 | **Strategies to cross the BBB and BTB for systemic treatments of GB.** The BBB has a finely regulated structure, maintained by endothelial cells of blood vessels, bound by tight junctions, the presence of pericytes, and astrocytic endfeet, ensuring a restrictive passage of blood elements to the brain. In the context of GB, the integrity of the BBB is heterogeneously compromised. Tumor growth weakens the BBB, creating a unique interface known as the brain-tumor barrier, devoid of astrocytic endfeet. Other tumor areas can disrupt the BBB due to rapid growth of tumor cells. In both scenarios, excessive angiogenesis in response to tumor hypoxia contributes to the development of a non-functional configuration of the BBB. However, given the heterogeneity of the disruption, bypassing or breaching the BBB remains a preferred strategy to ensure uniform administration of blood-borne therapies. Various vector types have been developed based on the therapy type to be administered (chemotherapy, mAbs, immunotherapy, oligonucleotides, radionuclides) to ensure their passage. Physical disruption, whether permanent or transient, of the BBB is also a means to ensure the effective distribution of the desired therapy. (Created with Biorender - biorender.com)

Intranasal (i.n.) administration is also a potential route that has yet to be explored in the context of radiopharmaceuticals. The nasal route has several advantages for drug delivery: it is easy to access, well irrigated with blood vessels, and can require lower medication doses because it avoids extensive first-pass metabolism[73]. However, nasal irritation, mucociliary clearance, and metabolic regulation inside the nose must be considered. For instance, Sukumar *et al.* developed nanoparticles loaded with microRNA (miRNA) therapy to improve temozolomide therapy for GB. These nanoparticles carrying miRNA accumulated in the targeted brain area, and resulted in a significant 42% reduction in tumor size. They exclusively accumulated in the brain region, leading to a significant increase in mice survival[70]. Other examples have demonstrated their potential for the administration of chemotherapy[74,75] or bevacizumab[76] *via* the i.n. route.

Coating drug carriers with a biological membrane also presents unexplored promising prospects for TRT in GB. Thus, therapeutic carriers like nanoparticles can be coated with membranes from red blood cells, white blood cells, platelets, tumor cells, stem cells, or bacteria[77]. Due to their inherent biocompatibility, this coating extends *in vivo* residence time by being recognized as self by the immune system. For example, the membranes of brain tumor cells, with their ability to cross the BBB, serve as an attractive vector to facilitate the homing of nanoparticles within the tumor[78]. Another example involves a hybrid membrane derived from cancer cells and mitochondria, as tested by Zou *et al.,* for coating Gboxin-loaded nanoparticles. This led to increased tumor accumulation and significantly improved survival in a murine model of GB[79].

External stimulation strategies also provide a potential avenue to breach the BBB. These strategies expand the range of possibilities for targeting radiopharmaceuticals, as the ability to cross the barrier is no longer a prerequisite for the vector. Light has been shown to be capable of reversibly disrupting the BBB, notably through the use of laser beams. Among light-based methods, near-infrared (NIR) light can penetrate deep into tissues to modulate BBB permeability in a transient way[80]. Recently, Cai *et al.* treated GB-bearing mice using a pulsed laser stimulation of gold nanoparticles targeting tight junctions on the blood vessels to induce a transient disruption of the BBB. This disruption subsequently increased the efficacy of paclitaxel chemotherapy. This protocol led to a reduction in tumor growth, with a significant increase in median survival, up to 50% in a mouse model of GB[81].

Focused ultrasound (FUS) methods have also attracted significant attention for BBB modulation, with recent clinical trials demonstrating the safety of this approach. In a recent phase I clinical trial, Sonabend *et al*. assessed an implantable device emitting low-intensity ultrasound for the delivery of albumin-bound chemotherapy agent (paclitaxel) in GB patients. Their method involved the administration of low-intensity pulsed ultrasound with simultaneous intravenous (i.v.) microbubble injection[82]. While the feasibility of this approach has been demonstrated, it should be noted that, in this context, the timeline for the restoration of the BBB depends on the technology employed and the molecular characteristics of the administered drug. Future pharmacokinetic data regarding drug accumulation and clearance will need to be addressed in subsequent research.

Strategies to bypass the BBB. Systemic approaches hold great promise but face persistent challenges: the heterogeneity of BBB and BTB disruptions, the high infiltrative behavior of tumor cells and the hard-to-reach hypoxic tumor foci. In this regard, we also must keep in mind that while there is a BBB from the periphery to the brain tissue, the BCB and the meningo-encephalic barrier that also play roles in the clearance of active molecules and further add to the complexity of drug administration. For instance, in multiple sclerosis, the immunoglobulins present in the CSF are distinct from those present in the blood, thus demonstrating their locoregional production, and not the result of the blood ultrafiltration[83].

In the case of a systemic injection, TRT itself has a variable range of action to reach tumoral margins and disseminated cells, depending on the radionuclide used, but a greater tissue penetration increases the risk of causing damage to healthy tissues. Intratumoral (i.t.) or intracavitary locoregional approaches can bypass these constraints by directly targeting the tumor mass (Fig. 2)[84]. Thus, they appear to be more compatible with α radionuclides with short half-lives (e.g., ^{211}At: 7.2 h), as their first decays could occur directly in the tumor site. To achieve this objective, convection-enhanced delivery (CED) represents a promising option. It involves the stereotactic placement of catheters intratumorally or into the post-surgical cavity. These catheters are connected to pumps that ensure a continuous, positive-pressure micro-infusion of the desired agents through the target tissues *via* principles of bulk flow, typically ranging from 0.1 to 10 µl/min, rather than a bolus injection[85,86]. Thus, by applying a pressure gradient in place of a concentration gradient, considerations about the molecular weight and diffusivity of the therapeutic agent are bypassed. This facilitates the homogeneous administration of low concentrations of drug to treat a specific brain region, while optimizing

its i.t. volume distribution. CED achieves a range of action on the order of centimeters in brain tissue, whereas diffusion-based methods are restricted to a few millimeters[87].

The administration of chemotherapy *via* CED is still under investigation, despite implementation challenges[88]. Similarly, the study of conjugated toxins or drugs encapsulated in liposomes is also explored. Phase I clinical trials have been completed to test liposomes loaded with irinotecan (NCT03086616) or Panobinostat nanoparticles (NCT03566199). The use of CED for radiopharmaceutical administration has shown promise in preclinical studies in GB-bearing rodents, including the use of lipid nanocapsules loaded with rhenium-188 (^{188}Re), a β^--emitter, which notably resulted in high cure rates after treatment[67,68,89]. This approach effectively treats large brain volumes, encompassing both radiographically defined tumor regions and the surrounding infiltrated brain tissues, while minimizing systemic toxicity, enabling safe and effective drug delivery.

Other localized treatment modalities are also available, such as implantable reservoirs (e.g., Ommaya or Rickham reservoirs), which are conventionally used in GB therapy[90]. Radionuclides with short half-lives could be suitable for use of reservoirs to administer single or fractionated doses of TAT to the resected cavity. In 2008, Zalutsky *et al*. showcased the viability of this method for TAT by administering ^{211}At conjugated with an anti-tenascin antibody in patients with GB[91].

Implants within resection cavities have also been explored. While chemotherapy wafers of carmustin (Gliadel®) have indicated slight improvements in patient survival, they soon revealed limitations[92]. Beyond these limited additional benefits, retrospective studies have highlighted an elevated risk of adverse effects[93,94]. The issue with carmustine wafers arises the lack of information interactions they create between the healthy brain tissue cells and the tumor cells in the cavity walls. The recent proposition to use locoregional tumor traps represents a significant advancement. Here, the concept is to offer implants that are integrated with the tissue being treated. This strategy aims to lure disseminated cells to a well-defined region, which can serve multiple purposes: it can possess antitumor properties through the release of active substances, act as a convergence point for cancer cells and local immune cells *via* chemoattraction, or allow local colonization to designate an easily accessible area for targeted antitumor drug administration or TRT[95,96]. Thus, biocompatible scaffolds using collagen-based hydrogels[97] and bacterial cellulose[98] to attract tumor cells validated their capability to trap tumor cells. Their combination with TAT could potentially minimize the risk of recurrence.

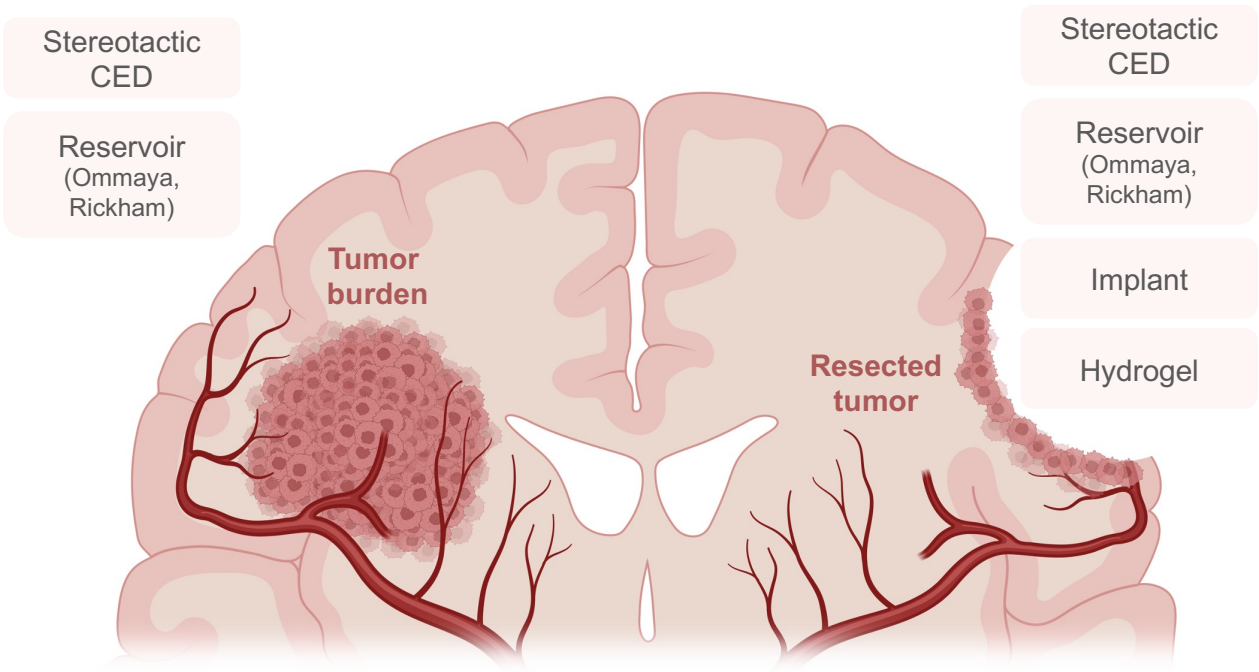

Fig. 2 | **Locoregional strategies for the treatment of GB.** The current management of GB in patients includes surgical resection followed by the Stupp regimen. However, depending on the location of the tumor, surgery is not always feasible. Resection does not eliminate all residual cells, even when removing with a significant margin. The search for suitable therapies to prevent recurrence thus addresses two distinct clinical scenarios. Inoperable tumors can be locally targeted through convection-enhanced delivery (CED) using an intratumoral catheter. The establishment of Ommaya or Rickham reservoirs is another method for catheter-based treatment administration and allow a repetitive access to the intrathecal space. The placement of the catheter is crucial for effective therapy delivery. Within the resection cavity, the same approaches can be applied. Additionally, a method that uses the cavity, such as a biocompatible implant or hydrogel, might be considered. These could be loaded with chemokines to attract residual tumor cells or infused with a therapeutic agent. (Created with Biorender - biorender.com)

2. Hypoxic niches

O_2 is a fundamental component of cellular metabolism. A deficiency in O_2 initiates a condition known as hypoxia, which is prevalent in many cancers and contributes to tumor progression[99]. While often essential for proper organ function, physiological hypoxia can vary across different niches due to organ anatomy or rapid cellular expansion. For example, the bone marrow, a notably hypoxic organ, requires this condition to maintain hematopoietic stem cell homeostasis[100]. Similarly, germinal centers, reproductive organs, and the intestinal mucosa also exhibit physiological hypoxia, which can impact immune function, cell differentiation, and barrier function[101–103]. The brain accounts for 20% of the body's O_2 consumption[104]. Oxygenation levels in the brain vary across regions, ranging from 0.5 % to 8 %. For reference, brain tumors typically exhibit an average oxygenation rate of 1.25 %, but comprise areas with highly heterogeneous oxygen supply[105].

Hypoxia in GB. In GB, hypoxia arises due to VEGF overexpression, which causes irregular vasculature, subsequently hindering the delivery of O_2, therapeutic agents, and immune cells. Moreover, the expansion of GB rapidly outstrips the existing blood supply. Regions of hypoxia are characterized by the presence of dense cellular zones around the necrotic foci of GB, called pseudopalisades. Studies indicate that these pseudopalisades represent the invasive front of tumors by gathering GB cells that migrate away from oxygen-deprived areas. The excessive secretion of proangiogenic factors by these cells results in an amplified angiogenic response termed microvascular hyperplasia[106]. Genetic alterations can also activate hypoxia-inducible factor 1α (HIF-1α) independently of hypoxia. This is evident in the case of epidermal growth factor receptor (EGFR), where the mutant EGFRvIII is constitutively activated and upregulates HIF-1α *via* the PI3K-AKT-mTOR pathway[107]. Similarly, inactivation or loss of p53 expression downregulates mdm2 expression, thereby stabilizing HIF-1α[108]. At the cellular level, the hypoxic environment is sensed through the HIF pathway, wherein HIF-1α and HIF-2α transcription factors play pivotal roles. Consequently, transcription driven by HIF modulates a multitude of genes which enhance processes such as angiogenesis, erythropoiesis, cell movement, survival, proliferation, epithelial-mesenchymal transition (EMT), inflammatory cell recruitment, invasion, metastasis, and metabolic adaptation[109–111].

Hypoxia and radioresistance in GB. Hypoxia is known to induce radioresistance, notably in GB. The extent of DNA damage caused by external beam radiation with X-rays directly correlates with the O_2 levels in the irradiated tissues. Under hypoxic conditions, the severity of DNA damage is attenuated due to reduced levels of ROS generated by ionizing radiation. This leads to indirect DNA strand breaks with an absence of oxygen-mediated fixation of DNA damage[99]. In addition, radiation itself can induce hypoxic pathways, leading to the overexpression of HIF-1α[112]. This overexpression fosters radioresistance through a range of mechanisms including modulation of ATP metabolism, p53 activation[113,114], mitigation of radiation-induced DNA damage [115], activation of angiogenesis, repair of double-strand DNA breaks, cell cycle arrest, suppression of apoptosis, and initiation of autophagy. Within the context of GB, it has been recently shown that hypoxia stimulates autophagy through the mediation of the Beclin-1 protein. In their study, Wei *et al.* demonstrated that the depletion of Beclin-1 markedly downregulated autophagy, enhanced the function of DNA-Dependent Protein Kinase (DNA-PK), and heightened radiosensitivity in C6 rat glioma cells[116].

Targeting hypoxic niches to overcome treatment resistance. Hypoxia plays a pivotal role in many features of GB and its microenvironment. Given that it is exacerbated in response to radiotherapy, concurrent detection and targeting of hypoxia alongside novel therapeutic approaches appear crucial. Detection can be achieved using PET/SPECT as detailed in Bolcaen *et al.'s* comprehensive review[56]. Specifically, the association of Diacetyl-bis(N4-methylthiosemicarbazone) (ATSM) with either copper-62 (^{62}Cu) or ^{64}Cu for PET imaging can help pinpoint hypoxic regions in GB patients[117–119]. In the case of radiotherapy, tumor radiosensitization remains a significant research focus. For instance, the temporary exposure of hypoxic GB tumor cells to normoxic conditions has been shown to make these cells susceptible to radiation for a specified duration[120]. Furthermore, since hypoxic regions have diminished blood supply, they undermine the efficacy of systemic approaches to ensure uniform distribution of TRT. However, a locoregional approach could be a viable strategy to target these remote and resistant tumor zones. Moreover, the use of α particles might offer a solution as Wulbrand *et al.* have shown that TAT maintain its efficacy in hypoxic regions, a feature that β^--emitters could not achieve[28].

3. Glioblastoma stem-like cells (GSLCs)

Neural stem-cells (NSCs). During the development of the CNS, NSCs are localized within the cerebral ventricles. In adulthood, only two NSC niches remain in the brain, located in the subventricular zone (SVZ) and the subgranular zone (SGZ) of the dentate gyrus in the hippocampus[121,122]. NSCs give rise to glial cells populating the brain, including astrocytes, oligodendrocytes, and neurons[123,124]. At the end of development, progenitor cells undergo terminal differentiation. The only exception is the oligodendrocyte precursor cells (OPCs), which retain the ability to proliferate in the adult brain[125]. Similarly, astrocytes maintain a proliferative capacity in response to brain injury[126]. Since GB originates from astrocytes, these cells must undergo dedifferentiation and acquire tumorigenic characteristics. NSCs are the primary suspects in inducing these phenomena in these cells, leading to the generation of GB.

Glioma stem-like cells. GSLCs, more commonly and somewhat inaccurately referred to as glioma stem cells, were first pinpointed by Singh *et al.* as a cell population with the ability to initiate *in vivo* tumor growth[127]. These cells exhibit self-renewal capabilities, differentiation potential, and a heightened resistance to therapies, enabling them to drive tumor development through invasion and angiogenesis. They are characterized by a plethora of markers, with the

primary ones being CD133, CD15, A2B5, L1CAM, integrin α6, CD44, ALDH, and ABCG2[128]. While this list of markers facilitates studies on stem-like phenotypes, it quickly reaches a threshold in accurately representing the true nature of GSLCs. In reality, GSLCs form a much broader and intricate mosaic, influenced by interactions within their microenvironment that impact their phenotype[129]. Recent findings have indicated that stem-like subclones derived from single cells clinical samples exhibited distinct profiles in therapy resistance, underscoring that different GSLC populations contribute to the progression of GBM[130].

Targeting NSCs in GB. Recent data accumulation has highlighted the involvement of NSCs in GB development, especially in their interaction with GSLCs. Consequently, GBs that develop near the SVZ have demonstrated increased resistance to chemotherapy and radiotherapy, leading to a reduced overall survival in patients[131,132]. In addition to functional overlap, the shared molecular programming between NSCs and GSLCs is underscored by the similar expression patterns of genes such as CD133, Sox10, Nestin, Musashi, Glial fibrillary acidic protein (GFAP), and Olig1/2[133]. This highlights the potential significance of the SVZ, as a reservoir of NSCs, in GB recurrence and treatment resistance. Consequently, the potential of targeting the SVZ for GBM treatment has attracted research interest. Several studies have demonstrated that external beam radiation of ipsilateral SVZ and even contralateral SVZ could significantly improve progression-free survival and overall survival of patients[134,135]. Therefore, targeting the NSCs in the SVZ as part of locoregional TAT therapeutic strategies could be advantageous to inhibit gliomagenesis.

4. Cancer-associated fibroblasts (CAFs)

CAFs also form a component of the TME in cancer. However, they were long considered absent in the GB TME, given the lack of fibroblasts in the brain[136]. A recent study led by Jain *et al.* revealed the presence of these CAFs in GB using single-cell RNA sequencing (scRNA-seq) and spatial transcriptomics techniques. It was demonstrated that CAFs in GB originate from various sources, such as fibroblasts[137], endothelial cells[138], and pericytes[139]. The study indicated that CAFs are chemoattracted by GSLCs *via* platelet-derived growth factor (PDGF) and transforming growth factor β (TGF-β). In return, they can facilitate GSLC enrichment modulated by osteopontin (OPN) and hepatocyte growth factor (HGF). *In vivo*, this results in enhanced tumor growth. CAFs have the capacity to polarize TAMs toward an M2

phenotype through the production of an extra-domain-A splice variant of fibronectin that binds toll-like receptor 4 (TLR4) on TAMs[140].

CAFs are known for their overexpression of fibroblast activation protein (FAP), a protease that is absent in fibroblasts under physiological conditions. In GB, before the discovery of CAFs in the TME, this marker was detected within GB cells and on non-malignant stromal cells. It is associated with a mesenchymal GB phenotype, a phenotype linked with enhanced migratory capacity, invasion, and resistance to apoptosis. *In vivo*, FAP is expressed in GB subgroups that do not express the astrocytic marker GFAP[141].

5. The immune landscape of GB

While it shares similarities with other solid tumors in terms of resident immune cell presence, GB distinctively activates immunosuppressive factors over stimulatory ones. This bias not only helps the tumor in evading immune detection but also poses challenges for therapeutic interventions.

Immunosuppression in GB. Tumor-associated macrophages (TAMs) are key components within the GB microenvironment, constituting up to 50% of the total tumor mass[142]. They encompass both the resident tissue macrophages of the brain, called microglia, and the peripheral infiltrating macrophages. These macrophages play a significant role in both immunosuppression and tumor progression[143]. Historically, TAMs have been categorized into two primary phenotypes: M1 and M2[144]. The M1 TAMs, activated by pro-inflammatory cytokines, exert anti-tumor effects by secreting inflammatory factors such as ROS, TNF-α, IL-1β, IL-6, IL-12, and IL-23, leading to the elimination of tumor cells. In contrast, M2 TAMs are less cytotoxic to the tumor and release anti-inflammatory cytokines like IL-4, IL-10, and IL-13[145]. It is worth noting that this initial classification, primarily based on *in vitro* observations, appears to be oversimplified. Recent evidence suggests that the TAM phenotype is more of a dynamic continuum within the tumor microenvironment, with macrophages displaying characteristics of both M1 and M2 markers being identified[146].

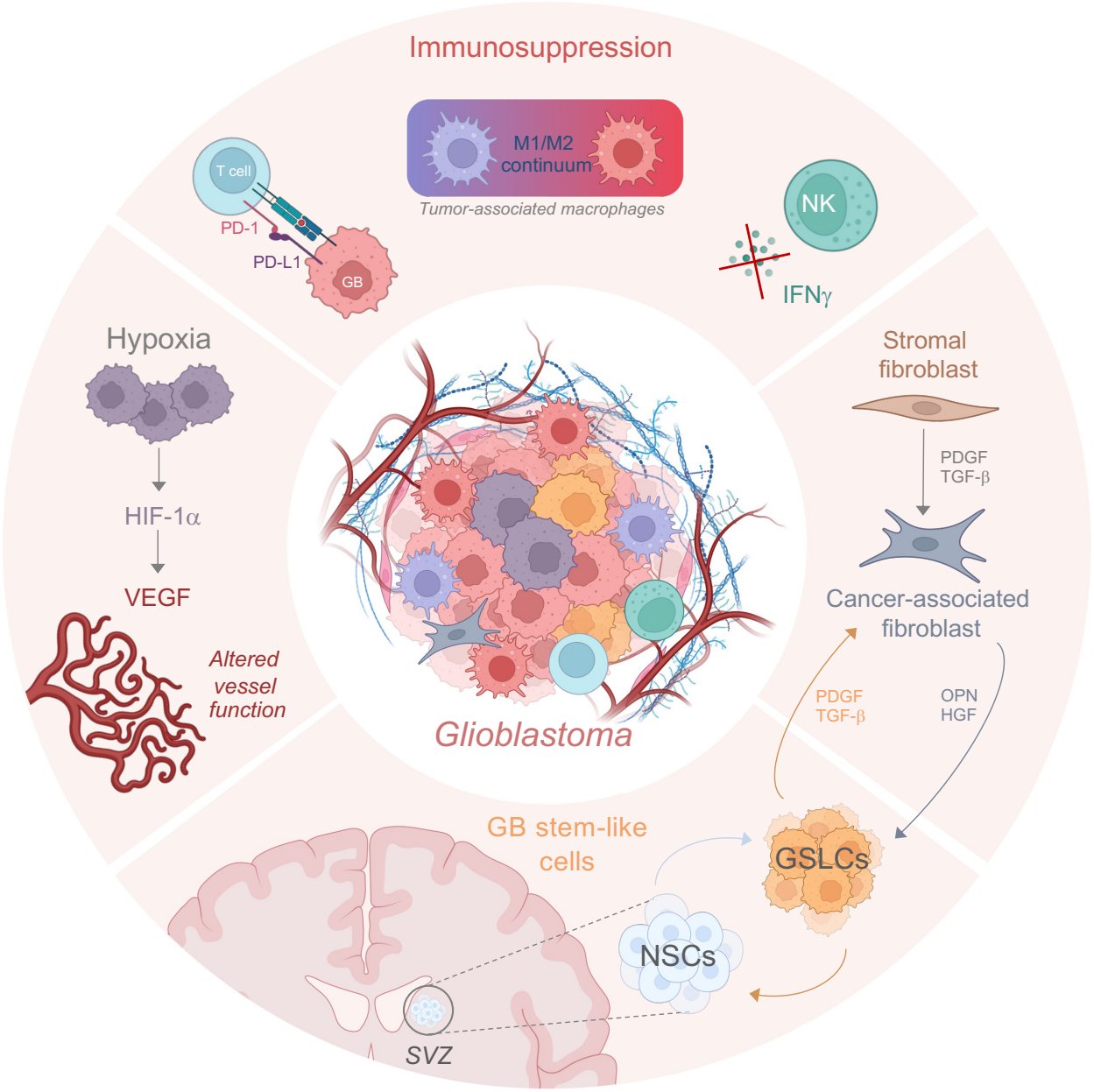

Fig. 3 | **Main characteristics of the TME to consider for the design of future TAT in GB.** GB is characterized by a strong immunosuppression, primarily through the increased expression of PD-L1 on tumor cells, allowing them to evade T cells detection, the modulation of microglia towards a pro-inflammatory and cytotoxic phenotype (M2), and the inactivation of natural killer cells (NK cells). Hypoxia resulting from rapid tumor growth activates signaling pathways, notably the HIF-1α pathway, which triggers excessive angiogenesis through the expression of VEGF. As previously mentioned, these newly formed vessels exhibit a disorganized BBB, and their immaturity restricts the supply of oxygen and nutrients to tumor cells. The heterogeneous populations of neural stem cells (NSCs), especially those residing in the subventricular zone (SVZ), interact with GB stem cells (GSLCs), which are also marked by significant heterogeneity. This interaction enhances the aggressiveness of GB and contributes to its chemoresistance and radioresistance. More recently, the presence of cancer-associated fibroblasts has been identified within GB. These are induced by platelet-derived growth factor (PDGF) and transforming growth factor β (TGF-β) signaling. They are involved in an interplay with GSLCs, facilitating their enrichment through the secretion of osteopontin (OPN) and hepatocyte growth factor (HGF). (Created with Biorender - biorender.com)

During tumor development, tumor-infiltrating T lymphocytes (TILs) are also present within the GB TME. GB tumors have a reduced expression of MHC on their cells, thereby hindering antigen presentation and recognition by dendritic cells, effectively evading T cell intervention[147]. Additionally, tumor cells overexpress programmed death-ligand 1 (PD-L1), which binds to the PD-1 receptor on T cells, resulting in the inhibition of their proliferation, cytokine production, and cytolytic function[148]. Regulatory T cells (Tregs) also contribute to this immunosuppressive microenvironment. These cells are a subset of T helper cells that express FOXP3, essential for their immunosuppressive activity. They promote immune system tolerance towards GB cells through the secretion of TGF-β and IL-10[149]. They also modulate immunosuppression *via* another immune checkpoint called cytotoxic T-Lymphocyte Antigen-4 (CTLA-4). CTLA-4 is a negative regulator of T cell costimulation. It is expressed on the surface of Tregs to compete with CD28 to bind CD80 and CD86 at the surface of antigen-presenting cells (APCs), and therefore inhibits T-cell expansion and activation in lymph nodes[150].

Natural killer (NK) cells are components of the innate immune system. They represent one of the least abundant immune cells within the GB TME. NK cells are equipped with granules rich in perforin and granzyme. When these granules are released in proximity to a target cell, perforin creates pores in the cell membrane, facilitating the entry of granzyme, which subsequently induces apoptosis. The activation of these cells is contingent upon the local secretion of interferons or cytokines[151]. NK cells are responsive to various receptors that either activate or inhibit their function. They have the capability to target cancer cells regardless of the reduced expression of MHC on these cells. However, studies have shown that NK cells identified within lesions exhibit increased expression of CXCR3, essential for their infiltration, and a decreased expression of interferon gamma, rendering them non-cytolytic[152].

Immunogenicity of α-emitting radionuclides. Numerous preclinical investigations have highlighted the potential of α emitters to elicit an immune response, and despite the limited extensive research on α-emitter TRT, emerging evidences indicate that α-radiation can induce immunogenic cell death. *In vitro* studies revealed that ^{223}Ra dichloride (Xofigo®) enhances T cell-mediated tumor cell lysis, elevates protein expression of MHC-I and calreticulin in human prostate, breast, and lung carcinoma cells[153]. in cell line and patient-derived xenograft models of breast, colorectal, lung, ovarian, and pancreatic cancer, thorium-227 (^{227}Th) conjugates aimed at mesothelin measured an increase in damage-associated molecular patterns

(DAMPs)[154]. *In vivo*, the same radioconjugate demonstrated a DAMP release as well as DCs activation and $CD8^+$ T cells infiltration in a colorectal cancer model[155]. The same results were obtained in an adenocarcinoma mouse model with bismuth-213 (^{213}Bi) bound to albumin. In this model, administration of cancer cells irradiated with ^{213}Bi-albumin conferred protection against tumor proliferation in immunocompetent mice for two months[156]. In a murine model of multiple myeloma treated with ^{213}Bi in conjunction with anti-SDC1 mAb, an upregulation was detected in the production of IL-2, CCL-5, and IFNγ[157]. Protective outcomes were also documented with lead-212 (^{212}Pb) directed at the melanocortin 1 receptor in a melanoma model with an augmentation of the presence of tumor-infiltrating lymphocytes[158].

Clinical data have underscored the ability of α-emitters to modulate immune responses. In patients with prostate cancer, treatment with ^{223}Ra led to changes in circulating immune cells and the modulation of immune checkpoint expression. Specifically, ^{223}Ra treatment resulted in a reduction of PD-1 expressing $CD8^+$ T cells[159]. An abscopal effect, characterized by the elimination of distant and untreated lesions, was also observed in a patient with cutaneous squamous cell carcinoma following treatment with ^{224}Ra[160].

II. Primary α-emitters for targeted-α-therapy of glioblastoma

Considering the inherent physical, cellular, molecular, and microenvironmental constraints of GB, the challenge for α emitters to outperform β^- emitters, and thus achieve a curative effect with a lower toxicity, is substantial (Fig. 4). In this section, the α-emitting radionuclides employed in preclinical *in vivo* studies and clinical trials for the treatment of GB are introduced. Their availability, production and chemistry have been recently addressed in detail[161,162] and will be briefly discussed here.

1. Astatine-211

^{211}At is characterized by a branching decay, with each pathway involving in the release of an α particle, making it as a 100% α-emitter. In this decay scheme, ^{211}At directly contributes to 42% of α emission with an energy of 5.9 MeV, and subsequently decays to bismuth-207 (^{207}Bi). The remaining α particles (7.5 MeV) are emitted by its second daughter radionuclide, polonium-211 (^{211}Po). The entire decay sequence of ^{211}At ultimately concludes in the formation of the stable isotope lead-207 (^{207}Pb) (Fig. 5a). This single α emission reduces potential

complications associated with uncontrolled dissemination, given the fact that daughter nuclides typically dissociate from the intended vector during decay. Moreover, the daughter nuclides stemming from ^{211}At decay exhibit a markedly reduced radiotoxic profile. Thus, ^{211}Po possesses an exceedingly transient half-life of 0.52 s, while the generation of ^{207}Bi remains insubstantial. Furthermore, with its limited tissue penetration range of 50-90 µm and a half-life of 7.21 h, ^{211}At is ideally suited for patient application as residual radioactivity is less than 1% after 48 h. Nonetheless, the half-life duration of ^{211}At is sufficient for radiolabeling operations involving multiple steps. It is also worth noting that ^{211}At emits X-rays in the range of 72-92 keV, facilitating detection *via* Single Photon Emission Computed Tomography (SPECT) imaging modalities[163].

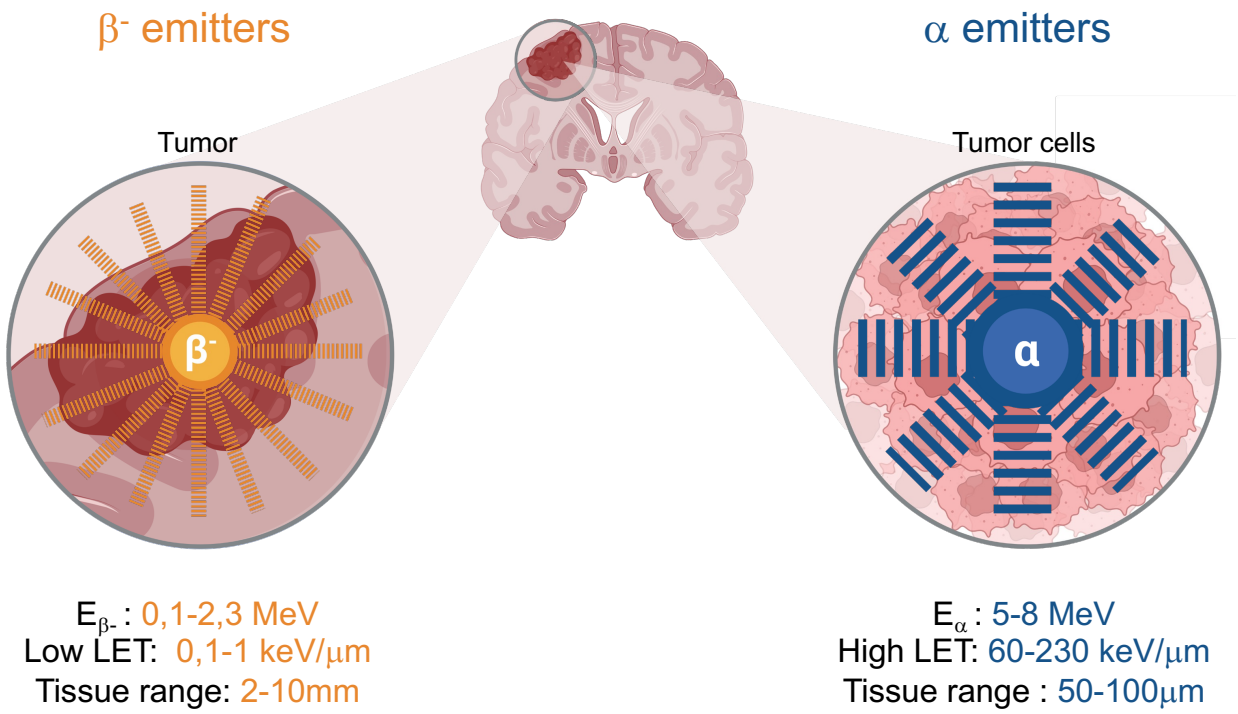

Fig. 4 | **Energy, Linear energy transfer (LET) and tissue range of β- and α-emitters.** (Created with Biorender - biorender.com)

The standard method to produce ^{211}At relies on the nuclear reaction ^{209}Bi(α,2n)^{211}At, which takes place when a natural bismuth target is bombarded with an α particle beam. A cyclotron capable of delivering over 20 MeV of incident energy is required for this reaction. Depending on the incident energy level, this process can also generate astatine-210 (^{210}At). ^{210}At carries a significant risk of toxicity due to its decay into polonium-210 (^{210}Po). As an α-emitter with a half-life of 138 days, the toxicity of ^{210}Po, even at low doses, is well-

established[164]. Thus, the optimal window of incident energy ranges from 28 to 29 MeV to minimize ^{210}At production and achieve a satisfactory yield of ^{211}At[165]. Currently, 13 cyclotrons across the USA, Europe, and Asia (mainly in Japan) meet the necessary criteria to perform this reaction. Projections indicate up to 30 operational cyclotrons in the coming years[166]. While the present supply is yet to match a steadily rising demand due to upcoming clinical needs, governmental initiatives have been addressing this disparity for several years. The recent formation of the World Astatine Community emerging from the European, American, and Japanese networks, aims to unify these efforts on a global scale by sharing ^{211}At production technology.

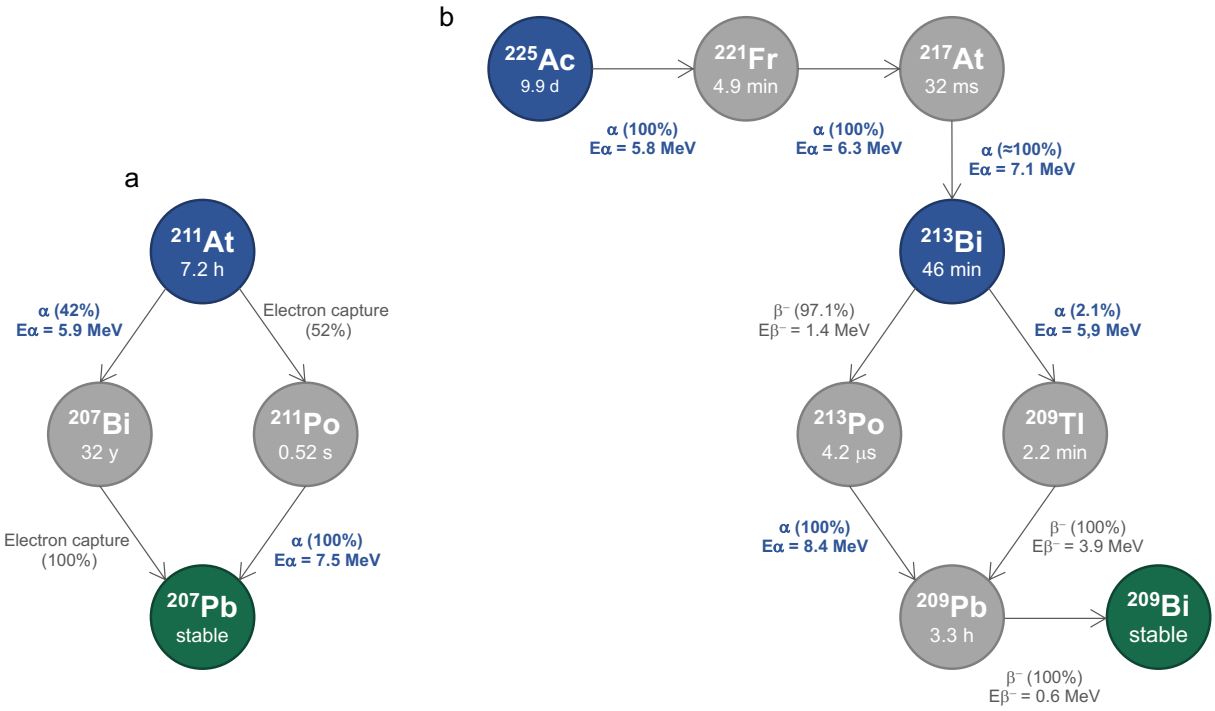

Fig. 5 | **Decay schemes and main characteristics of ^{211}At (a), ^{225}Ac, and ^{213}Bi (b).**

Preclinical studies. Discovered in 1940[167], ^{211}At experienced a resurgence in interest in the 1980s for the development of cancer targeted therapies, including GB. Following promising clinical outcomes achieved with ^{131}I radiopharmaceuticals[168–170], efforts shifted to ^{211}At in order to design less toxic therapies, primarily through the radiolabeling of mAb directed against tenascin-C (81C6 mAb) and epidermal growth factor vIII (EGFRvIII) (L8A4 mAb). Tenascin-C is a component of the extracellular matrix and is overexpressed in 90% of GBs, correlating with an unfavorable GB prognosis[171,172]. Concurrently, the active mutant EGFRvIII was identified as a key target, owing to its overexpression in GB and its involvement in processes such as angiogenesis, cellular migration, and proliferation[173,174]. A substantial challenge in this

endeavor was addressing the deastatination of the *in vitro* synthesized conjugates. However, in 1989, Zalutsky *et al.* proposed a technique that not only curtailed this deastatination but also preserved the *in vitro* immunoreactivity of labeled mAb or F(ab')$_2$ fragments[175]. The accumulation of preclinical data has enabled the determination of the lethal dose for 10% of animals (LD_{10}) to be 46 kBq/g for female mice and 102 kBq/g for males at 360 days after injection of ^{211}At-labeled 81C6 mAb (^{211}At-81C6)[176–181]. These studies showed that the primary toxicity risks are based on the potential deastatination of the mAb *in vivo*, with the [^{211}At]astatide then possibly accumulating in the stomach, spleen, thyroid, and lungs, in that order[182]. These results subsequently paved the way for the initiation of the first clinical trial in 2008, to assess safety and feasibility of intracranial (i.c.) injection of ^{211}At-81C6 in GB patients[183] (detailed in the next section).

Since then, successful astatination of new vectors has been achieved to test several targets in GB, including the L-type amino acid transporter 1 receptor (LAT1R)[59,184], poly(ADP-ribose) polymerase (PARP)[185], FAP[186], VEGF, and certain integrins[187]. ^{211}At encapsulation into gold nanoparticles has also been investigated. These nanoparticles provide the flexibility to be subsequently decorated with a targeting vector, such as a mAb or a peptide[71,72]. The majority of these investigations were conducted on mouse models bearing subcutaneous GB grafts, either as xenografts or allografts, with the TAT being administered *via* the tail vein. An exception is the study by Borrmann *et al.* published in 2013, which involved an orthotopic GB model treated with an i.c. injection of TAT[184] (Table 1).

Overall, the various preclinical approaches proposed over the past decade have demonstrated satisfactory stability of ^{211}At conjugates both *in vitro* and *in vivo*. Thus, these strategies are capable of inhibiting tumor growth and significantly enhancing survival in certain scenarios[184,186,187], all while maintaining reduced systemic toxicity. However, none of these methods have shown curative effects on the proposed *in vivo* models. Furthermore, the critical issue of tumor retention of radioactivity, which is paramount for ensuring therapeutic efficiency, was not always addressed in these studies. When considered, low percentages of the injected dose were observed following either i.v. or i.t. administration (with maximal retention ranging from ~0.4 to 4 %ID/g)[184,187]. As expected, i.t. administration displayed superior retention into the tumor mass. Ma *et al.* have reported the highest i.t. retention to date with the injection of ^{211}At-labeled FAP inhibitor (FAPi), exceeding 130 %ID/g after 30 min. However, rapid elimination was evident as it fell below 20% after just 2 h[186]. Despite the above discussed advances, no single strategy distinctly emerges. Almost all of these studies were based on

subcutaneous GB models, and future research should be conducted and replicated in orthotopic models to validate the relevance of these approaches and to investigate TAT efficacy.

Clinical studies. To date, the only clinical trial for the treatment of GB with ^{211}At was conducted by Zalutsky *et al*. and completed in 2005 (NCT00003461). This study enrolled 18 patients with recurrent brain tumors. All participants had previously undergone resection surgery and external beam radiation treatment, and 44% of them had received prior chemotherapy. Following surgical resection, these patients were administered a single dose of 71-347 MBq of ^{211}At-81C6 *via* a Rickham reservoir connected to a catheter placed in the resection cavity. After TAT injection, 14 patients (78%) received chemotherapy. Initially, 96.7 ± 3.6% of ^{211}At decays occurred within the resection cavity, with an estimated total residence time of 10.05 ± 0.4 h. The procedure was well-tolerated, with no observed grade 3 or higher neurotoxicity. Six patients experienced grade 2 neurotoxicity, which resolved within six weeks for five of them. The maximum tolerated dose (MTD) was not reached in this study. Encouraging median survival rates were reported: 13.5 months for all patients, 13 months for the 14 GB patients, and 29 months for astrocytoma or oligodendroglioma patients[91]. These median survival times were similar to those from a previous clinical study with ^{131}I-81C6[168], showing equivalent efficacy of ^{211}At (Table 2).

Currently, there are no ongoing clinical trial for the treatment of GB using ^{211}At. However, another clinical trial has also been completed with ^{211}At-labeled antibody for ovarian cancer (NCT04461457)[188–190] and several trials are ongoing or planned to investigate safety, feasibility and dose escalation in multiple myeloma (NCT04466475, NCT04579523), acute leukemia (NCT03670966, NCT03128034) and thyroid cancer (NCT05275946). Thus, in the upcoming years, it will be essential to initiate comprehensive, randomized clinical trials with broader patient cohorts.

2. Actinium-225

The nuclear properties of ^{225}Ac present promising potential to devise effective TAT strategies for GB. ^{225}Ac emits four α particles during its decay, as well as two β^- particles. The first three α particles exhibit radiation energies of 5.8, 6.3, and 7.1 MeV with ^{225}Ac successively decaying into francium-217 (^{217}Fr), ^{217}At and ^{213}Bi. At this point, a branched decay occurs. In the first branch, 97.1 % of ^{213}Bi decays into ^{213}Po by emitting a β^- particle (1.4 MeV), and ^{213}Po

decays into ^{209}Pb by emitting an α particle (8.4 MeV). In the second branch (2.1%), ^{213}Bi emits an α particle (5.9 MeV) to decay into thallium-209 (^{209}Tl), which emits a β^- particle (3.9 MeV) to decay into ^{209}Pb. The final β^- particle is emitted by ^{209}Pb, decaying to stable ^{209}Bi (Fig. 5b)[161]. These six emissions represent a pertinent tool to design efficient TAT. However, they also introduce risks and challenges, especially concerning dose control. During decay, the decoupling of the vector can lead to the uncontrolled dissemination of high-energy particles by the daughter nuclides and lead to toxicity in non-targeted tissues[191]. Unlabeled ^{225}Ac would thus preferentially accumulate into liver and bones[192]. Therefore, chelating ^{225}Ac, meaning binding to a vector, is crucial to mitigate this risk and ensure effective targeting. ^{225}Ac has a half-life of 9.9 days, which makes it compatible with macromolecular vectors, such as mAb or peptides with extended *in vivo* lifespans. This half-life also simplifies its logistical handling and clinical site distribution but could be too long depending on the treated pathology.

Similar to ^{211}At, current ^{225}Ac production falls short of clinical demands, and primarily relies on ^{229}thorium (^{229}Th)/^{225}Ac generators, with ^{229}Th originating from uranium-233 (^{233}U) decay. To date, ^{225}Ac used in all clinical studies was produced with this method. Direct production alternatives exist *via* cyclotron-mediated radium-226 (^{226}Ra) bombarding or ^{232}Th irradiation with high energy protons, but challenges arise from the availability and manipulation of ^{226}Ra, and the production of long half-life radionuclides during ^{232}Th decay requires heavy logistics[193–195]. However, global investments have been made to scale up the production of ^{225}Ac. Over the next decade, the worldwide supply of ^{225}Ac is expected to significantly increase, aligning with the rising clinical demands.

Preclinical studies. The use of ^{225}Ac in cancer treatment has attracted significant attention, particularly through its straightforward complexation with 1-,4-,7-,10-tetraazcyclododecane-1,4-,7-,10-tetra acetic acid (DOTA), which has become the current gold standard for ^{225}Ac chelators[196,197], and is a key component of the FDA-approved agents [^{177}Lu]Lu-DOTATATE and [^{68}Ga]Ga-DOTATOC for the treatment and diagnosis of neuroendocrine tumors[198,199]. Consequently, advancements have been made in treating acute myeloid leukemia (AML), prostate cancer, neuroendocrine tumors, and cancers of the bladder, ovary, breast, and colon[200]. However, strides concerning GB are more recent and in a limited number. Among the six related studies presented here, four of them used an orthotopic GB model to assess biodistribution, toxicity or therapeutic efficacy.

Table 1 | **Preclinical studies of targeted-α-therapy in GB *in vivo* models**

Reference	Investigation	Model	Tumor model			TAT agent				
			Cell line	Injection site	Initial cell nb or treated vol.	Activity per animal (MBq)	Vector	Target	Vector quantity per animal (mg)	Injection route, injected vol. per animal (µL)
Astatine-211										
Zalutsky *et al.*, 1989[175]	Biodistribution	BALB/c	D54MG	s.c.	300 mm^3	0.296	RPC 5 $F(ab')_2$	n/a	5	i.v.
	Biodistribution	BALB/c	D54MG	s.c.	300 mm^3	0.259	Mel-14 $F(ab')_2$	Chondroitin sulfate	5	i.v.
Zalutky *et al.*, 1997[176]	Biodistribution	Athymic mouse	D54MG	s.c.	n/a	0.074	ch81C6 mAb	Tenascin-C	2	i.v. or i.th.
Reist *et al.*, 1999[179]	Biodistribution	Athymic mouse	U87MG ΔEGFR	s.c.	150-250 mm^3	0.148	L8A4 mAb	EGFRvIII	2.5	i.v.
McLendon *et al.*, 1999[180]	Toxicity	B6C3F1	n/a	n/a	n/a	m: 0.317 - 1.710 f: 0.301 - 1.560	ch81C6 mAb	Tenascin-C	m: 8 - 43 f: 7.5 - 39	i.v.
Vaidyanathan *et al.*, 2003[181]	Biodistribution	BALB/c	U87MG ΔEGFR	s.c.	n/a	0.037	L84A mAb	EGFRvIII	0.5 - 1	i.v. 100
Borrmann *et al.*, 2013[184]	Biodistribution	BDIX/Ztm rat	BT4Ca	i.c.	1.10^4	2	Phe	LAT1R	n/a	i.v. 300
	Survival	BDIX/Ztm rat	BT4Ca	i.c.	1.10^4	1.6 - 3 (1 - 2 cycles)	Phe	LAT1R	n/a	i.v. 320 - 600
Watabe *et al.*, 2020[59]	Biodistribution	ICR mouse	n/a	n/a	n/a	0.53 ± 0.04	Phe	LAT1R	n/a	i.v.
	Efficacy	Nude mouse	C6	s.c.	5.10^6	0.3 - 1	Phe	LAT1R	n/a	i.v.
	Efficacy	C57BL/6J	GL261	s.c.	1.10^7	1	Phe	LAT1R	n/a	i.v.
Dabagian *et al.*, 2021[185]	Survival (anti-PD-L1 combination)	C57BL/6J	GL261	s.c.	1.10^6 200 mm^3	0.24 – 0.72	MM4	PARP1	n/a	i.p.
Kato *et al.*, 2021[71]	Efficacy	Nude rat	C6	s.c. (x 2)	$0.9.10^7$	1.4 ± 0.4 / tumor	Gold np	n/a	n/a	i.t. 100
Liu *et al.*, 2021[72]	Biodsitribution	Nude mouse	n/a	n/a	n/a	0.185	Gold np	n/a	100	i.v. 100
	Efficacy	Nude mouse	U87MG	s.c.	3.10^6 100 mm^3	1.11	Gold np	n/a	n/a	i.t. 30
Ma *et al.*, 2022[186]	Biodistribution	BALB/c	U87MG	s.c.	3.10^6	0.3	FAPi	FAP	n/a	i.v. or i.t.
	Survival	BALB/c	U87MG	s.c.	3.10^6	0.18 - 0.55	FAPi	FAP	n/a	i.t.
Liu *et al.*, 2022[187]	Biodistribution	Nude mouse	U87MG	s.c.	5.10^6	3.5 ± 0,2	iRGD-C6-lys -C6-DA7R	VEGFR + integrins	n/a	i.v.
	Survival	Nude mouse	U87MG	s.c.	5.10^6	0.18 - 0.74	iRGD-C6-lys -C6-DA7R	VEGFR + integrins	n/a	i.v.
Actinium-225										
Pandya *et al.*, 2016[201]	Biodistribution	BALB/c	U87MG	s.c.	1.10^6	0.7	RGDγK	$\alpha_v\beta3$ integrin	0.04	i.v. 150
	Toxicity, efficacy	BALB/c	U87MG	s.c.	1.10^6	0.010 - 0.16	RGDγK	$\alpha_v\beta3$ integrin	n/a	i.v.
Behling *et al.*, 2016a[202]	Biodistribution	Ink4a-Arf$^{-/-}$ mouse	DF-1	i.c.	2.10^5	0.0111	E4G10 mAb	VE-cadh	n/a	i.v. 100
	Efficacy, BBB remodeling	Ink4a-Arf$^{-/-}$ mouse	DF-1	i.c.	2.10^5	0.0074	E4G10 mAb	VE-cadh	n/a	i.v. 100
Behling *et al.*, 2016b[203]	Efficacy, BBB remodeling	Ink4a-Arf$^{-/-}$ mouse	DF-1	i.c.	2.10^5	0.0074	E4G10 mAb	VE-cadh	n/a	i.v. 100
Sattiraju *et al.*, 2017a[204]	Efficacy, BBB remodeling	Athymic nude mouse	U87MG	i.c.	1.10^5	0.037	Liposome	$\alpha_v\beta3$ integrin	n/a	i.c. 5
Sattiraju *et al.*, 2017b[205]	Safety, efficacy	Athymic nude mouse	U251-*f*Luc	i.c. 5 mL	1.10^5	0.037	Pep-1L	IL13RA2	n/a	i.c. 5
Salvanou *et al.*, 2020[206]	Biodistribution	SCID mouse	U87MG	s.c.	300 mm^3	0.005	Gold np	n/a	n/a	i.v. or i.t.
Radium-224										
Nishri *et al.*, 2022[207]	Safety, efficacy (TMZ and BEV combination)	Athymic nude mouse	U87MG	s.c. 100 mL	5.10^6	0.075 - 0.110	Coated steel seed	n/a	n/a	i.t.

s.c.: subcutaneous, i.v.: intraveinous, i.c.: intracranial, i.t.: intratumoral, mAb: monoclonal antibody, m: male, f: female, Phe: phenylalanine, np: nanoparticle, VE-cadh: vascular endothelial cadherin, BTB: brain-tumor barrier, BBB: brain-blood barrier, TMZ: temozolomide, BEV: bevacizumab.

The targeting of proangiogenic integrin $\alpha_v\beta_3$, overexpressed in high-grade gliomas[208–210], was investigated by Pandya *et al.* in a subcutaneous murine GB model using the RGDyK peptide vector. The study evaluated the biodistribution and longitudinal imaging of ^{225}Ac distribution. This imaging approach was not reliant on the γ emission of ^{213}Bi from the decay chain, but on the Cerenkov luminescence emitted by various ^{225}Ac daughter nuclides[201]. Cerenkov Luminescence Imaging (CLI) captures the ultraviolet light emission when specific charged particles surpass the phase velocity of light in a given medium[211]. This approach allowed for effective detection, but could not anticipate some toxic effects observed in animals. Notable nephrotoxicity was observed at high doses, although the treatment was generally well-tolerated. MTD was determined at 0.04 MBq in this model. With all three tested doses, a significant regression in tumor growth was observed after 14 days at doses of 0.01, 0.02, and 0.04 MBq[201]. In 2017, Sattiraju *et al.* also explored $\alpha_v\beta_3$ targeting in an orthotopic GB model, *via* an i.t. injection. Here, $\alpha_v\beta_3$-targeted liposomes demonstrated an induction of permeabilization of the BBB and BTB, locally but also distantly from the injection site, in areas unaffected by the DNA double-strand breaks (DSB), suggesting a modification of the BBB independent from ^{225}Ac radiation[204].

Monomeric vascular endothelial cadherin (VE-cadherin or cadherin 5), is expressed on tumor neovasculature and progenitor endothelial cells and represent a promising target for altering the vascular microenvironment of GB[212,213]. Its targeting was examined in two *in vivo* studies using the ^{225}Ac-labeled E4G10 mAb for i.v. injection in a subcutaneous GB model[202,203]. A notable modification of the BBB was observed, especially a reduction in the number of epithelial and perivascular cells at a 0.074 MBq dose. This approach also led to the reduction of tumor-related edema and necrosis zones, and depleted Tregs, which are known for their immunosuppressive role in GB[203]. This method significantly increased the survival of the treated animals, either as a standalone treatment or in combination with temozolomide[202].

Targeting Interleukine-13 receptor subunit α2 (IL13RA2), a highly studied GB biomarker due to its involvement in tumor progression[214], with ^{225}Ac has also been explored. Locoregional CED administration in an orthotopic GB model using a peptide targeting IL13RA2 (Pep-1L) labeled with actinium showed significant progress. A dose of 0.037 MBq enabled optimal brain retention, substantially reducing tumor growth without noticeable toxic effects. Survival was significantly improved, with a median survival of 41 days compared to 23 days for mice injected with a saline solution[205].

Gold nanoparticles loaded with ^{225}Ac have also demonstrated their utility as potential platforms for association with targeting antibodies or peptides. In an orthotopic murine model of GB, these nanoparticles showed strong local uptake after i.t. injection and slow clearance over 12 days. The efficacy was notable since these nanoparticles were not associated with a targeting vector. A previous study with gold nanoparticles labeled with ^{177}Lu has already demonstrated strong tumor uptake both with and without targeting[215]. However, over the same period, the gradual uptake in the liver, kidneys, and spleen, though moderate, needs consideration in terms of toxicity. This could be attributed to the clearance of the nanoparticles through the hepatobiliary pathway or the partial release of ^{225}Ac from the chelator. A delay in tumor growth over 22 days was achieved after three injections of treatment, with a total activity of 0.015 MBq, underscoring the benefits of dose fractionation in minimizing adverse effects[206] (Table 1).

Clinical studies. ^{225}Ac has only been the subject of one pilot study for the treatment of patients with GB. Following two pilot studies centered on treating GB patients with ^{213}Bi, which will be detailed later, Krolicki *et al.* sought to explore the clinical potential of ^{225}Ac. They hypothesized enhanced efficacy due to the four α particles emitted by this radionuclide, combined with its considerably longer half-life compared to that of ^{13}Bi (46 min)[216]. This study, therefore, introduced a TAT using ^{225}Ac-labeled substance P (^{225}Ac-DOTA-SP) to target neurokinin type 1 receptors (NK_1R)[216]. These receptors are overexpressed in GB, where they contribute to the proliferation, invasion, and survival of cancer cells[217–219]. 21 patients with recurrent primary (15) and secondary glioblastoma (6) were selected for this study. All these patients had previously undergone the standard therapeutic protocol (Stupp regimen: surgery, radiotherapy, chemotherapy). The dose for this study was determined based on previous human trials. Thus, treating prostate cancer patients with 3 doses of 8 MBq of ^{225}Ac-PSMA-617 was shown to be safe and effectiveCliquez ou appuyez ici pour entrer du texte.. Additionally, 3 cycles of 18.5 MBq of ^{225}Ac-DOTATOC were demonstrated to be safe and effective in patients with neuroendocrine tumors[221]. TAT was delivered directly into the resection cavity using one or two catheters. Patients received doses ranging from 10 MBq to 30 MBq over 1 to 6 cycles, with the total activity varying between 10 and 120 MBq. This dose escalation approach was generally well tolerated. Some patients experienced temporary side effects like edema, seizures, aphasia, and hemiparesis. Importantly, no adverse effects related to kidney, liver, or blood were linked to the TAT. While the primary tumor often showed signs of stabilization, prognosis sometimes deteriorated due to the emergence of satellite tumors not initially identified by MRI.

Interestingly, patients with secondary GB had a notably extended survival post-diagnosis compared to those with recurrent primary GB. Yet, both groups showed similar progression-free survival (PFS) and overall survival durations. While there were positive effects on survival, the therapeutic benefit did not directly correlate with the dose administered, and survival medians were less significant than results from preliminary studies using ^{213}Bi (Table 2).

3. Bismuth-213

As previously described, ^{213}Bi originates from the decay chain of ^{225}Ac, and emits one α particle and two β^- particles (Fig. 5b). Additionally, its γ emission of 435 keV provides a valuable avenue for longitudinal tracking *via* SPECT imaging[161]. Its brief half-life of 45.6 min dictates the selection of biological vectors with a compatible *in vivo* half-life, but also introduces constraints given the extended reaction times inherent to radiolabeling chemistry. The presence of a stable isotope of bismuth facilitated the swift development of suitable chelators. Consequently, the CHX-A″-DTPA ligand has been identified as an optimal choice for ^{213}Bi chelation, and DOTA also proved to be suitable, forming robustly stable complexes with high kinetic stability, thus limiting the well-described accumulation of unlabeled ^{213}Bi in kidneys and urine[192].

The production of ^{213}Bi relies on its parent radionuclide, ^{225}Ac, which can be loaded into a radionuclide generator. This setup allows for the production of ^{213}Bi with high specific activity and purity. Moreover, the ^{225}Ac required for this process doesn't need to be pure, as the co-production of ^{227}Ac is not problematic. These ^{225}Ac / ^{213}Bi generators typically use cation and anion exchange or extraction chromatography techniques[222,223]. In clinical studies, the main production route relies on AG MP-50 organic resin support, designed for cation exchange, on which is deposited ^{225}Ac. This device allows production for several weeks, with up to six therapeutic doses of radionuclide per day[224].

Preclinical Studies. To date, no preclinical studies involving ^{213}Bi have been conducted specifically for GB. However, *in vitro* investigations have been conducted on the LN18 cell line of GB to examine the impacts of ^{213}Bi-labeled anti-EGFR mAb on cellular metabolism. In this context, the cellular conversion of hyperpolarized [1-^{13}C]pyruvate to [1-^{13}C]lactate was assessed using magnetic resonance spectroscopy (MRS). Significant increase in lactate/pyruvate ratio, suggesting an increased metabolic activity, and cell death by induction

of DNA DSB were demonstrated after treatment221,222. Several preclinical studies have also demonstrated the *in vivo* stability of ^{213}Bi conjugates223. Additionally, biodistribution and efficacy studies have been conducted, primarily using mAb vectors, on models such as melanoma224, multiple myeloma225, ovarian cancer226, or metastatic breast cancer227.

Clinical studies. The first pilot study involving ^{213}Bi for the treatment of GB was carried out by Kneifel *et al.* on a very limited cohort[232]. The use of ^{213}Bi was introduced as an alternative to ^{90}Y-DOTAGA-SP for some patients to circumvent the crossfire effect on critically located brain tumors. Accordingly, one patient with GB and another with grade II oligodendroglioma received injections of ^{213}Bi-DOTAGA-SP. The GB patient was previously treated with the standard protocol (surgery, radiotherapy and chemotherapy) and was administered a dose of 375 MBq. The oligodendroglioma patient underwent two surgical interventions before injection of a dose of 825 MBq. The treatment was well-tolerated by both patients. However, evaluating the GB progress was challenging due to the presence of a residual tumor. For the oligodendroglioma patient, the resection of a tumor lesion after 33 months revealed radionecrosis and the absence of viable tumor cells, with an additional 34 months passing without recurrence[232].

Another trial on a small cohort was led by Cordier *et al.*, to assess ^{213}Bi efficacy as a primary therapeutic modality in patients bearing critically located GB. Depending on the size and configuration of the tumor, one or more catheters were placed intratumorally for the administration of the treatment. Thus, two GB patients and three grade III astrocytoma patients received doses ranging from 1.07 to 29.44 GBq over 1 to 4 cycles. Patients showing tumor progression or recurrence subsequently received chemotherapy and/or radiotherapy. Once again, the safety and feasibility of the treatment were confirmed. The therapy induced radionecrosis and allowed for the delineation of the tumor as observed through MRI. High retention of the radioisotope at the injection site was verified by SPECT[233].

Krolicki *et al.* conducted two similar studies on GB patients to assess the administration of ^{213}Bi-DOTA-SP. In both studies, patients had a catheter placed either in the resection cavity or intratumorally. In the first one, nine patients were treated with one to six cycles over two months, receiving a total injected activity ranging from 1.4 to 9.7 GBq of ^{213}Bi-DOTA-SP. The treatment was well-tolerated, with observed symptoms being primarily mild transient adverse

reactions, most notably headaches due to temporary perifocal edema. FLAIR imaging indicated the presence of an edema or a non-enhancing tumor. Median PFS was 5.8 months, median OS-t was 16.4 months, and median OS-d was 52.3 months[234].

Table 2 | **Completed pilot studies and clinical trials in high-grade glioma treated with TAT**

Reference	Clinical situation	Number of patients	Investigation	Vector	Target	Injection route	Total activity (GBq)	Median PFS (months)	Median OS-t (months)	Median OS-d (months)	Conclusion
Astatine-211											
Zalutsky *et al.*, 2008[91] (NCT00003461)	GB	18 - GB (14), O (3), A (1)	Feasibity, safety	SAB-ch81C6 mAb	Tenascin-C	i.c.	0.071 - 0.347	n/a	n/a	All: 13.5 GB: 13 A+O: 29	Feasible, safe, MTD not reached, small cohort
Bismuth-213											
Kneifel *et al.*, 2006[232]	GB, glioma	2 - GB (1), OII (1)	Feasibility, biodistribution, safety	DOTAGA-SP	NK_1R	i.t. / i.c	0.375 - 0.825	n/a	n/a	n/a	Feasible, very small cohort
Cordier *et al.*, 2010[233]	GB, glioma	5 - GB (2), AII-III (3)	Feasibity, safety	DOTA-SP	NK_1R	i.t.	1.07 - 29.44 (1 - 4 cycles)	n/a	n/a	n/a	Feasible, safe, radiation-induced necrosis, tumor demarcation, very small cohort
Krolicki *et al.*, 2018[234]	GB	9	Feasibity, safety	DOTA-SP	NK_1R	i.t. / i.c.	1.4 - 9.7 (1 - 6 cycles)	5.8	16.4	52.3	Feasible, safe
Krolicki *et al.*, 2019[235]	GB	20	Feasibity, safety	DOTA-SP	NK_1R	i.t. / i.c.	1.6 - 11.2 (1 - 7 cycles)	2.7	7.5	23.6	Feasible, safe, longer PFS/OS with dose repetition
Actinium-225											
Krolicki *et al.*, 2021[216]	GB	21	Dose escalation, safety	DOTA-SP	NK_1R	i.c.	0.0116 - 0.1495 (1 - 6 cycles)	2.4	9	35	Feasible, safe, no dose-dependent effect

GB: glioblastoma, A: astrocytoma, O: oligodendroglioma, SP: substance P, i.c.: intracavitary, i.t.: intratumoral, PFS: progression-free survival, OS-t: overall survival from treatment injection, OS-d: overall survival from diagnosis, MTD: maximal tolerated dose

In the second study, 20 patients received 1-7 cycles of ^{213}Bi-DOTA-SP treatment, which was largely well-tolerated. Side effects included facial flushing in two patients and ventricular enhancement in one. Ten patients had epileptic seizures post-injection but had prior seizure histories. One had a brief paresis increase. No severe side effects were noted. The median OS-d was 23.6 months, while median OS-r was 10.9 months, with a median PFS of 2.7 months. These findings suggest that localized treatment with high radioisotope doses is a promising approach for recurrent GB, offering survival rates that compared favorably to conventional treatments, as median survival after Stupp regimen ranges from 9.7 to 15.9 months[235] (Table 2).

4. Promising α-emitters for the treatment of GB

Significant progress has been made in TAT for GB using ^{211}At, ^{225}Ac, and ^{213}Bi, yet much of this domain remains uncharted. As previously mentioned, other α-emitters such as ^{223}Ra or ^{212}Pb have shown promises in both preclinical and clinical settings for the treatment of various cancers, as previously mentioned, and are pending comprehensive preclinical assessment for GB therapy. Each α radionuclide has its set of advantages and drawbacks. Understandably, those that are readily available and easier to manipulate tend to be more extensively studied. Similarly, the presence of a stable isotope for these radionuclides, as is the case for ^{213}Bi, considerably simplifies radiochemical processes for producing new stable vectors. However, evolution in the global supply of α-emitters and advancements in radiochemistry foster hope for a shift towards these less studied nuclides for GB treatment. Here, we suggest a few potential directions regarding upcoming α-emitters for GB therapy.

For example, a ^{223}Ra-based therapy (half-life of 11.43 days, emitting four α and two β^- particles) has been assessed *in vitro* using a nanozeolite-SP conjugate. This study demonstrated robust retention of TAT and pronounced affinity for NK_1R, resulting in significant cytotoxicity in the T98G cell line[236]. Furthermore, the potential of ^{224}Ra-loaded seeds as implantable sources was explored *via* a subcutaneous GB xenograft in an athymic mouse model, in combination with temozolomide or bevacizumab (Table 1). ^{224}Ra has a half-life of 3.66 days and emits four α and two β^- particles. ^{224}Ra treatment considerably impeded tumor growth in this model. The most effective strategy seemed to involve the administration of bevacizumab prior to TAT[207]. ^{212}Pb is also an α-emitter of interest, with a half-life of 10.6 h and emission of one α and two β^- particles. Its combination with DOTAMTATE to target somatostatin receptor (SSTR) has shown positive outcomes in preclinical models[237] and holds promise in clinical trials for neuroendocrine tumors (NCT03466216)[238]. Given the expression of SSTR as markers for GB, the stability of this conjugate may offer a seamless transition for GB testing.

Other prospective α-emitters, including thorium-227 (^{227}Th), terbium-149 (^{149}Tb), and bismuth-212 (^{212}Bi), could be future potential candidates yet to be examined for GB. Currently, the former two face challenges in terms of production, while ^{212}Bi, with its relatively short half-life of 60.6 min, is frequently overlooked in favor of its parent nuclide ^{212}Pb in therapeutic strategies[161]. Essential parameters such as radiochemical yield, purity, daughter element safety, and *in vivo* stability must be considered for a transfer to clinical application.

III. Preclinical challenges and prospects

Before addressing some future prospects of TAT in terms of new avenues to explore or therapeutic combinations, it is imperative to emphasize the importance of employing appropriate preclinical GB models to obtain meaningful results and facilitate the transition to clinical trials. The pursuit of the ideal therapeutic combination, integrating radionuclide, vector, and target, should continue and will undeniably benefit from new GB models that more closely mirror the clinical reality (Fig. 6).

1. *In vivo* models

GB cell lines. The GB models explored herein for TAT primarily rely on human GB cell lines for xenograft models, such as U87MG, U251, DF-1, D54MG, or rodent cell lines for syngeneic models, including GL261 in mice and C6 and BT4Ca in rats. It is a prevalent practice to maintain cell lines through *in vitro* culture in two-dimensional environments, employing non-physiological culture media and often involving enzymatic dissociation. Such methodologies increase the propensity for clonal selection and genetic drift during cultivation, potentially influencing drug response outcomes[239,240]. Furthermore, extended *in vitro* culture exacerbates this issue, with noted gradual deterioration of the GB signature accompanied by the accumulation of genomic duplications and depletions over time[210].

Xenograft models. For xenograft models, U87MG and U251 cell lines are among the most frequently used in research. Although genetically similar to human GB[241], U87MG cells exhibit a limited i.t. heterogeneity and a moderate invasive profile[242]. Similarly, U251 cells also show limited heterogeneity and are responsive to both chemotherapy and external beam radiotherapy in contrast to human GB[243]. Each cell line presents its own set of advantages and drawbacks. Given that classical GB cell lines do not accurately replicate GB features, the ideal approach would involve the use of patient-derived xenografts (PDX), which closely reflect the heterogeneity and histology of human GB[244,245]. These allow for the creation of a single cell suspension derived directly from a patient's tumor sample, which can then be injected into a mouse. Culturing in serum-free media supplemented with fibroblast growth factor b (bFGF) and EGF is also a viable option, especially considering the genomic stability of GB cells under such conditions[246]. However, several challenges persist. Firstly, accessing patient samples and challenges associated with establishing these models in culture makes the procedures more

intricate. Moreover, there is a pronounced variability between patients, leading to significant variability between models, which in turn complicates the production of reproducible data. Additionally, using PDX to investigate immune responses invariably necessitates the use of humanized mice[247,248].

Syngeneic models. The radiobiological effects of α particles on GB cells, particularly in terms of their immunogenicity, remain largely unexplored. Syngeneic murine models serve as pertinent tools to probe these *in vivo* dynamics. Within murine studies, the GL261 cell line is predominantly employed, being a well-characterized cell line that retains an infiltrative profile as well as higher tumorogenicity in serum free media[249]. Nonetheless, this cell line displays a high mutational load and strong immunogenicity through high major histocompatibility complex I (MCH-I) expression compared to human GB[250], potentially leading to a stronger adaptive immune response following TAT. Mouse cell lines exhibiting a diminished immunogenicity closer to human GB, such as the SB28 line, appear more apt for investigating immune repercussions post-TAT application[250]. Moreover, the SB28 cell line manifests therapeutic responses mirroring those seen in human GB[251,252]. Yet, it is worth noting that this particular cell line is conspicuously homogeneous and is underrepresented in literature, especially in the context of its histological attributes and microenvironment.

Tumor site. In both scenarios, the tumor injection site is of paramount importance. For GB, orthotopic cerebral grafting is vastly preferable as it recapitulates the authentic GB microenvironment. Indeed, subcutaneous GB models lack both BBB and BTB, and they often display a more robust anti-tumoral immunity. Additionally, these models do not present certain GB features like single-cell invasion, tumor necrosis, and microvascular proliferation. In essence, the TME of subcutaneous models does not reflect the actual clinical scenario. The TME plays a key role in treatment response, especially to radiotherapy[253]. So far, most preclinical investigations addressing TAT for GB so far have predominantly relied on subcutaneous GB models. Despite their limitations, subcutaneous GB models remain widely used due to their ease of execution and visual follow-up of the induced tumors. Among the 19 preclinical GB studies examining TAT approaches, 13 conducted their experiments with such ectopic models. Despite the promising results described in this Review, it remains challenging to assess the actual efficacy of treatment on a subcutaneous GB. Similarly, tumor retention of TAT is inevitably different, whether the treatment is administered systemically or intratumorally.

TAT administration route. The preclinical studies discussed herein predominantly employed i.v. delivery of TAT, with less frequent use of direct i.c. injection. Success hinges upon the precise interplay between radionuclide, vector, and target. The administration route, whether i.v. or i.c., is pivotal for the success of this combination.

The i.v. delivery necessitates the injection of a high activity of α-emitter associated with a high concentration of vector and poses an elevated risk of off-target toxicity due to its prior circulation in the bloodstream. Achieving specific targeting and ensuring predominant tumor retention are imperative with this method. This approach is less invasive as it does not demand additional surgery, making it particularly appealing for GB patients for whom surgical resection is not viable. The primary challenges lie in addressing the BBB and BTB, which exhibit significant heterogeneity in patients. Additionally, since this method relies on blood-mediated distribution, poorly vascularized tumor regions and isolated infiltrating cells stand a higher chance of escaping the radiations emitted by TAT.

The i.c. administration, on the other hand, bypasses the constraints of the BBB/BTB. This procedure can be integrated with surgical resection in patients, taking advantage of the resultant resection cavity for TAT administration, or it can be directly injected intratumorally. Cordier *et al.* observed that this latter approach as a primary therapeutic intention was feasible and the demarcation of the tumor post-TAT could aid in potential resection[233]. Intratumoral retention is also a primary determinant of success for this method, and it depends as much on the inherent properties of the vector as on the choice of a therapeutic target exclusive to GB. Thus, it is conceivable that using a mAb for i.t. administration allows for extended retention due to its size (~150 kDa) and its prolonged biological half-life in tissues.

Joining both methods is also a possibility. α particles appear capable of permeabilizing the BBB following i.c. administration[202–204]. An initial i.c. treatment might not only manage the BBB while retaining therapeutic efficacy but could also potentially aid in the permeabilization of both the BBB and BTB, optimizing TAT distribution for subsequent i.v. injections.

Model Standardization. In addition to the aspects previously discussed, the introduction of BBB integrity monitoring through DCE-MRI in orthotopic models treated with i.v. TAT could assist the evaluations of the limitations of certain approaches and help determining which radioconjugates are best suited to penetrate the BBB and target the tumor[254]. In orthotopic models, ensuring accurate tumor injection coordinates is crucial due to the diverse risks of cell

infiltration and migration, especially when injecting near the ventricles[255,256]. Future directions should encompass greater explorations towards these types of approaches and the use of CED, given the advantages it offers. Incorporating the Stupp regimen would also be of great interest. Le Reste *et al.* have developed a murine GB model that emulates the Stupp regimen, encompassing resection surgery, chemotherapy, and radiotherapy. Incorporating TAT during the surgical stage of this protocol, as opposed to using it as a standalone primary treatment, would enable an assessment of the positioning of TAT within the context of the standard of care protocol[257]. As we have observed, locoregional i.c. treatments have demonstrated their safety and feasibility in clinical settings, yet they are significantly underrepresented in the preclinical landscape of TAT for GB.

2. Targeting innovations and emerging vectors

The predominant challenge in GB is the intratumoral heterogeneity, which complicates the determination of an appropriate therapeutic target. The objective of targeted therapy is the complete eradication of tumor cells. The therapeutic administration window is critically important to effectively target cells with invasive potential before they become inaccessible. Today, preclinical studies of TAT for GB rely on the use of mAbs, peptides, non-peptidic small molecules, and gold nanoparticles. Thus, many promising vector types remain unexplored. A recent review by Lepareur *et al.* delved into these issues in detail[258].

Antibodies and derivates. The use of mAb for TRT in GB has demonstrated clinical efficacy with both β^- and α-emitting radionuclides. Some FDA-approved TRT treatments are indeed based on anti-CD20 mAb, such as Zevalin® and Bexxar®[22,23]. Monoclonal antibodies have a significant molecular weight, leading to low tissue diffusivity, which results in slow clearance. These properties can be advantageous for locoregional administration of TRT combined with a short-lived radionuclide, allowing prolonged retention of the radionuclide throughout its decay within the tumor. However, these characteristics can pose challenges for the systemic administration of TRT, especially if the radionuclide has a long half-life, increasing the risk of off-target toxicity.

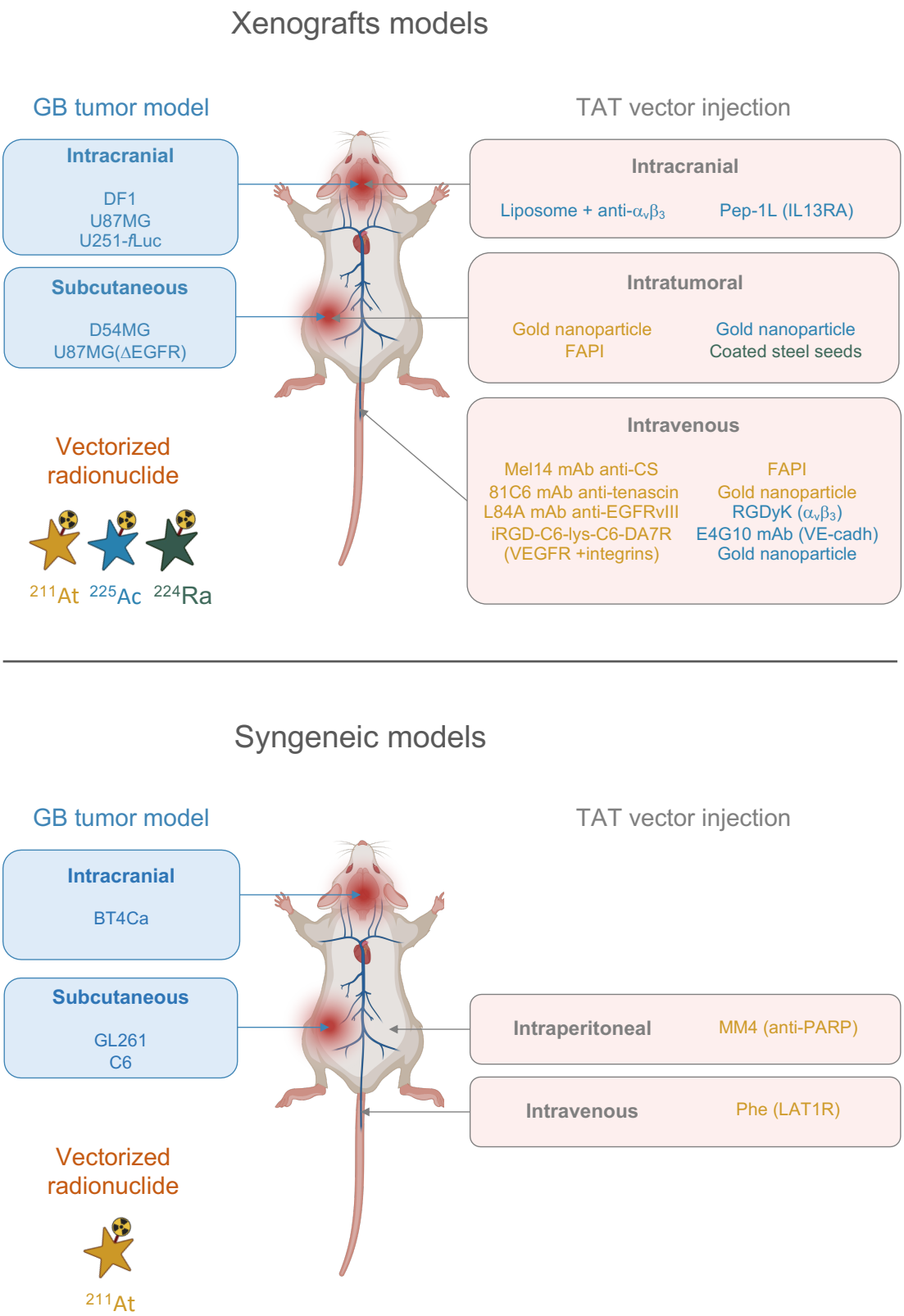

Fig. 6 | **Overview of current preclinical models and strategies for TAT in GB.** The majority of studies focusing on TAT in rodent models of GB have been conducted using xenograft models, most commonly with subcutaneous tumor grafts. Intravenous administration of TAT is the most explored route *in vivo*, with isotopes like ^{211}At or ^{225}Ac, and ^{224}Ra in one study. Syngeneic models are still underused, and no study has investigated locoregional administration of TAT in such models. Only ^{211}At has been studied in a syngeneic *via* intravenous and intraperitoneal routes. For further details, please refer to Table 1. *CS: chondroitin sulfate, mAb: monoclonal antibody Phe: phenylalanine.* (Created with Biorender - biorender.com)

When it comes to TAT based on mAb, only the targeting of tenascin-C[91,176,180], EGFRvIII[179,181], and VE-cadherin[202,203] have undergone testing. Historical targets addressed by TRT might offer promising avenues given some satisfactory results achieved. For instance, DNA-Histone H1 is an intracellular antigen expressed in the necrotic core of tumor cells[259]. Its targeting has shown encouraging overall survival in patients when labeled with ^{131}I[260,261]. C-X-C chemokine receptor type 4 (CXCR4) is a G-protein coupled chemokine receptor involved in tumor survival, proliferation and migration[262–264]. A TRT based on lipid nanocapsules loaded with ^{188}Re and targeting CXCR4 demonstrated an improved survival in a GB mouse model[68].

Reducing the vector size may provide several benefits in terms of diffusivity, clearance, and access to hard-to-reach epitopes. Hence, mAb derivatives of varying sizes have been developed. Among these, F(ab) and F(ab')$_2$ retain one and two variable fragments of the mAb, respectively, maintaining their affinity while being depleted of their constant region (Fc). Monobodies, nanobodies, affibodies, anticalins, and designed ankyrin repeat proteins (DARPins) are examples of non-immunoglobulin synthetic scaffolds out of the approximately 20 existing today that possess affinity and selectivity comparable to mAbs for a given target. They generally weigh less than 10 kDa. Unlike mAbs, their modular nature allows for the creation of bispecific molecules, an advantageous feature when considering pretargeting for TAT[265].

Pretargeting. Pretargeting helps minimize off-target radiation exposure by first targeting the tumor and subsequently injecting the radionuclide of interest. This method involves the administration of a bispecific antibody that recognizes the therapeutic target, followed by the introduction of a radiolabeled bivalent hapten peptide[266]. In the case of GB, pre-targeting strategies based on the biotin-streptavidin interaction[267], or initial targeting of fibronectin[268] have been conducted with ^{131}I. The limitations of this approach, however, include poor mAb uptake, dose-limiting toxicities, and the secretion of antidrug antibodies in patients. Pretargeting might also be relevant for TAT considering the high energy levels of α-emitters. Recently, a three-step pretargeting approach based on ^{225}Ac was evaluated for targeting human epidermal growth factor receptor 2 (HER2) in a murine model of ovarian cancer. Mice received an intraperitoneal injection of a bispecific antibody targeting both HER2 and DOTA. This was followed by an i.v. administration of a clearing agent, prior to the injection of the ^{225}Ac-labeled hapten. The results demonstrated extended survival with minimal observed toxicity[269].

Aptamers. Often termed "chemical antibodies", aptamers are short RNA or DNA oligonucleotides capable of binding targets with notable affinity and selectivity. These molecules form specific three-dimensional structures that recognize their targets similarly to antibodies. Aptamers are produced using the SELEX process, which iteratively refines an oligonucleotide library for optimal target binding. This method enhances the specificity and selectivity of the resultant aptamers. Unlike antibodies, aptamers have superior stability, reduced batch variation, and are generally non-toxic and non-immunogenic. Their smaller size allows for better tissue penetration and the ability to access epitopes inaccessible to larger antibodies, making them promising for diagnostic imaging[270].

The first radiolabeled aptamer, TTA1, was synthetized in 2006 and targets the tenascin-C. This aptamer uptake relies on the presence of human tenascin-C protein found in various solid tumors. The aptamer was detected in GB models, showing rapid tumor uptake after i.v. administration, with notable tumor diffusion at 3 h and effective clearance from the kidneys and liver[271]. A DNA aptamer named U2 was developed to target U87-EGFRvIII cells. The study found that U2 can bind effectively to U87-EGFRvIII cells, inhibiting their proliferation, migration, invasion, and affecting downstream signaling. Additionally, the U2 aptamer enhanced the radiosensitivity of these cells *in vitro* and showed improved antitumor effects when combined with ^{188}Re *in vivo*[272].

Peptides. Peptides, typically classified as molecules containing fewer than 50 amino acids, are small biomolecules. As vectors for TRT, they offer numerous advantages, such as non-immunogenicity, favorable pharmacokinetics, and simple production. Natural peptides have high affinity for their receptors, but their rapid degradation makes them unsuitable for targeting in imaging or therapy. However, peptides can be modified to improve their stability, receptor affinity, and facilitate the grafting of radiolabels. Challenges arise when modifications to improve stability and labeling disturb their properties due to modifications of essential amino acids or to steric hindrance from the chelating agent. Regulatory peptide receptors, many of which belong to the G protein-coupled receptors (GPCRs) superfamily, are overexpressed in many human tumors[273].

Peptide receptor radionuclide therapies (PRRT) have exhibited significant clinical promise. Somatostatin is one of the earliest clinically investigated peptides. This peptide has a role in regulating the endocrine system, influencing neurotransmission, and modulating cell proliferation, primarily through its binding to the SSTR receptor family (SSTR 1-5). Notably,

these SSTRs are overexpressed in gastroentero-pancreatic neuroendocrine tumors (GEP-NET) and several other tumor types, including GB[274]. The most renowned therapeutic success is illustrated by the NETTER-1 clinical trial for the treatment of neuroendocrine tumors. ^{177}Lu-DOTATE (Lutathera) has demonstrated its efficacy in targeting SSTRs in patients and is now approved both in the USA and Europe[275,276]. The safety and efficacy of this treatment were further corroborated in the recent NETTER-2 phase III clinical trial (NCT03972488).

This success has paved the way for the exploration of additional peptide vectors for cancer therapy, and targeting SSTRs in GB appears particularly promising. To date, PRRT preclinical developments concerning α-emitters encompass targeting IL13RA2 with ^{225}Ac-labeled Pep-1L peptide[205], and $\alpha_v\beta_3$ with ^{225}Ac or ^{211}At-labeled RGD peptides[187,204]. The encouraging clinical outcomes of ^{211}At-DOTA-SP to target NK_1R motivates an intensification of research with this peptide[216,234,235]. Another promising target for PRRT could be CXCR4. A ^{177}Lu-labeled binding peptide, known as FC231, is currently under investigation in clinical trials, demonstrating potential for both radiopharmaceutical imaging and therapy. This therapy known as ^{177}Lu-Pentixather could hold promise for GB treatment[277,278]. Finally, gastrin-releasing peptide receptors (GRPR) are overexpressed in numerous cancer types, including GB[279]. Current clinical investigation in targeting GRPR with ^{212}Pb-labeled bombesin analogs (NCT05283330) could be adapted to GB treatment as well.

Small molecules. Small molecules offer several benefits over antibody-based radiopharmaceuticals, such as lower cost, faster pharmacokinetics, and the ability to be radiolabeled under varied conditions.

Given the discovery of CAFS in GB TME and the expression of FAP in GB cells and non-malignant stromal cells in its TME, FAP is an appealing target for radiopharmaceuticals. FAP-specific agents have exhibited encouraging results in preliminary studies, underscoring the need for more extensive clinical evaluations. Ma *et al.* addressed the investigation of ^{211}At-labeled FAPi. The study illustrated favorable intratumoral retention in a murine GB model and displayed a significant impact on tumor volume reduction and *in vivo* survival extension[186].

Another compelling therapeutic target is the PARP enzymes family, known for its overexpression in various tumor cells. PARPs are involved in transferring ADP-ribose to proteins, impacting processes like chromatin modulation, transcription, and DNA repair. PARPs are overexpressed in cancer, and tumors with defective homologous recombination may

depend on PARP-mediated DNA repair, making them vulnerable to PARP inhibition[280]. PARP inhibitors (PARPi) have unveiled therapeutic potential in preclinical studies in GB mouse models[281]. Dabagian *et al.* explored this avenue using ^{211}At-labeled MM4 targeting PARP in a GB mouse model, showing an extended progression-free survival[185].

Other promising small molecules, effective for diverse cancer types, might be repurposed for TAT in GB. The prostate-specific membrane antigen (PSMA), an antigenic glycoprotein initially linked to prostate cancer, is found to be overexpressed in GB, establishing it as a promising therapeutic target[282]. Indeed, PSMA targeting has already achieved market approval with Pluvicto® for the treatment of mCRPC[25] and has demonstrated efficacy with ^{177}Lu in GB[283,284]. Moreover, PSMA radiolabeling with ^{211}At has been explored and could be beneficial for GB as well[285,286].

3. Therapeutic combinations

Current TRT methods have seen some clinical success, but improvements are still needed. Challenges arise from tumor heterogeneity and the difficulty to deliver radioactive drugs to all tumor cells and tumor heterogeneity. As addressed by Obata *et al.*, three potential strategies to enhance TRT's effectiveness should be addressed: i) Amplifying the difference in cytotoxicity between normal and cancer cells, ii) Boosting the radiation sensitivity of resistant cancer cells, iii) Using inflammatory/immune responses to target non-irradiated cells. Combining TAT with other therapeutic approaches could help to resolve these issues[287].

BBB disruption. In the context of i.v. administration, selecting a vector for TAT inherently tackles the challenge of crossing the BBB. Until now, only ^{225}Ac has been demonstrated to permeabilize the BBB with $\alpha_v\beta_3$-targeted liposomes[204] and an anti-VE-cadh mAb[203] while other α radionuclides have not yet been investigated regarding this aspect. Integrating TAT with active techniques to permeabilize or breach the BBB could allow an extension of the vectorization possibilities to molecules that cannot naturally cross the BBB. For example, using FUS might ensure a more homogeneous distribution of TAT within the tumor and promote prolonged retention. This could potentially enhance therapeutic efficacy while minimizing systemic toxicity. This concept was recently addressed upon a review by Sharma *et al.*, discussing the use of ultrasound-stimulated microbubbles (USMB) to optimize radiation effects at various sites, even eliciting an anti-tumoral response[288].

Immunotherapy. Given the immunogenic properties of α-particles, their combination with immune checkpoint inhibitors (ICIs) could enhance therapeutic outcomes by exploiting a potential abscopal effect. In the sole example related to GB, Dabagian *et al.* demonstrated the benefits of combining ^{211}At-MM4 targeting PARP with an anti-PD-1 antibody. A significantly extended survival compared to monotherapy was reported with a significant neutrophil increase four weeks post-administration[185]. TATs tested in other tumor models have yielded mixed results. In a murine melanoma model, the combination of melanocortin 1 receptor (MC1R)-targeted radiopeptide ^{212}Pb-VMT01 with the ICIs anti-CTLA-4 and anti-PD-1 was superior in inhibiting tumor growth than either treatment in isolation. Mice exhibiting a complete response showed minimal to no tumor regrowth upon rechallenge, indicative of adaptive antitumor immunity[289]. Some studies also reported T-cell activation with combination treatments involving ^{227}Th and ^{223}Ra in colorectal cancer and bone metastatic prostate cancer mouse models respectively[290,291].

Conversely, certain combinations, such as melanin-targeted or PD-L1-targeted ^{225}Ac-TRT-ICI, did not surpass the efficacy of monotherapies in a melanoma mouse model[292]. Another study suggests that the success of such combination depends on the treatment scheduling. In a murine melanoma model treated with ^{213}Bi-anti-melanin and anti–PD-1, the highest survival rate was achieved when ICI administration was interspersed between two TAT injections[293]. Future research should focus on this aspect, especially since α radiations can also exert detrimental effects on local immune responses. Premature stimulation of the immune system might thus be counterproductive.

Radiosensitizers. Radiosensitization of GB is an evolving area of research. As vectors, gold and iron oxide nanoparticles augment the radiosensitization of GB cells *in vitro*[294]. Interestingly, gold nanoparticles have been investigated for TAT with ^{211}At[62,72] and ^{225}Ac[206], though they have not yet shown superior progress compared to other strategies. To enhance the radiosensitivity of tumor cells, targeting the DNA damage response (DDR) is a viable strategy. The DDR encompasses pathways that rectify DNA damage, ensuring genomic stability. However, many cancers exhibit defects in DDR machinery, leading to genome instability - a hallmark of cancer. This instability, resulting from DDR deficiencies, elevates the mutational burden, potentially activating oncogenes and deactivating tumor suppressor genes, thus promoting tumorigenesis. DDR mechanisms are nevertheless vital for tumor cell survival, especially when exposed to genotoxic agents like chemotherapy and radiotherapy, which

induce DNA breaks. Overexpression of DDR regulatory proteins facilitates DNA repair, ensuring cell survival. Consequently, inhibiting these mechanisms is a promising approach to increase tumor cell sensitivity to genotoxic agents. In TAT, combination with DDR inhibitors could amplify radiation effects, promoting tumor eradication.

Central DDR kinases, such as ataxia telangiectasia mutated (ATM), ataxia telangiectasia and rad3-related (ATR), DNA-dependent protein kinase (DNA-PK), and PARP have significant roles in DDR. Specifically, ATM is integral for DDR and cell cycle regulation post DNA damage, predominantly double-strand breaks (DSBs). ATR, a serine/threonine-specific kinase, is involved in sensing DNA damage, especially single-strand breaks (SSBs). For SSBs, repair mechanisms include base excision repair (BER), nucleotide excision repair (NER), and mismatch repair (MMR). On the other hand, DSBs are primarily repaired through homologous recombination (HR) and non-homologous end joining (NHEJ). Aberrant activation of the DDR kinases is linked to resistance to genotoxic cancer treatments, making them prime targets to enhance tumor cell sensitivity to these agents[295].

Clinical trials on DDR inhibitor (DDRi) therapy in glioma patients have been extensively reviewed. In the context of TRT, most DDRi have been labeled with isotopes like ^{123}I, ^{131}I, ^{18}F, and ^{211}At[296]. Notably, Makvandi *et al.* labeled a PARPi with ^{211}At, showing its efficacy in a neuroblastoma mouse model. This labeled PARPi was considerably more potent than the PARPi talazoparib alone, suggesting that cell lethality was primarily due to α particle-induced DNA damage rather than pharmacological PARP inhibition[297]. In their review, Everix *et al.* proposed that the ATM inhibitor AZD1390, the DNA-PK inhibitor Nedisertib (M3814), and the checkpoint-kinase 1 (Chk1) inhibitors SAR-020106 and MK8776 might be potential candidates for combination with TRT. Indeed, their molecular structures feature a halogen in an aryl position, rendering them suitable for radiohalogenation with radionuclides like ^{125}I, ^{131}I, or ^{211}At[296].

Epigenetic regulation of DNA, which governs gene activation or silencing, could also be targeted in combination with TRT by focusing on (DNMT) and histone deacetylases (HDAC). Indeed, epigenetic modifications play a role in aberrant gene expression that facilitates cancer progression. Given that numerous inhibitors of DNMT and HDAC have already received FDA approval, they present promising candidates for combination with TRT[287].

Conclusion

In the endeavor to transpose potent radiopharmaceuticals and therapeutic combinations into clinical practice, to date, one mAb (81C6 anti-tenascin-C) and one peptide (substance P) have reached the clinical phase. The α-emitters under scrutiny are ^{211}At, ^{225}Ac, and ^{213}Bi which have yielded promising yet not entirely satisfactory results. While clinical investigations lean towards locoregional strategies, the emphasis is predominantly on systemic interventions in preclinical studies.

To enhance relevance, preclinical model standardization is crucial. A direct benchmark against the Stupp regimen is imperative to determine the position of TAT in the therapeutic arsenal against GB. The prevailing dependence on subcutaneous GB models should evolve towards the adoption of orthotopic models, ideally derived from genetically pertinent GB cell lines or, optimally, from PDXs. Similarly, incorporating a monitoring of the BBB integrity in future models could contribute to informed decisions regarding TAT design for systemic strategies.

The growing production of α-emitters, in tandem with progress in radiochemistry and the development of compact vectors, indicates a bright horizon. However, mAbs should not be prematurely sidelined; their intrinsic properties may enhance the efficacy of locoregional strategies in suitable TAT configurations. Presently, no distinct leader emerges in the TAT arena for GB. Each vector, radionuclide, and target offers unique prospects for clinical progression. Given the intricate nature of GB, crafting approaches that holistically address every aspect of the TME, including GSLCs and immunosuppressive mechanisms, remains a daunting task. Targeting pivotal components within this microenvironment through pertinent TAT designs and therapeutic combinations has the potential to destabilize the entire GB ecosystem, paving the way for its complete elimination.

References

1. Stupp, R. *et al.* Radiotherapy plus concomitant and adjuvant temozolomide for glioblastoma. *N Engl J Med* **352**, 987–996 (2005).

2. Fu, M. *et al.* Use of Bevacizumab in recurrent glioblastoma: a scoping review and evidence map. *BMC Cancer* **23**, 1–23 (2023).

3. Stupp, R. *et al.* Effect of Tumor-Treating Fields Plus Maintenance Temozolomide vs Maintenance Temozolomide Alone on Survival in Patients With Glioblastoma: A Randomized Clinical Trial. *JAMA* **318**, 2306–2316 (2017).

4. Mehta, M., Wen, P., Nishikawa, R., Reardon, D. & Peters, K. Critical review of the addition of tumor treating fields (TTFields) to the existing standard of care for newly diagnosed glioblastoma patients. *Crit Rev Oncol Hematol* **111**, 60–65 (2017).

5. Sanders, S. & Debinski, W. Challenges to Successful Implementation of the Immune Checkpoint Inhibitors for Treatment of Glioblastoma. *Int J Mol Sci* **21**, (2020).

6. Heynckes, S. *et al.* Crosslink between Temozolomide and PD-L1 immune-checkpoint inhibition in glioblastoma multiforme. *BMC Cancer* **19**, 1–7 (2019).

7. Taylor, M. A., Das, B. C. & Ray, S. K. Targeting autophagy for combating chemoresistance and radioresistance in glioblastoma. *Apoptosis* **23**, 563–575 (2018).

8. Wu, Y., Song, Y., Wang, R. & Wang, T. Molecular mechanisms of tumor resistance to radiotherapy. *Mol Cancer* **22**, (2023).

9. Eisenbarth, D. & Wang, Y. A. Glioblastoma heterogeneity at single cell resolution. *Oncogene 2023 42:27* **42**, 2155–2165 (2023).

10. Wang, X. *et al.* Decoding key cell sub-populations and molecular alterations in glioblastoma at recurrence by single-cell analysis. *Acta Neuropathologica Communications 2023 11:1* **11**, 1–19 (2023).

11. Sattiraju, A. *et al.* Hypoxic niches attract and sequester tumor-associated macrophages and cytotoxic T cells and reprogram them for immunosuppression. *Immunity* **56**, 1825-1843.e6 (2023).

12. Li, S., Dong, L., Pan, Z. & Yang, G. Targeting the neural stem cells in subventricular zone for the treatment of glioblastoma: an update from preclinical evidence to clinical interventions. *Stem Cell Res Ther* **14**, 1–11 (2023).

13. Yeo, A. T. *et al.* Single-cell RNA sequencing reveals evolution of immune landscape during glioblastoma progression. *Nature Immunology 2022 23:6* **23**, 971–984 (2022).

14. Osswald, M. *et al.* Brain tumour cells interconnect to a functional and resistant network. *Nature* **528**, 93–98 (2015).

15. Wu, D. *et al.* The blood–brain barrier: structure, regulation, and drug delivery. *Signal Transduction and Targeted Therapy 2023 8:1* **8**, 1–27 (2023).

16. Bigner, D. D. *et al.* Iodine-131-labeled antitenascin monoclonal antibody 81C6 treatment of patients with recurrent malignant gliomas: phase I trial results. *J Clin Oncol* **16**, 2202–2212 (1998).

17. Reardon, D. A. *et al.* Phase II trial of murine (131)I-labeled antitenascin monoclonal antibody 81C6 administered into surgically created resection cavities of patients with newly diagnosed malignant gliomas. *J Clin Oncol* **20**, 1389–1397 (2002).

18. Cokgor, I. *et al.* Phase I trial results of iodine-131-labeled antitenascin monoclonal antibody 81C6 treatment of patients with newly diagnosed malignant gliomas. *J Clin Oncol* **18**, 3862–3872 (2000).

19. Grana, C. *et al.* Pretargeted adjuvant radioimmunotherapy with Yttrium-90-biotin in malignant glioma patients: A pilot study. *Br J Cancer* **86**, 207 (2002).

20. Casacó Parada, A. *et al.* Phase I single-dose study of intracavitary-administered Nimotuzumab labeled with 188 Re in adult recurrent high-grade glioma. *Cancer Biol Ther* **7**, 333–339 (2008).

21. Brenner, A. J. *et al.* 277O The ReSPECT-GBM™ phase I/IIa trial of rhenium-186 nanoliposome (186RNL) in recurrent glioma via convection enhanced delivery (CED) and planned phase IIb trial. *Annals of Oncology* **33**, S666 (2022).

22. Grillo-López, A. J. Zevalin: the first radioimmunotherapy approved for the treatment of lymphoma. *Expert Rev Anticancer Ther* **2**, 485–493 (2002).

23. Friedberg, J. W. & Fisher, R. I. Iodine-131 tositumomab (Bexxar®): radioimmunoconjugate therapy for indolent and transformed B-cell non-Hodgkin's lymphoma. *Expert Rev Anticancer Ther* **4**, 18–26 (2004).

24. Strosberg, J. *et al.* Health-Related Quality of Life in Patients With Progressive Midgut Neuroendocrine Tumors Treated With 177Lu-Dotatate in the Phase III NETTER-1 Trial. *J Clin Oncol* **36**, 2578–2584 (2018).

25. Fallah, J. *et al.* FDA Approval Summary: Lutetium Lu 177 Vipivotide Tetraxetan for Patients with Metastatic Castration-Resistant Prostate Cancer. *Clin Cancer Res* **29**, 1651–1657 (2023).

26. Marcu, L., Bezak, E. & Allen, B. J. Global comparison of targeted alpha vs targeted beta therapy for cancer: In vitro, in vivo and clinical trials. *Crit Rev Oncol Hematol* **123**, 7–20 (2018).

27. Sgouros, G. *et al.* MIRD Pamphlet No. 22 (abridged): radiobiology and dosimetry of alpha-particle emitters for targeted radionuclide therapy. *J Nucl Med* **51**, 311–328 (2010).

28. Wulbrand, C. *et al.* Alpha-particle emitting 213Bi-anti-EGFR immunoconjugates eradicate tumor cells independent of oxygenation. *PLoS One* **8**, (2013).

29. Parker, C. *et al.* Alpha emitter radium-223 and survival in metastatic prostate cancer. *N Engl J Med* **369**, 213–223 (2013).

30. Abbott, N. J., Patabendige, A. A. K., Dolman, D. E. M., Yusof, S. R. & Begley, D. J. Structure and function of the blood-brain barrier. *Neurobiol Dis* **37**, 13–25 (2010).

31. Atchley, T. J., Vukic, B., Vukic, M. & Walters, B. C. Review of Cerebrospinal Fluid Physiology and Dynamics: A Call for Medical Education Reform. *Neurosurgery* **91**, 1–7 (2022).

32. Møllgård, K. *et al.* A mesothelium divides the subarachnoid space into functional compartments. *Science (1979)* **379**, 84–88 (2023).

33. Castellani, G., Croese, T., Peralta Ramos, J. M. & Schwartz, M. Transforming the understanding of brain immunity. *Science* **380**, (2023).

34. Doetsch, F., Caille, I., Lim, D. A., Garcia-Verdugo, J. M. & Alvarez-Buylla, A. Subventricular zone astrocytes are neural stem cells in the adult mammalian brain. *Cell* **97**, 703–716 (1999).

35. Obernier, K. & Alvarez-Buylla, A. Neural stem cells: origin, heterogeneity and regulation in the adult mammalian brain. *Development* **146**, (2019).

36. Venkataramani, V. *et al.* Glutamatergic synaptic input to glioma cells drives brain tumour progression. *Nature 2019 573:7775* **573**, 532–538 (2019).

37. Venkatesh, H. S. *et al.* Electrical and synaptic integration of glioma into neural circuits. *Nature 2019 573:7775* **573**, 539–545 (2019).

38. Krishnan, N., Fang, R. H. & Zhang, L. Cell membrane-coated nanoparticles for the treatment of cancer. *Clin Transl Med* **13**, (2023).

39. Kadry, H., Noorani, B. & Cucullo, L. A blood–brain barrier overview on structure, function, impairment, and biomarkers of integrity. *Fluids and Barriers of the CNS 2020 17:1* **17**, 1–24 (2020).

40. Betz, A. L., Firth, J. A. & Goldstein, G. W. Polarity of the blood-brain barrier: distribution of enzymes between the luminal and antiluminal membranes of brain capillary endothelial cells. *Brain Res* **192**, 17–28 (1980).

41. Oldendorf, W. H., Cornford, M. E. & Brown, W. J. The large apparent work capability of the blood-brain barrier: a study of the mitochondrial content of capillary endothelial cells in brain and other tissues of the rat. *Ann Neurol* **1**, 409–417 (1977).

42. Armulik, A. *et al.* Pericytes regulate the blood-brain barrier. *Nature* **468**, 557–561 (2010).

43. Sengillo, J. D. *et al.* Deficiency in mural vascular cells coincides with blood-brain barrier disruption in Alzheimer's disease. *Brain Pathol* **23**, 303–310 (2013).

44. Zhao, Z., Nelson, A. R., Betsholtz, C. & Zlokovic, B. V. Establishment and Dysfunction of the Blood-Brain Barrier. *Cell* **163**, 1064–1078 (2015).

45. Wolburg, H., Noell, S., Wolburg-Buchholz, K., MacK, A. & Fallier-Becker, P. Agrin, aquaporin-4, and astrocyte polarity as an important feature of the blood-brain barrier. *Neuroscientist* **15**, 180–193 (2009).

46. Schaeffer, S. & Iadecola, C. Revisiting the neurovascular unit. *Nature Neuroscience 2021 24:9* **24**, 1198–1209 (2021).

47. Sarkaria, J. N. *et al.* Is the blood-brain barrier really disrupted in all glioblastomas? A critical assessment of existing clinical data. *Neuro Oncol* **20**, 184–191 (2018).

48. Mo, F., Pellerino, A., Soffietti, R. & Rudà, R. Blood–Brain Barrier in Brain Tumors: Biology and Clinical Relevance. *Int J Mol Sci* **22**, (2021).

49. Wen, L. *et al.* Vegf-mediated tight junctions pathological fenestration enhances doxorubicin-loaded glycolipid-like nanoparticles traversing bbb for glioblastoma-targeting therapy. *Drug Deliv* **24**, 1843–1855 (2017).

50. Zhao, C., Wang, H., Xiong, C. & Liu, Y. Hypoxic glioblastoma release exosomal VEGF-A induce the permeability of blood-brain barrier. *Biochem Biophys Res Commun* **502**, 324–331 (2018).

51. Wen, P. Y. *et al.* Updated response assessment criteria for high-grade gliomas: response assessment in neuro-oncology working group. *J Clin Oncol* **28**, 1963–1972 (2010).

52. Santarosa, C. *et al.* Dynamic contrast-enhanced and dynamic susceptibility contrast perfusion MR imaging for glioma grading: Preliminary comparison of vessel compartment and permeability parameters using hotspot and histogram analysis. *Eur J Radiol* **85**, 1147–1156 (2016).

53. Ware, J. B. *et al.* Dynamic contrast enhanced MRI for characterization of blood-brain-barrier dysfunction after traumatic brain injury. *Neuroimage Clin* **36**, 103236 (2022).

54. Arvanitis, C. D., Ferraro, G. B. & Jain, R. K. The blood–brain barrier and blood–tumour barrier in brain tumours and metastases. *Nature Reviews Cancer 2019 20:1* **20**, 26–41 (2019).

55. Gu, Y. T. *et al.* Minoxidil sulfate induced the increase in blood-brain tumor barrier permeability through ROS/RhoA/PI3K/PKB signaling pathway. *Neuropharmacology* **75**, 407–415 (2013).

56. Bolcaen, J. *et al.* A perspective on the radiopharmaceutical requirements for imaging and therapy of glioblastoma. *Issue 16 Theranostics* **11**, 7911–7947 (2021).

57. Tylawsky, D. E. *et al.* P-selectin-targeted nanocarriers induce active crossing of the blood–brain barrier via caveolin-1-dependent transcytosis. *Nature Materials 2023 22:3* **22**, 391–399 (2023).

58. Królicki, L. *et al.* 225Ac- and 213Bi-Substance P Analogues for Glioma Therapy. *Semin Nucl Med* **50**, 141–151 (2020).

59. Watabe, T. *et al.* Targeted alpha therapy using astatine (211At)-labeled phenylalanine: A preclinical study in glioma bearing mice. *Oncotarget* **11**, 1388–1398 (2020).

60. Zalutsky, M. R., Stabin, M. G., Larsen, R. H. & Bigner, D. D. Tissue distribution and radiation dosimetry of astatine-211-labeled chimeric 81C6, an alpha-particle-emitting immunoconjugate. *Nucl Med Biol* **24**, 255–261 (1997).

61. Larsen, R. H., Akabani, G., Welsh, P. & Zalutsky, M. R. The cytotoxicity and microdosimetry of astatine-211-labeled chimeric monoclonal antibodies in human glioma and melanoma cells in vitro. *Radiat Res* **149**, 155–162 (1998).

62. Kato, T. *et al.* Efficient delivery of liposome-mediated MGMT-siRNA reinforces the cytotoxity of temozolomide in GBM-initiating cells. *Gene Therapy 2010 17:11* **17**, 1363–1371 (2010).

63. Gao, J. Q. *et al.* Glioma targeting and blood-brain barrier penetration bydual-targeting doxorubincin liposomes. *Biomaterials* **34**, 5628–5639 (2013).

64. Jhaveri, A., Deshpande, P., Pattni, B. & Torchilin, V. Transferrin-targeted, resveratrol-loaded liposomes for the treatment of glioblastoma. *Journal of Controlled Release* **277**, 89–101 (2018).

65. Lam, F. C. *et al.* Enhanced efficacy of combined temozolomide and bromodomain inhibitor therapy for gliomas using targeted nanoparticles. *Nature Communications 2018 9:1* **9**, 1–11 (2018).

66. Vanpouille-Box, C. *et al.* Tumor eradication in rat glioma and bypass of immunosuppressive barriers using internal radiation with (188)Re-lipid nanocapsules. *Biomaterials* **32**, 6781–6790 (2011).

67. Cikankowitz, A. *et al.* Characterization of the distribution, retention, and efficacy of internal radiation of 188Re-lipid nanocapsules in an immunocompromised human glioblastoma model. *J Neurooncol* **131**, 49–58 (2017).

68. Séhédic, D. *et al.* Locoregional Confinement and Major Clinical Benefit of 188Re-Loaded CXCR4-Targeted Nanocarriers in an Orthotopic Human to Mouse Model of Glioblastoma. *Theranostics* **7**, 4517–4536 (2017).

69. Galstyan, A. *et al.* Blood–brain barrier permeable nano immunoconjugates induce local immune responses for glioma therapy. *Nat Commun* **10**, (2019).

70. Sukumar, U. K. *et al.* Intranasal delivery of targeted polyfunctional gold–iron oxide nanoparticles loaded with therapeutic microRNAs for combined theranostic multimodality imaging and presensitization of glioblastoma to temozolomide. *Biomaterials* **218**, (2019).

71. Kato, H. *et al.* Intratumoral administration of astatine-211-labeled gold nanoparticle for alpha therapy. *J Nanobiotechnology* **19**, (2021).

72. Liu, Y. *et al.* Gold nanostars: A novel platform for developing211at-labeled agents for targeted alpha-particle therapy. *Int J Nanomedicine* **16**, 7297–7305 (2021).

73. Morales, D. E. & Mousa, S. Intranasal delivery in glioblastoma treatment: prospective molecular treatment modalities. *Heliyon* **8**, e09517 (2022).

74. Ullah, I. *et al.* Nose-to-Brain Delivery of Cancer-Targeting Paclitaxel-Loaded Nanoparticles Potentiates Antitumor Effects in Malignant Glioblastoma. *Mol Pharm* **17**, 1193–1204 (2020).

75. Chung, K. *et al.* Intranasal delivery of cancer-targeting doxorubicin-loaded PLGA nanoparticles arrests glioblastoma growth. *https://doi.org/10.1080/1061186X.2019.1706095* **28**, 617–626 (2020).

76. Sousa, F., Dhaliwal, H. K., Gattacceca, F., Sarmento, B. & Amiji, M. M. Enhanced anti-angiogenic effects of bevacizumab in glioblastoma treatment upon intranasal administration in polymeric nanoparticles. *Journal of Controlled Release* **309**, 37–47 (2019).

77. Fang, R. H., Gao, W. & Zhang, L. Targeting drugs to tumours using cell membrane-coated nanoparticles. *Nat Rev Clin Oncol* **20**, 33–48 (2023).

78. Liu, S. *et al.* Neutrophil-Biomimetic 'Nanobuffer' for Remodeling the Microenvironment in the Infarct Core and Protecting Neurons in the Penumbra via Neutralization of Detrimental Factors to Treat Ischemic Stroke. *ACS Appl Mater Interfaces* **14**, 27743–27761 (2022).

79. Zou, Y. *et al.* Cancer cell-mitochondria hybrid membrane coated Gboxin loaded nanomedicines for glioblastoma treatment. *Nat Commun* **14**, 4557 (2023).

80. Kiessling, M., Herchenhan, E. & Eggert, H. R. Cerebrovascular and metabolic effects on the rat brain of focal Nd:YAG laser irradiation. *J Neurosurg* **73**, 909–917 (1990).

81. Cai, Q. *et al.* Optical blood-brain-tumor barrier modulation expands therapeutic options for glioblastoma treatment. *Nature Communications 2023 14:1* **14**, 1–17 (2023).

82. Sonabend, A. M. *et al.* Repeated blood–brain barrier opening with an implantable ultrasound device for delivery of albumin-bound paclitaxel in patients with recurrent glioblastoma: a phase 1 trial. *Lancet Oncol* **24**, 509–522 (2023).

83. Bogers, L. *et al.* Selective emergence of antibody-secreting cells in the multiple sclerosis brain. *EBioMedicine* **89**, (2023).

84. van Solinge, T. S., Nieland, L., Chiocca, E. A. & Broekman, M. L. D. Advances in local therapy for glioblastoma — taking the fight to the tumour. *Nature Reviews Neurology 2022 18:4* **18**, 221–236 (2022).

85. Hunt Bobo, R. *et al.* Convection-enhanced delivery of macromolecules in the brain. *Proc Natl Acad Sci U S A* **91**, 2076–2080 (1994).

86. D'Amico, R. S., Aghi, M. K., Vogelbaum, M. A. & Bruce, J. N. Convection-enhanced drug delivery for glioblastoma: a review. *J Neurooncol* **151**, 415–427 (2021).

87. Lonser, R. R., Sarntinoranont, M., Morrison, P. F. & Oldfield, E. H. Convection-enhanced delivery to the central nervous system. *J Neurosurg* **122**, 697–706 (2015).

88. Spinazzi, E. F. *et al.* Chronic convection-enhanced delivery of topotecan for patients with recurrent glioblastoma: a first-in-patient, single-centre, single-arm, phase 1b trial. *Lancet Oncol* **23**, 1409–1418 (2022).

89. Vanpouille-Box, C. *et al.* Tumor eradication in rat glioma and bypass of immunosuppressive barriers using internal radiation with (188)Re-lipid nanocapsules. *Biomaterials* **32**, 6781–6790 (2011).

90. Yang, D. Y. *et al.* Enhanced antitumor effects of radiotherapy combined local nimustine delivery rendezvousing with oral temozolomide chemotherapy in glioblastoma patients. *J Cancer Res Ther* **14**, 78–83 (2018).

91. Zalutsky, M. R. *et al.* Clinical experience with α-particle-emitting 211 At: Treatment of recurrent brain tumor patients with 211 At-labeled chimeric antitenascin monoclonal antibody 81C6. *Journal of Nuclear Medicine* **49**, 30–38 (2008).

92. Westphal, M. *et al.* A phase 3 trial of local chemotherapy with biodegradable carmustine (BCNU) wafers (Gliadel wafers) in patients with primary malignant glioma. *Neuro Oncol* **5**, 79–88 (2003).

93. De Bonis, P. *et al.* Safety and efficacy of Gliadel wafers for newly diagnosed and recurrent glioblastoma. *Acta Neurochir (Wien)* **154**, 1371–1378 (2012).

94. Bregy, A. *et al.* The role of Gliadel wafers in the treatment of high-grade gliomas. *Expert Rev Anticancer Ther* **13**, 1453–1461 (2013).

95. Van Der Sanden, B. *et al.* Translation of the ecological trap concept to glioma therapy: the cancer cell trap concept. *http://dx.doi.org/10.2217/fon.13.30* **9**, 817–824 (2013).

96. Caballero, D., Reis, R. L. & Kundu, S. C. Cancer Traps: Implantable and On-Chip Solutions for Early Cancer Detection and Treatment. *Adv Mater Technol* (2023) doi:10.1002/ADMT.202300491.

97. Jain, A. *et al.* Guiding intracortical brain tumour cells to an extracortical cytotoxic hydrogel using aligned polymeric nanofibres. *Nat Mater* **13**, 308–316 (2014).

98. Autier, L. *et al.* A new glioblastoma cell trap for implantation after surgical resection. *Acta Biomater* **84**, 268–279 (2019).

99. Chen, Z., Han, F., Du, Y., Shi, H. & Zhou, W. Hypoxic microenvironment in cancer: molecular mechanisms and therapeutic interventions. *Signal Transduction and Targeted Therapy 2023 8:1* **8**, 1–23 (2023).

100. Parmar, K., Mauch, P., Vergilio, J. A., Sackstein, R. & Down, J. D. Distribution of hematopoietic stem cells in the bone marrow according to regional hypoxia. *Proc Natl Acad Sci U S A* **104**, 5431–5436 (2007).

101. Cho, S. H. *et al.* Germinal centre hypoxia and regulation of antibody qualities by a hypoxia response system. *Nature 2016 537:7619* **537**, 234–238 (2016).

102. He, G. *et al.* Noninvasive measurement of anatomic structure and intraluminal oxygenation in the gastrointestinal tract of living mice with spatial and spectral EPR imaging. *Proc Natl Acad Sci U S A* **96**, 4586–4591 (1999).

103. Reyes, J. G. *et al.* The hypoxic testicle: Physiology and pathophysiology. *Oxid Med Cell Longev* (2012) doi:10.1155/2012/929285.

104. Erecińska, M. & Silver, I. A. Tissue oxygen tension and brain sensitivity to hypoxia. *Respir Physiol* **128**, 263–276 (2001).

105. Beppu, T. *et al.* Change of oxygen pressure in glioblastoma tissue under various conditions. *J Neurooncol* **58**, 47–52 (2002).

106. Monteiro, A. R., Hill, R., Pilkington, G. J. & Madureira, P. A. The Role of Hypoxia in Glioblastoma Invasion. *Cells 2017, Vol. 6, Page 45* **6**, 45 (2017).

107. Clarke, K., Smith, K., Gullick, W. J. & Harris, A. L. Mutant epidermal growth factor receptor enhances induction of vascular endothelial growth factor by hypoxia and insulin-like growth factor-1 via a PI3 kinase dependent pathway. *British Journal of Cancer 2001 84:10* **84**, 1322–1329 (2001).

108. Ravi, R. *et al.* Regulation of tumor angiogenesis by p53-induced degradation of hypoxia-inducible factor 1α. *Genes Dev* **14**, 34 (2000).

109. Joseph, J. V. *et al.* Hypoxia enhances migration and invasion in glioblastoma by promoting a mesenchymal shift mediated by the HIF1α–ZEB1 axis. *Cancer Lett* **359**, 107–116 (2015).

110. Mao, X. gang *et al.* CEBPD is a master transcriptional factor for hypoxia regulated proteins in glioblastoma and augments hypoxia induced invasion through extracellular matrix-integrin mediated EGFR/PI3K pathway. *Cell Death & Disease 2023 14:4* **14**, 1–17 (2023).

111. Zhao, S. *et al.* Hypoxia-induced circADAMTS6 in a TDP43-dependent manner accelerates glioblastoma progression via ANXA2/ NF-κB pathway. *Oncogene 2022 42:2* **42**, 138–153 (2022).

112. Moeller, B. J., Cao, Y., Li, C. Y. & Dewhirst, M. W. Radiation activates HIF-1 to regulate vascular radiosensitivity in tumors: Role of reoxygenation, free radicals, and stress granules. *Cancer Cell* **5**, 429–441 (2004).

113. Unruh, A. *et al.* The hypoxia-inducible factor-1 alpha is a negative factor for tumor therapy. *Oncogene* **22**, 3213–3220 (2003).

114. Moeller, B. J. *et al.* Pleiotropic effects of HIF-1 blockade on tumor radiosensitivity. *Cancer Cell* **8**, 99–110 (2005).

115. Suwa, T. *et al.* SPINK1 as a plasma marker for tumor hypoxia and a therapeutic target for radiosensitization. *JCI Insight* **6**, (2021).

116. Wei, J. *et al.* Hypoxia-Induced Autophagy Is Involved in Radioresistance via HIF1A-Associated Beclin-1 in Glioblastoma Multiforme. *Heliyon* **9**, e12820 (2023).

117. Hino-Shishikura, A. *et al.* Tumor hypoxia and microscopic diffusion capacity in brain tumors: a comparison of (62)Cu-Diacetyl-Bis (N4-Methylthiosemicarbazone) PET/CT and diffusion-weighted MR imaging. *Eur J Nucl Med Mol Imaging* **41**, 1419–1427 (2014).

118. Gangemi, V. *et al.* Impact of [64Cu][Cu(ATSM)] PET/CT in the evaluation of hypoxia in a patient with Glioblastoma: a case report. *BMC Cancer* **19**, (2019).

119. Pérès, E. A. *et al.* 64Cu-ATSM/64Cu-Cl2 and their relationship to hypoxia in glioblastoma: a preclinical study. *EJNMMI Res* **9**, 1–15 (2019).

120. Clarke, R. H. *et al.* Sustained radiosensitization of hypoxic glioma cells after oxygen pretreatment in an animal model of glioblastoma and in vitro models of tumor hypoxia. *PLoS One* **9**, (2014).

121. Doetsch, F., Caille, I., Lim, D. A., Garcia-Verdugo, J. M. & Alvarez-Buylla, A. Subventricular zone astrocytes are neural stem cells in the adult mammalian brain. *Cell* **97**, 703–716 (1999).

122. Gage, F. H. Mammalian Neural Stem Cells. *Science (1979)* **287**, 1433–1438 (2000).

123. Ge, W. P., Miyawaki, A., Gage, F. H., Jan, Y. N. & Jan, L. Y. Local generation of glia is a major astrocyte source in postnatal cortex. *Nature 2012 484:7394* **484**, 376–380 (2012).

124. Gage, F. H. & Temple, S. Neural Stem Cells: Generating and Regenerating the Brain. *Neuron* **80**, 588–601 (2013).

125. Ffrench-Constant, C. & Raff, M. C. Proliferating bipotential glial progenitor cells in adult rat optic nerve. *Nature 1986 319:6053* **319**, 499–502 (1986).

126. Bardehle, S. *et al.* Live imaging of astrocyte responses to acute injury reveals selective juxtavascular proliferation. *Nature Neuroscience 2013 16:5* **16**, 580–586 (2013).

127. Singh, S. K. *et al.* Identification of human brain tumour initiating cells. *Nature* **432**, 396–401 (2004).

128. Lathia, J. D., Mack, S. C., Mulkearns-Hubert, E. E., Valentim, C. L. L. & Rich, J. N. Cancer stem cells in glioblastoma. *Genes Dev* **29**, 1203–1217 (2015).

129. Mitchell, K., Troike, K., Silver, D. J. & Lathia, J. D. The evolution of the cancer stem cell state in glioblastoma: emerging insights into the next generation of functional interactions. *Neuro Oncol* **23**, 199 (2021).

130. Reinartz, R. *et al.* Functional Subclone Profiling for Prediction of Treatment-Induced Intratumor Population Shifts and Discovery of Rational Drug Combinations in Human Glioblastoma. *Clin Cancer Res* **23**, 562–574 (2017).

131. Lim, D. A. *et al.* Relationship of glioblastoma multiforme to neural stem cell regions predicts invasive and multifocal tumor phenotype. *Neuro Oncol* **9**, 424–429 (2007).

132. Comas, S. *et al.* Influence of glioblastoma contact with the subventricular zone on survival and recurrence patterns. *Clin Transl Oncol* **23**, 554–564 (2021).

133. Bakhshinyan, D., Savage, N., Salim, S. K., Venugopal, C. & Singh, S. K. The Strange Case of Jekyll and Hyde: Parallels Between Neural Stem Cells and Glioblastoma-Initiating Cells. *Front Oncol* **10**, 603738 (2021).

134. Adeberg, S. *et al.* Do Increased Doses to Stem-Cell Niches during Radiation Therapy Improve Glioblastoma Survival? *Stem Cells Int* **2016**, (2016).

135. Ermiş, E. *et al.* Therapy Resistance of Glioblastoma in Relation to the Subventricular Zone: What Is the Role of Radiotherapy? *Cancers (Basel)* **15**, 1677 (2023).

136. LeBleu, V. S. & Neilson, E. G. Origin and functional heterogeneity of fibroblasts. *FASEB J* **34**, 3519–3536 (2020).

137. Li, Z. *et al.* Nodal Facilitates Differentiation of Fibroblasts to Cancer-Associated Fibroblasts that Support Tumor Growth in Melanoma and Colorectal Cancer. *Cells* **8**, (2019).

138. Kim, K. *et al.* Cancer-Associated Fibroblasts Differentiated by Exosomes Isolated from Cancer Cells Promote Cancer Cell Invasion. *Int J Mol Sci* **21**, 1–18 (2020).

139. Hosaka, K. *et al.* Pericyte-fibroblast transition promotes tumor growth and metastasis. *Proc Natl Acad Sci U S A* **113**, E5618–E5627 (2016).

140. Jain, S. *et al.* Single-cell RNA sequencing and spatial transcriptomics reveal cancer-associated fibroblasts in glioblastoma with protumoral effects. *J Clin Invest* **133**, (2023).

141. Busek, P. *et al.* Fibroblast activation protein alpha is expressed by transformed and stromal cells and is associated with mesenchymal features in glioblastoma. *Tumour Biol* **37**, 13961–13971 (2016).

142. Xuan, W., Lesniak, M. S., James, C. D., Heimberger, A. B. & Chen, P. Context-Dependent Glioblastoma–Macrophage/Microglia Symbiosis and Associated Mechanisms. *Trends Immunol* **42**, 280–292 (2021).

143. Simonds, E. F. *et al.* Deep immune profiling reveals targetable mechanisms of immune evasion in immune checkpoint inhibitor-refractory glioblastoma. *J Immunother Cancer* **9**, e002181 (2021).

144. Martinez, F. O. & Gordon, S. The M1 and M2 paradigm of macrophage activation: time for reassessment. *F1000Prime Rep* **6**, (2014).

145. Shapouri-Moghaddam, A. *et al.* Macrophage plasticity, polarization, and function in health and disease. *J Cell Physiol* **233**, 6425–6440 (2018).

146. Müller, S. *et al.* Single-cell profiling of human gliomas reveals macrophage ontogeny as a basis for regional differences in macrophage activation in the tumor microenvironment. *Genome Biol* **18**, 1–14 (2017).

147. Yang, W., Li, Y., Gao, R., Xiu, Z. & Sun, T. MHC class I dysfunction of glioma stem cells escapes from CTL-mediated immune response via activation of Wnt/β-catenin signaling pathway. *Oncogene 2019 39:5* **39**, 1098–1111 (2019).

148. Xue, S., Song, G. & Yu, J. The prognostic significance of PD-L1 expression in patients with glioma: A meta-analysis. *Scientific Reports 2017 7:1* **7**, 1–8 (2017).

149. Lu, L., Barbi, J. & Pan, F. The regulation of immune tolerance by FOXP3. *Nature Reviews Immunology 2017 17:11* **17**, 703–717 (2017).

150. Ribas, A. & Wolchok, J. D. Cancer immunotherapy using checkpoint blockade. *Science* **359**, 1350–1355 (2018).

151. Wolf, N. K., Kissiov, D. U. & Raulet, D. H. Roles of natural killer cells in immunity to cancer, and applications to immunotherapy. *Nature Reviews Immunology 2022 23:2* **23**, 90–105 (2022).

152. Fu, W. *et al.* Single-Cell Atlas Reveals Complexity of the Immunosuppressive Microenvironment of Initial and Recurrent Glioblastoma. *Front Immunol* **11**, 530579 (2020).

153. Malamas, A. S., Gameiro, S. R., Knudson, K. M. & Hodge, J. W. Sublethal exposure to alpha radiation (223Ra dichloride) enhances various carcinomas' sensitivity to lysis by antigen-specific cytotoxic T lymphocytes through calreticulin-mediated immunogenic modulation. *Oncotarget* **7**, 86937 (2016).

154. Hagemann, U. B. *et al.* Mesothelin-Targeted Thorium-227 Conjugate (MSLN-TTC): Preclinical Evaluation of a New Targeted Alpha Therapy for Mesothelin-Positive Cancers. *Clin Cancer Res* **25**, 4723–4734 (2019).

155. Lejeune, P. *et al.* Immunostimulatory effects of targeted thorium-227 conjugates as single agent and in combination with anti-PD-L1 therapy. *J Immunother Cancer* **9**, (2021).

156. Gorin, J. B. *et al.* Antitumor immunity induced after α irradiation. *Neoplasia* **16**, 319–328 (2014).

157. Perrin, J. *et al.* Targeted Alpha Particle Therapy Remodels the Tumor Microenvironment and Improves Efficacy of Immunotherapy. *Int J Radiat Oncol Biol Phys* **112**, 790–801 (2022).

158. Li, M. *et al.* Targeted Alpha-Particle Radiotherapy and Immune Checkpoint Inhibitors Induces Cooperative Inhibition on Tumor Growth of Malignant Melanoma. *Cancers (Basel)* **13**, (2021).

159. Kim, J. W., Shin, M. S., Kang, Y., Kang, I. & Petrylak, D. P. Immune Analysis of Radium-223 in Patients With Metastatic Prostate Cancer. *Clin Genitourin Cancer* **16**, e469–e476 (2018).

160. Bellia, S. R. *et al.* Clinical evidence of abscopal effect in cutaneous squamous cell carcinoma treated with diffusing alpha emitters radiation therapy: a case report. *J Contemp Brachytherapy* **11**, 449–457 (2019).

161. Eychenne, R., Chérel, M., Haddad, F., Guérard, F. & Gestin, J. F. Overview of the Most Promising Radionuclides for Targeted Alpha Therapy: The "Hopeful Eight". *Pharmaceutics 2021, Vol. 13, Page 906* **13**, 906 (2021).

162. Radchenko, V. *et al.* Production and Supply of α-Particle–Emitting Radionuclides for Targeted α-Therapy. *Journal of Nuclear Medicine* **62**, 1495–1503 (2021).

163. Eychenne, R., Chérel, M., Haddad, F., Guérard, F. & Gestin, J. F. Overview of the Most Promising Radionuclides for Targeted Alpha Therapy: The 'Hopeful Eight'. *Pharmaceutics* **13**, (2021).

164. Jefferson, R. D., Goans, R. E., Blain, P. G. & Thomas, S. H. L. Diagnosis and treatment of polonium poisoning. *Clin Toxicol (Phila)* **47**, 379–392 (2009).

165. Henriksen, G., Messelt, S., Olsen, E. & Larsen, R. H. Optimisation of cyclotron production parameters for the 209Bi(α, 2n) 211At reaction related to biomedical use of 211At. *Applied Radiation and Isotopes* **54**, 839–844 (2001).

166. Feng, Y. & Zalutsky, M. R. Production, purification and availability of 211At: Near term steps towards global access. *Nucl Med Biol* **100–101**, 12–23 (2021).

167. Corson, D. R., MacKenzie, K. R. & Segrè, E. Artificially Radioactive Element 85. *Physical Review* **58**, 672 (1940).

168. Bigner, D. D. *et al.* Iodine-131-labeled antitenascin monoclonal antibody 81C6 treatment of patients with recurrent malignant gliomas: phase I trial results. *J Clin Oncol* **16**, 2202–2212 (1998).

169. Akabani, G. *et al.* Dosimetry and dose-response relationships in newly diagnosed patients with malignant gliomas treated with Iodine-131-Labeled anti-tenascin monoclonal antibody 81C6 therapy. *Int J Radiat Oncol Biol Phys* **46**, 947–958 (2000).

170. Reardon, D. A. *et al.* Phase II trial of murine (131)I-labeled antitenascin monoclonal antibody 81C6 administered into surgically created resection cavities of patients with newly diagnosed malignant gliomas. *J Clin Oncol* **20**, 1389–1397 (2002).

171. Tenascin-C promotes microvascular cell migration and phosphorylation of focal adhesion kinase - PubMed. https://pubmed.ncbi.nlm.nih.gov/11980665/.

172. Angel, I., Pilo Kerman, O., Rousso-Noori, L. & Friedmann-Morvinski, D. Tenascin C promotes cancer cell plasticity in mesenchymal glioblastoma. *Oncogene 2020 39:46* **39**, 6990–7004 (2020).

173. Frederick, L., Wang, X.-Y., Eley, G., David James, C. & Biology Program E, T. G. Diversity and Frequency of Epidermal Growth Factor Receptor Mutations in Human Glioblastomas 1. *Cancer Res* **60**, 1383–1387 (2000).

174. An, Z., Aksoy, O., Zheng, T., Fan, Q. W. & Weiss, W. A. Epidermal growth factor receptor and EGFRvIII in glioblastoma: signaling pathways and targeted therapies. *Oncogene 2018 37:12* **37**, 1561–1575 (2018).

175. Zalutsky, M. R., Garg, P. K., Friedman, H. S. & Bigner, D. D. Labeling monoclonal antibodies and F(ab')2 fragments with the α-particle-emitting nuclide astatine-211: Preservation of immunoreactivity and in vivo localizing capacity. *Proc Natl Acad Sci U S A* **86**, 7149–7153 (1989).

176. Zalutsky, M. R., Stabin, M. G., Larsen, R. H. & Bigner, D. D. Tissue distribution and radiation dosimetry of astatine-211-labeled chimeric 81C6, an α-particle-emitting immunoconjugate. *Nucl Med Biol* **24**, 255–261 (1997).

177. Reist, C. J., Batra, S. K., Pegram, C. N., Bigner, D. D. & Zalutsky, M. R. In vitro and in vivo behavior of radiolabeled chimeric anti-EGFRvIII monoclonal antibody: comparison with its murine parent. *Nucl Med Biol* **24**, 639–647 (1997).

178. Larsen, R. H., Akabani, G., Welsh, P. & Zalutsky, M. R. The Cytotoxicity and Microdosimetry of Astatine-211-Labeled Chimeric Monoclonal Antibodies in Human Glioma and Melanoma Cells In Vitro. *Radiat Res* **149**, 155–162 (1998).

179. Reist, C. J., Foulon, C. F., Alston, K., Bigner, D. D. & Zalutsky, M. R. Astatine-211 labeling of internalizing anti-EGFRvIII monoclonal antibody using N-succinimidyl 5-[211At]astato-3-pyridinecarboxylate. *Nucl Med Biol* **26**, 405–411 (1999).

180. McLendon, R. E. *et al.* Radiotoxicity of systemically administered 211At-labeled human/mouse chimeric monoclonal antibody: a long-term survival study with histologic analysis. *Int J Radiat Oncol Biol Phys* **45**, 491–499 (1999).

181. Vaidyanathan, G., Affleck, D. J., Bigner, D. D. & Zalutsky, M. R. N-succinimidyl 3-[211At]astato-4-guanidinomethylbenzoate: An acylation agent for labeling internalizing antibodies with α-particle emitting 211At. *Nucl Med Biol* **30**, 351–359 (2003).

182. Garg, P., Harrison, C. L. & Zalutsky, M. Comparative tissue distribution in mice of the alpha-emitter 211At and 131I as labels of a monoclonal antibody and F(ab')2 fragment. *Cancer Res* (1990).

183. Zalutsky, M. R. *et al.* Clinical experience with alpha-particle emitting 211At: treatment of recurrent brain tumor patients with 211At-labeled chimeric antitenascin monoclonal antibody 81C6. *J Nucl Med* **49**, 30–38 (2008).

184. Borrmann, N. *et al.* Systemic treatment with 4-211Atphenylalanine enhances survival of rats with intracranial glioblastoma. *Nuklearmedizin* **52**, 212–221 (2013).

185. Dabagian, H. *et al.* PARP Targeted Alpha-Particle Therapy Enhances Response to PD-1 Immune-Checkpoint Blockade in a Syngeneic Mouse Model of Glioblastoma. *ACS Pharmacol Transl Sci* **4**, 344–351 (2021).

186. Ma, H. *et al.* In vitro and in vivo evaluation of 211At-labeled fibroblast activation protein inhibitor for glioma treatment. *Bioorg Med Chem* **55**, (2022).

187. Liu, W. *et al.* Targeted Alpha Therapy of Glioma Using 211At-Labeled Heterodimeric Peptide Targeting Both VEGFR and Integrins. *Mol Pharm* **19**, 3206–3216 (2022).

188. Andersson, H. *et al.* Intraperitoneal alpha-particle radioimmunotherapy of ovarian cancer patients: pharmacokinetics and dosimetry of (211)At-MX35 F(ab')2--a phase I study. *J Nucl Med* **50**, 1153–1160 (2009).

189. Cederkrantz, E. *et al.* Absorbed Doses and Risk Estimates of (211)At-MX35 F(ab')2 in Intraperitoneal Therapy of Ovarian Cancer Patients. *Int J Radiat Oncol Biol Phys* **93**, 569–576 (2015).

190. Hallqvist, A. *et al.* Intraperitoneal α-Emitting Radioimmunotherapy with 211At in Relapsed Ovarian Cancer: Long-Term Follow-up with Individual Absorbed Dose Estimations. *Journal of Nuclear Medicine* **60**, 1073 (2019).

191. de Kruijff, R. M., Wolterbeek, H. T. & Denkova, A. G. A Critical Review of Alpha Radionuclide Therapy—How to Deal with Recoiling Daughters? *Pharmaceuticals 2015, Vol. 8, Pages 321-336* **8**, 321–336 (2015).

192. Deal, K. A., Davis, I. A., Mirzadeh, S., Kennel, S. J. & Brechbiel, M. W. Improved in vivo stability of actinium-225 macrocyclic complexes. *J Med Chem* **42**, 2988–2992 (1999).

193. Melville, G. & J Allen, B. Cyclotron and linac production of Ac-225. *Appl Radiat Isot* **67**, 549–555 (2009).

194. Fitzsimmons, J., Griswold, J., Medvedev, D., Cutler, C. S. & Mausner, L. Defining Processing Times for Accelerator Produced 225Ac and Other Isotopes from Proton Irradiated Thorium. *Molecules 2019, Vol. 24, Page 1095* **24**, 1095 (2019).

195. Nagatsu, K. *et al.* Cyclotron production of 225Ac from an electroplated 226Ra target. *Eur J Nucl Med Mol Imaging* **49**, 279 (2021).

196. McDevitt, M. R. *et al.* Tumor therapy with targeted atomic nanogenerators. *Science (1979)* **294**, 1537–1540 (2001).

197. McDevitt, M. R., Ma, D., Simon, J., Frank, R. K. & Scheinberg, D. A. Design and synthesis of 225Ac radioimmunopharmaceuticals. *Applied Radiation and Isotopes* **57**, 841–847 (2002).

198. Hennrich, U. & Kopka, K. Lutathera®: The First FDA- and EMA-Approved Radiopharmaceutical for Peptide Receptor Radionuclide Therapy. *Pharmaceuticals* **12**, (2019).

199. Hennrich, U. & Benešová, M. [68Ga]Ga-DOTA-TOC: The First FDA-Approved 68Ga-Radiopharmaceutical for PET Imaging. *Pharmaceuticals* **13**, (2020).

200. Wiebe, L. I. *et al.* Recent Innovations and Nano-Delivery of Actinium-225: A Narrative Review. *Pharmaceutics 2023, Vol. 15, Page 1719* **15**, 1719 (2023).

201. Pandya, D. N. *et al.* Preliminary therapy evaluation of 225Ac-DOTA-c (RGDyK) demonstrates that Cerenkov radiation derived from 225Ac daughter decay can be detected by optical imaging for in vivo tumor visualization. *Theranostics* **6**, 698–709 (2016).

202. Behling, K. *et al.* Vascular targeted radioimmunotherapy for the treatment of glioblastoma. *Journal of Nuclear Medicine* **57**, 1576–1582 (2016).

203. Behling, K. *et al.* Remodeling the vascular microenvironment of glioblastoma with α-particles. *Journal of Nuclear Medicine* **57**, 1771–1777 (2016).

204. Sattiraju, A. *et al.* Alpha particle enhanced permeabilization of the blood tumor barrier using alpha-v beta-3 (αvβ3) specific nanoparticles. *Journal of Nuclear Medicine* **57**, 633–633 (2016).

205. Sattiraju, A. *et al.* IL13RA2 targeted alpha particle therapy against glioblastomas. *Oncotarget* **8**, 42997–43007 (2017).

206. Salvanou, E. A. *et al.* A proof-of-concept study on the therapeutic potential of au nanoparticles radiolabeled with the alpha-emitter actinium-225. *Pharmaceutics* **12**, (2020).

207. Nishri, Y. *et al.* Diffusing alpha-emitters radiation therapy in combination with temozolomide or bevacizumab in human glioblastoma multiforme xenografts. *Front Oncol* **12**, (2022).

208. Brooks, P. C., Clark, R. A. F. & Cheresh, D. A. Requirement of Vascular Integrin αvβ3 for Angiogenesis. *Science (1979)* **264**, 569–571 (1994).

209. Gladson, C. L. Expression of Integrin αvβ3 in Small Blood Vessels of Glioblastoma Tumors. *J Neuropathol Exp Neurol* **55**, 1143–1149 (1996).

210. Schittenhelm, J. *et al.* Longitudinal Expression Analysis of αv Integrins in Human Gliomas Reveals Upregulation of Integrin αvβ3 as a Negative Prognostic Factor. *J Neuropathol Exp Neurol* **72**, 194–210 (2013).

211. Shaffer, T. M., Pratt, E. C. & Grimm, J. Utilizing the power of Cerenkov light with nanotechnology. *Nature Nanotechnology 2017 12:2* **12**, 106–117 (2017).

212. Wang, R. *et al.* Glioblastoma stem-like cells give rise to tumour endothelium. *Nature* **468**, 829–835 (2010).

213. Maddison, K., Bowden, N. A., Graves, M. C. & Tooney, P. A. Characteristics of vasculogenic mimicry and tumour to endothelial transdifferentiation in human glioblastoma: a systematic review. *BMC Cancer* **23**, (2023).

214. Thaci, B. *et al.* Significance of interleukin-13 receptor alpha 2–targeted glioblastoma therapy. *Neuro Oncol* **16**, 1304 (2014).

215. Yook, S. *et al.* Intratumorally Injected 177Lu-Labeled Gold Nanoparticles: Gold Nanoseed Brachytherapy with Application for Neoadjuvant Treatment of Locally Advanced Breast Cancer. *Journal of Nuclear Medicine* **57**, 936–942 (2016).

216. Królicki, L. *et al.* Dose escalation study of targeted alpha therapy with [225Ac]Ac-DOTA-substance P in recurrence glioblastoma - safety and efficacy. *Eur J Nucl Med Mol Imaging* **48**, 3595–3605 (2021).

217. Hennig, I. M., Laissue, J. A., Horisberger, U. & Reubi, J. -C. Substance-P receptors in human primary neoplasms: tumoral and vascular localization. *Int J Cancer* **61**, 786–792 (1995).

218. Palma, C., Nardelli, F., Manzini, S. & Maggi, C. A. Substance P activates responses correlated with tumour growth in human glioma cell lines bearing tachykinin NK1 receptors. *British Journal of Cancer 1999 79:2* **79**, 236–243 (1998).

219. Muñoz, M. *et al.* The NK1 receptor is involved in the antitumoural action of L-733,060 and in the mitogenic action of substance P on neuroblastoma and glioma cell lines. *Neuropeptides* **39**, 427–432 (2005).

220. Kratochwil, C. *et al.* Targeted α-Therapy of Metastatic Castration-Resistant Prostate Cancer with 225Ac-PSMA-617: Dosimetry Estimate and Empiric Dose Finding. *J Nucl Med* **58**, 1624–1631 (2017).

221. Kratochwil, C. *et al.* Dosing 225Ac-DOTATOC in patients with somatostatin-receptor-positive solid tumors: 5-year follow-up of hematological and renal toxicity. *Eur J Nucl Med Mol Imaging* **49**, 54–63 (2021).

222. Morgenstern, A., Bruchertseifer, F. & Apostolidis, C. Bismuth-213 and actinium-225 -- generator performance and evolving therapeutic applications of two generator-derived alpha-emitting radioisotopes. *Curr Radiopharm* **5**, 221–227 (2012).

223. Ermolaev, S., Skasyrskaya, A. & Vasiliev, A. A Radionuclide Generator of High-Purity Bi-213 for Instant Labeling. *Pharmaceutics* **13**, (2021).

224. McDevitt, M. R., Finn, R. D., Sgouros, G., Ma, D. & Scheinberg, D. A. An 225Ac/213Bi generator system for therapeutic clinical applications: construction and operation. *Applied Radiation and Isotopes* **50**, 895–904 (1999).

225. Feuerecker, B. *et al.* Assessment of 213Bi-anti-EGFR MAb treatment efficacy in malignant cancer cells with [1-13C]pyruvate and [18F]FDG. *Scientific Reports 2019 9:1* **9**, 1–11 (2019).

226. Feuerecker, B. *et al.* Diverse metabolic response of cancer cells treated with a 213Bi-anti-EGFR-immunoconjugate. *Sci Rep* **11**, 6227 (2021).

227. Nikula, T. K. *et al.* Alpha-Emitting Bismuth Cyclohexylbenzyl DTPA Constructs of Recombinant Humanized Anti-CD33 Antibodies: Pharmacokinetics, Bioactivity, Toxicity and Chemistry. *Journal of Nuclear Medicine* **40**, 166–176 (1999).

228. Allen, K. J. H. *et al.* Comparative Radioimmunotherapy of Experimental Melanoma with Novel Humanized Antibody to Melanin Labeled with 213Bismuth and 177Lutetium. *Pharmaceutics 2019, Vol. 11, Page 348* **11**, 348 (2019).

229. Chérel, M. *et al.* 213Bi Radioimmunotherapy with an Anti-mCD138 Monoclonal Antibody in a Murine Model of Multiple Myeloma. *Journal of Nuclear Medicine* **54**, 1597–1604 (2013).

230. Gustafsson-Lutz, A. *et al.* Therapeutic efficacy of α-radioimmunotherapy with different activity levels of the 213Bi-labeled monoclonal antibody MX35 in an ovarian cancer model. *EJNMMI Res* **7**, 1–8 (2017).

231. Revskaya, E. *et al.* A Radiolabeled Fully Human Antibody to Human Aspartyl (Asparaginyl) β-Hydroxylase Is a Promising Agent for Imaging and Therapy of Metastatic Breast Cancer. *https://home.liebertpub.com/cbr* **32**, 57–65 (2017).

232. Kneifel, S. *et al.* Local Targeting of Malignant Gliomas by the Diffusible Peptidic Vector 1,4,7,10-Tetraazacyclododecane-1-Glutaric Acid-4,7,10-Triacetic Acid-Substance P. *Clinical Cancer Research* **12**, 3843–3850 (2006).

233. Cordier, D. *et al.* Targeted alpha-radionuclide therapy of functionally critically located gliomas with 213Bi-DOTA-[Thi8,Met(O2)11]-substance P: a pilot trial. *Eur J Nucl Med Mol Imaging* **37**, 1335–1344 (2010).

234. Krolicki, L. *et al.* Prolonged survival in secondary glioblastoma following local injection of targeted alpha therapy with 213Bi-substance P analogue. *Eur J Nucl Med Mol Imaging* **45**, 1636–1644 (2018).

235. Królicki, L. *et al.* Safety and efficacy of targeted alpha therapy with 213Bi-DOTA-substance P in recurrent glioblastoma. *Eur J Nucl Med Mol Imaging* **46**, 614–622 (2019).

236. Piotrowska, A. *et al.* Nanozeolite bioconjugates labeled with 223Ra for targeted alpha therapy. *Nucl Med Biol* **47**, 10–18 (2017).

237. Stallons, T. A. R., Saidi, A., Tworowska, I., Delpassand, E. S. & Torgue, J. J. Preclinical Investigation of 212Pb-DOTAMTATE for Peptide Receptor Radionuclide Therapy in a Neuroendocrine Tumor Model. *Mol Cancer Ther* **18**, 1012–1021 (2019).

238. Delpassand, E. S. *et al.* Targeted α-Emitter Therapy with 212Pb-DOTAMTATE for the Treatment of Metastatic SSTR-Expressing Neuroendocrine Tumors: First-in-Humans Dose-Escalation Clinical Trial. *J Nucl Med* **63**, 1326–1333 (2022).

239. Lenting, K., Verhaak, R., ter Laan, M., Wesseling, P. & Leenders, W. Glioma: experimental models and reality. *Acta Neuropathol* **133**, 263–282 (2017).

240. Ledur, P. F., Onzi, G. R., Zong, H. & Lenz, G. Culture conditions defining glioblastoma cells behavior: what is the impact for novel discoveries? *Oncotarget* **8**, 69185 (2017).

241. Patil, V., Pal, J. & Somasundaram, K. Elucidating the cancer-specific genetic alteration spectrum of glioblastoma derived cell lines from whole exome and RNA sequencing. *Oncotarget* **6**, 43452 (2015).

242. Radaelli, E. *et al.* Immunohistopathological and neuroimaging characterization of murine orthotopic xenograft models of glioblastoma multiforme recapitulating the most salient features of human disease. *Histol Histopathol* **24**, 879–891 (2009).

243. Chu, S. H., Zhou, Z. M., Karri, S., Li, Z. Q. & Zhao, J. M. In vitro and in vivo radiosensitization of human glioma U251 cells induced by upregulated expression of SLC22A18. *Cancer Gene Ther* **21**, 103–109 (2014).

244. Bao, S. *et al.* Glioma stem cells promote radioresistance by preferential activation of the DNA damage response. *Nature* **444**, 756–760 (2006).

245. Teng, J. *et al.* Dissecting inherent intratumor heterogeneity in patient-derived glioblastoma culture models. *Neuro Oncol* **19**, 820–832 (2017).

246. Lee, J. *et al.* Tumor stem cells derived from glioblastomas cultured in bFGF and EGF more closely mirror the phenotype and genotype of primary tumors than do serum-cultured cell lines. *Cancer Cell* **9**, 391–403 (2006).

247. Patrizii, M., Bartucci, M., Pine, S. R. & Sabaawy, H. E. Utility of Glioblastoma Patient-Derived Orthotopic Xenografts in Drug Discovery and Personalized Therapy. *Front Oncol* **8**, 23 (2018).

248. Alcaniz, J. *et al.* Clinically relevant glioblastoma patient-derived xenograft models to guide drug development and identify molecular signatures. *Front Oncol* **13**, 1129627 (2023).

249. Wu, A. *et al.* Persistence of CD133+ cells in human and mouse glioma cell lines: detailed characterization of GL261 glioma cells with cancer stem cell-like properties. *Stem Cells Dev* **17**, 173–184 (2008).

250. Genoud, V. *et al.* Responsiveness to anti-PD-1 and anti-CTLA-4 immune checkpoint blockade in SB28 and GL261 mouse glioma models. *Oncoimmunology* **7**, (2018).

251. Guan, X. *et al.* Blockade of Na/H exchanger stimulates glioma tumor immunogenicity and enhances combinatorial TMZ and anti-PD-1 therapy. *Cell Death Dis* **9**, (2018).

252. Garcia, L. B., Reiners, O., Gonzalez-Junca, A., Okada, H. & Barcellos-Hoff, M. H. RDNA-09. Radiation primes sb28 glioblastoma for response to tgfβ and pd-l1 neutralizing antibodies. *Neuro Oncol* **21**, vi208 (2019).

253. Stribbling, S. M. & Ryan, A. J. The cell-line-derived subcutaneous tumor model in preclinical cancer research. *Nature Protocols 2022 17:9* **17**, 2108–2128 (2022).

254. Harris, W. J. *et al.* In vivo methods for imaging blood–brain barrier function and dysfunction. *European Journal of Nuclear Medicine and Molecular Imaging 2022 50:4* **50**, 1051–1083 (2022).

255. Resende, F. F. B. *et al.* Evaluation of TgH(CX3CR1-EGFP) mice implanted with mCherry-GL261 cells as an in vivo model for morphometrical analysis of glioma-microglia interaction. *BMC Cancer* **16**, 1–13 (2016).

256. Irtenkauf, S. M. *et al.* Optimization of Glioblastoma Mouse Orthotopic Xenograft Models for Translational Research. *Comp Med* **67**, 300 (2017).

257. Reste, P. J. Le *et al.* Development of a novel preclinical glioblastoma mouse model and therapeutic impact of IRE1 inhibition. *bioRxiv* 841296 (2019) doi:10.1101/841296.

258. Lepareur, N., Ramée, B., Mougin-Degraef, M. & Bourgeois, M. Clinical Advances and Perspectives in Targeted Radionuclide Therapy. *Pharmaceutics* **15**, 1733 (2023).

259. Amatori, S., Tavolaro, S., Gambardella, S. & Fanelli, M. The dark side of histones: genomic organization and role of oncohistones in cancer. *Clinical Epigenetics 2021 13:1* **13**, 1–21 (2021).

260. Shapiro, W. R., Carpenter, S. P., Roberts, K. & Shan, J. S. (131)I-chTNT-1/B mAb: tumour necrosis therapy for malignant astrocytic glioma. *Expert Opin Biol Ther* **6**, 539–545 (2006).

261. Hdeib, A. & Sloan, A. Targeted radioimmunotherapy: the role of ^{131}I-chTNT-1/B mAb (Cotara) for treatment of high-grade gliomas. *Future Oncol* **8**, 659–669 (2012).

262. J. Richardson, P. CXCR4 and Glioblastoma. *Anticancer Agents Med Chem* **16**, 59–74 (2016).

263. Han, J. H. *et al.* CXCR4-STAT3 Axis Plays a Role in Tumor Cell Infiltration in an Orthotopic Mouse Glioblastoma Model. *Mol Cells* **43**, 539 (2020).

264. Khan, A. B. *et al.* CXCR4 expression is associated with proneural-to-mesenchymal transition in glioblastoma. *Int J Cancer* **152**, 713 (2023).

265. Škrlec, K., Štrukelj, B. & Berlec, A. Non-immunoglobulin scaffolds: a focus on their targets. *Trends Biotechnol* **33**, 408–418 (2015).

266. Cheal, S. M., Chung, S. K., Vaughn, B. A., Cheung, N. K. V. & Larson, S. M. Pretargeting: A Path Forward for Radioimmunotherapy. *J Nucl Med* **63**, 1302–1315 (2022).

267. Paganelli, G. *et al.* Antibody-guided three-step therapy for high grade glioma with yttrium-90 biotin. *Eur J Nucl Med* **26**, 348–357 (1999).

268. Moosmayer, D. *et al.* Bispecific antibody pretargeting of tumor neovasculature for improved systemic radiotherapy of solid tumors. *Clin Cancer Res* **12**, 5587–5595 (2006).

269. Chung, S. K. *et al.* Efficacy of HER2-Targeted Intraperitoneal 225Ac α-Pretargeted Radioimmunotherapy for Small-Volume Ovarian Peritoneal Carcinomatosis. *J Nucl Med* **64**, jnumed.122.265095 (2023).

270. Khalid, U. *et al.* Radiolabelled Aptamers for Theranostic Treatment of Cancer. *Pharmaceuticals* **12**, (2019).

271. Hicke, B. J. *et al.* Tumor Targeting by an Aptamer. *Journal of Nuclear Medicine* **47**, (2006).

272. Zhang, X. *et al.* Effects of Aptamer to U87-EGFRvIII Cells on the Proliferation, Radiosensitivity, and Radiotherapy of Glioblastoma Cells. *Mol Ther Nucleic Acids* **10**, 438–449 (2018).

273. Wang, L. *et al.* Therapeutic peptides: current applications and future directions. *Signal Transduct Target Ther* **7**, (2022).

274. Kiviniemi, A. *et al.* Somatostatin receptor subtype 2 in high-grade gliomas: PET/CT with 68Ga-DOTA-peptides, correlation to prognostic markers, and implications for targeted radiotherapy. *EJNMMI Res* **5**, (2015).

275. Strosberg, J. *et al.* Phase 3 Trial of 177 Lu-Dotatate for Midgut Neuroendocrine Tumors . *New England Journal of Medicine* **376**, 125–135 (2017).

276. Strosberg, J. R. *et al.* 177Lu-Dotatate plus long-acting octreotide versus high-dose long-acting octreotide in patients with midgut neuroendocrine tumours (NETTER-1): final overall survival and long-term safety results from an open-label, randomised, controlled, phase 3 trial. *Lancet Oncol* **22**, 1752–1763 (2021).

277. Hänscheid, H. *et al.* Biokinetics and Dosimetry of 177Lu-Pentixather. *Journal of Nuclear Medicine* **63**, 754–760 (2022).

278. Chen, Z., Xue, Q. & Yao, S. Nuclear Medicine Application of Pentixafor/Pentixather Targeting CXCR4 for Imaging and Therapy in Related Disease. *Mini Rev Med Chem* **23**, 787–803 (2023).

279. Moody, T. W. *et al.* Bombesin Receptor Family Activation and CNS/Neural Tumors: Review of Evidence Supporting Possible Role for Novel Targeted Therapy. *Front Endocrinol (Lausanne)* **12**, (2021).

280. Bhamidipati, D., Haro-Silerio, J. I., Yap, T. A. & Ngoi, N. PARP inhibitors: enhancing efficacy through rational combinations. *British Journal of Cancer 2023 129:6* **129**, 904–916 (2023).

281. Jannetti, S. A. *et al.* PARP-1-Targeted Radiotherapy in Mouse Models of Glioblastoma. *J Nucl Med* **59**, 1225–1233 (2018).

282. Wang, J. H. & Kiess, A. P. PSMA-targeted therapy for non-prostate cancers. *Front Oncol* **13**, (2023).

283. Kunikowska, J. *et al.* Tumor uptake in glioblastoma multiforme after IV injection of [177Lu]Lu-PSMA-617. *Eur J Nucl Med Mol Imaging* **47**, 1605 (2020).

284. Kumar, A. *et al.* 177u-/68Ga-PSMA Theranostics in Recurrent Glioblastoma Multiforme: Proof of Concept. *Clin Nucl Med* **45**, E512–E513 (2020).

285. Kiess, A. P. *et al.* (2S)-2-(3-(1-Carboxy-5-(4-211At-Astatobenzamido)Pentyl)Ureido)-Pentanedioic Acid for PSMA-Targeted α-Particle Radiopharmaceutical Therapy. *J Nucl Med* **57**, 1569–1575 (2016).

286. Mease, R. C. *et al.* An Improved 211At-Labeled Agent for PSMA-Targeted α-Therapy. *J Nucl Med* **63**, 259–267 (2022).

287. Obata, H., Ogawa, M. & Zalutsky, M. R. DNA Repair Inhibitors: Potential Targets and Partners for Targeted Radionuclide Therapy. *Pharmaceutics 2023, Vol. 15, Page 1926* **15**, 1926 (2023).

288. Sharma, D., Leong, K. X. & Czarnota, G. J. Application of Ultrasound Combined with Microbubbles for Cancer Therapy. *Int J Mol Sci* **23**, (2022).

289. Li, M. *et al.* Targeted Alpha-Particle Radiotherapy and Immune Checkpoint Inhibitors Induces Cooperative Inhibition on Tumor Growth of Malignant Melanoma. *Cancers (Basel)* **13**, (2021).

290. Lejeune, P. *et al.* Immunostimulatory effects of targeted thorium-227 conjugates as single agent and in combination with anti-PD-L1 therapy. *J Immunother Cancer* **9**, (2021).

291. Vardaki, I. *et al.* Radium-223 Treatment Increases Immune Checkpoint Expression in Extracellular Vesicles from the Metastatic Prostate Cancer Bone Microenvironment. *Clin Cancer Res* **27**, 3253–3264 (2021).

292. Malo, M. E. *et al.* Mechanistic Insights into Synergy between Melanin-Targeting Radioimmunotherapy and Immunotherapy in Experimental Melanoma. *Int J Mol Sci* **21**, (2020).

293. Jiao, R., Allen, K. J. H., Malo, M. E., Rickles, D. & Dadachova, E. Evaluating the Combination of Radioimmunotherapy and Immunotherapy in a Melanoma Mouse Model. *Int J Mol Sci* **21**, (2020).

294. Guerra, D. B. *et al.* Intercomparison of radiosensitization induced by gold and iron oxide nanoparticles in human glioblastoma cells irradiated by 6 MV photons. *Scientific Reports 2022 12:1* **12**, 1–11 (2022).

295. Li, Q. *et al.* A new wave of innovations within the DNA damage response. *Signal Transduction and Targeted Therapy 2023 8:1* **8**, 1–26 (2023).

296. Everix, L. *et al.* Perspective on the Use of DNA Repair Inhibitors as a Tool for Imaging and Radionuclide Therapy of Glioblastoma. *Cancers (Basel)* **14**, (2022).

297. Makvandi, M. *et al.* Targeting PARP-1 with alpha-particles is potently cytotoxic to human neuroblastoma in preclinical models. *Mol Cancer Ther* **18**, 1195–1204 (2019).

Acknowledgements

This work is funded by the National Agency for Research (ANR) under the framework of the LabEx IRON (Innovative Radiopharmaceuticals in Oncology and Neurology, grant number ANR-11-LABX-0018-01).

Author contributions

L.R. researched data and wrote the original manuscript. E.G., M.C, and F.H. supervised this work, and contributed to writing, editing and reviewing. All authors have read and approved the final version of the manuscript.

Competing interests

The authors declare no competing interest.

CHAPTER IV

Brain Intratumoral Astatine-211 Radiotherapy Targeting Syndecan-1 Cures Glioblastoma and Elicits Memory Immunity in Mice

Loris Roncali, Séverine Marionneau-Lambot, Charlotte Roy, Romain Eychenne, Sébastien Gouard, Sylvie Avril, Nicolas Chouin, Mathilde Allard, Audrey Rousseau, François Guérard, François Hindré, Michel Chérel* & Emmanuel Garcion*

Submitted to Nature Communications

Brain intratumoral astatine-211 radiotherapy targeting syndecan-1 cures glioblastoma and elicits memory immunity in mice

Loris Roncali[1,2], Séverine Marionneau-Lambot[2,3,4], Charlotte Roy[1,5], Romain Eychenne[2,6], Sébastien Gouard[2,4], Sylvie Avril[1], Nicolas Chouin[2,7], Mathilde Allard[2], Audrey Rousseau[1,8], François Guérard[2], François Hindré[1,5], Michel Chérel[2,4,9*] & Emmanuel Garcion[1,5,10*]

[1] Université d'Angers, INSERM, CNRS, CRCI[2]NA, F-49000 Angers, France

[2] Nantes Université, INSERM, CNRS, CRCI[2]NA, F-44000 Nantes, France

[3] CHU Nantes, Nantes Université, Service de médecine nucléaire, F-44000 Nantes, France

[4] CIMA (Centre d'Imagerie Multimodale Appliquée), Nantes Université, INSERM, CNRS, CRCI[2]NA, F-44000 Nantes, France

[5] PRIMEX (Plateforme de Radiobiologie et d'Imageries Expérimentales), Université d'Angers, SFR 4208, F-49000 Angers, France

[6] GIP ARRONAX, F-44160 Saint-Herblain, France

[7] ONIRIS, F-44000 Nantes, France

[8] CHU Angers, Université d'Angers, Service de pathologie cellulaire et tissulaire, F-49000 Angers, France

[9] Institut de Cancérologie de l'Ouest, Service de médecine nucléaire, F-44160 Saint-Herblain, France

[10] PACEM (Plateforme d'Analyse Cellulaire et Moléculaire), Université d'Angers, SFR 4208, F-49000 Angers, France

[*]Corresponding authors: emmanuel.garcion@univ-angers.fr (Emmanuel Garcion), michel.cherel@univ-nantes.fr (Michel Chérel)

Abstract

Glioblastoma (GB), the most devastating form of brain cancer, remains a critical clinical challenge due to its aggressiveness and resistance to conventional treatments. Here, we introduce a locoregional therapy with a rat monoclonal antibody targeting murine syndecan-1 (SDC1) coupled to the α-emitter radionuclide astatine-211 (^{211}At-9E7.4). This targeted-α-therapy (TAT) demonstrates robust efficacy to eliminate orthotopic tumors and achieve improved cure rates in a syngeneic mouse model. Targeting SDC1 ensures brain retention of the treatment over an optimal time window and consequently enables a low-activity administration with a minimal toxicity profile. Moreover, ^{211}At-9E7.4 TAT substantially reduces secondary tumor occurrence and provides resistance to new tumor formation through the activation of central and effector memory T cells. This study is the first exploration of locoregional ^{211}At therapy in an orthotopic mouse model of GB, underscoring ^{211}At-9E7.4 TAT as a promising advancement to improve the treatment and quality of life of GB patients.

Key points

- The mAb-mediated targeting of SDC1 is decisive for maximal cerebral distribution and animal survival
- The 100 kBq activity provides low systemic toxicity and major brain retention in the hemisphere of interest
- A single infusion of locoregional TAT eliminates the tumor locally and reduces secondary tumor occurrence
- Locoregional TAT elicits a memory immune response involving $CD4^+$ and $CD8^+$ memory T cells

Introduction

Glioblastoma (GB) is the most aggressive form of brain cancer. Classified as a grade 4 astrocytoma by the World Health Organization[1], its annual incidence is 3.27 cases per 100,000 people[2]. After a maximum safe resection, when feasible, the conventional treatment protocol, known as the "Stupp regimen", consists of external radiotherapy and concomitant temozolomide chemotherapy. Despite this intensive therapeutic approach, the median overall survival of patients does not exceed 15 months[3]. The failure of conventional treatments is attributed to the radioresistance[4] and chemoresistance[5] of the remaining tumor cells following surgical resection. Intratumoral heterogeneity[6] and genomic instability[7] foster a tumor microenvironment that maintains immunosuppression[8], along with a high infiltrative potential[9]. Another key obstacle to therapeutic success is the blood-brain barrier (BBB), which shields the brain from systemic circulation and consequently hampers the intravenous administration of therapeutic agents[10]. As a result, phase III clinical trials over the past 20 years have culminated in failures, leaving the clinical need for GB unmet[11].

Locoregional vectorized radiotherapy represents a promising approach to overcome these specific constraints and improve tumor targeting. β^--emitting radionuclides were the first to be investigated, conferring an optimal range in tissues (1-2 mm), high energy emission (0.1-2.3 MeV), and low linear energy transfer (LET, 0.2 keV/µm). In this context, we previously demonstrated the efficacy of lipid nanocapsules loaded with rhenium-188 (^{188}Re) in a syngeneic rat model of GB[12]. To achieve an adapted distribution volume from a small injection volume, the radiotherapy was locally administered by convection-enhanced delivery (CED), allowing the safe and homogeneous distribution of highly concentrated agents independently of their molecular weight or diffusivity[13,14]. This approach was then applied to other *in vivo* GB models and succeeded in extending the survival of treated animals[15,16].

α emitters have significant advantages over β^- emitters: a shorter range in tissues (50-100 µm), higher energy emission (2-10 MeV), higher linear energy transfer (LET; approximately 100 keV/µm)[17], and better efficacy in hypoxic conditions[18]. Thus, they represent ideal candidates to eliminate tumors burdens and potential isolated tumor cells with limited toxicity on healthy tissues. Over the past decade, clinical trials and pilot studies have demonstrated the feasibility and low toxicity of intracranial administration of tenascin-targeted monoclonal antibody (mAb) labeled with astatine-211 (^{211}At)[19], and substance P labeled with bismuth-213 (^{213}Bi)[20,21] or actinium-225 (^{225}Ac)[22] in GB patients. For the treatment of GB, ^{211}At

shows optimal characteristics. Its increasing worldwide supply, coupled with advancements in its chemistry make it a prime candidate to develop new targeted-α-therapies (TATs)[23,24]. Based on a branching decay, ^{211}At generates one α particle of 5.9 MeV or 7.5 MeV with a LET of 99 keV/μm. Its half-life of 7.21 h is convenient for multistep-radiolabeling and suitable for injection to patients. Recent preclinical studies have demonstrated the ability of ^{211}At to reduce tumor growth using various vectorization approaches, such as peptides and gold nanoparticles, through intravenous[25–27], intraperitoneal[28] or intratumoral administration[29–31]. These studies were primarily conducted on subcutaneous rodent models of GB. While some significant improvements in survival were observed[25,27,31], no curative effect was found.

In this context, we aimed to develop a locoregional therapeutic weapon capable of directly targeting the tumor burden and disseminated cells. Thus, the vectorization strategy is an essential factor for the optimal exploitation of ^{211}At attributes. MAbs appear to be ideal vectors for locoregional treatment due to their high affinity and specificity for their target and extensive biological half-life. In this study, we selected the 9E7.4 rat mAb directed against the murine cell surface proteoglycan syndecan-1 (SDC1, also known as CD138) to target GB. The labeling of the 9E7.4 mAb with ^{211}At previously demonstrated efficient systemic targeting and elimination of disseminated cells in a multiple myeloma model, without altering its specific binding to SDC1[32].

SDC1 establishes a critical interface between tumor cells and their microenvironment by engaging them with the extracellular matrix and with numerous growth factors and cytokines[33], thus influencing tumoral anchoring, invasion, immunosuppression, and radioresistance[34–36]. Its overexpression is associated with a poor prognosis in numerous tumor types, including GB, and it is thus an optimal target given the challenging variability of GB[37]. Targeting SDC1, apart from its recognition as a GB biomarker, could ensure extended retention of radioactivity and potentially enable the disruption of the entire tumor ecosystem.

In this study, we developed an orthotopic and syngeneic mouse model of GB to assess the efficacy of ^{211}At TAT when coupled to the 9E7.4 mAb (^{211}At-9E7.4). Therapeutic efficacy and toxicity were assessed by magnetic resonance imaging (MRI) and weekly blood sampling. Importantly, we carefully tracked tumor regression and the emergence of potential secondary tumors within brain parenchyma, while measuring the effects of the TAT in the induction of possible antitumor immune responses.

Results

1. *In vivo* GL261 tumors as a relevant model to target SDC1 in GB

The interest in targeting SDC1 in GB treatment arises primarily from its correlation with a poor prognosis in patients. Using the information provided by the REMBRANDT database (Repository for Molecular Brain Neoplasia Data) accessible *via* the GlioVis portal (http://gliovis.bioinfo.cnio.es), we observed that $SDC1^{HIGH}$ patients have a significantly lower median overall survival (12.1 months) than $SDC1^{LOW}$ patients (17 months) (Fig. 1a). We established a preclinical model using the murine GB cells GL261, which were stereotactically injected into immunocompetent C57BL/6JRj mice. We assessed the relevance of SDC1 targeting with the 9E7.4 mAb in our model by quantifying the level of *in vitro* expression of SDC1 by flow cytometry in the GL261 cell line (n = 6). The ratio of the median fluorescence intensity (MFI) between the 9E7.4 mAb and the IgG2a, κ isotype control was > 3.19. As the MFI ratio > 2, we estimated that SDC1 is expressed in a majority of the cell population (Fig. 1b, Supplementary Table 1).

We confirmed the expression of SDC1 by tumor cells *in vivo* in C57BL/6JRj mice that received a stereotactic intra-striatal graft of 50,000 GL261 cells (n = 4). Mice were sacrificed after a weight loss > 20% at d32, d38, d38 and d44, respectively, and the brains were harvested. The analysis of frozen brain sections by immunofluorescence showed SDC1 to be significantly expressed at higher levels in the developed tumor than in the healthy parenchyma (*p = 0.029) (Fig. 1c, d). In our study, the ^{211}At-9E7.4 TAT was injected on day 11 (d11) at the same stereotactic coordinates *via* CED after confirming tumor growth by MRI the same day. The global efficacy of the treatment was evaluated by weekly MRI and blood sampling (Fig. 1e). The ^{211}At-labeling experiments were performed using five distinct productions of ^{211}At characterized by a ^{210}At/^{211}At ratio < 10^{-3} (0.002 ± 0.001). The resulting astatinated antibody was prepared with a radiochemical purity of 98 ± 1%, hence, above the minimum requirement of 95% for *in vivo* experiments (Supplementary Table 2).

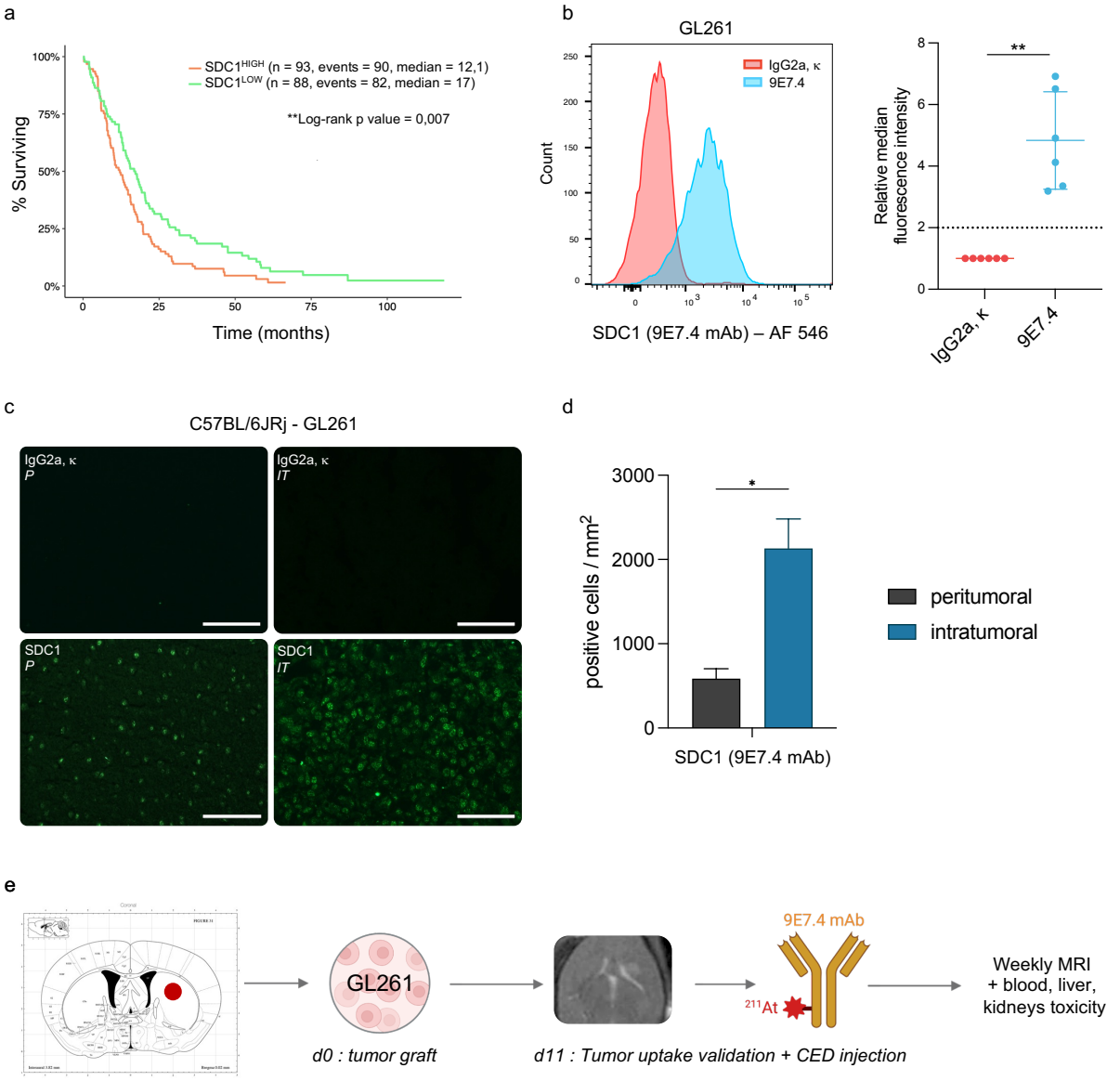

Fig. 1 | ***In vivo* GL261 tumors as a relevant model to target SDC1 in GB.** **a** Kaplan-Meier survival curves in GB patients according to their level of SDC1 expression. $SDC1^{HIGH}$ patients: n = 93, $SDC1^{LOW}$ patients: n = 88. A Log-rank test was performed to assess significance between the two groups. **p < 0.01. The GlioVis data portal was used for visualization and analysis of SDC1 expression in GB patients from the Rembrandt dataset. **b** Expression level of SDC1 in the murine GB cell line GL261 by flow cytometry (n = 6). SDC1 was detected with the 9E7.4 mAb as primary antibody. Data are presented as mean ± standard deviation (sd). A Mann-Whitney test was used to assess significance between the two groups. **p < 0.01. **c** Immunofluorescence staining showing *in vivo* expression of SDC1 in orthotopic GL261 tumors. C57BL/6JRj mice were injected with 50,000 GL261 cells and sacrificed after a weight loss > 20%. SDC1 was detected with the 9E7.4 mAb as primary antibody. *P*: parenchyma, *IT*: intratumoral. Scale bar = 100mm (n = 4). **d** SDC1 positive cells counting in intratumoral and peritumoral areas. Data are presented as mean ± sd. A Mann-Whitney test was used to assess significance between the two groups (n = 4). *p < 0.05. **e** Schematic overview of the application of locoregional ^{211}At TAT targeting SDC1. C57BL/6JRj mice received an orthotopic graft of 50,000 GL261 cells in the right striatum by stereotaxis. After MRI confirmation of tumor uptake, the 9E7.4 mAb labeled with ^{211}At was injected on d11 at the same coordinates by CED. Mice were subsequently monitored weekly by MRI. Blood toxicity was assessed on a weekly basis. Renal and hepatic toxicity were monitored monthly. Illustration was made with the online Mouse Brain Atlas from labs.gaidi.ca/mouse-brain-atlas and BioRender (biorender.com).

2. The 9E7.4 mAb enables a prolonged and localized cerebral retention of ^{125}I in tumor-bearing mice

We assessed the relevance of a locoregional therapeutic approach by evaluating the duration of cerebral retention of the radiolabeled 9E7.4 mAb. Due to limited availability and short half-life of ^{211}At, 9E7.4 and its isotype control (IgG2a, κ) were labeled with iodine-125 (^{125}I) to mimic the fate of ^{211}At in the biodistribution study, as these two radiohalogens share close physicochemical properties and similar biodistribution profiles[38].

Tumor-bearing C57BL/6JRj mice underwent a striatal CED administration of ^{125}I-9E7.4 or ^{125}I-IgG2a, κ on d11. Mice were sacrificed and organs were harvested 2, 7, 21, and 72 h post-injection (n = 3 for each). The radioactivity in each organ was measured in a gamma counter. CED administration of both radiolabeled 9E7.4 and IgG2a, κ demonstrated predominant cerebral retention (Fig. 2a, Supplementary Fig. 1a, b). A comparison of the biodistribution of the two radioconjugates revealed a significantly higher cerebral retention of ^{125}I-9E7.4 than IgG2a, κ (**p = 0.0079) throughout the 2 to 72 h period (Fig. 2a). This retention profile was, thus, consistent with the 7.2-hour half-life of ^{211}At. A moderate retention of ^{125}I-9E7.4 was also observed in the spleen, small intestine, and liver. The complete biodistribution study is available in Supplementary Fig. 1.

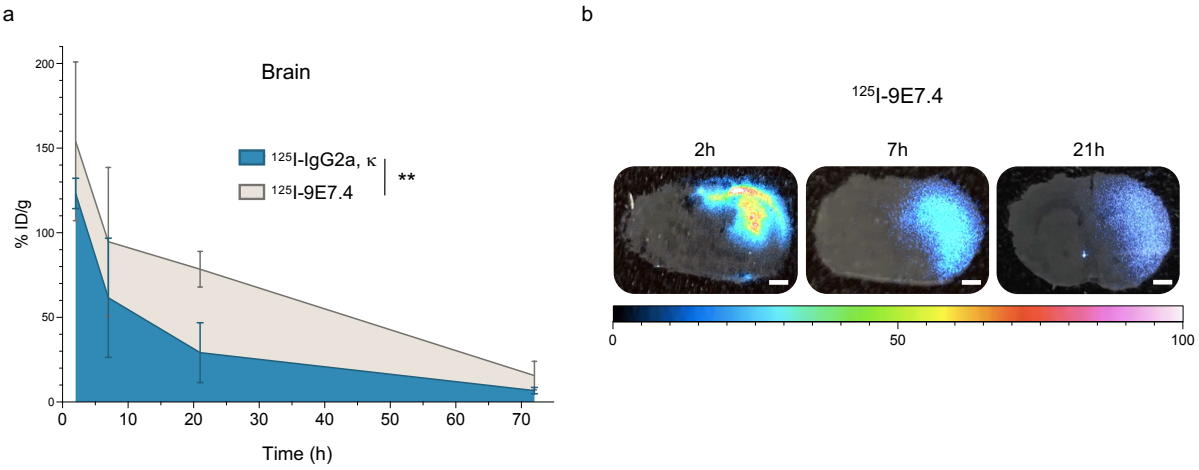

Fig. 2 | **The 9E7.4 mAb enables a prolonged and localized cerebral retention of ^{125}I in tumor-bearing mice. a** Comparative biodistribution of ^{125}I-IgG2a, κ and ^{125}I-9E7.4 in the brain between 2h and 72 h after locoregional CED injection in GB-bearing C57BL/6JRj mice (n = 3 for each time point). Radioconjugates were injected 11 days after tumor graft. Data are shown as a percentage of injected dose per gram (%ID/g) and presented as mean ± sd. Statistical significance was determined using multiple t-tests based on the AUC of each group. **p < 0.01. **b** Digital autoradiography performed on mouse brains at 2 h, 7 h or 21 h after ^{125}I-9E7.4 injection in GB-bearing C57BL/6JRj mice. n = 3 for each time point. Scale bar = 1 mm.

We visualized the brain distribution of ^{125}I-9E7.4 by digital autoradiography of brain cryosections produced under the same experimental conditions (n = 3 for each time point). These images displayed a high concentration of radioactivity 2 h post-injection, confined to the area of tumor cell injection. Within 7 h following the administration of ^{125}I-9E7.4, the area of distribution had expanded within the ipsilateral cerebral hemisphere without complete coverage and never reached the contralateral hemisphere. After 21 h, equivalent to three ^{211}At half-lives, measurable activity persisted within the same extended area (Fig. 2b).

3. Locoregional treatment of GB with ^{211}At-9E7.4 TAT leads to improved survival and minimal toxicity

We investigated the preclinical effects of ^{211}At locoregional therapy for GB by exploring the hypothesis of the targeting of SDC1. The lethal dose for 10% of animals (LD_{10}) was previously established by McLendon *et al.* at 46 MBq/g for an intravenous (i.v.) injection of ^{211}At-labeled mAb in female mice[39], equivalent to 920 kBq for a 20 g mouse. As we were conducting the first study of intracranial administration of ^{211}At in mice, we hypothesized that the treatment could be effective with a significantly lower activity than i.v. preclinical tests[25–27], leading us to set the highest injected activity at 470 kBq in our study. After confirming GB presence by MRI on d11, three groups of mice received a single injection of ^{211}At-9E7.4 *via* CED: 470 kBq (n = 5), 200 kBq (n = 16), or 100 kBq (n = 10). As a control, injection of 100 kBq of ^{211}At-IgG2a, κ (n = 4), 100 kBq of unlabeled ^{211}At ([^{211}At]NaAt) (n = 5), and 2.8 μg of unlabeled 9E7.4 mAb (n = 6), were tested. Untreated mice received an injection of saline solution (0.9% NaCl; n = 15). Mice were euthanized upon weight loss exceeding 20% of initial weight, combined with the deterioration of general condition and the appearance of significant pain symptoms like reduced activity, reduced food and drink intake, orbital tightening, abnormal ear position, aggression and vocalization (Fig. 1e).

All three tested activities showed striking efficacy in contrast to a median overall survival of 34 days for untreated animals. After 162 days, the survival rate of mice that received 470 kBq was 60% (3/5, *p = 0.0225), the survival rate of those that received a 200 kBq injection was 43.75% (7/16, ***p = 0.0003), and the survival rate of those that received a 100 kBq injection was 70% (7/10, ****p < 0.0001). None of the control conditions had a significant impact on the survival of the animals relative to the untreated group (Fig. 3a, Table 1, Supplementary Table 3).

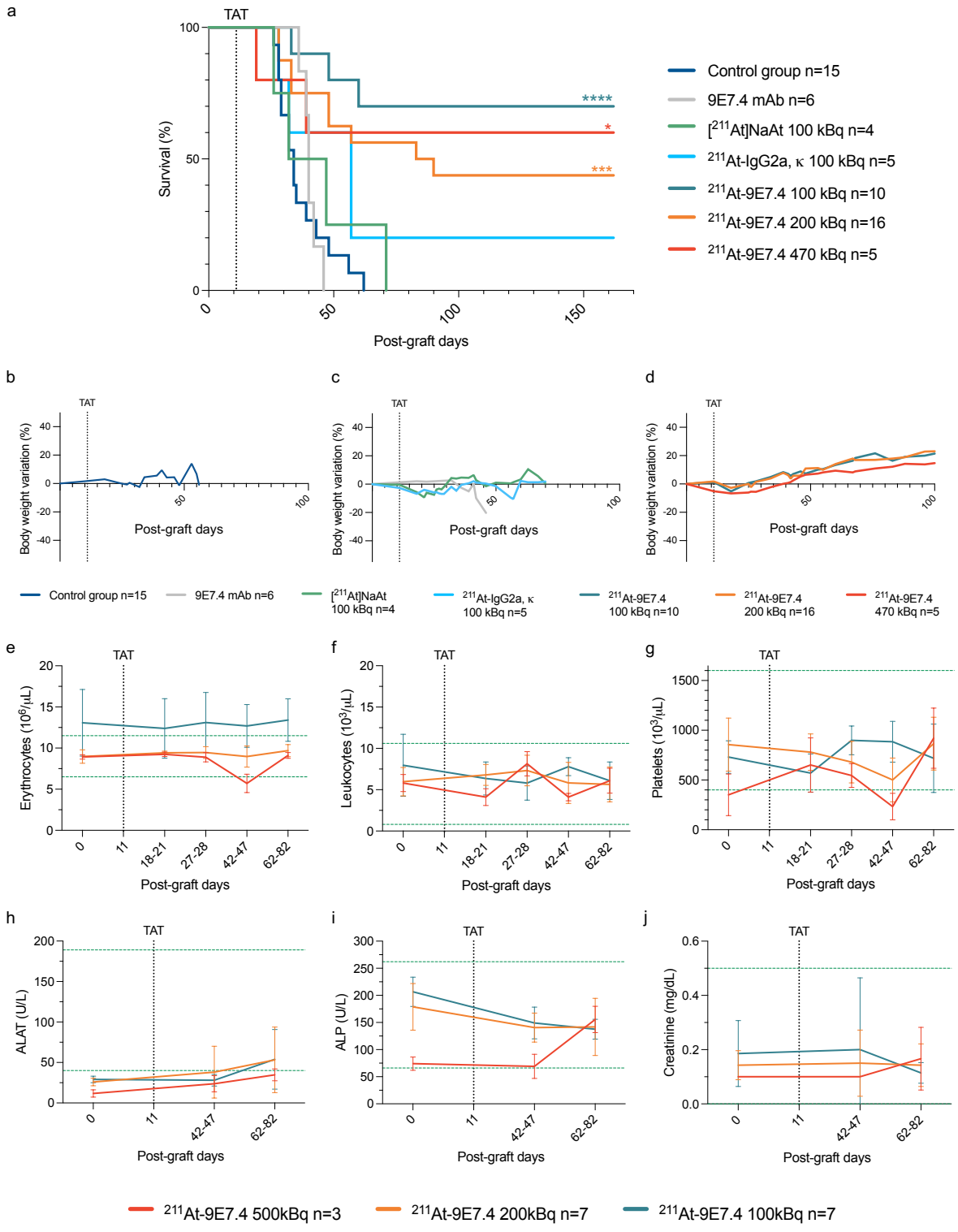

Fig. 3 | **Locoregional treatment of GB with ^{211}At-9E7.4 TAT leads to improved survival and minimal toxicity. a** Kaplan-Meier survival curves. C57BL/6JRj mice were injected at d0 with 50,000 GL261 cells into the right striatum by stereotaxis. Mice received at d11 a 5 µL CED injection of ^{211}At-9E7.4 (470, 200 or 100 kBq), ^{211}At-IgG2a, κ (100 kBq), [^{211}At]NaAt (100 kBq), unlabeled 9E7.4 mAb (2.8 µg) or saline solution (0.9% NaCl). A log-rank test was used to establish statistical significance in comparison with the control group: *p < 0.05, ***p < 0.001, ****p < 0.0001. **b-d** Weight curves of the different groups: control (0.9% NaCl) (**b**), non-targeting groups (^{211}At-IgG2a, κ, [^{211}At]NaAt, unlabeled 9E7.4 mAb) (**c**), and groups treated with 470, 200 or 100 kBq of ^{211}At-9E7.4 (**d**). Data are presented as mean ± sd. **e-j** Erythrocytes (**e**), leukocytes (**f**), platelets (**g**), alanine aminotransferase (ALAT) (**h**), alkaline phosphatase (ALP) (**i**) and creatinine levels (**j**) were measured to assess blood, hepatic, and renal toxicity. Data are presented as mean ± sd. Dotted green lines indicate toxicity thresholds provided by the device for C57BL/6JRj mice.

Weight loss was monitored on a weekly basis to evaluate treatment-induced toxicity. With the exception of a minor transient decline post-treatment, the therapy did not affect the weight (Fig. 3 b-d). Individual data of weight monitoring is available in Supplementary Fig. 2. In long-term survivors treated with 200kBq and 100 kBq, we observed no significant hematological impairment in the long-term surviving animals, as evidenced by stable erythrocytes (Fig. 3e), leukocytes (Fig. 3f), and platelets (Fig. 3g) levels up to the end of the study. The 470 kBq activity exhibited a transient decrease in erythrocytes and platelets at d42-47, below toxicity threshold provided by our hematology analyzer (Fig. 3 e, g). Blood levels of lymphocytes, monocytes, neutrophils, eosinophils, basophils and hemoglobin were also monitored and did not exhibit any significant variation associated with toxicity (Supplementary Fig. 3), except for a transient hemoglobin decrease at d42-47 in mice treated with 470 kBq (Supplementary Fig. 3f). Decreasing trends in erythrocyte counts and hemoglobin levels were observed on day 11 in groups treated with ^{211}At alone and with IgG2a, κ (Supplementary Figure 4). Individual hematology follow-up for TAT-injected mice sacrificed during the survival study is available in Supplementary Figure 5.

							Cause of sacrifice		
Protocol	**^{211}At activity (kBq)**	**mAb quantity (µg)**	**n**	**Surviving mice**	**Dead mice**	**Median survival time (days)**	**Striatal tumor**	**Secondary tumor**	**Radionecrosis**
Untreated (saline solution (0.9% NaCl)	-	-	15	0	15	34	6	9	0
9E7.4 mAb	-	2.8	6	0	6	40	6	0	0
[^{211}At]NaAt	100	-	4	0	4	39.5	2	2	0
^{211}At-IgG2a, κ	100	0.56	5	1	4	57	3	1	0
	100	0.56	10	7	3	not reached at d162	1	2	0
^{211}At-9E7.4	200	1.12	16	7	9	86.5	2	7	0
	470	2.8	5	3	2	not reached at d162	0	1	1

Table 1 | **Summary of the survival study.** Data from 5 independent experiments.

Regarding the hepatic enzymes alanine aminotransferase (ALT) and alkaline phosphatase (ALP), no significant increase associated with toxicity was detected for the three activities (Fig. 3h, i). Creatinine level, indicating kidney status, did not show any variation (Fig. 3j). We also assessed blood levels of glucose, phosphate, total proteins, albumin, globulin,

bilirubin, and calcium. The values remained below the thresholds associated with systemic toxicity (Supplementary Fig. 6). Individual data for the control groups and for TAT-injected mice sacrificed during the survival study are available in Supplementary Figures 7 and 8.

4. Activity-dependent radionecrosis resolves over time only in the case of a 100 kBq injection of TAT

We monitored tumor growth and studied the direct effects of α emissions on the brain tissue by MRI. The T2-weighted axial MRI images showed growing tumors in control groups after d11 (Fig. 4a), whereas mice treated with ^{211}At-9E7.4 TAT exhibited an activity-related hypersignal similar to that of radionecrosis (Fig. 4b). This result was confirmed by the simultaneous acquisition of T1-weighted MRI images which validated the presence of free water in the injection area (Supplementary Fig. 9a, b). These areas were initially diffuse and then decreased over time until stabilizing. Interestingly, it only occurred with the association of ^{211}At with the 9E7.4 mAb. Despite its efficacy, the 470 kBq activity was subsequently discontinued in the ensuing series due to the severity of the radionecrosis induced by the treatment.

Reduced tumor growth in the ^{211}At-IgG2a, k condition was also observed, even though 4 out of 5 mice eventually succumbed to their tumor (Fig. 4c, Supplementary Fig. 9f). Tumor volumes also confirmed a strong inhibition of tumor growth in TAT conditions (Fig. 4d, Supplementary Fig. 9g, h, i). The calculation of radionecrosis volumes in long-term survivors confirmed their evolution towards a stable dimension and their proportionality to the injected activities previously observed by MRI. At the end of the follow-up, mice treated with 470 kBq had an average volume of radionecrosis of 16 ± 5.5 mm^3, and those treated with 200 kBq had an average volume of necrosis of 4 ± 3.8 mm^3, whereas it was no longer detectable in survivors treated with 100 kBq (Fig. 4e). The survival study is resumed in Table 1.

5. Locoregional ^{211}At-9E7.4 TAT decreases the occurrence of secondary tumors

In an independent cohort of mice, we studied the direct effects of TAT on locoregional tumor expansion by histology and MRI. We followed the same protocol as for the survival study with a single CED injection at d11 of ^{211}At-9E7.4 (200 kBq, n = 4; 100 kBq, n = 4) or saline solution (0.9% NaCl, n = 4). Mice were sacrificed at d18, seven days after injection of the TAT.

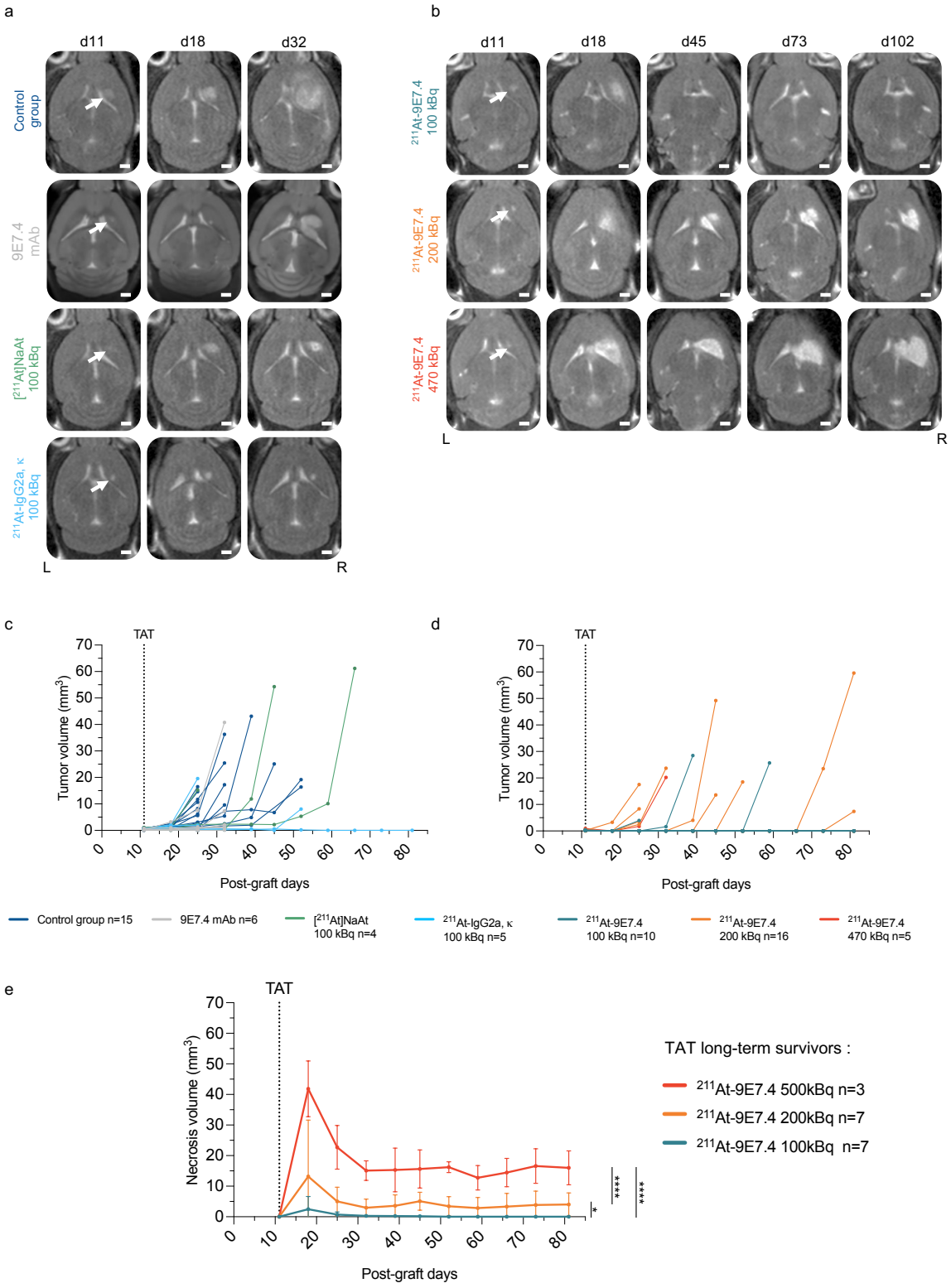

Fig. 4 | **Activity-dependent radionecrosis resolves over time only in the case of a 100 kBq injection of TAT. a-b** Axial T2-weighted MRI brain images of C57BL6/JRj mice from the survival study. Tumor-bearing mice were injected at d11 with saline solution (0.9% NaCl) (control group, n = 15), 100 kBq of ^{211}At-IgG2a, κ (n = 4), 100 kBq of [^{211}At]NaAt (n = 5), unlabeled 9E7.4 mAb (n = 6) (**a**), 470 kBq (n = 5), 200 kBq (n = 16), or 100 kBq (n = 10) of ^{211}At-9E7.4 (**b**). White arrows indicate tumor uptake at d11. Left and right sides are indicated by the corresponding initials at the bottom of the image set. Scale bar = 1 mm**. c-d** Mean tumor volumes measured from MRI images in non-targeting groups (^{211}At-IgG2a, κ, [^{211}At]NaAt, unlabeled 9E7.4 mAb; **c**), and groups treated with 470, 200 or 100 kBq of ^{211}At-9E7.4 of the survival study (**d**). Data are presented as mean ± sd. **e** Mean radionecrosis areas volumes measured from MRI images in long-term survivors treated with 470 kBq (n = 3), 200 kBq (n = 7) or 100 kBq (n = 7) of ^{211}At-9E7.4. Data are presented as mean ± sd. A one-way ANOVA test followed by a Tukey's multiple comparison test were performed on the AUC of each group. *p < 0.05, ****p < 0.0001.

Histopathological analyses carried out on brain cryosections revealed the presence of tumor cell foci in both ventricles at d18 in 100% of control mice and 87.5% of treated mice, although each group showed strong heterogeneity (Table 2). In control mice, we detected substantial proliferation of tumor cells in the striatum, with the presence of large and atypical glial cells. In addition, tumor cells were identified within the right (RV) and left (LV) ventricular regions (tumor cells in RV: 3/4, in LV: 4/4). In mice treated with 200 kBq, necrotic material at the site of injection was observed, corroborating the radionecrosis previously detected in MRI scans (Fig. 4b). Tumor cells were also discerned in both ventricular zones (tumor cells in RV: 4/4, in LV: 1/4). Mice injected with 100 kBq showed moderate chronic lymphocytic infiltrates and very few radionecrosis. They also exhibited tumor foci in both ventricles, excepted in one case (tumor cells in RV: 2/4, in LV: 3/4) (Fig. 5a, Table 2).

Group	Mouse	Tumor infiltrate			Radionecrosis	Inflammation
		Injection site	Right ventricle	Left ventricle	Injection site	Injection site
Control (Saline solution, 0.9% NaCl)	1	+	+	+	-	+
	2	+	+	+	-	+
	3	+	-	+	-	+
	4	+	+	+	-	+
200 kBq	1	-	+	-	+++	+
	2	+	+	-	++	+
	3	+	+	-	+++	+
	4	-	+	+	++	+
100 kBq	1	+	+	+	+	+
	2	-	-	+	+	+
	3	+	+	+	+	+
	4	-	-	-	+	+

Table 2 | **Histopathological analysis of brain sections 7 days after locoregional injection of the ^{211}At–9E7.4 TAT.**

In the survival study, the resolution of the MRI images was insufficient to distinguish such foci at d18. We identified the development of a secondary tumor located next to the hypothalamus from d25 in some mice within each group of the survival study (Fig. 5b). The census of these secondary tumors indicated that 60% of the untreated mice died due to this type of tumor mass. However, the proportion of animals that died due to this reason was reduced when they were treated with TAT: 20% (1/5) for the 470 kBq activity, 43.75% (7/16) for the 200 kBq activity, and 20% (2/10) for the 100 kBq activity (Fig. 5c).

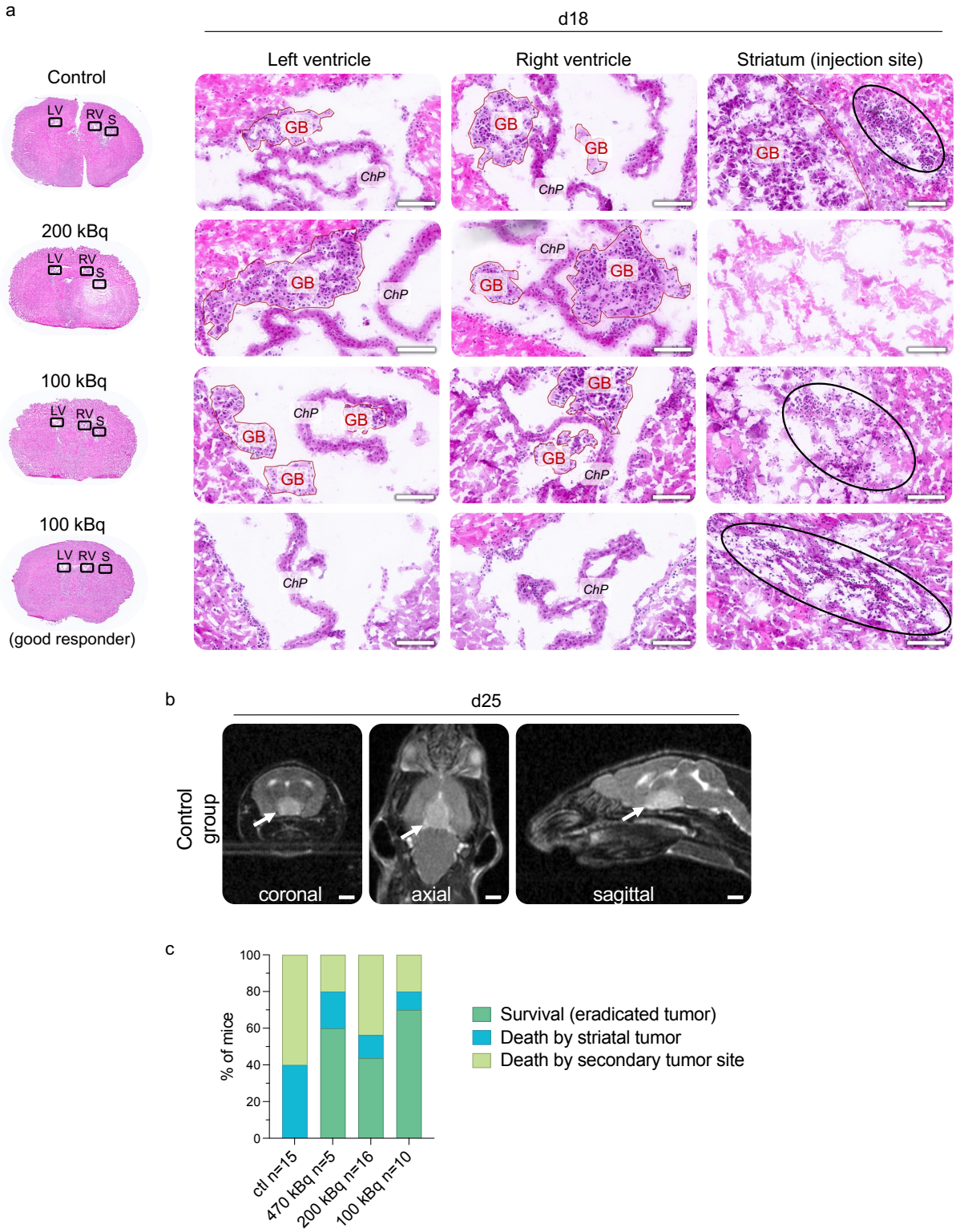

Fig. 5 | **Locoregional ^{211}At-9E7.4 TAT decreases the occurrence of secondary tumors. a** Histological analysis of tumor-bearing mouse brains treated with 200 kBq or 100 kBq of ^{211}At-9E7.4, or injected with saline solution (0.9% NaCl; n = 4 for each group). C57BL/6JRj mice were injected at d0 with 50,000 GL261 cells into the right striatum by stereotaxis. They received at d11 at the same coordinates a CED injection of TAT or saline solution (0.9% NaCl). Mice were euthanized 18 days post-tumor grafting, specifically 7 days following the administration of TAT. Tumor cells are delineated with a red line. Black circles indicate inflammation zones. *LV: left ventricle, RV: right ventricle, S: striatum, GB*: *glioblastoma, ChP*: choroid plexus. Scale bar = 100 μm. **b** T2-weighted images of a control mouse brain from the survival study displaying a secondary tumor indicated by the white arrow. Scale bar = 2 mm. **c** Overview of the survival/death proportions and types of induced tumors (striatal or secondary tumors) during the survival study in relation to the injected dose of ^{211}At-9E7.4 (470, 200 or 100 kBq).

6. Locoregional ^{211}At-9E7.4 TAT elicits vascular remodeling and local inflammation after 7 days

We studied the responses of the tumor environment by immunofluorescence analysis on brain sections. The same protocol as for the survival study was used. At d11, mice received a single CED injection of 200 kBq of TAT (n = 4) or saline solution (0.9% NaCl, n = 4), and were sacrificed at d18. We studied two areas of the brain: the injection area in the striatum (S) and the area adjacent to the right ventricle (V). Here, our aim was to assess responses of three components of the GB microenvironment: vasculature, inflammation, and adaptative immunity. Given the known effects of radiation on blood vessels, we performed CD31 labeling. Markers of innate immunity were also investigated: CD45 for all leukocytes, and CD11b for monocytes/macrophages, granulocytes, and NK cells. T cells were detected by CD3, CD4, and CD8 staining.

Immunofluorescence staining revealed a size increase of $CD31^+$ blood vessels in mice treated with TAT, suggesting functional alterations (Fig. 6a). Quantification of the fluorescence indicated a superior $CD31^+$ expression in these vessels compared to brain sections of control mice. This observation was significant in the injection area and followed the same trend in the area adjacent to the right ventricle (Fig. 6b). In addition, the number of vessels was significantly lower in these two areas for mice treated with TAT (Fig. 6c).

High expression of CD45 and CD11b indicated an increase in the local inflammatory infiltrate (Fig. 6d). In treated mice, CD11b quantification showed a significantly higher expression at the injection site but not in the area adjacent to the right ventricle. Very few T cells were detected in the brain tissue and no significant difference was observed regarding the fluorescence levels of CD3, CD4 and CD8 measured in both areas (Fig. 6e).

7. Locoregional ^{211}At-9E7.4 TAT protects the brain from contralateral tumor injection

Given the extensive research on immune responses induced by ionizing radiation, we investigated if antitumor immunity was operational in long-term survivors. Immune responses could indeed contribute to reduce the development of secondary tumors by eliminating cells migrating from the primary implantation site.

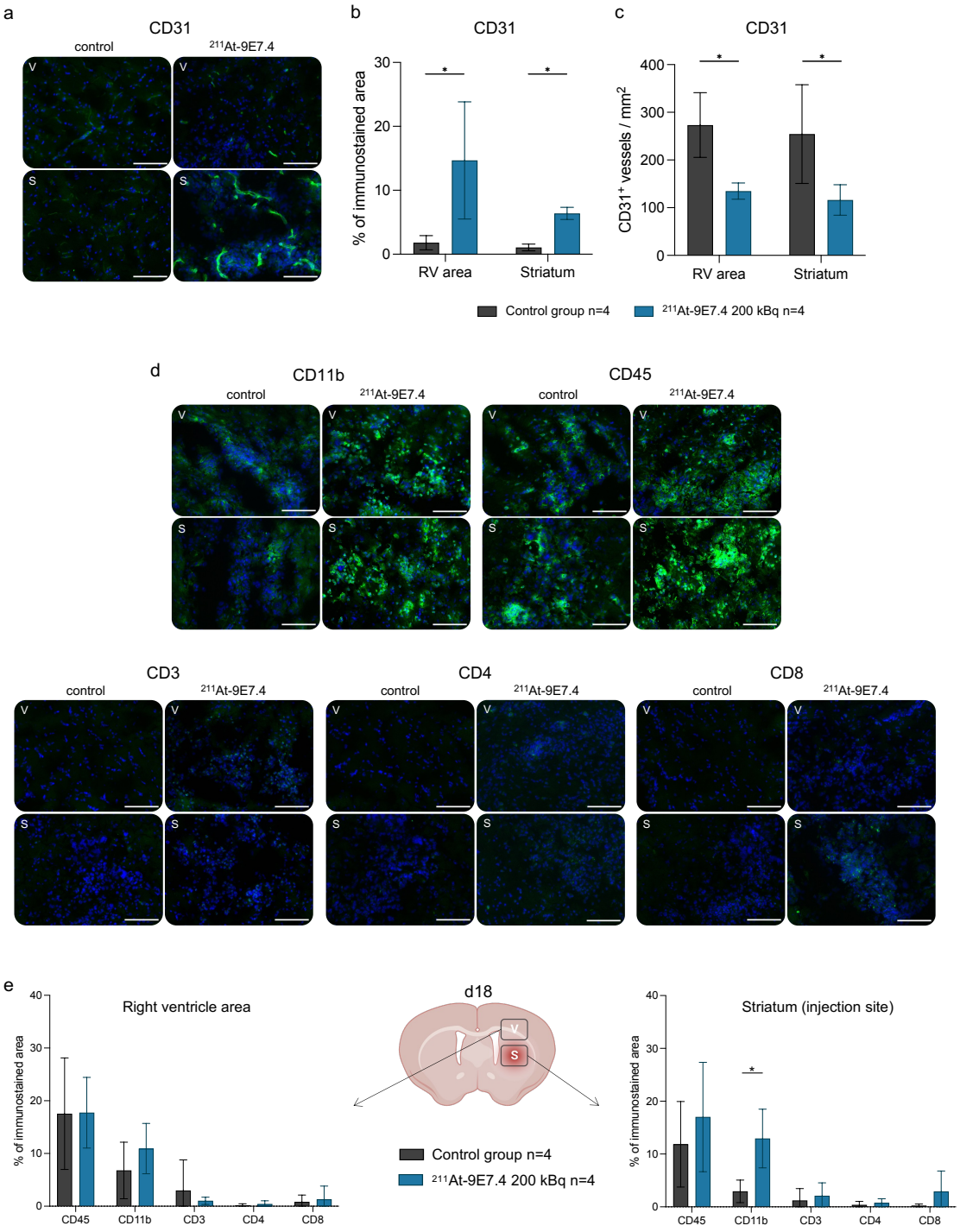

Fig. 6 | **Locoregional ^{211}At-9E7.4 TAT elicits vascular remodeling and local inflammation after 7 days. a** Immunofluorescence labeling of CD31 in mouse brain cryosections. Mice received a tumor graft of 50,000 GL261 cells at d0, followed by 200 kBq of ^{211}At-9E7.4 (n = 4) or saline solution (0.9% NaCl, n = 4) at d11. Mice were sacrificed at d18 (7 days post-TAT). *S: striatum area. V: right ventricle area.* Scale bar = 100 µm. **b** Fluorescence quantification of the CD31 staining. Data are expressed in percentage of immunostained area and presented as mean ± sd. A Mann-Whitney test was performed to assess significance between groups. *p < 0.05. **c** CD31$^+$ blood vessels counting. Data are expressed in number of CD31$^+$ vessels per mm^2 of tissue and presented as mean ± sd. A Mann-Whitney test was performed to assess significance between groups. *p < 0.05. **d** Immunofluorescence labeling of CD45, CD11b, CD3, CD4 and CD8 in mouse brain cryosections. Mice received a tumor graft of 50,000 GL261 cells at d0, followed by a CED injection of 200 kBq of ^{211}At-9E7.4 (n = 4) or saline solution (0.9% NaCl, n = 4) at d11. Mice were then sacrificed at d18 (7 days post-TAT). *S: striatum area. V: right ventricle area*. Scale bar = 100 µm. **e** Fluorescence quantification. Data are expressed in percentage of immunostained area and presented as mean ± sd. A Mann-Whitney test was performed to assess significance between groups. *p < 0.05. Illustration made with BioRender (biorender.com).

15 of the 17 long-surviving mice were rechallenged on d162 with a contralateral graft of 50,000 GL261 cells, divided into the following groups according to their previous treatment: 470 kBq, n = 3; 200 kBq, n = 6, and 100 kBq, n = 6. The new graft was placed in the striatum of the contralateral hemisphere, which had not been previously exposed to ^{211}At radiations as demonstrated in Fig. 2b. Follow-up was performed by weekly MRI scans.

Remarkably, 93% (14/15) of the rechallenged mice survived for 100 more days (Fig. 7a). Weight tracking indicated that the long-term survivors, which were 31-week-old at the time of rechallenge, tolerated the surgical intervention and were still able to gain weight (Fig. 7b and Supplementary Fig. 10 a-d). In all rechallenged mice, no tumor was detectable by MRI (Fig. 7c, d). The previously observed zones of radionecrosis (Fig. 4b) were still visible in mice treated with 470 and 200 kBq and remained undetectable in the 100 kBq group (Fig. 7d, Supplementary Fig. 10e). To detect tumor growth, positron emission tomography (PET) was used to assess the cerebral uptake of [^{18}F]fluorodeoxyglucose ([^{18}F]FDG) in an untreated mouse and two long-term survivors previously treated with 200 or 100 kBq of TAT. In the control mouse, a strong [^{18}F]FDG accumulation confirmed the presence of a tumor that was detected in T2-weighted images (Fig. 7e). In the rechallenged mice, no [^{18}F]FDG fixation was detected at d34 in the injection site nor in the radionecrosis area (Fig. 7f). This study is summarized in the Supplementary Table 4.

8. Locoregional ^{211}At-9E7.4 TAT elicits the activation of immune memory

With the aim of detecting memory T cells associated with this long-term protection, whole blood cytometry was assessed in a fraction of rechallenged mice (n = 5) and control mice (n = 6) at three time points (d4, d7, and d10 after the contralateral tumor graft). The rechallenged subset included mice treated with 200 kBq (n = 3) and 100 kBq (n = 2) of TAT, given that they met the shared criterion of surviving beyond 162 days post-initial transplantation. From the $CD45^+/CD3^+$ blood population, we investigated the $CD4^+$ and $CD8^+$ central memory T phenotypes ($CD44^+/CD62L^+$; T_{CM}) and effector phenotypes ($CD44^+/CD62L^-$; T_{EM}).

At d4, a larger number of $CD3^+$ T_{CM} was detected in rechallenged mice compared to the control group. This phenomenon only relied on $CD8^+$ T_{CM} and not on $CD4^+$ T_{CM}. By d7, in rechallenged mice, $CD4^+$ T_{CM} significantly increased in number while $CD8^+$ T_{CM} declined. In control mice, $CD4^+$ T_{CM} level remained stable over time and $CD8^+$ T_{CM} increased by d7 (Fig.8a).

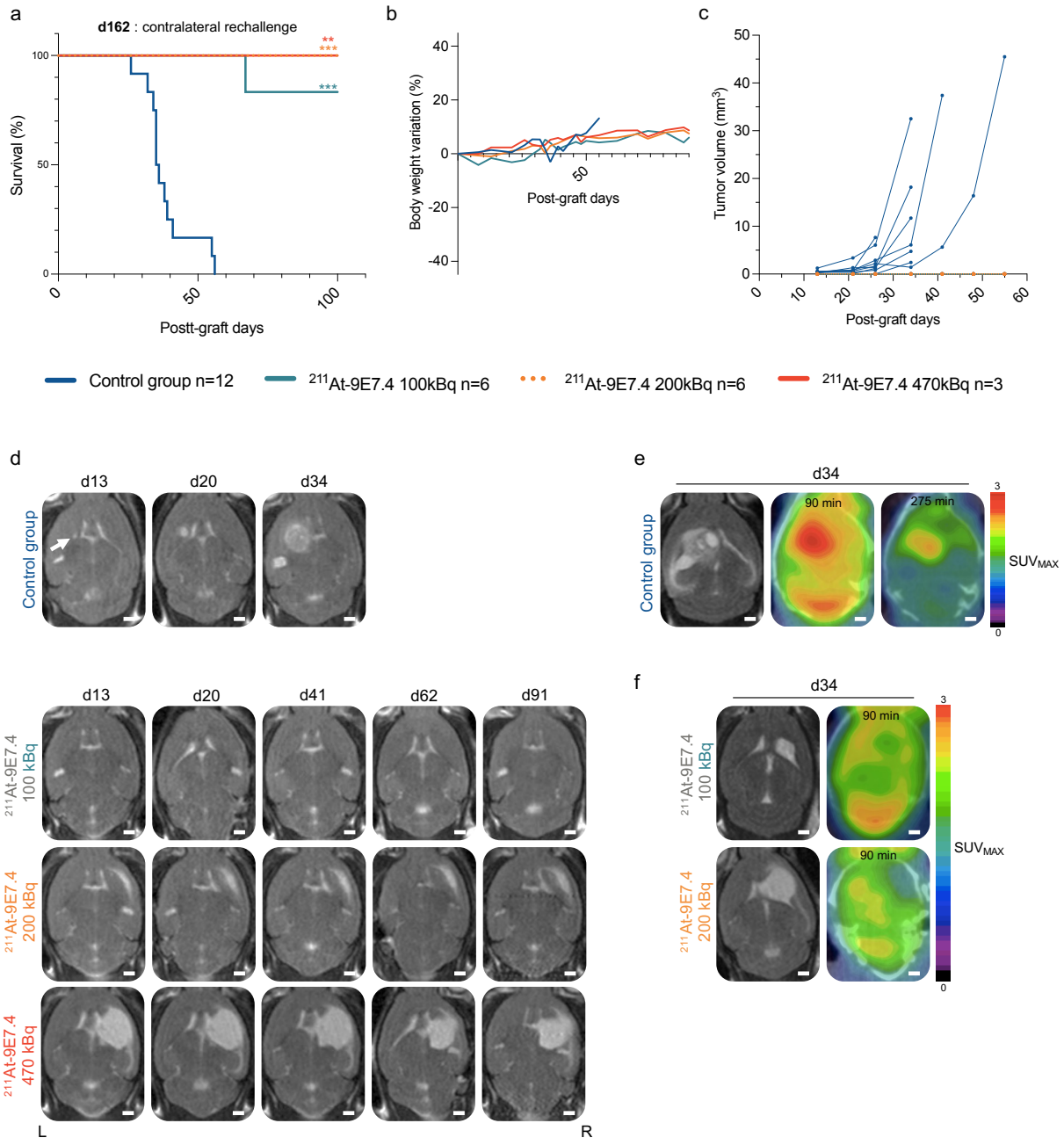

Fig. 7 | **Locoregional ^{211}At-9E7.4 TAT protects the brain from contralateral tumor injection. a** Kaplan-Meier survival curves. After 162 days of survival, long-term survivors and a control group of C57BL/6JRj mice were injected with 50,000 GL261 cells into the left striatum by stereotaxis. 15 mice were rechallenged in total (TAT injection at d11: 470 kBq n = 3, 200 kBq n = 6, 100 kBq n = 6) and 12 control mice. Data come from three independent experiments. Log-rank test was used to establish statistical significance in comparison with the control group. **p < 0.01, ***p < 0.001. **b** Weight monitoring (percentage of initial weight variation). Data are expressed as mean ± sd. **c** Mean tumor volumes measured from MRI images for each group. Data are presented as mean ± sd. **d** Axial T2-weighted MRI brain images of C57BL6/JRj mice from the rechallenge study. White arrows indicate tumor uptake at d13. Left and right sides are indicated by the corresponding initials at the bottom of the image set. Scale bar = 1 mm. **e-f** T2-weighted MRI and [^{18}F]fluorodeoxyglucose ([^{18}F]FDG) PET/CT images of brain from a control mouse (saline solution, 0.9% NaCl as initial treatment) and two rechallenged mice (200 or 100 kBq of ^{211}At-9E7.4 as initial treatment) 34 days after the contralateral rechallenge. Images were acquired 90 min after [^{18}F]FDG injection and additionally after 275 min for the control mouse. Scale bar = 1 mm. SUV_{MAX} = Maximal Standardized Uptake Value.

We also detected a larger number of $CD3^+$ T_{EM} at d4 in the rechallenged mice than in the controls. In this case, both $CD4^+$ and $CD8^+$ T_{EM} phenotypes were responsible for this observation; by d7, both phenotypes started to decline. In control mice, only a slight yet significant increase of $CD4^+$ T_{EM} was detected by d10 (Fig. 8b). For this study, additional information about the monitoring of $CD44^-/CD62L^+$ naïve and $CD44^-/CD62L^-$ T cells is available in Supplementary Fig. 11.

Discussion

In the GB clinical landscape, TAT is typically explored after surgical resection and application of the Stupp regimen[19,21,22], although chemotherapy and external radiotherapy promote radioresistance in residual GB cells[4,5]. To bypass these constraints, we aimed to evaluate the efficacy of locoregional ^{211}At-9E7.4 TAT on an unresected and untreated GB mouse model. In addition, the presence of the tumor could enhance the retention of TAT and help to reach infiltrative cells typically spared by surgery. The feasibility and safety of this kind of approach was previously demonstrated by Cordier *et al.* in a pilot study involving five GB-bearing patients[20].

A single injection of ^{211}At-9E7.4 TAT was able to generate long-term survivors, with the 100 kBq activity achieving the best cure rate of 70%. This is the first study to achieve a curative effect using TAT in an *in vivo* GB model. In contrast, the recapitulation of a Stupp-like regimen in the orthotopic C57BL/6JRj-GL261 model reaches a survival median of 60 days[40], underlying the strong benefit of TAT as a first-line approach. The activities of 200 kBq and 100 kBq were well-tolerated without any observable toxicity in blood, liver, or kidneys. Only the 470 kBq activity resulted in a temporary blood toxicity after 42 days which normalized after 20 days. The activity-dependent radionecrosis induced by TAT was resolved in the 100 kBq group, likely due to the compensation by the surrounding healthy tissues. Nevertheless, further exploration of cerebral toxicity through behavioral experiments should be conducted. Thus, the 100 kBq activity displays both the highest cure rate and the lowest toxicity. This also represents the lowest activity ever tested for ^{211}At *in vivo* in a GB model. Conversely, prior preclinical investigations used activities ranging from 180 kBq to 1.11 MBq of ^{211}At in subcutaneous GB mouse models, yet without a curative outcome[26–28,30,31].

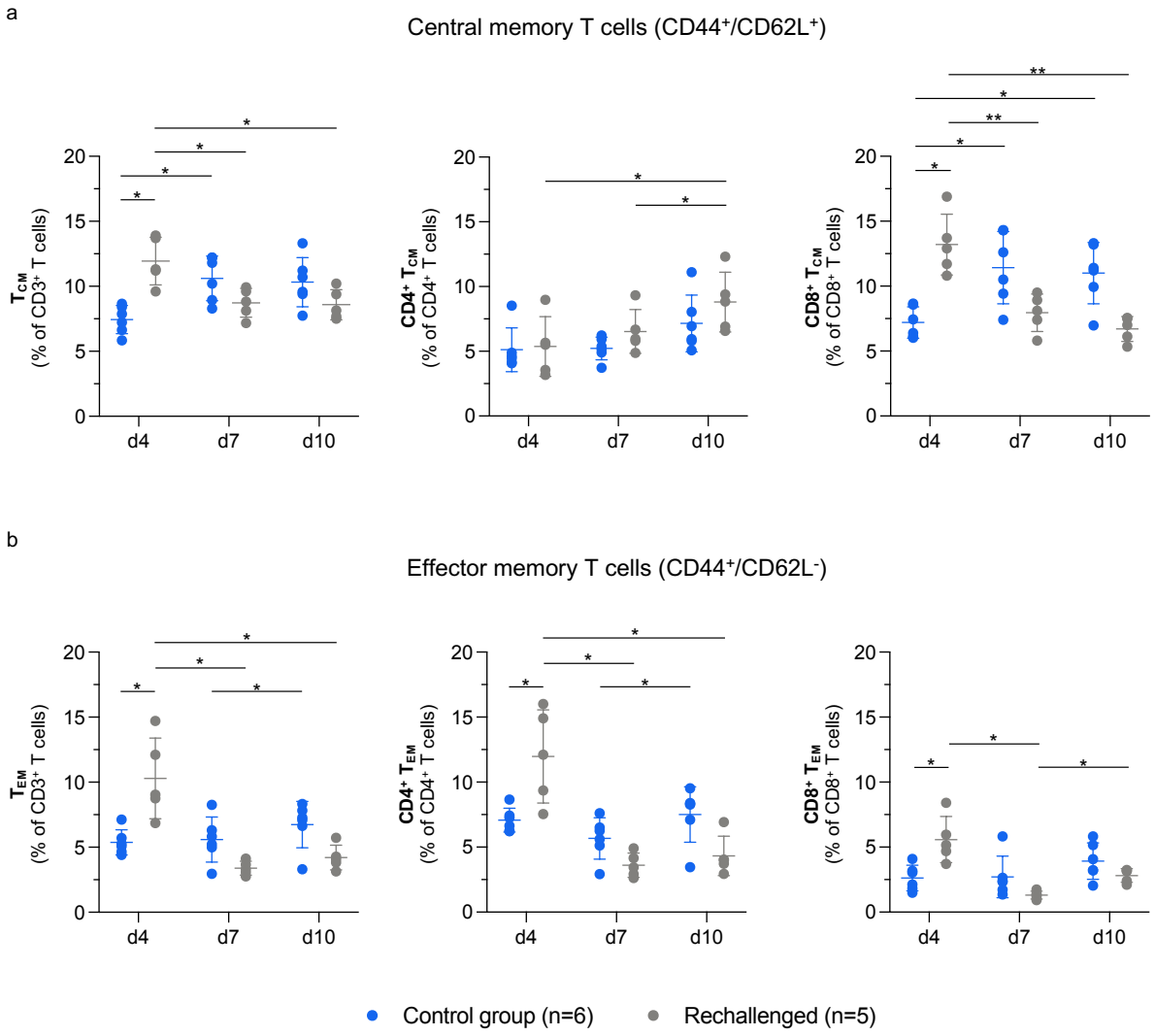

Fig. 8 | **Locoregional ^{211}At-9E7.4 TAT elicits the activation of immune memory. a** Flow cytometry analysis of the central memory phenotype CD44$^+$/CD62L$^+$ among circulating T lymphocytes 4, 7, and 10 days after rechallenge. Central CD4$^+$ and CD8$^+$ phenotypes were also investigated. Data are expressed as mean ± sd. Multiple Mann-Whitney tests were performed to assess significance between groups for each time point. *p < 0.05. A two-way ANOVA test followed by a Tukey's multiple comparison test were performed to assess significance between time points for each group. *p < 0.05, **p < 0.01. **b** Flow cytometry analysis of the effector memory phenotype CD44$^+$/CD62L$^-$ among circulating T lymphocytes 4, 7, and 10 days after rechallenge. Effector CD4$^+$ and CD8$^+$ phenotypes were also investigated. Data are expressed as mean ± sd. Multiple Mann-Whitney tests were performed to assess significance between groups for each time point. *p < 0.05. A two-way ANOVA test followed by a Tukey's multiple comparison test were performed to assess significance between time points for each group. *p < 0.05.

Despite the complete eradication of orthotopic tumors in long-term survivors, ventricular tumor foci were detected on d18 in distinct cohorts of treated mice (Table 2). This raises questions regarding their fate in these long-survivors, as they remained undetected by MRI during the monitoring period. Conversely, hypothalamic tumors developed from d25 in some mice of each group of the survival study (Fig. 5b). This observation is consistent with the ability of the GL261 cell line to produce secondary tumors after an intra-striatal injection[41], thereby mirroring multifocal GBs observed in 17.2% of patients[42]. The presence of

hypothalamic tumors in our model supports the hypothesis of GB cell migration through the cerebrospinal fluid after contact with the ventricles and the subventricular zone (SVZ) during the growth of the primary tumor. Indeed, in patients, neural stem cells (NSCs) of the SVZ facilitate the migration of GB stem-like cells (GSLCs)[43]. Therefore, the ventricular tumor foci observed at d18 could be the origin of these hypothalamic tumors. In our study, these tumors accounted for the mortality of 60% of the control group. In treated mice, this death rate dropped to 20% in the 470 kBq and 100 kBq groups, and to 43.75% in the 200 kBq group, highlighting an inhibitory effect of TAT on secondary tumor occurrence (Fig. 5c). In our protocol, the SVZ in the right hemisphere was subjected to TAT irradiation, which could directly impact the influence of NSCs on GB development. Indeed, it has been demonstrated that irradiating them can suppress their pro-tumoral capacity[43]. On the other hand, the left ventricle and the hypothalamic region were not subjected to ionizing radiation (Fig. 2b). As TAT is not capable of suppressing ventricular foci, the subsequent reduction in hypothalamic tumor occurrence post-TAT could arise from a bystander effect, either by modulating the immune response or by inducing modifications in the brain parenchyma, which in turn restricts the anchoring of tumor cells[44].

The tumor retention of TAT is essential to obtain the direct and indirect effects of α particles, as insufficient exposure may fail to eliminate tumor cells[45]. Locoregional CED administration of radiolabeled 9E7.4 mAb demonstrated a prolonged and localized cerebral retention of radioactivity over 72 h, superior to that obtained with the control isotype (Fig. 2a, b). This SDC1-dependent retention proved to be essential for tumor eradication, as only mice treated with ^{211}At-9E7.4 TAT became long-survivors (Fig. 3a). Additionally, this resulted in a reduced distribution in peripheral organs compared to intravenous injection previously assessed with ^{211}At-9E7.4[32]. A specific binding was observed in the liver, spleen, and small intestine, organs that exhibit substantial expression of SDC1[46–48], but no related toxicity was detected during the survival study (Fig. 3 e-i, Supplementary Fig. 3 and 6). In this context, the SDC1-targeted TAT is revealed as a highly sensitive system, requiring a minimal amount of 9E7.4 mAb (down to 0.56 µg per mouse, equivalent to 28 µg/kg) to retain ^{211}At within the tumor. By comparison, efficient mAb concentrations in systemic and intracranial approaches for GB vary from 5 to 10 mg/kg[49,50]. Contrary to current systemic modalities that require low molecular weight vectors with short biological half-lives to overcome the BBB and minimize systemic toxicity, the elevated molecular weight (~150 kDa) and extended half-life of mAbs stand as favorable properties to achieve therapeutic efficacy in a locoregional context.

In addition to ensuring intratumoral retention of TAT, targeting SDC1 could also play a role in mediating biological effects within GB. SDC1 performs distinct functions depending on its location: membrane-bound, nucleus-translocated, or present in a soluble form after proteolytic shedding[33]. In GB, SDC1 may have a role in modulating the epithelial-to-mesenchymal transition (EMT), as in other cancers[51], given its regulation by NF-κB[52] and its overexpression in the GB mesenchymal phenotype[53]. The 9E7.4 mAb might promote its internalization and thus its nuclear translocation, consequently repressing the activation of pro-EMT genes such as NF-κB and TGF-β[54]. Furthermore, the potential reduction of its shedding by 9E7.4 could prevent its interaction with several partners in pro-invasive signaling pathways[55]. These hypotheses are strengthened by the fact that we observed no secondary tumors in the six mice treated with the 9E7.4 mAb alone, in addition to their reduced occurrence in response to ^{211}At-9E7.4 TAT (Table 1). In the brain, SDC1 is primarily expressed in the choroid plexus[56] and plays a crucial role in stimulating adult neurogenesis by increasing the proliferation of NSCs in the SVZ[57]. Thus, its targeting could also reduce the stimulation of GSLCs, as previously mentioned. In its shed form, SDC1 is involved in the radioresistance of GB cells through the formation of a copolymer enabling the interaction of lysosomes and autophagosomes, thus maintaining an autophagic flux in irradiated cells[36]. In breast cancer, it also contributes to immune evasion by mediating the coupling of VEGFR2 to VLA-4, which blocks the T cell migration mediated by LFA-1[58]. The potential interference of 9E7.4 might contribute to reducing radiation resistance and to reactivating T cell migration in GB, thereby enhancing the efficacy of TAT.

These effects might enable the full exploitation of the immunogenic power of TAT. Indeed, several *in vivo* studies reported the ability of α particles to trigger an immune response, such as the release of damage-associated molecular patterns (DAMPs) in an adenocarcinoma model[59], increased production of IL-2, CCL-5, and IFNγ in a multiple myeloma model[60] or migration of dendritic cells and tumor infiltration of $CD8^+$ T cells in a colorectal carcinoma model[61]. In patients, a decrease of PD-L1-expressing $CD8^+$ T cells after irradiation[62] and an abscopal effect by the eradication of distant and untreated lesions, have also been reported[63]. In our research, we noted vascular hypertrophy and significant $CD11b^+$ cell infiltration at d18 in treated mice. This hypertrophy suggests a disruption of the BBB, which could account for the heightened infiltration by peripheral $CD11b^+$ cells. These observations stand in contrast to the findings of Behling *et al.*, who documented BBB remodeling accompanied by a reduction in CD31 expression in blood vessels after i.v. administration of TAT in a mouse model[64]. Our

findings were limited by the analysis of the response at a single time point, and likely missed events occurring earlier. Consequently, we observed no significant response from the adaptive immune system at d18 (Fig. 6d, e). However, the 93% long-term survival rate after contralateral rechallenge (Fig. 7) and the induction of memory immunity (Fig. 8) proves that adaptive immunity was indeed activated post-TAT. Four days post-rechallenge, a significant increase in $CD8^+$ T_{CM} and both $CD4^+$ and $CD8^+$ T_{EM} was measured in the blood of mice previously treated with TAT (Fig. 8). Control mice exhibited a delayed increase in blood T_{CM}, also indicating a potential antigenic presentation following tumor graft, but no change in the number of T_{EM} was observed. Although both naïve T cells and T_{CM} are known to interact with antigens[65], the significant increase in blood T_{CM} suggests that they predominantly facilitated antigen presentation. Furthermore, T_{EM} are known to be redirected from the blood towards non-lymphoid organs following the cleavage of L-selectin (CD62L) on their surface. Thus, the decline in blood T_{EM} in rechallenged mice on d7 suggests a blood-to-tissue flow towards the newly grafted tumor cells. It should be noted that the GL261 cell line is highly immunogenic[66]. Taking this into account, future studies should use less immunogenic GB cell lines, such as SB28, to thoroughly evaluate the immunogenicity induced by ^{211}At. Nevertheless, the widespread use and invasive capacity of GL261 maintains it as a relevant model. A longitudinal assessment of adaptive immune responses, including DAMPs release and cytokines secretion following treatment with ^{211}At-9E7.4 TAT, should also be conducted.

To take into account the tumor microenvironment, especially the immunological aspects of GB after the standard-of-care, the inclusion of ^{211}At-9E7.4 TAT in a protocol that combines tumor resection with the Stupp regimen would be instrumental to pinpoint the optimal therapeutic timeframe for its efficacy. In addition, exploring therapeutic combinations could further enhance outcomes in both inoperable tumor and resection cavity. Specifically, when used in conjunction with immune checkpoint inhibitors, early immune responses could be amplified and further reduce the formation of secondary tumor foci, as shown in breast and colon cancer models by association of ^{211}At with anti-PD-L1[67]. Combination to chimeric antigen receptor T cells (CAR-T cells) or dendritic cell vaccine could also contribute to eradicate distant foci of tumor cells[68,69]. Finally, association of TAT with DNA repair inhibitors has recently been suggested to be an efficient way to improve therapeutic efficacy[70].

Currently, both preclinical and clinical therapeutic studies on GB are focused on improving surgical resection and using both systemic and local approaches with chemotherapy, radiotherapy, and immunotherapy[71], but the outcomes have not been satisfactory yet. Regarding

TAT, the remarkable results observed in other models have not been replicated for GB[72], remaining non-curative even though delay in tumor growth was observed in some studies[25,27,31]. ^{211}At-9E7.4 is therefore one of the most effective TAT in the GB preclinical landscape. By optimizing the radioligand/vector/target association, we were able to significantly reduce the amount of vector and activity needed for robust therapeutic efficacy. This places mAb back at the forefront of potential TAT strategies and validates SDC1 as a relevant GB target. Reflecting on the initiative of Cordier *et al.* who investigated TAT as a first intention treatment, and the clinical trial of Zalutsky *et al.* underscoring the feasibility and minimal toxicity of locoregional ^{211}At[19], forthcoming studies should explore the potential of a humanized SDC1 antibody. This direction promises a clinical adaptation of our strategy to address both established tumors and post-operative residual cells. In future perspectives, the brief half-life of ^{211}At also seems compatible with CED implant systems, facilitating treatment delivery without additional surgical procedures.

Methods

1. Ethical statement

This project was conducted with the authorization of the French Ministry of Higher Education and Research, in accordance with the stipulations of European Directive 2010/63/EU dated September 22, 2010. All surgical procedures were performed under Ketamine/Xylazine anesthesia and all measures were taken to minimize the discomfort and pain endured by the animals. The preclinical studies were conducted on the UTE platform (SFR François Bonamy, IRS-UN, University of Nantes, France, authorisation D44-278). The authorisation for the animal experimentation project (APAFIS #34964 for biodistributions, APAFIS #22777 for survival and rechallenge studies) was delivered by the Ministry of Higher Education and Research, after a favorable review from the local animal experimentation ethics committee “Pays de Loire (CEEA-06)”.

2. Mice

Specific Pathogen Free (SPF) 7-weeks female C57BL/6JRj mice were procured from Janvier Labs and used for experimentation one week after delivery. Mice were accommodated in polycarbonate cages within a specific pathogen-free environment with regulated conditions

including a temperature of 22 °C, humidity within the range of 50-70%, and a 12-hour light/dark cycle. The room ambient air was frequently refreshed at a rate of 10 volume/h. Mice were provided with ad libitum access to tap water and food.

3. Cell line

The GL261 cell line was produced and kindly provided by Corinne Griguer and G. Yancey Gillepsie of the University of Alabama at Birmingham, AL, USA. GL261 cells were detached from culture dishes using accutase (A6964, Sigma-Aldrich) for 5 min at 37 °C, and then suspended in Dulbecco's Modified Eagle's Medium (DMEM) (D6429, Sigma-Aldrich) supplemented with 10% fetal bovine serum (FBS) (CVFSVF00-01, Eurobio Scientific) and 1% antibiotic solution (A5955, Sigma-Aldrich). Cells were then centrifuged at 120 x g and counted. Subsequently, the cells were cultured in a humidified incubator containing 21% O_2, 5% CO_2 at 37 °C and used when 80-90% confluence was reached.

4. 9E7.4 mAb production

The 9E7.4 mAb was produced by immunization of a rat with a 40-amino-acid peptide, derived from the murine SDC1 protein (amino acid sequence 90-130, GenBank: CAA80254.1), which was procured from GeneCust. The isotype of the rat used in generating 9E7.4 was determined by utilizing a RMT1 Rat Isotyping Kit (Bio-Rad) in strict adherence to the protocols provided by the manufacturer. The specificity and affinity of 9E7.4 mAb towards SDC1 was previously demonstrated by flow cytometry[32].

5. ^{125}I or ^{211}At-labeling of 9E7.4 and IgG2a, κ mAb

[^{125}I]NaI was obtained commercially from PerkinElmer in 10^{-5} M NaOH solution with a volumic activity of 3.70 MBq/µL (2 mCi/mL). [^{211}At]NaAt was produced at the Arronax cyclotron facility (Saint-Herblain, France) using the ^{209}Bi(α,2n)^{211}At reaction and recovered from the irradiated target in chloroform using a dry distillation protocol adapted from the procedure previously reported by Lindegren *et al.*[73]. [^{211}At]NaAt was then obtained by reducing to dryness the chloroformic astatine solution under a gentle stream of nitrogen to obtain dry astatine, followed by dissolution in an appropriate volume of 10 mg/mL dithiothreitol aqueous solution. The isotype control used for experiments was a rat IgG2a, κ purchased from R&D

Systems. Radioiodination or astatination of 9E7.4 and IgG2a, κ mAb were performed using a two-step process, from a biaryliodonium salt precursor of *N*-succinimidyl-3-[^{125}I]-iodobenzoate ([^{125}I]SIB) or *N*-succinimidyl-3-[^{211}At]-astatobenzoate ([^{211}At]SAB) and adapted from a previous work[74]. 3-(succinimidyloxycarbonyl)phenyl(4-methoxyphenyl)iodonium triflate (for astatination) or 3-(succinimidyloxycarbonyl)phenyl(2-thienyl)iodonium triflate for radioiodination (2.5 mM in CH_3CN, 190 µL) was incubated with [^{125}I]NaI or [^{211}At]NaAt solution for 30 min at 100 °C and 60 °C respectiverly. The crude reaction solution was then deposited on a dry disposable Sep-Pak C_{18} Plus Long cartridge (Waters), washed with 45 mL of CH_3CN 20% in H_2O and 2 mL of CH_3CN 100% to dissolve the expected product. CH_3CN fraction was diluted with 10 mL of H_2O, concentrated on a Sep-Pak C_{18} Plus Light (Waters) and recovered with 600 µL of MeCN. After evaporation under a stream of nitrogen, the resulting dry [^{125}I]SIB or [^{211}At]SAB was dissolved in 10 µL DMSO, followed by the addition of 60µL of either the 9E7.4 mAb or the isotype control IgG2a, κ (concentration of 5 mg/mL in 0.3M borate buffer at pH 8.6 using a disposable Amicon Ultra-4 centrifugal unit (Millipore)). The solution was incubated for 30 min at 20 °C, and conjugation yields were assessed by ITLC-SG analysis of a sample aliquot (methanol as eluent) and scanned with a Cyclone phosphorimaging scanner (Perkin Elmer). Unbound [^{125}I]SIB or [^{211}At]SAB was removed using a NAP-5 size exclusion chromatography column (Sephadex G25, Cytiva) with saline solution (0.9 %NaCl) as eluent. 200µL fractions were collected and only the fraction with most activity was kept in order to isolate the highest volumic activity. Ultimately, the radiochemical purity was evaluated by ITLC-SG analysis. The ^{211}At-labeling experiments were performed using five distinct ^{211}At productions (Supplementary Table 2).

6. Orthotopic tumor grafts

GL261 cells were detached with accutase (A6964, Sigma-Aldrich), counted and measured for viability by eosin exclusion. Animals were anesthetized intraperitoneally with ketamin 0.8 mL/kg (Imalgene 1000, Mérial) and xylazin 0.62 mL/kg (Rompun 2%, Bayer). The mouse skull was pierced with a burr (Microtorque II) following these coordinates from the bregma (= 0 mm): lateral: - 2.1 mm, anteroposterior: + 0.5 mm, depth: - 3 mm. C57BL/6JRj mice received a tumor graft of 50,000 GL261 cells in the right striatum using a stereotaxis frame (Stoelting) with a 32G syringe (1702N, Hamilton Company), in a 5µL volume of DMEM medium (D6429, Sigma-Aldrich) without FBS nor antibiotic. For the rechallenge grafts, 50,000 GL261 cells were injected into the left striatum with the same procedure at the following

coordinates from the bregma (= 0 mm): lateral: + 2.1 mm, anteroposterior: + 0.5 mm, depth: -3 mm.

7. MRI

For each MRI procedure, mice were anesthetized with 5% isoflurane and then maintained at 2% isoflurane. MRI follow-up was conducted using a 3T magnetic field RS^2D device to assess tumor development and detect potential oedema/necrotic areas. Two types of sequences were employed to obtain axial sections. T2-weighted parameters were: field of view (FOV): 78 mm / 32 mm / 27.9 mm, echo time (TE): 64.48 ms, repetition time (TR): 5000 ms, flip angle: 90 °, acquisition matrix: 450 / 144 / 31 / 1, acquisition voxel size: 173.4 µm / 177.8 µm / 800 µm, bandwidth: 110.1 kHz, duration: 6 min 10 s. T1-weighted parameters were: FOV: 80 mm / 40 mm / 31mm, TE: 12,07 ms, TR: 769 ms, flip angle: 90 °, acquisition matrix: 450 / 144 / 31 / 1, acquisition voxel size: 178.8 µm / 277.8 µm / 800 µm, bandwidth: 50.09 kHz, duration: 9 min 21 s. Due to a technical maintenance issue with the RS^2D device, the group treated with unlabeled 9E7.4 mAb in the survival study was imaged with a Bruker Biospec 70/20 device equipped with a 1H cryoprobe and which operates at a magnetic field of 7T (Bruker). T2-weighted sequence: FOV: 2 cm x 2 cm, TE: 14 ms, TR: 2000 ms, acquisition matrix: 256 x 256, slice thickness: 0.5 mm (separated from 0.1 mm), 2 averages, rare factor = 4, fat saturation. T1-weighted sequence: FOV: 2 cm x 2 cm, TE: 2.6 ms, TR: 2000 ms, acquisition matrix: 256 x 256, slice thickness: 0.5 mm (separated from 0.1 mm), 2 averages, flip angle = 80 °, fat saturation. Images were analysed using OsiriX MD software.

8. Radioconjugates locoregional injection

11 days after the GL261 cells inoculation, tumor growth was firstly evaluated by MRI. The radioconjugates and their controls were injected into the striatum at the same coordinates as the tumor graft, using a stereotaxic frame (Stoelting) equipped with a 32G syringe (1702N, Hamilton Company) connected to a convective infusion pump (Pump 11 Elite, Harvard Apparatus) delivering at a rate of 1 µL/min. The ^{125}I-labeled conjugates were prepared to obtain 2.8 µg of labeled antibodies (9E7.4 mAb or IgG2a, κ) with 30 kBq of ^{125}I in a volume of 5 µL of saline solution (0.9% NaCl). ^{211}At-labeled conjugates were injected at three different activities in a single injection of 5 µL. In one experiment (n = 5), the 470 kBq group received 473.7 ± 17.7 kBq (2.8 µg of antibody). In 3 independent experiments (n = 16), the 200 kBq

group received 206.4 ± 9.3 kBq (1.12 µg of antibody). In 2 independent experiments (n = 10), the 100 kBq group received 99.7 ± 9 kBq (0.56 µg of antibody). Additionally, four mice received 93.5 ± 3.5 kBq of ^{211}At-IgG2a, κ (0.56 µg of antibody), 5 mice received 98.2 ± 4.2 kBq of [^{211}At]NaAt and 6 mice received 2.8 µg of unlabeled 9E7.4 mAb. The activities were obtained by diluting the stock solutions with saline solution (0.9% NaCl), taking into account the decay of ^{211}At. All untreated mice (n = 15) received an injection of 5 µL of saline solution (0.9% NaCl) under the same conditions.

9. Biodistribution

C57BL/6JRj mice received a tumor graft of 50,000 GL261 cells in the right striatum. After a striatal injection of ^{125}I-9E7.4 or IgG2a, κ at d11, blood, thyroid, skin, muscle, spleen, stomach, small intestine, kidneys, liver, heart, lungs, salivary glands, and brain were collected and weighed (except for the thyroid due to difficulty in sampling alone) at 2 h, 7 h, 21 h, and 72 h after injection. The radioactivity was then counted for each sample with a Hidex automatic gamma counter (calibrated and normalized). The measured radioactivity values were decay-corrected to be normalized over the given sacrifice time.

10. Digital autoradiography

C57BL/6JRj mice received a tumor graft of 50,000 GL261 cells in the right striatum. After a striatal injection of ^{125}I-9E7.4 at d11, the brain was harvested after 2 h, 7 h, and 21 h post-injection, and quickly frozen in 2-methyl-butane at -25 °C for 1 min 30 s. 10 µm coronal brain cryosections were obtained using a cryostat (CM3050S, Leica) and were placed on SuperFrost Plus slides (VWR). Digital autoradiography was performed using a BeaQuant digital autoradiography instrument with the Beavacq software (Ai4R) for an acquisition time of 8 h, following the supplier's instructions.

11. Survival and rechallenge studies

In the survival study, C57BL/6JRj mice received a tumor graft of 50,000 GL261 cells in the right striatum. On d11, tumor presence was validated by MRI and a CED injection of the radioconjugates or their corresponding control condition was carried out at the same coordinates. Mice were weighed and monitored by MRI on a weekly basis. A retro-orbital blood

sampling was conducted once a week to measure hematological toxicity using a hematology analyzer (Element HT5, Scil). Once a month, a retro-orbital blood sample was taken to measure biochemical parameters (Element RC, Scil). In the rechallenge study, mice were weighed and monitored by MRI on a weekly basis. Animals were euthanized upon weight loss exceeding 20% of initial weight, combined with the deterioration of general condition and the appearance of significant pain symptoms (reduced activity, reduced food and drink intake, orbital tightening, abnormal ear position, aggression and vocalization).

12. Histopathological analysis

C57BL/6JRj mice received a tumor graft of 50,000 GL261 cells in the right striatum. After striatal injection of ^{211}At-9E7.4 mAb at d11, mice were sacrificed at d18 and brains were harvested and quickly frozen in 2-methyl-butane that had been chilled to -25 °C for 1 min 30 s. 10 µm coronal brain cryosections were obtained using a cryostat (CM3050S, Leica) and were placed on SuperFrost Plus slides (VWR). They were stained with hematoxylin and eosin (HE) and scanned using a Nanozoomzer slide scanner (Hamamatsu). Histopathological analyses were carried out at the Department of Cellular and Tissue Pathology of the University Hospital Center of Angers (CHU-Angers, France). Images were analysed with the NPD.view 2 software.

13. Immunofluorescence

C57BL/6JRj mice received a tumor graft of 50,000 GL261 cells in the right striatum. Following the injection of ^{211}At-9E7.4 TAT into the striatum on day 11, mice were sacrificed on day 18. The brains were collected and rapidly frozen in 2-methyl-butane at -25 °C for 1 min 30 s, and then stored at -80 °C. Coronal brain cryosections of 10 µm thickness were obtained using a cryostat (CM3050S Leica) and placed on SuperFrost Plus slides (VWR). The sections were fixed with acetone for 10 s, rehydrated with PBS for 5 min, and then fixed with 4% paraformaldehyde (PFA) for 15 min at -20 °C. To minimize nonspecific binding, saturation with 10% normal goat serum (NGS) was conducted at room temperature (RT) for 45 min, followed by three PBS washes (5 min each). The sections were incubated overnight at 4 °C with primary antibodies diluted in PBS/4% Bovine Serum Albumin (BSA) to a final concentration of 5 µg/mL. The primary mAbs used were anti-CD31 (550274, BD Biosciences), anti-CD45 (14-0451-82, eBioscience), anti-CD11b (14-0112-82, eBioscience), anti-CD3 (14-0032-82, eBioscience), anti-CD4 (14-0041-82, eBioscience), anti-CD8 (14-0081-82,

eBioscience) and control isotypes rat IgG2a, κ (553927, BD Pharmingen) and rat IgG2b, κ (559478, BD Pharmingen). Following a PBS wash (3 x 5 min), biotinylated anti-rat, anti-rabbit, or anti-mouse IgG secondary antibodies (1:100, Vector Laboratories) diluted in PBS/4% BSA were used for detection of the primary antibodies. After 1 h at RT, the sections were washed with PBS (3 x 5 min). Subsequently, the sections were developed using FITC-conjugated streptavidin (1:500, Dako) diluted in PBS for 45 min at RT, followed by a PBS wash (3 x 5 min). DAPI was added to the slides (1:1000) for 1 min, followed by another PBS wash (3 x 5 min). Finally, the slides were mounted using Dako Fluorescent Mounting Medium. The labeled cryosections were analyzed under an epifluorescence microscope (Axioscope 2 MOT, Zeiss) equipped with a camera (Axiocam 305, Zeiss). Images were acquired using the ZEN Blue 3.2 software (Zeiss). Quantitative analysis was performed using FIJI software.

14. PET/CT

[^{18}F]FDG was provided by the Nuclear Medicine service of the University Hospital Center of Nantes, France. PET/CT acquisitions were obtained at d34 after the rechallenge graft using an Iris PET/CT (Inviscan imaging system) scanner following the injection into the caudal vein of 4.725 ± 0.05 MBq of [^{18}F]FDG in a volume of 100 µL. For the control mouse, two acquisition times were implemented, at 90 min and 285 min post-injection. For the long-surviving mice, only one time point at 90 min post-injection was carried out. Images were reconstructed using the OsiriX MD software.

15. Flow cytometry

After a PBS/BSA 1% wash, cells were saturated in a PBS/BSA 5% solution for 30 min at 4 °C. They were subsequently incubated with the primary antibody 9E7.4 or its isotype control rat IgG2a, κ (553927, BD Pharmingen) for 30 min at RT, shielded from light. The secondary antibody anti-rat IgG conjugated with Alexa Fluor 546 (A11081, Invitrogen), was added for a 30 min incubation at 4 °C, also protected from light. After two washes with PBS / 1% BSA, the cells were resuspended in PBS for analysis on a CytoFLEX LX cytometer (Beckman Coulter). For post-rechallenge blood sample analysis, 100µL of blood were sampled for each mouse into EDTA tubes (control group: n = 6, rechallenge group: n = 5). An erythrocytes lysis step was performed using a BD Pharm Lyse lysis buffer and cells were then incubated for 15 min at RT, protected from light. After a PBS/BSA 1% wash, cells were

saturated in a PBS/BSA 5% solution complemented with Purified Rat Anti-Mouse CD16/CD32 (Mouse BD Fc Block, BD Biosciences) for 30 min at 4 °C. Cells were then incubated with coupled primary antibodies during 30 min at RT, protected from light: anti-CD45 (130-110-803, Miltenyi), anti-CD3 (11-0031-82, Invitrogen), anti-CD4 (552775, BD Pharmingen), anti-CD8 (47-0081-82, Invitrogen), anti-CD44 (563114, BD Horizon), anti-CD62L (553152, BD Pharmingen). The samples were analyzed on an Attune NxT cytometer (Invitrogen). All cytometry data were processed using FlowJo software (v10.8.2).

16. Statistical analysis

All data are presented as mean ± sd. Statistical tests, n and significance are indicated in the figures and legends. All p-values are indicated in the Source Data. For biodistribution, multiple t-tests were conducted based on the AUCs determined for each group to assess significance between the two groups. Regarding volumes of necrotic areas, a one-way ANOVA was used, using the AUCs determined for each group to evaluate significance between the three groups. A log-rank test was used on survival curves (survival and rechallenge studies). For cytometry assays, a Mann-Whitney test was used to determine significance between two groups at each time point, and a two-way ANOVA was used to compare data of each time point (Three time points). The tests were considered significant when p-values were < 0.05. GraphPad Prism Version 9.5.0 was used for data analysis.

Data Availability

The data corresponding to Fig. 1a can be accessed at http://gliovis.bioinfo.cnio.es. Comprehensive data are contained within the Article, Supplementary Information, and Source Data. Requests for additional information should be directed to Emmanuel Garcion (emmanuel.garcion@univ-angers.fr) and Michel Chérel (michel.cherel@univ-nantes.fr).

References

1. Louis, D. N. *et al.* The 2021 WHO Classification of Tumors of the Central Nervous System: a summary. *Neuro Oncol* **23**, 1231–1251 (2021).
2. Ostrom, Q. T. *et al.* CBTRUS Statistical Report: Primary Brain and Other Central Nervous System Tumors Diagnosed in the United States in 2016-2020. *Neuro Oncol* **25**, IV1–IV99 (2023).
3. Stupp, R. *et al.* Radiotherapy plus concomitant and adjuvant temozolomide for glioblastoma. *N Engl J Med* **352**, 987–996 (2005).
4. Wu, Y., Song, Y., Wang, R. & Wang, T. Molecular mechanisms of tumor resistance to radiotherapy. *Molecular Cancer 2023 22:1* **22**, 1–21 (2023).
5. Taylor, M. A., Das, B. C. & Ray, S. K. Targeting autophagy for combating chemoresistance and radioresistance in glioblastoma. *Apoptosis* **23**, 563–575 (2018).
6. Eisenbarth, D. & Wang, Y. A. Glioblastoma heterogeneity at single cell resolution. *Oncogene 2023 42:27* **42**, 2155–2165 (2023).
7. Wang, X. *et al.* Decoding key cell sub-populations and molecular alterations in glioblastoma at recurrence by single-cell analysis. *Acta Neuropathologica Communications 2023 11:1* **11**, 1–19 (2023).
8. Yeo, A. T. *et al.* Single-cell RNA sequencing reveals evolution of immune landscape during glioblastoma progression. *Nature Immunology 2022 23:6* **23**, 971–984 (2022).
9. Osswald, M. *et al.* Brain tumour cells interconnect to a functional and resistant network. *Nature* **528**, 93–98 (2015).
10. Wu, D. *et al.* The blood–brain barrier: structure, regulation, and drug delivery. *Signal Transduction and Targeted Therapy 2023 8:1* **8**, 1–27 (2023).
11. Mandel, J. J. *et al.* Inability of positive phase II clinical trials of investigational treatments to subsequently predict positive phase III clinical trials in glioblastoma. *Neuro Oncol* **20**, 113–122 (2018).
12. Vanpouille-Box, C. *et al.* Tumor eradication in rat glioma and bypass of immunosuppressive barriers using internal radiation with (188)Re-lipid nanocapsules. *Biomaterials* **32**, 6781–6790 (2011).
13. Hunt Bobo, R. *et al.* Convection-enhanced delivery of macromolecules in the brain. *Proc Natl Acad Sci U S A* **91**, 2076–2080 (1994).
14. D'Amico, R. S., Aghi, M. K., Vogelbaum, M. A. & Bruce, J. N. Convection-enhanced drug delivery for glioblastoma: a review. *J Neurooncol* **151**, 415–427 (2021).

15. Cikankowitz, A. *et al.* Characterization of the distribution, retention, and efficacy of internal radiation of 188Re-lipid nanocapsules in an immunocompromised human glioblastoma model. *J Neurooncol* **131**, 49–58 (2017).
16. Séhédic, D. *et al.* Locoregional Confinement and Major Clinical Benefit of 188Re-Loaded CXCR4-Targeted Nanocarriers in an Orthotopic Human to Mouse Model of Glioblastoma. *Theranostics* **7**, 4517–4536 (2017).
17. Eychenne, R., Chérel, M., Haddad, F., Guérard, F. & Gestin, J. F. Overview of the Most Promising Radionuclides for Targeted Alpha Therapy: The "Hopeful Eight". *Pharmaceutics 2021, Vol. 13, Page 906* **13**, 906 (2021).
18. Wulbrand, C. *et al.* Alpha-Particle Emitting 213Bi-Anti-EGFR Immunoconjugates Eradicate Tumor Cells Independent of Oxygenation. *PLoS One* **8**, e64730 (2013).
19. Zalutsky, M. R. *et al.* Clinical experience with alpha-particle emitting 211At: treatment of recurrent brain tumor patients with 211At-labeled chimeric antitenascin monoclonal antibody 81C6. *J Nucl Med* **49**, 30–38 (2008).
20. Cordier, D. *et al.* Targeted alpha-radionuclide therapy of functionally critically located gliomas with 213Bi-DOTA-[Thi8,Met(O2)11]-substance P: a pilot trial. *Eur J Nucl Med Mol Imaging* **37**, 1335–1344 (2010).
21. Królicki, L. *et al.* Safety and efficacy of targeted alpha therapy with 213Bi-DOTA-substance P in recurrent glioblastoma. *Eur J Nucl Med Mol Imaging* **46**, 614–622 (2019).
22. Królicki, L. *et al.* Dose escalation study of targeted alpha therapy with [225Ac]Ac-DOTA-substance P in recurrence glioblastoma - safety and efficacy. *Eur J Nucl Med Mol Imaging* **48**, 3595–3605 (2021).
23. Feng, Y. & Zalutsky, M. R. Production, purification and availability of 211At: Near term steps towards global access. *Nucl Med Biol* **100–101**, 12–23 (2021).
24. Guérard, F. *et al.* Advances in the Chemistry of Astatine and Implications for the Development of Radiopharmaceuticals. *Acc Chem Res* **54**, 3264–3275 (2021).
25. Borrmann, N. *et al.* Systemic treatment with 4-211Atphenylalanine enhances survival of rats with intracranial glioblastoma. *Nuklearmedizin* **52**, 212–221 (2013).
26. Watabe, T. *et al.* Targeted alpha therapy using astatine (211At)-labeled phenylalanine: A preclinical study in glioma bearing mice. *Oncotarget* **11**, 1388–1398 (2020).
27. Liu, W. *et al.* Targeted Alpha Therapy of Glioma Using 211At-Labeled Heterodimeric Peptide Targeting Both VEGFR and Integrins. *Mol Pharm* **19**, 3206–3216 (2022).

28. Dabagian, H. *et al.* PARP Targeted Alpha-Particle Therapy Enhances Response to PD-1 Immune-Checkpoint Blockade in a Syngeneic Mouse Model of Glioblastoma. *ACS Pharmacol Transl Sci* **4**, 344–351 (2021).
29. Kato, H. *et al.* Intratumoral administration of astatine-211-labeled gold nanoparticle for alpha therapy. *J Nanobiotechnology* **19**, 1–12 (2021).
30. Liu, Y. *et al.* Gold nanostars: A novel platform for developing211at-labeled agents for targeted alpha-particle therapy. *Int J Nanomedicine* **16**, 7297–7305 (2021).
31. Ma, H. *et al.* In vitro and in vivo evaluation of 211At-labeled fibroblast activation protein inhibitor for glioma treatment. *Bioorg Med Chem* **55**, 116600 (2022).
32. Gouard, S. *et al.* Targeted-Alpha-Therapy Combining Astatine-211 and anti-CD138 Antibody in A Preclinical Syngeneic Mouse Model of Multiple Myeloma Minimal Residual Disease. *Cancers (Basel)* **12**, 1–18 (2020).
33. Gondelaud, F. & Ricard-Blum, S. Structures and interactions of syndecans. *FEBS J* **286**, 2994–3007 (2019).
34. Shi, S. *et al.* Syndecan-1 knockdown inhibits glioma cell proliferation and invasion by deregulating a c-src/FAK-associated signaling pathway. *Oncotarget* **8**, 40922–40934 (2017).
35. Zhong, J. *et al.* Weighted Gene Co-Expression Network Analysis (WGCNA) Reveals the Functions of Syndecan-1 to Regulate Immune Infiltration by Influenced T Cells in Glioma. *Front Genet* **13**, 792443 (2022).
36. Zeng, L. *et al.* SDC1-TGM2-FLOT1-BHMT complex determines radiosensitivity of glioblastoma by influencing the fusion of autophagosomes with lysosomes. *Theranostics* **13**, 3725–3743 (2023).
37. Yang, Z., Chen, S., Ying, H. & Yao, W. Targeting syndecan-1: new opportunities in cancer therapy. *Am J Physiol Cell Physiol* **323**, C29–C45 (2022).
38. Ogawa, K. *et al.* Radiotheranostics coupled between an At-211-Labeled RGD peptide and the corresponding radioiodine-labeled RGD peptide. *ACS Omega* **4**, 4584–4591 (2019).
39. McLendon, R. E. *et al.* Radiotoxicity of systemically administered 211At-labeled human/mouse chimeric monoclonal antibody: a long-term survival study with histologic analysis. *Int J Radiat Oncol Biol Phys* **45**, 491–499 (1999).
40. Le Reste, P. J. *et al.* Local intracerebral inhibition of IRE1 by MKC8866 sensitizes glioblastoma to irradiation/chemotherapy in vivo. *Cancer Lett* **494**, 73–83 (2020).
41. Resende, F. F. B. *et al.* Evaluation of TgH(CX3CR1-EGFP) mice implanted with mCherry-GL261 cells as an in vivo model for morphometrical analysis of glioma-microglia interaction. *BMC Cancer* **16**, 1–13 (2016).

42. Li, Y. *et al.* A systematic review of multifocal and multicentric glioblastoma. *Journal of Clinical Neuroscience* **83**, 71–76 (2021).
43. Li, S., Dong, L., Pan, Z. & Yang, G. Targeting the neural stem cells in subventricular zone for the treatment of glioblastoma: an update from preclinical evidence to clinical interventions. *Stem Cell Res Ther* **14**, 1–11 (2023).
44. Daguenet, E. *et al.* Radiation-induced bystander and abscopal effects: important lessons from preclinical models. *British Journal of Cancer 2020 123:3* **123**, 339–348 (2020).
45. Fletcher-Sananikone, E. *et al.* Elimination of Radiation-Induced Senescence in the Brain Tumor Microenvironment Attenuates Glioblastoma Recurrence. *Cancer Res* **81**, 5935–5947 (2021).
46. Henry-Stanley, M. J., Hess, D. J., Erlandsen, S. L. & Wells, C. L. Ability of the heparan sulfate proteoglycan syndecan-1 to participate in bacterial translocation across the intestinal epithelial barrier. *Shock* **24**, 571–576 (2005).
47. Reszegi, A., Tátrai, P., Regs, E., Kovalszky, I. & Baghy, K. Syndecan-1 in liver pathophysiology. *Am J Physiol Cell Physiol* **323**, C289–C294 (2022).
48. O'Connell, F. P., Pinkus, J. L. & Pinkus, G. S. CD138 (Syndecan-1), a Plasma Cell Marker: Immunohistochemical Profile in Hematopoietic and Nonhematopoietic Neoplasms. *Am J Clin Pathol* **121**, 254–263 (2004).
49. Green, D. J. *et al.* Astatine-211 conjugated to an anti-CD20 monoclonal antibody eradicates disseminated B-cell lymphoma in a mouse model. *Blood* **125**, 2111–2119 (2015).
50. Liu, Y. X., Liu, W. J., Zhang, H. R. & Zhang, Z. W. Delivery of bevacizumab by intracranial injection: assessment in glioma model. *Onco Targets Ther* **11**, 2673–2683 (2018).
51. Couchman, J. R. Syndecan-1 (CD138), Carcinomas and EMT. *International Journal of Molecular Sciences 2021, Vol. 22, Page 4227* **22**, 4227 (2021).
52. Watanabe, A. *et al.* Expression of syndecans, a heparan sulfate proteoglycan, in malignant gliomas: participation of nuclear factor-kappaB in upregulation of syndecan-1 expression. *J Neurooncol* **77**, 25–32 (2006).
53. Wade, A. *et al.* Proteoglycans and their roles in brain cancer. *FEBS J* **280**, 2399 (2013).
54. Kumar-Singh, A. *et al.* Nuclear syndecan-1 regulates epithelial-mesenchymal plasticity in tumor cells. *Biology (Basel)* **10**, 521 (2021).
55. Nikolova, V. *et al.* Differential roles for membrane-bound and soluble syndecan-1 (CD138) in breast cancer progression. *Carcinogenesis* **30**, 397–407 (2009).
56. Zhang, X., Wu, C., Song, J., Götte, M. & Sorokin, L. Syndecan-1, a cell surface proteoglycan, negatively regulates initial leukocyte recruitment to the brain across the choroid plexus in murine experimental autoimmune encephalomyelitis. *J Immunol* **191**, 4551–4561 (2013).

57. Mouthon, M. A. *et al.* Syndecan-1 Stimulates Adult Neurogenesis in the Mouse Ventricular-Subventricular Zone after Injury. *iScience* **23**, 101784 (2020).
58. Jung, O., Beauvais, D. M., Adams, K. M. & Rapraeger, A. C. VLA-4 phosphorylation during tumor and immune cell migration relies on its coupling to VEGFR2 and CXCR4 by syndecan-1. *J Cell Sci* **132**, jcs232645 (2019).
59. Gorin, J. B. *et al.* Antitumor immunity induced after α irradiation. *Neoplasia* **16**, 319–328 (2014).
60. Perrin, J. *et al.* Targeted Alpha Particle Therapy Remodels the Tumor Microenvironment and Improves Efficacy of Immunotherapy. *Int J Radiat Oncol Biol Phys* **112**, 790–801 (2022).
61. Lejeune, P. *et al.* Immunostimulatory effects of targeted thorium-227 conjugates as single agent and in combination with anti-PD-L1 therapy. *J Immunother Cancer* **9**, e002387 (2021).
62. Kim, J. W., Shin, M. S., Kang, Y., Kang, I. & Petrylak, D. P. Immune Analysis of Radium-223 in Patients With Metastatic Prostate Cancer. *Clin Genitourin Cancer* **16**, e469–e476 (2018).
63. Bellia, S. R. *et al.* Clinical evidence of abscopal effect in cutaneous squamous cell carcinoma treated with diffusing alpha emitters radiation therapy: a case report. *J Contemp Brachytherapy* **11**, 449–457 (2019).
64. Behling, K. *et al.* Remodeling the vascular microenvironment of glioblastoma with α-particles. *Journal of Nuclear Medicine* **57**, 1771–1777 (2016).
65. Jameson, S. C. & Masopust, D. Understanding subset diversity in T cell memory. *Immunity* **48**, 214 (2018).
66. Genoud, V. *et al.* Responsiveness to anti-PD-1 and anti-CTLA-4 immune checkpoint blockade in SB28 and GL261 mouse glioma models. *Oncoimmunology* **7**, e1501137 (2018).
67. Zhang, J. *et al.* Alpha radionuclide-chelated radioimmunotherapy promoters enable local radiotherapy/chemodynamic therapy to discourage cancer progression. *Biomater Res* **26**, 1–15 (2022).
68. Brown, C. E. *et al.* Regression of Glioblastoma after Chimeric Antigen Receptor T-Cell Therapy. *New England Journal of Medicine* **375**, 2561–2569 (2016).
69. Liau, L. M. *et al.* Association of Autologous Tumor Lysate-Loaded Dendritic Cell Vaccination With Extension of Survival Among Patients With Newly Diagnosed and Recurrent Glioblastoma: A Phase 3 Prospective Externally Controlled Cohort Trial. *JAMA Oncol* **9**, 112–121 (2023).
70. Obata, H., Ogawa, M. & Zalutsky, M. R. DNA Repair Inhibitors: Potential Targets and Partners for Targeted Radionuclide Therapy. *Pharmaceutics 2023, Vol. 15, Page 1926* **15**, 1926 (2023).

71. van Solinge, T. S., Nieland, L., Chiocca, E. A. & Broekman, M. L. D. Advances in local therapy for glioblastoma — taking the fight to the tumour. *Nature Reviews Neurology 2022 18:4* **18**, 221–236 (2022).
72. Zhang, J. *et al.* Alpha-emitters and targeted alpha therapy in cancer treatment. *iRADIOLOGY* **1**, 245–261 (2023).
73. Lindegren, S., Bäck, T. & Jensen, H. J. Dry-distillation of astatine-211 from irradiated bismuth targets: A time-saving procedure with high recovery yields. *Applied Radiation and Isotopes* **55**, 157–160 (2001).
74. Guérard, F. *et al.* Bifunctional aryliodonium salts for highly efficient radioiodination and astatination of antibodies. *Bioorg Med Chem* **25**, 5975–5980 (2017).

Acknowledgements

We thank Marie-Hélène Gaugler for critical review of the manuscript. We would like to thank the IRS-UN technical platforms for their support: the radioactivity technical platform, the UTE animal facility, the MicroPICell platform, Nicolas Jouand and Cécile Daussy from the Cytocell platform (SFR François Bonamy, Nantes University, France). We also thank the SCAHU animal facility, the Department of Cellular and Tissue Pathology (CHU Angers, France), the PACEM platform (SFR ICAT, University of Angers, France), and the PRISM core facility (Biogenouest, Univ Rennes, Univ Angers, INRAE, CNRS, France). We would also like to thank Corinne Griguer and G. Yancey Gillepsie of the University of Alabama (Birmingham, AL, USA) who provided the GL261 cell line. E.M. and M.C. thank the National Agency for Research (ANR) which funded this work under the framework of the LabEx IRON (Innovative Radiopharmaceuticals in Oncology and Neurology, grant number ANR-11-LABX-0018-01).

Author contributions

L.R., S.M.-L., and C.R. conducted the *in vivo* experiments. S.M.-L. monitored the mice weighing, sampling and MRI follow-up. F.G. and R.E. performed the antibodies radiolabeling. S.A. and L.R. handled the cell culture for tumor grafts. S.G. and L.R. conducted the autoradiography study. L.R. performed the flow cytometry assays, brain sampling, cryosections and immunofluorescence staining. M.A. contributed to data analysis of the flow cytometry assays. A.R. supervised and interpreted the histological analysis. E.G., M.C. and F.H. supervised the study. L.R. wrote the original manuscript. E.G., M.C., F.H, and R.E. contributed

to the writing. All authors reviewed and edited the manuscript before final version. All authors have read and approved the final published version of the manuscript.

Competing interests

The authors declare no competing interest.

Supplementary Figures

n	IgG2a, k MFI	9E7.4 MFI	Fluorescence intensity ratio
1	340	2213	6.51
2	273	1125	4.12
3	196	625	3.19
4	230	1130	4.91
5	324	2240	6.91
6	644	2163	3.36

Supplementary Table 1 | Median fluorescence intensity ratios from Flow cytometry analysis between IgG2a, k and mAb 9E7.4. Median fluorescence intensity (MFI) was measured for each group. The fluorescence intensity ratio (FIR) was then calculted from these values. When this ratio is > 2, the entire cell population is considered positive for the marker of interest.

Production	^{210}At / ^{211}At ratio	Radiolabeled mAb	Radiolabeling yield (%)	mAb RCP (%)
1	$3.2.10^{-3}$	9E7.4	34	96
2	3.10^{-3}	9E7.4	26	99
4	$2.1.10^{-3}$	IgG2a, κ	31	98
3	$< 2.10^{-5}$	9E7.4	23	99
5	$1.2.10^{-3}$	9E7.4	44	98

Supplementary Table 2 | ^{211}At purity and radiochemical purity of the ^{211}At-9E7.4 and 211At-IgG2a, κ conjugates. The production of ^{211}At generates a fraction of astatine-210 (^{210}At). The purity of ^{211}At is thus represented here in the form of the ratio ^{210}At / ^{211}At. The purity of the radiolabeling of 9E7.4 and IgG2a, κ mAbs is represented in the form of a radiochemical purity (RCP) percentage. In vivo experiments require a minimum RCP value of 95%.

Protocol	Untreated (saline solution, 0.9% NaCl)	9E7.4 mAb 2,8µg	[^{211}At]NaAt 100 kBq	^{211}At-IgG2a, k 100 kBq	^{211}At-9E7.4 470 kBq	^{211}At-9E7.4 200 kBq	^{211}At-9E7.4 100 kBq
Untreated (saline solution, 0.9% NaCl)	-	0.6145	0.3599	0.0948	**0.0225***	**0.0003*****	**< 0.0001******
9E7.4 mAb 2,8µg	0.6145	-	0.3953	0.1846	0.1410	**0.0080****	**0.0005*****
[^{211}At]NaAt 100 kBq	0.3599	0.3953	-	0.4694	0.1635	**0.0183***	**0.044***
^{211}At-IgG2a, k 100 kBq	0.0948	0.1846	0.4694	-	0.3892	0.3028	**0.0445***
^{211}At-9E7.4 470 kBq	**0.0225***	0.1410	0.1635	0.3892	-	0.7214	0.5866
^{211}At-9E7.4 200 kBq	**0.0003*****	**0.0080****	**0.0183***	0.3028	0.7214	-	0.2021
^{211}At-9E7.4 100 kBq	**< 0.0001******	**0.0005*****	**0.044***	**0.0445***	0.5866	0.2021	-

Supplementary Table 3 | Detailed statistical analysis of the survival study. Presentation of the corresponding p-values from the log-rank tests performed between each group in the survival study.

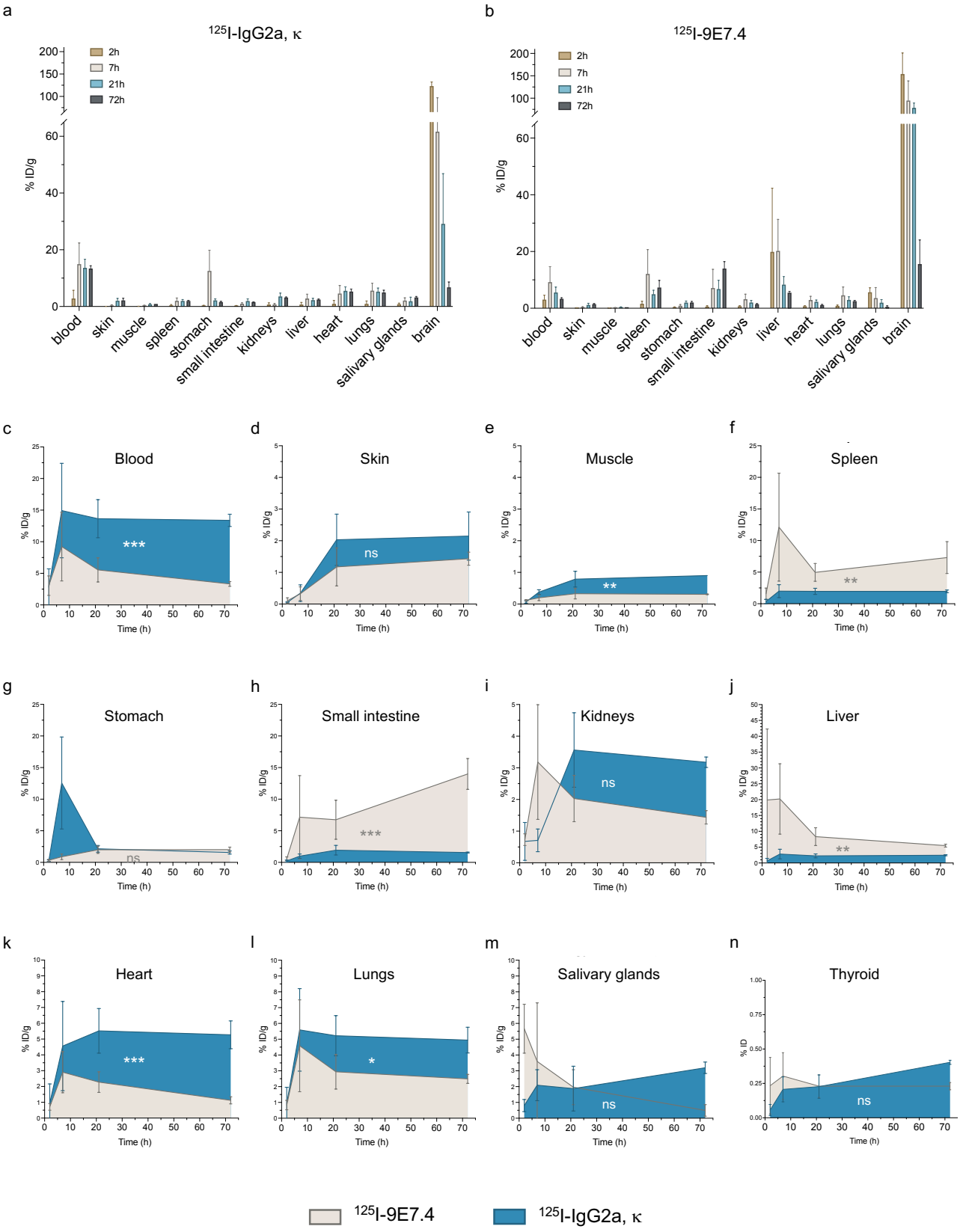

Supplementary Fig. 1 | Biodistribution study of ^{125}I-9E7.4 and ^{125}I-IgG2a, κ conjugates in GB-bearing C57BL/6JRj mice. a-b Biodistribution analysis conducted on ^{125}I-IgG2a, k and ^{125}I-9E7.4, conjugates where 2.8 µg of mAb were labeled with 30 kBq of ^{125}I. C57BL/6JRj mice were stereotactically injected with 50,000 GL261 cells into the right striatum on d0. On d11, mice were administered a CED injection of the radioconjugates at the same coordinates and sacrificed after 2 h, 7 h, 21 h or 72 h. n = 3 for each time point. Data are expressed as a percentage of injected dose per gram (%ID/g) and presented as mean ± sd. **c-n** Detailed biodistribution in blood, skin, muscle, spleen, stomach, small intestine, kidneys, liver, heart, lungs, salivary glands and thyroid. Mice were injected with 2,8µg of mAb 9E7.4 or isotype control IgG2a, κ labeled with 30 kBq of ^{125}I and sacrificed after 2, 7, 21 or 72h (three mice per time point). Data are expressed in percentage of injected dose per gram (%ID/g) and presented as mean ± sd. Because thyroid is difficult to extract alone, samples were not weighted and data are expressed in percentage of injected dose (%ID). Statistical significance was determined with multiple t tests from area under the curve (AUC). ns = $p > 0.05$, *$p < 0.05$, **$p < 0.01$, ***$p < 0.001$.

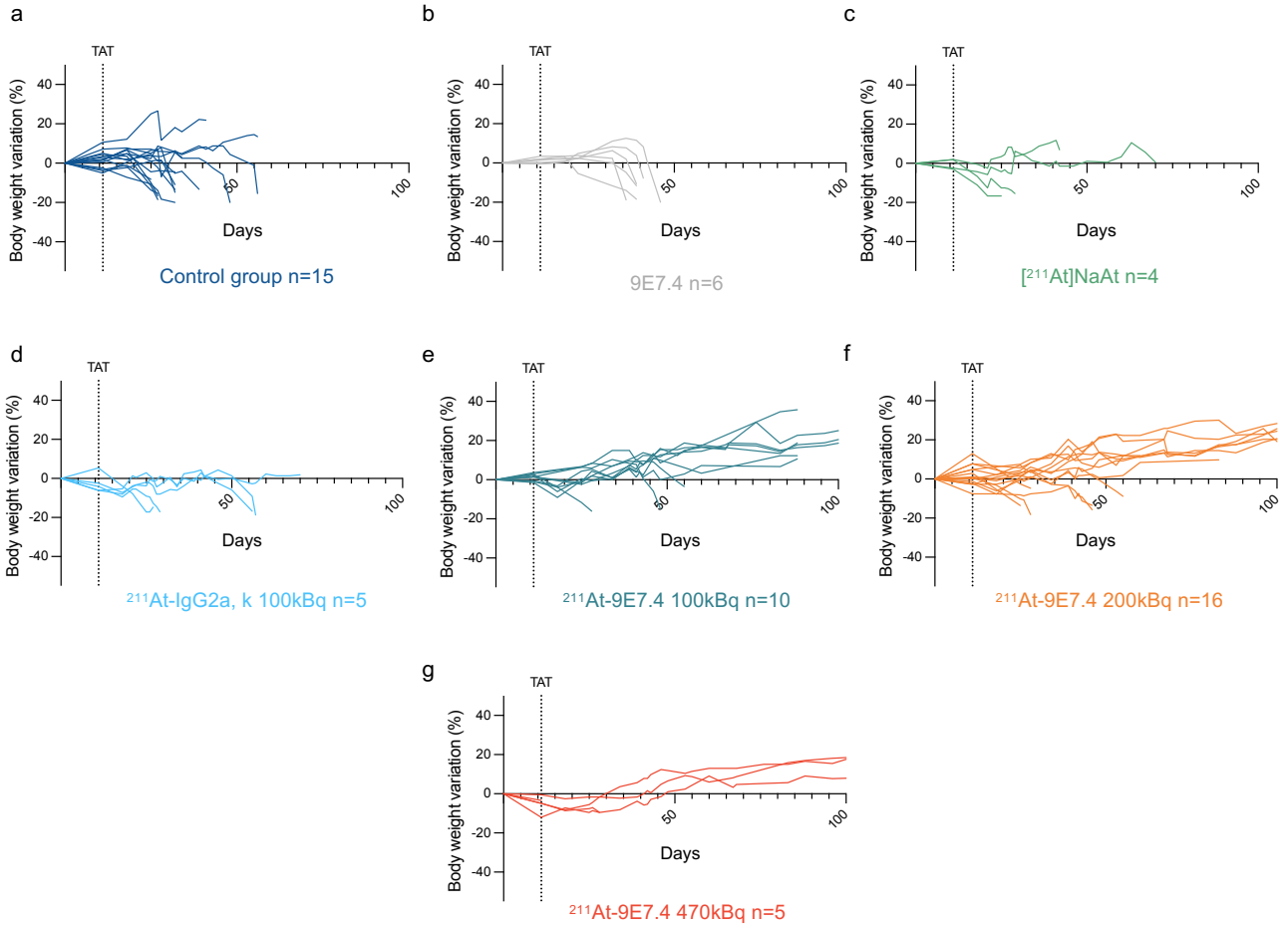

Supplementary Fig. 2 | Individual weight monitoring of C57BL/6JRj mice during the survival study. a-g Individual weight curves of the different groups. C57BL/6JRj mice were injected at d0 with 50,000 GL261 cells into the right striatum by stereotaxis. After validation of tumor uptake by MRI, mice received at d11, at the same coordinates, a CED injection of saline solution (0.9% NaCl; **a**), 2.8 µg of unlabeled 9E7.4 mAb (**b**), 100 kBq of [^{211}At]NaAt (**c**), 100 kBq of ^{211}At-IgG2a, κ (**d**), or 100 kBq (**e**), 200 kBq (**f**) or 470 kBq (**g**) of ^{211}At-9E7.4 in a volume of 5µL.

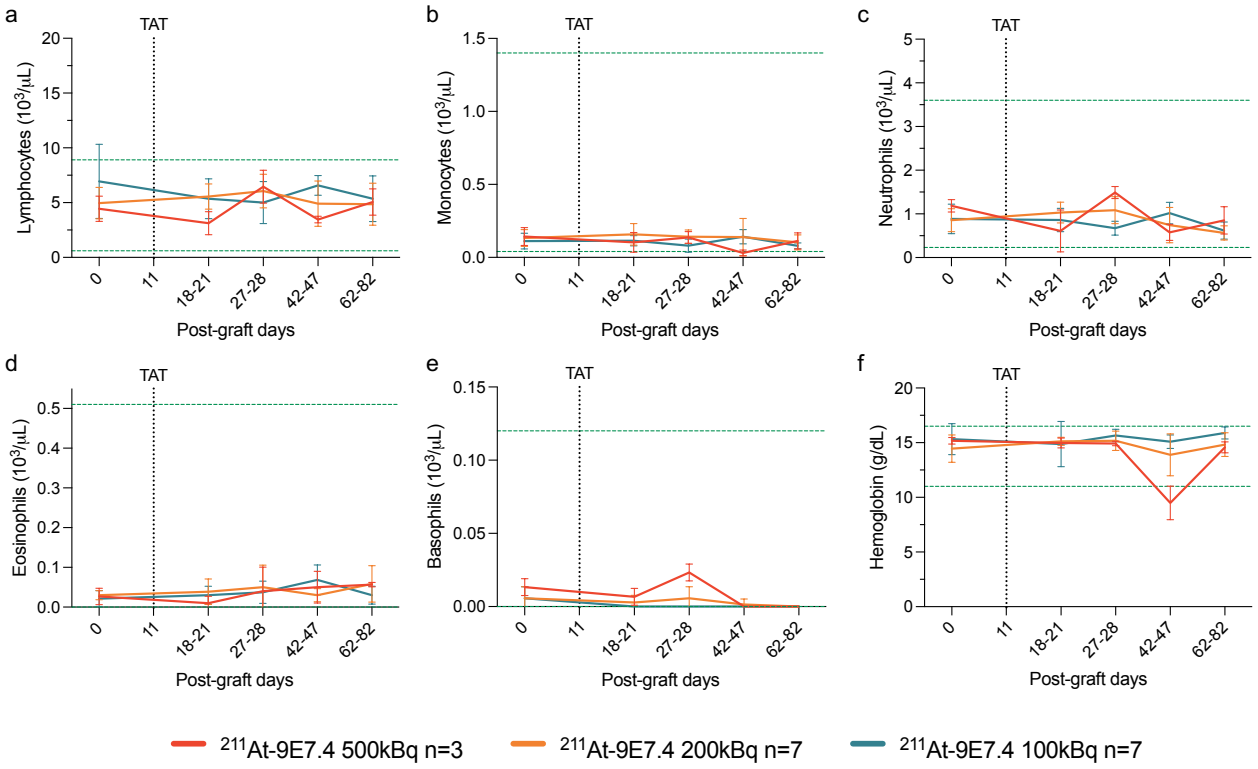

Supplementary Fig. 3 | Long-term monitoring of hematological toxicity in surviving mice. a-e C57BL/6JRj mice were injected at d0 with 50,000 GL261 cells into the right striatum by stereotaxis. After validation of tumor uptake by MRI, mice received at d11, at the same coordinates, a CED injection of ^{211}At-9E7.4 (470, 200 or 100 kBq) in a volume of 5µL. Blood levels of lymphocytes (**a**), monocytes (**b**), neutrophils (**c**), eosinophils (**d**), basophils (**e**), and hemoglobin (**f**) were analysed using a quantitative hematology analyzer. Data are presented as mean ± sd. Dotted green lines indicate toxicity tresholds provided by the device (Element HT5, Scil) for C57BL/6JRj mice.

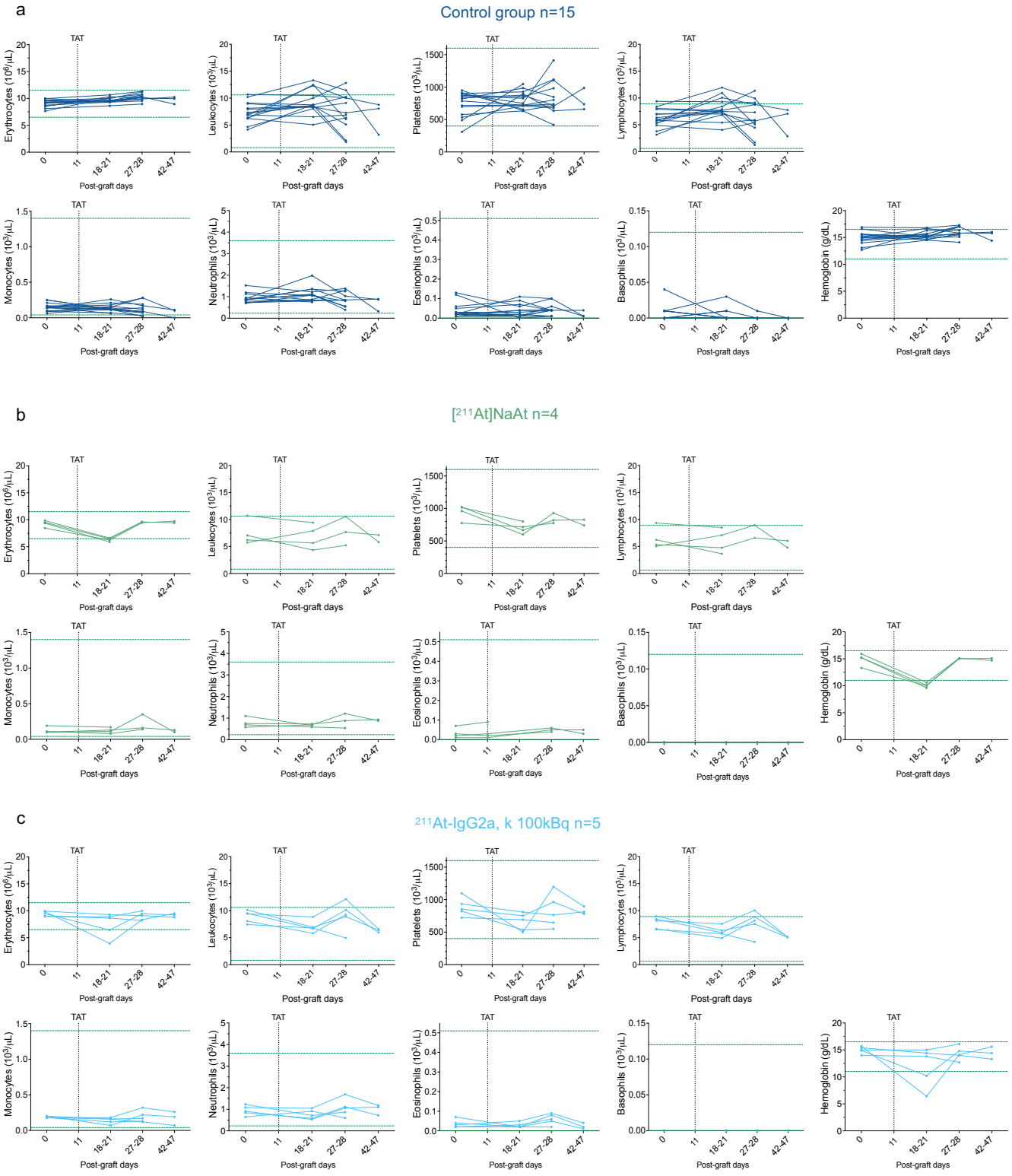

Supplementary Fig. 4 | Individual monitoring of hematological toxicity in control groups of the survival study. a-c Individual curves within each group of mice injected with saline solution (0.9% NaCl; **a**), 100kBq of [^{211}At]NaAt (**b**), or 100 kBq of ^{211}At-IgG2a, κ (**c**). Blood levels of erythrocytes, leukocytes, platelets, lymphocytes, monocytes, neutrophils, eosinophils, basophils, and hemoglobin were analysed using a quantitative hematology analyzer. Dotted green lines indicate toxicity tresholds provided by the device (Element HT5, Scil) for C57BL/6JRj mice.

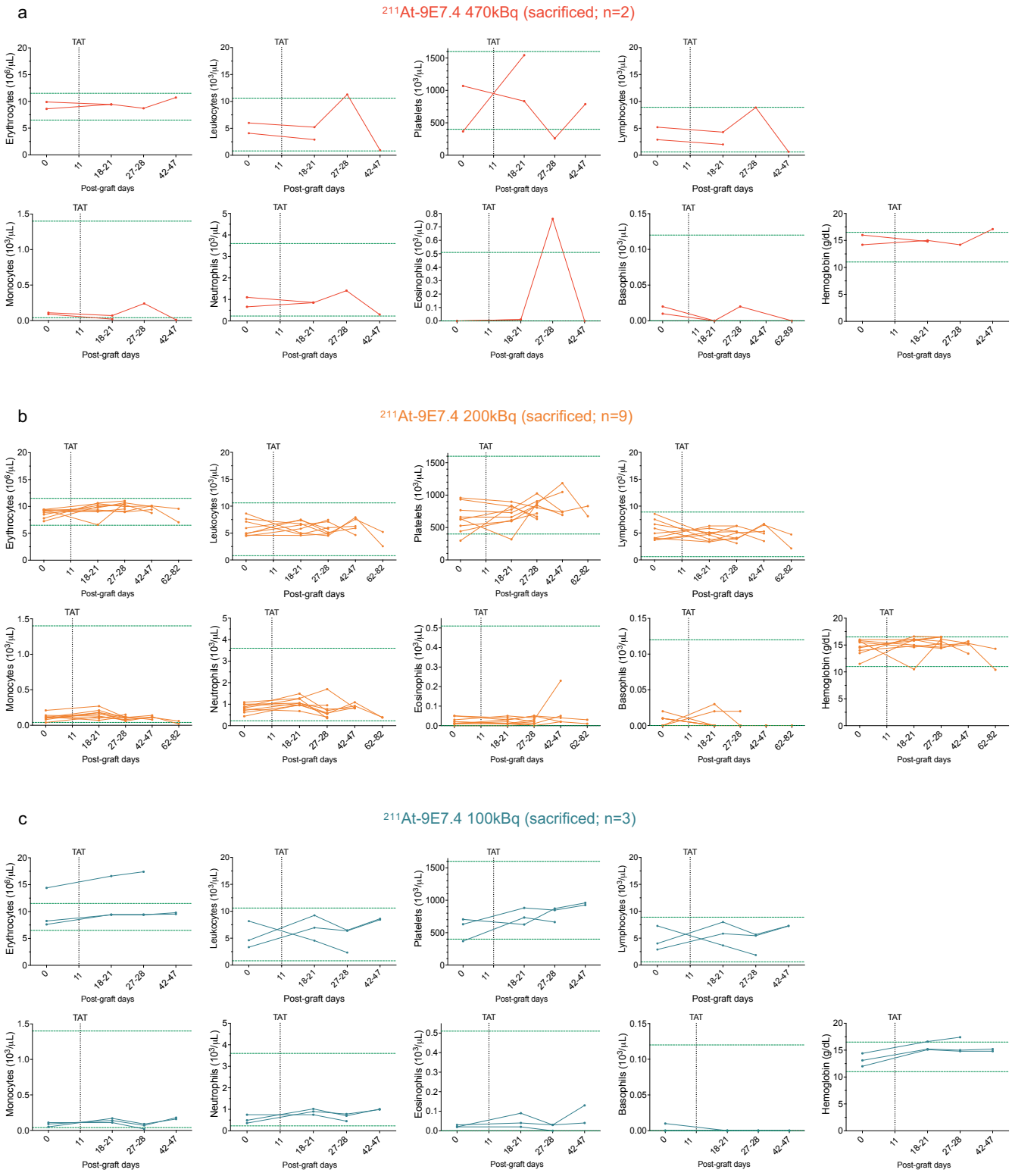

Supplementary Fig. 5 | Individual monitoring of hematological toxicity in sacrificed mice treated with TAT during the survival study. a-c Individual curves within each group of mice injected with 470 kBq (**a**), 200 kBq (**b**) or 100kBq of ^{211}At-9E7.4 (**c**). Blood levels of erythrocytes, leukocytes, platelets, lymphocytes, monocytes, neutrophils, eosinophils, basophils, and hemoglobin were analysed using a quantitative hematology analyzer. Dotted green lines indicate toxicity tresholds provided by the device (Element HT5, Scil) for C57BL/6JRj mice.

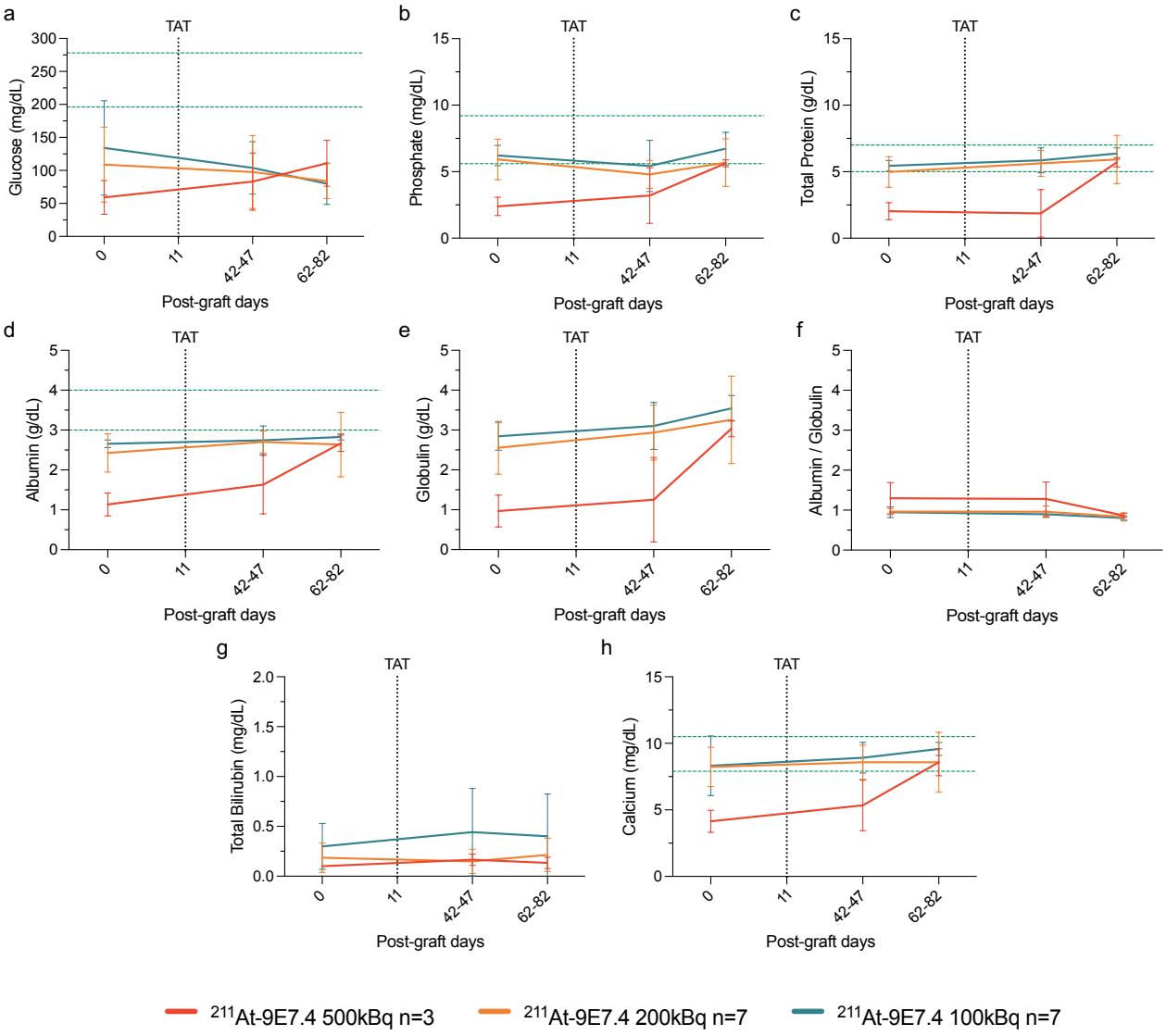

Supplementary Fig. 6 | Long-term monitoring of toxicity in surviving mice. a-h C57BL/6JRj mice were injected at d0 with 50,000 GL261 cells into the right striatum by stereotaxis. After validation of tumor uptake by MRI, mice received at d11, at the same coordinates, a CED injection of ^{211}At-9E7.4 (470, 200 or 100 kBq) in a volume of 5µL. Blood levels of glucose (**a**), phosphate (**b**), total protein (**c**), albumin (**d**), globulin (**e**), albumin/globulin ratio (**f**), total bilirubin (**g**), and calcium (**h**) were measured to assess hepatic and renal toxicity. Data are presented as mean ± sd. Dotted green lines indicate toxicity tresholds provided by the device (Element RC, Scil) for C57BL/6JRj mice.

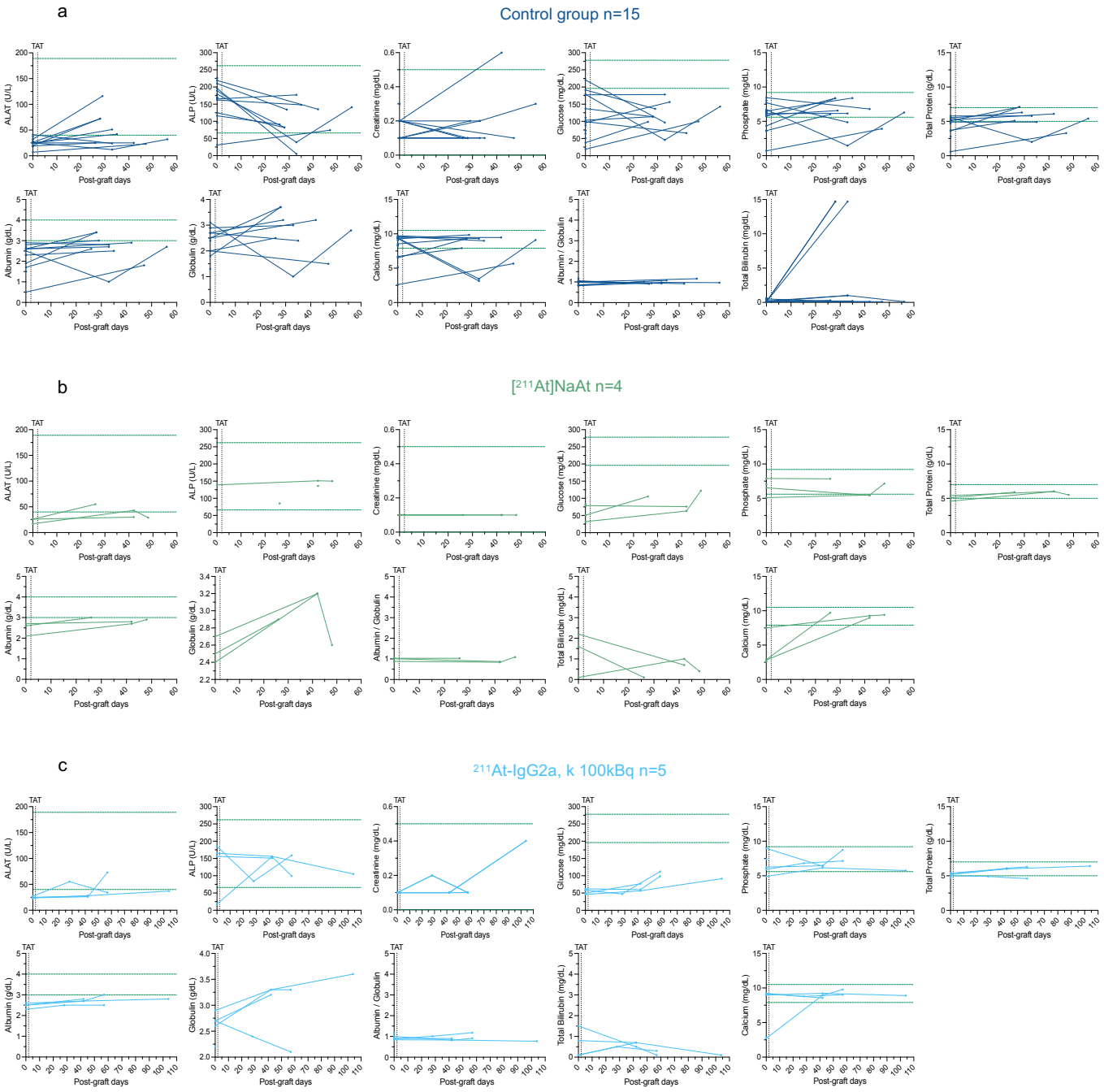

Supplementary Fig. 7 | Individual monitoring of toxicity in control groups of the survival study. a-c Individual curves within each group of mice injected with saline solution (0.9% NaCl; **a**), 100kBq of [^{211}At]NaAt (**b**), and 100 kBq of ^{211}At-IgG2a, κ (**c**). Blood levels of alanine aminotransferase (ALAT), alkaline phosphatase (ALP), creatinine, glucose, phosphate, total protein, albumin, globulin, albumin/globulin ratio, total bilirubin and calcium were measured to assess hepatic and renal toxicity. Dotted green lines indicate toxicity tresholds provided by the device (Element RC, Scil) for C57BL/6JRj mice.

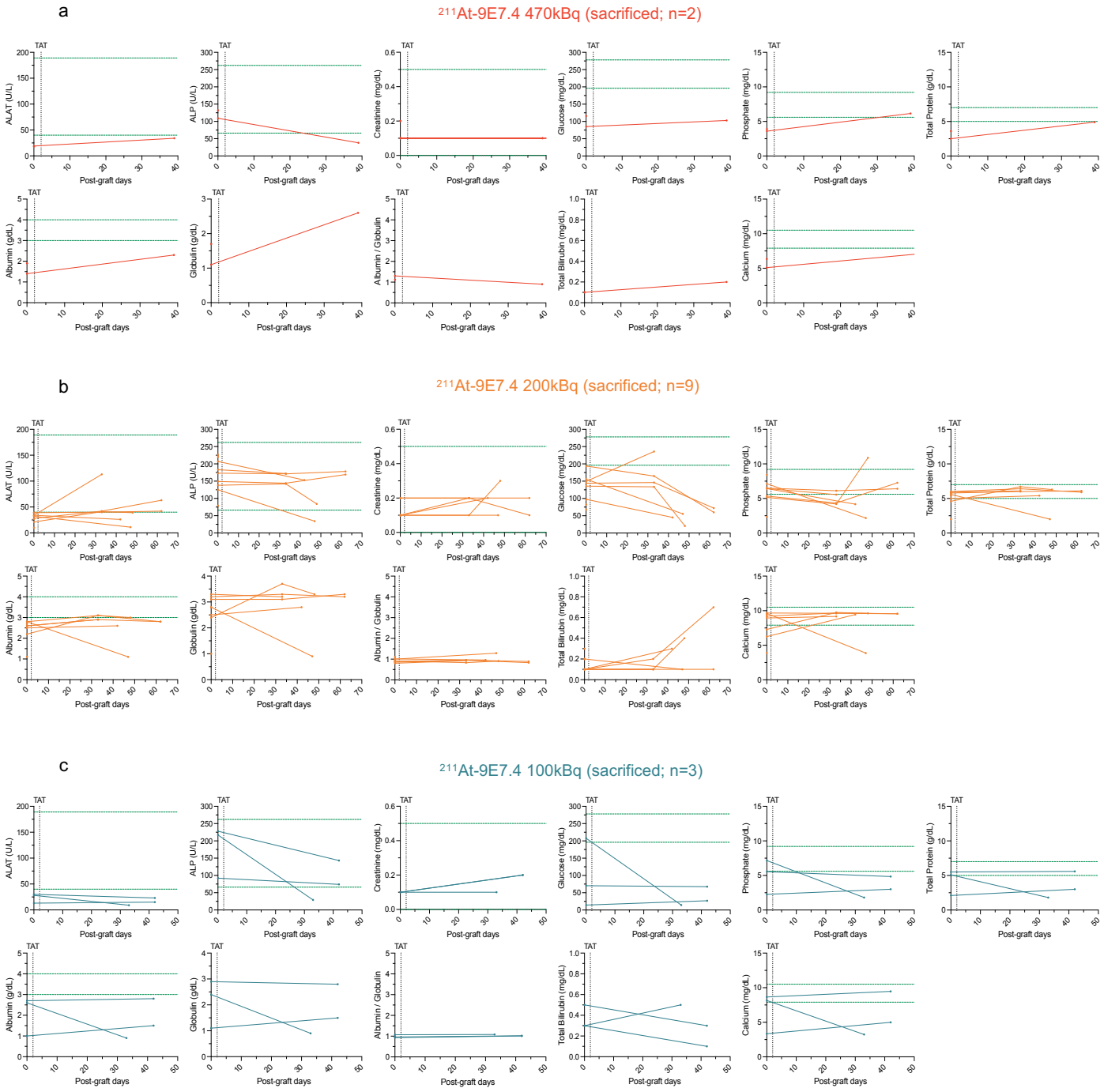

Supplementary Fig. 8 | Individual monitoring of toxicity in sacrificed mice treated with TAT during the survival study. a-c Individual curves within each group of mice injected with 470 kBq (**a**), 200 kBq (**b**) or 100kBq of ^{211}At-9E7.4 (**c**). Blood levels of alanine aminotransferase (ALAT), alkaline phosphatase (ALP), creatinine, glucose, phosphate, total protein, albumin, globulin, albumin/globulin ratio, total bilirubin and calcium were measured to assess hepatic and renal toxicity. Dotted green lines indicate toxicity tresholds provided by the device (Element RC, Scil) for C57BL/6JRj mice.

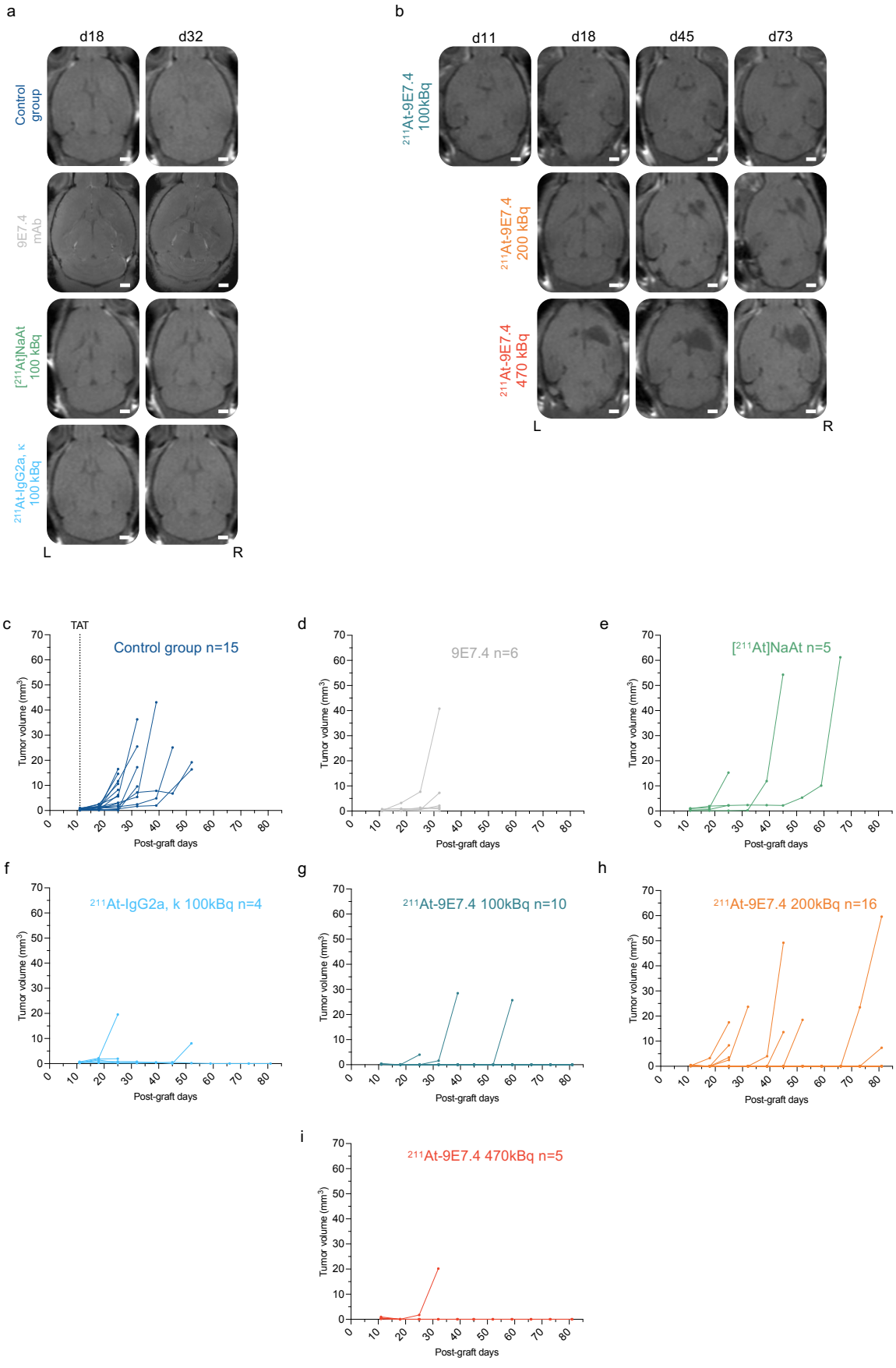

Supplementary Fig. 9 | T1-weighted MRI images and individual tumor growth follow-up during the survival study. a, b Axial T1-weighted MRI images of the brains of mice within each group. **c-i** Tumor-bearing mice were injected at d11 with saline solution (0.9% NaCl) (control group, n = 15; **c**), 2.8 µg of unlabeled 9E7.4 mAb (n = 6; **d**), 100 kBq of [^{211}At]NaAt (n = 5; **e**), 100 kBq of ^{211}At-IgG2a, κ (n = 4; **f**), 100 kBq (n = 10; **g**) , 200 kBq (n = 16; **h**), or 470 kBq (n = 5) of ^{211}At-9E7.4 (**i**).

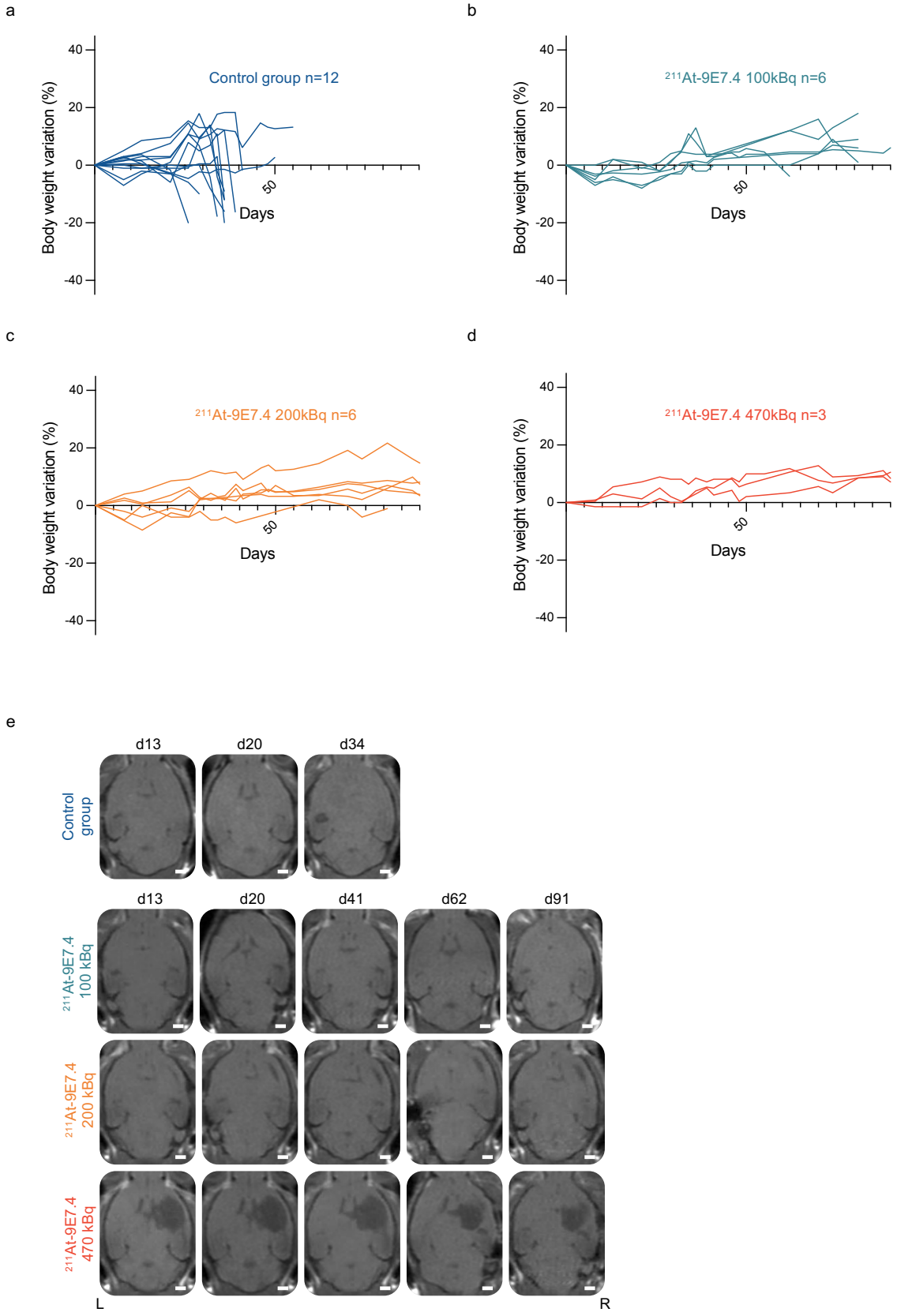

Supplementary Fig. 10 | T1-weighted MRI images and individual weight follow-up during the rechallenge study. a-d Invidual weight curves. After 162 days of survival, 15 long-term survivors and 12 C57BL/6JRj control mice were injected with 50,000 GL261 cells into the left striatum by stereotaxis. Control mice were injected with a saline solution (0.9% NaCl; **a**). Rechallenged mice were previously treated at d11 with TAT : 100 kBq n = 6 (**b**), 200 kBq n = 6 (**c**), or 470 kBq n = 3 (**d**). Data come from three independent experiments. **e** Axial T1-weighted MRI images of the brains of mice within each group.

Protocol	d11 TAT injection		n	Surviving mice	Dead mice	Median survival time (days)	Log-rank p-value to untreated group
	^{211}At activity (kBq)	mAb quantity (µg)					
untreated	-	-	12	0	12	35	-
^{211}At-9E7.4	100	0.56	6	5	1	undefined	**0.0001*****
	200	1.12	6	6	0	undefined	**0.0001*****
	470	2.8	3	3	0	undefined	**0.0042****

Supplementary Table 4 | Summary of the rechallenge study. Data issued from 3 independent experiments.

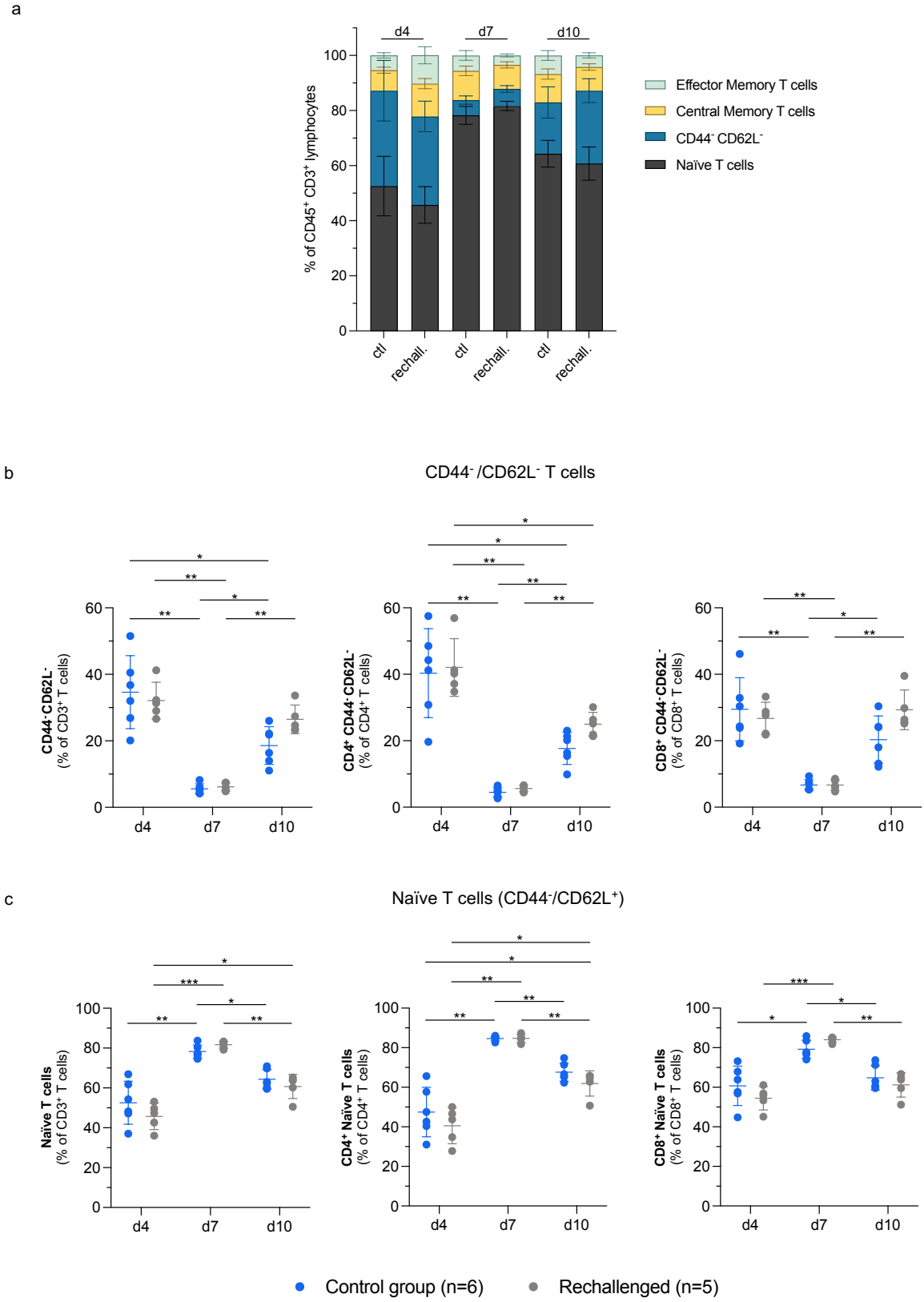

Supplementary Fig. 11 | Investigation of naïve and CD44-/CD62L- T cell phenotypes in the blood of rechallenged animals. a Comprehensive overview of the investigated T cell phenotypes and their levels assessed by flow cytometry after rechallenge. **b** Flow cytometry analysis of the CD44-/CD62L- phenotype among circulating T cells, 4, 7, and 10 days after rechallenge. The CD4+ and CD8+ double negative phenotypes were also investigated. Data are expressed as mean ± sd. Multiple Mann-Whitney tests were performed to assess significance between groups for each time point. A two-way ANOVA test followed by a Tukey's multiple comparison test were performed to assess significance between time points for each group. *p < 0.05, **p < 0.01. **c** Flow cytometry analysis of the naïve T cell phenotype among circulating T cells, 4, 7, and 10 days after rechallenge. The CD4+ and CD8+ naïve phenotypes were also investigated. Data are expressed as mean ± sd. Multiple Mann-Whitney tests were performed to assess significance between groups for each time point. A two-way ANOVA test followed by a Tukey's multiple comparison test were performed to assess significance between time points for each group. *p < 0.05, **p < 0.01, ***p < 0.001.

CHAPTER V

General discussion

General discussion

In view of the current limitations of conventional therapies applied to GB, this work has been focused on the development of a new therapeutic strategy based on the association of the α-emitting radionuclide ^{211}At with the rat monoclonal antibody 9E7.4 targeting murine SDC1. This study was carried out in an orthotopic, syngeneic mouse model to study early and long-term immune responses after TAT locoregional injection. We demonstrated the therapeutic potential of brain locoregional ^{211}At-9E7.4 TAT with a significantly improved survival rate *in vivo*, a strong reduction in the development of secondary tumors, and the establishment of an effective memory immune response in 93% of rechallenged animals. Our results were discussed in the previous section (Chapter IV, Discussion). This general discussion aims to more specifically position our strategy within the preclinical therapeutic landscape of TAT described in Chapter III, and to draw possible perspectives for the future development of this approach.

I. Therapeutic strategy

1. Locoregional TAT as first-line treatment

The therapeutic context for GB in patients primarily relies on the feasibility of surgical resection. Subsequently, two clinical scenarios must be taken into account: i) a diffuse GB that is inoperable, ii) a post-operative cavity created by the resection surgery, with a varying amount of residual tumor cells depending on the operated area. Only about 20 to 30 % of patients are actually considered suitable for surgery[1]. The Stupp regimen is then implemented, which combines radiotherapy with concomitant temozolomide chemotherapy[2]. Variations of this protocol exist, such as the adapted protocol by Perry *et al.* for older patients[3], but the core clinical approach remains the same.

GB is known for its strong resistance to conventional therapies. Firstly, genetic heterogeneity leads to the elimination of GB cells that are sensitive to treatment, resulting in a selection of more resistant and aggressive cells. Temozolomide chemotherapy has been shown to induce mechanisms such as autophagy and senescence which could be implicated in tumor recurrence and resistance to therapy[4,5]. Radiotherapy also contributes to induce radioresistance *via* several molecular pathways such as PI3K/Akt[6,7]. In addition, Knudson *et al.* recently indicated that surgical tumor resection was a driver for self-renewal of GSLCs[8]. These problems have triggered a reevaluation of the therapeutic positioning for new strategies, and especially

for TAT. In 2010, Cordier *et al.* demonstrated the clinical feasibility and safety of TAT administration as neoadjuvant treatment, using ^{213}Bi-labeled substance P to target NK_1R receptors in the tumor[9]. As a next step, we aimed to explore if TAT could address GB with a single injection, without any preceding treatment in a murine model, in order to bypass the radioresistance commonly induced by the post-treatment microenvironment.

2. Selecting ^{211}At for the treatment of GB

^{211}At is one of the three primary α-emitting radionuclides studied for TAT in GB, in both preclinical and clinical settings[10]. ^{211}At combines an optimal therapeutic duration in a context of future clinical considerations, with the formation of short-lived daughter radionuclides easy to manage. Zalutsky *et al.* showed that an ^{211}At-labeled anti-tenascin mAb locoregional administration was safe and feasible in GB-bearing patients[11]. To date, it is the only clinical trial based on the vectorization of a mAb for GB treatment (see Chapter III).

It should be noted that the maximum volume that can be injected intravenously in mice is 200 µL, while it should not surpass 5 µL for locoregional administration, given that the brain volume of a mouse is approximately 500 mm^3[(12)]. This raised the question of the feasibility of concentrating the activity of ^{211}At in a small volume after radiolabeling of the mAb. For this study, we managed to reach 100 kBq/µL as a starting concentration to prepare the different doses in a final volume of 5 µL.

3. Vectorization with the 9E7.4 mAb targeting SDC1

The choice of the mAb as a vector for TAT goes against the trend of newer, smaller synthetic vectors. This is due to the fact that current preclinical and clinical research for TAT in GB mainly focus on i.v. administration, for which small vectors might be superior to mAb (Chapter III). Nevertheless, mAb remain pertinent in a locoregional context. Their size and slow diffusion rate in tissue are advantageous for retention and thus prolonged exposure of tumor cells to radiation. Additionally, administration *via* CED allows for a homogeneous distribution within the tissues. Our previous study with the ^{211}At-9E7.4 targeting SDC1 provided positive results in a mouse model of multiple myeloma following an i.v. injection. It halted tumor development with an optimal dose of 740 kBq[13].

4. SDC1 as a therapeutic target for GB

Choosing a specific therapeutic target for GB is a challenging matter. GB is often viewed as a moving target. This perception primarily stems from the cellular heterogeneity of the tumor, leading to varied expression of biomarkers. Moreover, these epitopes or tumor antigens change their expression over time, leading to an evolutive heterogeneity[14]. Targeting a protein that represents both the GB and its TME increases the probability of detecting it at different stages of tumor progression. In the case of locoregional TAT, it is not essential for 100% of the tumor cells to express the target, as the primary efficacy criterion for radiotherapy is its local retention. Simultaneously targeting the TME, especially the ECM, can reach the invasive tumor front cells, potentially reducing recurrence rates. Indeed, beyond its structural role, the ECM maintains an active dialogue with the inflammatory and stem components of the TME[15].

SDC1 is overexpressed in GB and plays a frontline role in modulating the GB microenvironment through its interaction with the ECM. As previously discussed, SDC1 is an indicator of poor prognosis in GB[16,17], primarily linked to proliferation, invasion, and migration[18,19]. More recent studies have highlighted its role in modulating the immune response[20] and its contribution to radioresistance[21]. Furthermore, SDC1 operates at various cellular regulation levels. Initially at the membrane level, it has the ability to internalize and undergo nuclear translocation to induce EMT genes transcription, and also undergoes shedding to form various complexes[22]. Therefore, our hypothesis was that the targeting of SDC1 could help to disrupt the whole GB ecosystem.

II. Evaluation of the TAT distribution *in vivo*

1. Cerebral distribution

Targeting SDC1 notably extended the cerebral retention of TAT compared to its radiolabeled control isotype. it is interesting to compare our results with other preclinical studies using ^{211}At. Only one study by Borrmann *et al.* in 2013 used an orthotopic model but treated it with an i.v. injection of ^{211}At TAT[23]. However, this study did not mention the peripheral distribution of TAT. Despite their frequent use in preclinical studies, subcutaneous GB grafts for biodistribution experiments do not accurately represent tumor accessibility since this model lacks a BBB/BTB. Ma *et al.*, reported the best intratumoral retention observed in

preclinical studies, exceeding 130% ID/g, 30 min after injection in a subcutaneous murine GB. Yet, a swift elimination was with a drop to less than 20% in 2 h[24]. In our case, retention was still above 150% ID/g after 2 h, dropping below 20% after 21 h. Locoregional administration of 9E7.4 thus appears to be highly advantageous for extended TAT retention.

Digital autoradiography showed that the radioconjugate was distributed locally around the injection site in the brain. In our approach, the striatum, right ventricle, and SVZ are exposed to ^{211}At radiation. The NSCs from the SVZ are known to influence GSLCs, especially increasing their growth and spread[25]. Thus, their irradiation could potentially boost the efficacy of TAT. On the other hand, the hemisphere on the same side remained unaffected by radiation during the entire decay period of ^{211}At.

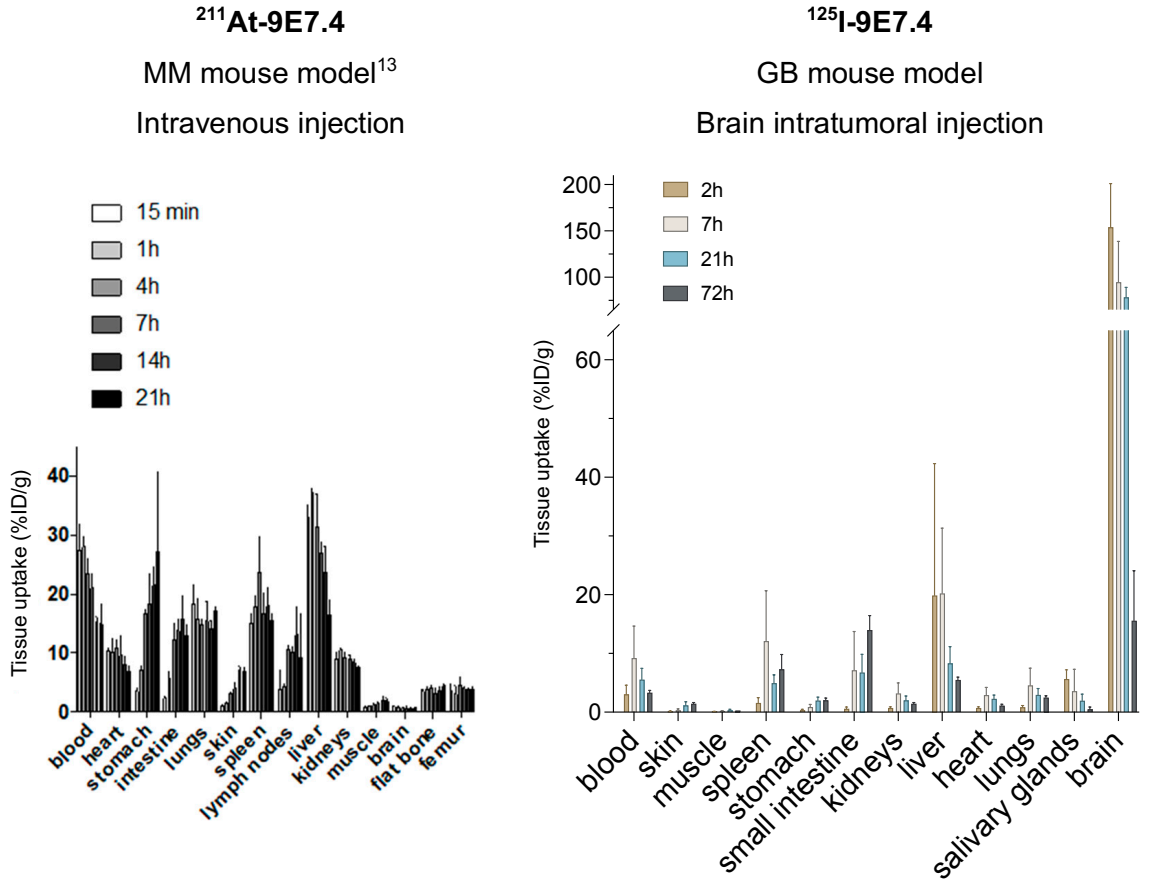

Fig. 1 | **Intravenous versus intracranial biodistribution of radiolabeled 9E7.4**. **a** Biodistribution of ^{211}At-9E7.4 after an i.v. injection of 370kBq in a mouse model of multiple myeloma, from Gouard *et al.* 2020. **b** Biodistribution of ^{125}I-9E7.4 after brain intratumoral injection of 30kBq. ^{125}I was used to mimic ^{211}At behavior (from Chapter IV, Supplementary Fig. 1b). *MM: multiple myeloma, GB: glioblastoma.*

2. Global distribution

The predominant cerebral retention observed in our study logically results in a less pronounced fixation of radioactivity in peripheral organs. For context, the biodistribution from an i.v. administration of ^{211}At-9E7.4 in a mouse model of multiple myeloma (MM) showed a significantly higher binding in peripheral organs (Fig. 1). However, it is worth noting that this protocol did not present any notable systemic toxicity[13].

This comparison, of course, has its limitations due to the inherent nature of the two models. As SDC1 is expressed on the surface of MM cells[26], an i.v. injection would naturally result in significant blood retention. Yet, this comparison provides insight into the potential off-target organs of ^{211}At, which are evidently more exposed in i.v. administration than in intracranial. In our study, the peripheral binding we observed suggests a compromised BBB in the C57BL/6JRj - GL261 tumor model. Notably, no related toxicity was observed during the survival study with the 200 and 100 kBq injections. This underscores the potential safety and specificity of our approach, even in the presence of a disrupted BBB.

III. Therapeutic efficacy of the TAT

1. Impact on the tumor

McLendon *et al.* determined the lethal dose to 10% of animals (LD_{10}) to be 46 MBq/g upon intravenous (IV) injection of ^{211}At-labeled mAb in female mice[27]. This translates to 920 kBq for a mouse weighing 20 g. Since our work represents the first study of intracranial delivery of ^{211}At in mice, we postulated that a considerably reduced dose might still prove efficient compared to the doses used in preclinical studies, reaching until 1 MBq for i.v. injections, and 1,11 MBq for i.t. injection, in subcutaneous GB models in mice (see Chapter III)[24,28–31]. We also needed an activity compatible with a 5 µL volume of injection as mentioned earlier. Consequently, we capped the maximum activity for our injections at 470 kBq and decided to test efficacy of 200 and 100 kBq. The latter is the lowest activity assessed in a survival study for ^{211}At TAT.

The 100 kBq allowed to reach a 70% survival rate. To the best of our knowledge, this is the first TAT study to produce long-term survivors. The only toxicity factor observed was dose-dependent radionecrosis, a response observed in 25% of patients after radiosurgery[32]. In

this regard, a comprehensive behavioral study should be undertaken to assess the impact of this radionecrosis and overall treatment on the motor and cognitive functions. The inherent variability in the lethality of different preclinical models makes direct efficacy comparisons delicate. Our model demonstrates a median survival of 34 days in the untreated group - consistent with the literature on GL261 cells[33]. In contrast, TAT studies in the literature report shorter median survival times (sometimes inferior to 15 days), often attributed to the use of subcutaneous GB models.

The doubling of survival with TAT must be discussed taking into account the specific characteristics of the model, particularly the growth rate, and the invasive and infiltrative capacities of the GB cells. The GL261 model is far from being perfect to mirror human GB, but it recapitulates the main features of GB regarding its pro-tumoral microenvironment and infiltrative behavior.

2. Effect on tumor dissemination

Several studies have reported the emergence of secondary tumors when using the GL261 cell line, an observation consistent with our model[34,35]. The occurrence of secondary tumors in orthotopic GL261 grafts mirrors the multifocal nature of GB observed in patients, with some reports suggesting this occurrence in up to 20% of cases[36]. This observation in patients aligns with the concept of "whole brain tumor" regarding GB, where a subset of undetectable disseminated cells eventually triggers a recurrence. Surprisingly, aside from technical studies focused on stereotaxis, this phenomenon has never been addressed before in TRT preclinical studies. In our model, TAT appears to decrease the occurrence of these secondary tumors. The mechanisms involved in this reduction process clearly deserves further exploration.

IV. Microenvironmental responses to TAT

1. The vascular component

In response to TAT, we observed vascular hypertrophy in the striatum 7 days post-treatment injection. Currently, no data exists regarding the effects of ^{211}At in this context. It remains uncertain whether these are pre-existing vessels that underwent morphological changes due to the treatment or if this is a result of angiogenesis. Similarly, it is ambiguous whether this

is a direct effect of α particles or a response of the TME to irradiation. While hypertrophy might suggest an adaptive or reactive change in response to the treatment, its direct impact on BBB permeability and function remains unclear.

Studies examining the integrity of the BBB following ^{225}Ac-based TAT have been previously conducted. As shown by Behling *et al.*, the targeting of Ve-cadherin with a mAb reduces the number of epithelial cells and pericytes around blood vessels[37]. A general decrease in vascularity was also demonstrated using the same protocol[38]. Sattiraju *et al.* highlighted an increased BBB permeability when using ^{225}Ac-labeled liposomes targeting integrin $\alpha_v\beta_3$[39]. This increased permeability was evidenced by the areas of extravasation of injected Evans Blue dye following intravenous injection. Intriguingly, the extravasation also occurred in areas devoid of DNA DSBs induced by ^{225}Ac, suggesting a bystander effect of α particles towards blood vessels. These properties need to be confirmed with ^{211}At but could provide an efficient way to permeabilize BBB beforehand in view of systemic administration of repeated doses of TAT, or to facilitate the delivery of active therapeutic agents in the context of combination therapies.

2. The immune component

Our study stands out as the first to generate long-term survivors with TAT, pioneering the exploration of memory immune responses post-treatment. From the entire population of $CD45^+/CD3^+$ T cells, we observed an increase in $CD4^+$ T_{CM} and both $CD4^+$ and $CD8^+$ T_{EM} in the blood of mice 4 days post-rechallenge. Interestingly, a similar increase in T_{CM} was noted at d10 in control mice, but without the associated rise in T_{EM}. These findings hint at antigenic recognition by APCs following TAT injection in both scenarios. However, only the mice treated with TAT were shielded against tumor growth upon regrafting. This suggests that the presence of T_{EM} is a key factor to provide an efficient immune response. Exploring the presence of resident memory T cells (T_{RM}) in the brain could represent a first step to understand the differential response of T_{EM} between control and treated mice. On the other hand, the characterization of tumor-associated antigen (TAA) and a comparison with other murine lines with lower immunogenicity are essential to assess the role of adaptive immunity in the response to TAT and overall survival outcomes. Notably, the GL261 cells maintain a high expression of MHC-I, which likely enhances the adaptive immune response[33].

V. Conclusions and perspectives

Locoregional ^{211}At-9E7.4 TAT provides the advantage of tumor eradication by treating with minimal ^{211}At activity and a low concentration of 9E7.4, with optimized retention of the therapeutic agent within the target site. However, several points need further investigations. Only a few data regarding adaptative immunity were obtained as immune reponses were recorded only 7 days after TAT injection.

Very few $CD4^+$ and $CD8^+$ T cells were detected locally, and only an increase in the infiltration of $CD11b^+$ myeloid cells was observed in the striatum. Consequently, a comprehensive study of the post-TAT microenvironment appears essential. It would be particularly insightful to focus on the kinetics of the early local recruitment of immune populations, including APCs and T cells. Additionally, the roles of macrophages/microglia and neutrophils should be explored on a kinetic scale within a short timeframe after TAT administration. Moreover, the dynamics of DAMP release, cytokines and chemokines has been shown to be influenced by α emitters, notably in adenocarcinoma and MM mouse models, and should be addressed here as well[40,41]. The potential of scRNA-seq in different stages of GB progression should be considered in this context to assess the impact of ^{211}At of the kinetics of GB and its TME.

Another crucial aspect is the preclinical evaluation of the post-TAT effect on the integrity of BBB. Mirroring studies achieved with ^{225}Ac, A specific emphasis on pericytes, epithelial cells, and astrocytes should provide insights into BBB permeability and about the compatibility of locoregional TAT with the optimization of a systemic approach.

Lastly, the efficacy experiments conducted should be replicated using a less immunogenic mouse cell GB model. This would offer a clearer perspective on the impact on adaptive immunity and the establishment of immune memory with TAT. Then, extending the study to a xenograft model, preferably patient-derived orthotopic xenograft (PDOX), would be beneficial to evaluating the effects on human GB. To go even further, using a humanized mouse model would enable further characterization of immune responses, and allow to identify the TAAs recognized by adaptive immunity[42,43]. These models can be generated with peripheral blood mononuclear cells (PBMCs) derived from the same patient as the PDX to recapitulate a specific GB-immune interface[44].

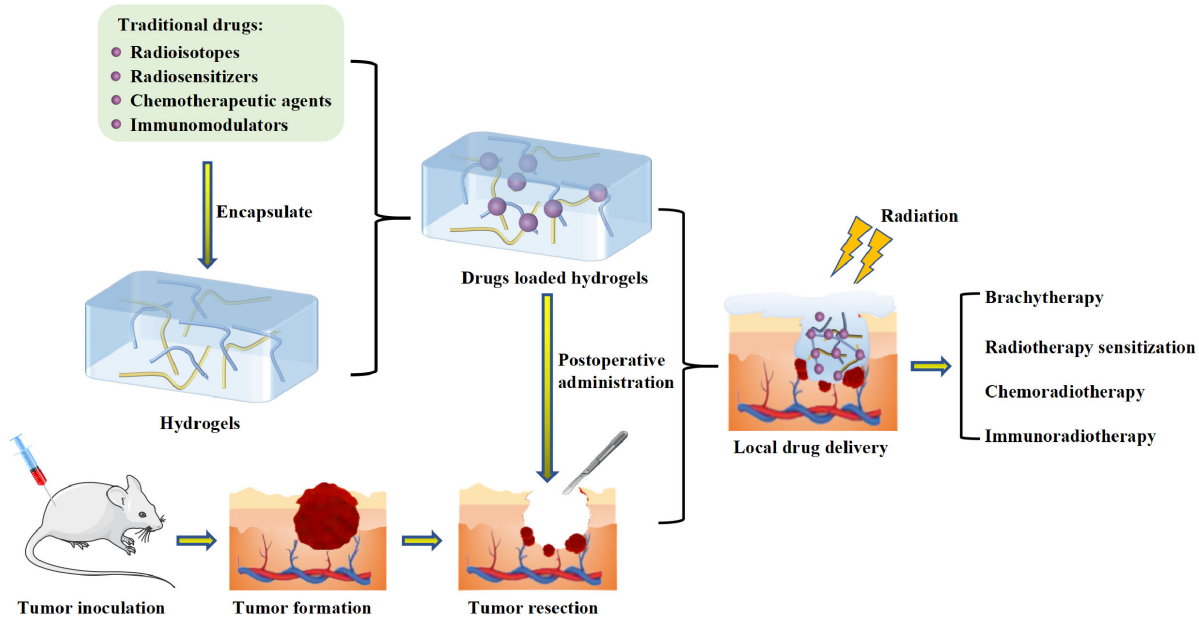

Fig. 2 | **Hydrogel-based local drug delivery systems for post-operative radiotherapy.** (From Xie *et al.*, 2023)[49]

In the future, therapeutic combinations should be explored. Given the increasing evidence of the ability of α particles to induce an antitumoral immune response, TAT could potentially leverage the benefits of immunotherapy, which, to date, has not been successful in clinical settings for GB[45]. Dabagian *et al.* highlighted the advantages of combining ^{211}At-MM4, which targets PARP, with an anti-PD-1 antibody. They demonstrated a notably prolonged survival when compared to monotherapy. Additionally, a significant increase in neutrophils was observed four weeks after administration[29]. As discussed in Chapter III, association with radiosensitizers through the targeting of DDR is also a promising avenue[46].

We should also explore new locoregional delivery methods to enhance retention, target all remaining cells, and prevent recurrence. Stereotaxic CED administration has proven to be efficient and offers several advantages over systemic injection. However, the challenge of accurately determining the real diffusion area of GB, whether surgically removed or not, remains. This issue is a significant cause of recurrence, making GB a tumor affecting the entire brain. Using hydrogels might be more adaptable to the two existing clinical scenarios, especially concerning the resection cavity (Fig. 2). These strategies are currently addressed to deliver molecules with chemoattractive properties or with the ability to induce differentiation of cancer stem-like cells[47–49] Some studies have investigated loading radionuclides into hydrogels, with β$^-$-emitters like ^{131}I, ^{188}Re and ^{125}I. To do so, a promising concept is the development of a system in which gelation of the polymer matrix is triggered by a NIR laser

beam, allowing a prolonged retention time of the radionuclide. Additionally, hyperthermia generated by NIR-responsive photothermal hydrogels might enhance blood flow and subsequently mitigate the hypoxic environment within the tumor[50,51]. These strategies have been validated in preclinical models of breast cancer and have yet to be tested in a GB model. The question arises whether the higher energy emitted by α particles is compatible with this approach, especially when combined with another active molecule. The idea of a device that combines the chemoattractive capabilities for residual GB cells with targeted eradication by α radiation, all while enhancing adaptive immunity, could offer promising prospects for the future of GB therapy.

References

1. Weller, M., Cloughesy, T., Perry, J. R. & Wick, W. Standards of care for treatment of recurrent glioblastoma—are we there yet? *Neuro Oncol* **15**, 4–27 (2013).
2. Stupp, R. *et al.* Radiotherapy plus concomitant and adjuvant temozolomide for glioblastoma. *N Engl J Med* **352**, 987–996 (2005).
3. Perry, J. R. *et al.* Short-Course Radiation plus Temozolomide in Elderly Patients with Glioblastoma. *N Engl J Med* **376**, 1027–1037 (2017).
4. Knizhnik, A. V. *et al.* Survival and Death Strategies in Glioma Cells: Autophagy, Senescence and Apoptosis Triggered by a Single Type of Temozolomide-Induced DNA Damage. *PLoS One* **8**, e55665 (2013).
5. Aasland, D. *et al.* Temozolomide induces senescence and repression of DNA repair pathways in glioblastoma cells via activation of ATR–Chk1, p21, and NF-kB. *Cancer Res* **79**, 99–113 (2019).
6. Li, H. F., Kim, J. S. & Waldman, T. Radiation-induced Akt activation modulates radioresistance in human glioblastoma cells. *Radiation Oncology* **4**, 43 (2009).
7. Li, W., Guo, F., Wang, P., Hong, S. & Zhang, C. miR-221/222 Confers Radioresistance in Glioblastoma Cells Through Activating Akt Independent of PTEN Status. *Curr Mol Med* **14**, 185–195 (2014).
8. Knudsen, A. M. *et al.* Surgical resection of glioblastomas induces pleiotrophin-mediated self-renewal of glioblastoma stem cells in recurrent tumors. *Neuro Oncol* **24**, 1074 (2022).
9. Cordier, D. *et al.* Targeted alpha-radionuclide therapy of functionally critically located gliomas with 213Bi-DOTA-[Thi8,Met(O2)11]-substance P: a pilot trial. *Eur J Nucl Med Mol Imaging* **37**, 1335–1344 (2010).
10. Bolcaen, J. *et al.* A perspective on the radiopharmaceutical requirements for imaging and therapy of glioblastoma. *Issue 16 Theranostics* **11**, 7911–7947 (2021).
11. Zalutsky, M. R. *et al.* Clinical experience with α-particle-emitting 211 At: Treatment of recurrent brain tumor patients with 211 At-labeled chimeric antitenascin monoclonal antibody 81C6. *Journal of Nuclear Medicine* **49**, 30–38 (2008).
12. Badea, A., Ali-Sharief, A. A. & Johnson, G. A. Morphometric analysis of the C57BL/6J mouse brain. *Neuroimage* **37**, 683 (2007).
13. Gouard, S. *et al.* Targeted-Alpha-Therapy Combining Astatine-211 and anti-CD138 Antibody in A Preclinical Syngeneic Mouse Model of Multiple Myeloma Minimal Residual Disease. *Cancers (Basel)* **12**, 1–18 (2020).

14. Schäfer, N. *et al.* Longitudinal heterogeneity in glioblastoma: Moving targets in recurrent versus primary tumors. *J Transl Med* **17**, 1–9 (2019).
15. Marino, S. *et al.* The Extracellular Matrix in Glioblastomas: A Glance at Its Structural Modifications in Shaping the Tumoral Microenvironment-A Systematic Review. *Cancers (Basel)* **15**, (2023).
16. Watanabe, A. *et al.* Expression of syndecans, a heparan sulfate proteoglycan, in malignant gliomas: participation of nuclear factor-kappaB in upregulation of syndecan-1 expression. *J Neurooncol* **77**, 25–32 (2006).
17. Xu, Y., Yuan, J., Zhang, Z., Lin, L. & Xu, S. Syndecan-1 expression in human glioma is correlated with advanced tumor progression and poor prognosis. *Mol Biol Rep* **39**, 8979–8985 (2012).
18. Shi, S. *et al.* Syndecan-1 knockdown inhibits glioma cell proliferation and invasion by deregulating a c-src/FAK-associated signaling pathway. *Oncotarget* **8**, 40922–40934 (2017).
19. Chen, J. *et al.* Effects of syndecan-1 on the expression of syntenin and the migration of U251 glioma cells. *Oncol Lett* **14**, 7217 (2017).
20. Zhong, J. *et al.* Weighted Gene Co-Expression Network Analysis (WGCNA) Reveals the Functions of Syndecan-1 to Regulate Immune Infiltration by Influenced T Cells in Glioma. *Front Genet* **13**, 792443 (2022).
21. Zeng, L. *et al.* SDC1-TGM2-FLOT1-BHMT complex determines radiosensitivity of glioblastoma by influencing the fusion of autophagosomes with lysosomes. *Theranostics* **13**, 3725–3743 (2023).
22. Gondelaud, F. & Ricard-Blum, S. Structures and interactions of syndecans. *FEBS J* **286**, 2994–3007 (2019).
23. Borrmann, N. *et al.* Systemic treatment with 4-211Atphenylalanine enhances survival of rats with intracranial glioblastoma. *Nuklearmedizin* **52**, 212–221 (2013).
24. Ma, H. *et al.* In vitro and in vivo evaluation of 211At-labeled fibroblast activation protein inhibitor for glioma treatment. *Bioorg Med Chem* **55**, 116600 (2022).
25. Li, S., Dong, L., Pan, Z. & Yang, G. Targeting the neural stem cells in subventricular zone for the treatment of glioblastoma: an update from preclinical evidence to clinical interventions. *Stem Cell Res Ther* **14**, 1–11 (2023).
26. Bayer-Garner, I. B., Sanderson, R. D., Dhodapkar, M. V., Owens, R. B. & Wilson, C. S. Syndecan-1 (CD138) immunoreactivity in bone marrow biopsies of multiple myeloma: Shed syndecan-1 accumulates in fibrotic regions. *Modern Pathology* **14**, 1052–1058 (2001).

27. McLendon, R. E. *et al.* Radiotoxicity of systemically administered 211At-labeled human/mouse chimeric monoclonal antibody: a long-term survival study with histologic analysis. *Int J Radiat Oncol Biol Phys* **45**, 491–499 (1999).
28. Watabe, T. *et al.* Targeted alpha therapy using astatine (211At)-labeled phenylalanine: A preclinical study in glioma bearing mice. *Oncotarget* **11**, 1388–1398 (2020).
29. Dabagian, H. *et al.* PARP Targeted Alpha-Particle Therapy Enhances Response to PD-1 Immune-Checkpoint Blockade in a Syngeneic Mouse Model of Glioblastoma. *ACS Pharmacol Transl Sci* **4**, 344–351 (2021).
30. Liu, Y. *et al.* Gold nanostars: A novel platform for developing211at-labeled agents for targeted alpha-particle therapy. *Int J Nanomedicine* **16**, 7297–7305 (2021).
31. Liu, W. *et al.* Targeted Alpha Therapy of Glioma Using 211At-Labeled Heterodimeric Peptide Targeting Both VEGFR and Integrins. *Mol Pharm* **19**, 3206–3216 (2022).
32. Kohutek, Z. A. *et al.* Long-term risk of radionecrosis and imaging changes after stereotactic radiosurgery for brain metastases. *J Neurooncol* **125**, 149 (2015).
33. Haddad, A. F. *et al.* Mouse models of glioblastoma for the evaluation of novel therapeutic strategies. *Neurooncol Adv* **3**, (2021).
34. Resende, F. F. B. *et al.* Evaluation of TgH(CX3CR1-EGFP) mice implanted with mCherry-GL261 cells as an in vivo model for morphometrical analysis of glioma-microglia interaction. *BMC Cancer* **16**, 1–13 (2016).
35. Irtenkauf, S. M. *et al.* Optimization of Glioblastoma Mouse Orthotopic Xenograft Models for Translational Research. *Comp Med* **67**, 300 (2017).
36. Li, Y. *et al.* A systematic review of multifocal and multicentric glioblastoma. *Journal of Clinical Neuroscience* **83**, 71–76 (2021).
37. Behling, K. *et al.* Remodeling the vascular microenvironment of glioblastoma with α-particles. *Journal of Nuclear Medicine* **57**, 1771–1777 (2016).
38. Behling, K. *et al.* Vascular targeted radioimmunotherapy for the treatment of glioblastoma. *Journal of Nuclear Medicine* **57**, 1576–1582 (2016).
39. Sattiraju, A. *et al.* Alpha particle enhanced permeabilization of the blood tumor barrier using alpha-v beta-3 (αvβ3) specific nanoparticles. *Journal of Nuclear Medicine* **57**, 633–633 (2016).
40. Gorin, J. B. *et al.* Antitumor immunity induced after α irradiation. *Neoplasia* **16**, 319–328 (2014).
41. Perrin, J. *et al.* Targeted Alpha Particle Therapy Remodels the Tumor Microenvironment and Improves Efficacy of Immunotherapy. *Int J Radiat Oncol Biol Phys* **112**, 790–801 (2022).

42. Leko, V. & Rosenberg, S. A. Identifying and Targeting Human Tumor Antigens for T Cell-Based Immunotherapy of Solid Tumors. *Cancer Cell* **38**, 454 (2020).
43. Chong, C., Coukos, G. & Bassani-Sternberg, M. Identification of tumor antigens with immunopeptidomics. *Nature Biotechnology 2021 40:2* **40**, 175–188 (2021).
44. Buqué, A. & Galluzzi, L. Modeling Tumor Immunology and Immunotherapy in Mice. *Trends Cancer* **4**, 599–601 (2018).
45. Mandel, J. J. *et al.* Inability of positive phase II clinical trials of investigational treatments to subsequently predict positive phase III clinical trials in glioblastoma. *Neuro Oncol* **20**, 113–122 (2018).
46. Obata, H., Ogawa, M. & Zalutsky, M. R. DNA Repair Inhibitors: Potential Targets and Partners for Targeted Radionuclide Therapy. *Pharmaceutics 2023, Vol. 15, Page 1926* **15**, 1926 (2023).
47. Bastiancich, C., Danhier, P., Préat, V. & Danhier, F. Anticancer drug-loaded hydrogels as drug delivery systems for the local treatment of glioblastoma. *J Control Release* **243**, 29–42 (2016).
48. Djoudi, A. *et al.* Hyaluronic Acid Scaffolds for Loco-Regional Therapy in Nervous System Related Disorders. *Int J Mol Sci* **23**, 12174 (2022).
49. Xie, Y. *et al.* Recent progress of hydrogel-based local drug delivery systems for postoperative radiotherapy. *Front Oncol* **13**, (2023).
50. Meng, Z. *et al.* Near-Infrared-Triggered in Situ Gelation System for Repeatedly Enhanced Photothermal Brachytherapy with a Single Dose. *ACS Nano* **12**, 9412–9422 (2018).
51. Wu, Y. *et al.* Tumor-Targeted Injectable Double-Network Hydrogel for Prevention of Breast Cancer Recurrence and Wound Infection via Synergistic Photothermal and Brachytherapy. *Advanced Science* **9**, (2022).

APPENDICES

Appendice I

Review: Targeting Tumor Associated Macrophages to Overcome Conventional Treatment Resistance in Glioblastoma

Hélène Grégoire, **Loris Roncali**, Audrey Rousseau, Michel Chérel, Yves Delneste, Pascale Jeannin, François Hindré and Emmanuel Garcion*

Grégoire H, Roncali L, Rousseau A, *et al.* Targeting Tumor Associated Macrophages to Overcome Conventional Treatment Resistance in Glioblastoma. Front Pharmacol. 2020;11:368. Published 2020 Apr 8. doi:10.3389/fphar.2020.00368

frontiers in Pharmacology

REVIEW
published: 08 April 2020
doi: 10.3389/fphar.2020.00368

Targeting Tumor Associated Macrophages to Overcome Conventional Treatment Resistance in Glioblastoma

*Hélène Grégoire[1], Loris Roncali[1], Audrey Rousseau[1,2], Michel Chérel[3], Yves Delneste[1,4], Pascale Jeannin[1,4], François Hindré[1,5] and Emmanuel Garcion[1,6]**

[1] CRCINA, INSERM, Université de Nantes, Université d'Angers, Angers, France, [2] Département de Pathologie Cellulaire et Tissulaire, CHU Angers, Angers, France, [3] CRCINA, INSERM, Université d'Angers, Université de Nantes, Nantes, France, [4] Laboratoire d'Immunologie et Allergologie, CHU d'Angers, Angers, France, [5] PRIMEX, Plateforme de radiobiologie et d'imagerie expérimentale, SFR ICAT, Université d'Angers, Angers, France, [6] PACeM, Plateforme d'analyses cellulaires et moléculaires, SFR ICAT, Université d'Angers, Angers, France

OPEN ACCESS

Edited by:
Robert Clarke, Georgetown University, United States

Reviewed by:
David Soto-Pantoja, Wake Forest School of Medicine, United States
Biana Godin, Houston Methodist Research Institute, United States

***Correspondence:**
Emmanuel Garcion
emmanuel.garcion@univ-angers.fr

Specialty section:
This article was submitted to Pharmacology of Anti-Cancer Drugs, a section of the journal Frontiers in Pharmacology

Received: *23 December 2019*
Accepted: *10 March 2020*
Published: *08 April 2020*

Citation:
Grégoire H, Roncali L, Rousseau A, Chérel M, Delneste Y, Jeannin P, Hindré F and Garcion E (2020) Targeting Tumor Associated Macrophages to Overcome Conventional Treatment Resistance in Glioblastoma. Front. Pharmacol. 11:368. doi: 10.3389/fphar.2020.00368

Glioblastoma (GB) is the most common and devastating form of brain cancer. Despite conventional treatments, progression or recurrences are systematic. In recent years, immunotherapies have emerged as an effective treatment in a number of cancers, leaving the question of their usefulness also faced with the particular case of brain tumors. The challenge here is major not only because the brain is the seat of our consciousness but also because of its isolation by the blood-brain barrier and the presence of a unique microenvironment that constitutes the central nervous system (CNS) with very specific constituent or patrolling cells. Much of the microenvironment is made up of immune cells or inflammation. Among these, tumor-associated macrophages (TAMs) are of significant interest as they are often involved in facilitating tumor progression as well as the development of resistance to standard therapies. In this review, the ubiquity of TAMs in GB will be discussed while the specific case of microglia resident in the brain will be also emphasized. In addition, the roles of TAMs as accomplices in the progression of GB and resistance to treatment will be presented. Finally, clinical trials targeting TAMs as a means of treating cancer will be discussed.

Keywords: glioblastoma, macrophages, microglia, resistance, radiation, crosstalks, tumor-associated macrophage

INTRODUCTION

Glioblastoma (GB) is the most frequent and malignant form of brain tumors. It is associated with a poor prognosis and the median overall survival of GB patients is about 15 months after standard of care (Stupp et al., 2009). Conventional treatments consist of maximal safe resection followed by external radiotherapy and concomitant chemotherapy based on the use of the alkylating agent temozolomide (TMZ) (Stupp et al., 2005). However, recurrence inevitably occurs. Currently, no therapy can completely cure GB; current treatments can only marginally improve the overall survival of patients. The current

strategy focuses mostly on targeting the tumor cells, failing to account for other cellular constituents present in the tumor. Hence, to cure and achieve a complete resection of GB tumors, new therapeutic strategies are in great demand.

GB is a highly heterogeneous tumor, with diverse co-existing cell types that include tumor cells, endothelial cells, fibroblasts and different cell types from the immune system (Charles et al., 2011; Quail and Joyce, 2017). A particular emphasis has been placed on the immune system and especially on tumor-associated macrophages (TAMs) as they are the dominant infiltrating immune cell population in GB. These cells interact with tumor cells to promote tumor growth and progression (Feng et al., 2015). The host defense is composed of both innate and adaptative immune cells and they are both involved in cancer immune surveillance in early stages of the disease. However, the tumor is able to escape this immune surveillance during its development. At that point, the tumor can recruit immune cells and change their original function to be one of its accomplices (Brown et al., 2018; Finn, 2018). Tumor cells can inhibit the cytotoxic function of the immune system by secreting immunosuppressive factors or recruiting immunosuppressive inflammatory cells. In relation to this, macrophages appear to be a promising target to improve the effectiveness of actual therapy as more and more information on their physiological and pathological roles in the brain is being uncovered.

Macrophages are the most abundant infiltrating immune cells in GB. Their function is different from their homolog in healthy tissues (Nishie et al., 1999; Hussain et al., 2006). They are able to discriminate the components of the self from the non-self (microbes) but also the altered components of the self. When recognizing the non-self or altered self-components, they can begin their process of elimination. Macrophages located in the tumor microenvironment are called tumor-associated macrophages. Under normal physiological conditions, macrophages are implicated in different processes such as organ development, tissue homeostasis, host defense against infections. These cells can also participate in metabolic disorders, immune diseases and cancer development (Sica et al., 2015). Normally, the myeloid population is the major player of the innate immune system and represents up to 30% of the tumor mass (Rossi et al., 1987; Graeber et al., 2002). Both the activation status and the number of TAMs present in the tumor microenvironment seem to influence GB prognosis (Komohara et al., 2008; Lu-Emerson et al., 2013; Pyonteck et al., 2013).

Macrophages are characterized by their plasticity and heterogeneity. They can be activated by different types of stimuli (growth factors, cytokines, microbial products, nucleotides) which in turn will affect macrophages differently (Poh and Ernst, 2018). *In vitro*, the stimulation of macrophages by interferon-γ (IFN–γ) and/or lipopolysaccharides (LPS) induces the classical (M1) macrophage polarization (Nielsen and Schmid, 2017). M1 macrophages favor the generation of T helper Type 1 (Th1) lymphocytes. Classically activated macrophages are good effectors to fight malignant tumors and are associated with chronic inflammation (Atri et al., 2018). Those macrophages are characterized by a high expression of IL-12, IL-23, and a low expression of IL-10. They can also produce high levels of pro-inflammatory cytokines IL-1β, tumor necrosis factor α (TNF-α), and IL-6, and increase the expression of inducible nitric oxide synthase (iNOS, NOSII) and reactive oxygen species (ROS). Another known stimulus for M1 macrophages is GM-CSF (Granulocyte Macrophage Colony-Stimulating Factor). It activates STAT5, which leads to the activation of the PI3K-AKT pathway (Jeannin et al., 2018).

On the contrary, macrophages stimulated *in vitro* by IL-4 and/or IL-13 are called alternatively activated (M2) macrophages (Murray et al., 2014). They are known effectors for promoting Th2 lymphocytes. They are involved in angiogenesis and tumor progression (Martinez and Gordon, 2014). This phenotype is associated with a low expression of IL-12, IL-23, and a high expression of IL-10 and TGF-β. Furthermore, M2 macrophages also have high levels of arginase 1 (Arg1), mannose receptors and scavenger receptors. M-CSF (Macrophage Colony-Stimulating Factor) and IL-34 also induce a M2 phenotype. M-CSF and IL-34 express the same receptor named CD115 and activate the MAP kinases signaling pathway (Jeannin et al., 2018).

Although the traditional M1/M2 dichotomy is useful for understanding the functionality of TAMs, recent analyzes, in particular of single-cell, revealed a spectrum of activation states much more complex than these traditional polarizations (Locati et al., 2020). Hence, macrophages in cancer are double-edged swords exerting pro- and antitumor functions. More than a real opposition, the M1/M2 signature crystallize a continuum of two extremes capable of specific adaptations (eg., chromatin remodeling, epigenetic marks, trained immunity, metabolic reprogramming,…) to various loco-regional cues (eg., cytokines, chemokines, miRNA, or immune checkpoints). In addition, proliferating monocytes could persist in a state of self-renewal within tumor tissues, rather than immediately differentiate into macrophages indicating a much higher complexity (Lin et al., 2019). It should again be emphasized that the M1 and M2 markers are distinct across species and in particular between humans and mice (eg., in human NOSII and Arg1 do not account for M1 and M2 macrophages, respectively) (Thomas and Mattila, 2014). In this regard, there are no specific surface markers in humans except a privileged panel of produced cytokines.

TAMs that are described in the tumor have in most cases pro-tumorigenic functions that promote tumor growth, invasion, angiogenesis, and tumor metastasis. In the GB microenvironment, both TAMs derive from blood monocytes; some originate from resident macrophages called microglia. Hence, macrophages appear to be an attractive target for new therapeutic strategies (Noy and Pollard, 2014).

The goal of this review is to discuss whether macrophages are worth considering as therapeutic targets in GB and to summarize the existing drugs targeting macrophages. In the second part of this review, the presence of microglia in brain tumor will be discussed. Then, the roles of TAMs in regulating the tumor

development, progression, and the response to conventional therapy will be reviewed. Finally, a survey of clinical trials testing drugs against macrophages in cancer will be presented.

THE PRESENCE OF TAMS IN GB: REALITY OR NOT?

The World Health Organization (WHO) classification of Central Nervous System (CNS) tumors was restructured in 2016. Diagnoses are based on both molecular alterations and histopathologic features (integrated diagnosis) in contrast to the 2007 WHO classification that only included histopathologic features (Louis et al., 2007; Louis et al., 2016). The tumor is essentially defined by the characteristics of the tumor cells that compose it, independently of the ecosystem in which they evolve and which they could themselves modify. GB also consists of many different noncancerous cells. The following cells are known to define the tumor microenvironment: endothelial cells, pericytes, fibroblasts, and immune cells in addition to cancer cells (Quail and Joyce, 2013).

The tumor microenvironment is now emerging as an important regulator of cancer progression (Quail and Joyce, 2017). Data from the literature seem to suggest that distinct molecular profiles in GB are correlated with differences in their microenvironment (Zhernakova et al., 2018). Even if the WHO classification now includes molecular data, no information on the tumor microenvironment has been integrated so far. Despite the fact that a solid tumor has never been seen without infiltrating immune cells, current diagnostic guidelines often forget voluntarily to take this into account. Although this does not necessarily modify the diagnosis as it is perceived today, it could be useful as regards the consideration of patient management and escape or not to new well identified therapies. The presence of TAMs has already been well described in GB (Saha et al., 2017; Séhédic et al., 2017; Roesch et al., 2018). In a mouse model, TAMs were observed in perivascular areas in the tumor and seem to be implicated in gliomagenesis Feng et al., 2015. Interestingly, their localization in the tumor appears to depend on their phenotypes Schiffer et al., 2018. In 2012, a meta-analysis showed that a high density of TAMs appeared to be associated with a poor prognosis in head and neck, ovarian and breast cancer and with a better prognosis in colorectal cancer (Zhang et al., 2012; Yuan et al., 2017; Zhao et al., 2017). Further evidence revealed that human GB display a mixed population of M1/M2 macrophages, and the ratio M1:M2 correlated with survival in IDH1 R132H wild type GB (Zeiner et al., 2018). In high-grade gliomas, M2 macrophages were correlated with an unfavorable prognostic (Sørensen et al., 2018). Caponegro et al. also described a correlation between the presence of TAMs and a poorest prognosis in GB (Caponegro et al., 2018). Furthermore, a study based on magnetic resonance imaging in GB showed that highly aggressive tumors were also correlated with the presence of TAMs (Zhou et al., 2018). Taking into account these findings, the presence of TAMs in GB has been well proven. Macrophages are important for the progression of GB and assessing them may give more information on the prognosis.

MICROGLIA: THE RESIDENT MACROPHAGES OF THE CNS

Microglia are the resident macrophages of the CNS and a healthy CNS macrophage population consists only of resident microglia. The blood brain barrier is impaired in neuropathological diseases, thus allowing an infiltration of monocytes form peripheral blood. In GB, both resident microglia and peripheral macrophages can be detected (Lisi et al., 2017). It is crucial to understand their molecular differences and their specific roles in the tumor. Resident microglia and newly recruited macrophages, hereafter referred to as peripheral macrophages have a distinct origin, as microglia arise from the yolk sac primitive macrophages (Ginhoux et al., 2013; Ginhoux and Guilliams, 2016). Although their origin differs, they share common histologic characteristics. Differentiating between microglia and peripheral macrophages is a difficult task, since they share common surface markers. The name TAM may very well include both resident microglia and monocyte-derived macrophages (Szulzewsky et al., 2015; Kloepper et al., 2016). In order to separate macrophages of hematopoietic origin from resident microglia, CD45 was used in flow cytometry analysis (Badie et al., 2000). However, resident microglia can upregulate their CD45 expression, making them indistinguishable from peripheral macrophages (Müller et al., 2015). Using a genetically engineered mouse, it was demonstrated that peripheral macrophages represent the majority of TAMs in the tumor, and resident microglia form a minor TAM population (Chen et al., 2017). Moreover, resident microglia and peripheral macrophages have different preferential localizations. Peripheral macrophages mostly appear in perivascular areas while resident macrophages are usually located in the peritumoral zone. A recent study showed that only a small batch of common genes toward species (rat, mice, human) differentiates GB-induced polarization of resident microglia (Walentynowicz et al., 2018). Although many studies tried to decipher the origin of TAMs in the tumor, no clear answer has yet been obtained.

Resident microglia are described to be involved in many processes including tumor growth and progression (Bryukhovetskiy et al., 2016; Matias et al., 2018). Microglia were shown to contribute to the invasiveness of GB by upregulating serpin family A member 3 (SERPINA3) expression in GB stem cells (GSCs), that is implicated in the remodeling of the extracellular matrix (Li et al., 2018). Resident microglia were also shown to mediate GB progression and stemness through the activation of interferon regulatory factor 7 (IRF7) that generates an inflammatory environment (Li Z. et al., 2017). Resident microglia are also involved in antitumor immunity processes through the expression of toll-like receptor 2 (TLR2) that down regulates their major histocompatibility complex class II (MHCII) expression (Qian et al., 2018). In a murine model, enhancer of zeste homolog 2 (EZH2) expression in GB was shown to be involved in the polarization of TAMs toward the M2 phenotype, creating an immune deficient environment (Yin et al., 2017). A 6 cytokine-related gene signature in resident microglia was shown to be sufficient to predict survival and identify M2 cells in GB (Cai et al., 2015). Both resident and peripheral macrophages are uniquely involved

in supporting GB growth and progression. Hence, if we wish to target TAMs as a mean to treat GB, we must first characterize this population as peripheral macrophages and/or resident microglia and counter their exact roles in GB initiation and maintenance.

TUMOR-ASSOCIATED MACROPHAGES: A PARTNER IN CRIME FOR TUMOR CELLS

A tumor can influence its microenvironment, and inversely. Thus, the interactions between the tumor cells and the nearby non-tumor cells are crucial to promote tumor angiogenesis, peripheral immune tolerance, and tumor growth. As previously said, TAMs are highly represented inside the tumor microenvironment. They are known for their heterogeneous phenotype, which by simplification can be with either anti-tumor (M1-like) or pro-tumor functions (M2-like). As TAMs are highly plastic cells, they can program themselves into both subpopulations. This gives them the ability to have different functions in different tumor areas and at different times during the tumor development.

Biology of the Tumor

Tumor Cells

The effect of TAMs on tumor cells is dependent on their type of activation. The reprogrammed M1 TAMs suppress the growth of GB cells (Li T. et al., 2017) meanwhile the M2 macrophages are described to favor tumor growth and resistance to therapy (Xue et al., 2017).

A macrophage with pro-tumor function in the tumor microenvironment is a macrophage that enhances tumor initiation and growth. TAMs and tumor cells actively communicate with each other leading to tumor progression. Their communication is mediated by interleukins IL-6 and IL-10 and transforming growth factor-β1 (TGF-β1) (Wagner et al., 1999; Ye et al., 2012). These cytokines activate signaling pathways in the tumor cells that boost processes such as proliferation, invasion and vascularization (**Figure 1**). TGF-β1 secretion by TAMs is responsible for the recruitment of cancer stem-like cells (CSCs) expressing CD133. Another consequence of TGF-β1 secretion is the production of metalloproteinase 9 (MMP-9) by CSCs rendering them highly invasive (Ye et al., 2012). TAMs are able to secrete pleiotrophin (PTN); CSCs express the PTN receptor PTPRZ1 on their cell surface. Once PTN is recognized by its receptor, it stimulates CSCs maintenance and tumorigenic potential, and therefore promotes GB growth (Shi et al., 2017). PTN- expressing TAMs also express CD163 which is an M2 lineage marker. Wang et al. showed that macrophages support GB invasiveness through the CCL4-CCR5 axis that enhances MMP-9 expression (Wang et al., 2016). Hypoxia was also shown to positively contribute to this mechanism by enhancing CCL4 and CCR5 expression. An increase of TAMs in a mouse model was shown to decrease the survival of the mice associated with a reduction of CD8+ T cells (Chae et al., 2015). On top of that, EGFR activation level correlates with TAM infiltration. Consequently, EGF can induce an upregulation of vascular cell adhesion molecule-1 (VCAM-1) that favors the interaction between TAMs and tumor cells, which in turn promoted tumor cell invasion (Zheng et al., 2013). MerTK (Myeloid-Epithelial-Reproductive Tyrosine Kinase) is a tyrosine kinase expressed by macrophages that suppresses the innate immune response. Its expression was shown to be higher in tumor recurrences. TAMs that express MerTK are also associated with tumor growth and resistance to treatment, making MerTK a potential therapeutic target (Wu et al., 2018). The molecular crosstalk between tumor cells and macrophages appears to be important for tumor growth and malignant progression. Therefore, modulating the exchange between those two cell populations may be therapeutically relevant.

Angiogenesis

GB is a highly hypoxic tumor with prominent necrotic regions due to the rapid proliferation of GB cells. The cell composition of the tumor core is quite different from that of the peritumoral area. The tumor core is more hypoxic, contains more $CD163^+$ TAMs and has a higher expression of VEGF-A (Tamura et al., 2018) (a major factor for vascularization). A downstream effect of hypoxia and necrosis is an increase in vascular proliferation. In the tumor microenvironment, TAMs are located near blood vessels. In mice, endothelial cells produce IL-6 that induces the expression of Arg1 and thus the alternative phenotype in TAMs (Wang et al., 2018). This alternative activation is mediated by the hypoxia-inducible factor-2α (HIF-2α). Wang et al. targeted IL-6 expression in a mouse model and improved the survival of GB-bearing mice. VEGF was shown to be implicated in promoting pro-angiogenic functions of TAMs in a GB rodent model (Turkowski et al., 2018). Gliomas overexpressing VEGF were correlated with an increase in the expression of MHCI and MHCII on macrophages. Endothelial cells and TAMs interaction leads to angiogenesis through the expression of TGF-β1 and integrin αvβ3, which induces the activation of the SRC-PI3K-YAP signaling (Cui et al., 2018) (**Figure 1**). The pro-angiogenic properties of TAMs are mediated by the protein CRCR1. This protein activates the PDGFB–PDGFRβ pathways and promotes pericytes recruitment, migration, and tumor angiogenesis (Zhu C. et al., 2017). In sum, TAMs have a proangiogenic function in GB. Thus, targeting macrophages may improve the response to anti-angiogenic therapies (Deng et al., 2017; Gagner et al., 2017). Indeed, blocking the macrophages recruitment by combining the chemokine SDF-1 and VEGF inhibitors was more effective and decreased tumor invasiveness and vascular density.

Immune Environment

Each tumor is characterized by an immune suppressive environment that forms one hallmark of cancer (Hanahan et al., 2011). This is in part due to the presence of TAMs in tumors but also to a complex regulation of the expression of immune and inflammatory genes by the global tumor ecosystem. It was found that IKKβ levels were reduced in GB; consequently, the NF-κB expression was decreased leading to defective immune and inflammatory gene expression in macrophages (Mieczkowski et al., 2015). NF-κB signaling is required for macrophage polarization and immune suppression in GB, making NF-κB a suitable target to improve overall survival in

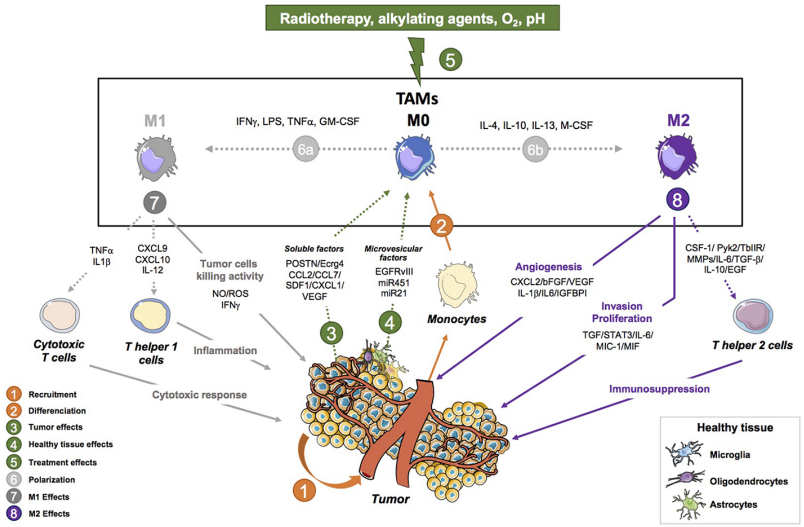

FIGURE 1 | Tumor-associated macrophage activities in glioblastoma progression. This figure shows the pro-tumoral (angiogenesis, invasion, proliferation and immunosuppressive properties) and anti-tumor (Tumor cell killing, Th1 response and anti-tumor activity) activities of tumor-associated macrophages (TAMs) in brain tumors. (1) Monocytes are recruited to the tumor where they differentiate into macrophages. The tumor is involved in their programming as it sends different signals to induce a specific phenotype in favor of the tumor. (2) TAMs that are recruited can either polarize into a continuum of macrophage states that are described with two extremes: an M1 (2a) or an M2 (2b) phenotype depending on the signal they receive (IFNγ/LPS/GM-CSF for M1 and IL-4/IL-13/M-CSF for M2) Pyonteck et al., 2013; Kast et al., 2017; Roesch et al., 2018. (3) M1-like TAMs are macrophages with anti-tumor properties such as tumor cell kill abilities mediated by the production of NO, ROS, IFNγ Kennedy et al., 2013; Leblond et al., 2017. They also mediate the Th1 response in the tumor through the activation of Th helper cells by secreting CXCL9, CXCL10, IL-12 Poon et al., 2017. Finally, they also display an anti-tumor activity by activating cytotoxic T cells *via* TNFα and IL1β. (4) M2-like TAMs have pro tumoral properties such as enhancing the invasive and proliferative ability of GB cells by secreting CSF-1, MMPs, Pyk2, TGFβIIR, TGFβ, IL-6, IL-10, and EGF. They can also mediate the immunosuppressive environment through the expression of IL-6, MIC-1, MIF, STAT3, and TGFβ. Finally, TAMs also regulate angiogenesis through the following factors: IL-6, MIC-1, MIF, STAT3, and TGFβ. (5) The tumor controls the polarization of TAMs through the production of soluble factors (CCL2/CCL7/SDF-1/CX3CL1/VEGF/POSTN/Ecrg4) Feng et al., 2015; Hambardzumyan et al., 2015; Lee et al., 2015; Zhou et al., 2015; Chang et al., 2016; Chen and Hambardzumyan, 2018; Turkowski et al., 2018 and microvesicle factors (EGFRvIII, miR451, miR21) Van Der Vos et al., 2016; Manda et al., 2018. (6) The tumor is also able to send signals to recruit new peripherical macrophages. (7) Environmental cues including radiotherapy, chemotherapy, O_2 level, pH are involved in the programing and functions of macrophages Hardee et al., 2012. (8) Healthy brain cells and TAMs probably interact and are involved in the programming of TAMs. Their interaction has yet to be studied. CCL2, C-C motif chemokine ligand 2; CCL7, C-C motif chemokine ligand 7; CSF-1, colony stimulating factor 1; CXCL2, C-X3-C motif chemokine ligand 2; CX3CL1, C-X3- C motif chemokine ligand 1; Ecrg4, esophageal cancer-related gene 4; EGF, endothelial growth fact; IGFBP1, insulin-like growth factor-binding protein 1; IL-1β, interleukin-1 beta; IL-10, interleukin-10; IL-6, interleukin-6; MIC-1, macrophage inhibitory cytokine 1; MIF, macrophage migration inhibitory factor; MMPs, matrix metalloproteinases; POSTN, periostin; Pyk2, proline rich tyrosine kinase 2; SDF-1, stromal cell-derived factor 1; STAT3, signal transducer and activator of transcription3; TGF-β, transforming growth factor-beta; TGFβIIR, TGF-beta type II receptor; VEGF, vascular endothelial growth factor; βFGF, basic fibroblast growth factor.

GB (Achyut et al., 2017). TAMs strongly inhibit the proliferation of antitumor T cells in the tumor microenvironment (Kumar et al., 2017). It was shown that an inhibition of transcription factors such as NF-κB, a mediator of M2 macrophages polarization, led to slower tumor growth and prolonged survival in a mouse model. It also decreased T cell induction which made the tumor less immunosuppressive (Barberi et al., 2018). Targeting NF-κB may improve the effectiveness of the current standard therapies.

TAMs express IL-4Rα that promotes immunosuppression. In mice, they also express Arg1 that is critical for T cell inhibition (Kohanbash et al., 2013). Chemokine ligand 22 (CCL22) is produced by TAMs and its expression is associated with a low survival rate and $CD4^+$ T cell activation (Zhou et al., 2015). One of the key regulators of the immunosuppressive environment in GB is fibrinogen-like protein 2 (FGL2). Its expression was correlated with a higher number of $CD4^+$ T cells and M2 macrophages (Latha et al., 2018). The colony stimulating factor receptor (CSF1R) is required for the recruitment of TAMs in the tumor microenvironment. It is also involved in promoting the polarization of macrophages toward the M2 phenotype. Inhibition of CSF1R attenuates the recruitment of TAMs and also increases the $CD8^+$ T cell infiltration (Strachan et al., 2013) (**Figure 1**). Another regulator of the immune microenvironment is the receptor tyrosine kinase AXL that is expressed in TAMs (Sadahiro et al., 2018). Its inhibition in a GB mouse model was

associated with prolonged survival. Furthermore, myeloid derived suppressor cells (MDSC) such as TAMs have been described to be activated by GB CSCs through MIF expression, having then an immunosuppressive activity on $CD8^+$ T cells, notably through the Arg1 expression in mice models (Flavahan et al., 2016). Overall, targeting TAMs may disturb the immunosuppressive environment of the tumor, allowing the immune cells to function more effectively.

Loco-Regional Cues for Metabolic Reprogramming

A peculiarity of GB is that it affects the seat of our consciousness, the CNS, whose immune status remains privileged due notably to the presence of the blood-brain barrier (BBB) and of unique resident cells (microglia, astrocytes, endothelial cells) (cf. **Box 1**). Although a precise control of the inflammatory or immune infiltrate is realized, the physiological and anatomical characteristics of the CNS is fed by the field of new recent knowledge, such as the identification of direct vascular channels connecting skull bone marrow to the brain surface enabling myeloid cell migration (Herisson et al., 2018), and make evolve our representation of its immune status. It should be stressed, however, that depending on the therapeutic strategy envisaged, the drug used can have a distinct impact when used according to a peripheral or loco-regional mode of administration (cf. **Tables 1**–**3**). Hence, if TAMs influence immune and adaptive signaling, reciprocally, loco-regional metabolic signals produced in tumor environments (glucose, glutamine, cystéine, lactate, IDO, adenosine, itaconic acid, acidic pH) impacted the polarization fate and immunosuppressive functions of TAMs, thus possibly resulting in immune tolerance and treatment resistance in GB (for review, see Won et al., 2019). Hence, tolerance can be reversed at both the promoters and enhancers of tolerized genes involved in metabolism and lipid biosynthesis, leading to transcriptional programs that rewired the intracellular signaling of innate immune cells thus increasing the capability of macrophages to respond to stimulation (for review see, Locati et al., 2020). In line with this, it has been observed that inhibition of fatty acid synthase (FAS), which catalyzes the synthesis of long-chain fatty acids, prevents the pro-inflammatory response in macrophages (Carroll et al., 2018). Interestingly, using metabolic profiling, it was found that exposure to β-amyloid triggers acute reactive microglial inflammation accompanied by metabolic reprogramming from oxidative phosphorylation to glycolysis while metabolic boosting with recombinant interferon-γ treatment reversed the defective glycolytic metabolism and inflammatory functions of microglia (Baik et al., 2019). Such microglial metabolic switch may also have a strong impact on GB development.

TAMs and Therapeutics

TAMs and Surgical Resection

Surgical resection is the current standard treatment for GB. However, limited data on the biological consequences of surgical resection have been published so far. It was reported that surgical resection increases proliferation and angiogenesis (Kong et al., 2010). After surgical resection, TAMs were shown to express higher levels of CD163, a M2 macrophage marker, and their localization was close to the site of recurrence (Zhu H. et al., 2017). Both TAMs and oligodendrocyte progenitor cells are localized near the tumor periphery. They enhance the stemness and chemo-radioresistance in GB cells (Hide et al., 2018). It was shown that tumor phenotypes associated with telomerase overexpression and TAMs infiltration were more complicated to resect, probably due to improvement of GB cell migratory capabilities (Hung et al., 2016). The inability to surgically remove the whole tumor contributes to the poor prognosis and recurrence of GB.

TAMs and Radiotherapy

Macrophages inside the tumor mass are involved in multiple phenomena that include radiation resistance. Radiation therapy itself induces changes in the tumor microenvironment and renders the tumor more aggressive. In fact, recurrence mostly appears near the irradiated area (Gupta and Burns, 2018). Radiotherapy induces a rapid inflammatory response leading to TAMs recruitment. This inflammatory response is correlated with a short survival time (Tabatabaei et al., 2017). TAMs participate in the induction of GB cell differentiation to a mesenchymal state through NF-κB production, an event that correlated with radiation resistance (Bhat et al., 2013). Recently, Leblond et al. showed that M1 macrophages are more sensitive to radiation than M2 macrophages (Leblond et al., 2017). The proportion of M2 macrophages in irradiated tissues is thus increased. Moreover, M2 macrophages were described to contribute to relapses in oral cancer by promoting vascularization after radiation treatment (Okubo

BOX 1 | Non-cancerous brain cells alter macrophages polarization and functions.

Tumor cells cooperate with its surroundings such as the tumor microenvironment. The brain is also the home of specific cell types with their own characteristics and functions; although those cells are not part of the tumor, they can also interact with it. The interaction between cells residing in the brain and TAMs are very poorly understood in cancer but has been studied in depth in other pathologies, which will be quickly reviewed in this box. Both neurons and astrocytes can produce CX3CL1R, the receptor for CX3CL1 found on microglia Matias et al., 2018. CX3CL1 promotes TAM recruitment and increases the expression of MMPs and thus invasive properties. When an ischaemic stroke happens, ischaemic neurons are able to prime microglia toward an M1 phenotype during an injury Hu et al., 2012. Another cell type is oligodendrocyte which accounts for the formation of the myelin sheath in the CNS. It was found that macrophages and oligodendrocyte progenitor cells colocalized near the tumor border. At this site of colocalization, those cells induced stemness and resistance to therapy in GB cells Hide et al., 2018. In the peripheral nervous system, Schwann cells are the cells responsible for myelin sheath formation. Schwann cells were shown to promote cancer invasion by direct contact with tumor cells Deborde et al., 2016. The mechanism involved in this process remains unclear. In neurofibromas (peripheral nerve sheath tumors due to NF1 loss in Schwann cells), macrophages were shown to be abundant Stratton et al., 2018. In this case, Schwann cells and macrophages communicate with each other and are involved in the regulation of inflammatory gene expression. As Schwann cells and oligodendrocytes share a common function in normal tissue, it may be interesting to further study the involvement of oligodendrocytes in GB. Non-cancerous cells of the CNS and peripheral nervous system interact with macrophages and lead them to polarize toward a specific phenotype.

TABLE 1 | Clinical trials targeting the recruitment of macrophages.

Target	Drugs	Inhibitor type	Clinical trial	Tumor type	Benefit
CCL2-CCR2 axis	Carlumab	mAb	NCT00992186 (2009) (completed, has results)	Metastatic Castrate-Resistant Prostate Cancer	Information about the disease's progression
			NCT01204996 (2010) (Completed)	Solid Tumors	
			NCT00537368 (2007) (Completed)	Solid Tumors	
	PF-04136309	Small molecule	NCT02732938 (2016) (Terminated)	Metastatic Pancreatic Cancer	Unknown
	MLN1202	mAb	NCT01015560 (2009) (Completed with results)	Bone Metastases	Well tolerated
	CCX872-B	Small molecule	NCT03778879 (2018) (Not yet recruiting)	Pancreatic Adenocarcinoma	Unknown
	BMS-813160	Small molecule	NCT03496662 (2018) (Recruiting)	Pancreatic Ductal Adenocarcinoma (PDAC)	Unknown
CD47	Hu5F9-G4	mAb	NCT02953509 (2016) (Recruiting)	B-cell Non-Hodgkin's Lymphoma	Unknown
			NCT03248479 (2017) (Recruiting)	Haematological Malignancies	
			NCT02216409 (2014) (Active, not recruiting)	Haematological Malignancies	
			NCT02678338 (2016) (Recruiting)	Haematological Malignancies	
			NCT02953782 (2016) (Recruiting)	Colorectal Cancer	
	TTI-621	Small molecule	NCT03530683 (2018) (Recruiting)	Refractory Lymphoma, Myeloma	Unknown
			NCT02663518 (2016) (Recruiting)	Hematologic Malignancies and Selected Solid Tumors	
	ALX148	Small molecule	NCT03013218 (2017) (Recruiting)	Solid Tumors and Lymphoma	Unknown
	SRF231	mAb	NCT03512340 (2018) (Recruiting)	Solid and Hematologic Cancers	Unknown
	CC-90002	mAb	NCT02367196 (2015) (Recruiting)	Solid and Hematologic Cancers	Unknown
	IBI188	mAb	NCT03763149 (2018) (Not yet recruiting)	Malignant Tumors and Lymphomas Advanced Malignancies	Unknown
			NCT03717103 (2018) (Recruiting)		

et al., 2016). In a radioresistant GB model, the total RNA was sequenced and it was found that there was a positive regulation of macrophage chemotaxis following radiation (Doan et al., 2018). Also, in a murine glioma model, an increase in SDF-1α at the tumor invasion front after radiotherapy was correlated with the recruitment of TAMs and radioresistance (Wang et al., 2013). Irradiation of the tumor leads to the alteration of multiple pathways. In particular, it modifies the macrophage activation type, rendering them more supportive of tumor growth.

TAMs and Chemotherapy

The standard treatment of GB affects the molecular profiles of the tumor. Temozolomide (TMZ) is commonly used to treat GB. TAMs that express CD74 were described to be involved in TMZ resistance by inducing AKT and Erk1/2 activation in tumor cells (Kitange et al., 2010). Gene expression profiling showed that the tumor that recurred after treatment did not match the primary treatment-naïve tumor. After treatment, the polarization toward the M2 phenotype was upregulated (Hudson et al., 2018). Tumor protein 53 (p53) is involved in promoting the development of the tumor. GB with the p53 isoform Δ133p53β had increased $CD163^+$ macrophages (Kazantseva et al., 2018). Moreover, Δ133p53β supports cancer stemness (Arsic et al., 2015). In addition, it is correlated with resistance to TMZ (Kazantseva et al., 2018). GB is able to evade the toxic effects of chemotherapy, but it can equally evade the action of the immune system. Hence, a cocktail of multiple drugs targeting different pathways may provide the most effective therapy for GB and improve overall survival.

CURRENT THERAPIES TARGETING TUMOR-ASSOCIATED MACROPHAGES IN CANCER

Targeting the Recruitment of TAMs

One strategy to target TAMs is to block their recruitment to the tumor site. It can be achieved by targeting the chemokine ligand 2 (CCL2) - chemokine receptor 2 (CCR2) axis. CCL2 is an inflammatory chemokine that can recruit macrophages and Treg lymphocytes leading to an immunosuppressive environment (Chang et al., 2016). To achieve this, a human IgG1k mAb called Carlumab was developed. A survey of clinical trials involving the CCL2-CCR2 axis is provided in **Table 1**.

A phase 2 study showed that this antibody was well-tolerated. However, it did not block the CCL2-CCR2 axis or have any antitumor activity as a single agent in metastatic prostate cancer (Pienta et al., 2013) (NCT00992186). When Carlumab was combined with four other chemotherapies, the treatment was still well tolerated but the suppression of CCL2-CCR2 axis remained elusive (Brana et al., 2015) (NCT01204996). In other studies, Carlumab was shown to transiently suppress CCL2 and had a preliminary antitumor activity (Sandhu et al., 2013) (NCT00537368, 2007). PF-04136309 combined with

TABLE 2 | Clinical trials with toll-like receptor (TLR) agonists for macrophages reprogramming.

Target	Drugs	Inhibitor type	Clinical trial	Tumor type	Benefit
CD40	APX005M	mAb	NCT03502330 (2018) (Recruiting) NCT02482168 (2015) (Active, not recruiting) NCT03123783 (2017) (Recruiting) NCT03389802 (2018) (Recruiting) NCT03165994 (2017) (Recruiting)	Non-small Cell Lung Cancer, Renal Cell Carcinoma Solid tumors Non-small Cell Lung Cancer or Metastatic Melanoma Pediatric CNS Tumors Resectable Esophageal and Gastroesophageal Junction Cancers	Unknown
	Selicrelumab	mAb	NCT02304393 (2014) (Recruiting)	Locally Advanced and/or Metastatic Solid Tumors	Unknown
	ChiLob 7/4	mAb	NCT01561911 (2012) (Completed)	Non-Hodgkin Lymphoma	Unknown
	CP-870,893	mAb	NCT00607048 (Completed)	Non-Hodgkin Lymphoma	Unknown
	CDX-1140	Small molecule	NCT03329950 (Recruiting)	Advanced Malignancies	Unknown
TLR7	LHC165	Small molecule	NCT03301896 (2017) (Recruiting)	Advanced Malignancies	Unknown
	Imiquimod	Small molecule	NCT01421017 (2011) (Completed) NCT00899574 (2009) (Completed with results)	Breast Cancer With Skin Metastases Chest Wall Recurrence or Skin Metastases	Well tolerated. Partial response: tumor regression and immune response
	NKTR-262	Small molecule	NCT03435640 (2018) (Recruiting)	Locally Advanced or Metastatic Solid Tumor Malignancies	Unknown
	IMO-8400	Small molecule	NCT02252146, (Completed with results)	Diffuse Large B Cell Lymphoma (DLBCL)	Lack of efficacy
	Resiquimod	Small molecule	NCT00821652 (2009) (Completed)	Surgically resected Stage IIB, IIC, Stage III or Stage IV (AJCC criteria) Melanoma	Unknown
	DSP-0509	Small molecule	NCT03416335 (2018) (Recruiting)	Advanced Solid Tumors	Unknown
TLR8	VTX-2337	Small molecule	NCT02431559 (2015) (Completed) NCT01294293, (Completed) NCT01334177, (Completed) NCT02452697 (2015) (Recruiting)	Platinum-Resistant Ovarian Cancer Ovarian Epithelial, Fallopian Tube, or Peritoneal Cavity Cancer Ovarian Epithelial, Fallopian Tube, or Peritoneal Cavity Cancer Myeloid and Lymphoid Malignancies	Unknown
TLR9	EMD 1201081	Small molecule	NCT01040832 (2009) (Completed with results)	Recurrent or Metastatic Squamous Cell Carcinoma of the Head and Neck	EMD 1201081 was well tolerated in combination with cetuximab, but no clinical efficacy was observed Ruzsa et al., 2014
	DUK-CPG-001	Small molecule	NCT02452697 (2015) (Recruiting)	Myeloid and Lymphoid Malignancies	Unknown
	IMO-2055	Small molecule	NCT00719199 (2008) (Completed) NCT00633529 (2008) (Completed)	Colorectal Cancer NSCLC	Unknown
	CMP-001	Small molecule	NCT03618641 (2018) (Recruiting) NCT03507699 (2018) (Recruiting)	Stage IIIB/C/D Melanoma Patients With Clinically Apparent Lymph Node Disease Metastatic Colorectal Cancer	Unknown
	SD-101	Small molecule	NCT03007732 (2017) (Recruiting) NCT03410901 (Recruiting) NCT02927964 (2016) (Recruiting) NCT02254772 (2014) (Completed with results)	Hormone-Naïve Oligometastatic Prostate Cancer Low-Grade B-Cell Non-Hodgkin Lymphoma Refractory Grade 1-3A Follicular Lymphoma Recurrent Low-Grade B-Cell Lymphoma	Well tolerated but progression of the tumor was observed

chemotherapy was also shown to be well-tolerated and led to a tumor response (Nywening et al., 2016).

Reprogramming of TAMs Toward an Antitumoral Phenotype

As mentioned previously, TAMs can exist in different functional states between the M1 and M2 phenotypes, making them highly heterogeneous and plastic cells (Biswas and Mantovani, 2010). Thus, they can be either pro- or anti-tumoral (Wynn et al., 2013). Reprogramming the TAMs toward a tumoricidal or a tumor-inhibition state may be a plausible therapeutic strategy. Different strategies are being studied in the clinic. These are reported in **Table 2** (please refer also to **Box 2**).

Inhibition of CD47

Inhibition of CD47 is a strategy that can facilitate phagocytosis of tumor cells by macrophages. Indeed, CD47 expressed by cancer cells inhibits phagocytosis through its interaction with signal

TABLE 3 | Clinical trials using drugs to deplete macrophages from the tumor's microenvironment.

Target	Drugs	Inhibitor type	Clinical trial		Benefit
CSF1R	Pexidartinib	Small molecule	NCT02777710 (2016) (Recruiting)	Metastatic/Advanced Pancreatic or Colorectal Cancers	Unknown
	DCC-3014	Small molecule	NCT03069469 (2017) (Recruiting)	Advanced Malignancies	Unknown
	LY3022855	mAb	NCT03153410 (2017) (Recruiting)	Pancreas Adenocarcinoma	Unknown
			NCT02718911 (2016) (Completed)	Advanced Solid Tumors Melanoma	
			NCT03101254 (2017) (Recruiting)		
	PLX3397	Small molecule	NCT01004861 (2009) (Completed)	Solid Tumors Melanoma and Other Solid Tumors	Unknown
			NCT02452424 (2015) (Completed)	Recurrent Glioblastoma Pigmented Villonodular Synovitis (PVNS) or Giant Cell	
			NCT01349036 (2011) (Completed)	Tumor of the Tendon Sheath (GCT-TS)	
			NCT02371369 (2015) (Active, not recruiting)		
	MCS110	Small molecule	NCT03694977 (2018) (Not yet recruiting)	Gastric Cancer	Unknown
	IMC-CS4	Small molecule	NCT01346358 (2011) (Completed)	Advanced Solid Tumors	Unknown
	Cabiralizumab	mAb	NCT03697564 (2018) (Not yet recruiting)	Stage IV Pancreatic Cancer	Unknown
			NCT02526017 (2015) (Active, not recruiting)		
	SNDX-6352	mAb	NCT03238027 (2017) (Recruiting)	Solid Tumors	Unknown
	JNJ-40346527	Small molecule	NCT03557970 (2018) (Not yet recruiting)	Acute Myeloid Leukemia	Unknown
	ARRY-382	Small molecule	NCT02880371, (Recruiting)	Acute Myeloid Leukemia	Unknown
			NCT01316822 (2011) (Completed)	Advanced or Metastatic Cancers	
	BLZ945	Small molecule	NCT02829723 (2016) (Recruiting)	Advanced Solid Tumors	Unknown
	RO5509554	Small molecule	NCT01494688 (2011) (Completed)	Advanced Solid Tumors	Unknown
NA	Clodronate	Bisphosphonate	NCT01198457 (2010) (Completed)	Breast Neoplasms, Prostatic Neoplasms, Multiple Myeloma Stage I or Stage II Breast Cancer	Treatment with clodronate suggests a benefit in recurrence rates for postmenopausal women with breast cancer Paterson et al., 2012
			NCT00009945 (2010) (2003) (Completed with results)	Bone neoplasms	
			NCT00909142 (2009) (Completed)	Hormone Refractory Metastatic Prostate Cancer Primary Breast Cancer	
			NCT00003232 (2004) (Completed)		
			NCT00127205 (2005) (Active, not recruiting)		
	Zoledronate	Bisphosphonate	NCT00301873 (2006) (Completed, has results)	Primary Malignant Glioma	
			NCT00885326 (2009) (Active, not recruiting)	High-Risk Neuroblastoma	
			NCT01345019 (2011), (Active, not recruiting)	Multiple Myeloma	

regulatory protein-α (SIRPα) expressed by macrophages thus sending out a "do not eat me" signal. Alternatively, CD47 can serve as a receptor for thrombospondin 1 (TSP1) to trigger specific signaling. Many tumors are described to overexpress CD47 (Zhang et al., 2015; Zhao et al., 2016). Inhibition of CD47 in a preclinical model showed a modification of microglia phenotypes in GB that was correlated with better survival (Hutter et al., 2019). Furthermore, *in vivo,* the anti-CD47 treatment is able to shift the macrophage phenotype toward an M1 type (Zhang et al., 2016) and induces anti-tumor effects (Li F. et al., 2017). The preclinical study of Hu5F9-G4 in pediatric malignant primary brain model demonstrated that this CD47 inhibitor is a safe and effective therapeutic agent (Gholamin et al., 2017). Hu5F9-G4 was also shown to be well tolerated in a clinical trial (Sikic et al., 2018) (NCT02216409, **Table 2**). TTI-621, a small molecule inhibiting CD47, is being investigated in an ongoing clinical trial. Interestingly, however, it has recently been observed that CD47 inhibition may result in cancer cell resistance to chemotherapy through escape to senescence (Guillon et al., 2019).

Activation of CD40

CD40 is expressed on monocytes, macrophages, dendritic cells, and B cells. It is a receptor that belongs to the TNF receptor superfamily. Many clinical trials targeting CD40 notably through agonistic or activating antibodies are ongoing (**Table 3**). In a mouse model, targeting CD40 was useful in producing antitumor effects that greatly improved the overall survival (Shoji et al.,

BOX 2 | The content of exosomes as a therapeutic target to control TAMs phenotype.

Exosomes are microvesicles (30-120μm) that are secreted through exocytosis by various cells. They exert a variety of biological effects. GB cells can secrete exosomes that carry proteins such as EGFR variant III (EGFRvIII) Manda et al., 2018. The content of exosomes was shown to be different depending on partial pressure in O_2 as cancer cells can adapt to their surroundings Zhang et al., 2017. Exosomes can mediate immunosuppressive properties in GB through their internalization in monocytes. Once they are internalized, they cause a rearrangement of the monocyte cytoskeleton and induce an M2 phenotype Gabrusiewicz et al., 2018. Vos et al. visualized the effect of GB-derived exosomes on TAMs and observed a shift of their cytokine profile to an immune-suppressive profile Van Der Vos et al., 2016. They also observed an elevation of miR-21 expression in TAMs associated with a decrease in c-Myc mRNA levels. GB-derived exosomes were shown to modify the expression of cell surface proteins and cytokines (IL-6 and VEGF), and to increase phagocytic activity in macrophages De Vrij et al., 2015. Also, blood samples from patients with GB were analyzed and shown to harbor GB-derived exosomes containing immunoglobulin (Ig) G2 and IgG4 antibody isotypes Harshyne et al., 2016. Those exosomes were able to induce the expression of CD163, associated with the M2 phenotype. Exosomes appear to be important for the communication between tumor cells and TAMs in GB. As key players from the tumor ecosystem, targeting them may impair the regulatory effects of GB cells on TAM immunosuppressive properties.

2016). Targeting CD40 modulated the immune cell number and led to an antitumor response (Vonderheide et al., 2013; Nowak et al., 2015). In a mouse model, the combination of CSF1R inhibition and CD40 activation induced the reprogramming of TAMs (Hoves et al., 2018), thus allowing the protective response of T cells (Perry et al., 2018).

TLR Agonist

Toll-like receptors (TLRs) are normally activated by microbial moieties (including nucleic acids) allowing macrophages to acquire a M1 phenotype. Using a TLR agonist to reprogram macrophages was thus of interest in cancer treatment (Feng et al., 2019). Numerous TLR7 ligands, TLR9 ligands, and one TLR8 ligand have been tested for their antitumoral properties in clinical trials (**Table 2**). For example, the TLR7 agonist Imiquimod has been tested. It was well tolerated and associated to tumor regression and increased lymphocytic infiltrate (Adams et al., 2013) (NCT00899574). The TLR7 agonist 852A was also well tolerated with reversible side effects (Dudek et al., 2007). IMO-2055, a TLR9 agonist, demonstrated a possible antitumor activity when combined with erlotinib and bevacizumab (Smith et al., 2014) (NCT00633529).

Depletion of TAMs

The activation of TAMs is dependent on the CSF1R signaling pathway. Therefore, CSF1R may be a way to target macrophages specifically. Many small molecules and antibodies were developed against CSF1R, and numerous clinical trials have been completed or are ongoing (**Table 3**). PLX3397 is a small molecule targeting CSF1R, it reduced the number of TAMs in a preclinical GB model and showed an antitumor activity (Coniglio and Segall, 2013; Yan et al., 2017). In clinical studies, PLX3397 was also well tolerated and showed anti-tumor responses after treatment (Tap et al., 2015) (NCT01004861). PLX3397 was also well tolerated but showed no efficacy in GB (Butowski et al., 2016) (NCT01349036). BLZ945, another small molecule inhibitor of CSF1R, can alter the polarization of TAMs in glioma (Pyonteck et al., 2013). It is currently being assessed in a clinical trial.

Another way to deplete the number of TAMs in the tumor is to use bisphosphonates. They are described for both direct and indirect anti-tumor effects such as induction of tumor apoptosis and inhibition of cell adhesion. More importantly, they alter the behavior of TAMs (Van Acker et al., 2016). Bisphosphonates are divided in two classes depending on their structure and mechanism of action. Clodronate belongs to the first group while zoledronate belongs to the second group. Both zoledronate and clodronate are still being assessed in clinical trials (**Table 3**).

CONCLUSION

In GB microenvironment, both resident and peripheral macrophages are present and there is an urgent need to understand their specific roles in tumor progression and resistance to treatment. It is obvious that macrophages may be a useful target to improve the outcome of cancer. Currently, many drugs targeting macrophages are being tested in the clinic. However, only a few are tested specifically in GB. The immune landscape in GB, and in cancer in general, has to be investigated further as there is a lack of efficacy in the clinic when only TAMs are targeted. The targeting of TAMs must be implemented hand in hand with the standard treatment to potentially improve the overall effect. In summary, TAMs seem to be a promising target to overcome resistance that arises in GB.

AUTHOR CONTRIBUTIONS

HG, LR and EG wrote the manuscript. FH and EG contributed to the conception and design of the work. HG, LR, AR, MC, YD, PJ, FH, and EG contributed to manuscript amendments and revisions. All authors read and approved the submitted version.

FUNDING

This work was supported by the French national research agency (ANR) through the LabEx IRON << *Innovative Radiopharmaceuticals in Oncology and Neurology*>> as part of the French government "Investissements d'Avenir" program (ANR-11-LABX-0018). It was also supported by the ANR under the frame of EuroNanoMed III (project GLIOSILK). The work was additionally funded by the "Institut National de la Santé et de la Recherche Médicale" (INSERM) and by the University of Angers (Angers, France). It was also related to: (i) the PL-BIO 2014-2020 INCa (Institut National du Cancer) consortium MARENGO <<; *MicroRNA agonist and antagonist Nanomedicines for*

GliOblastoma treatment: from molecular programmation to preclinical validation>>, (ii) to the MuMoFRaT project << *Multi-scale Modeling & simulation of the response to hypo-Fractionated Radiotherapy or repeated molecular radiation Therapies*>> supported by "La Région Pays-de-la-Loire" and by the Cancéropôle Grand-Ouest (Vectorization, imaging and radiotherapies network), (iii) the LabEX IGO and the ANR through the investment of the future program ANR-11-LABX-0016-01, (iv) the SIRIC ILIAD program supported by INCa, and (v) the Ministry of Health and the Institute for Health and Medical Research (Inserm) (contract INCa-DGOS-Inserm_12558). HG and LR were PhD fellows funded by the LabEx IRON and by the LabEx IRON-2 and the University of Angers, respectively.

REFERENCES

Achyut, B. R., Angara, K., Jain, M., Borin, T. F., Rashid, M. H., Iskander, A. S. M., et al. (2017). Canonical NFκB signaling in myeloid cells is required for the glioblastoma growth. *Sci. Rep.* 7, 1–12. doi: 10.1038/s41598-017-14079-4

Adams, S., Kozhaya, L., Martiniuk, F., Meng, T., Chiriboga, L., Liebes, L., et al. (2013). Rejection of Skin Metastases in Patients With Breast Cancer. *Clin. Cancer Res.* 18, 6748–6757. doi: 10.1158/1078-0432.CCR-12-1149

Arsic, N., Gadea, G., Lagerqvist, E. L., Busson, M., Cahuzac, N., Brock, C., et al. (2015). The p53 isoform Δ133p53β promotes cancer stem cell potential. *Stem Cell Rep.* 4, 531–540. doi: 10.1016/j.stemcr.2015.02.001

Atri, C., Guerfali, F. Z., and Laouini, D. (2018). Role of Human Macrophage Polarization in Inflammation during Infectious Diseases. *Int. J. Mol. Sci.* 19, 1801. doi: 10.3390/ijms19061801

Badie, B., Schartner, J., Vorpahl, J., and Preston, K. (2000). Interferon-γ Induces Apoptosis and Augments the Expression of Fas and Fas Ligand by Microglia in Vitro. *Exp. Neurol.* 162, 290–296. doi: 10.1006/exnr.1999.7345

Baik, S. H., Kang, S., Lee, W., Choi, H., Chung, S., Kim, J., et al. (2019). A Breakdown in Metabolic Reprogramming Causes Microglia Dysfunction in Alzheimer's Disease. *Cell Metab*. doi: 10.1016/j.cmet.2019.06.005

Barberi, T., Martin, A., Suresh, R., Barakat, D. J., Harris-Bookman, S., Drake, C. G., et al. (2018). Absence of host NF-κB p50 induces murine glioblastoma tumor regression, increases survival, and decreases T-cell induction of tumor-associated macrophage M2 polarization. *Cancer Immunol. Immunother.* 67, 1491–1503. doi: 10.1007/s00262-018-2184-2

Bhat, K. P. L., Balasubramaniyan, V., Vaillant, B., Ezhilarasan, R., Hummelink, K., Hollingsworth, F., et al. (2013). Mesenchymal Differentiation Mediated by NF-κB Promotes Radiation Resistance in Glioblastoma. *Cancer Cell* 24, 331–346. doi: 10.1016/j.ccr.2013.08.001

Biswas, S. K., and Mantovani, A. (2010). Macrophage plasticity and interaction with lymphocyte subsets: Cancer as a paradigm. *Nat. Immunol.* 11, 889–896. doi: 10.1038/ni.1937

Brana, I., Calles, A., LoRusso, P. M., Yee, L. K., Puchalski, T. A., Seetharam, S., et al. (2015). Carlumab, an anti-C-C chemokine ligand 2 monoclonal antibody, in combination with four chemotherapy regimens for the treatment of patients with solid tumors: an open-label, multicenter phase 1b study. *Targeting Oncol.* 10, 111–123. doi: 10.1007/s11523-014-0320-2

Brown, N. F., Carter, T. J., Ottaviani, D., and Mulholland, P. (2018). Harnessing the immune system in glioblastoma. *Br. J. Cancer* 119, 1171–1181. doi: 10.1038/s41416-018-0258-8

Bryukhovetskiy, I. S., Dyuizen, I. V., Shevchenko, V. E., Bryukhovetskiy, A. S., Mischenko, P. V., Milkina, E. V., et al. (2016). Hematopoietic stem cells as a tool for the treatment of glioblastoma multiforme. *Mol. Med. Rep.* 14, 4511–4520. doi: 10.3892/mmr.2016.5852

Butowski, N., Colman, H., De Groot, J. F., Omuro, A. M., Nayak, L., Wen, P. Y., et al. (2016). Orally administered colony stimulating factor 1 receptor inhibitor PLX3397 in recurrent glioblastoma: An Ivy Foundation Early Phase Clinical Trials Consortium phase II study. *Neuro. Oncol.* 18, 557–564. doi: 10.1093/neuonc/nov245

Cai, J., Zhang, W., Yang, P., Wang, Y., Li, M., Zhang, C., et al. (2015). Identification of a 6-cytokine prognostic signature in patients with primary glioblastoma harboring M2 microglia/macrophage phenotype relevance. *PloS One* 10, e0126022–e0126022. doi: 10.1371/journal.pone.0126022

Caponegro, M. D., Moffitt, R. A., and Tsirka, S. E. (2018). Expression of neuropilin-1 is linked to glioma associated microglia and macrophages and correlates with unfavorable prognosis in high grade gliomas. *Oncotarget* 9, 35655–35665. doi: 10.18632/oncotarget.26273

Carroll, R. G., Zasłona, Z., Galván-Peña, S., Koppe, E. L., Sévin, D. C., Angiari, S., et al. (2018). An unexpected link between fatty acid synthase and cholesterol synthesis in proinflammatory macrophage activation. *J. Biol. Chem.* doi: 10.1074/jbc.RA118.001921

Chae, M., Peterson, T. E., Balgeman, A., Chen, S., Zhang, L., Renner, D. N., et al. (2015). Increasing glioma-associated monocytes leads to increased intratumoral and systemic myeloid-derived suppressor cells in a murine model. *Neuro. Oncol.* 17, 978–991. doi: 10.1093/neuonc/nou343

Chang, A. L., Miska, J., Wainwright, D. A., Dey, M., Rivetta, C. V., Yu, D., et al. (2016). CCL2 Produced by the Glioma Microenvironment Is Essential for the Recruitment of Regulatory T Cells and Myeloid-Derived Suppressor Cells. *Cancer Res.* 76, 5671–5682. doi: 10.1158/0008-5472.CAN-16-0144

Charles, N. A., Holland, E. C., Gilbertson, R., Glass, R., and Kettenmann, H. (2011). The brain tumor microenvironment. *Glia* 59, 1169–1180. doi: 10.1002/glia.21136

Chen, Z., and Hambardzumyan, D. (2018). Immune Microenvironment in Glioblastoma Subtypes. *Front. Immunol.* 9, 1004. doi: 10.3389/fimmu.2018.01004

Chen, Z., Feng, X., Herting, C. J., Garcia, V. A., Nie, K., Pong, W. W., et al. (2017). Cellular and Molecular Identity of Tumor-Associated Macrophages in Glioblastoma. *Cancer Res.* 77, 2266–2278. doi: 10.1158/0008-5472.CAN-16-2310

Coniglio, S. J., and Segall, J. E. (2013). Review: Molecular mechanism of microglia stimulated glioblastoma invasion. *Matrix Biol.* 32, 372–380. doi: 10.1016/j.matbio.2013.07.008

Cui, X., Morales, R. T. T., Qian, W., Wang, H., Gagner, J. P., Dolgalev, I., et al. (2018). Hacking macrophage-associated immunosuppression for regulating glioblastoma angiogenesis. *Biomaterials* 161, 164–178. doi: 10.1016/j.biomaterials.2018.01.053

De Vrij, J., Niek Maas, S. L., Kwappenberg, K. M. C., Schnoor, R., Kleijn, A., Dekker, L., et al. (2015). Glioblastoma-derived extracellular vesicles modify the phenotype of monocytic cells. *Int. J. Cancer* 137, 1630–1642. doi: 10.1002/ijc.29521

Deborde, S., Hall, A., Wong, R.J., Deborde, S., Omelchenko, T., Lyubchik, A., et al. (2016). Schwann cells induce cancer cell dispersion and invasion Find the latest version : Schwann cells induce cancer cell dispersion and invasion. *J. Clin. Invest.* 126, 1538–1554. doi: 10.1172/JCI82658

Deng, L., Stafford, J. H., Liu, S. C., Chernikova, S. B., Merchant, M., Recht, L., et al. (2017). SDF-1 Blockade Enhances Anti-VEGF Therapy of Glioblastoma and Can Be Monitored by MRI. *Neoplasia (United States)* 19, 1–7. doi: 10.1016/j.neo.2016.11.010

Doan, N. B., Nguyen, H. S., Alhajala, H. S., Jaber, B., Al-Gizawiy, M. M., Ahn, E.-Y. E., et al. (2018). Identification of radiation responsive genes and transcriptome profiling via complete RNA sequencing in a stable radioresistant U87 glioblastoma model. *Oncotarget* 9, 23532–23542. doi: 10.18632/oncotarget.25247

Dudek, A. Z., Yunis, C., Harrison, L. I., Kumar, S., Hawkinson, R., Cooley, S., et al. (2007). First in human phase I trial of 852A, a novel systemic toll-like receptor 7 agonist, to activate innate immune responses in patients with advanced cancer. *Clin. Cancer Res.* 13, 7119–7125. doi: 10.1158/1078-0432.CCR-07-1443

Feng, X., Szulzewsky, F., Yerevanian, A., Chen, Z., Heinzmann, D., Rasmussen, R. D., et al. (2015). Loss of CX3CR1 increases accumulation of inflammatory monocytes and promotes gliomagenesis. *Oncotarget* 6, 15077–15094. doi: 10.18632/oncotarget.3730

Feng, Y., Mu, R., Wang, Z., Xing, P., Zhang, J., Dong, L., et al. (2019). A toll-like receptor agonist mimicking microbial signal to generate tumor-suppressive macrophages. *Nat. Commun.* 10, 2272. doi: 10.1038/s41467-019-10354-2

Finn, O. J. A. (2018). Believer's Overview of Cancer Immunosurveillance and Immunotherapy. *J. Immunol.* 200, 385–391. doi: 10.4049/jimmunol.1701302

Flavahan, W. A., Nakano, I., Rich, J. N., Otvos, B., Silver, D. J., Sinyuk, M., et al. (2016). Cancer Stem Cell-Secreted Macrophage Migration Inhibitory Factor

Stimulates Myeloid Derived Suppressor Cell Function and Facilitates Glioblastoma Immune Evasion. *Stem Cells* 34, 2026–2039. doi: 10.1002/stem.2393

Gabrusiewicz, K., Li, X., Wei, J., Hashimoto, Y., Marisetty, A. L., Ott, M., et al. (2018). Glioblastoma stem cell-derived exosomes induce M2 macrophages and PD-L1 expression on human monocytes. *Oncoimmunology* 7 (e1412909), 1–10. doi: 10.1080/2162402X.2017.1412909

Gagner, J. P., Sarfraz, Y., Ortenzi, V., Alotaibi, F. M., Chiriboga, L. A., Tayyib, A. T., et al. (2017). Multifaceted C-X-C Chemokine Receptor 4 (CXCR4) Inhibition Interferes with Anti–Vascular Endothelial Growth Factor Therapy–Induced Glioma Dissemination. *Am. J. Pathol.* 187, 2080–2094. doi: 10.1016/j.ajpath.2017.04.020

Gholamin, S., Mitra, S. S., Feroze, A. H., Liu, J., Kahn, S. A., Zhang, M., et al. (2017). Disrupting the CD47-SIRPα anti-phagocytic axis by a humanized anti-CD47 antibody is an efficacious treatment for malignant pediatric brain tumors. *Sci. Transl. Med.* 9, 1–14. doi: 10.1126/scitranslmed.aaf2968

Ginhoux, F., and Guilliams, M. (2016). Tissue-Resident Macrophage Ontogeny and Homeostasis. *Immunity* 44, 439–449. doi: 10.1016/j.immuni.2016.02.024

Ginhoux, F., Lim, S., Hoeffel, G., Low, D., and Huber, T. (2013). Origin and differentiation of microglia. *Front. Cell. Neurosci.* 7, 45. doi: 10.3389/fncel.2013.00045

Graeber, M. B., Scheithauer, B. W., and Kreutzberg, G. W. (2002). Microglia in brain tumors. *Glia* 40, 252–259. doi: 10.1002/glia.10147

Guillon, J., Petit, C., Moreau, M., Toutain, B., Henry, C., Roché, H., et al. (2019). Regulation of senescence escape by TSP1 and CD47 following chemotherapy treatment. *Cell Death Dis*. doi: 10.1038/s41419-019-1406-7

Gupta, K., and Burns, T. C. (2018). Radiation-Induced Alterations in the Recurrent Glioblastoma Microenvironment: Therapeutic Implications. *Front. Oncol.* 8, 503. doi: 10.3389/fonc.2018.00503

Hambardzumyan, D., Gutmann, D. H., and Kettenmann, H. (2015). The role of microglia and macrophages in glioma maintenance and progression. *Nat. Neurosci.* 19, 20. doi: 10.1038/nn.4185

Hanahan, D., Weinberg, R. A., Adams, J. M., Cory, S., Aguirre-Ghiso, J. A., Ahmed, Z., et al. (2011). Hallmarks of cancer: the next generation. *Cell* 144, 646–674. doi: 10.1016/j.cell.2011.02.013

Hardee, M. E., Marciscano, A. E., Medina-Ramirez, C. M., Zagzag, D., Narayana, A., Lonning, S. M., et al. (2012). Resistance of glioblastoma-initiating cells to radiation mediated by the tumor microenvironment can be abolished by inhibiting transforming growth factor-β. *Cancer Res.* 72, 4119–4129. doi: 10.1158/0008-5472.CAN-12-0546

Harshyne, L. A., Nasca, B. J., Kenyon, L. C., Andrews, D. W., and Hooper, D. C. (2016). Serum exosomes and cytokines promote a T-helper cell type 2 environment in the peripheral blood of glioblastoma patients. *Neuro. Oncol.* 18, 206–215. doi: 10.1093/neuonc/nov107

Herisson, F., Frodermann, V., Courties, G., Rohde, D., Sun, Y., Vandoorne, K., et al. (2018). Direct vascular channels connect skull bone marrow and the brain surface enabling myeloid cell migration. *Nat. Neurosci.* doi: 10.1038/s41593-018-0213-2

Hide, T., Komohara, Y., Miyasato, Y., Nakamura, H., Makino, K., Takeya, M., et al. (2018). Oligodendrocyte Progenitor Cells and Macrophages/Microglia Produce Glioma Stem Cell Niches at the Tumor Border. *EBioMedicine* 30, 94–104. doi: 10.1016/j.ebiom.2018.02.024

Hoves, S., Ooi, C.-H., Wolter, C., Sade, H., Bissinger, S., Schmittnaegel, M., et al. (2018). Rapid activation of tumor-associated macrophages boosts preexisting tumor immunity. *J. Exp. Med*. doi: 10.1084/jem.20171440

Hu, X., Li, P., Guo, Y., Wang, H., Leak, R. K., Chen, S., et al. (2012). Microglia/macrophage polarization dynamics reveal novel mechanism of injury expansion after focal cerebral ischemia. *Stroke* 43, 3063–3070. doi: 10.1161/STROKEAHA.112.659656

Hudson, A. L., Parker, N. R., Khong, P., Parkinson, J. F., Dwight, T., Ikin, R. J., et al. (2018). Glioblastoma Recurrence Correlates With Increased APE1 and Polarization Toward an Immuno-Suppressive Microenvironment. *Front. Oncol.* 8 (314), 1–10. doi: 10.3389/fonc.2018.00314

Hung, N. A., Eiholzer, R. A., Kirs, S., Zhou, J., Ward-Hartstonge, K., Wiles, A. K., et al. (2016). Telomere profiles and tumor-associated macrophages with different immune signatures affect prognosis in glioblastoma. *Mod. Pathol.* 29, 212–226. doi: 10.1038/modpathol.2015.156

Hussain, S. F., Yang, D., Suki, D., Aldape, K., Grimm, E., and Heimberger, A. B. (2006). The role of human glioma-infiltrating microglia/macrophages in mediating antitumor immune responses. *Neuro. Oncol.* 8, 261–279. doi: 10.1215/15228517-2006-008

Hutter, G., Theruvath, J., Graef, C. M., Zhang, M., Schoen, M. K., Manz, E. M., et al. (2019). Microglia are effector cells of CD47-SIRPα antiphagocytic axis disruption against glioblastoma. *Proc. Natl. Acad. Sci. U. S. A.* 116, 997–1006. doi: 10.1073/pnas.1721434116

Jeannin, P., Paolini, L., Adam, C., and Delneste, Y. (2018). The roles of CSFs on the functional polarization of tumor-associated macrophages. *FEBS J.* 285, 680–699. doi: 10.1111/febs.14343

Kast, R. E., Hill, Q. A., Wion, D., Mellstedt, H., Focosi, D., Karpel-Massler, G., et al. (2017). Glioblastoma-synthesized G-CSF and GM-CSF contribute to growth and immunosuppression: Potential therapeutic benefit from dapsone, fenofibrate, and ribavirin. *Tumor Biol.* 39, 1–10. doi: 10.1177/1010428317699797

Kazantseva, M., Eiholzer, R. A., Mehta, S., Taha, A., Bowie, S., Roth, I., et al. (2018). Elevation of the TP53 isoform Δ133p53β in glioblastomas: an alternative to mutant p53 in promoting tumor development. *J. Pathol.* 246, 77–88. doi: 10.1002/path.5111

Kennedy, B. C., Showers, C. R., Anderson, D. E., Anderson, L., Canoll, P., Bruce, J. N., et al. (2013). Tumor-associated macrophages in glioma: friend or foe? *J. Oncol.* 2013, 486912. doi: 10.1155/2013/486912

Kitange, G. J., Carlson, B. L., Schroeder, M. A., Decker, P. A., Morlan, B. W., Wu, W., et al. (2010). Expression of CD74 in high grade gliomas: a potential role in temozolomide resistance. *J. Neurooncol.* 100, 177–186. doi: 10.1007/s11060-010-0186-9

Kloepper, J., Riedemann, L., Amoozgar, Z., Seano, G., Susek, K., Yu, V., et al. (2016). Ang-2/VEGF bispecific antibody reprograms macrophages and resident microglia to anti-tumor phenotype and prolongs glioblastoma survival. *Proc. Natl. Acad. Sci.* 113, 4476 LP– 4481. doi: 10.1073/pnas.1525360113

Kohanbash, G., McKaveney, K., Sakaki, M., Ueda, R., Mintz, A. H., Amankulor, N., et al. (2013). GM-CSF promotes the immunosuppressive activity of glioma-infiltrating myeloid cells through interleukin-4 receptor-α. *Cancer Res.* 73, 6413–6423. doi: 10.1158/0008-5472.CAN-12-4124

Komohara, Y., Ohnishi, K., Kuratsu, J., and Takeya, M. (2008). Possible involvement of the M2 anti-inflammatory macrophage phenotype in growth of human gliomas. *J. Pathol.* 216, 15–24. doi: 10.1002/path.2370

Kong, B., Michalski, C. W., Friess, H., and Kleeff, J. (2010). Surgical procedure as an inducer of tumor angiogenesis. *Exp. Oncol.* 32, 186–189.

Kumar, R., De Mooij, T., Peterson, T. E., Kaptzan, T., Johnson, A. J., Daniels, D. J., et al. (2017). Modulating glioma-mediated myeloid-derived suppressor cell development with sulforaphane. *PloS One* 12, 1–26. doi: 10.1371/journal.pone.0179012

Latha, K., Yan, J., Yang, Y., Gressot, L. V., Kong, L.-Y., Manyam, G., et al. (2018). The Role of Fibrinogen-Like Protein 2 on Immunosuppression and Malignant Progression in Glioma. *JN7CI J. Natl. Cancer Inst.* 111, 1–9. doi: 10.1093/jnci/djy107

Leblond, M. M., Pérès, E. A., Helaine, C., Gérault, A. N., Moulin, D., Anfray, C., et al. (2017). M2 macrophages are more resistant than M1 macrophages following radiation therapy in the context of glioblastoma. *Oncotarget* 8, 72597–72612. doi: 10.18632/oncotarget.19994

Lee, J., Dang, X., Borboa, A., Coimbra, R., Baird, A., and Eliceiri, B. P. (2015). Thrombin-processed Ecrg4 recruits myeloid cells and induces antitumorigenic inflammation. *Neuro. Oncol.* 17, 685–696. doi: 10.1093/neuonc/nou302

Li, Z., Huang, Q., Chen, H., Lin, Z., Zhao, M., and Jiang, Z. (2017). Interferon Regulatory Factor 7 Promoted Glioblastoma Progression and Stemness by Modulating IL-6 Expression in Microglia. *J. Cancer* 8, 207–219. doi: 10.7150/jca.16415

Li, T.-F., Li, K., Wang, C., Liu, X., Wen, Y., Xu, Y.-H., et al. (2017). Harnessing the cross-talk between tumor cells and tumor-associated macrophages with a nano-drug for modulation of glioblastoma immune microenvironment. *J. Control. Release* 268, 128–146. doi: 10.1016/j.jconrel.2017.10.024

Li,F., Lv, B., Liu, Y., Hua, T., Han, J., Sun, C., et al. (2017). Blocking the CD47-SIRPα axis by delivery of anti-CD47 antibody induces antitumor effects in glioma and glioma stem cells. *Oncoimmunology* 7, e1391973–e1391973. doi: 10.1080/2162402X.2017.1391973

Li, Y., Dong, X., Cai, J., Yin, S., Sun, Y., Yang, D., et al. (2018). SERPINA3 induced by astroglia/microglia co-culture facilitates glioblastoma stem-like cell invasion. *Oncol. Lett.* 15, 285–291. doi: 10.3892/ol.2017.7275

Lin, J. D., Nishi, H., Poles, J., Niu, X., McCauley, C., Rahman, K., et al. (2019). Single-cell analysis of fate-mapped macrophages reveals heterogeneity, including stem-like properties, during atherosclerosis progression and regression. *JCI Insight* 4 (e124574), 1–15. doi: 10.1172/jci.insight.124574

Lisi, L., Ciotti, G. M. P., Braun, D., Kalinin, S., Currò, D., Dello Russo, C., et al. (2017). Expression of iNOS, CD163 and ARG-1 taken as M1 and M2 markers of microglial polarization in human glioblastoma and the surrounding normal parenchyma. *Neurosci. Lett.* 645, 106–112. doi: 10.1016/j.neulet.2017.02.076

Locati,M., Curtale,G., and Mantovani, A. (2020). Diversity, Mechanisms, and Significance of Macrophage Plasticity. *Annu. Rev. Pathol. Mech. Dis* 15, 123–147. doi: 10.1146/annurev-pathmechdis-012418-012718

Louis, D. N., Ohgaki, H., Wiestler, O. D., Cavenee, W. K., Burger, P. C., Jouvet, A., et al. (2007). The 2007 WHO classification of tumours of the central nervous system. *Acta Neuropathol.* 114, 97–109. doi: 10.1007/s00401-007-0243-4

Louis, D. N., Perry, A., Reifenberger, G., von Deimling, A., Figarella-Branger, D., Cavenee, W. K., et al. (2016). The 2016 World Health Organization Classification of Tumors of the Central Nervous System: a summary. *Acta Neuropathol.* 131, 803–820. doi: 10.1007/s00401-016-1545-1

Lu-Emerson, C., Snuderl, M., Kirkpatrick, N. D., Goveia, J., Davidson, C., Huang, Y., et al. (2013). Increase in tumor-associated macrophages after antiangiogenic therapy is associated with poor survival among patients with recurrent glioblastoma. *Neuro. Oncol.* 15, 1079–1087. doi: 10.1093/neuonc/not082

Müller, A., Brandenburg, S., Turkowski, K., Müller, S., and Vajkoczy, P. (2015). Resident microglia, and not peripheral macrophages, are the main source of brain tumor mononuclear cells. *Int. J. Cancer* 137, 278–288. doi: 10.1002/ijc.29379

Martinez, F. O., and Gordon, S. (2014). The M1 and M2 paradigm of macrophage activation: time for reassessment. *F1000Prime Rep.* 6, 13. doi: 10.12703/P6-13

Matias, D., Balça-Silva, J., da Graça, G. C., Wanjiru, C. M., Macharia, L. W., Nascimento, C. P., et al. (2018). Microglia/Astrocytes–Glioblastoma Crosstalk: Crucial Molecular Mechanisms and Microenvironmental Factors. *Front. Cell. Neurosci.* 12, 235. doi: 10.3389/fncel.2018.00235

Mieczkowski, J., Kocyk, M., Nauman, P., Gabrusiewicz, K., Sielska, M., Przanowski, P., et al. (2015). Down-regulation of IKKβ expression in glioma-infiltrating microglia/macrophages is associated with defective inflammatory/immune gene responses in glioblastoma. *Oncotarget* 6, 33077–33090. doi: 10.18632/oncotarget.5310

Murray, P. J., Allen, J. E., Biswas, S. K., Fisher, E. A., Gilroy, D. W., Goerdt, S., et al. (2014). Macrophage activation and polarization: nomenclature and experimental guidelines. *Immunity* 41, 14–20. doi: 10.1016/j.immuni.2014.06.008

NCT00003232 (2004). Combination Chemotherapy in Treating Pain in Patients With Hormone Refractory Metastatic Prostate Cancer. ClinicalTrials.gov. Available at https://clinicaltrials.gov/ct2/show/NCT00003232

NCT00009945 (2003). Clodronate With or Without Chemotherapy and/or Hormonal Therapy in Treating Women With Stage I or Stage II Breast Cancer. ClinicalTrials.gov. Available at: https://clinicaltrials.gov/ct2/show/NCT00009945

NCT00127205 (2005). S0307 Phase III Trial of Bisphosphonates as Adjuvant Therapy for Primary Breast Cancer. ClinicalTrials.gov. Available at: https://clinicaltrials.gov/ct2/show/NCT00127205

NCT00301873 (2006). Zoledronate in Preventing Osteoporosis in Patients With Primary Malignant Glioma. ClinicalTrials.gov. Available at: https://clinicaltrials.gov/ct2/show/NCT00301873

NCT00537368 (2007). First Study of the Safety of CNTO 888 in Patients With Solid Tumors. ClinicalTrials.gov. Available at: https://clinicaltrials.gov/ct2/show/NCT00537368

NCT00633529 (2008). Safety of Adding IMO-2055 to Erlotinib + Bevacizumab in 2nd Line Treatment for Patients With NSCLC. ClinicalTrials.gov. Available at: https://clinicaltrials.gov/ct2/show/NCT00633529

NCT00719199 (2008). Study of FOLFIRI Plus Cetuximab Plus IMO-2055 in Patients With Colorectal Cancer. ClinicalTrials.gov. Available at: https://clinicaltrials.gov/ct2/show/NCT00719199

NCT00821652 (2009). Randomized, Double Blind, Placebo-controlled Topical Resiquimod Adjuvant for NY-ESO-1 Protein Vaccination. ClinicalTrials.gov. Available at: https://clinicaltrials.gov/ct2/show/NCT00821652

NCT00885326 (2009). N2007-02:Bevacizumab,Cyclophosphamide,& Zoledronic Acid in Patients W/ Recurrent or Refractory High-Risk Neuroblastoma. ClinicalTrials.gov. Available at: https://clinicaltrials.gov/ct2/show/NCT00885326

NCT00899574 (2009). Imiquimod for Breast Cancer Patients With Chest Wall Recurrence or Skin Metastases. ClinicalTrials.gov. Available at: https://clinicaltrials.gov/ct2/show/NCT00899574

NCT00909142 (2009). Bonefos and the Consumption of Analgesics (BICAM). ClinicalTrials.gov. Available at: https://clinicaltrials.gov/ct2/show/NCT00909142

NCT00992186 (2009). A Study of the Safety and Efficacy of Single-agent Carlumab (an Anti-Chemokine Ligand 2 [CCL2]) in Participants With Metastatic Castrate-Resistant Prostate Cancer. ClinicalTrials.gov.Available at: https://clinicaltrials.gov/ct2/show/NCT00992186

NCT01004861 (2009). Safety Study of PLX108-01 in Patients With Solid Tumors. ClinicalTrials.gov. Available at: https://clinicaltrials.gov/ct2/show/NCT01004861

NCT01015560 (2009). S0916, MLN1202 in Treating Patients With Bone Metastases. ClinicalTrials.gov. Available at: https://clinicaltrials.gov/ct2/show/NCT01015560

NCT01040832 (2009). EMD 1201081 in Combination With Cetuximab in Second-Line Cetuximab-Naïve Subjects With Recurrent or Metastatic Squamous Cell Carcinoma of the Head and Neck. ClinicalTrials.gov. Available at: https://clinicaltrials.gov/ct2/show/NCT01040832

NCT01198457 (2010). Study to Investigate Adherence of Patients to Clodronate (Bonefos) Treatment (BONA). ClinicalTrials.gov. Available at: https://clinicaltrials.gov/ct2/show/NCT01198457

NCT01204996 (2010). A Study of the Safety and Efficacy of CNTO 888 in Combination With SoC (Standard of Care) Chemotherapy in Patients With Solid Tumors. ClinicalTrials.gov. Available at: https://clinicaltrials.gov/ct2/show/NCT01204996

NCT01294293 and NCT01334177 (2011). TLR8 Agonist VTX-2337 and Pegylated Liposomal Doxorubicin Hydrochloride or Paclitaxel in Treating Patients With Recurrent or Persistent Ovarian Epithelial, Fallopian Tube, or Peritoneal Cavity Cancer. ClinicalTrials.gov. Available at: https://clinicaltrials.gov/ct2/show/NCT01294293

NCT01316822 (2011). A Study of ARRY-382 in Patients With Selected Advanced or Metastatic Cancers. ClinicalTrials.gov. Available at: https://clinicaltrials.gov/ct2/show/NCT01316822

NCT01345019 (2011). Denosumab Compared to Zoledronic Acid in the Treatment of Bone Disease in Patients With Multiple Myeloma. ClinicalTrials.gov.

NCT01346358 (2011). A Study of IMC-CS4 in Subjects With Advanced Solid Tumors. ClinicalTrials.gov. Available at: https://clinicaltrials.gov/ct2/show/NCT01346358

NCT01349036 (2011). A Phase 2 Study of PLX3397 in Patients With Recurrent Glioblastoma. ClinicalTrials.gov. Available at: https://clinicaltrials.gov/ct2/show/NCT01349036

NCT01421017 (2011). Toll-like Receptor (TLR) 7 Agonist, Cyclophosphamide, and Radiotherapy for Breast Cancer With Skin Metastases. ClinicalTrials.gov. Available at: https://clinicaltrials.gov/ct2/show/NCT01421017

NCT01494688 (2011). A Study of RO5509554 as Monotherapy and in Combination With Paclitaxel in Participants With Advanced Solid Tumors. ClinicalTrials.gov. Available at: https://clinicaltrials.gov/ct2/show/NCT01494688

NCT01561911 and NCT00607048. (2012) A Phase I Study of the Chimeric Anti-CD40 Monoclonal Antibody ChiLob 7/4 to Treat Advanced Malignancies Refractory to Conventional Anti-cancer Treatment. ClinicalTrials.gov. Available at: https://clinicaltrials.gov/ct2/show/NCT01561911

NCT02216409 (2014). Phase 1 Trial of Hu5F9-G4, a CD47-targeting Antibody. ClinicalTrials.gov. Available at https://clinicaltrials.gov/ct2/show/NCT02216409

NCT02252146. Dose Escalation Study in Patients With Relapsed or Refractory DLBCL and MyD88 L265P Mutation. ClinicalTrials.gov.

NCT02254772 (2014). A Phase I/II Study of Intratumoral Injection of SD-101. ClinicalTrials.gov. Available at: https://clinicaltrials.gov/ct2/show/NCT02254772

NCT02304393 (2014). A Study of Selicrelumab (RO7009789) in Combination With Atezolizumab in Participants With Locally Advanced and/or Metastatic Solid Tumors. ClinicalTrials.gov.Available at: https://clinicaltrials.gov/ct2/show/NCT02304393

NCT02367196 (2015). A Phase 1, Dose Finding Study of CC-90002 in Subjects With Advanced Solid and Hematologic Cancers. ClinicalTrials.gov. Available at https://clinicaltrials.gov/ct2/show/NCT02367196

NCT02371369 (2015). Phase 3 Study of Pexidartinib for Pigmented Villonodular Synovitis (PVNS) or Giant Cell Tumor of the Tendon Sheath (GCT-TS) (ENLIVEN). ClinicalTrials.gov. Available at: https://clinicaltrials.gov/ct2/show/NCT02371369

NCT02431559 (2015). A Phase 1/2 Study of Motolimod (VTX-2337) and MEDI4736 in Subjects With Recurrent, Platinum-Resistant Ovarian Cancer for Whom Pegylated Liposomal Doxorubicin (PLD) is Indicated. ClinicalTrials.gov. Available at: https://clinicaltrials.gov/ct2/show/NCT02431559

NCT02452424 (2015). A Combination Clinical Study of PLX3397 and Pembrolizumab To Treat Advanced Melanoma and Other Solid Tumors. ClinicalTrials.gov. Available at: https://clinicaltrials.gov/ct2/show/NCT02452424

NCT02452697 (2015). Ph2 NK Cell Enriched DCIs w/wo RLR9 Agonist, DUK-CPG-001 From Donors Following Allogeneic SCT (NK-DCI). ClinicalTrials.gov. Available at: https://clinicaltrials.gov/ct2/show/NCT02452697

NCT02482168 (2015). Study of the CD40 Agonistic Monoclonal Antibody APX005M. ClinicalTrials.gov. Available at: https://clinicaltrials.gov/ct2/show/NCT02482168

NCT02526017 (2015). *Study of Cabiralizumab in Combination With Nivolumab in Patients With Selected Advanced Cancers (FPA008-003)*. ClinicalTrials.gov. Available at: https://clinicaltrials.gov/ct2/show/NCT02526017

NCT02663518 (2016). A Trial of TTI-621 for Patients With Hematologic Malignancies and Selected Solid Tumors. ClinicalTrials.gov. Available at: https://clinicaltrials.gov/ct2/show/NCT02663518

NCT02678338 (2016). CAMELLIA: Anti-CD47 Antibody Therapy in Haematological Malignancies. ClinicalTrials.gov. Available at: https://clinicaltrials.gov/ct2/show/NCT02678338

NCT02718911 (2016). A Study of LY3022855 in Combination With Durvalumab or Tremelimumab in Participants With Advanced Solid Tumors. ClinicalTrials.gov. Available at: https://clinicaltrials.gov/ct2/show/NCT02718911

NCT02732938 (2016). Ph1b/2 Study of PF-04136309 in Combination With Gem/Nab-P in First-line Metastatic Pancreatic Patients (CCR2i). ClinicalTrials.gov. Available at: https://clinicaltrials.gov/ct2/show/NCT02732938

NCT02777710 (2016). Evaluation of Safety and Activity of an Anti-PDL1 Antibody (DURVALUMAB) Combined With CSF-1R TKI (PEXIDARTINIB) in Patients With Metastatic/Advanced Pancreatic or Colorectal Cancers (MEDIPLEX). ClinicalTrials.gov. Available at: https://clinicaltrials.gov/ct2/show/NCT02777710

NCT02829723 (2016). Phase I/II Study of BLZ945 Single Agent or BLZ945 in Combination With PDR001 in Advanced Solid Tumors. ClinicalTrials.gov. Available at: https://clinicaltrials.gov/ct2/show/NCT02829723

NCT02927964 (2016). TLR9 Agonist SD-101, Ibrutinib, and Radiation Therapy in Treating Patients With Relapsed or Refractory Grade 1-3A Follicular Lymphoma. ClinicalTrials.gov. Available at: https://clinicaltrials.gov/ct2/show/NCT02927964

NCT02953509 (2016). Trial of Hu5F9-G4 in Combination With Rituximab in Relapsed/Refractory B-cell Non-Hodgkin's Lymphoma. ClinicalTrials.gov. Available at: https://clinicaltrials.gov/ct2/show/NCT02953509

NCT02953782 (2016). Trial of Hu5F9-G4 in Combination With Cetuximab in Patients With Solid Tumors and Advanced Colorectal Cancer. ClinicalTrials.gov. Available at: https://clinicaltrials.gov/ct2/show/NCT02953782

NCT03007732 (2017). Pembrolizumab in Combination With Intratumoral SD-101 Therapy. ClinicalTrials.gov. Available at: https://clinicaltrials.gov/ct2/show/NCT03007732

NCT03013218 (2017). A Study of ALX148 in Patients With Advanced Solid Tumors and Lymphoma. ClinicalTrials.gov. Available at: https://clinicaltrials.gov/ct2/show/NCT03013218

NCT03069469 (2017). Study of DCC-3014 in Patients With Advanced Malignancies. ClinicalTrials.gov. Available at: https://clinicaltrials.gov/ct2/show/NCT03069469

NCT03101254 (2017). LY3022855 With BRAF/MEK Inhibition in Patients With Melanoma. ClinicalTrials.gov. Available at: https://clinicaltrials.gov/ct2/show/NCT03101254

NCT03123783 (2017). CD40 Agonistic Antibody APX005M in Combination With Nivolumab. ClinicalTrials.gov.

NCT03153410 (2017). Pilot Study With CY, Pembrolizumab, GVAX, and IMC-CS4 (LY3022855) in Patients With Borderline Resectable Adenocarcinoma of the Pancreas. ClinicalTrials.gov. Available at: https://clinicaltrials.gov/ct2/show/NCT03153410

NCT03165994 (2017). APX005M With Concurrent Chemoradiation for Resectable Esophageal and Gastroesophageal Junction Cancers. ClinicalTrials.gov. Available at: https://clinicaltrials.gov/ct2/show/NCT03165994

NCT03238027 (2017). A Phase 1 Study to Investigate SNDX-6352 Alone or in Combination With Durvalumab in Patients With Solid Tumors. ClinicalTrials.gov. Available at: https://clinicaltrials.gov/ct2/show/NCT03238027

NCT03248479 (2017). Hu5F9-G4 Monotherapy or Hu5F9-G4 in Combination With Azacitidine in Patients With Hematological Malignancies. ClinicalTrials.gov. Available at: https://clinicaltrials.gov/ct2/show/NCT03248479

NCT03301896 (2017). Study of the Safety and Efficacy of LHC165 Single Agent and in Combination With PDR001 in Patients With Advanced Malignancies. ClinicalTrials.gov. Available at: https://clinicaltrials.gov/ct2/show/NCT03301896

NCT03329950 (2017). A Study of CDX-1140 as Monotherapy or in Combination in Patients With Advanced Malignancies. ClinicalTrials.gov. Available at: https://clinicaltrials.gov/ct2/show/NCT03329950

NCT03389802 (2018). Phase I Study of APX005M in Pediatric CNS Tumors. ClinicalTrials.gov. Available at: https://clinicaltrials.gov/ct2/show/NCT03389802

NCT03410901 (2018). TLR9 Agonist SD-101, Anti-OX40 Antibody BMS 986178, and Radiation Therapy in Treating Patients With Low-Grade B-Cell Non-Hodgkin Lymphomas. ClinicalTrials.gov. Available at: https://clinicaltrials.gov/ct2/show/NCT03410901

NCT03416335 (2018). A Study of DSP-0509 in Patients With Advanced Solid Tumors to Determine the Safety and the Pharmacokinetic Profile. ClinicalTrials.gov. Available at: https://clinicaltrials.gov/ct2/show/NCT03416335

NCT03435640 (2018). A Study of NKTR-262 in Combination With NKTR-214 and With NKTR-214 Plus Nivolumab in Patients With Locally Advanced or Metastatic Solid Tumor Malignancies (REVEAL). ClinicalTrials.gov. Available at: https://clinicaltrials.gov/ct2/show/NCT03435640

NCT03496662 (2018). BMS-813160 With Nivolumab and Gemcitabine and Nab-paclitaxel in Borderline Resectable and Locally Advanced Pancreatic Ductal Adenocarcinoma (PDAC). ClinicalTrials.gov. Available at: https://clinicaltrials.gov/ct2/show/NCT03496662

NCT03502330 (2018). APX005M With Nivolumab and Cabiralizumab in Advanced Melanoma, Non-small Cell Lung Cancer or Renal Cell Carcinoma. ClinicalTrials.gov. Available at: https://clinicaltrials.gov/ct2/show/NCT03502330

NCT03507699 (2018). Combined Immunotherapy and Radiosurgery for Metastatic Colorectal Cancer. ClinicalTrials.gov. Available at: https://clinicaltrials.gov/ct2/show/NCT03507699

NCT03512340 (2018). Study of SRF231 in Patients With Advanced Solid and Hematologic Cancers. ClinicalTrials.gov. Available at: https://clinicaltrials.gov/ct2/show/NCT03512340

NCT03530683 (2018). A Trial of TTI-622 in Patients With Advanced Relapsed or Refractory Lymphoma or Myeloma (TTI-622-01). ClinicalTrials.gov. Available at: https://clinicaltrials.gov/ct2/show/NCT03530683

NCT03557970 and NCT02880371 (2018). CSF1R Inhibitor JNJ-40346527 in Treating Participants With Relapsed or Refractory Acute Myeloid Leukemia. ClinicalTrials.gov. Available at: https://clinicaltrials.gov/ct2/show/NCT03557970

NCT03618641 (2018). CMP-001 in Combo With Nivolumab in Stage IIIB/C/D Melanoma Patients With Clinically Apparent Lymph Node Disease. ClinicalTrials.gov. Available at: https://clinicaltrials.gov/ct2/show/NCT03618641

NCT03694977 (2018). Biomarker Study of PDR001 in Combination With MCS110 in Gastric Cancer. ClinicalTrials.gov. Available at: https://clinicaltrials.gov/ct2/show/NCT03694977

NCT03697564 (2018). Nivolumab + Cabiralizumab + Gemcitabine Versus Gemcitabine in Patients With Stage IV Pancreatic Cancer Achieving Disease Control in Response to First-line Chemotherapy (GemCaN Trial). ClinicalTrials.gov.Available at: https://clinicaltrials.gov/ct2/show/NCT03697564

NCT03717103 (2018). A Phase 1 Study Evaluating the Safety, Tolerability, and Initial Efficacy of Recombinant Human Anti-cluster Differentiation Antigen 47 (CD47) Monoclonal Antibody Injection (IBI188) in Patients With Advanced Malignancies. ClinicalTrials.gov. Available at: https://clinicaltrials.gov/ct2/show/NCT03717103

NCT03763149 (2018). A Study Evaluating the Safety, Tolerability, and Initial Efficacy of Recombinant Human Anti-cluster Differentiation Antigen 47 (CD47) Monoclonal Antibody Injection (IBI188) in Patients With Advanced Malignant Tumors and Lymphomas. ClinicalTrials.gov.

NCT03778879 (2018). Pre-operative Stereotactic Body Radiation Therapy for Pancreatic Adenocarcinoma With or Without CCX872-B. ClinicalTrials.gov. Available at: https://clinicaltrials.gov/ct2/show/NCT03778879

Nielsen, S. R., and Schmid, M. C. (2017). Macrophages as Key Drivers of Cancer Progression and Metastasis. *Mediators Inflamm.* 2017. 9624760, 1–11. doi: 10.1155/2017/9624760

Nishie, A., Ono, M., Shono, T., Fukushi, J., Otsubo, M., Onoue, H., et al. (1999). Macrophage Infiltration and Heme Oxygenase-1 Expression Correlate with Angiogenesis in Human Gliomas. *Clin. Cancer Res.* 5, 1107 LP–1113.

Nowak, A. K., Millward, M. J., Cook, A. M., McDonnell, A. M., Creaney, J., Lake, R. A., et al. (2015). A phase 1b clinical trial of the CD40-activating antibody CP-870,893 in combination with cisplatin and pemetrexed in malignant pleural mesothelioma. *Ann. Oncol.* 26, 2483–2490. doi: 10.1093/annonc/mdv387

Noy, R., and Pollard, J. W. (2014). Tumor-Associated Macrophages: From Mechanisms to Therapy. *Immunity* 41, 49–61. doi: 10.1016/j.immuni.2014.06.010

Nywening, T. M., Wang-Gillam, A., Sanford, D. E., Belt, B. A., Panni, R. Z., Cusworth, B. M., et al. (2016). Targeting tumour-associated macrophages with CCR2 inhibition in combination with FOLFIRINOX in patients with borderline resectable and locally advanced pancreatic cancer: a single-centre, open-label, dose-finding, non-randomised, phase 1b trial. *Lancet Oncol.* 17, 651–662. doi: 10.1016/S1470-2045(16)00078-4

Okubo, M., Kioi, M., Nakashima, H., Sugiura, K., Mitsudo, K., Aoki, I., et al. (2016). M2-polarized macrophages contribute to neovasculogenesis, leading to relapse of oral cancer following radiation. *Sci. Rep.* 6, 1–12. doi: 10.1038/srep27548

Paterson, A. H. G., Anderson, S. J., Lembersky, B. C., Fehrenbacher, L., Falkson, C. I., King, K. M., et al. (2012). Oral clodronate for adjuvant treatment of operable breast cancer (National Surgical Adjuvant Breast and Bowel Project protocol B-34): a multicentre, placebo-controlled, randomised trial. *Lancet Oncol.* 13, 734–742. doi: 10.1016/S1470-2045(12)70226-7

Perry, C. J., et al. (2018). Myeloid-targeted immunotherapies act in synergy to induce inflammation and antitumor immunity. *J. Exp. Med.* 215, 877–893. doi: 10.1084/jem.20171435

Perry, C. J., Muñoz-Rojas, A. R., Meeth, K. M., Kellman, L. N., Amezquita, R. A., Thakral, D., et al. (2013). Phase 2 study of carlumab (CNTO 888), a human monoclonal antibody against CC-chemokine ligand 2 (CCL2), in metastatic castration-resistant prostate cancer. *Invest. New Drugs* 31, 760–768. doi: 10.1007/s10637-012-9869-8

Poh, A. R., and Ernst, M. (2018). Targeting Macrophages in Cancer: From Bench to Bedside. *Front. Oncol.* 8, 49. doi: 10.3389/fonc.2018.00049

Poon, C. C., Sarkar, S., Yong, V. W., and Kelly, J. J. P. (2017). Glioblastoma-associated microglia and macrophages: Targets for therapies to improve prognosis. *Brain* 140, 1548–1560. doi: 10.1093/brain/aww355

Pyonteck, S. M., Akkari, L., Schuhmacher, A. J., Bowman, R. L., Sevenich, L., Quail, D. F., et al. (2013). CSF-1R inhibition alters macrophage polarization and blocks glioma progression. *Nat. Med.* 19, 1264. doi: 10.1038/nm.3337

Qian, J., Luo, F., Yang, J., Liu, J., Liu, R., Wang, L., et al. (2018). TLR2 Promotes Glioma Immune Evasion by Downregulating MHC Class II Molecules in Microglia. *Cancer Immunol. Res.* 6, 1220 LP–1233. doi: 10.1158/2326-6066.CIR-18-0020

Quail, D. F., and Joyce, J. A. (2013). Microenvironmental regulation of tumor progression and metastasis. *Nat. Med.* 19, 1423–1437. doi: 10.1038/nm.3394

Quail, D. F., and Joyce, J. A. (2017). The Microenvironmental Landscape of Brain Tumors. *Cancer Cell* 31, 326–341. doi: 10.1016/j.ccell.2017.02.009

Manda, S. V., Kataria, Y., Tatireddy, B. R., Ramakrishnan, B., Ratnam, B. G., Lath, R., et al. (2018). Exosomes as a biomarker platform for detecting epidermal growth factor receptor–positive high-grade gliomas. *J. Neurosurg.* 128, 1091–1101. doi: 10.3171/2016.11.jns161187

Roesch, S., Rapp, C., Dettling, S., and Herold-Mende, C. (2018). When Immune Cells Turn Bad-Tumor-Associated Microglia/Macrophages in Glioma. *Int. J. Mol. Sci.* 19, 436. doi: 10.3390/ijms19020436

Rossi, M. L., Hughes, J. T., Esiri, M. M., Coakham, H. B., and Brownell, D. B. (1987). Immunohistological study of mononuclear cell infiltrate in malignant gliomas. *Acta Neuropathol.* 74, 269–277. doi: 10.1007/BF00688191

Ruzsa, A., Sen, M., Evans, M., Lee, L. W., Hideghety, K., Rottey, S., et al. (2014). Phase 2, open-label, 1:1 randomized controlled trial exploring the efficacy of EMD 1201081 in combination with cetuximab in second-line cetuximab-naïve patients with recurrent or metastatic squamous cell carcinoma of the head and neck (R/M SCCHN). *Invest. New Drugs* 32, 1278–1284. doi: 10.1007/s10637-014-0117-2

Séhédic, D., Chourpa, I., Tétaud, C., Griveau, A., Loussouarn, C., Avril, S., et al. (2017). Locoregional confinement and major clinical benefit of188re-loaded CXCR4-targeted nanocarriers in an orthotopic human to mouse model of glioblastoma. *Theranostics* 7, 4517–4536. doi: 10.7150/thno.19403

Sørensen, M. D., Dahlrot, R. H., Boldt, H. B., Hansen, S., and Kristensen, B. W. (2018). Tumour-associated microglia/macrophages predict poor prognosis in high-grade gliomas and correlate with an aggressive tumour subtype. *Neuropathol. Appl. Neurobiol.* 44, 185–206. doi: 10.1111/nan.12428

Sadahiro, H., Kang, K.-D., Gibson, J. T., Minata, M., Yu, H., Shi, J., et al. (2018). Activation of the Receptor Tyrosine Kinase AXL Regulates the Immune Microenvironment in Glioblastoma. *Cancer Res.* 78, 3002 LP–3013. doi: 10.1158/0008-5472.CAN-17-2433

Saha, D., Martuza, R. L., and Rabkin, S. D. (2017). Macrophage Polarization Contributes to Glioblastoma Eradication by Combination Immunovirotherapy and Immune Checkpoint Blockade. *Cancer Cell* 32, 253–267.e5. doi: 10.1016/j.ccell.2017.07.006

Sandhu, S. K., Papadopoulos, K., Fong, P. C., Patnaik, A., Messiou, C., Olmos, D., et al. (2013). A first-in-human, first-in-class, phase i study of carlumab (CNTO 888), a human monoclonal antibody against CC-chemokine ligand 2 in patients with solid tumors. *Cancer Chemother. Pharmacol.* 71, 1041–1050. doi: 10.1007/s00280-013-2099-8

Schiffer, D., Annovazzi, L., Casalone, C., Corona, C., and Mellai, M. (2018). Glioblastoma: Microenvironment and Niche Concept. *Cancers* 11 (5), 1–17. doi: 10.3390/cancers11010005

Shi, Y., Ping, Y.-F., Zhou, W., He, Z.-C., Chen, C., Bian, B.-S.-J., et al. (2017). Tumour-associated macrophages secrete pleiotrophin to promote PTPRZ1 signalling in glioblastoma stem cells for tumour growth. *Nat. Commun.* 8, 15080. doi: 10.1038/ncomms15080

Shoji,T., Saito, R., Chonan, M., Shibahara, I., Sato, A., Kanamori, M., et al. (2016). Local convection-enhanced delivery of an anti-CD40 agonistic monoclonal antibody induces antitumor effects in mouse glioma models. *Neuro. Oncol.* 18, 1120–1128. doi: 10.1093/neuonc/now023

Sica, A., Erreni, M., Allavena, P., and Porta, C. (2015). Macrophage polarization in pathology. *Cell. Mol. Life Sci.* 72, 4111–4126. doi: 10.1007/s00018-015-1995-y

Sikic, B. I., Lakhani, N. J., Patnaik, A., Shah, S., Chandana, S. R., Rasco, D. W., et al. (2018). A first-in-class, first-in-human phase 1 pharmacokinetic (PK) and pharmacodynamic (PD) study of Hu5F9-G4, an anti-CD47 monoclonal antibody (mAb), in patients with advanced solid tumors. *J. Clin. Oncol.* 36, 3002. doi: 10.1200/JCO.2018.36.15_suppl.3002

Smith, D. A., Conkling, P., Richards, D. A., Nemunaitis, J. J., Boyd, T. E., Mita, A. C., et al. (2014). Antitumor activity and safety of combination therapy with the Toll-like receptor 9 agonist IMO-2055, erlotinib, and bevacizumab in advanced or metastatic

non-small cell lung cancer patients who have progressed following chemotherapy. *Cancer Immunol. Immunother.* 63, 787–796. doi: 10.1007/s00262-014-1547-6

Strachan, D. C., Ruffell, B., Oei, Y., Bissell, M. J., Coussens, L. M., Pryer, N., et al. (2013). CSF1R inhibition delays cervical and mammary tumor growth in murine models by attenuating the turnover of tumor-associated macrophages and enhancing infiltration by CD8+T cells. *Oncoimmunology* 2, 1–12. doi: 10.4161/onci.26968

Stratton, J. A., Holmes, A., Rosin, N. L., Sinha, S., Vohra, M., Burma, N. E., et al. (2018). Macrophages Regulate Schwann Cell Maturation after Nerve Injury. *Cell Rep.* 24, 2561–2572.e6. doi: 10.1016/j.celrep.2018.08.004

Stupp, R., Mason, W. P., van den Bent, M. J., Weller, M., Fisher, B., Taphoorn, M. J. B., et al. (2005). Radiotherapy plus Concomitant and Adjuvant Temozolomide for Glioblastoma. *N. Engl. J. Med.* 352, 987–996. doi: 10.1056/NEJMoa043330

Stupp, R., Hegi, M. E., Mason, W. P., van den Bent, M. J., Taphoorn, M. J. B., Janzer, R. C., et al. (2009). Effects of radiotherapy with concomitant and adjuvant temozolomide versus radiotherapy alone on survival in glioblastoma in a randomised phase III study: 5-year analysis of the EORTC-NCIC trial. *Lancet Oncol.* 10, 459–466. doi: 10.1016/S1470-2045(09)70025-7

Szulzewsky, F., Pelz, A., Feng, X., Synowitz, M., Markovic, D., Langmann, T., et al. (2015). Glioma-associated microglia/macrophages display an expression profile different from M1 and M2 polarization and highly express Gpnmb and Spp1. *PloS One* 10, e0116644–e0116644. doi: 10.1371/journal.pone.0116644

Tabatabaei,P., Visse, E., Bergström, P., Brännström, T., Siesjö, P., and Bergenheim, A. T. (2017). Radiotherapy induces an immediate inflammatory reaction in malignant glioma: a clinical microdialysis study. *J. Neurooncol.* 131, 83–92. doi: 10.1007/s11060-016-2271-1

Tamura, R., Ohara, K., Sasaki, H., Morimoto, Y., Kosugi, K., Yoshida, K., et al. (2018). Difference in Immunosuppressive Cells Between Peritumoral Area and Tumor Core in Glioblastoma. *World Neurosurg.* 120, e601–e610. doi: 10.1016/j.wneu.2018.08.133

Tap, W. D., Wainberg, Z. A., Anthony, S. P., Ibrahim, P. N., Zhang, C., Healey, J. H., et al. (2015). Structure-Guided Blockade of CSF1R Kinase in Tenosynovial Giant-Cell Tumor. *N. Engl. J. Med.* 373, 428–437. doi: 10.1056/NEJMoa1411366

Thomas, A. C., and Mattila, J. T. (2014). 'Of mice and men': arginine metabolism in macrophages. *Front. Immunol.* 5, 479. doi: 10.3389/fimmu.2014.00479

Turkowski, K., Brandenburg, S., Mueller, A., Kremenetskaia, I., Bungert, A. D., Blank, A., et al. (2018). VEGF as a modulator of the innate immune response in glioblastoma. *Glia* 66, 161–174. doi: 10.1002/glia.23234

Van Acker, H. H., Anguille, S., Willemen, Y., Smits, E. L., and Van Tendeloo, V. F. (2016). Bisphosphonates for cancer treatment: Mechanisms of action and lessons from clinical trials. *Pharmacol. Ther.* 158, 24–40. doi: 10.1016/j.pharmthera.2015.11.008

Van Der Vos, K. E., Abels, E. R., Zhang, X., Lai, C., Carrizosa, E., Oakley, D., et al. (2016). Directly visualized glioblastoma-derived extracellular vesicles transfer RNA to microglia/macrophages in the brain. *Neuro. Oncol.* 18, 58–69. doi: 10.1093/neuonc/nov244

Vonderheide, R. H., Burg, J. M., Mick, R., Trosko, J. A., Li, D., Shaik, M. N., et al. (2013). Phase i study of the CD40 agonist antibody CP-870,893 combined with carboplatin and paclitaxel in patients with advanced solid tumors. *Oncoimmunology* 2, 1–10. doi: 10.4161/onci.23033

Wagner, S., Czub, S., Greif, M., Vince, G. H., Suss, N., Kerkau, S., et al. (1999). Microglial/macrophage expression of interleukin 10 in human glioblastomas. *Int. J. Cancer* 82, 12–16. doi: 10.1002/(SICI)1097-0215(19990702)82:1<12::AID-IJC3>3.0.CO;2-O

Walentynowicz, K. A., Ochocka, N., Pasierbinska, M., Wojnicki, K., Stepniak, K., Mieczkowski, J., et al. (2018). In Search for Reliable Markers of Glioma-Induced Polarization of Microglia. *Front. Immunol.* 9, 1329. doi: 10.3389/fimmu.2018.01329

Wang, S. C., Yu, C. F., Hong, J. H., Tsai, C. S., and Chiang, C. S. (2013). Radiation Therapy-Induced Tumor Invasiveness Is Associated with SDF-1-Regulated Macrophage Mobilization and Vasculogenesis. *PloS One* 8 (e69182), 1–10. doi: 10.1371/journal.pone.0069182

Wang, Y., Liu, T., Yang, N., Xu, S., Li, X., and Wang, D. (2016). Hypoxia and macrophages promote glioblastoma invasion by the CCL4-CCR5 axis. *Oncol. Rep.* 36, 3522–3528. doi: 10.3892/or.2016.5171

Wang, Q., He, Z., Huang, M., Liu, T., Wang, Y., Xu, H., et al. (2018). Vascular niche IL-6 induces alternative macrophage activation in glioblastoma through HIF-2α. *Nat. Commun.* 9, 559. doi: 10.1038/s41467-018-03050-0

Won, W.-J., Deshane, J. S., Leavenworth, J. W., Oliva, C. R., and Griguer, C. E. (2019). Metabolic and functional reprogramming of myeloid-derived suppressor cells and their therapeutic control in glioblastoma. *Cell Stress.* 3, 47–65 doi: 10.15698/cst2019.02.176

Wu, J., Frady, L. N., Bash, R. E., Cohen, S. M., Schorzman, A. N., Su, Y.-T., et al. (2018). MerTK as a therapeutic target in glioblastoma. *Neuro. Oncol.* 20, 92–102. doi: 10.1093/neuonc/nox111

Wynn, T. A., Chawla, A., and Pollard, J. W. (2013). Origins and Hallmarks of Macrophages: Development, Homeostasis, and Disease. *Nature* 496, 445–455. doi: 10.1038/nature12034

Xue, N., Zhou, Q., Ji, M., Jin, J., Lai, F., Chen, J., et al. (2017). Chlorogenic acid inhibits glioblastoma growth through repolarizating macrophage from M2 to M1 phenotype. *Sci. Rep.* 7, 39011. doi: 10.1038/srep39011

Yan, D., Kowal, J., Akkari, L., Schuhmacher, A. J., Huse, J. T., West, B. L., et al. (2017). Inhibition of colony stimulating factor-1 receptor abrogates microenvironment-mediated therapeutic resistance in gliomas. *Oncogene* 36, 6049–6058. doi: 10.1038/onc.2017.261

Ye, X., Xu, S., Xin, Y., Yu, S., Ping, Y., Chen, L., et al. (2012). Tumor-Associated Microglia/Macrophages Enhance the Invasion of Glioma Stem-like Cells via TGF-β1 Signaling Pathway. *J. Immunol.* 189, 444 LP–44 453. doi: 10.4049/jimmunol.1103248

Yin, Y., Qiu, S., Li, X., Huang, B., Xu, Y., and Peng, Y. (2017). EZH2 suppression in glioblastoma shifts microglia toward M1 phenotype in tumor microenvironment. *J. Neuroinflammation* 14, 220. doi: 10.1186/s12974-017-0993-4

Yuan, D., Zhao, Y., Banks, W. A., Bullock, K. M., Haney, M., Batrakova, E., et al. (2017). Macrophage exosomes as natural nanocarriers for protein delivery to inflamed brain. *Biomaterials* 142, 1–12. doi: 10.1016/j.biomaterials.2017.07.011

Zeiner, P. S., Preusse, C., Golebiewska, A., Zinke, J., Iriondo, A., Muller, A., et al. (2018). Distribution and prognostic impact of microglia/macrophage subpopulations in gliomas. *Brain Pathol.* 29, 513–529. doi: 10.1111/bpa.12690

Zhang, Q., et al. (2012). Prognostic significance of tumor-associated macrophages in solid tumor: a meta-analysis of the literature. *PloS One* 7, e50946–e50946. doi: 10.1371/journal.pone.0050946

Zhang, H., Lu, H., Xiang, L., Bullen, J. W., Zhang, C., Samanta, D., et al. (2015). HIF-1 regulates CD47 expression in breast cancer cells to promote evasion of phagocytosis and maintenance of cancer stem cells. *Proc. Natl. Acad. Sci.* 112, E6215–E6223. doi: 10.1073/pnas.1520032112

Zhang, M., Hutter, G., Kahn, S. A., Azad, T. D., Gholamin, S., Xu, C. Y., et al. (2016). Anti-CD47 Treatment Stimulates Phagocytosis of Glioblastoma by M1 and M2 Polarized Macrophages and Promotes M1 Polarized Macrophages In Vivo. *PloS One* 11, e0153550–e0153550. doi: 10.1371/journal.pone.0153550

Zhang, G., Zhang, Y., Cheng, S., Wu, Z., Liu, F., and Zhang, J. (2017). CD133 positive U87 glioblastoma cells-derived exosomal microRNAs in hypoxia-versus normoxia-microenviroment. *J. Neurooncol.* 135, 37–46. doi: 10.1007/s11060-017-2566-x

Zhao, H., Wang, J., Kong, X., Li, E., Liu, Y., Du, X., et al. (2016). CD47 promotes tumor invasion and metastasis in non-small cell lung cancer. *Sci. Rep.* 6 (29719), 1–11. doi: 10.1038/srep29719

Zhao, X., Qu, J., Sun, Y., Wang, J., Liu, X., Wang, F., et al. (2017). Prognostic significance of tumor-associated macrophages in breast cancer: a meta-analysis of the literature. *Oncotarget* 8, 30576–30586. doi: 10.18632/oncotarget.15736

Zheng, Y., Yang, W., Aldape, K., He, J., and Lu, Z. (2013). Epidermal growth factor (EGF)-enhanced vascular cell adhesion molecule-1 (VCAM-1) expression promotes macrophage and glioblastoma cell interaction and tumor cell invasion. *J. Biol. Chem.* 288, 31488–31495. doi: 10.1074/jbc.M113.499020

Zhernakova, A., Garmaeva, S., Fu, J., Chen, L., and Wijmenga, C. (2018). A system biology perspective on environment–host–microbe interactions. *Hum. Mol. Genet.* 27, R187–R194. doi: 10.1093/hmg/ddy137

Zhou, M., Bracci, P. M., McCoy, L. S., Hsuang, G., Wiemels, J. L., Rice, T., et al. (2015). Serum macrophage-derived chemokine/CCL22 levels are associated with glioma risk, CD4 T cell lymphopenia and survival time. *Int. J. Cancer* 137, 826–836. doi: 10.1002/ijc.29441

Zhou, W., Ke, S. Q., Huang, Z., Flavahan, W., Fang, X., Paul, J., et al. (2015). Periostin secreted by glioblastoma stem cells recruits M2 tumour-associated macrophages and promotes malignant growth. *Nat. Cell Biol.* 17, 170–182. doi: 10.1038/ncb3090

Zhou, J., Reddy, M. V., Wilson, B. K. J., Blair, D. A., Taha, A., Frampton, C. M., et al. (2018). MR Imaging Characteristics Associate with Tumor-Associated Macrophages in Glioblastoma and Provide an Improved Signature for Survival Prognostication. *Am. J. Neuroradiol.* 39, 252 LP–25 259. doi: 10.3174/ajnr.A5441

Zhu, C., Chrifi, I., Mustafa, D., Van Der Weiden, M., Leenen, P. J. M., Duncker, D. J., et al. (2017). CECR1-mediated cross talk between macrophages and vascular mural cells promotes neovascularization in malignant glioma. *Oncogene* 36, 5356–5368. doi: 10.1038/onc.2017.145

Zhu, H., Leiss, L., Yang, N., Rygh, C. B., Mitra, S. S., Cheshier, S. H., et al. (2017). Surgical debulking promotes recruitment of macrophages and triggers glioblastoma phagocytosis in combination with CD47 blocking immunotherapy. *Oncotarget* 8, 12145–12157. doi: 10.18632/oncotarget.14553

Conflict of Interest: The authors declare that the research was conducted in the absence of any commercial or financial relationships that could be construed as a potential conflict of interest.

Appendice II

Article: LentiRILES, a miRNA-ON Sensor System for Monitoring the Functionality of miRNA in Cancer Biology and Therapy

Viorel Simion, Claire Loussouarn, Yoan Laurent, **Loris Roncal**i, David Gosset, Flora Reverchon, Audrey Rousseau, Francisco Martin, Patrick Midoux, Chantal Pichon, Emmanuel Garcion*, and Patrick Baril*

Simion V, Loussouarn C, Laurent Y, *et al.* LentiRILES, a miRNA-ON sensor system for monitoring the functionality of miRNA in cancer biology and therapy. RNA Biol. 2021;18(sup1):198-214. doi:10.1080/15476286.2021.1978202

RNA BIOLOGY
2021, VOL. 18, NO. S1, 198–214
https://doi.org/10.1080/15476286.2021.1978202

Taylor & Francis
Taylor & Francis Group

TECHNICAL PAPER

LentiRILES, a miRNA-ON sensor system for monitoring the functionality of miRNA in cancer biology and therapy

Viorel Simion [a], Claire Loussouarn [b], Yoan Laurent [a], Loris Roncali [b], David Gosset [a], Flora Reverchon [a], Audrey Rousseau [b], Francisco Martin [c], Patrick Midoux [a], Chantal Pichon [a], Emmanuel Garcion [b,†], and Patrick Baril [a,†]

[a]Centre De Biophysique Moléculaire, CNRS UPR4301, Université d'Orléans, Orléans, France; [b]Université d'Angers, Université de Nantes, Inserm, CRCINA, Angers, France; [c]GENYO, Pfizer/University of Granada/Andalusian Regional Government, Granada, Spain

ABSTRACT

A major unresolved challenge in miRNA biology is the capacity to monitor the spatiotemporal activity of miRNAs expressed in animal disease models. We recently reported that the miRNA-ON monitoring system called RILES (RNAi-inducible expression Luciferase system) implanted in lentivirus expression system (LentiRILES) offers unique opportunity to decipher the kinetics of miRNA activity *in vitro*, in relation with their intracellular trafficking in glioblastoma cells. In this study, we describe in detail the method for the production of LentiRILES stable cell lines and employed it in several applications in the field of miRNA biology and therapy. We show that LentiRILES is a robust, highly specific and sensitive miRNA sensor system that can be used *in vitro* as a single-cell miRNA monitoring method, cell-based screening platform for miRNA therapeutics and as a tool to analyse the structure–function relationship of the miRNA duplex. Furthermore, we report the kinetics of miRNA activity upon the intracranial delivery of miRNA mimics in an orthotopic animal model of glioblastoma. This information is exploited to evaluate the tumour suppressive function of miRNA-200c as locoregional therapeutic modality to treat glioblastoma. Our data provide evidence that LentiRILES is a robust system, well suited to resolve the activity of endogenous and exogenously expressed miRNAs from basic research to gene and cell therapy.

ARTICLE HISTORY
Received 12 May 2021
Revised 27 July 2021
Accepted 6 September 2021

KEYWORDS
miRNA; molecular imaging; RILES; glioblastoma; RNA therapeutics

Introduction

MicroRNAs (miRNAs) are a large family of small, non-coding RNAs that play critical roles in the post-transcriptional regulation of gene expression. MiRNAs are predicted to regulate more than half of all mammalian protein-coding genes and are involved in almost all developmental and cellular processes [1–3]. The canonical pathway of miRNA biogenesis in animals is initiated by transcription of long primary miRNAs (pri-miRNAs) by RNA polymerase II [4]. The pri-miRNAs are processed in the nucleus by the microprocessor complex into pre-miRNAs, hairpin intermediates of approx. 70 nucleotides [5]. Pre-miRNAs are transported to the cytoplasm by exportin-5, where they are further cleaved by Dicer (RNase III enzyme) into approx. 22-bp duplex molecules with short 3′overhangs [6,7]. One strand of the duplex, the guide strand, is selectively incorporated into the RNA-induced silencing complex (RISC) containing the Argonaute (Ago) protein. The other strand, the passenger strand, is discarded. This class of non-coding RNAs bind to their target mRNAs by base pairing with partially complementary sequences in the 3′-untranslated region (3′UTR). Binding of miRNAs to target mRNAs results in translational repression and/or mRNA degradation [8–11]. Each miRNA is believed to regulate up to several hundred targets, making up extensive gene expression regulatory networks [12]. This evolutionarily conserved type of interaction between miRNAs and mRNAs has attracted great attention in the field of RNA biology and therapeutics [13]. MiRNAs fulfil their biological function through a dynamic spatiotemporal expression pattern that fine-tunes the expression of multiple mRNA targets and collectively orchestrates biological responses [14–17]. Beyond the well-illustrated spatiotemporal expression pattern of Lin 4 and let seven miRNAs during embryonic development [18–23], there are many other miRNAs that are dynamically regulated during disease progression [24–26]. For example, the miRNA-10b plays a role in the late stage of the metastatic process, whereas it has a negligible effect in the first stage of tumour development [27] In preclinical therapeutic studies, it was observed that the duration of gene silencing of therapeutic RNAi oligonucleotides is also variable and their biological activity depends on many parameters such as accessibility to the tumour site, diffusion through tumour-microenvironment, proliferation rate of tumour cells and the half-life of mRNA targets [28–30]. A better understanding of the dynamic expression pattern of miRNAs as well as miRNA delivery kinetics would be an advantage to better understand the functionality of miRNA and to optimize the benefits of miRNA-based therapeutics.

CONTACT Patrick Baril patrick.baril@cnrs-orleans.fr Centre De Biophysique Moléculaire, Cnrs UPR4301, Université d'Orléans, France

†The authors wish it to be known that, in their opinion, the last two authors should be regarded as joint last Authors.

To resolve the spatiotemporal dynamics of miRNA-mediated gene regulation, it is necessary to assess the kinetics of miRNA expression in targeted cells or tissues. Expression levels of miRNA can be analysed by northern blotting, quantitative PCR, microarrays, and deep sequencing. However, kinetic analysis is laborious due to the need to collect samples at multiple time points. Furthermore, these methods fail to capture information on cell-to-cell variations in miRNA expression that occur within individual cells. Non-invasive molecular imaging modalities have the potential to fulfil these limitations. There are several miRNA molecular imaging methods developed to monitor the expression of miRNAs in real time and non-invasively. Molecular beacons which typically consist of stem-loop DNA oligonucleotides complementary to a miRNA strand, a fluorophore, and a quenchercan overcome some of these limitations [31–33]. However, signals of molecular beacons arise from hybridization of mature miRNA to stem-loop DNA, regardless of Ago2 loading. Thus, molecular beacons do not discriminate between Ago-loaded functional miRNA and free, non-functional miRNA. Because miRNA expression levels do not necessarily correlate with miRNA activity, the miRNA functionality cannot be inferred from expression analysis alone [34]. Moreover, the dilution of the probes over the cell division rate of the biological systems studied is a limitation for the longitudinal analysis of miRNA expression. To directly measure miRNA activity, luciferase reporter gene with miRNA target sequences in their 3′UTR has been widely used as miR-OFF reporter assays, and are also successfully utilized for bioluminescent imaging *in vivo* [34,35]. Consequently, the expression of miRNA is negatively signed by the loss of optical signal, a readout that is somewhat constraining as the absence of signal in molecular imaging can have different causes such as cell death, low-resolution capacity or equipment dysfunction. The miR-ON gene reporter methods tackle some of these limitations. These systems rely on engineering of genetic-switch expression systems to induce optical signal in cells when the miRNA of interest is expressed and, importantly, functionally processed by the RISC machinery. Pichard et al. [36], Amendola et al. [37], and more recently Rossetti et al. [38] engineered the Tetracycline-Inducible tTR-KRAB System and revealed the temporal dynamic expression pattern of miRNAs in several types of cells *in vitro*. However, the principle of regulation of this miR-ON system requires several hours to days for the tTR-KRAB regulator protein [39–41] to switch-ON the inducible expression cassette. Furthermore, KRAB-mediated silencing can act over several tens of kilobases and thus might affect the biology and behaviour of cells [42,43]. We previously designed the RILES system (RNAi-Inducible Luciferase Expression System) for spatiotemporal detection of miRNA activity in vivo by engineering the Cumate genetic-switch operon [44–46] and, more recently, the Tetracycline genetic-switch operon systems in the Tet R configuration [47]. We demonstrated that RILES switched ON the expression of luciferase and the hNIS reporter genes in a specific and dose-dependent manner and provided a temporal and spatial resolution of miRNA regulation *in vitro* and *in vivo*, that conventional detection methods can hardly achieve [45,46]. More recently [47], we demonstrated that subcloning the RILES in a lentiviral expression system provides the opportunity to monitor in real time the fate of miRNA activity in glioblastoma cells. We demonstrated that the time frame for the LentiRILES to be accurately switched ON in cells is indeed rapid, starting 3 hours after transfection. When combined with confocal microscopy studies, this miR-ON monitoring system enabled us to decipher the critical steps of miRNA internalization, processing and exocytosis in U87MG glioblastoma cells [47].

Here, we fully characterized the LentiRILES in cells by challenging the sensitivity, specificity and robustness of this miRNA-ON monitoring system using several cell types. We employed lentiRILES to visualize miRNA regulation in single-cells, as a cell-based miRNA screening platform and as rationale to perform structure-function analysis of the miRNA duplex. We report, for the first time to our knowledge, the kinetic of miRNA-mediated mRNA silencing activity in a preclinical animal model of glioblastoma after the locoregional infusion of synthetic miRNA by convection-enhanced delivery. We exploit the bioluminescence data generated by lentiRILES system to evaluate the tumour suppressive function of miRNA-200c as a locoregional treatment of glioblastoma.

Methods

Tissue culture and reagents

The U87MG, HEK 293 T, Hela, B16F10, 4T1 and C2C12 cell lines were purchased from ATCC (American Type Culture Collection) and maintained in culture according to standardized conditions. Cells were mycoplasma-free as evidenced by the MycoAlert Mycoplasma Detection Kit (Lonza). The commercial transfection reagents and synthetic miRNAs were purchased from several companies as indicated in the text. The polybrene (hexadimethrine bromide) used to increase lentiviral transduction efficiency and proteinase K was from Sigma. The Tet R (clone 17 795) and Argonaute 2 antibodies were from Abcam (Abcam, USA). The luciferin substrate for *in vitro* and *in vivo* use was from Promega. Our home-made lipopolyplexe transfection reagent, LPRi, was prepared as described recently [47].

Lentiriles Stable Cell Line Production and Selection

The LentiRILES harbouring the CMV-TetO regulatable cassette encoding the luciferase reporter gene and the spleen focus-forming virus promoter driving the expression of the Tet R repressor gene originated from the Francisco Martin laboratory (Genyo, Pfizer/University of Granada, PTS Granada, Spain) and derived from a previous publication [48]. Procedures to place the Tet R transcriptional repressor under control of miRNA of interest as well as the protocol to produce the LentiRILES cell lines were the same as described recently [47] and according to conditions indicated in the text. The screening procedure to identify the LentiRILES cell lines that were the most responsive to miRNA of interest was carried out 7 days post-infection with the LentiRILES viral

particles and by transfecting the cells with miRNA mimic at a final concentration of 100 nM using our LPRi lipopolyplexes transfection reagent.

Mirna mimics transfections and luciferase assay

The transfection procedure to evaluate the potency of commercially available synthetic miRNA mimic and transfection reagents was performed strictly according to manufacturer's recommendations. At the indicated time point post transfection, the relative luciferase activity units (RLU) in wells were quantified using a luminometer equipped with automatic injectors and normalized to protein content (RLU/mg protein) as previously described [45]. Alternatively, tissue culture plates were scanned using an IVIS Lumina II imaging scanner (PerkinElmer) after renewing the tissue culture media with determined from a standard procedure as previously described PBS containing the luciferin substrate at a final concentration of 150 µg/ml. The plates were scanned for 2 min. Light emission from regions of interest (ROI) was drawn manually and quantified as photons/second/pixel/sr using the living Image Software (PerkinElmer).

Quantitative Real-Time PCR

The relative expression of Tet R and Luciferase mRNA as well as miRNAs was determined from a standard procedure as previously described [45]. Briefly, short and long RNAs were collected simultaneously using the miRNAVANA isolation kit (ThermoFisher) then reverse-transcribed using the NCode VILO miRNA cDNA synthesis kit according to the manufacturer's instructions (ThermoFisher). Real time quantitative PCR was performed with SYBR green dyes (QuantiFast SYBR Green master mix, Qiagen) using specific Tet R (forward 5′-GCCCAGAAGCTAGGTGTAGA and reverse 5′-TGTACTTTTGCTCCATCGCG), luciferase (forward 5′-TCATAGAACTGCCTGCGTGA and reverse 5′-AGCAGCGCACTTTGAATCTT), E-caherin (forward 5′-CGTACATGTCAGCCAGCTTC and reverse 5′-TGGAGGAATTCTTGCTTTGC), Vimentin (forward 5′-TGTCCAAATCGATGTGGATGTTTC and reverse 5′-TTGTACCATTCTTCTGCCTCCTG), Zeb-1 (forward 5′-TTTCTTGCCCTTCCTTTCTG and reverse 5′-GGGAGGAGCAGTGAAAGAG) and Zeb-2 (forward 5′-CCACACTCTGTGCATTTGAACT and reverse 5′-AAGCCAGGGACAGATCAGC) primers and commercially available primers to miRNA-122, −133a, and −21.5 (Qiagen). The specificity of the PCR amplicon (size and product) and absence of primer-dimer were verified by melt-curve analysis using LightCycler 480 equipment and software (Roche). Samples were normalized to the GAPDH level for quantification of the mRNA transcripts and to the snU6 level for quantification of miRNA. Finally, the relative levels of expression of mRNAs and miRNAs were determined using the $2^{-\Delta\Delta Ct}$ method. To quantify the number of lentivirus vector copies integrated per genome, genomic DNA was extracted by lysing 10^6 cells in the SNET buffer (20 mM Tris-HCl pH 8, 5 mM EDTA pH 8, 400 mM NaCl, 1% SDS) containing proteinase K used at a final concentration of 100 mg/ml. After a phenol–chloroform extraction step to remove proteins, the genomic DNA was ethanol precipitated and quantified by spectrophotometry. Then 50 ng of extracted genomic DNA samples were used in each quantitative PCR reaction performed in triplicate using the Tet R and luciferase primers. The vector copy number (v.g.c) per host-cell genome was determined by interpolation to a standard curve prepared from serial dilution of the Tet R and Tet-o-Luc plasmids. Data were finally expressed as v.g.c value by assuming that 50 ng of genomic DNA is equivalent to 8 334 genomes as described previously [48].

Mirna labelling and confocal microscopy analysis

For confocal microscopy studies of the intracellular distribution of transfected miRNAs in cells, miRNA mimics were labelled using the Label IT nucleic acid labelling kit according to the manufacturer's protocol (Mirus, USA) with some modification as described recently [47]. After plating, the cell monolayers were transfected with LPRi complexed with 50 nM final concentration of Cyanine 3 (Cy-3)-labelled blunt or overhang miRNA-133a mimics for 6 h in tissue culture. The cells were thereafter fixed in 3% paraformaldehyde/PBS solution at room temperature, washed and stained with the Argonaute 2 antibody overnight at 4°C. Coverslips were collected, mounted in Vectashield medium for fluorescence (H-100, Vector Laboratories) and analysed using the Zeiss LSM 510 confocal laser scanning microscope with an apochromat 63×/1.4 oil differential interference contrast (DIC) objective (Carl Zeiss). Colocalization analysis was monitored using the ImageJ plug-in JACoP (Just Another Co-localization Plugin). Each coloured image was split into respective red and green channels. The Mander's R coefficient was calculated based on the red and green channels. Final data were expressed as the co-localization coefficient, r2, from three independent experiments collected from a minimum of 50 independent cells per condition each time.

Cell viability assay, cell cycle and apoptosis flow cytometry analysis and In Vitro wound scratch assay

Cell viability upon transfection of miRNA-200c in U87MG cells was performed using the Alamar Blue assay following the manufacturer's recommendations (Sigma-Aldrich). Briefly described, at the time of the assay, the Alamar Blue stock solution was directly loaded in the tissue culture plate at a final dilution of 1/10 and incubated for 90 min at 37°C, 5% CO2. The plates were thereafter read using a fluorescence-based plate reader with a fluorescence excitation wavelength of 540–560 nm and an emission wavelength of 590–610 nm. The raw fluorescence values were corrected by subtracting the background fluorescence values detected in wells treated in the same condition but without cells. Fluorescence cell cycle analysis was performed by incubating 10^6 cells in suspension with 3 mL of 70% ethanol followed by an incubation period of 1 h at −20°C. Ethanol was removed after centrifugation and total RNA discarded by treatment for 30 min at 37°C with

RNAse A solution (ThermoFisher) used at the final concentration of 500 U/ml. The pellets were washed twice in DPBS, resuspended in 300 µL of DPBS containing 0.2% Triton X-100 and analysed using Becton Dickinson FACSort (Becton Dickinson) after addition of propidium iodide solution used at the final concentration of 10 ng/µL. Fluorescence was collected from 30,000 events and analysed using the CellQuestTM Pro software (Becton Dickinson). Cell death and apoptosis analysis were performed after staining cells with a combination of Annexin V conjugated FITC and propidium iodide (ANNEX300F kit, Bio-Rad). Cells in suspension were first resuspended in binding buffer provided by the Annexin V:FITC Assay Kit before adding 5 µL of Annexin V conjugated FITC solution to 3 10^5 cells for 10 min of incubation at room temperature in the dark. Then, propidium iodide was added to the cell suspension at a final concentration of 1 ng/ml before analysing the cell population by flow cytometry using the Becton Dickinson FACSort. A minimum of 30,000 events were acquired and analysed using CellQuestTM Pro software. *In vitro* wound scratch assays were performed by culturing the U87MG cells in 24-well plates to reach a nearly confluent cell monolayer the following day. The miRNA-200c mimics formulated with the LPRi transfection reagent were transfected to cells according to the protocol described above. Then, 3 days later, vertical wounds were performed with sterile 20–200 μl plastic pipette tips. The plates were placed in a time lapse videomicroscope (Zeiss) placed in an environmental chamber at 37°C, 5% CO2. Pictures of the wounds were recorded automatically every 2 h for a total of 3 days. Wound areas at individual time points were measured using the ZEN LE Digital Imaging Software (Zeiss). Data were expressed as % of closure by normalizing the calculated area to 100% of wound area of untreated cells.

Orthotopic glioblastoma animal model and locoregional delivery of LPRi Mimic.

All mouse experiments were carried out in strict accordance with the rules of the French Ministry of Agriculture and the European Communities Council Directive (86/609/EEC). The experimental protocol used in this study was approved by the 'Pays de la Loire' Ethics Committee of Animal Experiments (Permit No. CEEA. 2012.60; Authorization n°A 49–2012-04). Female CB-17/Icr-Prkdc scid/Rj mice (7 weeks old, Janvier Labs, France) were maintained in pathogen-free conditions with controlled temperature (20–22°C), humidity (50–70%), light (12 h light/dark cycles) and housed with unlimited access to food and water. Tumour implantations were done by stereotactic surgery according to detailed procedures recently described [47,49]. The miRNA mimics (2 µg miRNA mimic formulated in 7 µl of PBS using a 10-fold concentrated LPRi solution) were infused into solid tumours by the convection-enhanced delivery method (CED). The CED infusion was performed using syringes equipped with a 32-G needle connected to the Harvard apparatus Pump and carried out automatically at a constant flow rate of 0.5 µL/min over a period of time of 18 min. After injection, the needles were left in place for an additional 5 min and gradually removed over an additional period of 5 min. The mice were monitored daily for mobility, grooming and weight.

Bioluminescence imaging

Bioluminescence imaging was performed rigorously as previously described [45,47]. The Living Image Software (PerkinElmer, USA) was used to express the data as photons/second/pixel/sr monitored from region of interest covering the brain of mice after a 2 min integration time with the following acquisition parameters: relative aperture F/Stop = 1, binning of 4, field of View D. The sensitivity of the imaging scanner was tested monthly with commercially available positive sources of bioluminescence.

MRI imaging

MRI of mice was performed according to procedure described previously [49]. Briefly, mice were isoflurane-anesthetized and scanned using a Burker Biospec 70/20 device, operating at a magnetic field of 7 T (Bruker, Wissembourg, France), equipped with a 1 H cryoprobe. Anatomical proton images were generated using a acquisition with relaxation enhancement (RARE) sequence [TR = 3200 ms; mean echo time (TE) = 21.3 ms; RARE factor = 4; FOV = 2 cm x 2 cm; matrix 256 x 256; 11 contiguous slices of 0.5 mm, Nex = 1]. For monitoring tumour development overtime, a total of 8 MRI slices by brain were taken during the imaging session. Then, regions of interest covering visible tumours areas were drawn using Paravision 6.0.1 software, summed and multiplied by the slice thickness to obtain the tumour volume at each time point and for each group of mice.

Statistical analysis

The results were expressed as mean ± S.E.M. and all the experiments were performed at least in triplicate. Statistical evaluation was carried out by one-way analysis of variance between groups (ANOVA program of Origin, OriginLab, Northampton, MA) or Student's t-test for comparisons between two groups. Statistical significance for survival experiments in animal was determined using the log rank test. Differences were considered to be statistically significant when $p < 0.05$.

Results and discussion

Strategy of production of LentiRILES cell lines

Recently, we engineered the Tet R-based lentiviral system developed by Benabdellah et al. [48] to produce a U87 MG stable cell line expressing the miR-ON RILES system constitutively (LentiRILES, Figure 1a). The system is based on two lentiviral vectors, one expressing the Tet R through the spleen focus forming virus (SFFV) promoter (Lenti Tet R) and the other expressing the firefly luciferase (FLuc) driven by the regulatable inducible CMV-Tet O promoter (Lenti Tet_O_Luc). We subcloned a block of 4 complementary

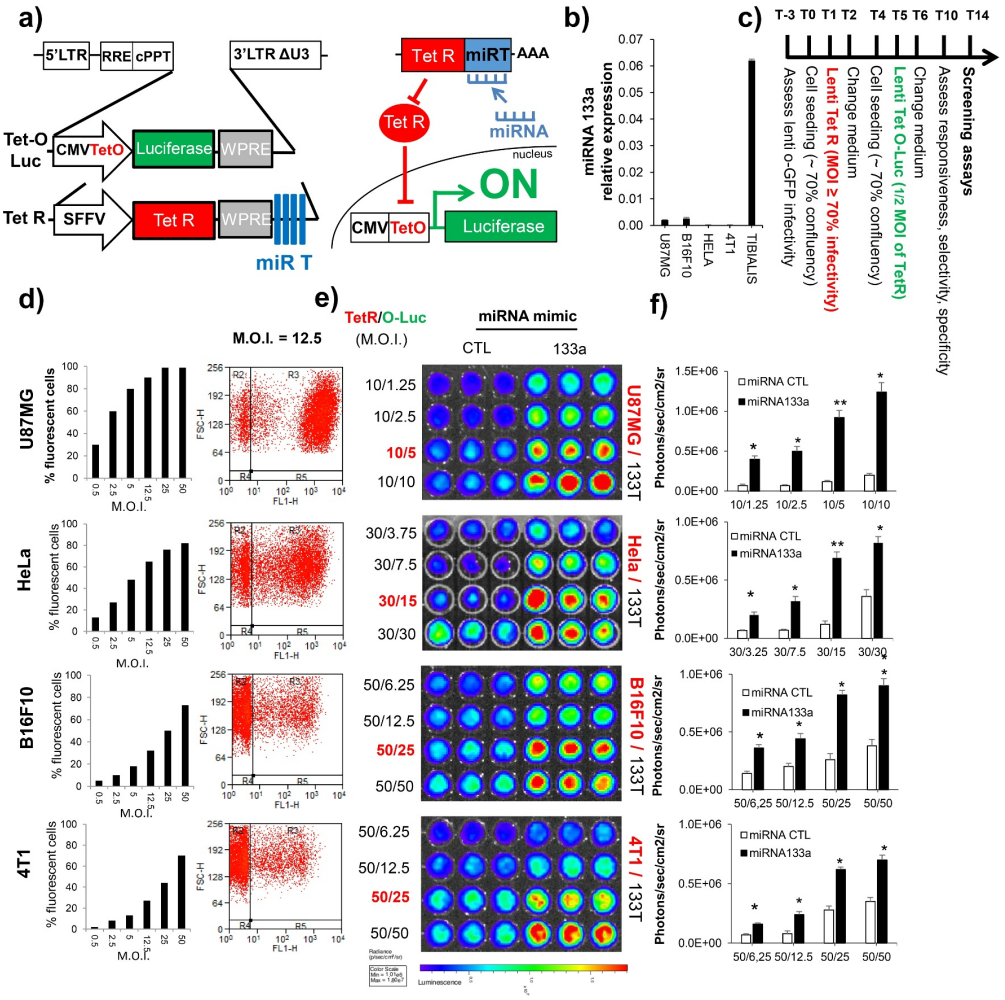

Figure 1. Schematic representation of the lentiRILES system and strategy to generate LentiRILES stable cell lines. **a)** Maps of the two lentiviral expression plasmids encoding for the RILES system. *Left panel*, Tet-O-Luc: lentivirus expression plasmid encoding for the firefly luciferase reporter gene driven by the inducible minimal CMV promoter containing 2 Tet O operators. Tet R: lentivirus expression plasmid encoding for the Tet R repressor protein controlled by the presence of a miRNA targeting sequence cassette (miR T) complementary to a miRNA sequence of interest. *Right panel*, Scheme showing luciferase induction upon miRNA activity. When expressed in cells, the miRNA of interest will bind to the miR T cassette located in the 3'UTR of the Tet R mRNA, inducing activation of the RISC machinery and transcriptional repression of the Tet R protein. In the absence of Tet R, the RNA polymerase transcribes the luciferase reporter gene, switching-ON the LentiRILES system. Bioluminescence signals emitted from the cells can be collected by bioluminescence imaging equipment. **b)** Quantitative RT-PCR analysis of miRNA-133a expression in several cancer cell lines and in the tibialis anterior skeletal muscles of mice used as positive control. **c)** Schematic representation of the procedure used to generate stable cell lines expressing the LentiRILES/133 T system. The cells are first transduced with a constant MOI value of the Lenti Tet R/133 T viral particles followed by the infection with different MOI values of lenti Tet-O-Luc viral particles to find the best balance between expression of the Tet R protein and the number of Tet O operators integrated in the host genome of cells. **d-f)** Production of different stable LentiRILES/133 T cancer cell lines. **d**) Permissiveness of U87MG, Hela, B16F10 and 4T1 cells to lentivirus infection evaluated by flow cytometry using lentivirus particles encoding for the eGFP reporter gene at various MOI. **e**) Responsiveness to miRNA-133a of different U87MG, Hela, B16F10 and 4T1 cells LentiRILES/133 T cell lines generated using different MOIs of TetR and Tet-O-Luc as indicated at the left of each lane of each wells of tissue culture plate. The LentiRILES/133 T cell lines were plated on 24 well plates and then transfected with miRNA-133a before scanning the plate 3 days later using a bioluminescence imaging scanner. **f**). Quantitative bioluminescence signals collected from region of interest from E. Data are expressed as mean ± SEM of one representative experiment performed at least 3 times. Statistics by the two-tailed t-test, *P < 0.05, **P < 0.01, compared to control cells transfected with a miRNA mimic control (CTL)

sequences to a miRNA of interest (miR T cassette) downstream to the WPRE viral gene of the Lenti Tet R vector to place the expression of the Tet R repressor under control of the miRNA (Figure 1a). When the given miRNA is expressed in cells, it will bind to the miR T cassette, activating the RISC machinery and inhibiting the production of the Tet R protein. Consequently, in the absence of the Tet R protein bound on the Tet O operator, the inducible promoter is switched ON, resulting in the expression of the FLuc and emission of a positive bioluminescence signature in cells that can be easily collected using a bioluminescence imaging scanner (Figure 1a).

To achieve a high signal-to-noise ratio readout, we placed RILES under the control of miRNA-133a (LentiRILES/133 T),

a muscle-specific miRNA that is highly enriched in cells from cardiac and skeletal muscles lineages and undetectable in most other cell types derived from different organ sources (Figure 1b). Therefore, as illustrated in Figure 1a, it is expected that the background level of the Luciferase reporter gene in the OFF configuration, *i.e.* in the absence of miRNA-133a, will be at lower levels, as being not expressed neither endogenously nor exogenously, this miRNA could not bind to the TET R mRNA repressor to switch ON the RILES. In contrast, when transfected in cells, the miRNA-133a mimic will bind to TET R mRNA resulting in RNAi activation and TET R mRNA degradation. As a consequence, the LentiRILES will be switched at the higher and maximal levels in the ON configuration in the presence of maximal dose of transfected miRNA.

We challenged the LentiRILES/133 T system by evaluating the responsiveness of the LentiRILES produced in several cancer cell lines, derived from different tissue origins, such as human cervical cancer (HeLa) cells, murine melanoma (B16F10) cells, mouse mammary carcinoma (4T1) cells and, for comparison, the human glioblastoma U87MG cell line (U87MG). We first developed and optimized the procedure to generate optimal-responsive LentiRILES/133 T stable cell lines to the miRNA-133a used as the inducer of the OFF-to-ON shift of the RILES configuration. The general procedure (Figure 1c) consists in the transduction of cells with first a MOI value of the Lenti Tet R/133 T viral particles to transfer expression of the Tet R protein in at least 80% of the whole-cell population. Then, 4 days later, cells were infected with different MOI values of the Lenti Tet_O_Luc viral particles to find an appropriate balance between expression of the Tet R protein and the number of Tet O operator sequences integrated in the host genome of cells.

To rationalize the best MOI values of Lenti Tet R/133 and Lenti_o_Luc viral particles, we first evaluated the transduction efficiency of each cell line using a lentivirus encoding for the eGFP reporter gene. Flow cytometry analysis of cells transduced at a MOI of 12.5 indicated (Figure 1d) that the most permissive cell line was the U87MG (80% of GFP positive cells), followed by the HeLa cells (63% of GFP positive cells), the B16F10 cells (35% of GFP positive cells) and finally the 4T1 cells (35% of GFP positive cells). According to this result, we selected for each cell line an appropriate MOI value of Lenti Tet R/133 T viral particles to transfer expression of the Tet R protein in 70% of the whole-cell populations. We then infected the cells with increasing MOI values of Lenti Tet_O_Luc viral particles to find the best ratio of infection between the Lenti Tet R/133 and Lenti_o_Luc viral particles. We produced a total of 16 LentiRILES/133 T cell lines and evaluated their responsiveness to miRNA-133a transfected in 96-well plates using a bioluminescence imaging scanner. The results demonstrate that all the LentiRILES/133 T stable cell lines generated were responsive to the miRNA-133a mimic with however different efficiency (Figure 1e). Quantification of bioluminescence signals emitted from the cells indicated that a Lenti Tet R 133 T to Lenti Tet_O_Luc MOI ratio of 2/1 was the best ratio to generate optimal-responsive cells to miRNA-133a. As shown in Figure 1e, Hela cells transduced with a MOI ratio of 30/15 had a maximum 5.8-fold increase in luciferase activity in response to transfected miRNA-133a, while the B16F10 melanoma cells transduced with a MOI ratio of 50/25 had a maximum 3.1-fold increase of luciferase activity. The 4T1 breast cancer cells were found to be the less responsive LentiRILES/133 T cell line as a maximum 2.2-fold increase in luciferase activity was detected in these cells for a MOI ratio of 50/25. In contrast, the U87MG glioblastoma cells were the most responsive cell line to transfected miRNA-133a as a maximum of 7.7-fold increase in luciferase activity was detected at a MOI ratio of 10/5.

This first set of data indicates that an optimal balance between the Tet R protein and the Tet O operator sequence integrated in cells is a key determinant to generate responsive cell lines to miRNA mimic used as inducer to switch OFF-to-ON the RILES configuration. Accordingly, the permissiveness of cells to lentivirus infection has to be taken into account when generating LentiRILES stable cell lines and might require optimized transduction procedures to bypass the low rate of viral infection of some cell lines [50].

Characterization of the U87MG LentiRILES/133 T cell line

We next performed a systematic analysis to gain insight into the molecular mechanism of the OFF-to-ON shift of the RILES/133T stably integrated in the genome of the LentiRILES U87MG/133 T cell line (ratio 10/5). Results from qPCR analysis indicated that there were 2.1-times more viral integrated copies of Lenti TetR/133 T than of Lenti_o_Luc virus in the host genome of these cells leading to to 64.1-fold higher relative production of Tet R mRNA in cells than Luciferase mRNA (Figure 2b and 2c). In the ON-configuration, *i.e.* after transfection of miRNA-133a, the relative expression of Tet R mRNA was reduced by 77.4% (Figure 2b) corresponding to a reduction by 68.2% of Tet R protein expression (Figure 2c). This downregulation process was correlated with the induction by 5.1-fold of the luciferase mRNA (Figure 2c) proving, as anticipated theoretically in Figure 1, that the mode of shifting OFF-to-ON of the RILES system is dependent on the transcriptional repression of Tet R mRNA that, in turn, induces the expression of the Firefly Luciferase protein. We then evaluated the sensitivity of U87MG LentiRILES/133 T cells. We found that the rate of luciferase fold induction was well correlated (R^2 = 0.97) with the concentration of miRNA-133a transfected in cells ranging from 0 to 3 nM (Figure 2e). However, above this concentration, the RILES read-out saturated. No statistically significant difference in terms of luciferase fold change was found between cells transfected with 3 nM and 100 nM of miRNA-133a (Figure 2e). The same trend was observed when the study was performed at the molecular level. The range of Tet R mRNA down-regulation was well correlated (R^2 = 0.92) with the increasing concentrations of miRNA-133a transfected in cells up to 3 nM, and was, as expected, inversely correlated (R^2 = 0.90) with the induction of luciferase reporter mRNA (Figure 2f). Again, above this miRNA concentration, the relative expression of both Tet R and luciferase mRNAs was not significantly different when 3 or 100 nM of miRNA-133a were transfected (Figure 2f). We finally assayed the specificity of the LentiRILES/133 T to several miRNA mimics transfected

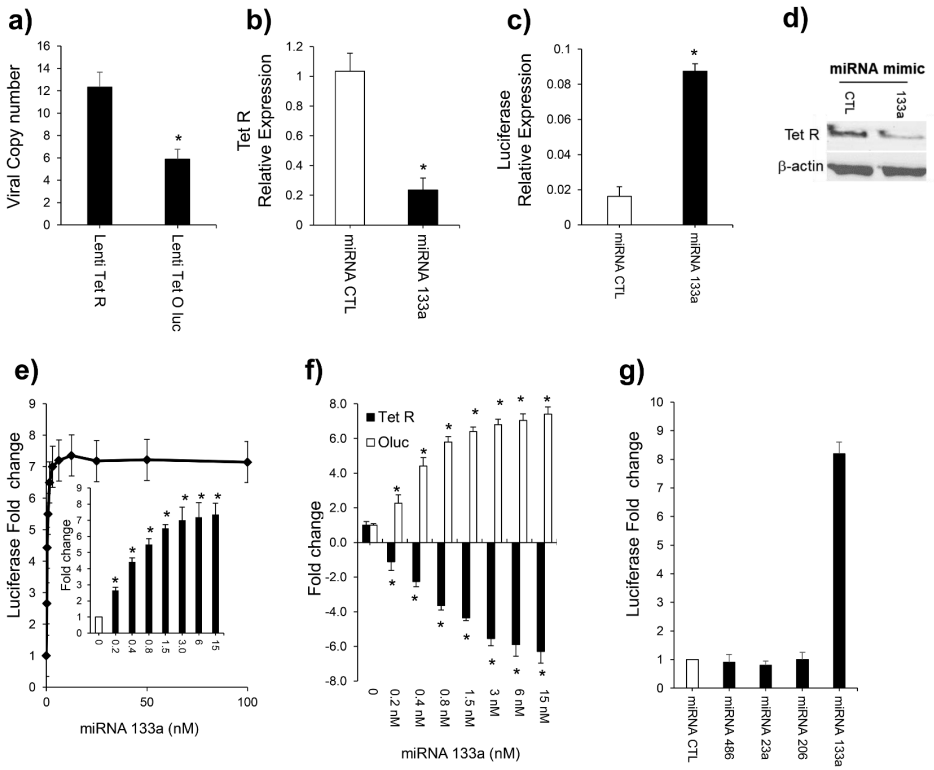

Figure 2. Functional characterization of the U87MG LentiRILES/133 T cell line. **a)** Absolute quantitative PCR quantification to determine the number of viral copies of Lenti Tet R/133 T and Lenti Tet-O-Luc expression plasmids integrated into the host genome of the U87MG LentiRILES/133 T cell line. Relative Tet R (b) and luciferase (c) expression detected by quantitative RT-PCR in the U87MG LentiRILES/133T cell line before and after transfection of miRNA. **d)** Relative protein expression of Tet R protein detected by western blot in the U87MG LentiRILES/133T cell line before and after transfection of miRNA. **e)** Dose response study of luciferase fold change induction detected in the U87MG LentiRILES/133 T cell line in response to increasing concentration of miRNA-133a mimic. Forty-eight hours after transfection, luciferase activity in cells was quantified and expressed as fold induction relative to control, not-transfected cells, and set to the arbitral value of 1. *Inset*: the same results but shown on a linear scale for miRNA concentration ranging from 0 to 3 nM. **f)** Relative Luciferase and Tet R fold change mRNA expression quantified by quantitative RT-PCR in U87MG LentiRILES/133T cells in response to increasing concentration of miRNA 133a. Data are expressed as mean ± SEM of one representative experiments performed at least 3 times. Statistics by the two-tailed t-test, *P < 0.05, **P < 0.01, ns (not significant), compared to control cells transfected with a miRNA mimic control (CTL, B, C, G) or not-transfected cells (A, E, F)

in cells. As shown in Figure 2g, no leakage or non-specific induction of the luciferase reporter gene was detected when irrelevant or unspecific miRNA mimics were used attesting again the great specificity of the RILES system [45–47].

This second set of data demonstrates that the LentiRILES system is a reliable, specific, sensitive OFF-to-ON shift miRNA-ON reporter system, capable to monitor the functionality of transfected miRNAs in several cancer cell lines. However, the saturation of RILES detected at intermediate concentrations of transfected miRNA mimics is perceptible and might be a limitation.

In Vitro monitoring of endogenous expressed Mirna Using the LentiRILES System

We then challenged a key aspect of miRNA biology that is related to the need for monitoring methods capable of resolving the dynamic expression pattern of endogenously expressed miRNAs during the development of physiological and pathological processes. We evaluated this challenging aspect using the two different cell types, C2C12 myoblast cells that are known to express the miRNA-133a upon differentiation in myotubes [51] (Figure 3a) and U87MG cells that are known to have opposite expression patterns of miRNA-122 and −21.5p [52]. To visualize the dynamic expression of these endogenously expressed miRNAs by fluorescence imaging on live cells, we replaced the Firefly Luciferase with the GFP reporter gene. The generated system was then denoted RIFES system, standing for RNAi-Inducible Fluorescence Expression System.

C2C12 cells were transduced with an optimal Lenti Tet R/133T to Lenti Tet_O_eGFP MOI ratio according to the procedure described in Figure 1. Then, the most responsive C2C12 LentiRIFES 133T stable cell line was differentiated in myotubes to induce expression of miRNA-133a [51]. Fluorescence microscopy analysis of cell monolayers revealed the presence of intense fluorescent signals in the differentiated myotubes formed, with stronger emitted fluorescence detected

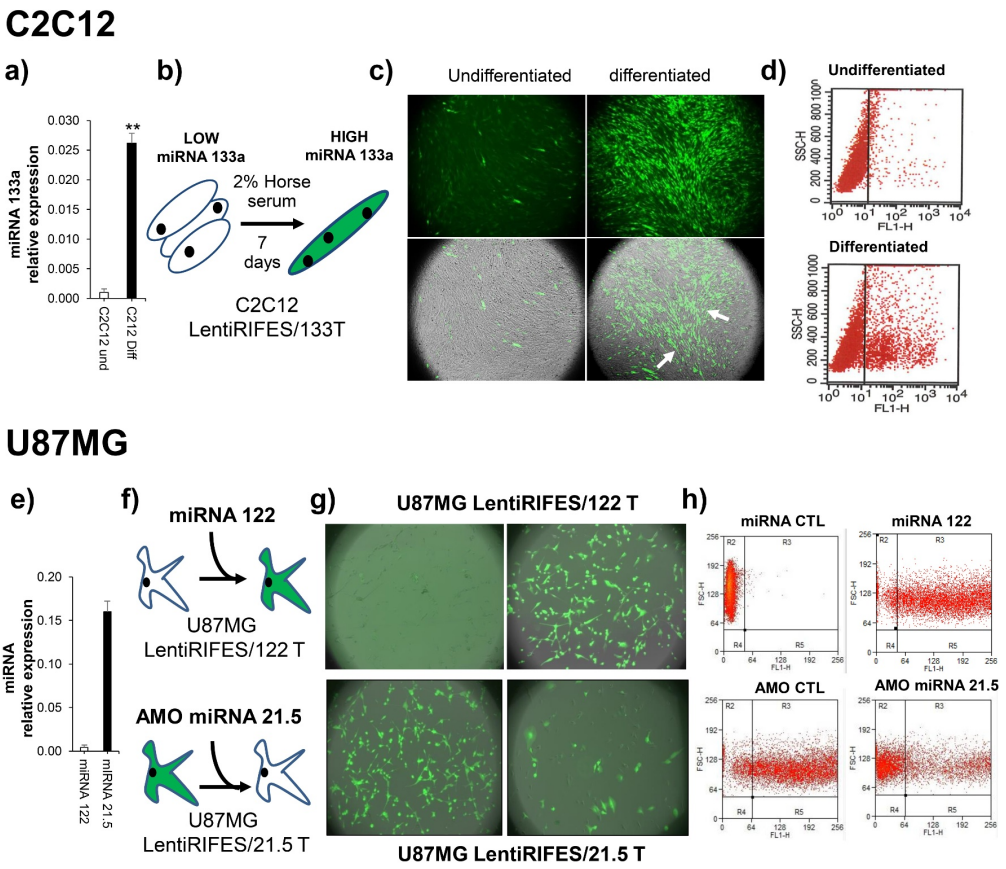

Figure 3. Real time, fluorescence monitoring of endogenously expressed miRNA in cell lines. **a**) Quantitative RT-PCR analysis of miRNA-133a expression in C2C12 cells cultured in undifferentiated and differentiated media to induce differentiation of these cells in myotubes and the endogenous expression of miRNA-133a. **b)** Schematic representation of the procedure used to monitor expression of miRNA-133a in the myotubes using the RIFES/133T system and a fluorescence imaging microscope. The C2C12 cells were transduced with the Lenti Tet R/133T virus and then with Lenti_o_eGFF according to the procedure described in Figure 1c and then cultured in media containing 2% of horse serum to induce their differentiation in myotubes and expression of this miRNA. **c)** *Upper quadrant*, Live-cell fluorescence imaging of monolayers from undifferentiated and differentiated C2C12 LentiRIFES/133T cells performed at day 7. *Lower quadrant* superimposition of bright field and fluorescence images of the same field of view of cell monolayers to show the more pronounced localization of fluorescence signals in the myotubes (arrows). **d)** Flow cytometry quantification of eGFP expression in the same cells as C collected by trypsinization. **e)** Quantitative RT-PCR analysis of expression of miRNA-122 and −21.5 in U87MG cells. **f)** Schematic representation of the procedure to monitor expression of these two miRNAs in real-time by fluorescence imaging after transfection of miRNA-122 mimic or miRNA-21.5 inhibitor (AMO, antisense miRNA) in U87MG RIFES/122T and U87MG RIFES/21.5T cells respectively. **g)** Live-cell fluorescence imaging and **h)** flow cytometry analysis of the U87MG RIFES cells from F. Data are expressed as mean ± SEM of one representative experiments performed at least 3 times. Statistics by the two-tailed t-test, **P < 0.01 compared to control undifferentiated cells (C2C12 und)

in areas where myotubes were more apparent (Figure 3c, arrows). In contrast, lower fluorescence signal was detected in undifferentiated, myoblast cell monolayers (Figure 3c) with a uniform distribution pattern of the fluorescence detected among the cellular monolayer. Quantitative flow cytometry analysis of the cells collected by trypsinization indicated that the mean GFP intensity was 3.9-fold higher in differentiated C2C12/133T myotubes compared to undifferentiated C2C12/133T myoblast cells (Figure 3d). Next, we monitored the endogenous expression pattern of miRNA-122 and −21.5p in U87MG cells, which were found to be, respectively, faintly and highly expressed by qRT-PCR (Figure 3e). We constructed two novel LentiRIFES expression plasmids by replacing the miRNA-133T cassette with a miRNA- 122T or 21.5T cassettes to produce the corresponding U87MG LentiRIFES/122 T and −21.5 T stable cell lines. We transfected these two cell lines with miRNA-122 mimic or with an inhibitor of miRNA-21.5 (AMO miRNA-21.5) (Figure 3f). Fluorescence microscopic analysis of cells monolayers in basal conditions revealed high fluorescence signal in the U87MG LentiRIFES/21.5T cells and low-to-almost undetectable fluorescence signal in the U87MG LentiRIFES/122T (Figure 3g) that correlated well with the endogenous expression pattern of these miRNAs detected by qRT-PCR (Figure 3e). Remarkably, a clear positive shift of fluorescence intensity, from 94 to 4 755 MFI was quantified when the U87MG LentiRIFES/122T cells were transfected with miRNA-122 while, in contrast, a clear negative fluorescence shift from 7 547 to 3 231 MFI was detected

when the U87MG LentiRIFES/21.5 T cells were transfected with the miRNA-21.5 inhibitor.

This third set of data demonstrates that the LentiRILES system can not only monitor the expression of ectopic miRNA but also endogenously expressed miRNAs using two main optical molecular imaging modalities (*e.g.* bioluminescent and fluorescent imaging). The fluorescent reporter gene offers an additional advantage for RILES by providing a single and live-cell resolution of miRNA expression that can be exploited to cell-sort homogeneous populations of cells according to their miRNA expression pattern.

The lentiriles cell line can be used as a positive screening platform to identify optimal synthetic mirna mimics and transfection reagents

We next explored some applications of the LentiRILES system in the field of miRNA therapy. Having demonstrated the good sensitivity and specificity of the U87MG LentiRILES/133T cell line, we then anticipated that this cell line could be used as a novel, positive cell-based screening platform to evaluate the performance of miRNA mimics and transfection reagents. We screened the efficacy of eight miRNA mimics and seven transfection reagents commercially available. We included our homemade lipopolyplexes (LPRi) formulation, previously reported as a potent siRNA [53] and miRNA [47] transfection reagent as well as a synthetic homemade miRNA-133a mimic. Results of this screening procedure performed in 96-wells plate and monitored using a bioluminescence scanner indicated (Figure 5a) that the gold standard Lipofectamine RNAi max (7.24 x 10^{10} RLU/mg) and LPRi (6.82 x 10^{10} RLU/mg) transfection reagents were the two most efficient miRNA transfection reagents. The transfection reagent Transit X2 (4.93 x 10^{10} RLU/mg) and Hyperfect (4.63 x 10^{10} RLU/mg) exhibited a similar range of efficacy but were less efficient than the RNAi max and LPRi. The transfection reagents HappyFect (3.69 x 10^{10} RLU/mg), Viromer Blue (2.69 x 10^{10} RLU/mg), Fugene HD (2.63 x 10^{10} RLU/mg) and Fugene 6 (2.46 x 10^{10} RLU/mg) were found the less efficient (Figure 4a, lower panel). Using a similar approach (Figure 5b), we found that the best miRNA mimic tested was the miRVANA mimic from ThermoFisher (7.59 x 10^{10} RLU/

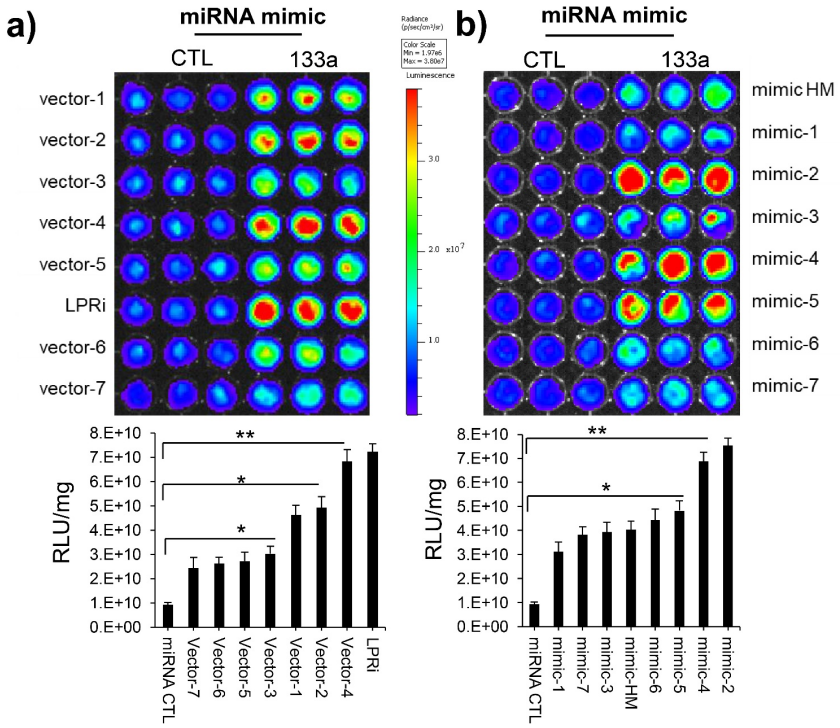

Figure 4. Cell-based miRNA screening platform using the U87MG LentiRILES/133T cell line. The U87MG LentiRILES/133T cells were plated on 96-well plates and then transfected with commercially available **a)** transfection reagents and **b)** miRNA-133a mimics. A homemade miRNA-133 mimic (mimic HM) and lipopolyplexes transfection reagent (LPRi) were included. *Upper panel*: the plates were scanned 3 days later using a bioluminescence scanner. *Lower panel*: same experiment performed on 24-wells plate to normalize bioluminescence values to protein contents in each wells. The data were expressed as mean of RLU/mg ± SEM of one representative experiment performed at least 3 times. Statistics by the two-tailed t-test, *P < 0.05, **P < 0.01, compared to control cells transfected with a miRNA mimic control (miRNA CTL)

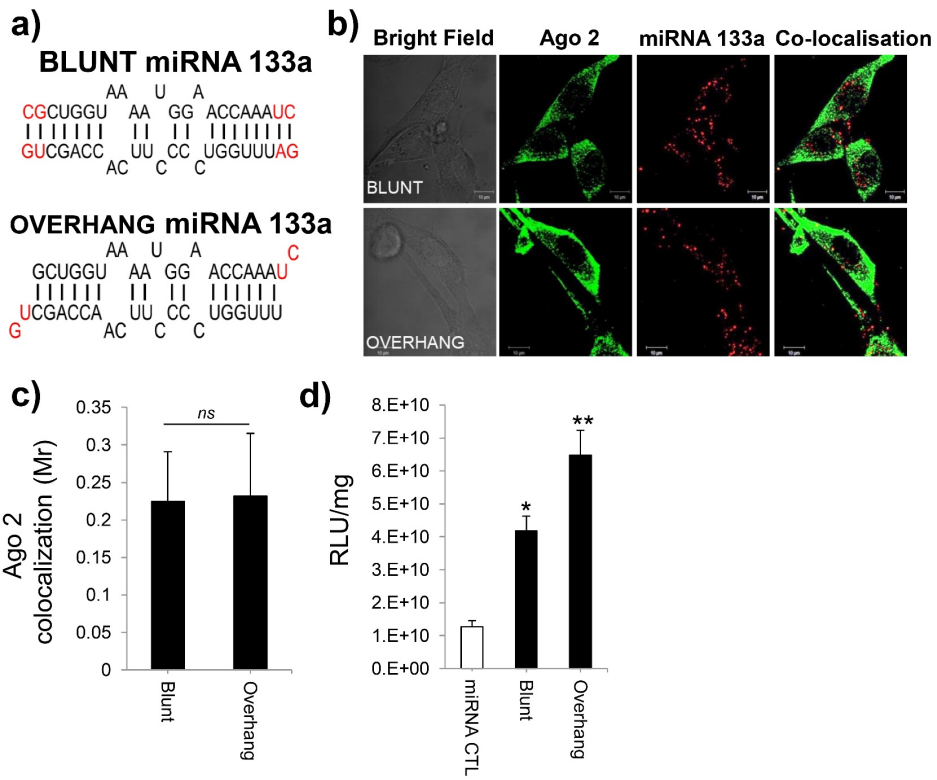

Figure 5. Structure and function relationship study of miRNA-133a duplexes using the U87MG LentiRILES/133 T cell line. **a**) Schematic representation of the structure of the two synthetic miRNA-133a duplexes produced in our laboratory that harbour either blunt-end or 3′ dinucleotide overhang extremities. **b**) Confocal microscopy analysis of U87MG cells transfected with Cy3-labelled miRNA-133a from A. **c**) Percentage of co-localization of Cy3-labelled miRNA-133a from B with Argonaute 2 protein revealed by immunofluorescence staining. **d**) Luciferase activities normalized to protein content (RLU/mg) from U87MG LentiRILES/133T cells transfected with miRNA-133a from A. Data are expressed as mean ± SEM of representative experiments performed at least 3 times. Statistics by the two-tailed t-test, *P < 0.05; **P < 0.01, compared to control cells transfected with a miRNA mimic control (miRNA CTL)

mg) followed closely by the mimic produced by Qiagen (6.89 x 10^{10} RLU/mg). The miRNA mimics produced by Dharmacon (4.83 x 10^{10} RLU/mg), Active Motif (4.66 x 10^{10} RLU/mg), by our laboratory (HM, 4.43 10^{9} RLU/) and by Sigma (4.03 x 10^{10} RLU/mg) were less efficient. We also found that the first generation of miRNA mimic produced by ThermoFisher, called pre-miRNA, was less efficient (3.93 × 10^{10} RLU/mg) than miRVANA (7.24 x 10^{10} RLU/mg) which is the latest generation of miRNA mimics produced by the company. According to this company, the difference between these two generations of synthetic miRNAs can be attributed to proprietary-based chemical modifications of miRNA oligonucleotides. It is therefore interesting to point out that the LentiRILES monitoring system is sensitive enough to discriminate by an almost twofold difference in sensitivity between these two generations of miRNA mimics.

We then examined another possible application of our LentiRILES system by exploring some key features of the relationship between the structure and function of miRNA duplexes [54–56]. We prepared two types of miRNA-133a mimic (Figure 5a): a blunt-end extremity of miRNA-133a duplex and a 3′ dinucleotide overhang miRNA-133a duplex identical to the double-stranded miRNA-133a duplex produced endogenously by the cells and annotated in the mirBAse data base. As impact of the miRNA structures on their intracellular fate in cells after transfection was not reported to our knowledge, we first investigated whether the change in the miRNA structure duplex from asymmetric 3′overhang structure to symmetric blunt structure would affect their intracellular distribution as well as their co-localization with the Argonaute 2 protein. Confocal fluorescence microscopy analysis in Figure 5b demonstrated that the intracellular distribution of the two miRNA structures labelled with Cyanine 3 was similar and also equally co-localized with the Argonaute 2 protein as revealed by immunofluorescence labelling. The determination of the Pearson coefficient (PC) index confirmed this observation as no statistically significant difference was found between the co-localization indices of Argonaute 2 with the overhang (PC = 0.225) and blunt (PC = 0.232) miRNA duplexes (Figure 5c). In contrast, the functionality of these two miRNA duplexes were different (Figure 5d). The overhang, asymmetric miRNA-133a duplex activated by 4.2-fold the RILES/133T system while the

symmetric miRNA-133a duplex activated by only 2.4-fold. This demonstrates that the RISC machinery preferentially processed the overhang, asymmetric miRNA-133a duplex rather than the blunt, symmetric miRNA-133a duplex. These results are in line with previous studies indicating that 3′ nucleotide overhang asymmetric duplex miRNA is a key structural parameter that governs the incorporation and selection of one strand from the miRNA duplex by the RISC machinery, a phenomenon referred to as the thermodynamic asymmetry rule of RNAi duplex [57]. We therefore anticipated that the blunt-end miRNA duplex does not favour such a selection and thus that the RISC machinery might process equally the two strands of miRNA duplexes. The lower luciferase induction monitored by RILES with the blunt-end miRNA duplex can be explained by a direct competition of the two strands of the miRNA-133a duplex for binding to the miR-133 T cassette in cells, which is specific to the mature strand sequence of miRNA 133a, not the passenger strand.

In Vivo bioluminescence monitoring of the kinetic of mirna activity upon delivery in an orthotopic animal model of glioblastoma

A key aspect that has not yet been fully achieved in the field of miRNA therapeutics is the ability to resolve the kinetic of miRNA functionality once delivered in the tumour mass. Better understanding of the long-term activity of synthetic miRNA mimics or inhibitors in targeted tissues would be an advantage to optimize an administration protocol to deliver maximal dose of therapeutic miRNA with minimal toxicity [58,59]. This point is particularly of interest when considering the locoregional treatment of tumour mass located in vulnerable organs such as the brain furthermore isolated from the rest of the body by the blood-brain barrier. Recent advances into clinical practice indicated that the convection-enhanced delivery method is a reliable approach to deliver high drug content in specific areas of the brain, bypassing as such the

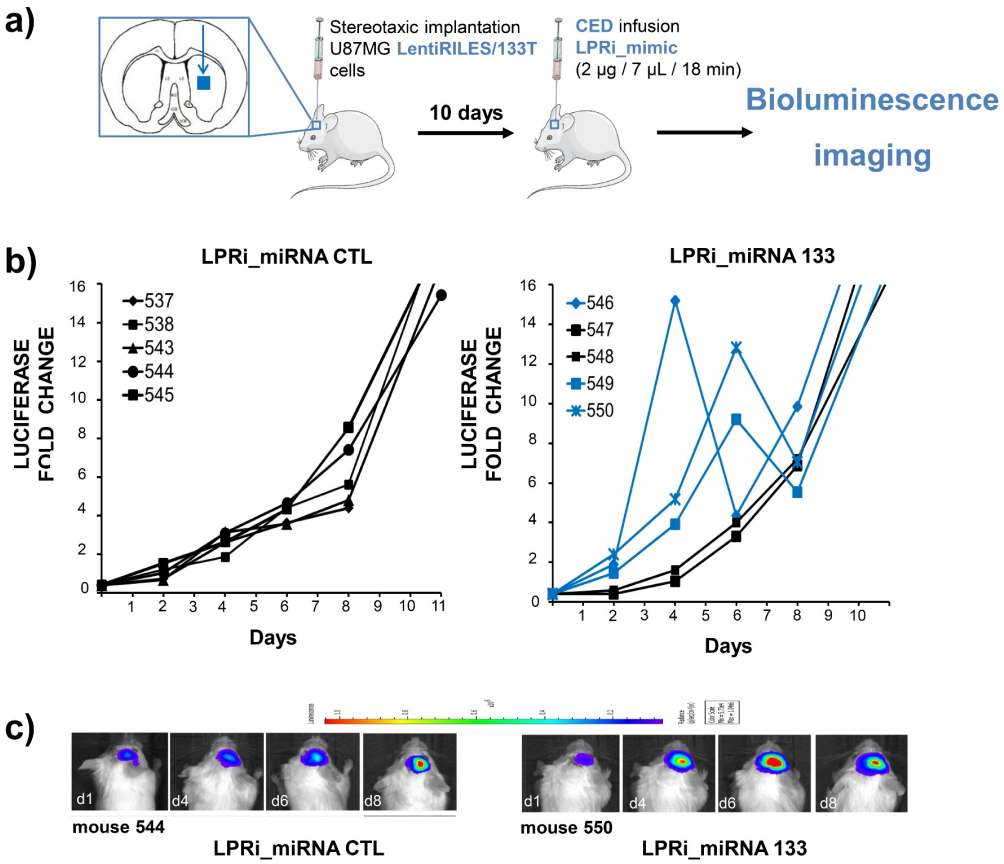

Figure 6. *In vivo* bioluminescence monitoring of kinetic of miRNA-133a activity upon delivery in an orthotopic glioblastoma mouse model. **a**) Schematic representation of the procedure used to establish the kinetic of miRNA-133a *in vivo*. The U87MG LentiRILES/133T cells were implanted in the striatum of mice by stereotaxic surgery and then, 10 days later when the mice developed solid tumours, the miRNA-133a or miRNA control (CTL) were formulated with the LPRi lipopolyplexes and infused locally in tumour masses by convection-enhanced delivery. **b**) Quantitative bioluminescence signals emitted from the brain of mice infused with the LPRi_miRNA-133a and LPRi_miRNA CTL and collected in real time using an *in vivo* bioluminescence scanner. Data are expressed as luciferase activity fold change by normalizing bioluminescence values detected for each mouse at the indicated time point to the minimal value detected on the day of infusion and set to the arbitral value of 1. **c**) Representative bioluminescence images collected from one representative mouse from the LPRi_miRNA-133a and LPRi_miRNA CTL group of animals

blood-brain barrier that prevents therapeutic drugs from reaching the central nervous system. The principle of this delivery method consists in applying a constant pressure gradient to an infusion tip in such way that the fluid flow driven by the convection force allows the drugs to diffuse over large distance and period of time [49,60–62]. However, as this locoregional procedure can be considered as invasive, optimal administration procedures are required to limit the repetition of surgical intervention to implant catheters into the brain without compromising the therapeutic outcome.

Using bioluminescence imaging, we attempted to resolve the dynamics of miRNA activity upon delivery in glioblastoma tumour mass by CED. We implanted the U87MG LentiRILES/133T cells into the striatum of SCID mice. Ten days later, the developed tumour mass was infused with the miRNA-133a complexed with our LPRi nanocarrier by CED (Figure 6a). The mice were thereafter scanned using a bioluminescence imaging scanner over a longitudinal study of 2 weeks (Figure 6b). Typical bioluminescence images collected at several time points from one illustrative mouse per group are shown in Figure 6c.

Bioluminescence analysis of each mice followed over time revealed that the basal luciferase activity of RILES detected in the LPRi_miRNA control group of mice increased proportionally with the tumour proliferation over time (Figure 6b, left panel). In contrast, upon CED infusion of miRNA-133a and thus switching lentiRILES in the ON-configuration, a different pattern of luciferase activity was detected in the LPRi_miRNA-133a group of mice (Figure 6b, right panel). Three of the five mice exhibited two peaks of luciferase activity detected either at day 4 (mouse 546) or day 6 (mice 550 and 549), indicating that the delivery of miRNA-133a mimic was successful in these 3 tumours but also variable. As shown in the right panel of Figure 6b, the luciferase fold change values monitored in mouse #550 and #549 increased gradually over time, reached a maximum peak of activity at day 6 and then dropped, two days later, to the basal level, similar to that detected in the control group (LPRi_miRNA CTL mice, Figure 6b). In contrast, the luciferase activity monitored in mice #546 increased more rapidly in the first 4 days, reached a maximum at this time point (*e.g* day 4) and decreased quickly thereafter to finally reaching the basal bioluminescence levels detected in the control group.

The factors contributing to the heterogeneity of miRNA delivery observed by RILES in these mice are currently not clear and several hypothesis can be inferred. The interaction with the extracellular matrix might allow the LPRi_miRNA-133a nanoparticles to be gradually released in the tumour microenvironment, thus serving as extra-cellular reservoirs [63]. Physical parameters, such as pH values, salt concentration, interstitial tumour fluid pressure can also impact the release rate of LPRi_miRNA-133a nanocarriers from infusion tips into the solid tumours [64–67]. Tumour cells intrinsic processing or recycling of transfected miRNAs through extracellular vesicles can also be involved [68,69] resulting in a long-lasting activity of transfected miRNAs in solid tumour as we recently reported in U87MG cells [47]. While deciphering the exact mechanism of miRNAs diffusion into the brain was not the scope of this study, future experiments are planned to elucidate this process. This study is the first to our knowledge that reports in real time and as a positive readout the kinetic of miRNA delivery and activity in a preclinical animal model of brain tumour.

Taken together, in this first part of this study, we provide evidence that lentiRILES is a relevant miRNA sensor system with several advantages as compared to conventional miRNA monitoring methods such as: 1) detection of miRNA expression/delivery in live cells by real-time fluorescence imaging operating at the single cell level in dividing (cancer) cells; 2) positive readout signal, avoiding the potential confounding factors associated with negative readout such as such as cell death or low-resolution capacity; 3) exploitation as positive readout cell-based miRNA screening platform for screening of innovative miRNA oligonucleotides/transfection reagents and 4) visualization of the kinetic of miRNA activity in a preclinical animal model of cancer that can be exploited to guide the development of more efficient miRNA-delivery systems with potential clinical application. Finally, 5) while miR-ON reporter systems such as tetR KRAB have been used to follow miRNAs regulation during cell fate differentiation over extended periods of time (weeks), the lentiRILES can be employed to follow the endogenous miRNA regulation during cell differentiation over less than one week (Figure 3a-d). Disadvantages of the lentiRILES miR-ON reporter may include the time needed to establish the stable cell line (Figure 1c) and the dependence on cell line permissiveness to lentivirus infection (Figure 1d).

Therapeutic Evaluation of Mirna-200 c in the Orthotopic Animal Model of Glioblastoma

Finally, we decided to evaluate the therapeutic relevancy of a locoregional RNAi treatment of glioblastoma by infusion of tumour beds with a tumour suppressor miRNA by CED guided by the RILES (Figure 6). Over the last decade, a growing number of tumour suppressor miRNAs have been discovered to play pivotal roles in tumorigenesis [70,71]. We decided to focus our experiments on the tumour suppressor miRNA-200c [72,73]. Gain-of-function studies performed in our laboratory indicated that transfection of miRNA-200c in U87MG cells impaired significantly the proliferation rate of these tumour cells (Figure 7a) by inducing cell cycle arrest in G1 phase (Figure 7b) but without inducing apoptosis (Figure 7c). We observed a drastic change in the morphology of U87MG cells after miRNA-200c transfection (data not shown) and investigated whether the ectopic expression miRNA-200c in these cells might induce a reversal phenotype from the mesenchymal to the epithelial phenotype (MET). As shown in Figure 7d, significant reduction of relative mRNAs expression of mesenchymal markers, ZEB-1 (38.2% reduction), ZEB-2 (49.4% reduction) and Vimentin (21% reduction) were detected after miRNA-200c transfection, which correlated with the *de novo* expression of epithelial E-Cadherin marker (16.3-fold increase). Based on these data, we evaluated the impact of this change in the cell morphology on the migratory behaviour of the U87MG cells. Wound-healing scratch assay in Figure 7e

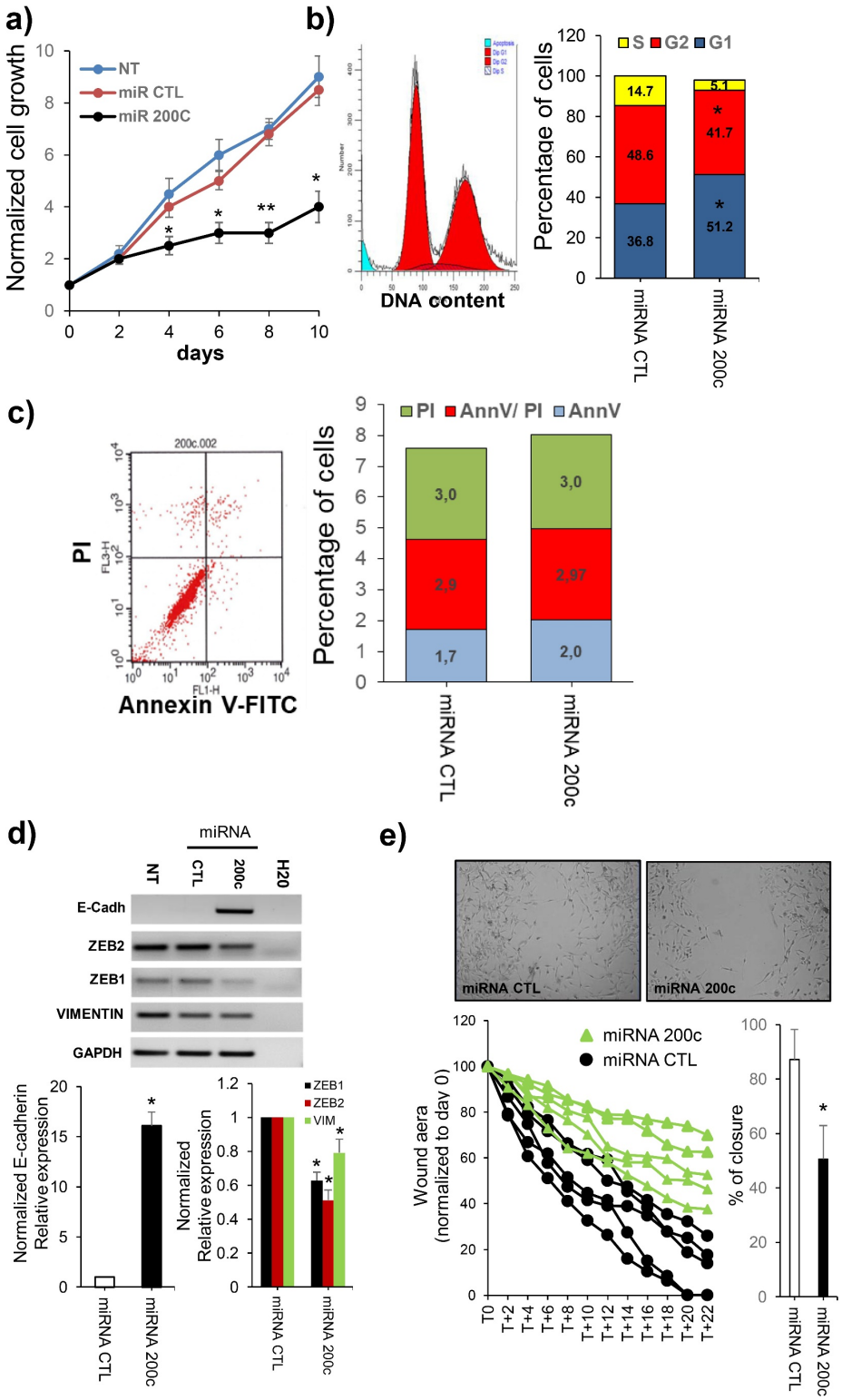

Figure 7. Tumour suppressive function evaluation of miRNA-200c in U87MG cells *in vitro*. **a**) Alamar Blue cell proliferation assay, **b**) flow cytometry analysis of cell cycle and **c**) apoptosis assay of U87MG cells transfected with miRNA-200c or miRNA control (miRNA CTL). **d**) *Upper panel*: Agarose gel analysis of the RT-PCR products generated with specific primers to detect expression of the E-cadherin, vimentin, ZEB1 and ZEB2 EMT markers after transfection of U87MG cells with miRNA-200c or miRNA control (miRNA CTL). *Lower panel*: the same experiment analysed by quantitative RT-PCR. **e)** Wound healing assay of U87MG cells transfected with miRNA-

200c or miRNA control (miRNA CTL). *Upper panel*, representative pictures of cell monolayers collected 16 hours after wound scratch. *Lower panel, left*, time lapse of wound area closure measured by imaging software from pictures taken every 2 hours over a period of time of 24 hours. *Lower panel, right*, percentage of wound closure from U87MG cell transfected with miRNA-200c or miRNA control (miRNA CTL) normalized to the wound surface area detected at T0 and set to the arbitral value of 1. Data are expressed as mean ± SEM of one representative experiments performed at least 3 times. Statistics by the two-tailed t-test, *P < 0.05, **P < 0.01, compared to control cells transfected with miRNA mimic control (miRNA CTL)

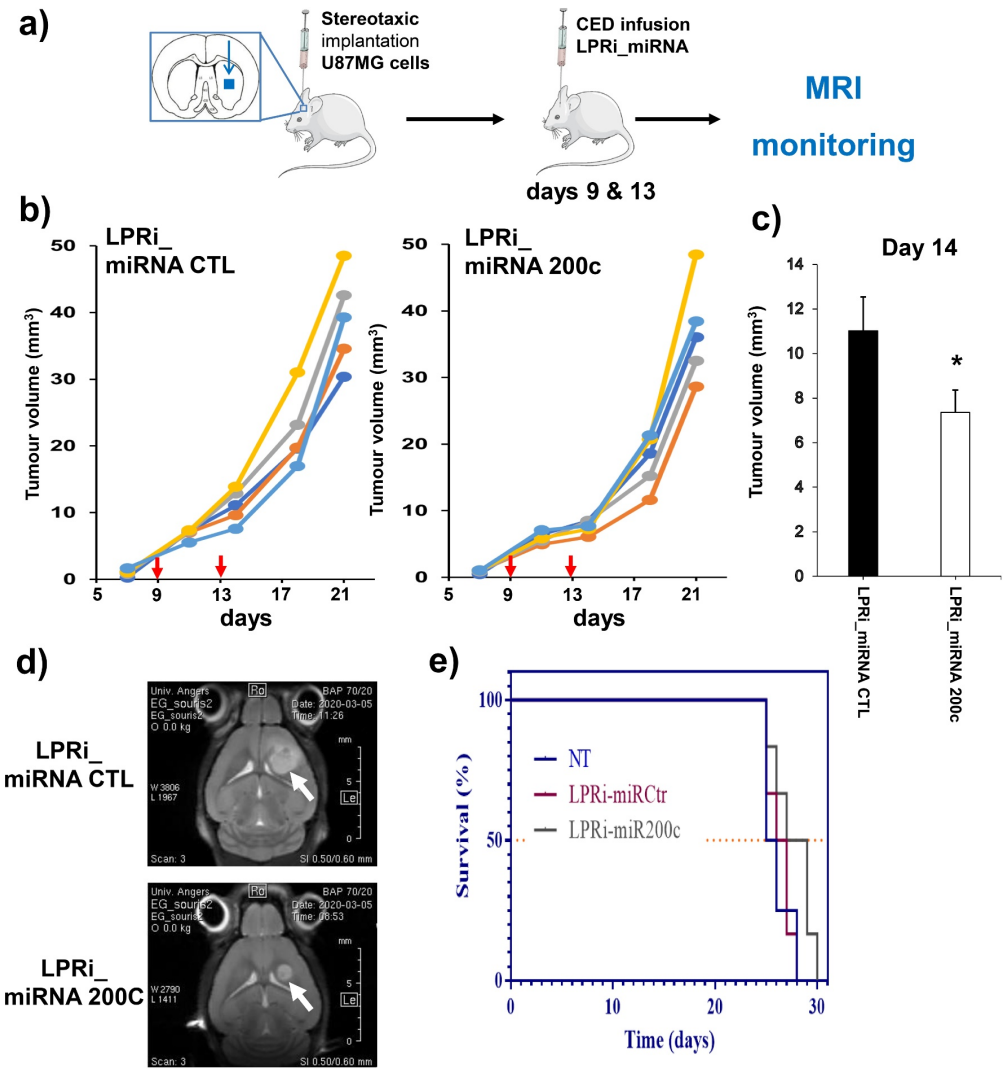

Figure 8. Tumour suppressive evaluation of miRNA-200c in a preclinical animal model of glioblastoma. **a**) Schematic representation of the procedure used to evaluate the therapeutic potential of miRNA-200c. The U87MG cells were implanted in the brain of mice and then when the mice developed solid tumours, the miRNA-200c or miRNA control were formulated with the LPRi lipopolyplexes and infused locoregionally, twice, at days 9 and 13 by convection-enhanced delivery. **b**) Tumour growth in both treatment groups monitored by MRI imaging once a week. **c**) Statistical analysis of tumour volumes collected at day 14 from the two groups of animals (n = 5 for each). **d**) Representative MRI performed at day 14 after implantation of U87MG cells (arrows indicate tumour tissue). **e**) Kaplan Meier curve. Data are expressed as mean ± SEM of one representative experiment performed twice. Statistics by the two-tailed t-test, *P < 0.05 compared to control group of animal infused with the LPRi_miRNA CTL

demonstrated that transfection of miRNA-200c significantly delayed (p = 0.028) the migratory capability of the U87MG cells, notably at the 22 hours time point, where the percentage of wound closure was reduced by 51.3 %. Overall, these biological changes in U87MG cells are relevant for glioblastoma treatment as this tumour type is characterized by rapid growth and local invasion of surrounding tissue [74–76]. Furthermore, Quin et al. [77] demonstrated that the stable overexpression of miRNA-200c in glioblastoma reduced the proliferation and invasion rate of glioma cells *in vitro* and *in vivo* in a subcutaneous xenografts animal model of glioblastoma. Although this study has merit as it

provides novel insights into the mode of action of miRNA-200c in a glioblastoma context, it cannot objectively, as acknowledged by the authors, inquire into the therapeutic value of miRNA-200c to treat brain tumours.

We decided to address this point using a miRNA delivery approach to closely mimic a clinical intervention in which the miRNA-200c will be infused directly into the tumour mass using a miRNA-nanocarrier, the LPRi lipopolyplexes and the CED as delivery method. As the RILES system indicated that the delivered miRNAs are active for 4 to 6 days upon delivery (Figure 6), we infused the U87MG solid tumours twice with the LPRi_miRNA-200c by CED, spaced by an interval of time of 4 days (Figure 8a). The therapeutic impact of this targeted miRNA-200c delivery approach in glioblastoma development was evaluated by magnetic resonance imaging (MRI) performed over a 3 weeks period of time.

As shown in Figure 8b, the overall growth rate of tumour development was found similar between the LPRi_miRNA CTL and LPRi_miRNA-200c group of animals although a plateau of growth of tumour mass was visible between days 11 to 14 in the LPRi_miRNA-200c group of animals. Statistical analysis performed at day 14 indicated that tumour volumes in the LPRi_miRNA-200c group of animals were significantly smaller (p = 0.03, Figure 8c) than those detected in the LPRi_miRNA CTL group of animals. Representative MRI of one representative tumour mass by group of animals is showed in Figure 8d. Smaller size of tumour mass is noticeably visible at this time point. However, beyond this time frame no other statistically significant difference was found. These results indicate that the treatment of glioblastoma tumours twice with the LPRi_miRNA-200c can significantly delay the proliferation rate of tumour cells but this effect is transient and reversible. The Kaplan-Meier survival curves draw from this experience confirm the above statement. Although the median survival time of the two groups of animals differed by 2 days in beneficial of the miRNA-200c group of animals, no statistically significant difference was observed between these two groups of animals (Figure 8e).

Based on this data, it might be tempting to speculate that repeated administrations (*i.e.* more than twice) of the LPRi_miRNA-200c might be necessary to reach a better therapeutic outcome. However, as we observed *in vitro* that miRNA-200c exerted a mild cytostatic effect in U87MG tumour cells, characterized by a cell cycle arrest of U87MG cells in G1 and S-phase without inducing apoptosis (Figure 7a-c), locoregional therapeutic intervention of glioblastoma with miRNA-200c mimic needs to be addressed with caution. A combinatorial treatment with another therapeutic agent might be required to reach a better curative treatment. In the specific context of glioblastoma, a combined treatment of miRNA-200c with radiotherapy seems particularly suitable. External beam therapy has long been used as a keystone treatment in glioblastoma patients but results from clinical studies indicated that combinatory treatments are required for an optimal therapeutic outcome [78]. Interestingly, it was recently reported that overexpression of miRNA-200c in different cancer cells including glioblastoma inhibited invasion, migration, and vascular tube formation and increased the radiosensitivity of tumour cells by modulating the EGFR signalling pathway and favouring persistence of the γH2AX focus [79]. Exploiting the radio-sensitizing properties of miRNA-200c in combination with a radiotherapy protocol deserves to be addressed *in vivo*. Repeated administration of miRNA-200c, guided by RILES after radiotherapy, might provide a therapeutic advantage. We are currently assaying this point as well as investigating the radiosensitizing role of other miRNA candidates recently identified through a molecular screening procedure applied on biopsies of patients with radioresistant glioblastoma tumours.

Conclusion

Taken together, our work demonstrates that the genetic-switch RILES expression system integrated in a lentivirus is a relevant approach to monitor the endogenous and exogenous dynamic expression of miRNAs in fast-dividing biology systems such as cancer cells. We performed a complete set of validation studies at the molecular and cellular level and demonstrated that LentiRILES is a robust, specific and sensitive integrative miR-ON monitoring system that can be exploited to resolve the dynamic of miRNA activity over short [47] and, here, long periods of time. We explored several applications of LentiRILES in the field of miRNA biology and therapeutics *in vitro* and demonstrated the feasibility of this novel system for *in vivo* monitoring of miRNA mimic delivery. Because of its relatively easy production and versatility, we anticipate that the LentiRILES system holds promise for multiple applications in the field of miRNA biology as well as gene and cellular therapy.

Acknowledgments

We thank Stéphanie Lerondel, Maryline Le Mée, Stéphanie Rétif and Julien Sobilo (TAAM/CIPA, CNRS UPS 44, Orléans) for their technical assistance and for access to the Lumina Bioluminescence scanner. We also thank Elizabeth Rowley-Jolivet (elizabeth.rowley-jolivet@orange.fr) for English language editing.

Disclosure statement

Francisco Martin is inventor of 'Highly inducible dual-promoter lentiviral Tet-On' (CT/EP2012/059408) licensed to Canvax Biotech.

Funding

This work was funded by the Institut National du Cancer (INCa) [PL-BIO 2014–2020, consortium MARENGO: MicroRNA agonist and antagonist Nanomedicines for GliOblastoma treatment: from molecular programming to preclinical validation to P.B and E.G]; La Ligue Contre le Cancer [Région du Loiret 2017-2019 to P.B]; ARD 2020 Biopharmaceuticals [RNA cell factory 2017-2020 to C.P]. The work was also related to the French National Research Agency (ANR) through the LabEx IRON (Innovative Radiopharmaceuticals in Oncology and Neurology to E.G) as part of the French government Investissements d'Avenir program (ANR-11-LABX-0018 to E.G) and to the ANR under the frame of EuroNanoMed III (project GLIOSILK to E.G). LR was a PhD fellow funded by the LabEx IRON-2 and the University of Angers. h[;

ORCID

Viorel Simion http://orcid.org/0000-0002-2683-2871

References

[1] Nazarov PV, Reinsbach SE, Muller A, et al. Interplay of microRNAs, transcription factors and target genes: linking dynamic expression changes to function. Nucleic Acids Res. 2013;41(5):2817–2831. PMCID: 3597666
[2] O'Brien J, Hayder H, Zayed Y, et al. Overview of MicroRNA biogenesis, mechanisms of actions, and circulation. Front Endocrinol (Lausanne). 2018;9:402. PMCID: 6085463
[3] Osada H, Takahashi T. MicroRNAs in biological processes and carcinogenesis. Carcinogenesis. 2007;28(1):2–12.
[4] Cai X, Hagedorn CH, Cullen BR. Human microRNAs are processed from capped, polyadenylated transcripts that can also function as mRNAs. RNA. 2004;10(12):1957–1966. PMCID: 1370684
[5] Lee Y, Ahn C, Han J, et al. The nuclear RNase III Drosha initiates microRNA processing. Nature. 2003;425(6956):415–419.
[6] Grishok A, Pasquinelli AE, Conte D, et al. Genes and mechanisms related to RNA interference regulate expression of the small temporal RNAs that control C. elegans developmental timing. Cell. 2001;106(1):23–34.
[7] Hutvagner G, McLachlan J, Pasquinelli AE, et al. A cellular function for the RNA-interference enzyme Dicer in the maturation of the let-7 small temporal RNA. Science. 2001;293(5531):834–838.
[8] Jonas S, Izaurralde E. Towards a molecular understanding of microRNA-mediated gene silencing. Nat Rev Genet. 2015;16(7):421–433.
[9] Wu J, Yang J, Cho WC, et al. Argonaute proteins: structural features, functions and emerging roles. J Adv Res. 2020;24:317–324. PMCID: 7235612
[10] Gebert LFR, MacRae IJ. Regulation of microRNA function in animals. Nat Rev Mol Cell Biol. 2019;20(1):21–37. PMCID: 6546304
[11] Huntzinger E, Izaurralde E. Gene silencing by microRNAs: contributions of translational repression and mRNA decay. Nat Rev Genet. 2011;12(2):99–110.
[12] Shivdasani RA. MicroRNAs: regulators of gene expression and cell differentiation. Blood. 2006;108(12):3646–3653. PMCID: 1895474
[13] Rupaimoole R, Slack FJ. MicroRNA therapeutics: towards a new era for the management of cancer and other diseases. Nat Rev Drug Discov. 2017;16(3):203–222.
[14] Lim LP, Lau NC, Weinstein EG, et al. The microRNAs of Caenorhabditis elegans. Genes Dev. 2003;17(8):991–1008. PMCID: 196042
[15] Sokol NS. Small temporal RNAs in animal development. Curr Opin Genet Dev. 2012;22(4):368–373. PMCID: 3419770
[16] Pauli A, Rinn JL, Schier AF. Non-coding RNAs as regulators of embryogenesis. Nat Rev Genet. 2011;12(2):136–149. PMCID: 4081495
[17] Ebert MS, Sharp PA. Roles for microRNAs in conferring robustness to biological processes. Cell. 2012;149(3):515–524. PMCID: 3351105
[18] Wightman B, Ha I, Ruvkun G. Posttranscriptional regulation of the heterochronic gene lin-14 by lin-4 mediates temporal pattern formation in C. elegans. Cell. 1993;75(5):855–862.
[19] Reinhart BJ, Slack FJ, Basson M, et al. The 21-nucleotide let-7 RNA regulates developmental timing in Caenorhabditis elegans. Nature. 2000;403(6772):901–906.
[20] Johnson SM, Lin SY, Slack FJ. The time of appearance of the C. elegans let-7 microRNA is transcriptionally controlled utilizing a temporal regulatory element in its promoter. Dev Biol. 2003;259(2):364–379.
[21] Bracht JR, Van Wynsberghe PM, Mondol V, et al. Regulation of lin-4 miRNA expression, organismal growth and development by a conserved RNA binding protein in C. elegans. Dev Biol. 2010;348(2):210–221. PMCID: 2982876
[22] Kai ZS, Finnegan EF, Huang S, et al. Multiple cis-elements and trans-acting factors regulate dynamic spatio-temporal transcription of let-7 in Caenorhabditis elegans. Dev Biol. 2013;374(1):223–233. PMCID: 3548979
[23] Kucherenko MM, Barth J, Fiala A, et al. Steroid-induced microRNA let-7 acts as a spatio-temporal code for neuronal cell fate in the developing Drosophila brain. EMBO J. 2012;31(24):4511–4523. PMCID: 3545287
[24] Li T, Pan H, Li R. The dual regulatory role of miR-204 in cancer. Tumour Biol. 2016;37(9):11667–11677. PMCID: 5080331
[25] Jiang H, Zhang G, Wu JH, et al. Diverse roles of miR-29 in cancer (review). Oncol Rep. 2014;31(4):1509–1516.
[26] Dykxhoorn DM. MicroRNAs and metastasis: little RNAs go a long way. Cancer Res. 2010;70(16):6401–6406. PMCID: 2922433
[27] Ma L. Role of miR-10b in breast cancer metastasis. Breast Cancer Res. 2010;12(5):210. PMCID: 3096969
[28] Lee SJ, Kim MJ, Kwon IC, et al. Delivery strategies and potential targets for siRNA in major cancer types. Adv Drug Deliv Rev. 2016;104:2–15. PMCID: 4958528
[29] Jones D. Setbacks shadow microRNA therapies in the clinic. Nat Biotechnol. 2018;36(10):909–910.
[30] Setten RL, Rossi JJ, Han SP. The current state and future directions of RNAi-based therapeutics. Nat Rev Drug Discov. 2019;18(6):421–446.
[31] Kang WJ, Cho YL, Chae JR, et al. Molecular beacon-based bioimaging of multiple microRNAs during myogenesis. Biomaterials. 2011;32(7):1915–1922.
[32] Hernandez R, Orbay H, Cai W. Molecular imaging strategies for in vivo tracking of microRNAs: a comprehensive review. Curr Med Chem. 2013;20(29):3594–3603. PMCID: 3749288
[33] Baker MB, Bao G, Searles CD. In vitro quantification of specific microRNA using molecular beacons. Nucleic Acids Res. 2012;40(2):e13. PMCID: 3258119
[34] Schug J, McKenna LB, Walton G, et al. Dynamic recruitment of microRNAs to their mRNA targets in the regenerating liver. BMC Genomics. 2013;14(1):264. PMCID: 3639193
[35] Kim HJ, Kim YH, Lee DS, et al. In vivo imaging of functional targeting of miR-221 in papillary thyroid carcinoma. J Nucl Med. 2008;49(10):1686–1693.
[36] Pichard V, Aubert D, Boni S, et al. Specific micro RNA-regulated TetR-KRAB transcriptional control of transgene expression in viral vector-transduced cells. PloS One. 2012;7(12):e51952. PMCID: 3522580
[37] Amendola M, Giustacchini A, Gentner B, et al. A double-switch vector system positively regulates transgene expression by endogenous microRNA expression (miR-ON vector). Mol Ther. 2013;21(5):934–946. PMCID: 3666624
[38] Rossetti S, Anauo MJ, Sacchi N. MiR-221-regulated KIT level by wild type or leukemia mutant RUNX1: a determinant of single myeloblast fate decisions that - collectively – drives or hinders granulopoiesis. Oncotarget. 2017;8(49):85783–85793. PMCID: 5689646
[39] Ecco G, Imbeault M, Trono D. KRAB zinc finger proteins. Development. 2017;144(15):2719–2729.
[40] Rowe HM, Jakobsson J, Mesnard D, et al. KAP1 controls endogenous retroviruses in embryonic stem cells. Nature. 2010;463(7278):237–240.
[41] Stieger K, Belbellaa B, Le Guiner C, et al. In vivo gene regulation using tetracycline-regulatable systems. Adv Drug Deliv Rev. 2009;61(7–8):527–541.
[42] Wolf G, Yang P, Fuchtbauer AC, et al. The KRAB zinc finger protein ZFP809 is required to initiate epigenetic silencing of endogenous retroviruses. Genes Dev. 2015;29(5):538–554. PMCID: 4358406
[43] Groner AC, Meylan S, Ciuffi A, et al. KRAB–Zinc finger proteins and KAP1 can mediate long-range transcriptional repression through heterochromatin spreading. PLoS Genet. 2010;6(3):e1000869. PMCID: 2832679
[44] Baril P, Pichon C. Positive bioluminescence imaging of MicroRNA expression in small animal models using an

engineered genetic-switch expression system, RILES. Methods Mol Biol. 2016;1372:193–208.
[45] Ezzine S, Vassaux G, Pitard B, et al. RILES, a novel method for temporal analysis of the in vivo regulation of miRNA expression. Nucleic Acids Res. 2013;41(20):e192. PMCID: 3814383
[46] Simion V, Sobilo J, Clemoncon R, et al. Positive radionuclide imaging of miRNA expression using RILES and the human sodium iodide symporter as reporter gene is feasible and supports a protective role of miRNA-23a in response to muscular atrophy. PloS One. 2017;12(5):e0177492. PMCID: 5426778
[47] Simion V, Henriet E, Juric V, et al. Intracellular trafficking and functional monitoring of miRNA delivery in glioblastoma using lipopolyplexes and the miRNA-ON RILES reporter system. J Control Release. 2020;327:429–443.
[48] Benabdellah K, Cobo M, Munoz P, et al. Development of an all-in-one lentiviral vector system based on the original TetR for the easy generation of Tet-ON cell lines. PloS One. 2011;6(8):e23734. PMCID: 3158098
[49] Sehedic D, Chourpa I, Tetaud C, et al. Locoregional confinement and major clinical benefit of (188)Re-Loaded CXCR4-targeted nanocarriers in an orthotopic human to mouse model of glioblastoma. Theranostics. 2017;7(18):4517–4536. PMCID: 5695146
[50] Denning W, Das S, Guo S, et al. Optimization of the transductional efficiency of lentiviral vectors: effect of sera and polycations. Mol Biotechnol. 2013;53(3):308–314. PMCID: 3456965
[51] Chen JF, Mandel EM, Thomson JM, et al. The role of microRNA-1 and microRNA-133 in skeletal muscle proliferation and differentiation. Nat Genet. 2006;38(2):228–233. PMCID: 2538576
[52] Yang CH, Yue J, Pfeffer SR, et al. MicroRNA-21 promotes glioblastoma tumorigenesis by down-regulating insulin-like growth factor-binding protein-3 (IGFBP3). J Biol Chem. 2014;289(36):25079–25087. PMCID: 4155674
[53] Goncalves C, Berchel M, Gosselin MP, et al. Lipopolyplexes comprising imidazole/imidazolium lipophosphoramidate, histidinylated polyethyleneimine and siRNA as efficient formulation for siRNA transfection. Int J Pharm. 2014;460(1–2):264–272.
[54] Bramsen JB, Laursen MB, Nielsen AF, et al. A large-scale chemical modification screen identifies design rules to generate siRNAs with high activity, high stability and low toxicity. Nucleic Acids Res. 2009;37(9):2867–2881. PMCID: 2685080
[55] Rana TM. Illuminating the silence: understanding the structure and function of small RNAs. Nat Rev Mol Cell Biol. 2007;8(1):23–36.
[56] Yoshioka K, Kunieda T, Asami Y, et al. Highly efficient silencing of microRNA by heteroduplex oligonucleotides. Nucleic Acids Res. 2019;47(14):7321–7332. PMCID: 6698647
[57] Hu HY, Yan Z, Xu Y, et al. Sequence features associated with microRNA strand selection in humans and flies. BMC Genomics. 2009;10:413. PMCID: 2751786
[58] Pierce RL. Translational nanomedicine–through the therapeutic window. Nanomedicine (Lond). 2015;10(21):3249–3260.
[59] Cooney L, Loke YK, Golder S, et al. Overview of systematic reviews of therapeutic ranges: methodologies and recommendations for practice. BMC Med Res Methodol. 2017;17(1):84. PMCID: 5455119
[60] Saucier-Sawyer JK, Seo YE, Gaudin A, et al. Distribution of polymer nanoparticles by convection-enhanced delivery to brain tumors. J Control Release. 2016;232:103–112. PMCID: 4893898
[61] Mehta AM, Sonabend AM, Bruce JN. Convection-Enhanced Delivery. Neurotherapeutics. 2017;14(2):358–371. PMCID: 5398992
[62] Seo YE, Bu T, Saltzman WM. Nanomaterials for convection-enhanced delivery of agents to treat brain tumors. Curr Opin Biomed Eng. 2017;4:1–12. PMCID: 5761746
[63] Engin AB, Nikitovic D, Neagu M, et al. Mechanistic understanding of nanoparticles' interactions with extracellular matrix: the cell and immune system. Part Fibre Toxicol. 2017;14(1):22. PMCID: 5483305
[64] Khawar IA, Kim JH, Kuh HJ. Improving drug delivery to solid tumors: priming the tumor microenvironment. J Control Release. 2015;201:78–89.
[65] Dzobo K, Senthebane DA, Thomford NE, et al. Not everyone fits the mold: intratumor and intertumor heterogeneity and innovative cancer drug design and development. OMICS. 2018;22(1):17–34.
[66] Sagnella SM, McCarroll JA, Kavallaris M. Drug delivery: beyond active tumour targeting. Nanomedicine. 2014;10(6):1131–1137.
[67] Dagogo-Jack I, Shaw AT. Tumour heterogeneity and resistance to cancer therapies. Nat Rev Clin Oncol. 2018;15(2):81–94.
[68] Ipas H, Guttin A, Issartel JP. Exosomal MicroRNAs in Tumoral U87 MG versus normal astrocyte cells. Microrna. 2015;4(2):131–145.
[69] Luhtala N, Aslanian A, Yates JR 3rd, et al. Secreted glioblastoma nanovesicles contain intracellular signaling proteins and active ras incorporated in a Farnesylation-dependent Manner. J Biol Chem. 2017;292(2):611–628. PMCID: 5241736
[70] Zhang B, Pan X, Cobb GP, et al. microRNAs as oncogenes and tumor suppressors. Dev Biol. 2007;302(1):1–12.
[71] Frixa T, Donzelli S, Blandino G. Oncogenic MicroRNAs: key players in malignant transformation. Cancers (Basel). 2015;7(4):2466–2485. PMCID: 4695904
[72] Mutlu M, Raza U, Saatci O, et al. miR-200c: a versatile watchdog in cancer progression, EMT, and drug resistance. J Mol Med (Berl). 2016;94(6):629–644.
[73] Kumar S, Nag A, Mandal CC, et al. Review on miR-200c, A promising cancer biomarker with therapeutic potential. Curr Drug Targets. 2015;16(12):1381–1403.
[74] Huse JT, Holland EC. Targeting brain cancer: advances in the molecular pathology of malignant glioma and medulloblastoma. Nat Rev Cancer. 2010;10(5):319–331.
[75] Hatoum A, Mohammed R, Zakieh O. The unique invasiveness of glioblastoma and possible drug targets on extracellular matrix. Cancer Manag Res. 2019;11:1843–1855. PMCID: 6395056
[76] Feng X, Wang Z, Fillmore R, et al. MiR-200, a new star miRNA in human cancer. Cancer Lett. 2014;344(2):166–173. PMCID: 3946634
[77] Qin Y, Chen W, Liu B, et al. MiR-200c inhibits the tumor progression of glioma via targeting moesin. Theranostics. 2017;7(6):1663–1673. PMCID: 5436519
[78] Mirimanoff RO, Gorlia T, Mason W, et al. Radiotherapy and temozolomide for newly diagnosed glioblastoma: recursive partitioning analysis of the EORTC 26981/22981-NCIC CE3 phase III randomized trial. J Clin Oncol. 2006;24(16):2563–2569.
[79] Koo T, Cho BJ, Kim DH, et al. MicroRNA-200c increases radiosensitivity of human cancer cells with activated EGFR-associated signaling. Oncotarget. 2017;8(39):65457–65468. PMCID: 5630345

Appendice III

Article: Rapamycin-Loaded Lipid Nanocapsules Induce Selective Inhibition of the mTORC1-Signaling Pathway in Glioblastoma Cells

Delphine Séhédic, **Loris Roncali**, Amel Djoudi, Nela Buchtova, Sylvie Avril, Michel Chérel, Frank Boury, Franck Lacoeuille, François Hindré and Emmanuel Garcion*

Séhédic D, Roncali L, Djoudi A, *et al.* Rapamycin-Loaded Lipid Nanocapsules Induce Selective Inhibition of the mTORC1-Signaling Pathway in Glioblastoma Cells. Front Bioeng Biotechnol. 2021;8:602998. Published 2021 Feb 25. doi:10.3389/fbioe.2020.602998

frontiers in Bioengineering and Biotechnology

ORIGINAL RESEARCH
published: 25 February 2021
doi: 10.3389/fbioe.2020.602998

Rapamycin-Loaded Lipid Nanocapsules Induce Selective Inhibition of the mTORC1-Signaling Pathway in Glioblastoma Cells

*Delphine Séhédic[1], Loris Roncali[1], Amel Djoudi[1], Nela Buchtova[1], Sylvie Avril[1], Michel Chérel[2], Frank Boury[1], Franck Lacoeuille[1], François Hindré[1] and Emmanuel Garcion[1]**

[1] Univ Angers, Université de Nantes, Inserm, CRCINA, SFR ICAT, Angers, France, [2] Université de Nantes, Inserm, CNRS, CRCINA, Nantes, France

Inhibition of the PI3K/Akt/mTOR signaling pathway represents a potential issue for the treatment of cancer, including glioblastoma. As such, rapamycin that inhibits the mechanistic target of rapamycin (mTOR), the downstream effector of this signaling pathway, is of great interest. However, clinical development of rapamycin has floundered due to the lack of a suitable formulation of delivery systems. In the present study, a novel method for the formulation of safe rapamycin nanocarriers is investigated. A phase inversion process was adapted to prepare lipid nanocapsules (LNCs) loaded with the lipophilic and temperature sensitive rapamycin. Rapamycin-loaded LNCs (LNC-rapa) are ∼110 nm in diameter with a low polydispersity index (<0.05) and the zeta potential of about −5 mV. The encapsulation efficiency, determined by spectrophotometry conjugated with filtration/exclusion, was found to be about 69%, which represents 0.6 wt% of loading capacity. Western blot analysis showed that LNC-rapa do not act synergistically with X-ray beam radiation in U87MG glioblastoma model *in vitro*. Nevertheless, it demonstrated the selective inhibition of the phosphorylation of mTORC1 signaling pathway on Ser2448 at a concentration of 1 μM rapamycin in serum-free medium. Interestingly, cells cultivated in normoxia (21% O_2) seem to be more sensitive to mTOR inhibition by rapamycin than those cultivated in hypoxia (0.4% O_2). Finally, we also established that mTOR phosphorylation inhibition by LNC-rapa induced a negative feedback through the activation of Akt phosphorylation. This phenomenon was more noticeable after stabilization of HIF-1α in hypoxia.

Keywords: rapamycin, nanoparticles, radiation, hypoxia, mTOR, Akt, HIF-1α, cancer

OPEN ACCESS

Edited by:
Guillermo Raul Castro, Consejo Nacional de Investigaciones Científicas y Técnicas (CONICET), Argentina

Reviewed by:
Maria Do Carmo Pereira, University of Porto, Portugal
Antonio Giordano, Temple University, United States

***Correspondence:**
Emmanuel Garcion
emmanuel.garcion@univ-angers.fr

Specialty section:
This article was submitted to Nanobiotechnology, a section of the journal Frontiers in Bioengineering and Biotechnology

Received: *07 September 2020*
Accepted: *29 December 2020*
Published: *25 February 2021*

Citation:
Séhédic D, Roncali L, Djoudi A, Buchtova N, Avril S, Chérel M, Boury F, Lacoeuille F, Hindré F and Garcion E (2021) Rapamycin-Loaded Lipid Nanocapsules Induce Selective Inhibition of the mTORC1-Signaling Pathway in Glioblastoma Cells. Front. Bioeng. Biotechnol. 8:602998. doi: 10.3389/fbioe.2020.602998

INTRODUCTION

Glioblastoma (GB) is the most common and deadly primary brain tumor in adults (Ostrom et al., 2017). Despite remarkable advances in surgical techniques and treatment options including chemotherapy and radiotherapy, the prognosis of this disease remains very poor with a median survival under 15 months (Stupp et al., 2005, 2009). Therefore, the understanding of the molecular mechanisms that drive malignancy in glioblastoma is seriously needed for the development of new agents specifically targeting tumor cells and the tumor microenvironment (Touat et al., 2017; Najberg et al., 2019).

The phosphatidylinositol 3-kinase (PI3K)/protein kinase B (Akt)/mechanistic target of rapamycin (mTOR) intracellular signaling pathway plays a central role in the regulation of cell proliferation, growth, differentiation, and survival (Sonoda et al., 2001; Bjornsti and Houghton, 2004; Knobbe et al., 2005; Castellino and Durden, 2007; Jiang and Liu, 2009). Stimulation of this pathway results in the activation of a receptor tyrosin kinase (RTK) by a cytokine or a growth factor, which drive a sequential phosphorylation of PI3K, Akt, and mTOR. mTOR regulates cell growth and survival *via* two different multiprotein complexes, mTORC1 and mTORC2. The complex mTORC1 is composed of mTOR, regulatory-associated protein of mTOR (Raptor), mammalian lethal with Sec13 protein 8 (mLST8), proline-rich AKT substrate 40 kDa (PRAS40), and DEP-domain-containing mTOR-interacting protein (Deptor) (Saxton and Sabatini, 2017). mTORC1 activates the eukaryotic initiation factor 4E (eIF4E)-binding protein, releasing the transcription factor eIF4E and the p70 ribosomal S6 kinase 1 (S6K1 or p70S6K) implicated in translation (Heimberger et al., 2005).

This pathway can be activated through numbers of mechanisms, including growth factors, overexpression or amplification of Akt family members, inactivation of the inhibitory effects of PTEN (phosphatase and tensin homolog) tumor suppressor or by non-canonical Wnt pathway (Saxton and Sabatini, 2017). Furthermore, radiation can also activate mTOR signaling in vascular endothelium and in glioblastoma cell lines (Eshleman et al., 2002; Shinohara et al., 2005; Anandharaj et al., 2011). Consequently, mutations in the PI3K or AKT genes, loss of PTEN, epigenetic modifications, or constitutive activation of upstream tyrosine kinase receptors will lead to dysregulation of this pathway in a variety of tumors, including GB (Engelman, 2009; Bai et al., 2011; Wick et al., 2011; Mao et al., 2012). As such, there are marked associations between alterations in the PI3K/AKT/mTOR pathway and the poor clinical survival (Engelman, 2009). Therefore, inhibition of the PI3K/Akt/mTOR signaling pathway has been widely investigated as a potential therapy for cancer including glioblastoma (Li et al., 2016). Interestingly, tumor cells in which the PI3K/Akt/mTOR pathway is dysregulated are more susceptible to the inhibition of mTOR, the downstream effector of this signaling pathway, than normal cells (Courtney et al., 2010). Hence, mTOR inhibitors such as rapamycin and its derivatives provide a new class of active agents and therapeutics for GB.

Rapamycin (Sirolimus) is a natural macrolide antibiotic (firstly isolated from samples of Streptomyces hygroscopicus found on Easter Island), which binds to FK506 binding protein 12 (FKBP12). The rapamycin-FKBP12 complex inhibits mTOR and prevents further phosphorylation of proteins involved in the transcription, translation, and cell cycle control (Heimberger et al., 2005). Anandharaj et al. studied three PTEN-null GB cell lines and demonstrated that rapamycin combined with radiotherapy inhibited the inhibitor of apoptosis protein (IAP) family protein surviving through repression of phospho-Akt. Thus, targeting Akt through mTOR with rapamycin increased the radiation sensitivity (Anandharaj et al., 2011). Preclinical trials showed that PTEN deficient tumors and those dependent on PI3K overexpression were most sensitive to rapamycin (Bjornsti and Houghton, 2004). These results provide a strong basis for investigation of mTOR inhibitors as potential tumor-selective therapeutic agents. Rapamycin and its derivatives, CCI-779 and RAD001, specifically inhibit the function of mTOR by blocking the phosphorylation of downstream molecules, such as p70S6 kinase (p70S6K) and eukaryotic initiation factor 4E-binding protein 1 (4E-BP1), leading to G1-phase cell cycle arrest. Accumulating evidence from preclinical and early clinical studies suggests that these mTOR inhibitors, alone or in combination, would be directly and indirectly effective as growth inhibitors against a broad range of tumors including GB (Mecca et al., 2018; Hsu et al., 2020; Wanigasooriya et al., 2020).

Despite the potency of rapamycin in preclinical studies, clinical development of rapamycin floundered due to the lack of suitable formulations. The low oral bioavailability (<15%) (Yatscoff et al., 1995) precludes tablet formulation except for low dosage treatments such as immunosuppression. Rapamycin's poor solubility in water, ca. 2.6 μg/mL, and common excipients make intravenous (i.v.) formulation difficult (Simamora et al., 2001). In addition, pharmacokinetic studies found that rapamycin strongly partition into the erythrocytes (Kd ca. 20) from where it may not readily access to solid tumors (Yatscoff et al., 1995). This led to the development of ester derivatives, e.g., Temsirolimus or CCI-779, which were more easily formulated. Despite the promise of CCI-779 for mTOR inhibition, intravenous formulations required ethanol that may cause hemolysis (Raymond et al., 2004). Furthermore, phase I trials established that the CCI-779 prodrug was rapidly hydrolyzed in the plasma back into rapamycin thus favoring again potential partition into erythrocytes and unsupportive for tumor accumulation. More recent evolutions with the derivative Everolimus in phase II leads to increase treatment-related toxicities (Chinnaiyan et al., 2018).

In order to improve rapamycine biodistribution, nanovectorization strategies have been developed. They provide a physical protection and allow freeing from solubility problems. In this work, lipid nanocapsules loaded with rapamycin (LNC-rapa) were developed as new nanocarriers for the treatment of GB. We demonstrated that encapsulated rapamycin keeps its biological effect and efficiently inhibits mTOR phosphorylation. LNC-rapa were more cytotoxics than rapamycin alone but, in association with 8Gy radiation, no synergistic effect were observed. This result could be explained by the complexity of the PI3k/Akt/mTOR in GB as demonstrated by activation of phosphorylated Akt with mTOR inhibition and dependence from oxic status.

MATERIALS AND METHODS

Materials

Lipoïd® S75-3 (soybean lecithin at 69% of phosphatidylcholine) and Solutol® HS15 (a mixture of polyethylene glycol 660 and polyethylene glycol 660 hydroxystearate) were kindly provided by LipoïdGmbh (Ludwigshafen, Germany) and BASH (Ludwigshafen, Germany), respectively. NaCl and DMSO were provided by Sigma Aldrich (St-Quentin, Fallavier, France). Deionized water was obtained from a Milli-Q plus

system (Millipore, Paris, France). Lipophilic Labrafac® CC (caprylic-capric acid triglycerides) was provided by Gattefosse S.A. (Saint-Priest, France). Rapamycin was purchased from Interchim (Montluçon, France).Captex® 8000 (Triglyceride of caprylic acid), Transcutol® HP (Diethylene glycol monoethyl ether), and Miglyol® 812 (caprylic/capric triglyceride) were purchased, respectively, from Abitec (Janesville, WI, USA), Gattefosse S.A. (Saint-Priest, France) and Sasol Germany GmbH (Marl, Germany).

Reagents and Antibodies

Rapamycin was dissolved in DMSO. The final concentration of DMSO in the culture medium did not exceed 0.2%. Anti-phospho-mTOR (ab109268, diluted 1:2,000) and anti-HIF-1α (ab51608, diluted 1:2,000) were from Abcam (Cambridge, UK). Anti-phospho-Akt (#4058, diluted 1:1,000) was from Cell Signaling Technology (Beverly, MA, USA) and anti-HSC70 (sc7298, diluted 1:10,000) was from Santa Cruz biotechnology (Dallas, TX, USA). Peroxidase-conjugated anti-mouse (#32430, diluted 1:2,000) and anti-rabbit (#32460, diluted 1:2,000) secondary antibody were from ThermoScientific (Waltham, MA, USA). Lysis buffer: [50 mM Hepes (pH 7.5), 150 mM sodium chloride, 1 mM EDTA (pH 8), 2.5 mM EGTA (pH 7.4), 0.1% Tween 20, 10% glycerol, 0.1 mM sodium orthovanadate, 1 mM sodium fluoride and 10 mM β-glycerophosphate] plus Protease inhibitor cocktail (#539134 Calbiochem, Darmstadt, Germany), PMSF and Phosphatase inhibitor Cocktail Set II (#524636 Calbiochem).

Solubility Assays

Rapamycin solubility assays were performed in different oils: Captex® 8000, Labrafac® CC and Miglyol® 812. Five microgram of rapamycine were dissolved in 250 mg of oil and kept under magnetic stirring during 3 h at room temperature (RT) or at 90°C. Rapamycin concentration was determined by reverse-phase high-performance liquid chromatography (RP-HPLC) after 24 h settling at 4°C, using μBondapack C18 column (Waters Corporation, Milford, MA) with an ultraviolet detector at 278 nm. The mixture of 90% acetonitrile and 10% water (v/v) was used as a mobile phase, and delivered at a flow rate of 2.0 mL/min. The injection volume was 10 μL and the retention time was about 2.3 min.

For spectral analysis of the stability of rapamycin in Labrafac®, rapamycin was solubilized at 1 mg/mL in Labrafac® under magnetic stirring before being submitted to 3 to 6 short cycles of heating (70°C for <1 min) and cooling (RT) or incubated for 1 to 3 h at 70°C in Labrafac. Spectral analysis was then made by use of the CLARIOstar microplate reader (BMG Labtech, Champigny-sur-Marne, France).

Formulation and Physico-Chemical Characterization of Empty (LNCs) and Rapamycin-Loaded Lipid Nanocapsules (LNC-rapa)

LNCs were prepared according to a phase-inversion process adapted from Heurtault et al. (2002). This process involves the formation of an oil/water microemulsion containing an oily/fatty phase (triglycerides: Labrafac® WL 1349), a non-ionic hydrophilic surfactant (polyethylene glycol hydroxystearate: Solutol® HS15), and a lipophilic surfactant (lecithin: Lipoïd® S75-3). Briefly, 21 mg of Lipoïd® S75-3, 138 mg of Solutol® HS15, 345 mg of Labrafac®, 104 mg of NaCl and 898 mg of deionized water were mixed by magnetic stirring. 5 mg of rapamycin were added to other reagents for a final concentration of 1 mg/mL. Three cycles of progressive heating and cooling between 30 and 70°C were then carried out and followed by an irreversible shock, induced by addition of 3.6 mL of 0°C deionized water. Afterwards, slow magnetic stirring was applied to the suspension for 5 min. LNCs were filtered through a Minisart® 0.2 μm filter (Sartorius, Goettingen, Germany) and kept at 4°C. The average diameter and polydispersity index were determined using Malvern Zetasizer® Nano Serie DTS 1060 (Malvern instruments S.A., Worcestershire, UK).

Encapsulation of drug: For determination of drug encapsulation yield, three samples of filtrate were prepared by dissolution of an exact quantity of LNC dispersion in a 96/4 (v/v) methanol/tetrahydrofurane solution. Free rapamycin (non-soluble) was removed by the filtration performed through the Minisart® 0.2 μm filter and its concentration measured by spectrophotometry at 289 nm. Quantification was achieved by comparison between observed peak area ratios of rapamycin of the samples and a calibration curve performed using the same conditions. Samples were performed in triplicate and the loading capacity (LC) was calculated using the following equation:

$$\text{Drug content (wt\%)} = \frac{\text{mass of encapsulated drug}}{\text{mass of encapsulated drug} + \text{mass of LNC excipients}} \times 100 \quad (1)$$

The encapsulation efficiency (EE) of rapamycin was calculated using the Equation (2):

$$\text{Encapsulation efficiency (wt\%)} = \frac{\text{mass of encapsulated drug}}{\textit{mass of initial drug}} \times 100 \quad (2)$$

For electrical conductivity measurements, an electrical conductivity meter (Cond 330i/SET, WTW, Germany) was used in non-linear temperature compensation mode according to EN 27888. The conductivity variations were followed as a function of temperature to determine the emulsion inversion zone.

Cell Culture and Exposure to Hypoxia

Human malignant glioma cell lines U87MG were purchased from American Tissue Culture Collection (Rockville, MD). Tumor cells were cultured in Dulbecco's modified Eagle's medium 4.5 g/L glucose and L-glutamine (DMEM, Lonza, Verviers, Belgium) supplemented with 10% of heat-inactivated fetal bovine serum (FBS, Lonza) and 1% antibiotics suspension (10

units/mL of penicillin, 10 mg/mL streptomycin and 25 μg/mL amphotericin B, Sigma-Aldrich, Saint-Louis, MO, USA). Tumor cells were incubated at 37°C in 5% CO_2 and 21% (normoxia) or 0.4% O_2 (hypoxia). Hypoxia conditions were obtained by use of an InVivo$_2$ 400 SCI-tive hypoxia workstation (Ruskinn Technology, Ltd., Leeds, UK).

Irradiation Procedure

Irradiation was performed with the CP-160 cabinet x-ray system (Faxitron, Edimex, Le Plessis Grammoire, Angers, France) which delivers a dose of 1,5 grays by min. Irradiation was performed during 5.33 min in order to reach the dose of 8 grays. Irradiation was performed with cells covered. Depending on the condition considered, the cells were placed throughout the experiment in a conventional 21% O_2 incubator at 37°C/5% CO_2 (normoxia) or 0.4% O_2 (hypoxia) at 37°C/5% CO_2 in an InVivO2 400 SCI-tive hypoxia workstation (Ruskinn); they are only placed in an isolated flask for the duration of the irradiations.

Cytotoxicity Evaluation

Two assays were performed to determine the cytotoxicity effect of LNC-rapa on the glioblastoma cell line U87MG:MTS (3-(4,5-dimethylthiazol-2-yl)-5-(3-carboxymethoxyphenyl)-2-(4-sulfophenyl)-2H-tetrazolium) (Promega, Charbonnières, France) and clonogenic assay by crystal violet coloration (Sigma-Aldrich).

For the MTS assay, U87MG cells (5×10^4 cells/mL) harvested in the exponential growth phase were seeded in a 24-well plate in DMEM medium with 10% FBS, in humidified atmosphere (5% CO_2) at 37°C. Once the cells incubated in the exponential growth phase, serum-contained medium was removed and replaced by serum-deprived DMEM supplemented with 1% N1 supplement (Sigma-Aldrich). Free rapamycin dissolved in DMSO (1/10,000, non-toxic) was applied at various concentrations (0.04; 0.2; 1; 5; 10; 20; 100; 200 μM) for 4 h. 8Gy radiation was performed 6 h after the onset of initial treatment by Faxitron CP-160 (Faxitron X-rays, Lincolnshire, UK). Medium was changed every day. Forty-eight hours following the treatment, MTS reagent was diluted (1:5) in U87MG cell medium and incubated for 2 h at 37°C. The absorbance was measured at 492 nm using Multiskan® microplate spectrophotometer (Thermo Scientific).

For the clonogenic assay, U87MG cells (10^3 cells/mL) harvested in the exponential growth phase were seeded in a 6-well plate in DMEM medium with 10% FBS, in humidified atmosphere (5% CO_2) at 37°C. Once the cells incubated in the exponential growth phase, serum-contained medium was removed and replaced by serum-deprived DMEM supplemented with 1 % N1 supplement. Cells were treated for 4 h with rapamycin, LNC-rapa at 1 μM (IC50 LNC-rapa at 21% O_2 corresponding to a 1/1,000 dilution from initial suspension) and with empty LNCs at the same dilution than LNC-rapa. 8Gy radiation was performed 6 h after the treatment by Faxitron CP-160. Ten days after treatment, colonies were colorized by crystal violet and their number was evaluated with ImageJ Software version 1.43.

Depending on the condition considered, the cells were placed throughout the experiment in a conventional 21% O_2 incubator at 37°C/5% CO_2 (normoxia) or 0.4% O_2 (hypoxia) at 37°C/5% CO_2 in an InVivO2 400 SCI-tive hypoxia workstation (Ruskinn); they are only placed in isolated flasks for the duration of the irradiations.

Western Blotting

U87MG cells (2.4×10^5 cells/mL) harvested in the exponential growth phase were seeded in dishes in DMEM medium with 10% FBS, at 37°C in humidified atmosphere containing 5% CO_2 and 21 or 0.4% O_2. Once the cells incubated in the exponential growth phase, serum-contained medium was removed and replaced by serum-deprived DMEM supplemented with 1% N1 supplement. Cells were treated with rapamycin, LNC-rapa at 1 μM and with empty LNCs at the same dilution than LNC-rapa. 8Gy radiation was performed 6 h after the treatment by Faxitron CP-160 (cf. section Irradiation Procedure).

Sixteen hours after rapamycin initial treatment (untreated, rapamycin, LNC, LNC-rapa), soluble proteins for immunobloting were harvested from tumor cells lysed in 300 μL lysis buffer on ice. Cells were scrapped and lysed by sonication for 10 s.

Equal amounts of protein from each sample, estimated by the Bio-Rad Protein Assay (Richmond, CA), were separated by electrophoresis through a 4–20% SDS-polyacrylamide gel (Mini-protean® TGX™ Ge, BioRad), transferred to PVDF membranes (AmershamHybond, GE Healthcare, Buckinghamshire, UK) and blocked with 4% non-fat dry milk in 1X TBS plus 0.1% Tween 20 at RT for 1 h. The membranes were washed and incubated with a primary antibody diluted in 2% BSA in 1X TBS plus 0.1% Tween 20 overnight at 4°C. The membranes were then washed and incubated again for 1 h at RT with peroxidase-conjugated anti-rabbit or anti-mouse secondary antibody. The bound antibody was detected using the enhanced chemiluminescence reagent kit SuperSignal West Femto (Thermo Scientific, Waltham, MA, USA) and read with a bioluminescence detector Image Quant Las 4000 (GE Healthcare, USA).

Statistical Analysis

Three independent biological replicates were performed for all experiments described in this manuscript. Statistical analyses were performed with R software using two-way *analysis* of variance (ANOVA) test. Differences were considered significant if the p-value was ≤ 0.05.

RESULTS

Formulation and Physicochemical Characterization of Rapamycin-Loaded LNCs

As a lipophilic molecule with logP = 4.3, rapamycin can be encapsulated in the lipophilic core of lipid nanocapsules. The formulation of LNCs *via* a phase-inversion process described by Heurtault et al. (2002) involves three cycles of heating/cooling between 60 and 90°C. However, rapamycin degrades at higher temperatures as observed during the solubility assay. Three different oils were tested for the dissolution of rapamycin at room temperature (RT) and at 90°C: Captex® 8000, Miglyol® 812

TABLE 1 | Rapamycin solubility in different oils at RT and at 90°C.

Oil	Temperature	Initial rapamycin (mg/mL)	Dissolved rapamycin (mg/mL)	Dissolution rate (%)
Captex® 8000	RT	19.0	1.8	9.5
	90°C	16.8	0	0
Miglyol® 812	RT	19.2	1.4	7.3
	90°C	17.1	0	0
Labrafac®	RT	24.0	1.5	6.3
	90°C	21.1	0	0

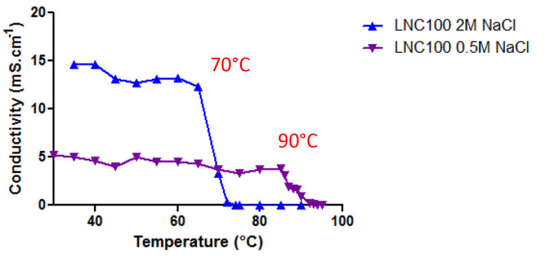

FIGURE 1 | Micro-emulsion conductivity. Micro-emulsion conductivity during cycles of heating/cooling for LNCs formulation performed with 2 M or 0.5 M NaCl aqueous solution.

and Labrafac®. Rapamycin concentration in the supernatant was determined by HPLC and the results are summarized in **Table 1**. At 90°C, rapamycin is completely degraded whatever the oil used. At RT, rapamycin has a comparable solubility in all three oils.

Finally, Labrafac®, pharmaceutically acceptable and in which the stability of rapamycin is confirmed during short cycles of heating and cooling at 70°C (**Supplementary Figure 1**), was used for the formulation of empty and rapamycin-loaded LNCs. Hence, a lower temperature (70°C) was employed in order to avoid rapamycin decomposition. To decrease the phase inversion temperature from 90 to 70°C, we increased the concentration of NaCl aqueous solution. Electrical conductivity of the micro-emulsion was measured as a function of temperature for the "classical formulation" with 0.5 M NaCl and for the formulation with 2 M NaCl (**Figure 1**). A steady state at a high conductivity value indicates that the continuous phase of the emulsion is water, whereas conductivity close to zero means that the continuous phase is oil. The region where the conductivity gradually changes with temperature represents the phase inversion from oil-in-water emulsion to water-in-oil emulsion. **Figure 1** shows that the phase inversion occurs at lower temperature (70°C) when 2 M NaCl aqueous solution is used as compared to 0.5 M NaCl solution (90°C). Thus, increasing NaCl concentration allows us to perform rapamycin encapsulation in non-degrading temperature range between 30 and 70°C.

Empty and rapamycin-loaded LNCs were characterized in terms of their average size and zeta potential. These values are presented in **Table 2**. LNC-rapa have an average size of 112.6 ± 8.4 nm with a polydispersity index (PDI) of 0.044 ± 0.011. The zeta potential is of −5.5 ± 0.4 mV. Rapamycin encapsulation efficiency and loading capacity were determined using the equations 1 and 2, these values are also reported in **Table 2**. The encapsulation efficiency is of 68.8 ± 7.1 wt% thus representing a loading capacity of the nanoparticle of 0.6 ± 0.1 wt%. This encapsulation efficiency rate was considered in the calculation of rapamycin concentration in biological assays. Insofar as low temperature-made LNC can exhibit fluctuations in their long-term stability with regard to preservation methods not yet fully elucidated, the LNCs used throughout of this work were prepared extemporaneously (**Supplementary Table 1**).

Effect of Rapamycin-Loaded LNCs (LNC-rapa) on mTOR Phosphorylation in U87MG Cells Depending on Oxic Condition and Exposure to Radiation Treatment

Rapamycin binds FKBP12 and the complex FKBP12/rapamycin inhibits mTOR phosphorylation that leads to 4E-BP1 dephosphorylation and inhibition of translation. To check if rapamycin encapsulated within LNCs keeps its biological proprieties, human U87MG glioblastoma cells, that are PTEN negative and thus overactivate Akt/mTOR signals, were treated with empty LNCs, LNC-rapa and free rapamycin dissolved in DMSO. The cells were cultured in serum-free medium in atmosphere containing either 21% O_2 or 0.4% O_2.

As cytotoxicity assay performed by MTS with free rapamycin demonstrated a toxic effect only at high concentrations, with more impact in normoxia than in hypoxia (IC50 of 20.54 µM at 21% pO_2 and 34.65 µM at 21% pO_2 and 0.4% pO_2, respectively, **Supplementary Figure 2**), the choice to use a relevant far much lower concentration while using the LNC nanocarrier was made. Hence a concentration of 1 µM (corresponding to the IC50 LNC-rapa at 21% O_2 and to a 1/1,000 dilution from the initial suspension while using LNC) was applied all throughout the work.

Western blot analysis was performed and relative phosphorylation was determined by volumetric ratio of p-mTOR/HSC70. The results presented in **Figure 2A** indicate that rapamycin-encapsulated within LNCs effectively inhibits mTOR phosphorylation (Ser2448) with modalities much more effective in hypoxia than in normoxia.

This observation is consistent with the one made by Brugarolas and coworkers who notably showed that hypoxia induced mTOR inhibition through TSC1/TSC2 tumor suppressor complex and the hypoxia-inducible gene REDD1/RTP801. They demonstrated that in contrast to energy depletion, mTOR inhibition by hypoxia does not require AMPK or LKB1 but depend on increased expression of the hypoxia inducible *REDD1* gene. They also showed that down-regulation of S6K, an mTOR target, phophorylation by Redd1 requires Tsc2 and Redd1 probably acts up-stream of the Tsc1/Tsc2 complex to down-regulate mTOR function in response to hypoxia (Brugarolas et al., 2004). Thus, at 0.4% oxygenation, mTOR is inhibited by rapamycin and hypoxia, with loaded-LNCs also exerting a higher effect in these conditions (**Figure 2A**).

TABLE 2 | Physicochemical parameters of LNC-rapa.

	Inversion phase (°C)	Size (nm)	PdI	Zeta-potential (mV)	Encapsulation efficiency (% w/w)	Loading capacity (%w/w)
LNC-rapa	70	112.6 ± 8.4	0.04 ± 0.01	−5.5 ± 0.5	68.8 ± 7,1	0.6 ± 0.1
LNC	90	92.3 ± 2.6	0.05 ± 0.02	−8.6 ± 0.6	0	0

Average particle size, PDI, zeta potential, encapsulation efficiency (EE) and loading capacity (LC) of empty and rapamycin-loaded LNCs.

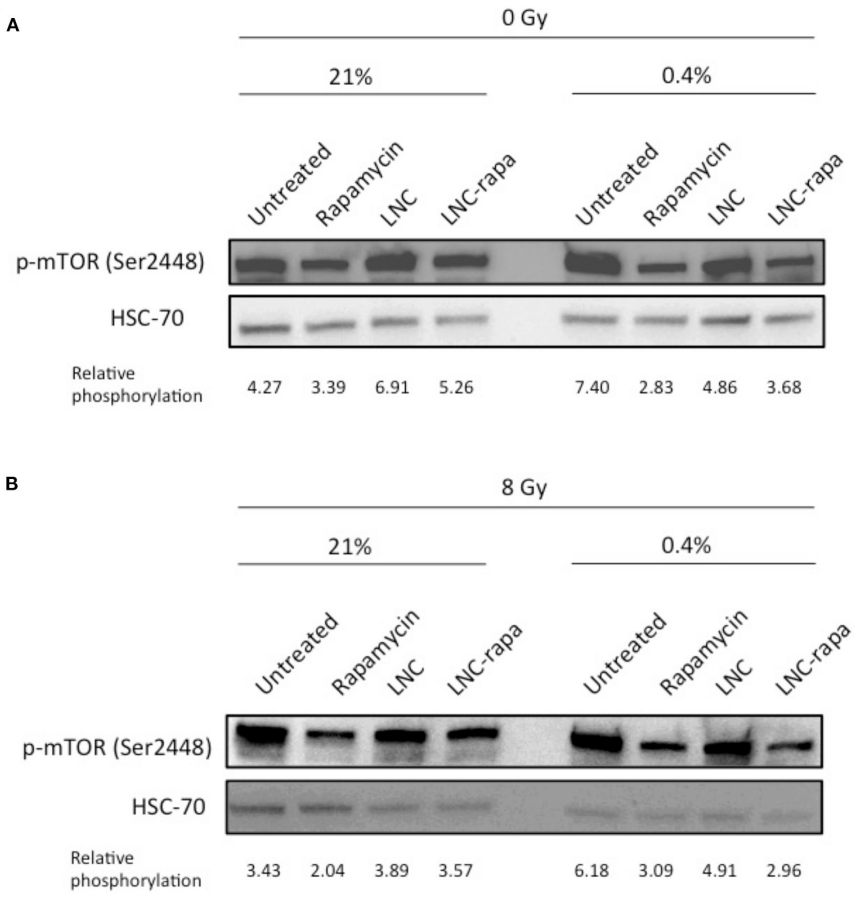

FIGURE 2 | Effects of LNC-rapa assessed on mTOR phosphorylation in U87MG cells depending on oxic condition and exposure to radiation treatment. U87MG cells were treated with rapamycin, empty LNCs (LNC) or rapamycin-loaded LNCs (LNC-rapa), and maintained at two oxygenation conditions: 21 and 0.4% O_2 before proceeding to western blot analysis. Relative phosphorylation of one representative experiment was determined by volumetric ratio of p-mTOR/HSC70. **(A)** 0Gy. **(B)** 8Gy irradiation.

As various synergies have been tested and since the conventional treatment of glioblastoma involves beam radiation, the impact of LNC-rapa on mTOR phosphorylation in U87MG cells was also tested after exposure to 8Gy irradiation. Similar results to the non-irradiated condition are obtained (**Figure 2B**).

Effect of LNC-rapa on U87MG Cell Growth Depending on Oxic Condition and Exposure to Radiation Treatment

To determine the effect of rapamycin encapsulated within LNCs on cancer cell survival and growth depending on the oxygen status and exposure to radiation treatment, a clonogenic assay

was performed. Hence, U87MG cells were grown under two oxygenation conditions (21 or 0.4% O_2) and treaded with either empty LNCs, LNC-rapa or free rapamycin at 1 μM before being exposed, 6 h later, to 0 or 8Gy irradiation. They were then maintained in culture for 10 days and colorized by crystal violet (**Figure 3A**). Under all the conditions tested, a very clear effect of the irradiations, in normoxia (21% pO_2) as in hypoxia (0.4% O_2), was observed (**Figures 3B,C**). Rapamycin, nanovectorized or as free, exerts only moderate effects, however significant at 0.4% O_2, demonstrating the similarity of action of encapsulated LNC-rapa vs. the free form (**Figure 3C**). Interestingly, rapamycin and LNC-rapa do not exert any synergistic effect related to radiation treatment and even slight but significant inhibitory effects impacted radiation efficacy at 0.4% O_2 (**Figure 3C**).

Activation of Alternative Signaling Pathways in Response to Exposure to LNC-rapa in U87MG

The observed duality of the effects of rapamycin and LNC-rapa associating a strong inhibition of mTOR phosphorylation to a moderated cytotoxic effect whatever the environmental conditions used (low/high oxygen or irradiating) led us to focus on the mechanisms that control the PI3K/Akt/ mTOR pathway. Since HIF exerts negative feedback on mTOR (Brugarolas et al., 2004) and mTORC2 complex also exerts feedback control while capable to phosphorylate Akt (Sarbassov et al., 2005; O'Reilly et al., 2006), HIF-1α protein expression and phosphorylation of Akt on Ser473 (Akt-p) were evaluated. Western Blot presented in **Figure 4A** shows that HIF-1α protein expression is reduced when cells are treated with free rapamycin and LNC-rapa whatever oxygenation condition considered. Inversely, these treatments enhance Akt-p protein level. **Figure 4B** shows that at 8Gy, Akt-p protein expression is reduced related to HSC70 in comparison with the 0Gy control condition. Again the down regulation of HIF-1α protein expression by free rapamycin and LNC-rapa is observed concomitantly with the induction of phosphorylation of Akt, thus emphasizing the possible double edge sword impact of LNC-rapa due to the multiplicity of signals downstream mTOR inhibition.

DISCUSSION

This work demonstrated that a new safe formulation of rapamycin encapsulated in lipid nanocapsules at low temperature and without the use of organic solvent, allows keeping its activity while specifically inhibiting mTOR phosphorylation. These observations also established that the mechanism of action of rapamycin-loaded LNCs, to some extent like free rapamycin, involve distinct modalities of responses at 0.4 vs. 21% oxygenation. Indeed, protein expression analysis shows that, if mTOR phosphorylation inhibition is higher at 0.4% O_2, the up-stream effector of PI3k/Akt/mTOR pathway, Akt phosphorylation, is higher too. Furthermore, free rapamycin and LNC-rapa inhibit HIF-1α expression at 21% O_2 and to a lesser extent at 0.4% O_2. This difference is linked to HIF-1α stabilization under hypoxia.

LNC-rapa as a New Safe Nanocarrier of Rapamycin

In the present study, we developed lipid nanocapsules capable to efficiently encapsulate rapamycin with yield close to 70%. The formulation was done between 30 and 70°C, a temperature range that protects rapamycin from thermal degradation. Capable to cope with poor water solubility of rapamycin and bioavailability due to their capability to effectively reached intracellular cell compartment (Paillard et al., 2010), rapamycin-loaded LNCs keep rapamycin biological proprieties with an effective inhibition of mTOR phosphorylation. Although this tool fulfills its role as a vector, it does not strengthen the activity of rapamycin or one of its selective aspects in our *in vitro* model tested as well as through multiple conditions (8Gy irradiation, 0.4% hypoxia, 21% normoxia).

In the plethora of new rapamycin nanovector formulations currently available, the loading capacities of each of them, their application methods and loco-regional bioavailability should make it possible to resolve the problem of efficiency and possibly synergy with conventional treatments. Thus a loading capacity of 0.6% for LNC-rapa remains low compared to other systems such as polysorbate 80-coated PLGA nanoparticles (Escalona-Rayo et al., 2019), lipid-polyaniline nanoparticles (Wang J. P. et al., 2016) or PEO/PDLLA electrospun nanofibers (Wang B. L. et al., 2016). Comparative studies in particular *in vivo* should make it possible to understand the rationale which makes one of these vectors an appropriate tool or not.

Forrest and coworkers have developed poly(ethylene glycol)-b-poly(ε-caprolactone) (PEG-PCL) micelles loaded with rapamycin and showed that this drug was efficiently loaded within PEG-PCL up to 10 wt% (more than 1 mg/mL) (Forrest et al., 2006). Other group also demonstrated that rapamycin encapsulation within poly(ethylene glycol)-Block-poly(2-methyl-2-benzoxycarbonyl-propylene carbonate) (PEG-b-PBC) micelles reduced its toxicity (Lu et al., 2011). Shi et al. (2013) developed elastin-based protein polymer nanoparticles loaded with rapamycin and decorated with its ligand FKBP. They showed that these objects slowed down the drug release as compared to non-decorated nanoparticles. Moreover, rapamycin elastin-like polypeptide nanoparticles decreased the gross toxicity and enhanced the anti-cancer activity on human breast cancer mice model (Dhandhukia et al., 2017a,b; Peddi et al., 2020). Finally, Tyler and coworkers incorporated rapamycin into biodegradable caprolactone-glycolide (35:65) polymer beads (Tyler et al., 2011). *In vitro*, rapamycin was cytotoxic toward 9L cells (rat glioma cells), causing growth inhibition at a concentration of 0.01 μg/mL. No *in vivo* toxicity was observed at 0.3, 3, and 30% loading doses implanted intracranially. Animals treated with the highest dose of rapamycin beads (30%) consistently demonstrated

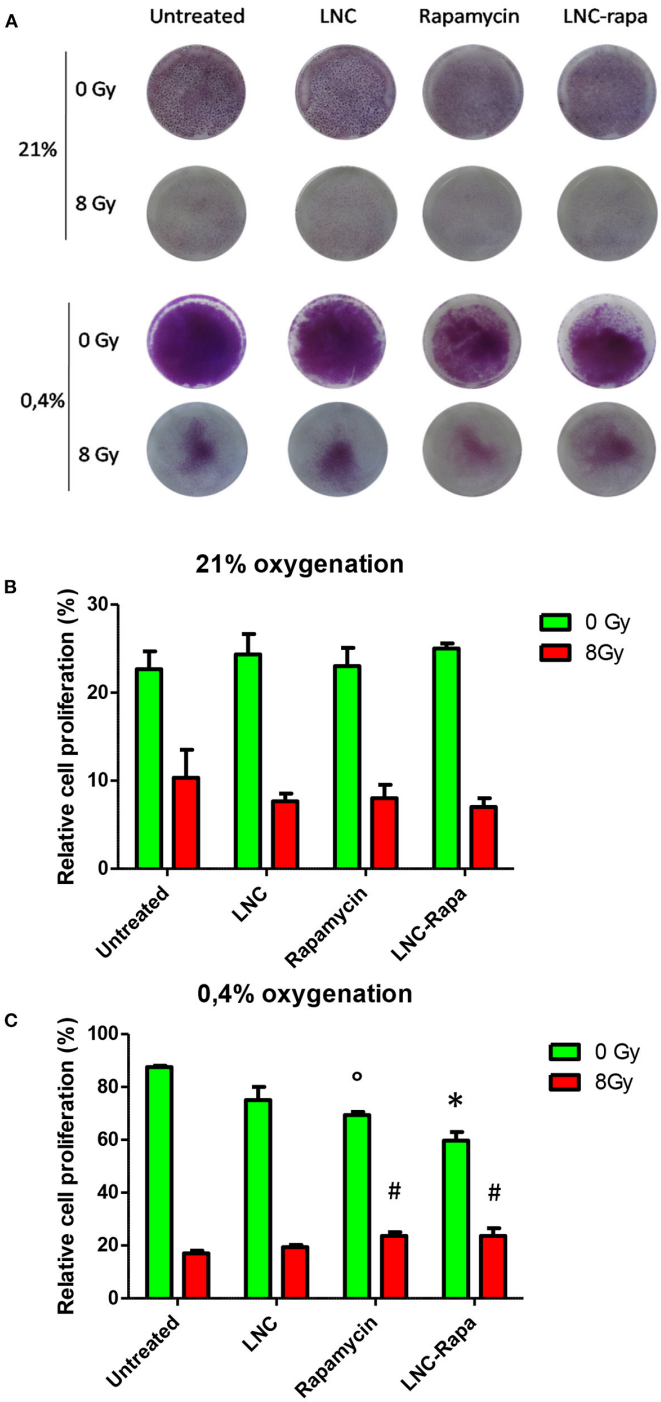

FIGURE 3 | Effects of LNC-rapa assessed by clonogenic assay on U87MG cell growth depending on oxic condition and exposure to radiation treatment. **(A)** Photography of 6-wells plates containing U87MG cells treated with LNCs, rapamycin or LNC-rapa, radiated at 0 Gy (top row) or 8Gy (bottom row) at 21 and 0.4% pO_2

(Continued)

FIGURE 3 | and stained with crystal violet. **(B,C)** Cell survival was determined by measuring crystal violet staining of wells exposed to 0 and 8Gy at 21% pO_2 **(B)** or 0.4% pO2 **(C)**. Data show the average values from a combination of three independent experiments and error bars display the standard deviation. Two-way ANOVA test was performed between LNC-rapa condition compared to LNC condition (*$p \leq 0.05$) or between rapamycin treatment condition and untreated control condition ($^{\circ}p \leq 0.05$) or between rapamycin treatment condition and untreated condition ($^{\#}p \leq 0.05$).

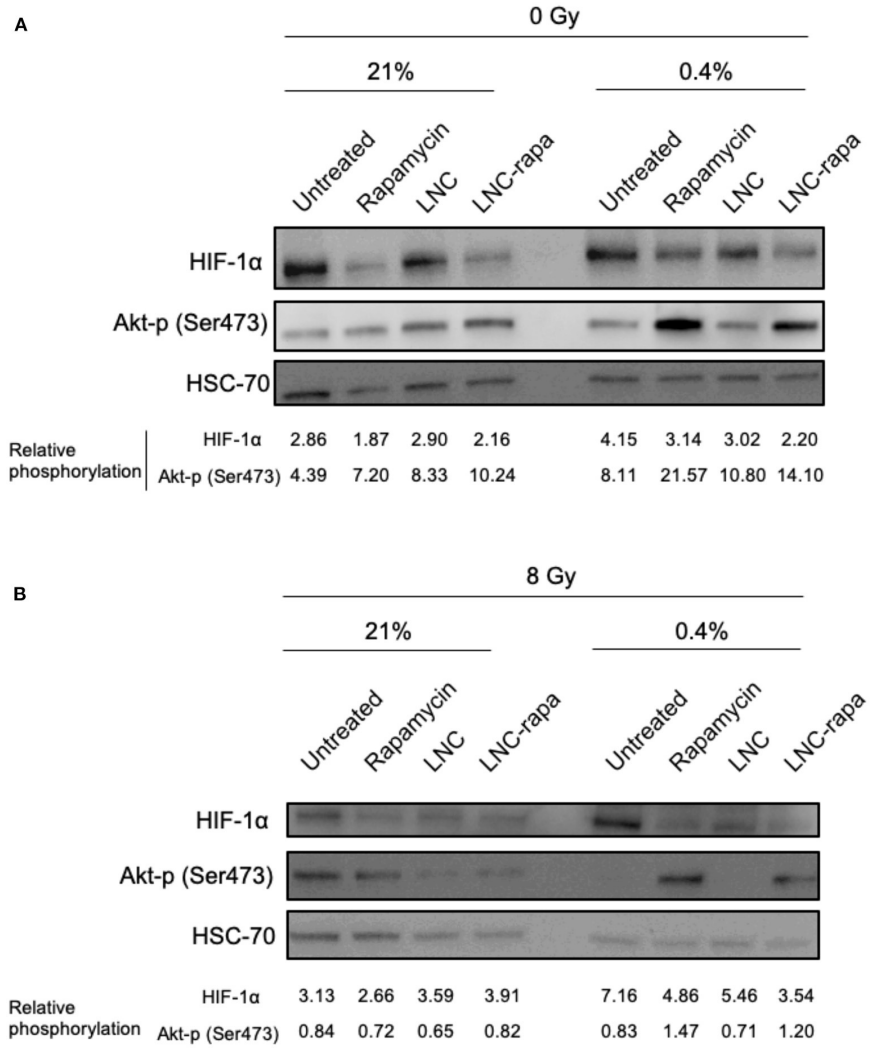

FIGURE 4 | Activation of alternative signaling pathways in response to exposure to LNC-rapa in U87MG. **(A,B)** U87MG cells were treated with free rapamycin, empty LNCs or LNC-rapa, radiated at 0 Gy **(A)** or 8Gy **(B)** and maintained at two oxygenation conditions: 21 and 0.4% before proceeding to western blot analysis. Relative phosphorylation of one representative experiment was measured by volumetry ratio of p-mTOR/HSC70.

significantly longer survival duration than the control and placebo groups. They also showed that radiation therapy in addition to the simultaneous treatment with 30% rapamycin beads led to significantly longer survival duration than each therapy alone.

Vectorized Rapamycin: A Double-Edge Sword "Interactor" in Cancer Cells

The result we obtained on mTOR phosphorylation by rapamycin and LNC-rapa associated with of HIF-1α down regulation and Akt phosphorylation can be linked to the observation made

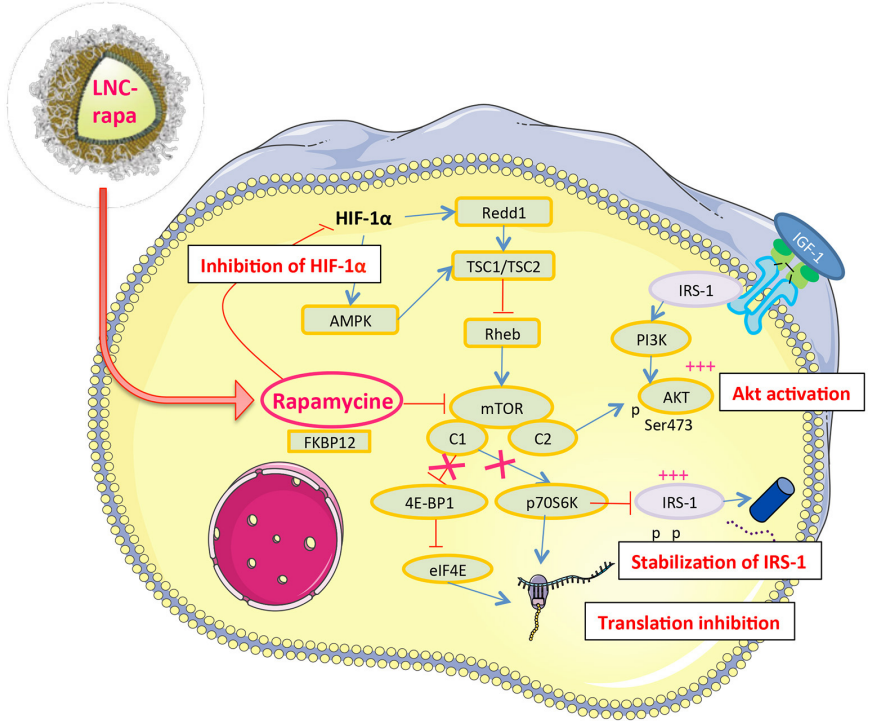

FIGURE 5 | Rapamycin a likely double-edge sword molecular interactor in U87MG glioblastoma cells. Nanovectorized rapamycin (LNC-rapa) or rapamycin as free, solubilized in DMSO, inhibits the stabilization and transcriptional activity of HIF1α which in turn inhibits the TSC1/TSC2 inhibitor and thus promotes the activation of mTOR. On the other hand, rapamycin inhibits mTORC1 but not mTORC2, which in turn induces Akt phosphrylation. Finally, by inhibiting mTORC1, rapamycin lifts the inhibition exerted by p70s6k on IRS-1, which stabilizes this protein and induces Akt phosphorylation *via* the IGF-1 receptor.

by Hudson et al. who reported that rapamycin inhibits both stabilization of HIF-1α and the transcriptional activity of HIF-1 in hypoxic cancer cells and mTOR dependent signals stimulate HIF-1α accumulation and HIF-1 mediated transcription in cells exposed to hypoxia or hypoxia-mimetic agent (Zhong et al., 2000). Rapamycin-sensitive functions of mTOR are not essential for the accumulation of HIF-1α but are needed for maximal expression of this protein, as well as for optimal HIF-1-dependent gene expression under hypoxic conditions. The notion that mTOR is a nutrient sensor may be particularly relevant to HIF-1 function, since decrease oxygen tensions are almost inevitable accompanied by limited supplies of glucose and amino-acids in mammalian tissues (Hudson et al., 2002). *In vivo*, rapamycin enhance thrombosis and also an increase in the hypoxic zone (Weppler et al., 2007). Hypoxia causes activation of the TSC1/2 complex, which functions to inhibit mTOR. This can occur both *via* induction of the HIF-dependent gene REDD1, and/or through activation of AMPK (Brugarolas et al., 2004; Liu et al., 2006). Rapamycin may be less effective in hypoxic regions of tumors since mTOR may already be at least partially inactivated by TSC. Thus the amount of hypoxia present at the start of treatment may play a part in determining sensitivity to rapamycin *in vivo* (Weppler et al., 2007) (**Figure 5**).

The higher Akt phosphorylation at 0.4% could also explain that cells are less sensitive to rapamycin than at 21%. Indeed, U87MG cell line is PTEN *null* that drives to a constitutive activation of the PI3K/Akt/mTOR pathway and could explains its radioresistance. Thus, mTOR inhibition could restore radiosensitivity but our results show that maximal cytotoxic effect was observed with 8Gy radiation and rapamycin or LNC-rapa were not sufficient to improve the cytotoxicity at the concentration of 1 μM. To well-understand this phenomenon, it is important to remind that mTOR exist in two complexes: mTORC1 and mTORC2. mTORC1 contains the mTOR, Raptor, mLST8/GβL, and PRAS40 proteins and controls cell size and protein translation *via* two major substrates, p70S6K and 4E-BP1. Activated S6 kinase causes feedback inhibition of insulin-like growth factor 1 (IGF-1)/insulin signaling by phosphorylating insulin receptor substrate 1 (IRS-1) and causing its degradation (Tremblay et al., 2007). mTORC2 has been shown to phosphorylate Akt at the serine 473 site, which enhances the catalytic activity of Akt already phosphorylated

on threonine 308 (Sarbassov et al., 2005). Rapamycin binds to FKBP-12 and this complex then binds to and causes the allosteric inhibition of mTORC1. Rapamycin effectively blocks S6K phosphorylation and also induces Akt S473 phosphorylation and Akt activity (O'Reilly et al., 2006). Physiologic activation of PI3k/Akt signaling is regulated by mTOR-dependent feedback inhibition of IRS expression and, consequently, IGF-1 receptor (IGF-1R)/insulin receptor signaling (Tremblay et al., 2007). Rapamycin relieves this feedback and induces Akt S473 phosphorylation in an mTORC2-dependent manner, leading to Akt activation, which may attenuate its therapeutic effects (O'Reilly et al., 2006). Furthermore, mTOR inhibitory drug rapamycin up-regulates IRS-1 protein levels and induces Akt phosphorylation that increase IGF—IR/IRS-1/PI3K signaling to Akt (O'Reilly et al., 2006) (**Figure 5**). In line with this, mTORC2, not inhibited by LNC-rapa, has recently been described as a downstream integrator of metabolic and epigenetic landscape leading to tumor cell survival and cancer durg resistance (Masui et al., 2019, 2020).

In response of those problems, Rodrik-Outmezguine et al. (2011) used a selective ATP-competitive mTOR kinase inhibitor AZD8055. This drug inhibits 4E-BP1 phosphorylation more effectively than rapamycin. It also inhibits mTORC2 and Akt S473 phosphorylation, which leads to Akt T308 dephosphorylation and suppression of Akt activity and downstream signaling. Unfortunately, even though mTORC2 inhibition is potent and persistent, inhibition of Akt T308 and Akt substrate phosphorylation is only transient. Authors demonstrated that this re-induction resulted from hyperactivation of PI3K. In cells in which mTOR kinase inhibitors relieve feedback inhibition of receptor tyrosine kinase, leading to activation of PI3K, the result is a new steady state in which mTORC1 is potently inhibited and Akt is phosphorylated on T308 but not on the S473. This Akt species is activated and able to phosphorylate key substrates in the cells. Induction of PI3K activation depends also from cell directory of activated tyrosine kinase receptors and from active ligands available (Rodrik-Outmezguine et al., 2011).

Alternatively, Kahn and coworkers showed *in vitro* that addition of AZD2014, another mTORC1/mTORC2 inhibitor, to culture media 1 h before irradiation enhanced the radiosensitivity of $CD133^+$ and $CD15^+$ glioblastoma stem-like cells (Kahn et al., 2014). The combination of AZD2014 and radiation delivered to mice bearing GSC-initiated orthotopic xenografts significantly prolonged survival of these animals as compared to individual treatments.

In parallel, dual PI3K/mTOR inhibitors were developed, notably the NVP-BEZ235. It demonstrated suppression of mTORC1 (S6K1, S6K, and 4E-BP1) and mTORC2 (AKT) downstream components resulting in cell cycle arrest and induced autophagy (Cerniglia et al., 2012). NVP-BEZ235 showed inhibited *in vivo* glioma proliferation and improved anti-tumor effects compared to rapamycin analogs. Mukherjee et al. (2012) showed that NVP-BEZ235 can inhibit DNA repair proteins ATM and DNA-PKC in GB that lead to a radiosensitizing effect. Nevertheless, because of the induction of autophagy that seems to be cytoprotective (Cerniglia et al., 2012), combination therapies with NVP-BEZ235 have been explored. One strategy utilized NVP-BEZ235 with autophagy inhibitor chloroquine to show a synergistic effect in *in vivo* tumor apoptosis (Fan et al., 2010). In line with this, Heinze et al., underlined that under hypoxia and nutrient-poor conditions, second generation mTORC1/C2 inhibitors displayed even stronder cytoprotective effect by reducing oxygen and glucose consumption (Heinzen et al., 2019).

However, those experiences were performed mainly *in vitro* and could yield different results *in vivo*. Indeed, some groups have reported that rapamycin sensitized U87MG xenografts to fractionated radiation therapy. Eshleman and coworkers also showed that there were no radiosensitizing effects of rapamycin on U87MG in the radiation clonogenic survival assays, nevertheless, they observed a great effect in the U87 xenograft and spheroids models (Eshleman et al., 2002). They proposed that other factors could also be important for the sensitizing effect of rapamycin. For example, rapamycin induces significant changes in glucose and nitrogen metabolism, and the starvation-like metabolic state induced by rapamycin could potentially decrease oxygen consumption in solid tumors and improve overall tumor oxygenation (Hardwick et al., 1999). Any decrease in the proportion of radioresistant hypoxic cells should significantly increase the efficacy of radiation. The authors also suggested that rapamycin could inhibit host-dependent processes that contribute to the profound sensitizing effect of rapamycin in xenograft model. Furthermore, rapamycin is a potent inhibitor of endothelial cell proliferation *in vitro*, therefore its systemic administration can inhibit angiogenesis. It reduces VEGF production by tumor cells and the inhibition of VEGF-induced proliferation in endothelial cells (Guba et al., 2002).

In the same way, Weppler et al. (2007) investigated the combination of rapamycin with short course of fractionated radiotherapy to minimize the anti-proliferative effect of rapamycin and thus evaluate its potential to contribute to the direct cytotoxic effect of radiation. They found that rapamycin did not significantly improve radiation response but increased variability in tumor response to radiotherapy, with several individual tumors showing large increases in growth delay. Thus, they underlined the importance to determine the biological factors that mediated this differential response in order to potentially identify patients that may benefit from combination treatment.

CONCLUSION

To conclude, rapamycin-loaded lipid nanocapsules for peripheral or loco-regional administration developed in this study represent a new safe nanocarrier of rapamycin capable to convey rapamycin and preserves its biological activity on cancer cells. We showed that activation of a negative feedback following mTOR phosphorylation inhibition is a serious brake on rapamycin cytotoxicity. The first solution could consist of changing rapamycin for dual PI3K/mTOR inhibitors like the NVP-BEZ235 which has demonstrated effectiveness *in vivo* (Cerniglia et al., 2012), or mTORC1/mTORC2 inhibitor is

AZD2014 which radiosensitizes glioma (Kahn et al., 2014). Nevertheless, rapamycin radiosensitizer effect have been proved *in vivo* or using fractionated radiation protocol (Eshleman et al., 2002). Moreover, if patients are biologically screened to select the most responsive ones, as underlined by Weppler et al., LNC-rapa can potentially be effective with an adapted radiation protocol.

DATA AVAILABILITY STATEMENT

All data generated or analyzed during this study are included in this published article (and its **Supplementary Information** files).

AUTHOR CONTRIBUTIONS

DS and EG wrote the manuscript. EG, FH, MC, FB, and FL contributed to the conception, design, and funding of the work. DS and SA contributed to the experiments. DS, NB, LR, AD, and EG contributed to manuscript revisions. All authors read and approved the submitted version.

FUNDING

This work was supported by the French National Research Agency (ANR) through the LabEx IRON (Innovative Radiopharmaceuticals in Oncology and Neurology) as part of the French government Investissements d'Avenir program (ANR-11-LABX-0018). It was also supported by the Institut National de la Santé et de la Recherche Médicale (INSERM) and by the University of Angers (Angers, France). This work was also supported by the NanoFar program (European doctorate in nanomedicine and pharmaceutical innovation) (Erasmus Mundus Joint Doctorate) funded by EACEA and by the NanoFar+ program (International strategy) funded by La Région Pays-de-la-Loire. The work was also related to: (i) the ANR under the frame of EuroNanoMed III (project GLIOSILK), (ii) the PL-BIO 2014–2020 INCa (Institut National du Cancer) consortium MARENGO (MicroRNA agonist and antagonist Nanomedicines for GliOblastoma treatment: from molecular programmation to preclinical validation), (iii) to the MuMoFRaT project (Multi-scale Modeling & simulation of the response to hypo-Fractionated Radiotherapy or repeated molecular radiation Therapies) supported by La Région Pays-de-la-Loire and by the Cancéropole Grand-Ouest (Vectorization, imaging, and radiotherapies network). DS and LR were PhD fellows funded by La Région Pays de la Loire and by the LabEx IRON-2/University of Angers, respectively. AD was a Ph.D. fellow from La Ligue Nationale contre le Cancer and was funded in this context by the Comité de Loire-Atlantique.

ACKNOWLEDGMENTS

The content of this manuscript has been published in part as part of the thesis of DS, Développement de nouvelles stratégies en nanomédecine pour le ciblage et la radiosensibilisation des cellules souches dans le glioblastome (Séhédic, 2014).

SUPPLEMENTARY MATERIAL

The Supplementary Material for this article can be found online at: https://www.frontiersin.org/articles/10.3389/fbioe.2020.602998/full#supplementary-material

Supplementary Figure 1 | Spectral analysis of rapamycin stability in Labrafac®. **(A)** Labrafac spectra at RT. **(B)** Labrafac spectra after 3 h heating at 70°C. **(C)** Rapamycin spectra after 3 h at RT in Labrafac. **(D)** Rapamycin spectra after six short cycles of heating and cooling (70°C to RT) in Labrafac. **(E)** Rapamycin spectra after 1 h heating at 70°C in Labrafac. **(F)** Rapamycin spectra after 3 h heating at 70°C in Labrafac. **(G)** Spectra of rapamycin, previously dissolved in methanol (MeOH), after three short cycles of heating and cooling (70°C to RT) in Labrafac. **(H)** Spectra of rapamycin, previously dissolved in methanol (MeOH), after 3 h heating at 70°C in Labrafac. Each curve represents one representative analysis of a triplicate.

Supplementary Figure 2 | Survival of U87MG cells in response of free-rapamycin treatment assessed by use of MTS assay. **(A)** U87MG cells were treated with free rapamycin at 21% (green curve) and 0.4% (red curve) oxygenation. **(B)** Calculated IC50 at 21 and 0.4% oxygenation following rapamycin treatment.

Supplementary Table 1 | Stability of 50 nm blank and rapamycin loaded LNC during storage at different temperatures. Note the modification of size and loss of polydispersity after 7 days storage (boxes highlighted in gray).

REFERENCES

Anandharaj, A., Cinghu, S., and Park, W. Y. (2011). Rapamycin-mediated mTOR inhibition attenuates survivin and sensitizes glioblastoma cells to radiation therapy. *Acta Biochim. Biophys. Sin.* 43, 292–300. doi: 10.1093/abbs/gmr012

Bai, R. Y., Staedtke, V., and Riggins, G. J. (2011). Molecular targeting of glioblastoma: drug discovery and therapies. *Trends Mol. Med.* 17, 301–312. doi: 10.1016/j.molmed.2011.01.011

Bjornsti, M. A., and Houghton, P. J. (2004). The TOR pathway: a target for cancer therapy. *Nat. Rev. Cancer* 4, 335–348. doi: 10.1038/nrc1362

Brugarolas, J., Lei, K., Hurley, R. L., Manning, B. D., Reiling, J. H., Hafen, E., et al. (2004). Regulation of mTOR function in response to hypoxia by REDD1 and the TSC1/TSC2 tumor suppressor complex. *Genes Dev.* 18, 2893–2904. doi: 10.1101/gad.1256804

Castellino, R. C., and Durden, D. L. (2007). Mechanisms of disease: the PI3K-Akt-PTEN signaling node - an intercept point for the control of angiogenesis in brain tumors. *Nat. Clin. Pract. Neurol.* 3, 682–693. doi: 10.1038/ncpneuro0661

Cerniglia, G. J., Karar, J., Tyagi, S., Christofidou-Solomidou, M., Rengan, R., Koumenis, C., et al. (2012). Inhibition of autophagy as a strategy to augment radiosensitization by the dual phosphatidylinositol 3-kinase/mammalian target of rapamycin inhibitor NVP-BEZ235. *Mol. Pharmacol.* 82, 1230–1240. doi: 10.1124/mol.112.080408

Chinnaiyan, P., Won, M., Wen, P. Y., Rojiani, A. M., Werner-Wasik, M., Shih, H. A., et al. (2018). A randomized phase II study of everolimus in combination with chemoradiation in newly diagnosed glioblastoma: results of NRG oncology RTOG 0913. *Neuro Oncol.* 20, 666–673. doi: 10.1093/neuonc/nox209

Courtney, K. D., Corcoran, R. B., and Engelman, J. A. (2010). The PI3K pathway as drug target in human cancer. *J. Clin. Oncol.* 28, 1075–1083. doi: 10.1200/JCO.2009.25.3641

Dhandhukia, J. P., Li, Z., Peddi, S., Kakan, S., Mehta, A., Tyrpak, D., et al. (2017a). Berunda polypeptides: multi-headed fusion proteins promote subcutaneous administration of rapamycin to breast cancer *in vivo*. *Theranostics* 7, 3856–3872. doi: 10.7150/thno.19981

Dhandhukia, J. P., Shi, P., Peddi, S., Li, Z., Aluri, S., Ju, Y. P., et al. (2017b). Bifunctional elastin-like polypeptide nanoparticles bind rapamycin and integrins and suppress tumor growth *in vivo*. *Bioconjug. Chem.* 28, 2715–2728. doi: 10.1021/acs.bioconjchem.7b00469

Engelman, J. A. (2009). Targeting PI3K signalling in cancer: opportunities, challenges and limitations. *Nat. Rev. Cancer* 9, 550–562. doi: 10.1038/nrc2664

Escalona-Rayo, O., Fuentes-Vazquez, P., Jardon-Xicotencatl, S., Garcia-Tovar, C. G., Mendoza-Elvira, S., and Quintanar-Guerrero, D. (2019). Rapamycin-loaded polysorbate 80-coated PLGA nanoparticles: optimization of formulation variables and *in vitro* anti-glioma assessment. *J. Drug Deliv. Sci. Technol.* 52, 488–499. doi: 10.1016/j.jddst.2019.05.026

Eshleman, J. S., Carlson, B. L., Mladek, A. C., Kastner, B. D., Shide, K. L., and Sarkaria, J. N. (2002). Inhibition of the mammalian target of rapamycin sensitizes U87 Xenografts to fractionated radiation therapy. *Cancer Res.* 62, 7291–7297.

Fan, Q. W., Cheng, C., Hackett, C., Feldman, M., Houseman, B. T., Nicolaides, T., et al. (2010). Akt and autophagy cooperate to promote survival of drug-resistant glioma. *Sci. Signal.* 3:ra18. doi: 10.1126/scisignal.2001017

Forrest, M. L., Won, C. Y., Malick, A. W., and Kwon, G. S. (2006). *In vitro* release of the mTOR inhibitor rapamycin from poly(ethylene glycol)-b-poly(epsilon-caprolactone) micelles. *J. Control. Release* 110, 370–377. doi: 10.1016/j.jconrel.2005.10.008

Guba, M., von Breitenbuch, P., Steinbauer, M., Koehl, G., Flegel, S., Hornung, M., et al. (2002). Rapamycin inhibits primary and metastatic tumor growth by antiangiogenesis: involvement of vascular endothelial growth factor. *Nat. Med.* 8, 128–135. doi: 10.1038/nm0202-128

Hardwick, J. S., Kuruvilla, F. G., Tong, J. K., Shamji, A. F., and Schreiber, S. L. (1999). Rapamycin-modulated transcription defines the subset of nutrient-sensitive signaling pathways directly controlled by the Tor proteins. *Proc. Natl. Acad. Sci. U.S.A.* 96, 14866–14870. doi: 10.1073/pnas.96.26.14866

Heimberger, A. B., Wang, E., McGary, E. C., Hess, K. R., Henry, V. K., Shono, T., et al. (2005). Mechanisms of action of rapamycin in gliomas. *Neuro Oncol.* 7, 1–11. doi: 10.1215/S1152851704000420

Heinzen, D., Dive, I., Lorenz, N. I., Luger, A. L., Steinbach, J. P., and Ronellenfitsch, M. W. (2019). Second generation mTOR inhibitors as a double-edged sword in malignant glioma treatment. *Int. J. Mol. Sci.* 20:4474. doi: 10.3390/ijms20184474

Heurtault, B., Saulnier, P., Pech, B., Proust, J. E., and Benoit, J. P. (2002). A novel phase inversion-based process for the preparation of lipid nanocarriers. *Pharm. Res.* 19, 875–880. doi: 10.1023/A:1016121319668

Hsu, S. P. C., Chen, Y.-C., Chiang, H.-C., Huang, Y.-C., Huang, C.-C., Wang, H.-E., et al. (2020). Rapamycin and hydroxychloroquine combination alters macrophage polarization and sensitizes glioblastoma to immune checkpoint inhibitors. *J. Neurooncol.* 146, 417–426. doi: 10.1007/s11060-019-03360-3

Hudson, C. C., Liu, M., Chiang, G. G., Otterness, D. M., Loomis, D. C., Kaper, F., et al. (2002). Regulation of hypoxia-inducible factor 1 alpha expression and function by the mammalian target of rapamycin. *Mol. Cell. Biol.* 22, 7004–7014. doi: 10.1128/MCB.22.20.7004-7014.2002

Jiang, B. H., and Liu, L. Z. (2009). PI3K/PTEN signaling in angiogenesis and tumorigenesis. *Adv. Cancer Res.* 102, 19–65. doi: 10.1016/S0065-230X(09)02002-8

Kahn, J., Hayman, T. J., Jamal, M., Rath, B. H., Kramp, T., Camphausen, K., et al. (2014). The mTORC1/mTORC2 inhibitor AZD2014 enhances the radiosensitivity of glioblastoma stem-like cells. *Neuro Oncol.* 16, 29–37. doi: 10.1093/neuonc/not139

Knobbe, C. B., Trampe-Kieslich, A., and Reifenberger, G. (2005). Genetic alteration and expression of the phosphoinositol-3-kinase/Akt pathway genes PIK3CA and PIKE in human glioblastomas. *Neuropathol. Appl. Neurobiol.* 31, 486–490. doi: 10.1111/j.1365-2990.2005.00660.x

Li, X., Wu, C., Chen, N., Gu, H., Yen, A., Cao, L., et al. (2016). PI3K/Akt/mTOR signaling pathway and targeted therapy for glioblastoma. *Oncotarget* 7, 33440–33450. doi: 10.18632/oncotarget.7961

Liu, L. P., Cash, T. P., Jones, R. G., Keith, B., Thompson, C. B., and Simon, M. C. (2006). Hypoxia-induced energy stress regulates mRNA translation and cell growth. *Mol. Cell* 21, 521–531. doi: 10.1016/j.molcel.2006.01.010

Lu, W. L., Li, F., and Mahato, R. I. (2011). Poly(ethylene glycol)-block-poly(2-methyl-2-benzoxycarbonyl-propylene carbonate) micelles for rapamycin delivery: *in vitro* characterization and biodistribution. *J. Pharm. Sci.* 100, 2418–2429. doi: 10.1002/jps.22467

Mao, H., LeBrun, D. G., Yang, J. X., Zhu, V. F., and Li, M. (2012). Deregulated signaling pathways in glioblastoma multiforme: molecular mechanisms and therapeutic targets. *Cancer Invest.* 30, 48–56. doi: 10.3109/07357907.2011.630050

Masui, K., Harachi, M., Cavenee, W. K., Mischel, P. S., and Shibata, N. (2020). mTOR complex 2 is an integrator of cancer metabolism and epigenetics. *Cancer Lett.* 478, 1–7. doi: 10.1016/j.canlet.2020.03.001

Masui, K., Harachi, M., Ikegami, S., Yang, H. J., Onizuka, H., Yong, W. H., et al. (2019). mTORC2 links growth factor signaling with epigenetic regulation of iron metabolism in glioblastoma. *J. Biol. Chem.* 294, 19740–19751. doi: 10.1074/jbc.RA119.011519

Mecca, C., Giambanco, I., Donato, R., and Arcuri, C. (2018). Targeting mTOR in glioblastoma: rationale and preclinical/clinical evidence. *Dis. Markers.* 2018:9230479. doi: 10.1155/2018/9230479

Mukherjee, B., Tomimatsu, N., Amancherla, K., Camacho, C. V., Pichamoorthy, N., and Burma, S. (2012). The dual PI3K/mTOR inhibitor NVP-BEZ235 is a potent inhibitor of ATM- and DNA-PKCs-mediated DNA damage responses. *Neoplasia* 14, 34–43. doi: 10.1593/neo.111512

Najberg, M., Haji Mansor, M., Boury, F., Alvarez-Lorenzo, C., and Garcion, E. (2019). Reversing the tumor target: establishment of a tumor trap. *Front. Pharmacol.* 10:887. doi: 10.3389/fphar.2019.00887

O'Reilly, K. E., Rojo, F., She, Q. B., Solit, D., Mills, G. B., Smith, D., et al. (2006). mTOR inhibition induces upstream receptor tyrosine kinase signaling and activates Akt. *Cancer Res.* 66, 1500–1508. doi: 10.1158/0008-5472.CAN-05-2925

Ostrom, Q. T., Gittleman, H., Liao, P., Vecchione-Koval, T., Wolinsky, Y., Kruchko, C., et al. (2017). CBTRUS statistical report: primary brain and other central nervous system tumors diagnosed in the united states in 2010–2014. *Neuro Oncol.* 19, v1–v88. doi: 10.1093/neuonc/nox158

Paillard, A., Hindre, F., Vignes-Colombeix, C., Benoit, J. P., and Garcion, E. (2010). The importance of endo-lysosomal escape with lipid nanocapsules for drug subcellular bioavailability. *Biomaterials* 31, 7542–7554. doi: 10.1016/j.biomaterials.2010.06.024

Peddi, S., Roberts, S. K., and MacKay, J. A. (2020). Nanotoxicology of an elastin-like polypeptide rapamycin formulation for breast cancer. *Biomacromolecules* 21, 1091–1102. doi: 10.1021/acs.biomac.9b01431

Raymond, E., Alexandre, J., Faivre, S., Vera, K., Materman, E., Boni, J., et al. (2004). Safety and pharmacokinetics of escalated doses of weekly intravenous infusion of CCI-779, a novel mTOR inhibitor, in patients with cancer. *J. Clin. Oncol.* 22, 2336–2347. doi: 10.1200/JCO.2004.08.116

Rodrik-Outmezguine, V. S., Chandarlapaty, S., Pagano, N. C., Poulikakos, P. I., Scaltriti, M., Moskatel, E., et al. (2011). mTOR kinase inhibition causes feedback-dependent biphasic regulation of AKT signaling. *Cancer Discov.* 1, 248–259. doi: 10.1158/2159-8290.CD-11-0085

Sarbassov, D. D., Guertin, D. A., Ali, S. M., and Sabatini, D. M. (2005). Phosphorylation and regulation of Akt/PKB by the rictor-mTOR complex. *Science* 307, 1098–1101. doi: 10.1126/science.1106148

Saxton, R. A., and Sabatini, D. M. (2017). mTOR signaling in growth, metabolism, and disease. *Cell* 168, 960–976. doi: 10.1016/j.cell.2017.02.004

Séhédic, D. (2014). *Development of new nano-medicine strategies for the targeting and the radiosensization of glioblastoma stem cells* (Université d'Angers). Available online at: https://www.theses.fr/2014ANGE0028

Shi, P., Aluri, S., Lin, Y. A., Shah, M., Edman, M., Dhandhukia, J., et al. (2013). Elastin-based protein polymer nanoparticles carrying drug at both corona and core suppress tumor growth *in vivo*. *J. Control. Release* 171, 330–338. doi: 10.1016/j.jconrel.2013.05.013

Shinohara, E. T., Cao, C., Niermann, K., Mu, Y., Zeng, F. H., Hallahan, D. E., et al. (2005). Enhanced radiation damage of tumor vasculature by mTOR inhibitors. *Oncogene* 24, 5414–5422. doi: 10.1038/sj.onc.1208715

Simamora, P., Alvarez, J. M., and Yalkowsky, S. H. (2001). Solubilization of rapamycin. *Int. J. Pharm.* 213, 25–29. doi: 10.1016/S0378-5173(00)00617-7

Sonoda, Y., Ozawa, T., Aldape, K. D., Deen, D. F., Berger, M. S., and Pieper, R. O. (2001). Akt pathway activation converts anaplastic astrocytoma to glioblastoma multiforme in a human astrocyte model of glioma. *Cancer Res.* 61, 6674–6678.

Stupp, R., Hegi, M. E., Mason, W. P., van den Bent, M. J., Taphoorn, M. J., Janzer, R. C., et al. (2009). Effects of radiotherapy with concomitant and adjuvant temozolomide vs. radiotherapy alone on survival in glioblastoma in

a randomised phase III study: 5-year analysis of the EORTC-NCIC trial. *Lancet Oncol.* 10, 459–466. doi: 10.1016/S1470-2045(09)70025-7

Stupp, R., Mason, W. P., van den Bent, M. J., Weller, M., Fisher, B., Taphoorn, M. J., et al. (2005). Radiotherapy plus concomitant and adjuvant temozolomide for glioblastoma. *N. Engl. J. Med.* 352, 987–996. doi: 10.1056/NEJMoa043330

Touat, M., Idbaih, A., Sanson, M., and Ligon, K. L. (2017). Glioblastoma targeted therapy: updated approaches from recent biological insights. *Ann. Oncol.* 28, 1457–1472. doi: 10.1093/annonc/mdx106

Tremblay, F., Brule, S., Um, S. H., Li, Y., Masuda, K., Roden, M., et al. (2007). Identification of IRS-1 Ser-1101 as a target of S6K1 in nutrient- and obesity-induced insulin resistance. *Proc. Natl. Acad. Sci. U.S.A.* 104, 14056–14061. doi: 10.1073/pnas.0706517104

Tyler, B., Wadsworth, S., Recinos, V., Mehta, V., Vellimana, A., Li, K., et al. (2011). Local delivery of rapamycin: a toxicity and efficacy study in an experimental malignant glioma model in rats. *Neuro Oncol.* 13, 700–709. doi: 10.1093/neuonc/nor050

Wang, B. L., Li, H. Y., Yao, Q. Y., Zhang, Y. L., Zhu, X. D., Xia, T. L., et al. (2016). Local *in vitro* delivery of rapamycin from electrospun PEO/PDLLA nanofibers for glioblastoma treatment. *Biomed. Pharmacother.* 83, 1345–1352. doi: 10.1016/j.biopha.2016.08.033

Wang, J. P., Guo, F., Yu, M., Liu, L., Tan, F. P., Yan, R., et al. (2016). Rapamycin/DiR loaded lipid-polyaniline nanoparticles for dual-modal imaging guided enhanced photothermal and antiangiogenic combination therapy. *J. Control. Release* 237, 23–34. doi: 10.1016/j.jconrel.2016.07.005

Wanigasooriya, K., Tyler, R., Barros-Silva, J. D., Sinha, Y., Ismail, T., and Beggs, A. D. (2020). Radiosensitising cancer using phosphatidylinositol-3-kinase (PI3K), protein kinase B (AKT) or mammalian target of rapamycin (mTOR) inhibitors. *Cancers* 12:1278. doi: 10.3390/cancers12051278

Weppler, S. A., Krause, M., Zyromska, A., Lambin, P., Baumann, M., and Wouters, B. G. (2007). Response of U87 glioma xenografts treated with concurrent rapamycin and fractionated radiotherapy: possible role for thrombosis. *Radiother. Oncol.* 82, 96–104. doi: 10.1016/j.radonc.2006.11.004

Wick, W., Weller, M., Weiler, M., Batchelor, T., Yung, A. W. K., and Platten, M. (2011). Pathway inhibition: emerging molecular targets for treating glioblastoma. *Neuro Oncol.* 13, 566–579. doi: 10.1093/neuonc/nor039

Yatscoff, R. W., Wang, P., Chan, K., Hicks, D., and Zimmerman, J. (1995). Rapamycin - distribution, pharmacokinetics, and therapeutic range investigations. *Ther. Drug Monit.* 17, 666–671. doi: 10.1097/00007691-199512000-00020

Zhong, H., Chiles, K., Feldser, D., Laughner, E., Hanrahan, C., Georgescu, M. M., et al. (2000). Modulation of hypoxia-inducible factor 1 alpha expression by the epidermal growth factor/phosphatidylinositol 3-kinase/PTEN/AKT/FRAP pathway in human prostate cancer cells: implications for tumor angiogenesis and therapeutics. *Cancer Res.* 60, 1541–1545.

Conflict of Interest: The authors declare that the research was conducted in the absence of any commercial or financial relationships that could be construed as a potential conflict of interest.

Appendice IV

Article: Implantable SDF-1α-loaded Silk Fibroin Hyaluronic Acid Aerogel Sponges as an Instructive Component of the Glioblastoma Ecosystem: Between Chemoattraction and Tumor Shaping into Resection Cavities

Rodolfo Molina-Pena, Natalia Helen Ferreira, Charlotte Roy, **Loris Roncali**, Mathie Najberg, Sylvie Avril, Mariana Zarour, William Bourgeois, Alba Ferreiros, Chiara Lucchi, Francesco Cavalieri, François Hindré, Giovani Tosi, Giuseppe Biagini, Franco Valzania, François Berger, Miguel Abal, Audrey Rousseau, Frank Boury, Carmen Alvarez-Lourenzo*, Emmanuel Garcion*

Molina-Peña R, Ferreira NH, Roy C, et al. Implantable SDF-1α-loaded silk fibroin hyaluronic acid aerogel sponges as an instructive component of the glioblastoma ecosystem: Between chemoattraction and tumor shaping into resection cavities. Acta Biomater. Published online October 20, 2023. doi:10.1016/j.actbio.2023.10.022

ARTICLE IN PRESS
JID: ACTBIO [m5G;November 17, 2023;23:43]
Acta Biomaterialia xxx (xxxx) xxx

Contents lists available at ScienceDirect

Acta Biomaterialia

journal homepage: www.elsevier.com/locate/actbio

Full length article

Implantable SDF-1α-loaded silk fibroin hyaluronic acid aerogel sponges as an instructive component of the glioblastoma ecosystem: Between chemoattraction and tumor shaping into resection cavities

Rodolfo Molina-Peña[a,1], Natália Helen Ferreira[a,1], Charlotte Roy[a], Loris Roncali[a], Mathie Najberg[a], Sylvie Avril[a], Mariana Zarur[b], William Bourgeois[c], Alba Ferreirós[g], Chiara Lucchi[e], Francesco Cavallieri[d], François Hindré[a], Giovani Tosi[f], Giuseppe Biagini[e], Franco Valzania[d], François Berger[c], Miguel Abal[g], Audrey Rousseau[a], Frank Boury[a], Carmen Alvarez-Lorenzo[b,1,*], Emmanuel Garcion[a,1,*]

[a] *Univ Angers, Nantes Université, Inserm, CNRS, CRCI2NA, SFR ICAT, F-49000 Angers, France*
[b] *Departamento de Farmacología, Farmacia y Tecnología Farmacéutica, ID Farma (GI-1645), Facultad de Farmacia, iMATUS, and Health Research Institute of Santiago de Compostela (IDIS), Universidade de Santiago de Compostela, 15782 Santiago de Compostela, Spain*
[c] *Inserm UMR1205, Brain Tech Lab, Grenoble Alpes University Hospital (CHUGA), Grenoble, 38000, France*
[d] *Neurology Unit, Neuromotor and Rehabilitation Department, Azienda USL-IRCCS di Reggio Emilia, Reggio Emilia, Italy*
[e] *Department of Biomedical, Metabolic and Neural Sciences, University of Modena and Reggio Emilia, 41125 Modena, Italy*
[f] *Department of Life Sciences, University of Modena and Reggio Emilia, 41125 Modena, Italy*
[g] *NASASBIOTECH S.L., Cantón Grande nº 9, 15003, A Coruña, Spain*

ARTICLE INFO

Article history:
Received 25 May 2023
Revised 16 October 2023
Accepted 17 October 2023
Available online xxx

Keywords:
Resection cavity
Implantable device
Cancer cell trap
Chemoattraction
Ecosystem dynamic
Cell homing

ABSTRACT

In view of inevitable recurrences despite resection, glioblastoma (GB) is still an unmet clinical need. Dealing with the stromal-cell derived factor 1-alpha (SDF-1α)/CXCR4 axis as a hallmark of infiltrative GB tumors and with the resection cavity situation, the present study described the effects and relevance of a new engineered micro-nanostructured SF-HA-Hep aerogel sponges, made of silk fibroin (SF), hyaluronic acid (HA) and heparin (Hep) and loaded with SDF-1α, to interfere with the GB ecosystem and residual GB cells, attracting and confining them in a controlled area before elimination. 70 µm-pore sponges were designed as an implantable scaffold to trap GB cells. They presented shape memory and fit brain cavities. Histological results after implantation in brain immunocompetent Fischer rats revealed that SF-HA-Hep sponges are well tolerated for more than 3 months while moderately and reversibly colonized by immuno-inflammatory cells. The use of human U87MG GB cells overexpressing the CXCR4 receptor (U87MG-CXCR4+) and responding to SDF-1α allowed demonstrating directional GB cell attraction and colonization of the device *in vitro* and *in vivo* in orthotopic resection cavities in Nude rats. Not modifying global survival, aerogel sponge implantation strongly shaped U87MG-CXCR4+ tumors in cavities in contrast to random infiltrative growth in controls. Overall, those results support the interest of SF-HA-Hep sponges as modifiers of the GB ecosystem dynamics acting as "cell meeting rooms" and biocompatible niches whose properties deserve to be considered toward the development of new clinical procedures.

Statement of Significance

Brain tumor glioblastoma (GB) is one of the worst unmet clinical needs. To prevent the relapse in the resection cavity situation, new implantable biopolymer aerogel sponges loaded with a chemoattractant molecule were designed and preclinically tested as a prototype targeting the interaction between the initial tumor location and its attraction by the peritumoral environment. While not modifying global survival, biocompatible SDF1-loaded hyaluronic acid and silk fibroin sponges induce directional GB cell

* Corresponding authors.
E-mail addresses: carmen.alvarez.lorenzo@usc.es (C. Alvarez-Lorenzo), emmanuel.garcion@univ-angers.fr (E. Garcion).
[1] Eq contribution.

https://doi.org/10.1016/j.actbio.2023.10.022

Please cite this article as: R. Molina-Peña, N.H. Ferreira, C. Roy et al., Implantable SDF-1α-loaded silk fibroin hyaluronic acid aerogel sponges as an instructive component of the glioblastoma ecosystem: Between chemoattraction and tumor shaping into resection cavities, Acta Biomaterialia, https://doi.org/10.1016/j.actbio.2023.10.022

ARTICLE IN PRESS
JID: ACTBIO [m5G;November 17, 2023;23:43]
R. Molina-Peña, N.H. Ferreira, C. Roy et al. Acta Biomaterialia xxx (xxxx) xxx

attraction and colonization *in vitro* and in rats *in vivo*. Interestingly, they strongly shaped GB tumors in contrast to random infiltrative growth in controls. These results provide original findings on application of exogenous engineered niches that shape tumors and serve as cell meeting rooms for further clinical developments.

1. Introduction

Glioblastoma (GB) is a lethal tumor with high recurrence rates. Most recurrences occur within 2 cm of the resection cavity due to the infiltration of GB cells into the brain parenchyma [1–3]. Targeting residual tumor cells is crucial to improve patient outcomes. New strategies are needed to selectively kill these cells while minimizing damage to normal brain tissue.

In contrast to direct targeting strategies that vectorize killing agents toward cancer cells, the reversal approach involves bringing the target toward a site of confinement by mimicking the preferred environment of infiltrating tumor cells [4,5]. Then, direct loco-regional delivery of a cell death signal, such as focalized radiotherapy or local delivery of cytotoxic chemotherapeutic agents, could be applied for more effective treatment.

The tumor cell trapping strategy has been applied by a few groups like De la Fuente et al. who designed a polyurethane scaffold coated with collagen that was able to confine metastatic ovarian cancer cells in mice peritonea showing an improvement in survival [6]. Jain et al. designed aligned fibers of polycaprolactone to direct GB cells toward an extracortical killing sink [7]. Reduced tumor size was observed; however, the invasive behavior of GB cells did not allow for a complete recovery. More research in this area shall be beneficial for the development of more effective glioblastoma treatment.

For this purpose, biocompatible biomaterials that can support cell infiltration should be chosen [8,9]. The scaffold should be biomimetically functionalized to adapt its structure and composition, including relevant extracellular matrix (ECM) components, such as hyaluronic acid (HA), which is a crucial element of the cerebral ECM [10,11]. Also, an active scaffold can contain specific cellular signals that respond to the desired application, such as a chemokine to increase the recruitment of cancer cells.

In this regard, it has been observed that infiltrative GB cells express the C-X-C chemokine receptor type 4 (CXCR4) [12–14]. This receptor binds the chemoattractant stromal cell-derived factor 1 α (SDF-1α), also known as CXCL12. A gradient of this chemokine induces the attraction of cells expressing the CXCR4 receptor [15,16]. Therefore, we hypothesize that implanting a scaffold containing SDF-1α in the resection cavity can attract and confine infiltrative GB cells into a specific site.

Previously, our group developed freeze-dried aerogel sponges for this purpose: a silk fibroin (SF) with Hyaluronic acid (HA) sponge (SF-HA), and a SF with HA and heparin (Hep) (SF-HA-Hep) sponge, where heparin acts as a complexation agent for SDF-1α [17]. This study aims to evaluate the capacity of this new scaffold to attract infiltrative GB cells in a rat model of the brain resection cavity.

The biocompatibility and biodegradability of sponges were first evaluated. Direct placement of GB cells and glioma spheroids in contact with the scaffolds was used to evaluate cellular interactions and their cell hosting capacity. SF-HA-Hep sponges were selected for further application based on their degradation profile and enhanced cell adhesion. Our results showed that SDF-1α-loaded sponges had a strong *in vitro* chemotactic response and enhanced colonization. *In vivo* assessment was conducted by the placement of sponges 1-mm away to human GB cells expressing the CXCR4 receptor. Sponges attracted GB cells and induced localized tumor development in the resection spaces, which can be potentially used for further focalized therapy in a concentrated area. The findings and limitations of this strategy are discussed for further development of a safer and more efficient GB cell confinement device.

2. Materials and methods

2.1. Materials

Hepes, bovine serum albumin (BSA), resazurin, paraformaldehyde (PFA), sucrose, low melting point low gelling temperature agarose, Sudan Black, Giemsa stain, Crystal violet, Phosphate Buffered Saline (PBS, pH 7.4), Dulbecco's Modified Eagle's Medium (DMEM) with high glucose and Aphidicolin (ADC) were purchased from Sigma-Aldrich; glycerol (86–89 wt%) from Fluka and heparin sodium salt (Mw 15,000 ± 2000 g/mol) from Calbiochem (Billerca MA, USA), N-(3-dimethylaminopropyl)-N′-ethylcarbodiimide hydrochloride (EDC) and N-hydroxysulfosuccinimide sodium salt (NHS) from Acros Organics (New Jersey, USA). Hyaluronic acid (HA) (Mw 360,000 g/mol) was purchased from Guinama (Valencia, Spain). Silk fibroin (SF) 8 wt% in an aqueous solution was provided by IMIDA (Murcia, Spain). SDF-1α was purchased from Miltenyi Biotec (Paris, France).

2.1.1. Sponges' preparation and characterization

SF (4 %) with HA (2 %) (SF-HA) and SF (4 %) with HA (2 %) and heparin (1 %) (SF-HA-hep) sponges were synthesized and physicochemically characterized as reported previously by Najberg et al. (2020) [17]. Briefly, HA was dissolved in Hepes buffer ($C_{Hepes} = 20.10^{-3}$ M, $C_{NaCl} = 0.15$ M, pH=7.4) to obtain a final concentration of 4% w/v. SF 8% w/v solution was gently mixed with an equivalent volume of HA 4 % solution in Hepes buffer with or without heparin sodium salt ($C_f = 1\%$ w/v). The SF-HA mixture was crosslinked using 5 mg/mL EDC and 1.8 mg/mL NHS. For formulations with heparin, 15 mg/mL EDC and 5.5 mg/mL NHS were used. The solutions were poured into a 96-well plate, covered, and allowed to crosslink for 15 h at 4 °C. The gels were then frozen at −20 °C for 24 h and freeze-dried in a Telstar® LyoQuest at −70 °C and 0.01 mBar overnight. The stabilization occurred by annealing the sponges in ethanol vapors, followed by freeze-drying again.

The porosity, thickness, and pore size of the sponges (n = 3) were evaluated by microcomputed tomography (microCT) using a Bruker SkyScan 1272 (Kontich, Belgium). Scans were acquired at a voltage of 50 kV and a current of 200 μA, with a rotation step of 0.3°, pixel size of 5 μm, and no filter. Reconstruction of the obtained tomograms was carried out using NRecon software (Bruker) and 3D rendered images of the samples were generated through original volumetric reconstructed images by CTVox (Bruker). The quantification of structure properties was evaluated using a cylindric volume of interest (VOI) of 30 mm^3 centered in the middle of the samples. Before the analysis, datasets were binarized using

a global threshold of 70–255 and a 3D despeckle process was applied to reduce image noise. Finally, analysis was performed using CTAn software (Bruker).

Sponges, measuring 2 mm - height and 3 mm - diameter, underwent sterilization under UV light for 30 min on each side prior to both *in vitro* and *in vivo* procedures.

2.1.2. Cell lines and culture conditions

NIH3T3 mouse fibroblast cells (CRL-1658^{TM}) and U87-MG cells were acquired from ATCC (Rockville, Maryland, USA). U87-MG cells, transduced to express the CXCR4 receptor and red fluorescent protein (RFP) as previously described [18]. Transduced cells were selected with Blasticidine treatment (10 µg/mL) followed by cell sorting of a pure subpopulation expressing RFP and the CXCR4 receptor. These cells were called here as U87MG-CXCR4^{+}. All cell lines were cultured at 37 °C and 5 % CO_2 in DMEM supplemented with 10 % fetal bovine serum (FBS) and 1 % penicillin/streptomycin and subcultured every 3.5 days.

2.2. In vitro methods

2.2.1. Flow cytometry

U87MG-CXCR4+ cells were dissociated with trypsin, washed and incubated with 10 μg/mL anti-CXCR4 primary antibody clone 12G5, or IgG2a [18] in PBS containing 0.5 % BSA for 40 min at 4 °C. After washing with PBS/BSA, cells were incubated with 8 µg/mL secondary Ab (Polyclonal goat α-mouse IGs-FITC, Dako F0479) in PBS containing 0.5 % BSA for 30 min at 4 °C protected from light. After washing in PBS/BSA cells were analyzed in a MACSQuant® Analyzer 10 Flow Cytometer (Miltenyi Biotec).

2.2.2. Western blot

Total proteins were isolated from U87MG-CXCR4+ cells by sonication in a lysis buffer composed of 50 mM HEPES, pH 7.5, 150 mM NaCl, 1 mM EDTA, pH 8, 2.5 mM EGTA, pH 7.4, 0.1 % Tween 20, 10 % glycerol, 0.1 mM sodium orthovanadate, 1 mM sodium fluoride, 10 mM glycerophosphate and 0.1 mM phenylmethylsulphonyl fluoride (PMSF). After quantification by spectrophotometry using the Quick Start^{TM} Bradford Protein Assay (Bio-rad), equal amounts of proteins (20 µg) were loaded onto 10 % polyacrylamide gels and transferred to an Amersham GE Healthcare nitrocellulose membrane (0.45 μm pore size; Fisher Scientific). The following antibodies were used according to the manufacturer's instructions: rabbit anti-human Akt (Cell Signaling, #9272), phosphor-Akt (Ser473; #9271), p44/42 MAPK Erk1/2 (#9102), phospho-p44/42 MAPK Erk1/2 (Thr202/Tyr204; #9101), paxillin (#2542), and phosphor-paxillin (Tyr118; #2541). A mouse anti-human actin (#MA5–11,869, Invitrogen) was used as a loading control. Anti-Rabbit IgG Secondary Antibody, HRP conjugate (Fisher Scientific) was used at a dilution of 1:10,000. Detection was performed on SuperSignal^{TM} West Femto Maximum Sensitivity Substrate (Fisher Scientific) with a ChemiCapt 3000 imaging system (Vilber Lourmat, Marne-la-Vallée France).

2.2.3. Viability assay

The cytotoxicity of sponges on NIH3T3 and U87MG cells was evaluated by the indirect and direct contact methods, by ISO 10,993–5:2009, at 24 h and 72 h intervals. 4×10^4 NIH3T3 cells were seeded per well (24-well plates) for the 24-h assay and 1×10^4 cells/well for the 72-h assay. 8×10^4 U87MG cells were seeded per well for the 24-h assay and 2×10^4 cells/well for the 72-h assay. Cells were kept at 37 °C and 5 % CO_2 for 24 h before adding the sponges. UV-sterilized 2 mm height and 3 mm diameter sponges were washed 3 times with PBS, for residual crosslinker removal, and equilibrated in complete medium before use. For the direct contact method, sponges were directly added on top of the cell monolayer. Wells without sponges were used as controls. 24 h or 72 h after, sponges were removed by aspiration, and the media was replaced with 500 µL of 44 µM resazurin. After 2 h, cell viability was estimated by the fluorescence intensity of the resorufin (545–600 nm) using the ClarioStar microplate fluorometer (BMG Labtech GmbH, Ortenberg, Germany). For the indirect contact method, suspended culture inserts with the sponges inside (MilliCell, PET, 8 µm) were placed in the wells containing cells. Inserts without sponges were used as controls. 200 µL of media was added to completely cover the sponges. The viability of the cells was measured as described above. Triplicates were performed for all used conditions.

2.2.4. Agarose drop assay

The ability of SDF-1α (Miltenyi Biotec) to induce the migration of U87MG-CXCR4+ cells was evaluated using an adapted agarose drop assay [19]. Briefly, a 24-well plate was coated with the extracellular matrix from U87MG cells. To do so, wells were first coated with poly-d-lysine (PDL, Sigma), then 5×10^4 U87MG cells were cultured for 48 h, lysed with deionized water, washed with PBS, and air-dried under sterile conditions before use. Then, a 2 µL drop of 1% w/v agarose in PBS containing 1×10^5 cells was placed in the center of a well. The agarose was allowed to solidify at 4 °C for 10 min. Then, 500 µL of serum-free DMEM with or without the chemokine (40 ng/mL of SDF-1α), and with or without 20 µg/mL aphidicolin (ADC) acting as an inhibitor of proliferation, was added on top of the drops. Plates were incubated for 3 days at 37 °C and 5 % CO_2. The distance of migration was measured at 4 points of the drop between the edge of the drop and the front of migration with ImageJ.

2.2.5. Boyden chamber assay

U87MG-CXCR4^{+}cells were starved in serum-free DMEM (SFM) for 24 h. Then cells were collected with Acutase solution, washed with PBS and resuspended in SFM. 5×10^4 cells were deposited on top of 8-µm pore PET inserts (Corning 353,097) in 100 µL of SFM. Then, 650 µL of SF DMEM containing 0, 40 or 120 ng/mL SDF-1α was deposited in the bottom well. After 18-h incubation cells were fixed with 4 % PFA for 15 min at room temperature (RT) and stained with 0.1 % crystal violet solution for 30 min. After washing, images were obtained in a VHX-7000 microscope (Keyence, France), and cells were counted with the QuPath software.

2.2.6. U87MG cells interaction with sponges

The cell response of U87MG cells when cultured into the sponges matrix was evaluated by direct seeding of cells into the sponges. SF-HA and SF-HA-Hep (1 % heparin) sponges were hydrated and cut in 2-mm height cylinders. After washing in PBS, they were sterilized by 30-min UV cycles each side. Sponges were washed with PBS and equilibrated in complete DMEM medium (10 % FBS and 1 % antibiotics). The excess medium was blotted in sterile gauzes for 20 s on each side. The sponges were then transferred to individual wells (24-well plate) and a drop containing 5×10^4 cells in 20 µL of medium was slowly deposited on top of the sponges. Sponges with cells were left for 30 min in the incubator to allow for cell adherence. Following this, 500 µL of complete DMEM was added and the sponges incubated for 2 days at 37 °C and 5 % CO_2. Revelation of the cellular response was performed by replacing the medium with complete DMEM containing 44 mM resazurin followed by incubation for 3 h. Controls well consisted in the same number of cells cultured on plastic.

The adherence and spreading of U87MG cells in SF-HA and SF-HA-Hep sponges were observed using a scanning electron microscope (SEM) Evo LS15 (Zeiss, USA). 60 µL DMEM containing 1×10^5 U87MG cells was deposited onto a 2-mm height sponge and cells were allowed to adhere for 1 h before the addition of

500 µL of complete DMEM in a 24-well plate. Constructs were cultured for 3 days at 37 °C and 5 % CO_2. 2.5 % glutaraldehyde in 0.1 M phosphate buffer was used for fixation for 2 h. After PBS and distilled water rinsing (1x for 5 min), constructs were incubated in 1 % osmium tetroxide aqueous solution for 1 h at RT. The samples were cut in half then rinsed with distilled water (3x for 5 min), followed by dehydration performed in increasing concentrations of ethanol solutions 50, 70, and 95 % for 20 min each, and 100 %, (3x for 30 min). Desiccation was performed in ethanol:hexamethyldisilazane (HDMS) 1:1 for 45 min, and HDMS overnight. A platinum coating was performed before the analysis of the surface and transverse sections of the different sponges.

2.2.7. Under agarose cell migration assay

The assay was adapted from Heit and Kubes, 2003 [20]. Agarose was dissolved in PBS by microwave heating and mixed with serum-free DMEM at 70 °C. The resulting mixture containing 1.2 % agarose in 75 % DMEM was sterile-filtered and equilibrated for 15 min at 37 °C before depositing 3 mL into each well of a 6-well plate. Casted gels were left to solidify for 30 min at RT and 1 h at 4 °C. Three punches were made in each gel using a homemade template and a 4-mm biopsy punch. The cut agarose was aspirated to create three reservoirs separated by equal distances of 2 mm. 5×10^4 U87MG-CXCR4+ cells previously treated with 1 µg/mL of ADC for 24 h in complete medium were seeded in 20 µL of DMEM containing either 1 % FBS or 10 % FBS, and 5 µg/mL of ADC, in the center well. Sterile sponges loaded with either 10 pmol or 100 pmol of SDF-1α were deposited in the right chamber and covered with 15 uL of serum-free DMEM. PBS was put in the left compartment acting as a control. To assess the effect of sponges without SDF-1α, the latter were evaluated against only PBS that was deposited in the left compartment. The comparison of the cell migration response to sponges loaded with SDF-1α (100 pmol) vs sponges alone was also carried out by placement of the former in the right wells and the sponges alone in the left well. After 3 days of incubation, the constructs were fixed with a mixture of methanol and acetic acid (3:1) and after removal of the gels, cells were stained with Giemsa stain (1:10), and washed 3x with distilled water. Pictures were taken with a VHX-7000 digital microscope (Keyence, France) and the areas of migration from the edge of the center well toward the left and right flanks were quantified with ImageJ.

2.2.8. Glioma spheroids assay

U87MG-CXCR4+ cells were cultured at a density of 6000 cells/cm^2 in defined medium consisting of a 1:1 mixture of low glucose DMEM and Ham's F12 supplemented with 20 ng/mL EGF and FGF-2, 5 µg/mL heparin, 1x B27 supplement and 1 % v/v Penicillin/Streptomycin. Half of the medium was changed every 3.5 days and spheroids were subcultured every 7 days. A single D7-neurospheroid of around 200 µm was collected and deposited on top of a 2-mm height and 6-mm diameter UV-sterilized sponge that was previously loaded with 60 µL serum-free DMEM containing 100 pmol of SDF-1α. Sponges without SDF-1α were used as controls. After 1-h of incubation at 37 °C and 5 % CO_2, 400 µL of DMEM supplemented with 1 % FBS, 1 % N1, and 1 % antibiotics was added carefully into the well (24 well plate). The constructs were left in culture for 6 days, fixed with 4 % PFA, permeabilized, and stained with DAPI before incubation in 0.3 % Soudan Black solubilized in 70 % ethanol to reduce the autofluorescence of sponges. Confocal images were obtained from the top view and the cross-section of sliced constructs. The on-top cell area and the cross-section invaded area were analyzed with the QuPath software.

2.3. In vivo studies

2.3.1. Animals

Fischer and nude athymic female rats aged 8–10 weeks were obtained from Janvier Labs (Le Genest-Saint-Isle, France). The protocol was approved by the Ethical Committee for Animal Experimentation of Pays de la Loire region, France (authorization number APAFIS #25889-2020032620074335 v3).

2.3.2. Evaluation of the biocompatibility of sponges

2.3.2.1. Implantation of sponges. Fisher rats were anesthetized by intraperitoneal injection of a mixture of ketamine (80 mg/kg) and xylazine (10 mg/kg) with subcutaneous administration of ketoprofen (5 mg/Kg) and positioned in a Kopf stereotaxic instrument. A 10 mm-long incision was made along the midline to create access to the surface of the skull. Following this, a burr hole (stereotactic coordinates: P: +0.8 mm; L: −3 mm (right from the bregma)) was drilled into the skull using a high-speed drill to expose the brain tissues underneath. A portion of the brain cortex was then carefully cut using a biopsy punch device and subsequently removed using vacuum suction to create a cavity that was approximately 3 mm wide and 2 mm deep. SF-HA and SF-HA-hep sponges were swollen in PBS, cut transversely to obtain 2 mm height cylinders, and sterilized under UV light for 1 hour. The sponges were then cut one by one before implantation with a 3 mm diameter biopsy punch with a push-button and, immediately after, implanted in the cavity with the biopsy punch. The wound was sutured, and the rats were allowed to wake without any further intervention. All rats became fully conscious within 2 h after surgery and did not display any sign of distress. In control rats, the same surgical procedure was also performed, but no scaffold was implanted. Ketoprofen was administered for 2 days after surgery. Two groups of rats were set up: one group consisted of 9 rats (3 implanted with SF-HA sponges, 3 implanted with SF-HA-hep sponges, and 3 cavity controls - with no implants), and was intended for the short-term study (euthanized after 7 days) while the other group, consisted of 12 rats (4 implanted with SF-HA sponges, 4 with SF-HA-hep sponges and 4 controls), was intended for the long-term follow-up (euthanized after 118 days). MRI follow-up was performed on days 6 and 76 post-implantation.

2.3.2.2. Histology. After euthanasia, the brains were collected and subsequently fixed in formalin for a duration of 10 days, followed by paraffin embedding. Next, 5 µm thick sections were obtained using an HM340E Microm Microtech microtome (France) and stained with hematoxylin and eosin (HE) for analysis. The histopathological parameters considered included multinucleated giant cells, acute inflammatory cells, necrosis, chronic inflammatory cells, neoangiogenesis, hemorrhage, hemosiderin deposition, and mineralization. These parameters were evaluated in randomly selected fields under 40× magnification in the tissue sections. The analyses were conducted at the Department of Cellular and Tissue Pathology, centre Hospitalier Universitaire d'Angers (CHU-Angers, France). Microscopic images were captured using an Olympus microscope.

2.3.3. Evaluation of SDF-1α release in rat brains

To study the potential release of SDF-1α from the sponge to the brain, an SDF-1α coupled with Alexa Fluor 647 (AF-SDF-1α) at the C terminal (Almac, Scotland) was used. The SF-HA-Hep sponge was used for further *in vivo* experiments, as the SF-HA sponge was mostly degraded after 7 days. The same methods to prepare the sponges, including cutting and sterilization, were used as cited before. Afterward, the 3 mm diameter sponges were taken out of the biopsy punch, the PBS excess was taken out by blotting them on a gauze, producing slight dehydration, and rehydrated by

ARTICLE IN PRESS
JID: ACTBIO [m5G;November 17, 2023;23:43]

adding 3 µL of AF-SDF-1α (150 ng) on the top of the sponge to finally implant them in the cavity of Fischer rats as described in Section 2.3.2.1. With this process, the full volume of AF-SDF-1α was absorbed by the sponge, resulting in a theoretical 100 % loading. Rats were euthanized after 7 days, and the brains were snap-frozen in isopentane and stored at −80 °C right after collection. Tissues were cut coronally in the region of interest with a Cryostat Leica CM3050 S (Leica Biosystems, Nussloch, Germany) to obtain 10 µm thick slices that were deposited on gelatinated Superfrost slides (Thermo Fisher Scientific, Braunschweig, Germany), and kept at −20 °C until immunolabeling.

2.3.4. Evaluation of the sponge's performance in vivo

To assess the GB cell attractant capacity of sponges *in vivo*, two orthotopic models were tested in nude female rats, aged 8 to 10 weeks. In the first model, 5×10^3 U87MG-CXCR4+ cells were injected into the striatum (P: +0.8 mm; L: −3 mm (right from the bregma); D: −2.5 mm from the cortex surface). After 10 days of tumor development, a 3-mm diameter and ∼2-mm depth resection cavity was performed in the same vertical axis of cell injection using a biopsy punch. The tissue was then aspirated, and SF-HA-Hep sponges (3-mm diameter and 2-mm height) were implanted loaded or not with 100 pmol of SDF-1α. After 7 days, animals were euthanized, and brains were collected and snapfrozen at −80 °C until analysis. GB cell identification was performed by RFP, CXCR4 and Ki67 analysis by IHC-IF.

In the second model, a resection cavity was created (P: +0.8 mm; L: −2.9mm (right from the bregma); D: ∼ −2 mm from the cortex surface). SF-HA-Hep sponges (3-mm diameter and 2-mm height) were implanted loaded or not with 100 pmol of SDF-1α in 5 µL of PBS. Following this, 2.5×10^4 U87MG-CXCR4+ cells were injected at 1 mm posterior from the edge of the resection (Stereotactic coordinates: P: −1.7, L: −2.9, D: −2 mm from the surface of the brain). Excess blood was removed with sterile gauze, the cavities were closed with non-absorbable bone wax and the wound was sutured.

The animals recovered after 2 h and did not show signs of distress. Animals were monitored daily, observing food and water intake, also weights were recorded. After 7 days, euthanasia was conducted, and all brains were extracted, snap-frozen and kept at −80 °C until analysis. The experimental design consisted of three groups: resection control, PBS swollen sponges, and sponges loaded with SDF-1α ($n = 3$). A survival experiment was performed using the same latter surgery procedures, but 1×10^3 U87MG-CXCR4+ cells were injected instead ($n = 6$ per group). Animals were followed by MRI weekly and euthanized at defined endpoints.

2.3.5. MRI analysis

MRI scans were performed with a Bruker Biospec 70/20 system operating at 7T, under isoflurane (0.5 % 1 L/min O_2) anesthesia, with the monitoring of respiratory parameters. T2-weighted images were acquired with a multi-spin echo sequence [FOV = 35×35 mm, slice thickness = 0.8 mm, spacing between slices = 1.1 mm, matrix 256×256, TR = 2.5 s, TE = 33 ms].

2.3.6. Immunohistochemistry and immunofluorescence

For the SDF-1α release study, 10 µm sections were fixed with PFA 4 % (w/v) at 4 °C for 20 min, permeabilized with 0.25 % (w/v) Triton X-100 in PBS for 10 min and saturated with NGS 10 % (w/v) in PBS for 2 h. They were then incubated overnight at 4 °C with polyclonal rabbit IgG anti-SDF-1α (1:500) (Abcam, Cambridge) followed by 1 h incubation at RT with the secondary antibody goat anti-rabbit AF 488 (#4412 Cell Signaling). Cell nuclei were stained with DAPI (1:2000, Thermo Fisher Scientific, Waltham, MA) before mounting sections with Dako fluorescence mounting media (Dako, CA, USA). Stained sections were visualized using a confocal microscope Leica TCS SP8 AOBS (Leica Microsystems, Wetzlar, Germany).

For the sponge's bioperformance study, 16 µm sections were fixed for 10 min in methanol at −20 °C and rehydrated in PBS (3 washes). After saturation in PBS/4 %BSA/10 %NGS/0.25 % TritonX100 for 1 h, sections were probed with the primary antibodies as follows: anti-CXCR4 polyclonal (1:2500, #PA3–305-Invitrogen) which does not cross-react with rat tissue, or anti-Ki67 (1:200, ab16667-ABCAM), both overnight at 4 °C in a humidified chamber. After washing (3x in PBS) the slices were incubated with a biotinylated secondary Ab (anti-mouse or anti-rabbit, 1:100 in PBS/4 %BSA, Vector Laboratories) for 1 h at RT. Slices were re-washed and incubated with Streptavidin-FITC (1:500, Interchim) or Streptevidin-AF647 (1:500, Life Technologies) in PBS for 45 min at RT. After washing, slices were incubated with DAPI, and finally with Sudan Black for 15 min before mounting slides. Fluorescence was analyzed in a Leyca confocal microscope.

2.4. Statistical analysis

Data are presented as mean ± SEM. Data were statistically analyzed using an ANOVA test with Prism 7 software. Tukey's multiple comparison test was used to compare individual groups. For analysis considering only two groups, a two-tailed t-test was performed. UACMA data was analyzed with a two-tailed paired t-test. In all statistical comparisons $p < 0.05$ was considered statistically significant. For the survival analysis, all and single groups were compared using the Log-rank (Mantel-Cox).

3. Results

In vitro studies

3.1. U87MG-CXCR4+ cells are responsive to SDF-1α

Human GB U87MG cells were transduced for the expression of the CXCR4 receptor (U87MG-CXCR4+) and the receptor expression was confirmed by flow cytometry (Fig. 1A). Then, their molecular response was evaluated by incubation of cells with serum-free medium containing 40 ng/mL of SDF-1α. Results showed an increased p-Akt/Akt ratio after 15 min, which was maintained at 1 h of incubation with SDF-1α, whereas the p-Erk/Erk ratio was increased after 15 min of incubation but then reduced at 1 h. These results match early findings on patient de-novo- and recurrent-derived GB cell lines [14,21]. On the other hand, p-Paxillin/Paxillin ratio was gradually increased at 15 min and 1 h of evaluation (Fig. 1B), suggesting a gradual formation of focal adhesions [22].

To assess the functional response of U87MG-CXCR4+ cells to SDF-1α, first, their ability to migrate across an 8-µm porous membrane was evaluated in Boyden chambers. On average, a 3-fold increase in the number of migrating cells was observed after 18 h of incubation for both 40 and 120 ng/mL of SDF-1α as compared to controls (Fig. 1C). Then, the ability of U87MG-CXCR4+ cells to leave a confined spot of agarose was measured by the length of the migrating cell halo surrounding the cell-laden agarose drop (Fig. 1D). On average a 2-fold increase in the migrated distance was observed for cells treated with 40 ng/mL of SDF-1α relative to controls.

To discriminate against the effect of proliferation, the latter assay was performed in the presence of the proliferation inhibitor Aphidicolin (ADC). Although a reduced cell hallo was observed as compared to non-ADC treated cells, approximately the same ratio of 2-fold increase in the migrated length for SDF-1α treated drops was maintained relative to controls. This result suggests that the chemoattractant effect of SDF-1α was independent of cell proliferation. Moreover, U87MG cells without receptor expression

ARTICLE IN PRESS
JID: ACTBIO [m5G;November 17, 2023;23:43]
R. Molina-Peña, N.H. Ferreira, C. Roy et al. Acta Biomaterialia xxx (xxxx) xxx

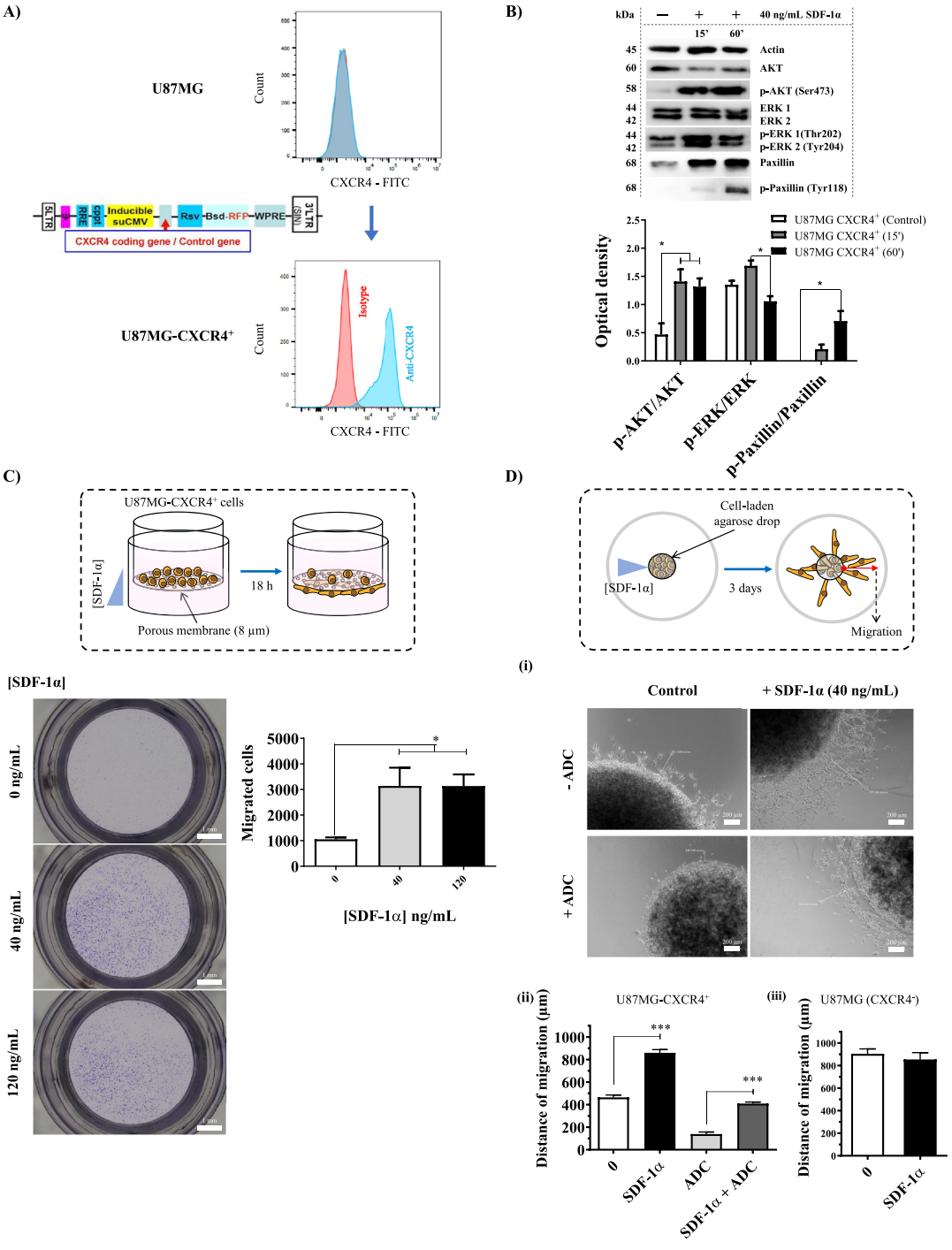

Fig. 1. Cellular model and its response to SDF-1α. A) Design of the cellular model: U87MG cells were transduced for constitutive expression of the CXCR4 receptor and red fluorescent protein (RFP). **B)** Molecular response: phosphorylation of Akt, Erk, and Paxillin shows the activation of the CXCR4/SDF-1α pathway in U87MG-CXCR4$^+$ cells in response to SDF-1α ($n = 3$). **C)** Transwell migration of U87MG-CXCR4$^+$ cells: after 18-h incubation of cells deposited on top of the porous membranes, migrating cells were more abundant in wells containing both 40 and 120 ng/mL of SDF-1α compared to controls ($n = 3$–4 replicates, with three repetitions). **D)** Agarose drop assay. (i)(ii) Migration of U87MG-CXCR4$^+$ from a confined spot of agarose was higher for cells treated with 40 ng/mL of SDF-1α as compared to controls. Inhibition of cell proliferation by the addition of Aphidicolin (+ADC) reduced the measured distance of migration but did not change the ratio of migration respective to controls. (iii) U87MG cells without expression of the CXCR4 receptor (U87MG-CXCR4$^-$) did not show a significative difference when treated with SDF-1α compared to control drops ($n = 3$ replicates, with two repetitions). Levels of significance are: $*$: $p < 0.05$, $**$: $p < 0.01$, $***$: $p < 0.001$.

ARTICLE IN PRESS
JID: ACTBIO [m5G;November 17, 2023;23:43]
R. Molina-Peña, N.H. Ferreira, C. Roy et al. Acta Biomaterialia xxx (xxxx) xxx

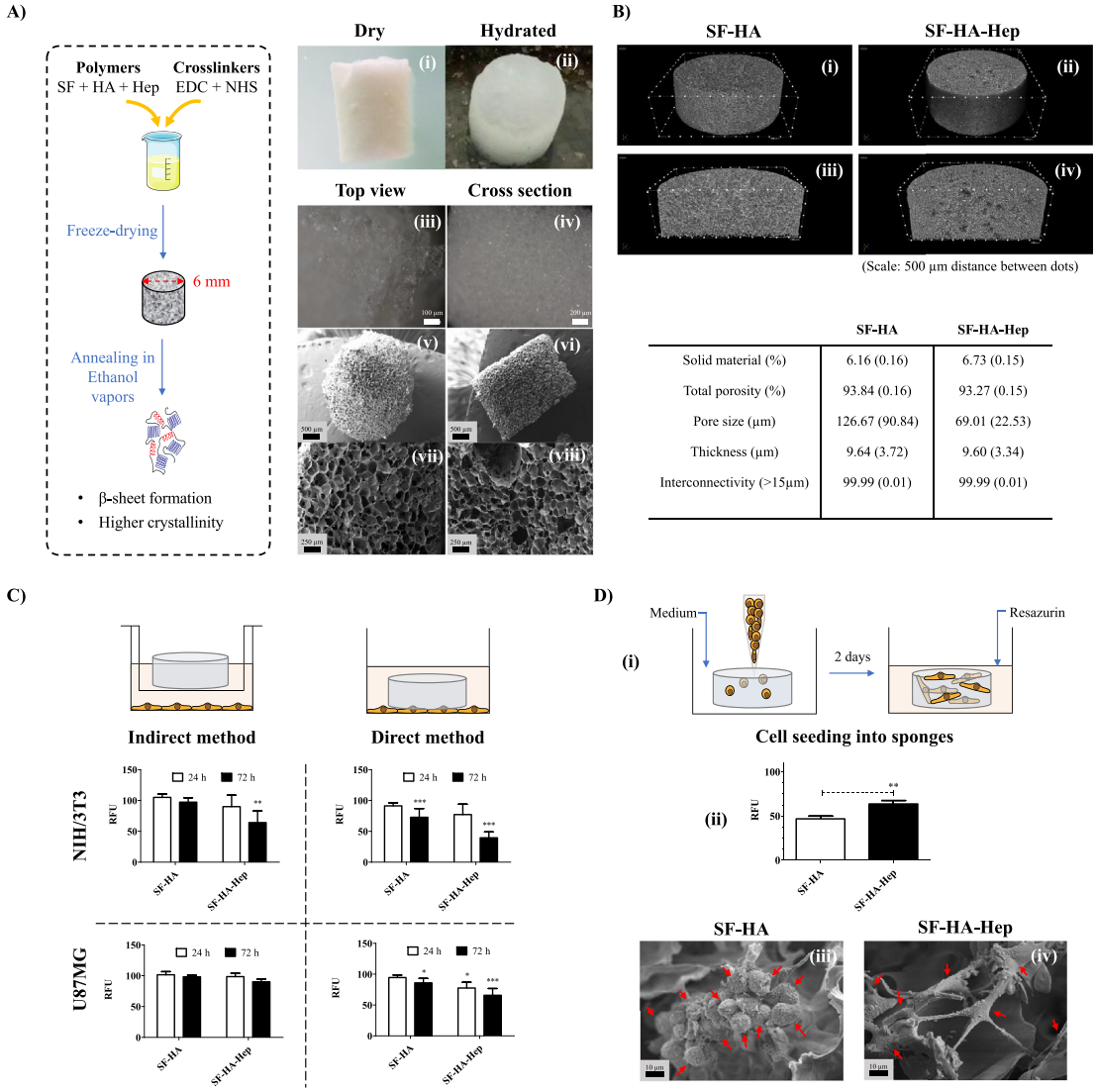

	SF-HA	SF-HA-Hep
Solid material (%)	6.16 (0.16)	6.73 (0.15)
Total porosity (%)	93.84 (0.16)	93.27 (0.15)
Pore size (µm)	126.67 (90.84)	69.01 (22.53)
Thickness (µm)	9.64 (3.72)	9.60 (3.34)
Interconnectivity (>15µm)	99.99 (0.01)	99.99 (0.01)

Fig. 2. Aerogel sponges, synthesis, structure, and cellular response. A) Synthesis and structure of the silk fibroin (SF), hyaluronic acid (HA), and heparin (Hep) sponges. Dry SF-HA-Hep sponges (i) rapidly absorb PBS and maintain their shape (ii). Stereomicroscopic images [(iii) and (iv)], and scanning electron micrographs [(v), (vi), (vii) and (viii)] showing the superficial and cross-sectional porous structure of SF-HA-Hep sponges. B) Microcomputed tomography (µCT) images for the evaluation of the porosity of sponges, the size and wall thickness of their pores, and the percentage of their connected pores with troughs > 15 µm. Depicted are representative µCT images of superficial [(i) and (ii)], and cross sections [(iii) and (iv)] of sponges without heparin (SF-HA) and with 1 % Heparin (SF-HA-Hep). C) The cell response of NIH/3T3 and U87MG cells after incubation with leachables from sponges (indirect method) and after direct contact of sponges with a cell monolayer (direct method) was evaluated using the resazurin assay. Depicted in the graphs are the percentages of the relative fluorescent units (RFU) respective to control wells that contained no scaffolds ($n = 3$ replicates, with three repetitions). D) The response of cells directly seeded into scaffolds. U87MG cells were directly deposited into scaffolds. After 2 days, the cellular response in SF-HA and SF-HA-Hep scaffolds was evaluated by incubation with media containing resazurin (i). The produced fluorescence in the media was normalized to control wells with cells seeded on plastic and is expressed as the percentages of RFU (ii) ($n = 5$ replicates, with 2 repetitions). U87MG cells (red arrows) seen under scanning electron microscopy 3 days after seeding in SF-HA sponges (iii) and SF-HA-Hep sponges (iv). Levels of significance are: ∗: $p < 0.05$, ∗∗: $p < 0.01$, ∗∗∗: $p < 0.001$.

(U87MG-CXCR4-) did not respond to SDF-1α, in terms of chemoattraction, as observed by the equal distances of migration for both non-treated and treated cells (Fig. 1D).

3.2. Sponges are highly porous, with interconnected pores and present shape memory

Aerogel sponges presented similar structure and physical appearance independently of heparin content (Fig. 2A). A porosity of ~ 93% was observed for both types of sponges SF-HA and SF-HA-Hep (1 % heparin). However, the pore size distribution was affected by the presence of heparin (Fig. 2B). A larger dispersion of pore sizes was observed in sponges without heparin 126.67 (90.84) µm, while sponges with heparin showed a narrower pore size distribution of on average 69.01 (22.53) µm. This reduction in the average pore size correlates to the higher content of total solids due to the addition of heparin.

ARTICLE IN PRESS
JID: ACTBIO [m5G;November 17, 2023;23:43]
R. Molina-Peña, N.H. Ferreira, C. Roy et al. Acta Biomaterialia xxx (xxxx) xxx

The thickness of the pore walls was consistent between all types of sponges. On average, a 9.6 µm wall thickness, which represents a ~9.6/69 = ~14 % of the diameter of a pore including walls for sponges containing heparin, reflects the spongy nature of the scaffolds. Thirdly, all sponges showed open, interconnected pores. This can be observed by tracking the maximal length of the path with troughs larger than 15 µm that can be followed without interruption in both orthogonal axes of the cross sections of sponges. Finally, all the sponges presented shape memory as observed by their capacity to regain their original shape upon an external force was applied, and then released, over the sponges' hydrated form (**Video S1**).

3.3. SF-HA-Hep sponges present mild to moderate cytotoxicity in vitro

The viability of NIH/3T3 mouse fibroblasts and U87MG glioblastoma cells was evaluated via the indirect and direct contact methods at 24 and 72 h incubation with SF-HA and SF-HA-Hep sponges (Fig. 2C). NIH/3T3 cells were chosen due their high sensitivity to chemical-induced toxicities (Xia et al., 2008). After 72 h of direct contact, SF-HA sponges significantly decreased the viability only for NIH/3T3 cells (71 ± 14 %). SF-HA-Hep sponges, however, presented mild cytotoxicity after 72 h of indirect contact (63 ± 19 % viability), and moderate cytotoxicity after 72 h of direct contact with NIH/3T3 cells (39 ± 9 % viability). Mild cytotoxicity was seen on U87MG cells after direct contact with SF-HA-Hep sponges at 24 (76 ± 9 % viability) and 72 h (64 ± 9 % viability).

Different washing techniques were tested aiming to eliminate traces of crosslinkers to improve the cytocompatibility of SF-HA-Hep1 % sponges. The first consisted in a 24-h wash in PBS under agitation, and the second in 5 × 30 s sonication cycles followed by agitation for 1 h in PBS. However, after 72-h of direct incubation of washed sponges with NIH/3T3 cells, no improvement was observed (**Fig. S1**). To determine whether EDC and NHS or Heparin were responsible for this cytotoxicity, two new sponges were produced. The first was composed of SF and HA crosslinked with the same concentration of crosslinkers as SF-HA-Hep (C_{EDC} = 15 mg/mL, C_{NHS} = 5.5 mg/mL) and was called SF-HA(+). The second was composed of SF, HA and Hep crosslinked with the same concentration of crosslinkers as SF-HA (C_{EDC} = 5 mg/mL, C_{NHS} = 1.8 mg/mL) and was called SF-HA-Hep(-). Because of the lower concentration of crosslinkers in the SF-HA-Hep(-) sponge, its shape was lost in the media.

Sponges with the same concentration of crosslinkers showed the same cytotoxicity, with a lower concentration of crosslinker leading to an increase in viability (**Fig. S1**). A tradeoff between stability and cytotoxicity had to be made, and therefore the original SF-HA-Hep1 % sponge was kept for further studies. Additional evaluation of its 24-h cytotoxicity by the direct contact method on cells resemblant to resident cells of the normal brain parenchyma was performed. In this case, murine BV-2 and human HMC3 microglial cells showed a viability of 64.4 and 82.3 %, respectively (**Fig. S2**).

3.4. The matrix of SF-HA-Hep sponges allowed a better U87MG GB cell response

To assess the response of cells in the scaffold's matrix, U87MG cells were directly deposited into the sponges as a cell suspension and cultured for 2 days. The cell response was evaluated by the resazurin assay (Fig. 2D-i). Results showed that SF-HA-Hep sponges allowed a better response compared to SF-HA sponges (Fig. 2D-ii). After 3 days of culture, SEM images showed cell aggregates in SF-HA sponges with no or little spreading of their soma (Fig. 2D-iii), whereas cells in SF-HA-Hep1 % sponges attached, spread, and formed large protrusions, suggesting a better interaction with GB cells (Fig. 2D-iv).

3.5. SDF-1α-loaded sponges directionally attract U87MG-CXCR4+ cells in vitro

To evaluate the chemoattractant capacity *in vitro*, sponges loaded with SDF-1α (10 and/or 100 pmol) were added in the right well, contiguous to a well containing U87MG-CXCR4+ cells in an agarose gel (Fig. 3). A well containing only PBS was also included to the left. After 3 days of culture with the addition of Aphidicolin as a proliferation inhibitor, results showed that there was a larger area of cells that migrated under the agarose towards the SDF-1α-loaded sponges as compared to controls located in the wells left to the cells. The migrated area depended on the dose of SDF-1α and the percentage of FBS used for cell seeding. Indeed, FBS was necessary for cells to adhere. This effect corresponded to a 3-fold increase of the invaded area for the 10 pmol loading and an 11.3-fold increase for the 100 pmol loading as compared to controls, in the case of 1 % FBS seeded cells (Fig. 3A-iii). A larger area in both directions, towards the sponges and controls, was observed when cells were seeded with medium containing 10 % FBS. However, increasing area ratios of 2.2-fold and 3-fold showed preferential migration of cells towards the sponges loaded with 10 and 100 pmol of SDF-1α, respectively (Fig. 3A-iii). To evaluate if the sponges alone were able to attract GB cells *in vitro*, the experiment was repeated with sponges containing only PBS compared to wells filled with only PBS (Fig. 3B-i). Results showed no significant difference in the areas of cell migration. When SDF-1α-loaded sponges were compared to sponges containing only PBS, only the former were able to show cell attraction (Fig. 3B-iii), showing a similar pattern than agarose gels where only PBS was used as a negative control (Fig. 3B-ii).

3.6. SDF-1α in SF-HA-Hep sponges enhanced their colonization in vitro

To assess the cell hosting capacity of sponges, single ~ 200-µm U87MG-CXCR4+ spheroids were cultured on top of SF-HA-Hep sponges that were loaded or not with 100 pmol of SDF-1α (Fig. 4B). Results showed that after 6 days of culture, there was a 1.4-fold larger area of glioma spheroids attachment on the surface of the sponges loaded with SDF-1α in relation to control sponges loaded with PBS (Fig. 4B-iii). In addition, a 1.6-fold larger infiltrated area and a 1.3-fold maximal infiltrated length in the sponges loaded with SDF-1α were observed compared to controls. However, cells remained within the contours of the glioma spheroids and did not spread out ubiquitously within the sponge in the 6-day time frame of the experiment.

***In vivo* studies**

3.7. Sponges are biocompatible and biodegradable in vivo

SF-HA and SF-HA-Hep sponges were implanted in the resection cavities of Fisher rats to evaluate the foreign body reaction in the brain as well as their biodegradability (Fig. 5). MRI images showed the presence of the sponges at D6 from implantation but completely degraded after 76 days as shown by the watery content in the cavities (Fig. 5A). SF-HA sponges were mostly absorbed after one week of implantation, which was confirmed by histological analysis (Fig. 5B). The cellular response was characteristic of a foreign body reaction with an acute inflammatory response at week one post-implantation, with the presence of polymorphonuclear (PMN) cells that was more important for SF-HA-Hep sponges compared to SF-HA sponges.

ARTICLE IN PRESS
JID: ACTBIO [m5G;November 17, 2023;23:43]
R. Molina-Peña, N.H. Ferreira, C. Roy et al. Acta Biomaterialia xxx (xxxx) xxx

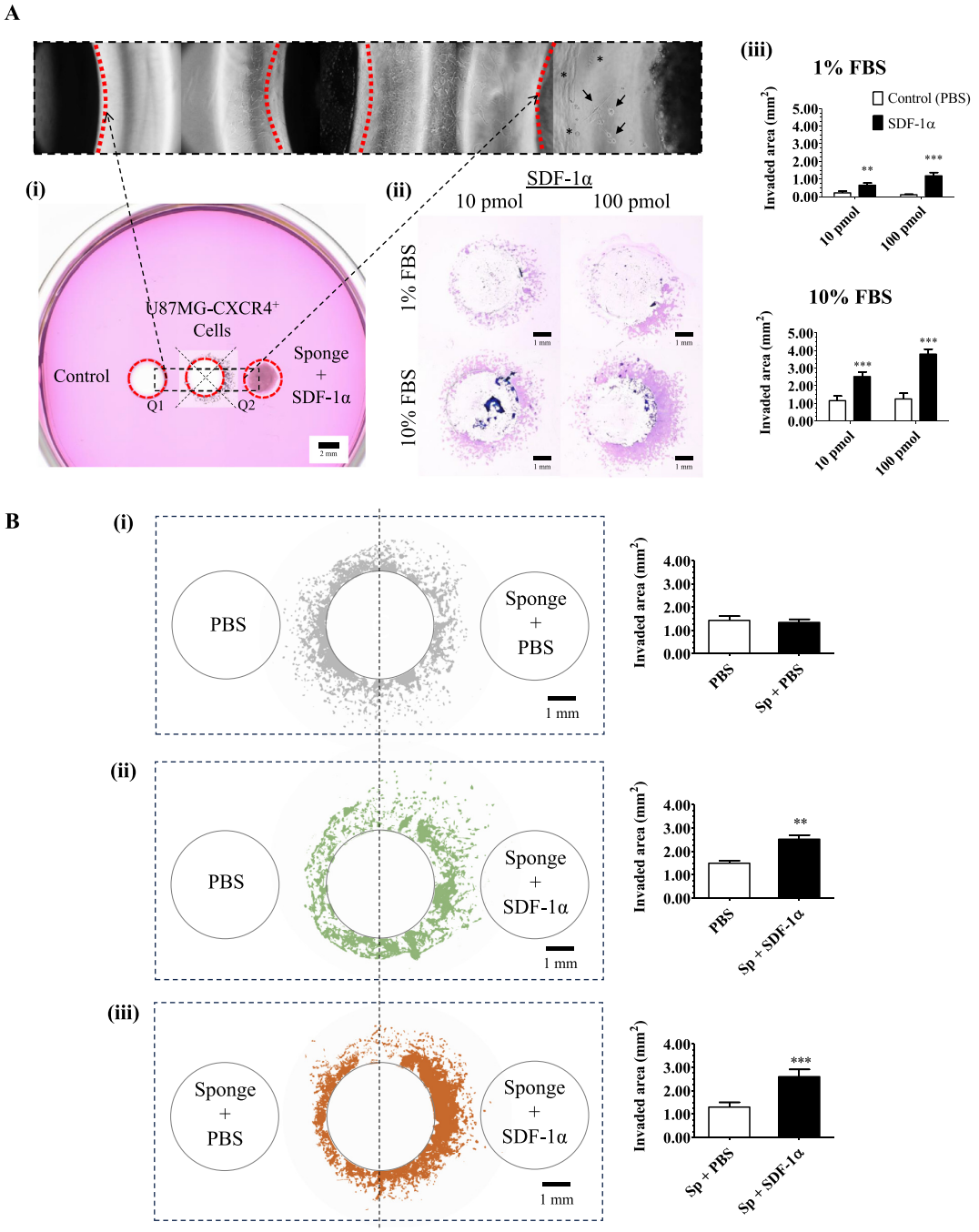

Fig. 3. *In vitro* cellular attraction. A) *In vitro* chemoattractant capacity of SDF-1α-loaded sponges: (i) agarose gel showing the disposition of cells (center well), sponges (right well), and control wells containing PBS (left well) to assess the induction of directional migration. Top panel: images (10x objective) of a representative experiment on day three after cell seeding. The assembled image shows the pattern of cell migration under the agarose gel. Some cells were detected near the sponges loaded with SDF-1α (100 pmol) (black arrows), with some cells undergoing cell death (asterisks). Of note is the "squeezed" shape of cells under the agarose, whereas cells that invade the right agarose-gel-free well regain a "spindle-like" morphology. (ii) Giemsa staining of cells that migrated under the agarose after three days of incubation. Cells were seeded in media containing either 1 % or 10 % FBS and 5 µg/mL of Aphidicolin as a proliferation inhibitor. (iii) Quantification of the cell area of the binary images in the most proximal quarters (Q) to either control wells (Q1) or sponges (Q2) as depicted in the representative image in the center well of (i) ($n = 3$ replicates, with three repetitions). B) The effect of the sponges alone containing only PBS (i) or of sponges loaded with 100 pmol of SDF-1α (ii), as compared to wells loaded with only PBS (left wells). (iii) The effect of sponges containing 100 pmol of SDF-1α vs. sponges loaded with only PBS. ($n = 3$ replicates, with three repetitions). Levels of significance are: $*$: $p < 0.05$, $**$: $p < 0.01$, $***$: $p < 0.001$.

ARTICLE IN PRESS
JID: ACTBIO [m5G;November 17, 2023;23:43]
R. Molina-Peña, N.H. Ferreira, C. Roy et al. Acta Biomaterialia xxx (xxxx) xxx

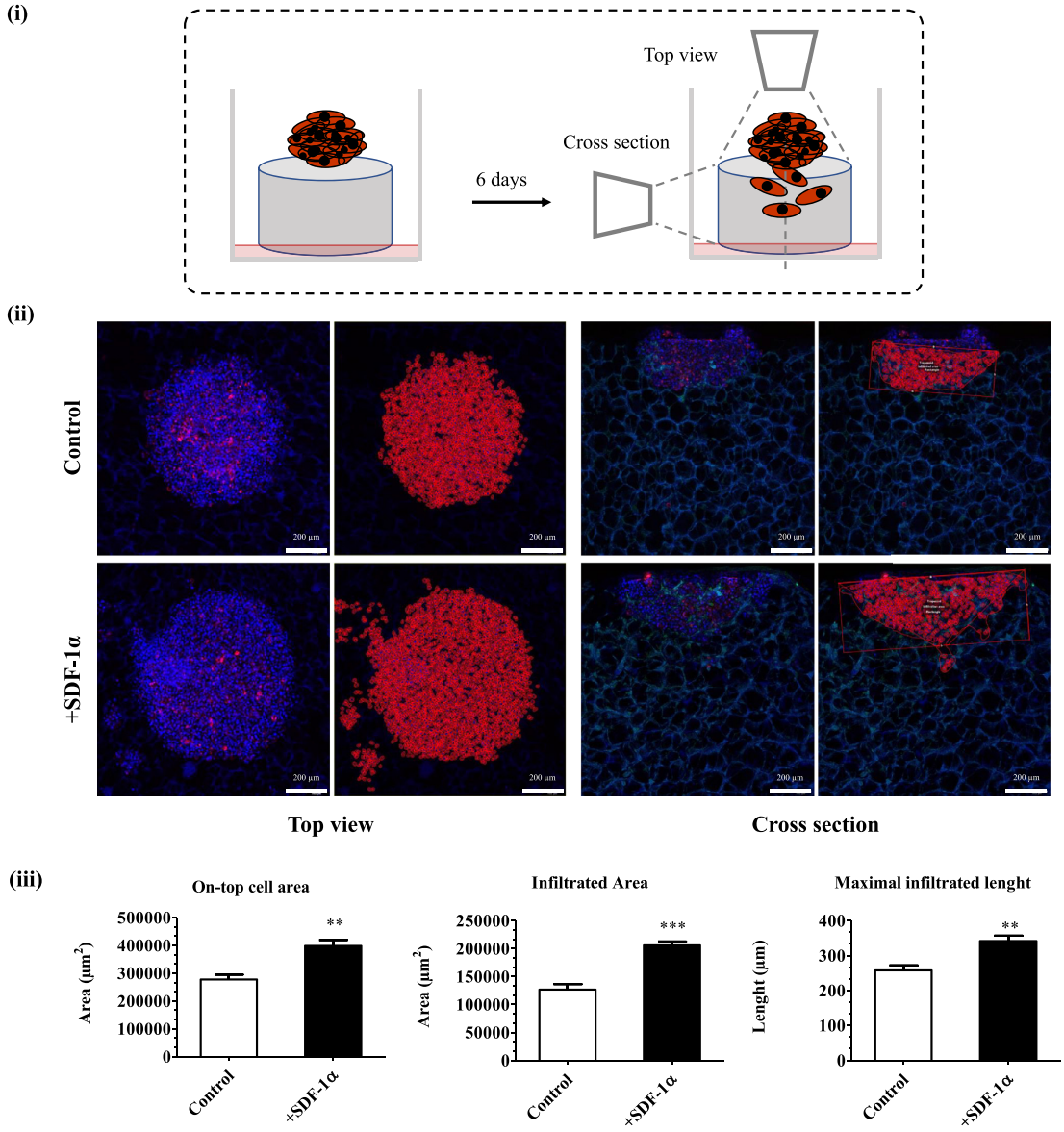

Fig. 4. *In vitro* cellular colonization of sponges. (i) Representation of the spheroid culture assay for the evaluation of the capacity of SF-HA-Hep sponges to be colonized by GB cells coming from GB spheroids. A single U87MG-CXCR4$^+$ gliomaspheroid was deposited on top of a SF-HA-Hep sponge loaded or not with SDF-1α. After 6 days of culture, the on-top cell area, the infiltrated cross-sectional area, and the maximal infiltrated length were imaged (ii) and quantified (iii) ($n = 3$; 2 experimental repetitions). Levels of significance are: $*$: $p < 0.05$, $**$: $p < 0.01$, $***$: $p < 0.001$.

The presence of multinucleated giant cells was rare, but the concomitant presence of macrophages and lymphocytes showing up from the initial stages after implantation demonstrates a process of debridement and chronic inflammation that was prolonged to up to the third month post-implantation. The formation of new blood vessels was more evident on day 7 of evaluation for all groups suggesting that the brain damage caused by the surgical resection and the consequent signals induced this neoangiogenic response. On the third month of evaluation, the acute inflammation was resolved, and the chronic inflammation lessened. Interestingly, only the cavities of rats implanted with sponges kept some lymphocytes in the long term compared to cavity controls alone. The presence of hemosiderin-laden macrophages and calcification zones (mineralization) showed the late stages of cicatrization. Overall, the residual cavities were porencephalic, i.e., filled with resident cerebral cells but with the loss of brain matter, however no collagen deposition nor fibrotic tissue was observed in the implantation zone, suggesting a good reabsorption of the sponges without the formation of a scar. As SF-HA sponges were mostly degraded within the first week of implantation, SF-HA-Hep sponges were chosen for further experiments.

ARTICLE IN PRESS
JID: ACTBIO [m5G;November 17, 2023;23:43]
R. Molina-Peña, N.H. Ferreira, C. Roy et al. Acta Biomaterialia xxx (xxxx) xxx

A)

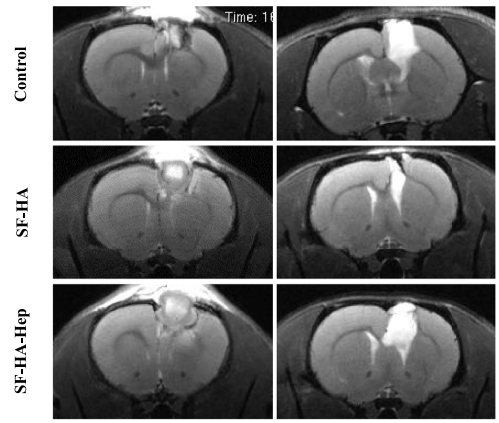

B)

Day 7			Day 118			[- -/+ + ++ +++]
Cavity Control	SF-HA	SF-HA-Hep	Cavity Control	SF-HA	SF-HA-Hep	
-	-	-/+	-	-	-	Multinucleated Giant cells
+	-	++	-	-	-	Acute inflammatory cells (PMN cells)
-	-	++	-	-	-	Necrosis
++	++	+	-	+	+	Chronic inflammatory cells
++	+	+	-	-	-	Neoangiogenesis
-	-	-	-	-	-	Haemorrhage
-/+	-	-	+	++	+	Hemosiderin
+	+	-	-/+	+	+	Mineralization

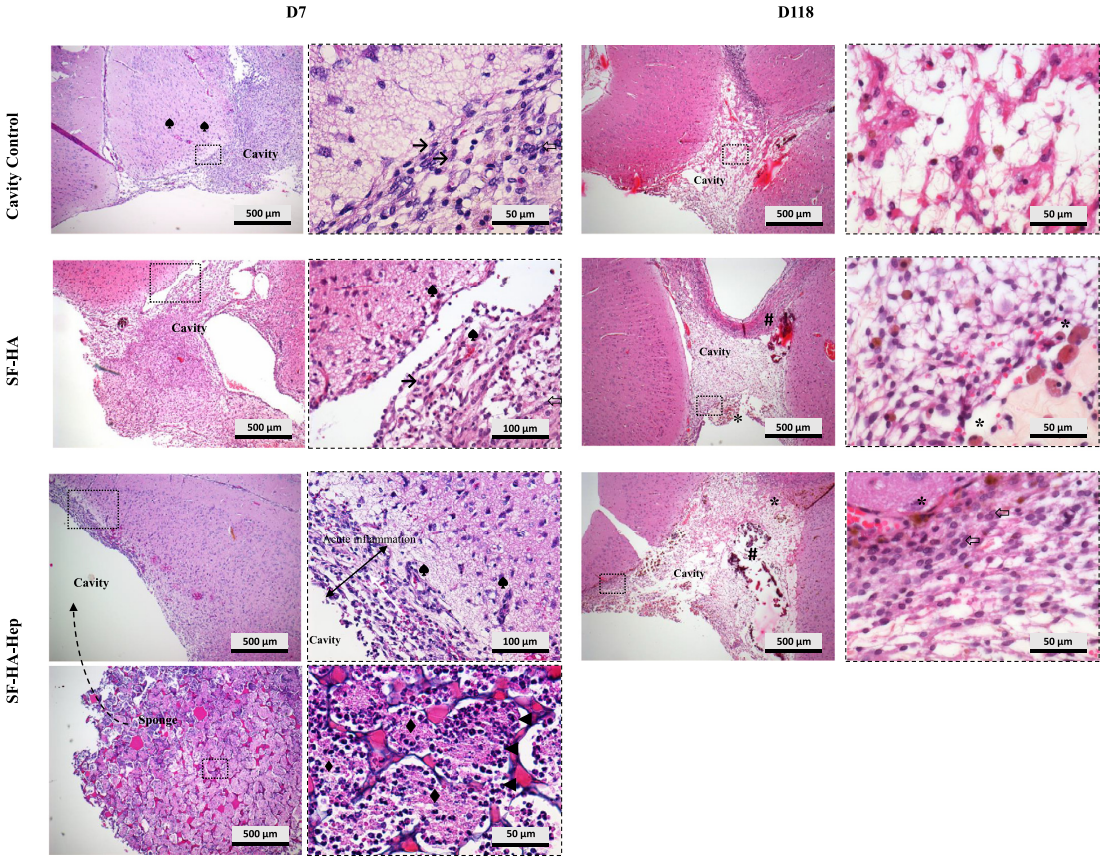

Fig. 5. *In vivo* biocompatibility and biodegradability of sponges. A) MRI scans of brains with implanted sponges. B) Characterization of the *in vivo* cellular response to implanted sponges in the rat brain cortex. Histological (H&E) staining (nuclei: blue/purple; cytoplasm: pink). SF-HA sponges were completely degraded after 7 days, while SF-HA-Hep sponges were still present. A representative image is shown of a SF-HA-Hep sponge that came out of the cavity during the slicing process (bottom left panel). Left panels: H&E representative images 7 days post-implantation showed an acute inflammatory response in rats implanted with SF-HA-Hep sponges. The acute response was less marked in the other groups. There was a local chronic inflammatory response with the presence of lymphocytes that were more frequent in the cavity controls and in SF-HA implanted rats. At this 1-week time point, the formation of blood vessels (neoangiogenesis) was observed in all groups. Right panels: After 3 months, the acute inflammation was resolved, and the chronic inflammation lessened in the control cavity and SF-HA groups and remained in the SF-HA-Hep group. At this 3-month time point, mineralization and hemosiderin deposition were observed in all groups. Symbols are as follows: infiltrating polymorphonuclear (PMN) cells (◂), Necrosis (♦), macrophages (→), lymphocytes (⇦), neoangiogenesis (♠), hemosiderin (*), mineralization (#). Scores are as follows: (−) = nil, (-/+) = rare, (+) = mild, (++) = moderate, and (+++) = marked. Interrupted-line bordered images are magnifications of the smaller squares indicated in their respective left images.

ARTICLE IN PRESS
JID: ACTBIO [m5G;November 17, 2023;23:43]

3.8. SDF-1α was retained in SF-HA-Hep sponges in vivo

To evaluate the *in vivo* biodistribution of SDF-1α in the brain after the sponge's implantation, SF-HA-Hep sponges were loaded with 150 ng of AF-647 tagged SDF-1α and implanted in the resection cavities of Fisher rats. Results showed that 7 days post-implantation, AF647-SDF-1α was detected inside the sponges, and in the margins of the resection cavity as bulges detaching from the edges of the sponges that were undergoing degradation; but was not detected in the brain tissues beyond the resection limits (Fig. 6A). Interestingly, AF647-SDF-1α was distributed as droplets of about 10–100 µm diameter which corresponded to the internal structures observed in the sponges (Fig. 6A-third panel). Endogenous SDF-1α was stained indirectly with an antibody coupled with FITC and was distinguished from the exogenous SDF-1α that was loaded into the sponges, as the latter was not recognized by the primary antibody (Fig. 6B). Endogenous SDF-1α was found only scarcely expressed in small blood vessels surrounding the resection cavity. Interestingly, more nuclei were observed inside the sponges containing SDF-1α compared to the brain tissue. This correlates with the colonization of sponges by PMN cells as observed in Fig.5B.

3.9. CXCR4+ GB cells interacted with SDF-1α loaded sponges 7 days post-implantation

To assess the GB cell attractant capacity of sponges *in vivo*, two orthotopic models were tested in nude rats. In the first model, 5×10^3 U87MG-CXCR4+ cells were injected into the striatum. After 10 days of tumor development, a ~2-mm depth resection cavity was performed in the same vertical axis of cell injection, and SF-HA-Hep sponges were implanted loaded or not with SDF-1α. After 7 days, animals were euthanized, and brains were collected and analyzed by IHC-IF. Cell tracking by RFP, CXCR4 and Ki67 expression revealed colonization in only one implant loaded with SDF-1α (out of 3 animals) (**Fig. S3**). Although this experiment showed that SDF-1α-loaded sponges can be colonized by tumor cells after resection, the main complication found here was the lack of a reproducible resection. For instance, the tumor was completely removed in some cases and the distances between the tumors and scaffolds were not reproducible. To overcome this limitation, the second experimental set-up consisted in placing the implants and cells distanced from ~1 mm in the horizontal plane of the frontal brain cortex at the same time. First, SF-HA-Hep sponges with PBS or SDF-1α were implanted in the frontal cortex, followed by stereotactic injection of 2.5×10^4 U87MG-CXCR4+ cells 1 mm backward from the cavity edges (Fig. 7). Control rats were subjected to the same surgical and tumor cell injection procedures in the absence of sponges. After euthanasia, 7 days post-implantation, the brains were removed, snap-frozen and analyzed by IHC-IF. We observed a modification in the behavior of cells near the sponges compared to the cavity control alone. Cells constituting the anterior front of the tumor were able to interact with the surface of the sponges with a significant portion of CXCR4+ cells detaching from the main tumor mass towards the cavity containing the SDF-1α-loaded sponges or PBS-loaded sponges as compared to and cavity controls (Fig. 7). However, at this point, the interaction of cells with sponges was only observed at the intermediate zone between the tumor leading edge and the edge of the sponges facing it.

3.10. SF-HA-Hep sponges shaped the tumors and allowed their localized development

To assess the effect of sponges in the long term, the same orthotopic model used to evaluate the colonization of sponges was implemented, but this time 1×10^3 U87MG-CXCR4+ cells were injected. Animals were followed up until the defined endpoint, and tumor evolution was followed by MRI every week. All animals recovered within 2 h after the procedure and did not show any signs of distress. Animals behaved normally and started to present symptoms from week 4 after surgery. Results showed that the survival of rats did not improve by sponge implantation in either case loaded or not with SDF-1α (Fig. 8A) compared to cavity controls. We observed that SDF-1α tended to reduce the median of survival to 27.5 days as compared to controls (31 days), though non-significant statistically (the fact that there is one animal from the SDF-1α group crossing the other survival curves makes this non-significant). This effect correlates with the average size of the tumor that tends to be larger (as a tendency as no statistical difference was observed) for rats implanted with SDF-1α-loaded sponges as shown in Fig. 8A **right panel**. Therefore, SDF-1α contained within the sponges may be exerting an effect on tumor evolution favoring its development. This result can be explained by the fact that no killing signal was included in the study. However, we observed an effect of the sponges on the tumor shape and localization. Interestingly, the shape of the tumors fitted better to the projections' shape of the cross sections of the sponges in the three axes imaged and they were more rounded compared to the tumors where sponges were not present (Fig. 8B). Indeed, the reduced tumoral areas outside the projection of sponges, suggest that the tumor is better confined in the volume behold by the sponge's structure. This result highlights the relevance of the sponge implantation as a strategy to confine the tumor in a controllable area and confer a spherical shape that can facilitate their further treatment.

4. Discussion

The main problem facing glioblastoma therapy is the infiltrative nature of GB cells remaining after standard treatment. cDNA expression analysis revealed that CXCR4 is overexpressed in 57 % of primary glioblastoma (GB) tumors and in 88 % of GB cell lines that were analyzed [23]. CXCR4 expression is considered a prognostic marker in gliomas. Patients with CXCR4-positive GB had a reduced postoperative life expectancy [24]. CXCR4 was expressed in more than 50 % of astrocytomas and 100 % activated form (phosphorylated) in grades 2–4 astrocytomas and 76 % in grade 1 astrocytomas [25]. Previously, it was shown that the CXCR4 receptor confers to GB cells increased infiltrative capacity into the brain parenchyma [18], and that the CXCR4/SDF-1α axis is related to the chemotaxis attraction of GB cells *in vitro* [14,26] and of glioma stem cells (GSCs) to the tumor vasculature [27]. Here, a rupture concept was investigated. The strategy was to exploit the CXCR4/SDF-1α axis to attract GB cells to a confining biodeposit consisting of a SF-HA-Hep sponge. This study aimed to investigate the preclinical feasibility and benefit of a new interventional approach using SDF-1α-loaded SF-HA-Hep aerogel sponges as implantable scaffolds into the brain resection cavity. Fischer rats were used to assess the *in vivo* biocompatibility of scaffolds to observe the complete foreign body reaction. However, to evaluate the *in vivo* performance of sponges, athymic nude rats were chosen because of the human cellular model that was used. The sponges are biodegradable. They were well tolerated for more than 3 months and reabsorbed after implantation into rat brains. The disappearance of the sponges is attributed to the inherent biodegradability of the scaffolds, primarily through hydrolysis and solubilization of the components. *In vitro* studies reported 85 % degradation within 3 weeks [17], under conditions mimicking *in vivo* enzyme presence. This gradual degradation can facilitate temporary accommodation of cancer cells within the cavity, minimizing the risk of long-term adverse reactions or the need for surgical removal. Their shape memory permitted fitting into the resection

ARTICLE IN PRESS
JID: ACTBIO [m5G;November 17, 2023;23:43]
R. Molina-Peña, N.H. Ferreira, C. Roy et al. Acta Biomaterialia xxx (xxxx) xxx

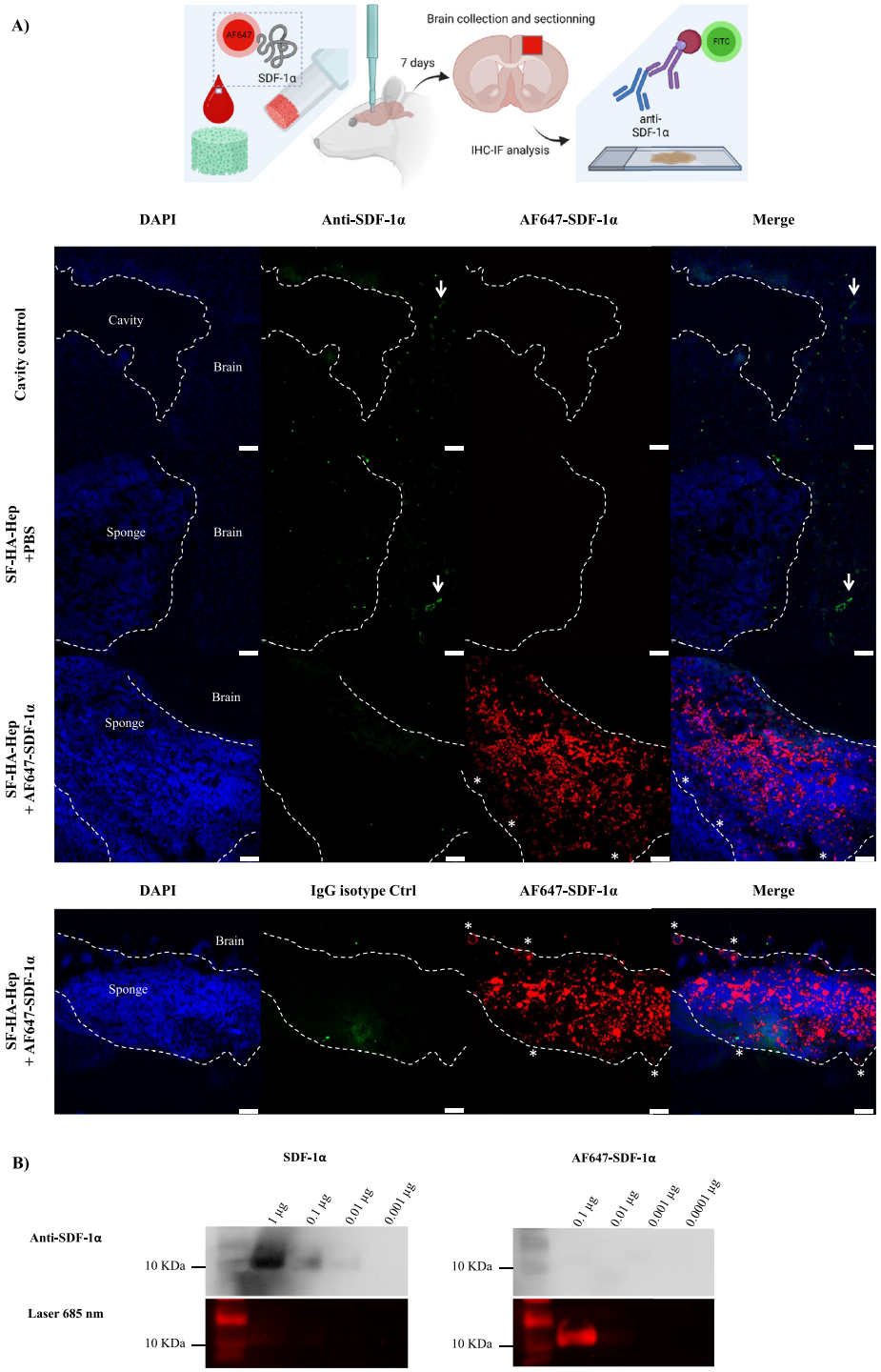

Fig. 6. *In vivo* distribution of SDF-1α. A) Implantation of SF-HA-Hep sponges containing SDF-1α tagged with AF-647, in the resection cavity in the frontal cortex of Fisher rats (Created with BioRender.com). Control sponges contained only PBS. Seven days after implantation, brains were collected and sliced. AF-647-SDF-1α was localized within the structure of the sponge (red channel, third column). Degradation of sponges was observed at their edges in contact with the borders of the resection cavity, and the detaching bulges containing AF-647-SDF-1α were located adjacent to the brain parenchyma (white asterisks). Further labeling with an anti-SDF-1α antibody and revelation by the Strep-FITC amplification method did not show the presence of AF-647-SDF-1α as the latter was not recognized by the anti-SDF-1α, see (B). The presence of small blood vessels positive for the anti-SDF-1α antibody was rarely observed in the margins of the resection (white arrows, second column, green channel). Scale bar = 100 µm. B) WB analysis for the immuno-detection of SDF-1α and AF-647-SDF-1α. The same anti-SDF-1α antibody recognized only the non-tagged SDF-1α but not the AF-647 tagged SDF-1α, which is however revealed by excitation with an IR laser.

ARTICLE IN PRESS
JID: ACTBIO [m5G;November 17, 2023;23:43]
R. Molina-Peña, N.H. Ferreira, C. Roy et al. Acta Biomaterialia xxx (xxxx) xxx

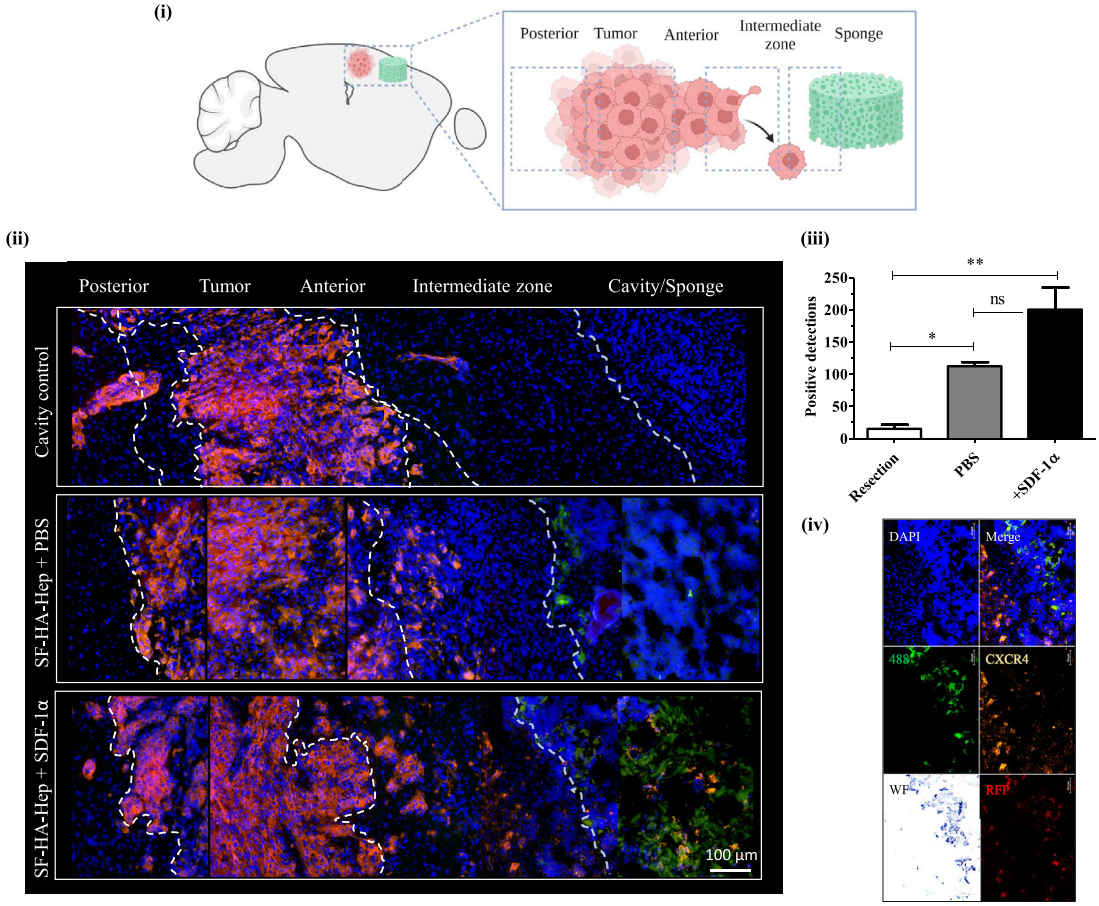

Fig. 7. *In vivo* response of GB cells to implantation of sponges. A model of the resection cavity in the brain cortex was developed in nude rats. U87MG-CXCR4^{+} cells were injected near the sponges loaded or not with SDF-1α, or near the created cavity alone (i) (Created with BioRender.com). After seven days following implantation, cell detection was performed in cryosections by RFP expression and CXCR4 immunolabeling (yellow) (ii). Depicted are the composite images resulting from the merging of the different channels. An increased cell number of dissociated cells lying in the anterior/intermediate zone between the tumor and the sponges in rats bearing SF-HA-Hep sponges loaded with SDF-1α (SF-HA-Hep + SDF-1α) or sponges alone (SF-HA-Hep + PBS) was observed as compared to rats with the resection cavity alone with no implanted sponge (iii) ($n = 3$; $*$: $p < 0.05$, $**$: $p < 0.01$). The right panel shows an example of images from single channels as follows: WF (white field), RFP (red fluorescent protein), CXCR4 (yellow), DAPI (cell nuclei), 488 (green autofluorescence of sponges) (iv).

cavities and their highly interconnected pores supported cell infiltration and growth.

To assess the *in vivo* sponges' bioperformence, a cavity resection model was developed. Due to the difficulty of reproducibility of resected tumors by using a punch biopsy pen and an aspiration method, the developed rat model here shows that concomitant placement of implants and GB cells is feasible to investigate the functionality of interventional scaffolds in a model of the residual disease were infiltrating cells are situated adjacent to the cavities in the brain parenchyma. This strategy might be used to assess different scenarios including the distance between cells and scaffolds, and the number of injected cells. Here, by 1-mm distant placement of GB cells relative to resected zones, it was revealed that GB cells interacted with the sponges 7 days post-implantation. Serving as a chemokine reservoir in the tissue, SDF-1α remained within the sponges after 7 days of implantation.

In vitro, sponges loaded with SDF-1α directionally attracted U87MG-CXCR4+ GB cells and enhanced cell colonization within the scaffold. The function of SDF-1α is observed in the under-agarose assay *in vitro* from a distance that is 2-fold larger than the sponge implanted *in vivo*. The sponges alone did not show a difference relative to only wells containing PBS (Fig. 3B-i). And sponges loaded with SDF-1α attracted cells vs sponges alone (Fig. 3B-iii). This means that the signaling provided by the released SDF-1α is necessary to attract GB cells distantly placed in a semi-confined site. In this case, the agarose gel provides a layer between the plastic and the gel that cells can invade. Moreover, the *in vitro* assay using tumor cells grown as spheroids demonstrated the importance of SDF-1α for improving the sponge colonization. *In vivo*, cells were injected approximately 1 mm away from sponges. This nearer placement of sponges as compared to the *in vitro* experiment, can influence the interaction of cells growing from the main tumor as observed in the intermediate zones and edges of the sponges facing the tumors in Fig. 7. Interestingly, SF-HA-Hep sponges were able to shape and locate the tumors inside the cavities. The effect of shaping of the tumor by sponges alone (Fig. 8D) can be explained by the attraction of cells by mechanisms yet undetermined and independent from SDF-1α. *In vivo*, on day 7 after cell injection, there was no significant difference between the positive detections of cells in the intermediate zone located be-

ARTICLE IN PRESS
JID: ACTBIO [m5G;November 17, 2023;23:43]
R. Molina-Peña, N.H. Ferreira, C. Roy et al. Acta Biomaterialia xxx (xxxx) xxx

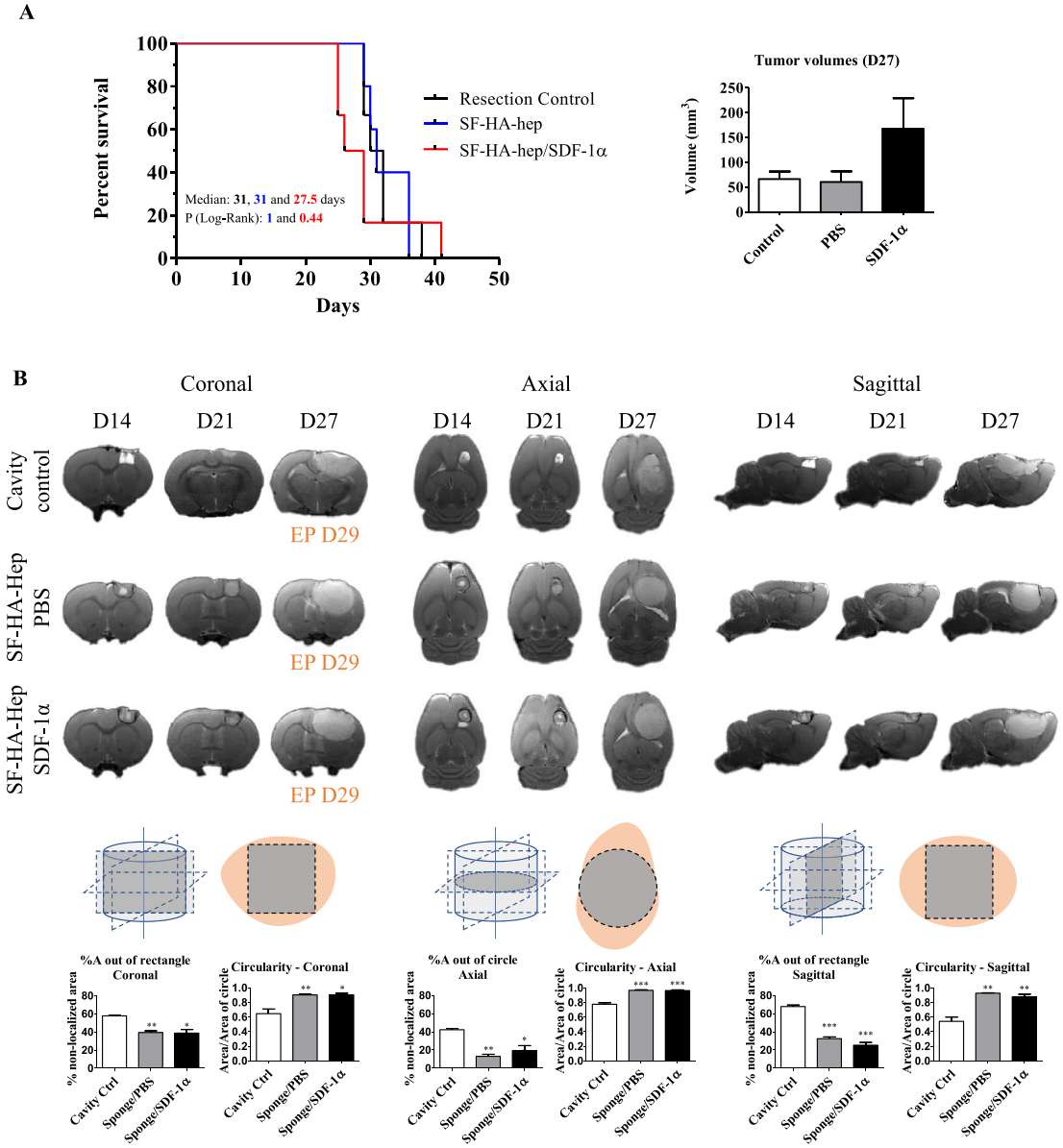

Fig. 8. Evolution of tumor growth and survival analysis of implanted rats vs cavity controls. A) Survival Analysis. Although no significant statistical difference is observed between groups, the calculated smaller median survival (27.5 d) for sponges loaded with SDF-1α correlates with a higher average tumor volume on day 27 (as a tendency as no statistical difference is observed, $P = 0.059$). **B)** The shape of the tumor is affected by the presence or absence of sponges. The area of the tumor out of the enclosed and shaped cross-sectional area projected from the sponge is depicted in the lower panels. The circularity is calculated as the area of the tumor cross-section divided by the area of the adjusted circle according to the tumor perimeter ($4\pi A/P^2$). Three slices were analyzed for each projection plane for each animal ($n = 3$ animals per group). Levels of significance are: $*$: $p < 0.05$, $**$: $p < 0.01$, $***$: $p < 0.001$.

tween the tumor and sponges loaded with SDF-1α or sponges alone (Fig. 7). This can be linked to the effect of sponges loaded or not with SDF-1α on tumor shaping. The MRI images provided on Fig. 8B corresponding to day 27 suggest a displacement of the tumor towards the cavities that contained sponges. Results did not reflect a survival improvement, but this was in part expected as no killing signal was introduced. The tumor-shaping and -sitting effect occurred regardless of SDF-1α loading, suggesting it is associated with the properties of the SF-HA-Hep sponges.

4.1. SF-HA-Hep sponges as a tool for intervention: instructing the tumor ecosystem

The dynamic crosstalk between cancer cells and their environment might be interfered to instruct the GB ecosystem and potentially improve treatment. Cancer cell behavior and fate are strongly associated with non-cellular components, such as the ECM. Thus, the unique composition and architecture of the brain ECM can offer opportunities, being implemented as a target and as an instru-

ARTICLE IN PRESS
JID: ACTBIO [m5G;November 17, 2023;23:43]

ment for various therapeutic strategies [28–30]. GB cell morphology, migration and proliferation can be influenced by the composition of the biomaterial [31–33]. And parameters such as porosity, permeability and the stiffness of the scaffold can be crucial in terms of cell ingrowth, cell growth, migration, and scaffold colonization [34].

Previously, the physicochemical and mechanical similarities between the brain ECM and SF-HA-Hep sponges were described [17]. Here, we demonstrated that the multiple interconnected 69µm-pore-channel networks of SF-HA-Hep sponges played a significant role in GB cells' infiltration and spreading by providing adequate internal space and support for cell growth. Pore size is a fundamental factor implicated in the invasion and migration of GB cells [35], which occur after matrix degradation when the cross-sectional area of the interfibrillar pore is less than 7 μm^2 [36]. Above this value, cells can undergo physical deformations to squeeze through the pores of the brain ECM and migrate [37]. The spatial arrangement of the matrix fibers near primary tumor sites can influence the motility of tumor cells, and aligned fibers offer tracks that are more conducive to migration [38,39]. With this regard, Jain et al. (2014) demonstrated that aligned fibers can be used as guidance elements to direct brain resident GB cells toward an extracortical zone. In contrast, SF-HA-Hep sponges presented here did not feature any structural alignment [7]. Other works using non-aligned porous scaffolds made use of an attracting signaling strategy, trying to imitate metastatic niches. For example, De la Fuente et al. (2015) used extracellular vesicles to demonstrate the luring capacity of ovarian cancer cells when loaded into the scaffold's matrix [6]. Moreover, Azarin et al. (2015) showed that the implantation of PLG microporous scaffolds in mice mammary fat pads induced the recruitment of immune cells by cytokines including CCL22, that in turn induced the recruitment of metastatic breast cancer cells [40]. In the context of glioblastoma, Gliadel wafers used for carmustine delivery are FDA approved, but no other porous scaffolds like sponges have been used for the trapping of GB cells. This paper hence describes a new system. Porous SF-HA-Hep sponges offer the possibility of covering a larger space and taking advantage of the resection cavity after implantation. These sponges are biodegradable, so a second surgery to remove the device would not be necessary.

In the present work, we explored the effect of loading a chemoattractant into SF-HA-Hep sponges and found that SDF-1α -loaded sponges were able to attract GB cells *in vitro*. *In vivo*, clusters of tumor cells and individual cells were observed infiltrating the intermediate zone between the anterior tumor border and the sponges, which was promoted by the SDF-1α load compared to the cavity controls. However, we also found that tumor shaping and localization were favored to fit the resection cavities containing implants, and this occurred independently of SDF-1α loading. Interestingly, the shape of the tumors matched the shape of the cross-sectional projections of the sponges in the three MRI axes imaged, being more rounded when compared to the tumors where sponges were absent. This suggests that the implants exerted an attraction force from the site of cell injection toward the resection cavity. Indeed, the sponge structure was not seen anymore during the 4th week of MRI imaging. This can be explained by 1) the total colonization of the sponges by U87MG-CXCR4+ cells during the experiment, hindering the sponges' structure, 2) the complete sponge's degradation favored by the tumoral environment, and 3) the ejection of sponges by the tumor's center of mass displacement and further elimination of the sponges.

Despite not knowing the precise mechanism, the attraction of GB cells seen at the sponge-parenchyma intermediate zone after 7 days of implantation, even in the absence of SDF-1α, suggests that sponges alone may modulate GB cell behavior. Cancer cells can be guided towards laminin and hyaluronan molecules in the ECM by internal integrins and CD44 receptors respectively, and via haptotaxis by chemokines and growth factors immobilized along tracks [41,42]. In line with this, HA may have contributed to tumor cell presence inside SF-HA-Hep sponges, via CD44/HA axis [43], as the majority of U87MG-CXCR4+ cells expressed the CD44 receptor (**Fig. S4**). In addition, *in vitro* U87MG cells responded better when directly seeded into SF-HA-Hep sponges as compared to SF-HA sponges (Fig. 2D), highlighting the effect of the matrix structure and composition. Heparin and other glycosaminoglycans (GAGs) can regulate glioma cell adhesion to ECM proteins leading to cell proliferation or cell migration, according to the ECM composition, thus modulating tumor cell properties [44]. Heparin can be safely used when it is modified or covalently incorporated into scaffolds for biomedical applications [45–47] offering cell contact sites by the recruitment of molecules promoting cell adhesion. Therefore, the enhanced *in-vitro* cell response observed here could be explained by the trapping of factors from the media containing FBS such as fibronectin and vitronectin, both of which harbor heparin binding sites [48,49].

Furthermore, the strong heparin-chemokine complex was responsible for SDF-1α retention in SF-HA-Hep sponges [17,50]. As this chemokine can be rapidly turned over [51] and inactivated by nitration *in vivo* [52], the SDF-1α immobilization in the sponges combined with their slow degradation rate can offer an advantage as a reservoir reinforcing its role in haptotaxis versus chemotaxis, here pivotal for directional cell migration and colonization of the sponge. SDF-1α linked to heparin-binding domains had similar activity to the free chemokine [53]. Here, fragments of SF-HA-Hep sponges as AF647-SDF-1α bulges were seen in the edges of the brain cavities containing a high number of cell nuclei. These bulges might have induced a haptotaxis response [54].

The recruitment of immune cells in the site of scaffold implantation has been described as having a role in the creation of premetastatic niches for the capture of breast cancer cells. Leukocytes can be recruited into scaffolds reorganizing as a site of premetastasis in a murine breast cancer model. This is due in part to the secretion of soluble factors from recruited Gr1hiCD11b+ cells that can attract cancer cells [40,55]. SDF-1α is a cytokine that can be secreted by immune cells including neutrophils [56]. Despite PMN cells were recruited into the sponges, endogenous SDF-1α in the site of implantation was not detected in both implanted and mock surgery resected rats. Besides, other soluble factors can attract cancer cells which do not exclude the possible effect of implantation of SF-HA-Hep sponges alone as a premetastatic niche. Further experiments need to consider the distant placement of sponges ($>$ 1 mm) from the primary tumor site to assess their premetastatic potential.

Alternatively, the attraction driving force might have been physical. Cells were injected after scaffold implantation, so the sponge was most probably not exerting any absorption of liquid, as they were already equilibrated with the liquids inside the cavity. By exclusion, this effect may be related to sponge stiffness, as stiffness gradients can induce cell migration [57,58]. Considering this, the young modulus of SF-HA-Hep sponges (13 KPa) [17] is larger than that of the human brain (1–10 KPa) [59,60], but may better suit the tumor microenvironment, where the altered ECM presents enhanced matrix stiffness (11.4 to 33.1 KPa) [61]. Thus, SF-HA-Hep sponges may confer to cells a suitable substrate with stronger mechanical forces than the brain ECM, allowing them to move upgradient, in a durotaxis response.

The reverse effect of the ECM on cancer cells and the progression of tumors remains to be investigated [28,29,62,63]. Here, we showed that alteration of the tumor ecosystem can be done by the implantation of SF-HA-Hep sponges in the resection cavity. The exact underlying mechanisms of how SF-HA-Hep sponges helped to the resection cavity siting and shaping of the tumors remain to

ARTICLE IN PRESS
JID: ACTBIO [m5G;November 17, 2023;23:43]
R. Molina-Peña, N.H. Ferreira, C. Roy et al. Acta Biomaterialia xxx (xxxx) xxx

be completely determined. Further studies including scaffold-to-tumor distance variation, the measuring of mechano-sensing markers and the identification of immune cells can give more clarification in this matter. Overall, the biological and mechanical properties of SF-HA-Hep sponges may allow the concentration of remaining GB cells in a controllable area for further elimination.

4.2. Limits and perspectives

Incorporating dynamic biological information into scaffolds to match the *in vivo* environment of the native tissue has gained great appreciation [64]. However, this design can be a colossal challenge considering the complexity of the aberrant cues and signaling of cancer. The increasing understanding of the pre-metastatic niches and their roles in welcoming metastatic dissemination [65–67] has inspired scientists to create different strategies to trap migrating cancer cells [6,68–70]. In our exploration of SDF-1α as a bait to attract GB cells, we have encountered several challenges.

4.2.1. Release and control of SDF-1α into the brain parenchyma

We were previously able to observe the capacity of SF-HA-Hep sponges to integrate SDF-1α into their structure according to the loading methods used by simple dropping [17]. The distribution profile of the protein inside the sponge was visualized using SDF-1α coupled to AlexaFluor 647 thus demonstrating a radial concentration gradient from the center (where the drop was deposited) toward the edges of the sponges [17]. The ability of heparin to bind SDF-1α in polymer matrices is a proven fact thus facilitating the loading of chemokine [71,72]. Here, the SDF-1α retention capacity displayed by the SF-HA-Hep sponge correlates with the presence of AF 647-SDF-1α within the sponges in the brain parenchyma on day 7 of evaluation.

For strategies envisaging to attract cancer cells from a distant site, chemoattraction is an attractive strategy. The first challenge is related to the design of the scaffold to provide a releasing signal so that it creates a gradient, perdures and gets to the site of cancer cell residence. SF-HA-Hep sponges showed strong retention of SDF-1α. The initial burst of SDF-1α that occurred during the first day was about 4 % of the total load, quickly reaching a 5 % cumulative release plateau thereafter [17]. *In vitro*, this initial burst of SDF-1α was enough to chemoattract U87MG-CXCR4+ cells. Indeed, the calculated concentration in 30 µL of liquid within the well of the agarose gel (1070 ng/mL) was sufficient to create a gradient of SDF-1α. And, even if all the released SDF-1α were diffused within the 3-mL gel, the final concentration (10.7 ng/mL) would still be active [14]. Nevertheless, these remarks may not apply to the *in vivo* scenario. In this case, 32 ng of SDF-1α are released in a watery volume of ~20 µL corresponding to the resection cavity. Assuming a homogeneous distribution, the after-burst concentration of the soluble SDF-1α within the resection would be 1600 ng/mL. However, the surgical procedure involves leakage from drained liquids, including blood; therefore, it seems difficult that this concentration remains within the cavity. Moreover, if we consider SDF-1α degradation by enzymes and the inflammatory environment, the calculated SDF-1α initial concentration would be further reduced. In addition, SDF-1α being a small cytokine is rapidly dispersed in a water environment but the diffusion coefficient in the brain may be different.

Importantly, no AF647-SDF-1α was detected by fluorescence in the brain parenchyma, apart from the signal present in the detaching bulges from the edges of the sponges corresponding to the heparin complexed form of SDF-1α (Fig. 6A). Of note is that the levels of detection of the fluorescent protein by WB were only possible at 100 ng of protein concentrated in a band (Fig. 6B**).** Therefore, it is possible that lower levels of AF-647 were not detected in the brain parenchyma. Further studies need to consider different time points to evaluate the *in vivo* releasing profile of SDF-1α from the sponges using a radiolabeled protein. Discerning between chemotaxis and haptotaxis can be addressed by varying the placement of cells relative to sponges. Here, the effect of SDF-1α can be explained in part by a combination of chemotaxis and haptotaxis signaling as cells were injected beside the sponges. Under the premise that if SDF-1α is not released then chemoattraction can be limited, to improve the releasing profile of the chemokine, another strategy can be envisaged such as the incorporation of the protein into nanoparticles [73,74] for further integration into the sponges.

The optimal concentration of SDF-1α for GB-cell attraction may depend on several factors such as the stage of the disease, the type of cells involved, and the presence of other factors that may influence the chemokine activity. The effects of SDF-1α on cancer cell behavior can be concentration-dependent. Low concentrations of SDF-1α can promote cancer cell migration and invasion, while high concentrations can inhibit these processes by causing receptor internalization and desensitization [75]. Pasquier et al. (2015) showed that low concentrations of SDF-1α promote the migration of breast cancer cells through the activation of RhoA, while high concentrations increased adhesion through the activation of Rac1 [76]. Therefore, the task involves the design of a releasing profile to reach a steady state biological concentration of the chemokine during the time required to reach the target, which implies further and in-depth knowledge of the system.

4.2.2. Pleiotropic effects of SDF-1a

The concept of tumor entrapment aims to confine and eliminate cancer cells within a controlled microenvironment. Two primary strategies involve synergy with locoregional irradiation and the use of compounds to counteract tumor cell growth and resistance. SDF-1α, a versatile signaling molecule, plays a pivotal role in various biological processes. Its initial advantages, such as chemoattraction and migration, can turn detrimental to inhibiting proliferation. Hence, the development of diverse SDF-1α analogs offers promise for selectively modulating its functions [77]. Exploring distinct SDF-1 isoforms like SDF-1γ, with unique biomatrix binding properties, can further optimize the balance between beneficial chemotaxis and reduced proliferation [78].

The SDF-1α network is intrinsically connected with several genetic and molecular events in the tumor microenvironment [79], reflecting in tumor growth and cell invasion. CXCR4-mediated chemotaxis can be mediated by the activation of PI3 kinase (PI3K) by both G$\beta\gamma$ and Gα subunits of the activated G-protein coupled receptor. PI3K activation results in the phosphorylation of several focal adhesion components, paxillin among them [80]. Tyr118, the main residue of paxillin phosphorylation by focal adhesion kinase (FAK) was found here in gradual phosphorylated levels according to the increasing time of exposure to SDF-1α, suggesting a gradual formation of focal adhesions [22]. However, we also found activation of Akt and Erk. Independent activation of Akt and ERK1/2 by SDF-1α can support cell growth [81], and exert a positive effect on the survival of GB cells [14].

Therefore, although the initial strategy of using SDF-1α as a chemoattractant was coherent with the observed gradual increase in p-paxillin and the strong chemotactic *in-vitro* response, the utilization of SDF-1α to attract infiltrative GB cells *in vivo* entails a risk of tumor progression and dissemination that must be evaluated. Indeed, we found that the effect of SDF-1α on migration was independent of cell proliferation *in vitro*. However, the reduced cell hallo observed in the ADC-treated agarose drops (proliferation inhibited), also suggests a positive effect of SDF-1α on survival and/or proliferation. Moreover, the *in vivo* observations about the larger average tumor size and reduced median survival suggest that SDF-1α contained within the sponges may favor the devel-

opment of the tumors. Therefore, this may lead to an increase in tumor aggressiveness if not controlled.

A better understanding of SDF-1α pathways' activation after loading into SF-HA-Hep sponges might help to find an optimal condition. For instance, SDF-1α forms oligomers upon binding to free GAGs in brain ECM, which implies the regulation of chemokine function [78]. Whether chemoattraction alone can be activated in the SDF1α /CXCR4 axis is not known. However, evidence exists that the SDF-1γ isoform did not induce robust cell motility unless it was bound to heparin [53,82]. Then, a modification of the scaffold-chemokine interaction or the use of a different isoform might favor chemotaxis against proliferation or survival.

4.2.3. Tumor heterogeneity, the evolution of cancer cells and endogenous signals

SDF-1α has been shown to exert a chemoattractant effect *in vitro* on GB patient-derived cell lines expressing the CXCR4 receptor [14]. In addition, U87MG-CXCR4+ cells are infiltrative into the normal mouse brain parenchyma [18]. However, cell lines may not represent completely GB as a heterogeneous tumor. Even if the cell of origin might be a common neural stem cell or progenitor cell [83], the evolution of the tumoral cell content is dictated by the tumoral ecosystem, and different glioma stem cells with their progeny may be present [84]. Therefore, the expression of the CXCR4 receptor might be variable, reducing the targeting efficiency.

Furthermore, the expression of endogenous signals in the brain can represent competitional zones for cell attraction. For example, we observed SDF-1α expression in blood vessels, which are sites of GB cell migration. Macrophage migration inhibitory factor (MIF) can also bind to the CXCR4 receptor, and it is expressed by U87MG cells (**Fig. S5**), therefore the autologous/paracrine signaling from the tumor itself can also interfere with the efficiency of the chemoattraction strategy.

4.2.4. Cellular/tissue barriers to migration

Another consideration is related to the body's reaction to the material itself. Fibrotic capsules are often formed in materials recognized as strange bodies as implanted devices [85]. The cellular and tissue barriers formed around them, represent then an obstacle to cell colonization. For example, the M-Trap device showed increased mean survival of human ovarian cancer xenografted rats [6], but has failed to demonstrate safety and efficacy in clinical trials. This was attributed to surgical complexity and the numerous intraperitoneal adhesions developed after implantation, preventing tumor cells from reaching the devices [86]. In the brain context, Autier et al. (2019), designed bacterial cellulose (BC) membranes for tumor bed implantation, as a system for trapping residual GB cells. *In vitro* assessments showed that F98 tumor cells were trapped and unable to move onto the surface of the membranes. However, a fibrous capsule was observed around the material after brain implantation, which may prevent or decrease cell access [87]. This reaction was not observed for any of the implanted sponges as demonstrated by the histological analysis in rats, however the host reaction might be different as observed in humans for the M-trap device.

4.2.5. Tumor microenvironment (TME)'s response

SF-HA-Hep sponges caused an acute and chronic inflammatory response that was characteristic of a foreign body reaction with the recruitment of PMN cells, macrophages and lymphocytes. The presence of diverse cell types within the GB TME can influence the progression of the disease. For instance, GB cells are thought to induce an immunosuppressive environment by secretion of different factors. Among them, M-CSF, TGFb-1 and IL-10 skew macrophages to the immunosuppressive M2 phenotype [88]. The presence of M2-stage macrophages is correlated with vessel dilation and malignancy in different human glioma samples [89]. Furthermore, normal monocytes exposed to glioma cells acquire properties like those of myeloid-derived suppressor cells (MDSCs) [90]. Secretion of VEGF induces neoangiogenesis, inhibits maturation of dendritic cells, hinders infiltration of effector T-cells and activates antigen-specific regulatory T cells [91]. In addition, reactive astrogliosis produces growth factors, cytokines and metabolites that promote gliomagenesis [92]. We observed the presence of PMN cells and chronic inflammatory cells in both SF-HA-Hep and control cavities without sponges. Although this observation was true in the immunocompetent Fischer rats, nude rats (with 70 % Fischer background, Janvier Labs) may have a similar response due to the presence of most of these immune cells except for mature T-cells. In nude animals, SF-HA-Hep implantation alone did not influence survival as compared to cavities, therefore the discrimination of a positive effect of the inflammatory response on tumor progression cannot be discerned. To explore the effect of the whole immune system, the complete immunocompetent model would have to be used. Whether these immune reactions could be exploited for targeting cancer cells remains to be explored, i.e., the reversion into a positive factor for GB treatment.

Taken together, these listed factors should be considered in the design of a tumor cell trapping strategy, independently of the molecules used. Their adequate consideration may increase the efficacy of the cell trapping capacity.

4.3. The resection cavity as a part of the pathology and perspectives on sponges as "meeting rooms" to direct the GB ecosystem

In operable GB, the resection cavity is part of the pathology. After tumor surgical resection, the brain parenchyma is extremely fragile, and the cavities present unpredictable shapes and sizes. These aspects hinder the local administration of post-operative treatments, resulting in a high probability of recurrence (~90 % of the cases) [93]. Mainly, tumor cells present in the peritumoral brain zone are responsible for that, and today it is impossible to image and target them using the maximum tolerated dose of radiotherapy after surgery [87]. However, the resection space can also offer an opportunity for the treatment of recurrent GB. The two main limitations contributing to the failure of conventional therapy are i) treatment resistance and ii) sub-optimal delivery of active principles. Different strategies have been investigated for the local and enhanced delivery of chemotherapeutic agents. Convection-enhanced delivery (CED) allows direct delivery of chemotherapeutics via a catheter in the tissue surrounding the GB resection cavity, but this method results in unpredictable brain diffusion and requires the use of several surgical procedures, leading to a high risk of infection or bleeding [94]. Other strategies include the use of hydrogels and other implantable scaffolds [95,96] for the sustained and local delivery of chemotherapeutics. However, only Gliadel wafers, consisting of an implantable copolymer that allows the controlled release of carmustine within the cavity, have reached the clinic. Recently, it was reported that adjuvant treatment with Gliadel may prolong the overall survival of malignant glioma patients [97], but their association with a high rate of complications is still controversial [98–100].

Alteration of the GB ecosystem may offer a new perspective for the targeting of the residual disease. Luring of GB cells is now being explored to concentrate GB cells for further elimination [7,87]. For this purpose, the use of an implantable support as means of direct contact with the brain parenchyma is fundamental for the targeting of residual GB cells. In this line, shape-memory lasting SF-HA-Hep sponges may allow the brain parenchyma to have better structural support, preventing a collapse of this tissue after surgery and lasting long enough to permit cell infiltration.

ARTICLE IN PRESS
JID: ACTBIO [m5G;November 17, 2023;23:43]

However, the limitations presented and discussed for the tumor cell trapping strategy may still impede the complete eradication of infiltrative GB cells. Combined approaches, such as the use of chemoattractants and killing agents [101], local radiotherapy [18], or the delivery of cellular components such as engineered tumoricidal neural stem cells [102] may help a better outcome.

Switching the focus from the cancer cell alone to one that includes the normal host environment offers new perspectives [28,103]. SF-HA-Hep sponges and other implants [6,87] caused a local inflammatory response. Moreover, the presence of CD11b/c-positive cells inside the sponges and GFAP-positive cells in the vicinity of the cavities seven days post-implantation (**Supp. Fig. 6**) indicate that various cell types can interact with the implant, regardless of whether it is loaded with SDF-1α or not. These interactions could potentially impact the TME. Integrin CD11b is primarily expressed in monocytes, macrophages, neutrophils, dendritic cells (DCs), NK cells, and a subset of B and T cells (absent in the case of nude rats). Conversely, CD11c is a widely used marker for defining DCs [104] . The Glial fibrillary acidic protein (GFAP), on the other hand, is specifically found in the astroglial cytoskeleton [105]. Ideally, implantable materials should have a regenerating anti-inflammatory and neuro-regenerative effect after surgical resection of the tumor [28,106]. However, the inflammatory cells observed in the cavities might be reeducated for the tackling of tumor cells. GB is known to create an immunosuppressive environment [107]. This is due to the crosstalk between glioma and immune cells, which opens the possibility of the immunomodulation of the TME. Therefore, the presence of macrophages and lymphocytes after implantation of SF-HA-Hep sponges could be reverted in a positive factor to improve the immune response against the tumor by loading other chemokines and immunostimulatory molecules. Additionally, the chronic inflammatory cells can help to break down the ECM and increase blood flow to the tumor, improving drug penetration and increasing treatment efficacy [108]. Further research is needed to fully understand the potential benefits of this approach as a "cell meeting room" implantable scaffold to remodel the GB ecosystem for better therapy outcomes.

5. Conclusion

The plethora of strategies investigated for GB treatment is impressive, but the reflection on patient survival is nowadays limited. This is due to the high infiltrative capacity of GB cells. Considering GB as an ecosystem disease may help in the designing of therapeutic strategies that explore the alteration of its elements such as migratory niches. Here, SF-HA-Hep sponges were able to attract GB cells from the parenchyma surrounding the created brain cavity in rats, and sited and shaped the tumors in the resection spaces. Besides, the sponges demonstrated to have characteristics compatible with an implantable biomaterial, adequate for the brain tissue. This work has shown this scaffold is a potential tool for GB treatment, although there are yet some limitations regarding the use of SDF-1α. The concentration of GB cells and the shaping of the tumor may improve cancer treatment by improving post-surgical outcomes, enhancing the effectiveness of chemotherapy and other targeted therapies, and improving the precision of radiation therapy. Still, limitations exist for the complete attraction of residual cells, therefore other combinatorial and immune-modulating approaches can be considered.

Data availability

The data that support the findings of this study are available from the corresponding authors, upon reasonable request.

Declaration of Competing Interest

The authors declare that they have no known competing financial interests or personal relationships that could have appeared to influence the work reported in this paper.

Acknowledgements

For critical platform assistance in developing this work, authors would like to thank Romain Mallet, Florence Manero and Rodolphe Perrot from SCIAM (Common Service for Imaging and Microscopy Analysis, SFR ICAT 4208, Université d'Angers, France), Florence Franconi and Samuel Bonnet from PRISM (Imagerie et spectroscopie multi-modales, SFR ICAT 4208, Université d'Angers, France), Catherine Guillet, Jérôme Cayon and Lydie Bonneau from PACeM (Plateforme d'Analyses Cellules et Moléculaire, SFR ICAT 4208, Université d'Angers, France), and Aurélia Rolland from IMAC (Imagerie Cellulaire, INRAE, Angers, France).The authors are also grateful to Luis Diaz-Gomez from USC (Universidade de Santiago de Compostela, Spain) for help with microCT analysis andLaurence Sindji and Anne Clavreul from CRCI2NA, team 5 GLIAD (Design and application of innovative local treatments in glioblastoma, Angers, France) for their useful advices.

Funding

This work was funded by the French National Research Agency (ANR) under the frame of EuroNanoMed III (project GLIOSILK "Silk-fibroin interventional nano-trap for the treatment of glioblastoma") [grant ANR-19-ENM3-0003-01]. It was also supported by the Instituto de Salud Carlos III (ISCIII) [AC19/00067] Cofinanciado FEDER, Spain, by the Italian Ministry of Health-Ricerca Corrente Annual Program 2023, by the Institut National de la Santé et de la Recherche Médicale (INSERM) and by the University of Angers (Angers, France). The work was in addition related to: (i) to the French ANR under the frame of the LabEx IRON (Innovative Radiopharmaceuticals in Oncology and Neurology) as part of the French government Investissements d'Avenir program (ANR-11-LABX-0018 to E.G.); (ii) the "Région Pays-de-la-Loire" under the frame of the Target'In project (Improvement of targeting radiopharmaceuticals for better diagnostic and therapy in nuclear medicine to E.G.); iii) the "Ligue Nationale contre le Cancer" and the "Comité Départemental de Maine-et-Loire de la Ligue contre le Cancer" (CD49) under the frame of the FusTarG project (Design and application of precision RNA oligonucleotides and aptamers for targeting gene fusion products in glioblastoma to E.G.) and iv) the "Tumour targeting, Imaging and radiotherapies network" of the "Cancéropôle Grand-Ouest" (France). RMP was a PhD fellow from the French "Ministère de l'Enseignement supérieur, de la recherche et de l'innovation" (MESRI). MN received a PhD fellowship from "La Région Pays-de-la-Loire" under the frame of the Erasmus Mundus Joint Doctorate program for Nanomedicine and Pharmaceutical Innovation (EMJD NanoFar).

Supplementary materials

Supplementary material associated with this article can be found, in the online version, at doi:10.1016/j.actbio.2023.10.022.

References

[1] C. Birzu, P. French, M. Caccese, G. Cerretti, A. Idbaih, V. Zagonel, G. Lombardi, Recurrent glioblastoma: from molecular landscape to new treatment perspectives, Cancers 13 (2021) 47, doi:10.3390/cancers13010047.
[2] T. Yamahara, Y. Numa, T. Oishi, T. Kawaguchi, T. Seno, A. Asai, K. Kawamoto, Morphological and flow cytometric analysis of cell infiltration in glioblastoma: a comparison of autopsy brain and neuroimaging, Brain Tumor Pathol. 27 (2010) 81–87, doi:10.1007/s10014-010-0275-7.

[3] A. Giese, R. Bjerkvig, M.E. Berens, M. Westphal, Cost of migration: invasion of malignant gliomas and implications for treatment, J. Clin. Oncol. 21 (2003) 1624–1636, doi:10.1200/JCO.2003.05.063.
[4] M. Najberg, M. Haji Mansor, F. Boury, C. Alvarez-Lorenzo, E. Garcion, Reversing the tumor target: establishment of a tumor trap, Front. Pharmacol. 10 (2019) 887, doi:10.3389/fphar.2019.00887.
[5] B. Van Der Sanden, F. Appaix, F. Berger, L. Selek, J.-P. Issartel, D. Wion, Translation of the ecological trap concept to Glioma therapy: the cancer cell trap concept, Fut. Oncol. (2013) 817–824, doi:10.2217/fon.13.30.
[6] A. de la Fuente, L. Alonso-Alconada, C. Costa, J. Cueva, T. Garcia-Caballero, R. Lopez-Lopez, M. Abal, M-Trap: exosome-based capture of tumor cells as a new technology in peritoneal metastasis, J. Natl. Cancer Inst. (2015) 107, doi:10.1093/jnci/djv184.
[7] A. Jain, M. Betancur, G.D. Patel, C.M. Valmikinathan, V.J. Mukhatyar, A. Vakharia, S.B. Pai, B. Brahma, T.J. MacDonald, R.V. Bellamkonda, Guiding intracortical brain tumour cells to an extracortical cytotoxic hydrogel using aligned polymeric nanofibres, Nat. Mater. 13 (2014) 308–316, doi:10.1038/nmat3878.
[8] Y. Xu, C. Chen, P.B. Hellwarth, X. Bao, Biomaterials for stem cell engineering and biomanufacturing, Bioact. Mater. 4 (2019) 366–379, doi:10.1016/j.bioactmat.2019.11.002.
[9] A. Sood, A. Gupta, G. Agrawal, Recent advances in polysaccharides based biomaterials for drug delivery and tissue engineering applications, Carbohydr. Polym. Technol. Appl. 2 (2021) 100067, doi:10.1016/j.carpta.2021.100067.
[10] G. Jensen, J.L. Holloway, S.E. Stabenfeldt, Hyaluronic acid biomaterials for central nervous system regenerative medicine, Cells 9 (2020) 2113, doi:10.3390/cells9092113.
[11] J. Nicolas, S. Magli, L. Rabbachin, S. Sampaolesi, F. Nicotra, L. Russo, 3D Extracellular matrix mimics: fundamental concepts and role of materials chemistry to influence stem cell fate, Biomacromolecules 21 (2020) 1968–1994, doi:10.1021/acs.biomac.0c00045.
[12] M. Ehtesham, J.A. Winston, P. Kabos, R.C. Thompson, CXCR4 expression mediates glioma cell invasiveness, Oncogene 25 (2006) 2801–2806, doi:10.1038/sj.onc.1209302.
[13] D. Zagzag, M. Esencay, O. Mendez, H. Yee, I. Smirnova, Y. Huang, L. Chiriboga, E. Lukyanov, M. Liu, E.W. Newcomb, Hypoxia- and vascular endothelial growth factor-induced stromal cell-derived factor-1alpha/CXCR4 expression in glioblastomas: one plausible explanation of Scherer's structures, Am. J. Pathol. 173 (2008) 545–560, doi:10.2353/ajpath.2008.071197.
[14] Y. Zhou, P.H. Larsen, C. Hao, V.W. Yong, CXCR4 is a major chemokine receptor on Glioma cells and mediates their survival, J. Biol. Chem. 277 (2002) 49481–49487, doi:10.1074/jbc.M206222200.
[15] V.V.V. Hira, U. Verbovšek, B. Breznik, M. Srdič, M. Novinec, H. Kakar, J. Wormer, B.V. der Swaan, B. Lenarčič, L. Juliano, S. Mehta, C.J.F. Van Noorden, T.T. Lah, Cathepsin K cleavage of SDF-1α inhibits its chemotactic activity towards glioblastoma stem-like cells, Biochim. Biophys. Acta. Mol. Cell Res. 1864 (2017) 594–603, doi:10.1016/j.bbamcr.2016.12.021.
[16] H. Kim, H.S. Roh, J.E. Kim, S.D. Park, W.H. Park, J.-Y. Moon, Compound K attenuates stromal cell-derived growth factor 1 (SDF-1)-induced migration of C6 glioma cells, Nutr. Res. Pract. 10 (2016) 259–264, doi:10.4162/nrp.2016.10.3.259.
[17] M. Najberg, M. Haji Mansor, T. Taillé, C. Bouré, R. Molina-Peña, F. Boury, J.L. Cenis, E. Garcion, C. Alvarez-Lorenzo, Aerogel sponges of silk fibroin, hyaluronic acid and heparin for soft tissue engineering: composition-properties relationship, Carbohydr. Polym. 237 (2020) 116107, doi:10.1016/j.carbpol.2020.116107.
[18] D. Séhédic, I. Chourpa, C. Tétaud, A. Griveau, C. Loussouarn, S. Avril, C. Legendre, N. Lepareur, D. Wion, F. Hindré, F. Davodeau, E. Garcion, Locoregional confinement and major clinical benefit of 188Re-loaded CXCR4-targeted nanocarriers in an orthotopic human to mouse model of glioblastoma, Theranostics 7 (2017) 4517–4536, doi:10.7150/thno.19403.
[19] R. Milner, G. Edwards, C. Streuli, C. Ffrench-Constant, A role in migration for the alpha V beta 1 integrin expressed on oligodendrocyte precursors, J. Neurosci. 16 (1996) 7240–7252.
[20] B. Heit, P. Kubes, Measuring chemotaxis and chemokinesis: the under-agarose cell migration assay, Science's STKE 2003 (2003) pl5–pl5, doi:10.1126/stke.2003.170.pl5.
[21] N. Ishii, D. Maier, A. Merlo, M. Tada, Y. Sawamura, A.-C. Diserens, E.G. Van Meir, Frequent co-alterations of TP53, p16/CDKN2A, p14ARF, PTEN tumor suppressor genes in human glioma cell lines, Brain Pathol. 9 (1999) 469–479, doi:10.1111/j.1750-3639.1999.tb00536.x.
[22] Y. Hu, J. Lu, X. Xu, J. Lyu, H. Zhang, Regulation of focal adhesion turnover in SDF-1α-stimulated migration of mesenchymal stem cells in neural differentiation, Sci. Rep. 7 (2017) 10013, doi:10.1038/s41598-017-09736-7.
[23] A. Sehgal, C. Keener, A.L. Boynton, J. Warrick, G.P. Murphy, CXCR-4, a chemokine receptor, is overexpressed in and required for proliferation of glioblastoma tumor cells, J. Surg. Oncol. 69 (1998) 99–104 2<99::aid–jso10>3.0.co;2-m., doi:10.1002/(sici)1096-9098(199810)69.
[24] S. Chatterjee, B. Behnam Azad, S. Nimmagadda, Chapter Two - The intricate role of CXCR4 in cancer, in: M.G. Pomper, P.B. Fisher (Eds.), Advances in Cancer Research, Academic Press, 2014, pp. 31–82, doi:10.1016/B978-0-12-411638-2.00002-1.
[25] B.M. Woerner, N.M. Warrington, A.L. Kung, A. Perry, J.B. Rubin, Widespread CXCR4 activation in astrocytomas revealed by phospho-CXCR4-specific antibodies, Cancer Res. 65 (2005) 11392–11399, doi:10.1158/0008-5472.CAN-05-0847.
[26] X. Bian, S. Yang, J. Chen, Y. Ping, X. Zhou, Q. Wang, X. Jiang, W. Gong, H. Xiao, L. Du, Z. Chen, W. Zhao, J. Shi, J.M. Wang, Preferential expression of chemokine receptor CXCR4 by highly malignant human gliomas and its association with poor patient survival, Neurosurgery 61 (2007) 570–579, doi:10.1227/01.NEU.0000290905.53685.A2.
[27] L. Cheng, Z. Huang, W. Zhou, Q. Wu, S. Donnola, J.K. Liu, X. Fang, A.E. Sloan, Y. Mao, J.D. Lathia, W. Min, R.E. McLendon, J.N. Rich, S. Bao, Glioblastoma stem cells generate vascular pericytes to support vessel function and tumor growth, Cell 153 (2013) 139–152, doi:10.1016/j.cell.2013.02.021.
[28] A. Belousov, S. Titov, N. Shved, M. Garbuz, G. Malykin, V. Gulaia, A. Kagansky, V. Kumeiko, The extracellular matrix and biocompatible materials in glioblastoma treatment, Front. Bioeng. Biotechnol. 7 (2019) https://www.frontiersin.org/articles/10.3389/fbioe.2019.00341. (Accessed 17 March 2023).
[29] D. Sood, M. Tang-Schomer, D. Pouli, C. Mizzoni, N. Raia, A. Tai, K. Arkun, J. Wu, L.D. Black, B. Scheffler, I. Georgakoudi, D.A. Steindler, D.L. Kaplan, 3D extracellular matrix microenvironment in bioengineered tissue models of primary pediatric and adult brain tumors, Nat. Commun. 10 (2019) 4529, doi:10.1038/s41467-019-12420-1.
[30] E. Mohiuddin, H. Wakimoto, Extracellular matrix in glioblastoma: opportunities for emerging therapeutic approaches, Am. J. Cancer Res. 11 (2021) 3742–3754.
[31] S.S. Rao, J. DeJesus, A.R. Short, J.J. Otero, A. Sarkar, J.O. Winter, Glioblastoma behaviors in three-dimensional collagen-hyaluronan composite hydrogels, ACS Appl. Mater. Interfaces 5 (2013) 9276–9284, doi:10.1021/am402097j.
[32] C. Wang, X. Tong, F. Yang, Bioengineered 3D brain tumor model to elucidate the effects of matrix stiffness on glioblastoma cell behavior using PEG-based hydrogels, Mol. Pharm. 11 (2014) 2115–2125, doi:10.1021/mp5000828.
[33] J.-W.E. Chen, S. Pedron, P. Shyu, Y. Hu, J.N. Sarkaria, B.A.C. Harley, Influence of hyaluronic acid transitions in tumor microenvironment on glioblastoma malignancy and invasive behavior, Front. Mater. 5 (2018) https://www.frontiersin.org/articles/10.3389/fmats.2018.00039. (Accessed 17 March 2023).
[34] M. Bartoš, T. Suchý, R. Foltán, Note on the use of different approaches to determine the pore sizes of tissue engineering scaffolds: what do we measure? Biomed. Eng. Online 17 (2018) 110, doi:10.1186/s12938-018-0543-z.
[35] M. Saif Ur Rahman, J. Wu, H. Chen, C. Sun, Y. Liu, S. Xu, Matrix mechanophysical factor: pore size governs the cell behavior in cancer, Adv. Phys. 8 (2023) 2153624, doi:10.1080/23746149.2022.2153624.
[36] K. Wolf, M. Te Lindert, M. Krause, S. Alexander, J. Te Riet, A.L. Willis, R.M. Hoffman, C.G. Figdor, S.J. Weiss, P. Friedl, Physical limits of cell migration: control by ECM space and nuclear deformation and tuning by proteolysis and traction force, J. Cell Biol. 201 (2013) 1069–1084, doi:10.1083/jcb.201210152.
[37] K. Polyak, R.A. Weinberg, Transitions between epithelial and mesenchymal states: acquisition of malignant and stem cell traits, Nat. Rev. Cancer 9 (2009) 265–273, doi:10.1038/nrc2620.
[38] P.P. Provenzano, D.R. Inman, K.W. Eliceiri, S.M. Trier, P.J. Keely, Contact guidance mediated three-dimensional cell migration is regulated by Rho/ROCK-dependent matrix reorganization, Biophys. J. 95 (2008) 5374–5384, doi:10.1529/biophysj.108.133116.
[39] C.D. Paul, P. Mistriotis, K. Konstantopoulos, Cancer cell motility: lessons from migration in confined spaces, Nat. Rev. Cancer 17 (2017) 131–140, doi:10.1038/nrc.2016.123.
[40] S.M. Azarin, J. Yi, R.M. Gower, B.A. Aguado, M.E. Sullivan, A.G. Goodman, E.J. Jiang, S.S. Rao, Y. Ren, S.L. Tucker, V. Backman, J.S. Jeruss, L.D. Shea, In vivo capture and label-free detection of early metastatic cells, Nat. Commun. 6 (2015) 8094, doi:10.1038/ncomms9094.
[41] S. Aznavoorian, M.L. Stracke, H. Krutzsch, E. Schiffmann, L.A. Liotta, Signal transduction for chemotaxis and haptotaxis by matrix molecules in tumor cells, J. Cell Biol. 110 (1990) 1427–1438, doi:10.1083/jcb.110.4.1427.
[42] Z. Fan, F. Zhang, T. Liu, B.Q. Zuo, Effect of hyaluronan molecular weight on structure and biocompatibility of silk fibroin/hyaluronan scaffolds, Int. J. Biol. Macromol. 65 (2014) 516–523, doi:10.1016/j.ijbiomac.2014.01.058.
[43] K.J. Wolf, P. Shukla, K. Springer, S. Lee, J.D. Coombes, C.J. Choy, S.J. Kenny, K. Xu, S. Kumar, A mode of cell adhesion and migration facilitated by CD44-dependent microtentacles, Proc. Natl. Acad. Sci. 117 (2020) 11432–11443, doi:10.1073/pnas.1914294117.
[44] C.B.N. Mendes de Aguiar, B. Lobão-Soares, M. Alvarez-Silva, A.G. Trentin, Glycosaminoglycans modulate C6 glioma cell adhesion to extracellular matrix components and alter cell proliferation and cell migration, BMC Cell Biol. 6 (2005) 31, doi:10.1186/1471-2121-6-31.
[45] W.I. Choi, A. Sahu, C. Vilos, N. Kamaly, S.-M. Jo, J.H. Lee, G. Tae, Bioinspired heparin nanosponge prepared by photo-crosslinking for controlled release of growth factors, Sci. Rep. 7 (2017) 14351, doi:10.1038/s41598-017-14040-5.
[46] E.M. Rodrigues, A.L.G. Cornélio, P.H. Godoi, P.I. da Costa, C. Rossa-Junior, G. Faria, J.M. Guerreiro Tanomaru, M. Tanomaru-Filho, Heparin is biocompatible and can induce differentiation of human dental pulp cells, Int. Endod. J. 52 (2019) 829–837, doi:10.1111/iej.13061.
[47] B. Zhao, Z. Zhao, J. Ma, X. Ma, Modulation of angiogenic potential of tissue-engineered peripheral nerve by covalent incorporation of heparin and loading with vascular endothelial growth factor, Neurosci. Lett. 705 (2019) 259–264, doi:10.1016/j.neulet.2019.01.017.
[48] E.G. Hayman, M.D. Pierschbacher, S. Suzuki, E. Ruoslahti, Vitronectin–a major cell attachment-promoting protein in fetal bovine serum, Exp. Cell. Res. 160 (1985) 245–258, doi:10.1016/0014-4827(85)90173-9.
[49] X. Zhong, O. Arnolds, O. Krenczyk, J. Gajewski, S. Pütz, C. Herrmann, R. Stoll, The structure in solution of fibronectin type III domain 14 reveals its syner-

gistic heparin binding site, Biochemistry 57 (2018) 6045–6049, doi:10.1021/acs.biochem.8b00771.
[50] F.H. Seeger, T. Rasper, A. Fischer, M. Muhly-Reinholz, E. Hergenreider, D.M. Leistner, K. Sommer, Y. Manavski, R. Henschler, E. Chavakis, B. Assmus, A.M. Zeiher, S. Dimmeler, Heparin disrupts the CXCR4/SDF-1 axis and impairs the functional capacity of bone marrow–derived mononuclear cells used for cardiovascular repair, Circ. Res. 111 (2012) 854–862, doi:10.1161/CIRCRESAHA.112.265678.
[51] N. Rusetska, K. Kowalski, K. Zalewski, S. Zięba, M. Bidziński, K. Goryca, B. Kotowicz, M. Fuksiewicz, J. Kopczynski, E. Bakuła-Zalewska, A. Kowalik, M. Kowalewska, CXCR4/ACKR3/CXCL12 axis in the lymphatic metastasis of vulvar squamous cell carcinoma, J. Clin. Pathol. 75 (2022) 324–332, doi:10.1136/jclinpath-2020-206917.
[52] R. Janssens, A. Mortier, D. Boff, V. Vanheule, M. Gouwy, C. Franck, O. Larsen, M.M. Rosenkilde, J.V. Damme, F.A. Amaral, M.M. Teixeira, S. Struyf, P. Proost, Natural nitration of CXCL12 reduces its signaling capacity and chemotactic activity in vitro and abrogates intra-articular lymphocyte recruitment in vivo, Oncotarget 7 (2016) 62439–62459, doi:10.18632/oncotarget.11516.
[53] C. Laguri, R. Sadir, P. Rueda, F. Baleux, P. Gans, F. Arenzana-Seisdedos, H. Lortat-Jacob, The Novel CXCL12γ isoform encodes an unstructured cationic domain which regulates bioactivity and interaction with both glycosaminoglycans and CXCR4, PLoS One 2 (2007) e1110, doi:10.1371/journal.pone.0001110.
[54] K.M. Yamada, M. Sixt, Mechanisms of 3D cell migration, Nat. Rev. Mol. Cell Biol. 20 (2019) 738–752, doi:10.1038/s41580-019-0172-9.
[55] B.A. Aguado, R.M. Hartfield, G.G. Bushnell, J.T. Decker, S.M. Azarin, D. Nanavati, M.J. Schipma, S.S. Rao, R.S. Oakes, Y. Zhang, J.S. Jeruss, L.D. Shea, Biomaterial scaffolds as pre-metastatic niche mimics systemically alter the primary tumor and tumor microenvironment, Adv. Healthc. Mater. 7 (2018) 1700903, doi:10.1002/adhm.201700903.
[56] E. Nakayama, Y. Shiratsuchi, Y. Kobayashi, K. Nagata, The importance of infiltrating neutrophils in SDF-1 production leading to regeneration of the thymus after whole-body X-irradiation, Cell. Immunol. 268 (2011) 24–28, doi:10.1016/j.cellimm.2011.01.006.
[57] K.M. Yamada, J.W. Collins, D.A. Cruz Walma, A.D. Doyle, S.G. Morales, J. Lu, K. Matsumoto, S.S. Nazari, R. Sekiguchi, Y. Shinsato, S. Wang, Extracellular matrix dynamics in cell migration, invasion and tissue morphogenesis, Int. J. Exp. Pathol. 100 (2019) 144–152, doi:10.1111/iep.12329.
[58] J.A. Davies, Chapter 11 - Guidance by contact, in: J.A. Davies (Ed.), Mechanisms of Morphogenesis (Second Edition), Academic Press, Boston, 2013, pp. 129–145, doi:10.1016/B978-0-12-391062-2.00011-5.
[59] M.M. Nava, M.T. Raimondi, R. Pietrabissa, Controlling self-renewal and differentiation of stem cells via mechanical cues, Biomed. Res. Int. 2012 (2012) e797410, doi:10.1155/2012/797410.
[60] G. Singh, A. Chanda, Mechanical properties of whole-body soft human tissues: a review, Biomed. Mater. 16 (2021), doi:10.1088/1748-605X/ac2b7a.
[61] Y. Peng, Z. Chen, Y. He, P. Li, Y. Chen, X. Chen, Y. Jiang, X. Qin, S. Li, T. Li, C. Wu, H. Yang, F. You, Y. Liu, Non-muscle myosin II isoforms orchestrate substrate stiffness sensing to promote cancer cell contractility and migration, Cancer Lett. 524 (2022) 245–258, doi:10.1016/j.canlet.2021.10.030.
[62] A.E. Erickson, S.K. Lan Levengood, J. Sun, F.-C. Chang, M. Zhang, Fabrication and characterization of chitosan–hyaluronic acid scaffolds with varying stiffness for glioblastoma cell culture, Adv. Healthc. Mater. 7 (2018) 1800295, doi:10.1002/adhm.201800295.
[63] A. Saleh, E. Marhuenda, C. Fabre, Z. Hassani, J. de Weille, H. Boukhaddaoui, S. Guelfi, I.L. Maldonado, J.-P. Hugnot, H. Duffau, L. Bauchet, D. Cornu, N. Bakalara, A novel 3D nanofibre scaffold conserves the plasticity of glioblastoma stem cell invasion by regulating galectin-3 and integrin-β1 expression, Sci. Rep. 9 (2019) 14612, doi:10.1038/s41598-019-51108-w.
[64] J. Litowczenko, M.J. Woźniak-Budych, K. Staszak, K. Wieszczycka, S. Jurga, B. Tylkowski, Milestones and current achievements in development of multifunctional bioscaffolds for medical application, Bioact. Mater. 6 (2021) 2412–2438, doi:10.1016/j.bioactmat.2021.01.007.
[65] B.A. Aguado, G.G. Bushnell, S.S. Rao, J.S. Jeruss, L.D. Shea, Engineering the pre-metastatic niche, Nat. Biomed. Eng. 1 (2017) 0077, doi:10.1038/s41551-017-0077.
[66] G. Bassi, S. Panseri, S.M. Dozio, M. Sandri, E. Campodoni, M. Dapporto, S. Sprio, A. Tampieri, M. Montesi, Scaffold-based 3D cellular models mimicking the heterogeneity of osteosarcoma stem cell niche, Sci. Rep. 10 (2020) 22294, doi:10.1038/s41598-020-79448-y.
[67] E. D'Angelo, D. Natarajan, F. Sensi, O. Ajayi, M. Fassan, E. Mammano, P. Pilati, P. Pavan, S. Bresolin, M. Preziosi, R. Miquel, Y. Zen, S. Chokshi, K. Menon, N. Heaton, G. Spolverato, M. Piccoli, R. Williams, L. Urbani, M. Agostini, Patient-derived scaffolds of colorectal cancer metastases as an organotypic 3D model of the liver metastatic microenvironment, Cancers 12 (2020) 364, doi:10.3390/cancers12020364.
[68] Y. Huang, A. Hakamivala, S. Li, A. Nair, R. Saxena, J.-T. Hsieh, L. Tang, Chemokine releasing particle implants for trapping circulating prostate cancer cells, Sci. Rep. 10 (2020) 4433, doi:10.1038/s41598-020-60696-x.
[69] R.S. Oakes, G.G. Bushnell, S.M. Orbach, P. Kandagatla, Y. Zhang, A.H. Morris, M.S. Hall, P. LaFaire, J.T. Decker, R.M. Hartfield, M.D. Brooks, M.S. Wicha, J.S. Jeruss, L.D. Shea, Metastatic conditioning of myeloid cells at a subcutaneous synthetic niche reflects disease progression and predicts therapeutic outcomes, Cancer Res. 80 (2020) 602–612, doi:10.1158/0008-5472.CAN-19-1932.
[70] Q. Xiong, N. Zhang, M. Zhang, M. Wang, L. Wang, Y. Fan, C.-Y. Lin, Engineer a pre-metastatic niched microenvironment to attract breast cancer cells by utilizing a 3D printed polycaprolactone/nano-hydroxyapatite osteogenic scaffold – an in vitro model system for proof of concept, J. Biomedic. Mater. Res. Part B 110 (2022) 1604–1614, doi:10.1002/jbm.b.35021.
[71] M.S. Krieger, J.M. Moreau, H. Zhang, M. Chien, J.L. Zehnder, M.A. Nowak, M. Craig, Novel cytokine interactions identified during perturbed hematopoiesis, (2018) 484170. https://doi.org/10.1101/484170.
[72] S. Prokoph, E. Chavakis, K.R. Levental, A. Zieris, U. Freudenberg, S. Dimmeler, C. Werner, Sustained delivery of SDF-1α from heparin-based hydrogels to attract circulating pro-angiogenic cells, Biomaterials 33 (2012) 4792–4800, doi:10.1016/j.biomaterials.2012.03.039.
[73] R. Molina-Peña, M. Haji Mansor, M. Najberg, J.-M. Thomassin, B. Gueza, C. Alvarez-Lorenzo, E. Garcion, C. Jérôme, F. Boury, Nanoparticle-containing electrospun nanofibrous scaffolds for sustained release of SDF-1α, Int. J. Pharm. 610 (2021) 121205, doi:10.1016/j.ijpharm.2021.121205.
[74] S. Gascon, A. Giraldo Solano, W. El Kheir, H. Therriault, P. Berthelin, B. Cattier, B. Marcos, N. Virgilio, B. Paquette, N. Faucheux, M.-A. Lauzon, Characterization and mathematical modeling of alginate/chitosan-based nanoparticles releasing the chemokine CXCL12 to attract glioblastoma cells, Pharmaceutics 12 (2020) 356, doi:10.3390/pharmaceutics12040356.
[75] S. Tavor, I. Petit, S. Porozov, A. Avigdor, A. Dar, L. Leider-Trejo, N. Shemtov, V. Deutsch, E. Naparstek, A. Nagler, T. Lapidot, CXCR4 regulates migration and development of human acute myelogenous leukemia stem cells in transplanted NOD/SCID mice, Cancer Res. 64 (2004) 2817–2824, doi:10.1158/0008-5472.CAN-03-3693.
[76] J. Pasquier, N. Abu-Kaoud, H. Abdesselem, A. Madani, J. Hoarau-Véchot, H.Al. Thawadi, F. Vidal, B. Couderc, G. Favre, A. Rafii, SDF-1alpha concentration dependent modulation of RhoA and Rac1 modifies breast cancer and stromal cells interaction, BMC Cancer 15 (2015) 569, doi:10.1186/s12885-015-1556-7.
[77] A. Faber, C. Roderburg, F. Wein, R. Saffrich, A. Seckinger, K. Horsch, A. Diehlmann, D. Wong, G. Bridger, V. Eckstein, A.D. Ho, W. Wagner, The many facets of SDF-1alpha, CXCR4 agonists and antagonists on hematopoietic progenitor cells, J. Biomed. Biotechnol. 2007 (2007) 26065, doi:10.1155/2007/26065.
[78] E. Migliorini, D. Thakar, J. Kühnle, R. Sadir, D.P. Dyer, Y. Li, C. Sun, B.F. Volkman, T.M. Handel, L. Coche-Guerente, D.G. Fernig, H. Lortat-Jacob, R.P. Richter, Cytokines and growth factors cross-link Heparan sulfate, Open Biol. 5 (2015) 150046, doi:10.1098/rsob.150046.
[79] E. Henke, R. Nandigama, S. Ergün, Extracellular matrix in the tumor microenvironment and its impact on cancer therapy, Front Mol. Biosci. 6 (2020) https://www.frontiersin.org/articles/10.3389/fmolb.2019.00160. (Accessed 17 March 2023).
[80] B.A. Teicher, S.P. Fricker, CXCL12 (SDF-1)/CXCR4 pathway in cancer, Clinic. Cancer Res. 16 (2010) 2927–2931, doi:10.1158/1078-0432.CCR-09-2329.
[81] R. Würth, A. Bajetto, J.K. Harrison, F. Barbieri, T. Florio, CXCL12 modulation of CXCR4 and CXCR7 activity in human glioblastoma stem-like cells and regulation of the tumor microenvironment, Front. Cell Neurosci. 8 (2014) 144, doi:10.3389/fncel.2014.00144.
[82] M. Janowski, Functional diversity of SDF-1 splicing variants, Cell Adh. Migr. 3 (2009) 243–249, doi:10.4161/cam.3.3.8260.
[83] S.R. Alcantara Llaguno, L.F. Parada, Cell of origin of glioma: biological and clinical implications, Br. J. Cancer 115 (2016) 1445–1450, doi:10.1038/bjc.2016.354.
[84] O.O. Kanu, A. Mehta, C. Di, N. Lin, K. Bortoff, D.D. Bigner, H. Yan, D.C. Adamson, Glioblastoma multiforme: a review of therapeutic targets, Expert Opin. Ther. Targets 13 (2009) 701–718, doi:10.1517/14728220902942348.
[85] C. Horejs, Preventing fibrotic encapsulation, Nat. Rev. Mater. 6 (2021) 554, doi:10.1038/s41578-021-00338-4.
[86] A. Gil-Moreno, L. Alonso-Alconada, B. Díaz-Feijoo, S. Domingo, A. Vilar, A. Hernández, J. Gilabert, A. Llueca, A. Torné, J. de Santiago, M. Carbonell-Socias, V. Lago, E. Arias, V. Sampayo, J. Siegrist, A. Chipirliu, J.L. Sánchez-Iglesias, A. Pérez-Benavente, P. Padilla-Iserte, M. Santacana, X. Matias-Guiu, M. Abal, R. Lopez-Lopez, M-TRAP: safety and performance of metastatic tumor cell trap device in advanced ovarian cancer patients, Gynecol. Oncol. 161 (2021) 681–686, doi:10.1016/j.ygyno.2021.03.022.
[87] L. Autier, A. Clavreul, M.L. Cacicedo, F. Franconi, L. Sindji, A. Rousseau, R. Perrot, C.N. Montero-Menei, G.R. Castro, P. Menei, A new glioblastoma cell trap for implantation after surgical resection, Acta Biomater. 84 (2019) 268–279, doi:10.1016/j.actbio.2018.11.027.
[88] E.K. Nduom, M. Weller, A.B. Heimberger, Immunosuppressive mechanisms in glioblastoma, Neuro. Oncol. 17 (Suppl 7) (2015) vii9–vii14, doi:10.1093/neuonc/nov151.
[89] T. Mathivet, C. Bouleti, M. Van Woensel, F. Stanchi, T. Verschuere, L.-K. Phng, J. Dejaegher, M. Balcer, K. Matsumoto, P.B. Georgieva, J. Belmans, R. Sciot, C. Stockmann, M. Mazzone, S. De Vleeschouwer, H. Gerhardt, Dynamic stroma reorganization drives blood vessel dysmorphia during glioma growth, EMBO Mol. Med. 9 (2017) 1629–1645, doi:10.15252/emmm.201607445.
[90] J.C. Rodrigues, G.C. Gonzalez, L. Zhang, G. Ibrahim, J.J. Kelly, M.P. Gustafson, Y. Lin, A.B. Dietz, P.A. Forsyth, V.W. Yong, I.F. Parney, Normal human monocytes exposed to glioma cells acquire myeloid-derived suppressor cell-like properties, Neuro-oncology 12 (2010) 351–365, doi:10.1093/neuonc/nop023.
[91] G.T. Motz, G. Coukos, Deciphering and reversing tumor immune suppression, Immunity 39 (2013) 61–73, doi:10.1016/j.immuni.2013.07.005.

[92] S. De Vleeschouwer (Ed.), Glioblastoma, Codon Publications, Brisbane (AU), 2017 http://www.ncbi.nlm.nih.gov/books/NBK469998/ (Accessed 23 January 2023).
[93] J.-M. Lemée, A. Clavreul, P. Menei, Intratumoral heterogeneity in glioblastoma: don't forget the peritumoral brain zone, Neuro-oncology 17 (2015) 1322–1332, doi:10.1093/neuonc/nov119.
[94] E. Cruz Da Silva, M.-C. Mercier, N. Etienne-Selloum, M. Dontenwill, L. Choulier, A systematic review of glioblastoma-targeted therapies in phases II, III, IV clinical trials, Cancers 13 (2021) 1795, doi:10.3390/cancers13081795.
[95] C. Bastiancich, P. Danhier, V. Préat, F. Danhier, Anticancer drug-loaded hydrogels as drug delivery systems for the local treatment of glioblastoma, J. Controll. Release 243 (2016) 29–42, doi:10.1016/j.jconrel.2016.09.034.
[96] A. Djoudi, R. Molina-Peña, N. Ferreira, I. Ottonelli, G. Tosi, E. Garcion, F. Boury, Hyaluronic acid scaffolds for loco-regional therapy in nervous system related disorders, Int. J. Mol. Sci. 23 (2022) 12174, doi:10.3390/ijms232012174.
[97] T. Iuchi, A. Inoue, Y. Hirose, M. Morioka, K. Horiguchi, A. Natsume, Y. Arakawa, K. Iwasaki, M. Fujiki, T. Kumabe, Y. Sakata, Long-term effectiveness of Gliadel implant for malignant glioma and prognostic factors for survival: 3-year results of a postmarketing surveillance in Japan, Neuro-Oncol. Adv. 4 (2022) vdab189, doi:10.1093/noajnl/vdab189.
[98] C. Buonerba, G. Di Lorenzo, A. Marinelli, P. Federico, G. Palmieri, M. Imbimbo, P. Conti, G. Peluso, S. De Placido, J.H. Sampson, A comprehensive outlook on intracerebral therapy of malignant gliomas, Crit. Rev. Oncol. Hematol. 80 (2011) 54–68, doi:10.1016/j.critrevonc.2010.09.001.
[99] A. Bregy, A.H. Shah, M.V. Diaz, H.E. Pierce, P.L. Ames, D. Diaz, R.J. Komotar, The role of Gliadel wafers in the treatment of high-grade gliomas, Expert Rev. Anticancer Ther. 13 (2013) 1453–1461, doi:10.1586/14737140.2013.840090.
[100] E. Yeini, P. Ofek, N. Albeck, D. Rodriguez Ajamil, L. Neufeld, A. Eldar-Boock, R. Kleiner, D. Vaskovich, S. Koshrovski-Michael, S.I. Dangoor, A. Krivitsky, C. Burgos Luna, G. Shenbach-Koltin, M. Goldenfeld, O. Hadad, G. Tiram, R. Satchi-Fainaro, Targeting glioblastoma: advances in drug delivery and novel therapeutic approaches, Adv. Therap.. 4 (2021) 2000124. https://doi.org/10.1002/adtp.202000124.
[101] P.M. Kasapidou, E.L. de Montullé, K.-P. Dembélé, A. Mutel, L. Desrues, V. Gubala, H. Castel, Hyaluronic acid-based hydrogels loaded with chemoattractant and anticancer drug – new formulation for attracting and tackling glioma cells, Soft Matter 17 (2021) 10846–10861, doi:10.1039/D1SM01003D.
[102] K.T. Sheets, M.G. Ewend, M. Mohiti-Asli, S.A. Tuin, E.G. Loboa, K.S. Aboody, S.D. Hingtgen, Developing implantable scaffolds to enhance neural stem cell therapy for post-operative glioblastoma, Mol. Therapy 28 (2020) 1056–1067, doi:10.1016/j.ymthe.2020.02.008.
[103] A. De Boeck, B.Y. Ahn, C. D'Mello, X. Lun, S.V. Menon, M.M. Alshehri, F. Szulzewsky, Y. Shen, L. Khan, N.H. Dang, E. Reichardt, K.-A. Goring, J. King, C.J. Grisdale, N. Grinshtein, D. Hambardzumyan, K.M. Reilly, M.D. Blough, J.G. Cairncross, V.W. Yong, M.A. Marra, S.J.M. Jones, D.R. Kaplan, K.D. McCoy, E.C. Holland, P. Bose, J.A. Chan, S.M. Robbins, D.L. Senger, Glioma-derived IL-33 orchestrates an inflammatory brain tumor microenvironment that accelerates glioma progression, Nat. Commun. 11 (2020) 4997, doi:10.1038/s41467-020-18569-4.
[104] M. Gallizioli, F. Miró-Mur, A. Otxoa-de-Amezaga, R. Cugota, A. Salas-Perdomo, C. Justicia, V.H. Brait, F. Ruiz-Jaén, M. Arbaizar-Rovirosa, J. Pedragosa, E. Bonfill-Teixidor, M. Gelderblom, T. Magnus, E. Cano, C. Del Fresno, D. Sancho, A.M. Planas, Dendritic cells and microglia have non-redundant functions in the inflamed brain with protective effects of type 1 cDCs, Cell Rep. 33 (2020) 108291, doi:10.1016/j.celrep.2020.108291.
[105] Z. Yang, K.K.W. Wang, Glial fibrillary acidic protein: from intermediate filament assembly and gliosis to neurobiomarker, Trends Neurosci. 38 (2015) 364–374, doi:10.1016/j.tins.2015.04.003.
[106] B. Newland, P.B. Welzel, H. Newland, C. Renneberg, P. Kolar, M. Tsurkan, A. Rosser, U. Freudenberg, C. Werner, Tackling cell transplantation anoikis: an injectable, shape memory cryogel microcarrier platform material for stem cell and neuronal cell growth, Small 11 (2015) 5047–5053, doi:10.1002/smll.201500898.
[107] J.R.D. Pearson, S. Cuzzubbo, S. McArthur, L.G. Durrant, J. Adhikaree, C.J. Tinsley, A.G. Pockley, S.E.B. McArdle, Immune escape in glioblastoma multiforme and the adaptation of immunotherapies for treatment, Front. Immunol. 11 (2020) https://www.frontiersin.org/articles/10.3389/fimmu.2020.582106. (Accessed 17 March 2023).
[108] J. Huang, L. Zhang, D. Wan, L. Zhou, S. Zheng, S. Lin, Y. Qiao, Extracellular matrix and its therapeutic potential for cancer treatment, Sig. Transduct. Target Ther. 6 (2021) 1–24, doi:10.1038/s41392-021-00544-0.

Titre : Développement d'une Radiothérapie Locorégionale à l'Astate-211 Ciblant Syndecan-1 dans un Modèle Murin Syngénique de Glioblastome

Mots clés : Glioblastome, Thérapie α Ciblée, Astate-211, Syndecan-1, Anticorps Monoclonal

Résumé : Le glioblastome (GB) est la tumeur la plus agressive du système nerveux central. Résistant aux approches thérapeutiques, conventionnelles ou novatrices, il constitue encore aujourd'hui un défi clinique urgent. Des avancées récentes dans la thérapie radionucléidique ciblée (targeted radionuclide therapy, TRT) ont mis en évidence des voies potentielles d'intervention pour le GB. Plus précisément, la thérapie α ciblée (targeted-α-therapy, TAT) est une TRT qui utilise des particules α de courte portée et de haute énergie. La TAT a montré des résultats prometteurs dans différents scénarios précliniques et cliniques de cancer. Cependant, les résultats spécifiques au GB restent insatisfaisants. Cette thèse commence par évaluer le potentiel thérapeutique de la TAT pour le GB, visant à mettre en évidence à la fois les avancées et les défis à venir. Sur cette base, notre étude introduit une approche thérapeutique locorégionale utilisant un anticorps monoclonal ciblant le syndécan-1 (SDC1), lié au radionucléide émetteur α astate-211 (^{211}At-9E7.4). Cette TAT démontre une efficacité accrue pour éradiquer les tumeurs orthotopiques dans un modèle murin syngénique de GB. Le ciblage stratégique de SDC1 assure une rétention optimale de l'agent thérapeutique dans le cerveau, permettant une administration à faible dose avec des effets secondaires minimes. De plus, la TAT réduit la formation de tumeurs secondaires et permet d'établir une résistance au développement de nouvelles tumeurs grâce à l'activation des lymphocytes T mémoire centraux et effecteurs. Ainsi, cette avancée significative offre le potentiel d'améliorer le traitement et la qualité de vie des patients atteints de GB.

Title: Development of a Locoregional Astatine-211 Radiotherapy Targeting Syndecan-1 in a Syngeneic Mouse Model of Glioblastoma

Keywords: Glioblastoma, Targeted-α-Therapy, Astatine-211, Syndecan-1, Monoclonal Antibody

Abstract: Glioblastoma (GB) is the most aggressive tumor of the central nervous system. Having consistently resisted both conventional and novel therapeutic approaches, it remains a pressing clinical challenge. Some recent breakthroughs in targeted radionuclide therapy (TRT) have highlighted potential pathways for GB intervention. Specifically, targeted-α-therapy (TAT) is a TRT that employs short-range, high-energy α particles. TAT has demonstrated promising outcomes in both preclinical and clinical cancer scenarios. However, the results specific to GB remain less than satisfactory. This thesis begins by assessing the therapeutic potential of TAT for GB, aiming to highlight both breakthroughs and future challenges. Building on this foundation, our study introduces a locoregional therapeutic approach using a monoclonal antibody that targets syndecan-1 (SDC1), linked to the α-emitter radionuclide astatine-211 (^{211}At-9E7.4). This TAT demonstrates enhanced efficacy in eradicating orthotopic tumors in a syngeneic mouse model of GB. The strategic targeting of SDC1 ensures optimal brain retention of the therapeutic agent, allowing low-dose administration with minimal side effects. Furthermore, TAT reduces the formation of secondary tumors and elicits resistance to new tumor development through the activation of central and effector memory T cells. Thus, this significant advancement holds the potential to improve treatment outcomes and quality of life of GB patients.